Physical, chemical and biological modelling for gold nanoparticle-enhanced radiation therapy : towards a better understanding and optimization of the radiosensitizing effect

Floriane Poignant

º d'ordre NNT : 2018LYSE1160

THÈSE DE DOCTORAT DE L'UNIVERSITÉ DE LYON
opérée au sein de
l'Université Claude Bernard Lyon 1

École Doctorale ED52
Physique & Astrophysique de Lyon

Spécialité de doctorat : Physique médicale
Discipline : Physique

Soutenue publiquement le 27/09/2019, par :
Floriane, Adélie, Marion Poignant

Physical, chemical and biological modelling for gold nanoparticle-enhanced radiation therapy: towards a better understanding and optimization of the radiosensitizing effect

---

Devant le jury composé de :

Nom Prénom, grade/qualité, établissement/entreprise	
	Président(e)
GUATELLI Susanna, Associate Professor, University of Wollongong, Australia	Rapporteure
MAIGNE Lydia, Maître de conférence HDR, Université Clermont Auvergne, France	Rapporteure
BRUN Emilie, Maître de conférence, Université Paris-Sud, France	Examinatrice
DELORME Rachel, Chargée de Recherche CNRS, Université Paris-Sud, France	Examinatrice
DUMONT Elise, Professeure, Ecole Normale Supérieure de Lyon, France	Examinatrice
GERVAIS Benoît, Ingénieur de Recherche CEA - E6, CIMAP, Caen, France	Examinateur
INCERTI Sébastien, Directeur de Recherche CNRS, CENBG, France	Examinateur
NEDELEC Patrick, Professeur des Universités, Université Claude Bernard Lyon 1, France	Examinateur

BEUVE Michaël, Professeur des Universités, Université Claude Bernard Lyon 1	Directeur de thèse
TESTA Étienne, Maître de conférence, Université Claude Bernard Lyon 1	Co-directeur de thèse

UNIVERSITE CLAUDE BERNARD - LYON 1

Président de l'Université	**M. le Professeur Frédéric FLEURY**
Président du Conseil Académique	M. le Professeur Hamda BEN HADID
Vice-président du Conseil d'Administration	M. le Professeur Didier REVEL
Vice-président du Conseil Formation et Vie Universitaire	M. le Professeur Philippe CHEVALIER
Vice-président de la Commission Recherche	M. Fabrice VALLÉE
Directrice Générale des Services	Mme Dominique MARCHAND

COMPOSANTES SANTE

Faculté de Médecine Lyon Est – Claude Bernard	Directeur : M. le Professeur G.RODE
Faculté de Médecine et de Maïeutique Lyon Sud – Charles Mérieux	Directeur : Mme la Professeure C. BURILLON
Faculté d'Odontologie	Directeur : M. le Professeur D. BOURGEOIS
Institut des Sciences Pharmaceutiques et Biologiques	Directeur : Mme la Professeure C. VINCIGUERRA
Institut des Sciences et Techniques de la Réadaptation	Directeur : M. X. PERROT
Département de formation et Centre de Recherche en Biologie Humaine	Directeur : Mme la Professeure A-M. SCHOTT

COMPOSANTES ET DEPARTEMENTS DE SCIENCES ET TECHNOLOGIE

Faculté des Sciences et Technologies	Directeur : M. F. DE MARCHI
Département Biologie	Directeur : M. le Professeur F. THEVENARD
Département Chimie Biochimie	Directeur : Mme C. FELIX
Département GEP	Directeur : M. Hassan HAMMOURI
Département Informatique	Directeur : M. le Professeur S. AKKOUCHE
Département Mathématiques	Directeur : M. le Professeur G. TOMANOV
Département Mécanique	Directeur : M. le Professeur H. BEN HADID
Département Physique	Directeur : M. le Professeur J-C PLENET
UFR Sciences et Techniques des Activités Physiques et Sportives	Directeur : M. Y.VANPOULLE
Observatoire des Sciences de l'Univers de Lyon	Directeur : M. B. GUIDERDONI
Polytech Lyon	Directeur : M. le Professeur E.PERRIN
Ecole Supérieure de Chimie Physique Electronique	Directeur : M. G. PIGNAULT
Institut Universitaire de Technologie de Lyon 1	Directeur : M. le Professeur C. VITON
Ecole Supérieure du Professorat et de l'Education	Directeur : M. le Professeur A. MOUGNIOTTE
Institut de Science Financière et d'Assurances	Directeur : M. N. LEBOISNE

Physical, chemical and biological modelling for gold nanoparticle-enhanced radiation therapy: towards a better understanding and optimization of the radiosensitizing effect

by Floriane Poignant

A thesis submitted in partial fulfilment for the

degree of Doctor of Philosophy

in

Université Claude Bernard Lyon 1

27/09/2019

Résumé

En radiothérapie, les nanoparticules faites de métaux lourds telles que les nanoparticules l'or (AuNPs) ont démontré des propriétés radiosensibilisantes particulièrement prometteuses. Une augmentation de la dose et du nombre de radicaux produits, à échelle tumorale (effet photoélectrique) et à échelle sub-cellulaire (électrons Auger) pourraient être responsables d'une partie des effets pour les rayons X de basse énergie. Dans le cadre de cette thèse, nous proposons d'étudier ces mécanismes physiques et chimiques précoces par des outils de simulation, afin de mieux les quantifier et comprendre leur impact sur la survie cellulaire. Nous avons d'abord finalisé et validé une simulation Monte Carlo développée pour suivre les électrons jusqu'à très basse énergie à la fois dans l'eau (meV) et dans l'or (eV). Nous avons obtenu de bons résultats de simulation pour l'or comparables aux données expérimentales de la littérature, en terme de production d'électrons et de perte d'énergie. Nous avons utilisé cet outil de simulation pour quantifier l'énergie déposée dans des nanocibles situées près d'une AuNP, énergie qui est corrélée à la probabilité de générer des dommages. Cette étude a nécessité d'importantes optimisations, afin d'atteindre des temps de calculs raisonnables. Nous avons montré une augmentation significative de la probabilité d'avoir un dépôt d'énergie dans la nanocible supérieur à une énergie seuil, dans un rayon de 200 nm autour de la AuNP, ce qui suggère qu'une AuNP pourrait efficacement détruire des cibles biologiques situées dans sa périphérie. Nous avons ensuite utilisé la simulation pour quantifier des effets chimiques. Á échelle macroscopique, nous avons estimé l'augmentation de la quantité de radicaux libres produits en présence d'une concentration d'AuNPs. Nous avons également comparé la distribution radiale des espèces chimiques d'une nanoparticule d'or ionisée, à celle d'une nanoparticule d'eau ionisée. Si le nombre total d'espèces chimiques par ionisation était en moyenne plus important pour l'or que pour l'eau, le nombre d'espèces chimiques produites en périphérie de la nanoparticule n'était pas systématiquement supérieur pour l'or par rapport à l'eau. Cela suggère que l'effet de l'AuNP dans sa périphérie réside surtout dans l'augmentation de la probabilité d'avoir une ionisation. Nous avons également étudié plusieurs scénarios pour expliquer l'augmentation expérimentale inattendue de la production d'espèces fluorescentes lors de l'irradiation d'une solution d'AuNPs et de coumarine. Notre étude suggère qu'un scénario plausible pouvant expliquer les observations expérimentales est l'interférence entre une AuNP et une des molécules intermédiaires produites suite à la réaction entre la coumarine et le radical hydroxyle. Pour finir, nous avons injecté les résultats des simulations dans le modèle biophysique NanOx, développé à l'IPNL pour calculer des doses biologiques en hadronthérapie, afin de prédire la survie cellulaire en présence de AuNPs. Nous avons aussi implémenté le 'Local Effect Model' (LEM), principal modèle biophysique utilisé dans le contexte des nanoparticules. Pour le LEM, nous nous sommes appuyés sur plusieurs approches dosimétriques proposées dans la littérature. Pour un système simpliste où les AuNPs étaient distribuées de façon homogène dans la cellule, nous avons montré que les prédictions de survies du LEM étaient significativement différentes en fonction de l'approche dosimétrique choisie. De plus, nous avons obtenu une augmentation de la mort cellulaire avec NanOx qui était due uniquement à l'augmentation macroscopique du dépôt de dose. Nous n'avons obtenu aucun effet supplémentaire dû aux électrons Auger, en contradiction avec les prédictions du LEM. Cette étude suggère que les modèles actuels proposés pour prédire l'effet radiosensibilisant des AuNPs doivent être améliorés pour être prédictifs, en prenant par exemple en compte de potentiels mécanismes biologiques mis en évidence par l'expérience.

Abstract

In radiation therapy, high-Z nanoparticles such as gold nanoparticles (GNPs) have shown particularly promising radiosensitizing properties. At an early stage, an increase in dose deposition and free radicals production throughout the tumour (photoelectric effect) and at sub-cellular scale (Auger cascade) might be responsible for part of the effect for low-energy X-rays. In this Ph.D work, we propose to study these early mechanisms with simulation tools, in order to better quantify them and better understand their impact on cell survival. We first finalised and validated Monte Carlo (MC) models, developed to track electrons down to low energy both in water (meV) and gold (eV). The comparison of theoretical predictions with available experimental data in the literature for gold provided good results, both in terms of secondary electron production and energy loss. This code allowed us to quantify the energy deposited in nanotargets located near the GNP, which is correlated with the probability to generate damages. This study required important optimisations in order to achieve reasonable computing time. We showed a significant increase of the probability of having an energy deposition in the nanotarget larger than a threshold, within 200 nm around the GNP, suggesting that GNPs may be particularly efficient at destroying biological nanotargets in its vicinity. The MC simulation was then used to quantify some chemical effects. At the macroscale, we quantified the increase of free radicals production for a concentration of GNPs. We also compared the radial distribution of chemical species following the ionisation of either a gold nanoparticle or a water nanoparticle. We showed that following an ionization, the average number of chemical species produced is higher for gold compared to water. However, in the vicinity of the nanoparticle, the number of chemical species was not necessarily higher for gold compared to water. This suggests that the effect of GNPs in its vicinity mostly comes from the increase of the probability of having an ionisation. We also studied several scenarios to explain the unexpectedly high experimental increase of the production of fluorescent molecules during the irradiation of a colloidal solution of GNPs and coumarin. Our study suggests that a plausible scenario to explain experimental measurements would be that GNPs interfere with an intermediate molecule, produced following the reaction between a coumarin molecule and a hydroxyl radical. During the last step of this Ph.D work, we injected our MC results in the biophysical model NanOx, originally developed at IPNL to calculate the biological dose in hadrontherapy, to predict cell survival in presence of GNPs. In addition, we implemented the Local Effect Model (LEM), currently the main biophysical model implemented for GNP-enhanced radiation therapy, to compare the NanOx and the LEM predictions with each other. In order to estimate cell survival with the LEM, we used various dosimetric approaches that were proposed in the literature. For a simple system where GNPs were homogeneously distributed in the cell, we showed that the LEM had different outcomes with regard to cell survival, depending on the dosimetric approach. In addition, we obtained an increase of cell death with the biophysical model NanOx that was purely due to the increase of the macroscopic dose. We did not obtain an increased biological effectiveness due to Auger electrons, which comes in contradiction with the LEM predictions. This study suggests that the current biophysical models available to predict the radiosensitizing effect of GNPs must be improved to be predictive. This may be done, for instance, by accounting for potential biological mechanisms evidenced by experimental works.

Acknowledgements

This work was performed within the framework of the LABEX PRIMES (ANR-11-LABX-0063) of Université de Lyon, within the program "Investissements d'Avenir" (ANR-11-IDEX-0007) operated by the French National Research Agency (ANR). This work has been supported by the Fondation ARC pour la recherche sur le cancer.

Contents

1. Introduction

1.1. Context

Nanoscience has revolutionized many fields. While the constant improvement of technology allows us to build smaller and smaller reproducible objects, nanotechnology is experiencing a growing interest and is particularly attractive in the domain of medical applications. Large scale research projects, such as Horizon 2020 (larger European Union's research endeavour with 80 billion euros over 7 years), aim at bridging the gap between nanotechnology research and markets, especially in medical applications[35]. Due to the infinite variety of nanomaterials (NMs), these new biotechnologies may concern therapeutics, diagnostics/imaging and regenerative medicine, and are of particular interest in cancer diagnosis and therapy. Considered as the new "Swiss knife" of medicine, NMs offer possibilities to deliver new treatments or optimize existing ones.

In particular, high-Z nanoparticles (NPs) may be used in radiotherapy to improve the therapeutic outcome. Radiation therapy is widely used for cancer therapy. Due to their penetrating properties, ionizing radiations may travel through the body and reach cancerous cells. When interacting with atoms and molecules of these cancerous cells, energy is deposited, which may lead to the destruction of the cells. The major challenge of radiotherapy is to deposit enough energy to kill all the diseased cells, while sparing surrounding healthy cells. The amount of dose that may be deposited to induce efficient cancer cells killing without inducing too severe adverse side effects is known as the therapeutic window. Several techniques are possible to improve this therapeutic window, among which the use of radiosensitizers. When located in the cancerous cells, these products increase the effects of the dose, thus increasing the contrast between the cellular response to radiation of cancerous cells *vs* healthy cells.

High-Z NPs, and in particular gold NPs (GNPs), have shown radiosensitizing properties. Its use is under clinical investigation and was recently granted European certification for cancer of soft tissues. Over the past decades, a lot of work has been dedicated to the understanding of the origin of the radiosensitization effect of GNPs to ensure a safe and optimised use in clinical routine. Currently, it is a topic of high interest with many teams around the world investigating the different mechanisms. At an early stage, the literature suggests that physical and chemical mechanisms could be responsible for the radiosensitizing effect of GNPs. For keV photon irradiation, high-Z nanoparticles have an increased probability to interact with photons, compared to soft-tissues. For a tumour loaded with GNPs, this results in an increase of dose deposition, potentially throughout the whole tumour. In addition, heavy atoms, when ionized, undergo desexcitation processes that induce the release of many low-energy electrons, a phenomenon called the Auger cascade. This generates a boost of local energy deposition, in the vicinity of the GNP. Both the macroscopic and nanoscopic increase of energy deposition may induce additional damages to the cell, through a direct destruction of cellular nanotargets and through the generation of toxic chemical species. In addition to these proposed mechanisms, there are growing evidences that GNPs are not inert when in contact with cells, and may trigger complex chemical and biological mechanisms that would further enhance the radiosensitization.

Despite the growing interest, there are yet many questions to answer. While many NPs have shown radiosensitizing effect *in vitro*, the absence of consensus regarding the mechanisms and the best NP candidates slow down translation to clinics[35]. A better understanding and quantification of the mechanisms may help optimize NPs to make them the most efficient for NP-aided radiation therapy. In a recent review, Brun and Sicard-Roselli [2016] pointed the need to better understand and quantify the relative contribution of the physical, chemical and biological steps on the final fate of the cell.

1.2. Scope, motivation and organisation of this Ph.D work

The global objective of this thesis is double. First, it aims at studying, at nano and microscale by simulation, the impact of GNPs on the physical and the chemical processes induced by radiations. Regarding physical processes, we focus in particular on the impact of GNPs on the probability to deposit energy in cellular nanotarget, i.e. targets that are of the order of tens of nanometers. In addition, the chemical part aims at estimating the production of free radicals in presence of GNPs, both at a micro and nanoscale. The second objective of this Ph.D is then to inject these results in the NanOx model to estimate cell survival in the presence of GNPs as an alternative to the LEM. We chose to focus on low keV photon irradiation, as we expect the effects to be at their maximum. Moreover, many works have been done in this energy range, allowing us to compare our theoretical results with other theoretical results but also with experimental data. This thesis is organised as follows.

Part I: State of the art In order to fully show nanotechonogy potential in radiation therapy, the first part of this thesis is dedicated to the description of the context. Chapter 2 introduces the concept of nanomaterials and how they may be used in medicine to improve current treatments or create new ones. Chapter 3 introduces the mechanisms of radiation therapy, from early sub-cellular damages to cellular death. It also discusses the limits of this therapeutic approach. Finally, it provides a first overview of how NPs may improve radiation therapy treatment, and *in vivo* evidences of the efficiency of the treatment. Then, Chapter 4 briefly explains how GNPs interact with the surrounding environment, from the molecular scale up to the full body scale. This is particularly important as such interactions have consequences on a toxicologic level. Besides, understanding such interactions enables to have an insight on the biodistribution of nanoparticles in cells, a key parameter for modelling radiosensitizing properties of NPs. Chapter 5 provides more in details (compared to Chapter 3) the experimental evidences of the radiosensitizing effect of GNPs. It describes the results for 3 types of systems: measurements of free radicals for an irradiation of a solution of GNPs and water; measurements of molecular damages when irradiating a solution of GNPs, biomolecules and water; measurements of cell death when cells are put in contact with GNPs and irradiated. This last part provides in particular insights on the extent of the radiosensitizing effect of GNPs, on the extreme variability of both the parameters and the results, and on the possible biological mechanisms that could partly explain GNP effects. Understanding not only the physical and chemical aspects but also the biological aspects enables to have a full picture of the complexity of the radiosensitizing effect of GNPs. It also enables to be aware of the different mechanisms, and therefore have every pieces of the puzzle for modelling purposes and for validation of the hypothesis. Finally, Chapter 6 provides an overview of simulation studies performed to better understand the radiosensitizing properties of GNPs. More specifically, this chapter summarizes dosimetric calculation and conclusion on the physical effects, from the tumour scale down to the sub-cellular scale.

Part II: Physical modelling The second part of this Ph.D work concerns the physical modelling for GNP-enhanced radiation therapy. We focused on a quantity that has not been investigated in this context yet: the specific energy. The specific energy is the energy deposited in a nanometric target following an irradiation. Its distribution enables to account for the variation of the energy deposition at nanoscale (e.g. of the order of the size of a DSB). Previous studies have focused

on average quantities. While average dose distribution enables to emphasize the heterogeneity of energy deposition at the sub-cellular scale, the link with biological damages is not direct. As further detailed in Chapter 9, the amount of damages at nanoscale does not scale with the average energy deposition. Indeed, nanometric biological targets have a probability of receiving energy of the order of 10^{-4} under low LET photon irradiation and clinical doses. Therefore, most of the time a nanotarget receives 0 Gy, but when it does receive energy it may reach doses as high as tens of kGy. Specific energy distribution thus allowed us to better quantify nanometric biological damages, in particular around GNPs. Such calculations are challenging, and require optimized algorithms in order to be achievable in reasonable time. Such algorithms were discussed and established with my supervisors. A program was already available in my team (Transfer Energy Distribution, TED) that performed nanodosimetry calculations for ion irradiation. Part of my work consisted in modifying this program to adapt it to the present context. Then, I performed all the calculations for several photon energies and GNP sizes, using the IN2P3 computing centre. I also implemented an analysis tool using ROOT in order to obtain the final specific energy distributions.

In order to study this quantity, we needed an accurate tracking of electrons both in water and gold. While many MC codes enable to track electrons in water down to meV[19,106], accurate modelling of electron transport in metals is scarce at such energies. As pointed in many MC studies, the MC simulations available at the beginning of this work did not have an event-by-event tracking of electrons in gold. Most of the models were accurate down to $\sim$ 1 keV, and with an energy cut in gold at either 100 or 250 eV. Only recently, the Geant4-DNA toolkit implemented physical models to track electrons in gold down to 10 eV[238]. In a recent work, Sakata et al. [2018] pointed out the importance of accurate tracking of electrons in gold when studying dose deposition at nanometric scale around GNPs. In line with these observations, the very first work of this thesis was to finalise and validate a physical model in order to track electrons in gold. In the late 90's, the Monte Carlo code LQD (LiQuiD) was developed at the CIMAP (Caen, France) in order to track ions and electrons in liquid water down to low energy. This code is part of a package (LQD for the physical stage, PHYCHEML for the physico-chemical stage and CHEM for the chemical stage) that also allows the tracking of chemical species. It was in particular used to study the radiochemistry following ion irradiation of liquid water. LQD was further developed to account for multiple ionisation of water molecules[105,106], in collaboration with our laboratory and the Instituto de Fisica (Rosario, Argentina). It was used for nanodosimetry calculations[23]. Then, it was developed to include additional materials such as silica[214], leading to a new branch of the code named MDM (MeDiuM). In 2014, A. Ipatov during his postdoctoral position developed models for the tracking of electrons in gold. At the beginning of my Ph.D., these models required validation and some improvements. As detailed in Chapter 8, the first part of my work consisted in performing an extensive benchmark against available data in the literature, both in terms of electron yields and energy distribution. In particular, I investigated the validity of the models for secondary electron emission. In collaboration with B. Gervais, I also improved the bulk plasmon cross sections, implemented the surface plasmon models, calculated the associated cross sections, and used the software ELSEPA[240] to calculate elastic cross sections.

Part III: Chemical modelling Following the study of physical mechanisms, the impact of GNPs on the radiolysis yields was studied. As previously said, the package MDM/PHYCHEML/CHEM[106] enables the tracking of radical species up to $\sim 10^{-6}$ s, and was used for the study of chemical species production under ion irradiation[60] or in the presence of radical scavengers[59]. In combination with an accurate physical tracking in gold, this MC simulation constituted an ideal tool to investigate the radical production following irradiation of GNPs in water. This part is organised in 3 chapters. Chapter 10 quantified the production, at a macroscale, of chemical species after irradiating a solution containing a concentration C_{NP} of GNPs. This may be linked to the average primary chemical boost a cell containing GNPs experiences following an irradiation. Chapter 11 focused on the production of chemical species in the vicinity of one GNP, following an ionization event. It may be used to quantify the primary chemical boost a sub-cellular target experiences

following the ionization of a GNP. For both of these studies, all the algorithms used to fasten the calculations were discussed and established with my Ph.D. director. I then performed all the calculations, and developed all the analysis tools required to compute the final results. Finally, Chapter 12 focused specifically on different scenarios in order to explain the unexpected high measurement of coumarin fluorescence in various studies[109,110,251]. The mechanism of this phenomenon is yet unknown, and various scenarios were studied with theoretical modelling. The scenarios I propose in this final chemical study were established following a careful reading of the experimental studies, and some discussions with my Ph.D. director, B. Gervais and the team of E. Dumont at the ENS Lyon. This study required minor changes in the Monte Carlo codes PHYCHEML/CHEM, such as the addition of new chemical species and new lists of reactions. I also developed the analytical approach in order to calculate chemical yields for times larger than the µs. I then performed all the calculations and analysis of the results, using the computing resources of the IN2P3 computing centre.

Part IV: Biological modelling The final part, constituted of Chapter 13, aims at predicting cell survival in presence of GNPs, in particular using the biophysical model NanOx. This study has to be viewed as a theoretical study to better estimate the influence of the integration of the physical and chemical processes in the biophysical modelling of cell survival in presence of NPs. Therefore, in line with the published application of the LEM, we considered the same simplistic uniform distribution of GNPs and we showed the crucial impact of the stochastic effects of energy deposition at nanoscale. We compared the LEM predictions to the NanOx ones for the same system. Different approaches were used for the LEM predictions, which I identified during my bibliography research. The methodology for the application of NanOx for GNP-enhanced radiation was established with my supervisors and C. Monini, who has a postdoctoral position and has worked on the application of NanOx for hadrontherapy. I then implemented both the Local Effect Model and the NanOx model, performed the calculations and analysed the results.

Part V: Conclusion Chapter 14 concludes on the results of this work and the future perspectives. This part also contains a summary of this work in French in chapter 15, and a 'CV' of my Ph.D. containing, among others, the list of the conferences I attended to present my work (oral/poster).

Each part or chapter may be read independently from one to another. Each chapter is written in the format of an article.

Part I.

State of the art

The topic of nanoparticle applications in radiation therapy encompasses many fields (nanoscience, physics, theoretical chemistry, experimental chemistry and biology, medicine). During my bibliographic research, I therefore came across a very large number of works, all reporting different aspects of the topic. In this thesis, I propose a dense "state of the art" composed of 5 chapters, to study many aspects of the topic with an emphasis on the biological and simulation components, as both are fundamental to accurately model the radiosensitizing effect of GNPs and understand its origin on a sub-cellular scale. This part may either be read by going through each chapter to fully understand the complexity of the topic, or by limiting the reading to the summary of each chapter to have the key points.

2. Nanomedicine

Contents

2.1. Nanoparticles: definitions and classifications

Definitions Due to their unique properties, nanoparticles (NPs) and nanomaterials (NMs) constitute an attractive area with increasing studies and applications. As pointed by Jeevanandam et al. [2018], a single internationally accepted definition for NMs does not exist, and varies according to international organizations. The International Organization for Standardization (ISO) described NMs as *"material with any external nanoscale dimension or having internal nanoscale surface structure"*, and include a variety of nanostructures such as nanofibers, nanoplates, nanowires or quantum dots. NMs may be categorized according to their size, composition, shape or origin and we follow here the categories proposed by Jeevanandam et al. [2018].

Size Although NMs could theoretically include any particle in the size range 1 - 1000 nm, they are commonly defined as objects with dimensions in the order of 1-100 nm. In particular, the British Standards Institution proposed to define NPs as nano-objects with three external nanoscale dimensions. Their size is thus between the molecule and the bulk material, and induces particularly interesting properties. These objects have a very large ratio of surface area over volume compared to macroscopic materials. As illustrated by Friberg and Nyström [2015], a cube of 1 cm $\times$ 1 cm $\times$ 1 cm has a volume of 1 cm^3 and a surface area of 6 cm^2. If this same cube is divided in smaller cubes of dimensions 100 nm $\times$ 100 nm $\times$ 100 nm, the volume remains identical but the surface area increases to 6×10^{14} cm^2. For spherical NPs, the surface to volume ratio is particularly high for a radius between 1 to 100 nm, with an increased number of the fraction of atoms located on the surface (Nel et al. [2006]). This may induce a particular chemical reactivity, as discussed in chapter 4. As illustrated in Fig. 2.1, the NP size is well below the size of a human cell and can penetrate them.

Composition Following the classification by Jeevanandam et al. [2018], NPs and NMs may be organized in four categories according to their core material:

1. Carbon-based NMs, such as carbon nanotubes, fullerenes, etc.
2. Inorganic-based NMs, which include metal oxide based NPs (zinc oxide, iron oxide, T_iO_2 etc.), metal based NPs (gold, silver or iron), or semi-conductors (silicon, ceramics). They are based on strong (covalent) interactions. In the review by Ju-Nam and Lead [2008], quantum dots (cadmium sulfite, cadmium selenide) were separated as a specific category.
3. Organic-based NMs, which are made from organic matter (excluding carbon-based NMs), are usually designed based on non-covalent (weak) interactions. It includes dendrimers, micelles, liposomes and polymer NPs.
4. Composite-based NMs, which refers to hybrids nanoplatforms. It may be based on any combination of the aforementioned materials.

The core composition of NPs might impact the interaction of NPs with cells. When studying such interactions, they may be separated into two categories: those formed via strong interactions (among which metallic NPs, which this thesis will focus on) and those formed by weak interactions, such as micelles (Canton and Battaglia [2012]). For the former, their interaction with their surrounding is dominated by interfacial forces. They have a high surface tension that can induce surface catalytic events that could lead to adverse outcomes for the cells.

Origin NMs may be either synthetic or natural. It should be noted that naturally occurring NMs are present through Earth regardless of human actions, which implies that humans have always been exposed to them. Natural NMs are produced for example during incidental events such as volcanic eruptions or forest fires. In the nature, they are also found anywhere in living organisms, as illustrated by Fig. 2.1. Any plant, insect or animals is made of nanostructures that are used for numerous purposes. A component as essential and basic as our DeoxyriboNucleic Acid (DNA) is a nanostructure. Viruses are also in the nanometer range, and some strategies in the synthesis of new biomedical nanostructures mimic virus behaviours inside cells. Some bacteria, algae, fungi or yeast also possess the ability to naturally produce NPs, and are used to generate NPs with low toxicity. Even small organisms have been found to reach nanometer scales: recently, nano-organisms were found in Triassic and Jurassic sandstones, composed of cells of diameters comprised between 20 and 150 nm (Jeevanandam et al. [2018]).

Regarding anthropogenic NMs, they may be produced by mechanical grinding, engine exhaust and smoke. Transportation, industrial operations and charcoal burning are among the major causes of synthetic NMs production. For example, diesel automobiles release 20-130 nm sized NPs, whereas gasoline engines release 20 - 60 nm sized NPs. Both are a cause of public concern and a major source of urban pollution. More than 90 % of carbon NPs in the atmosphere are diesel-generated NPs. Although 10 % of overall aerosols in the atmosphere come from human activity and 90 % come from natural activity, the hazardous effect on human health depends on the composition of NMs. As a consequence, inhalation of ultrafin particles emitted by pollution is a hot topic regarding public health issues. Foreign substances are generally blocked by the human skin, however some organs are particularly at risk when exposed to NMs, including lungs and gastrointestinal tract. Furthermore, NPs that are inhaled may reach the bloodstream and other sites in the human body, including liver, heart or blood cells. The study of their toxicology has been particularly active, and has led to the emergence of a new discipline: the nanotoxicology. NM toxicity depends on its origin and many NPs appear non-toxic, while others may even have positive health effects (Jeevanandam et al. [2018]).

Synthetic NMs are anthropogenic NMs that are manufactured intentionally to take benefit of their unique properties. Their preparation relies on physical, chemical, biological or hybrid methods. NMs have been used throughout ages since antiquity for their unique optical properties. For

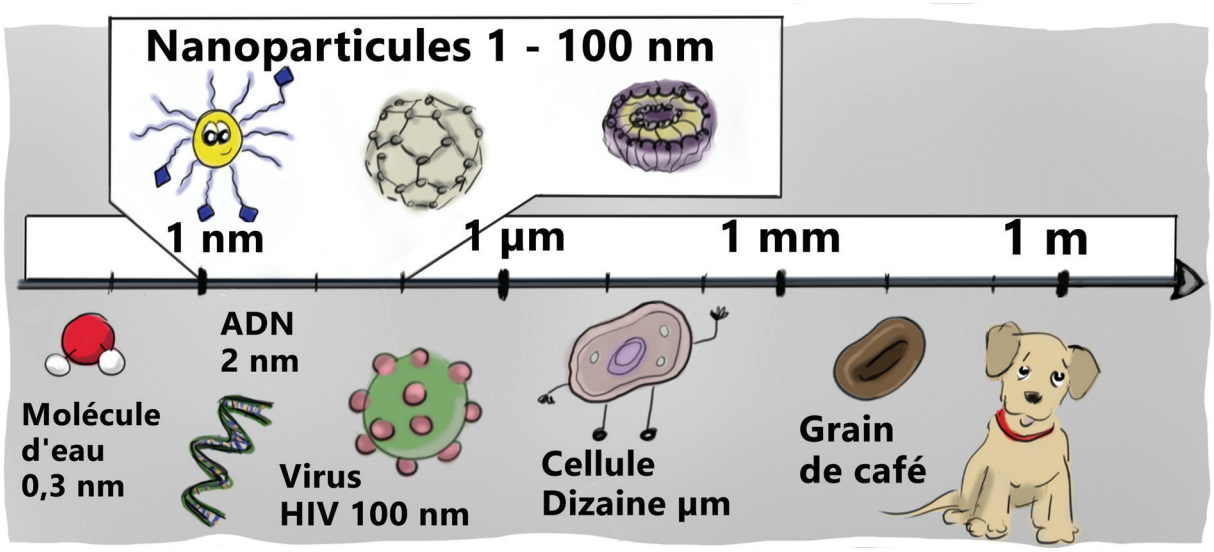

Figure 2.1.: Typical dimensions of various elements, as compared to NPs.

example, their usage dates as early as 4000 years ago, when ancient Egyptians used NPs for hair die. Michael Faraday was the first to report a scientific description of the synthesis of colloidal gold NP (GNP) solution in 1857 (Jeevanandam et al. [2018]). Nowadays, they are used on industrial scales for a variety of applications, such as cosmetics, sunscreens, electronics or catalysis (Ju-Nam and Lead, Nel et al. [2008, 2006]). In 2014, there were about 1814 nanotechnology-based consumer products commercially available over 20 countries (Jeevanandam et al. [2018]). As the number of engineered NMs and their release in the environment increase, the risk assessment has become a central question (Nel et al. [2006]). A key question is whether these engineered NMs will exhibit specific interactions and toxicities.

Because NMs are similar in scale to biological molecules, nanotechnology may be potentially useful for medical applications (Kim et al. [2010]). A succinct overview of these applications is listed in the next subsection, with an emphasis on the cancer area.

2.2. Medical applications of nanoparticles

The field of nanomedicine aims at using the properties and characteristics of NMs for the diagnosis and treatment of diseases at the molecular level (Kim et al. [2010]).

***In vitro* applications** For *in vitro* applications, NPs may be used for labelling and imaging of biological samples. They may either simplify the readout or amplify the detection threshold of biological devices. For instance, in immunostaining (use of antibody-based method to detect a specific protein in a sample), antibody-conjugated NPs that bind to cells provide a visualization by contrast using Transmission Electron Microscopy (TEM). Besides, they may be used for *in vitro* and *in vivo* labelling by loading fluorescent dyes or other probes on NPs (Doll et al. [2013]). NPs may also be used as biological sensors. For example, it is possible to use it in order to detect DNA sequences at very low concentration, including detection of genetic mutations. NPs may also be used as chemical biosensors, for example to mediate electrochemical reactions as redox catalysts. The list of these applications may be found in many reviews such as the ones written by Boisselier and Astruc, Daniel and Astruc, Kim et al. [2009, 2004, 2010] and Doll et al. [2013].

Clinical applications NPs have also many clinical applications (Boisselier and Astruc, Daniel and Astruc [2009, 2004]), and several NMs are being studied in clinical trials for numerous dis-

eases, that may be found on ClinicalTrials.gov[1]. They may be used, for example, as carriers to deliver diagnostic or therapeutic agents through biologic barriers. In the **drug delivery** field, they have shown in several cases to improve tolerance of drugs that are normally toxic at high dose when not associated with NPs (Kim et al. [2010]). NPs may be used in particular for targeted drug delivery or for gene delivery (Chithrani [2010]). Encapsulated drugs may be released by biological triggers, such as the reduction of pH if NPs are internalized and trapped in lysosomes. They may also be released by external stimuli (electromagnetic field or ultrasound). NPs may also **act as therapeutic** when activating them with an external stimuli. For instance, using near infrared photo-stimulation of NPs trapped inside lysosomes triggers necrotic and specific apoptotic signals. A local heating may also be generated by using an alternating magnetic field excitation combined with magnetic NPs. NPs may be used for **prevention** of different pathologies. For instance, dendrimers, which are nanostructures shaped like tree branches, have shown to prevent the transmission of HIV in macaque models (Kim et al. [2010]). In particular, NPs may be used as vaccines. Several studies are reported[1], including vaccination against influenza (NCT03293498) or Ebola (NCT02370589). Several clinical trials have reported the use of NPs coronary diseases for therapeutic or prevention purposes. Other therapeutic applications include Alzheimer, Hepatitis B, tuberculosis, improvement of cognitive dysfunction in Schizophrenia (NCT02104752), cataract management (NCT03001466) or plaque Psoriasis (NCT03004339). Regarding **diagnosis**, NPs may be conjugated with Magnetic Resonance Imaging (MRI) enhancing agents and used as contrast agents. All of the aforementioned techniques may be used for cancer prevention, diagnosis or therapy and is discussed more in details in the next section.

2.3. Nanomedicine in cancerology

This section provides an overview of cancer incidence, the main therapeutic strategies, and how nanomedecine has been developed to help improve their therapeutic balance.

2.3.1. Cancer: key numbers, definition and strategies

Cancer is a worldwide major public health issue and the second leading cause of death. In 2015, it was responsible for 8.8 million deaths[2], which represent one out of six death. In France, cancer is the first cause of death. In 2015, 385 000 new cases were detected, and 150 000 deaths were caused by cancer[3]. The economic impact of cancer is significant and increasing. According to the World Health Organization, it was estimated that cancer costs approximately US$ 1.16 trillion in 2010. Approximately 38.4 % of men and women will be diagnosed with cancer at some point during their lifetime[4]. These few statistical facts undeniably remind the importance of cancer incidence, and the urge to keep on finding new solutions to prevent, diagnose and cure this disease.

Cancer is a generic term that encompasses many different cases of cell dysfunction. In the two most cited *Cell* review papers by Hanahan and Weinberg, Hanahan and Weinberg [2000, 2011], ten hallmarks were listed that distinguish cancer cells to normal cells. (1) While normal cells have a finite ability to undergo mitosis, cancer cells have a replicative immortality. (2) Cancer cells are also characterised by a genome instability, and generally have severe chromosomal abnormalities. (3) They resist inhibitory signals that might stop their growth: while mitosis in normal cells is a tightly controlled process orchestrated by proteins known as tumour suppressor genes, these proteins are altered in cancer cells. This leads to uncontrolled cell division despite severe cell abnormalities. (4) Cancer cells may be resistant to cell death: normal cells can initiate apoptosis in response to abundant DNA damages or cellular stress, while cancer cells are less sensitive and avoid apoptosis. (5) They can stimulate their own growth. Normal cells require hormones or

[1] www.clinicaltrials.gov
[2] www.who.int
[3] www.fondation-arc.org
[4] www.cancer.gov

other molecules as a signal to grow and divide, while cancer cells do not necessarily require them. (6) They also use altered metabolic pathways to provide energy. (7) They have the ability to avoid immune system and despite this ability, (8) tumours promote inflammation. The tumour micro-environment is often infiltrated by cells from the immune system, that mimic inflammatory conditions and provide the tumour cells chemical substances essential to allow them to survive, move and proliferate. (9) Cancer cells promote the induction of angiogenesis, i.e. the formation of blood vessels to ensure blood supply. These newly formed vessels are usually poorly formed and leaky. At last, (10) tumour cells activate cell invasion and metastasis.

Regardless of the cancer type, cells from a specific part of the body begin to divide uncontrollably and eventually spread. There are more than 100 types of cancer, which are usually named after the organs or tissues the cancer started from. For instance, carcinoma, the most common type of cancer, designates a cancer type that originates from epithelial cells. These cells cover the inside and outside surfaces of the body in contact with the external world[4]. Facing such a diversity, once diagnosed a specific type of cancer requires a specific type of treatment, which can combine one or more modalities. These modalities may use strategies based on the previously listed hallmarks, and aim at either removing the cells, killing them or stopping their spread. The main modalities are surgery, radiation therapy, chemotherapy, immunotherapy, targeted therapy and hormone therapy.

- **Surgery** consists of removing the tumour by a medical procedure performed by surgeons. It is used in 80 % of the cases[3], and may be sufficient for some cases, if the entire tumour is removed. It works best for solid tumours contained in a well defined volume. Limits are mainly related to the fact that some cancers, like some cerebral cancers, may not be accessible. Besides, it is not applicable for spread cancers (metastatic cancer, or blood cancer).

- **Radiation therapy** is based on the ability of radiation to travel through matter and deposit energy thus destroying cancer cells. This treatment remains an important component, with approximately 50 % of patients undergoing cancer treatment receiving radiation and contributing towards 40 % of curative treatment (Baskar et al. [2012]). The mechanisms, limits and technological strategies for treatment improvement will be further discussed in Chapter 3.

- **Chemotherapy** uses cytotoxic drugs that have the ability to destroy tumoural cells. It may either stop or slow the growth of cancer cells, which divide quickly. Most of the time, it is combined with other treatments, although in some cancers chemotherapy may be the only treatment received. It usually causes severe side effects due to their non tumour-specificity. The drugs attack in particular quickly dividing healthy cells, such as the ones that cause hair growth resulting in hair loss.

- **Immunotherapy** aims at stimulating the immune system to attack cancer cells. As cancer cells have the ability to hide from the immune system, this treatment mark cancer cells or boost the immune system in order to enhance cancer cells destruction. It is a particularly active research area, and the two 2018 Nobel price winners of in physiology or medicine (James P. Allison, Tasuku Honjo) developed an immunotherapy technique. There are many types of immunotherapies, but it is not yet as widely used as surgery, chemotherapy and radiation therapy.

- **Targeted therapy** is among innovative treatments and uses drugs that specifically attack target cancer cells based on the recognition of their structure. They are usually small molecules which may enter cells or monoclonal antibodies that get attached to the surface of cancer cells. They have a variety of mode of action, and have side effects which depend

on the type of treatment received. They may be very expensive to design.

– Some cancer growth (prostate cancers and breast cancers) is associated with hormones, and thus **hormone therapy** consists of blocking these hormones. This treatment is usually combined with another.

All these treatments face limits and side-effects. First, chemical treatments and radiations induce a broad toxicity, and a key to improve their efficacy is to target their action onto cancerous cells. Besides, tumours have a specific microenvironment that contains high interstitial fluid pressure that may limit the distribution of drugs. Additionally, inner part of the tumour usually lacks blood supply and thus becomes hypoxic, hardly accessible and drug resistant. Tumours are heterogeneous with necrotic areas, making a mono-approach sometimes insufficient. These may explain resistance to treatment and relapses (Akhter et al., Wang et al. [2013, 2012]). Diagnosis tools could help better visualise the different parts of the tumour, while combining treatments all at once might help dealing with heterogeneity. An improved targeting of cancer cells is also required for reduced toxicity and higher tumour uptake. With the emergence of nanoscience, the design of smart molecules that could combine all the aforementioned elements has become possible. Next section explains the advantage of NPs over standard molecular drugs for the tumoural delivery, a key to accumulate or focus the treatment within cancerous cells.

2.3.2. Nanoparticles delivery to tumour: active *vs* passive targeting

The biodistribution of any medical drug in the human body is governed by three pharmacokinetic steps: vascular transport, transvascular transport and interstitial transport. NPs offer a new way of pharmacokinetics and biodistribution compared to other drugs, through the passive and the active targeting. These two strategies enable more accumulation in the target, and thus less toxicity (Friberg and Nyström [2015]).

Passive targeting and first generation of NPs Cancer cells proliferate quickly, and their tumour vasculature may be abnormal, with aberrant branching and leaky walls with pores as large as few hundreds of nanometres. It is much larger than normal vessel junctions (5 - 10 nm). This facilitates the extravasion of macromolecules in the tumour interstitial space. The size of NPs make them ideal for biodistribution: they have a size that is large enough not to penetrate normal vasculature and capillaries, leading to a lower accumulation in organs such as skin, lung and heart compared to smaller molecules. Additionally, solid tumours contain a defected lymphatic drainage, which allows the accumulation and a long retention time of macromolecules. This passive targeting, illustrated in Fig. 2.2 A, is known as the Enhanced Permeation and Retention (EPR) effect, and may be used for accumulation of NPs.

Strategies may be used to optimize this effect. The reticuloendothelial system (RES) is a part of the immune system and in charge of recognizing and sequestrating foreign macromolecules, through a process called opsonization. For a more efficient accumulation of NPs in tumour, a long blood circulation time is required. Thus, the use of hydrophilic NP surface coating to avoid phagocytosis by the RES is usually applied. Polyethylene glycol, or PEG is the most commonly used molecule. Others include poly(ethylene oxide) (PEO), poly(vinyl alcohol) (PVA), polysaccharides (dextran), poly(N-vinyl pyrrolidone) (PVP) (Canton and Battaglia [2012]). Such NPs are known as furtive NPs, as they escape the immune system. A dense coating is mandatory to be efficient to prevent opsonization and interaction with serum proteins. This combination of NPs coated with hydrophilic elements enabled the first clinically approved NPs. This approach may have drawbacks and limits. An extensive half-life might induce side effects, when the drug has a very long blood circulation life and reach distant capillaries (Friberg and Nyström [2015]). Besides, the EPR effect may only be applied to solid tumours, and not liquid tumours. In solid tumours, the effect is limited when tumour interstitium faces high pressure, limiting the diffusion of

drugs. While in small animal models existing in laboratories, the EPR effect exists due to selection of fast growing cancers, its existence in humans is still under debate (Friberg and Nyström [2015]). Some solid tumours may take years to develop, and thus have normal vessels. In any case, it is a heterogeneous phenomenon which varies dramatically from one tumour to another, and from one patient to another, thus room exists for improved targeting of cancer cells.

Active targeting and second generation of NPs Active targeting relies on the use of molecules that bind to specific tumour cells or tumour microenvironment, including blood vessels receptors as illustrated on Fig. 2.2. The first strategy that is illustrated facilitates intracellular accumulation of NPs *via* the receptor-mediated endocytosis. The second strategy that is illustrated causes accumulation in the interstitial spaces of the tumour, and NPs are eventually endocytosed by cancer cells (Biswas and Torchilin [2014]). Both strategies aim at inducing a higher uptake of the NP in the tumour, achieving high tumour to blood and tumour to normal tissue ratios. This may help decreasing potential side effects and increasing the therapeutic or diagnostic efficiency. With advances in cancer proteomics and bioinformatics, the discovery or many markers has allowed potential efficient targeting. Different strategies or molecules may be adopted:

- **Physico-chemical properties** (surface topology/charge). In that area, virus-like nanoparticles have a natural affinity to target some cells.

- **Proteins.** Some monoclonal antibodies (Mabs, proteins that recognise some pathogen agents) are generally overexpressed in primary and metastatic tumours, such as HER2 in breast cancer or the epidermal growth factor receptor in lymphoma. Some of Mabs-based drugs have already been approved while other are in clinical trials. There has been successful monoclonal antibody therapies, however this strategy faces difficulties, in particular in the conception and scale-up (i.e. industrial production) of the NPs. Other targeted proteins include proteins which can bind to transmembrane receptors, such as the transmembrane tyrosine kinase receptor, or integrins which play a key role in promoting tumour angiogenesis and metastasis. However, their effectiveness may be limited by their immunogenecity, and susceptibility to early clearance. The target receptors of these proteins are usually expressed in many healthy cells.

- **Peptides.** They might constitute a good alternative to targeting molecules due to their small size, high stability and relative low immunogenecity. A good example is the vasoactive intestinal peptide receptor, which is five times more abundant in breast cancer cells than normal breast cells.

- **Nucleic acids.** Aptamers are short Ribonucleic acid (RNA) or DNA oligonucleotides that fold into 3D conformations with high binding affinity and specificity. In particular, aptamers are being developed to bind selectively to vascular endothelial growth factor, a protein involved in angiogenesis. These molecules have the advantage of inducing low immunogenecity, leading to better stability and biodistribution. However, disadvantages include a lower affinity than antibodies as they tend to dissociate more easily from their receptors than antibodies.

- **Folic acids and other small molecules.** Folic acid is an essential vitamin for cell survival, due to its role in the synthesis of nucleotide bases. The folate receptor is overexpressed in many cancers, 100- to 300- times higher than normal tissues and may therefore be useful for targeting strategies.

Additionally, when needed, some ligands may improve cell internalization, and target specific organelles. Some ligands exist to favour (1) cell penetration, (2) endosomal escape, (3) mitochondrial targeting, (4) nuclear delivery and (5) endoplasmic reticulum delivery (Biswas and

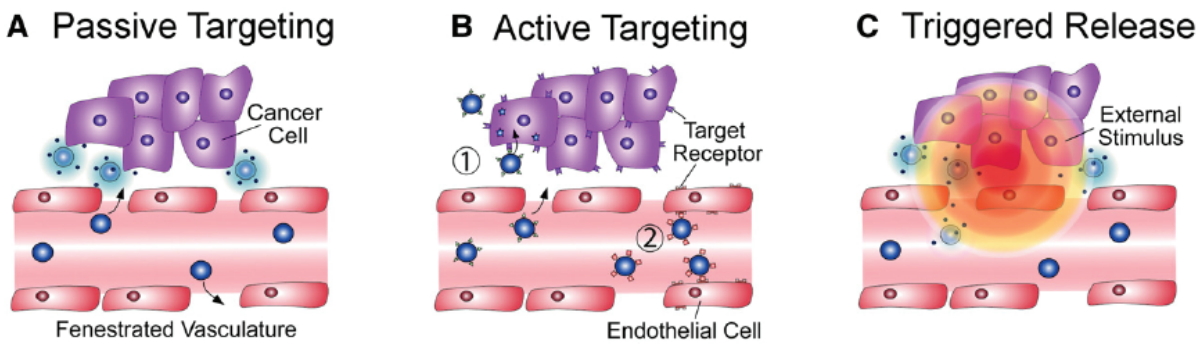

Figure 2.2.: Strategies for drug targeting using NPs. On Fig. 2.2 A, NPs are delivered to the tumour through passive targeting. The leaky blood vessel and lymphatic impairment allows for accumulation of macromolecules such as NPs. On Fig. 2.2 B, NPs are delivered through active targeting, by using ligands on NP surface that preferentially attach themselves to tumours or to blood vessels. On Fig. 2.2 C, the NP action (drug delivery, photothermal thermapy, radiosensitization, etc.) is activated by an external stimuli. Taken from Wicki et al. [2015].

Torchilin [2014]). For a successful targeting, a key is to find the proper ligand density to maximize the attachment, along with a good stability of ligand attachment (Wicki et al. [2015]). Targeting cancer cells has however faced many issues, including poor tumour penetration. While *in vitro* experiments have shown very promising results, the transition to *in vivo* condition is challenging. The situation is much more complex with NPs facing much more obstacles such as high viscosity, rigid barriers and long distances to travel before reaching the target. For an interaction between the ligand and the receptor to occur, both must be very close (< 0.5 nm). The time for a single NP to cross one cell is long, estimated to a few hours. Thus, if the distance from the vessel to the cell target is a few cell layer, it might take a few days for the NP to diffuse and whether the drug remains intact or not is a relevant question (Friberg and Nyström [2015]). Besides, interaction of NPs with biomolecules might "cover" the targeting ligand and prevents it from bonding to the receptor. No guideline exists yet on how to design the perfect targeted NP. In particular, there is no indication on how to place the ligand in the most efficient way, to achieve the highest targeted-uptake while minimizing non-specific binding (Polo et al. [2017]). *In vivo* targeting is particularly challenging because it may imply the targeting of a specific cell organelle, to a specific type of cell which possess a non-specific phenotype. Rather than targeting the cancerous cells, another strategy is to preferentially target vascular cells that compose the solid tumour. The partial destruction of tumour vasculature may help further enhance the EPR effect by making the vasculature more leaky, and thus reach higher tumoural concentration of NPs.

In the next section, we list some of the main NPs that are currently used for cancer applications.

2.3.3. Main nanoparticles in cancer applications

While there is a large number of applications in medicine, most of the nanoparticles are used for cancer applications. Thereafter are listed the most common NPs designed or under investigation in the field of cancerology. Their specific use will be further introduced in the next subsection. Some of these NPs are illustrated in Fig. 2.3, following the classification introduced in section 2.1.

Lipid based NPs The biomedical use of nanotechnology began more than 50 years ago, before the use of the terminology *nano*, with the discovery of liposomes. Liposomes are self-assembling vesicles with lipid bilayers. The outer and inner part of the liposome is hydrophilic. To protect them from the body's defenses, they are often coated with a polymer layer (PEG). The resulting products are known as stealth liposomes (Friberg and Nyström [2015]). These nano-objects are used as vessels to deliver active agents, and have been clinically approved for cancer treatment.

The first Food and Drug Administration (FDA) approved liposome-based product is Doxil^{TM} in 1995 as a chemotherapeutic agent for the treatment of Kaposi's sarcoma, a refractory breast and ovarian cancer. The drug doxorubicin, used to prevent cell division, is encapsulated in the lyposome to enable a safer delivery of the drug. Another type of lipid-based NPs are solid lipid NPs which are stable colloidal carrier systems with low toxicity.

Dendrimers Dendrimers are highly branched, globular, monodisperse, uniformly distributed polymeric macromolecules, shaped like tree branches. They contain both hydrophobic and hydrophilic areas. They can be made of amino acids, sugars, nucleotides, etc. The dendrimer poly(amidoamine) (PAMAM) is the most well known dendrimer.

Micelles Micelles are lipid-based or polymer-based NPs that contain an inner hydrophobic core and an outer shell made of hydrophilic part. They have a good stability. There are contradicting results with regard to their longevity, with some studies showing long circulation time and others short circulation time.

Other polymeric NPs NPs that are designed with biocompatible, biodegradable polymers. Polymer chains with different hydrophilicity self assemble into a core-shell structure in an aqueous environment. They are among the most investigated nanomedicines, due to their flexibility that allows customized composition, molecular weight and topology.

Nucleic acid-based nanoassemblies Nucleic acids are small biomolecules, composed of nucleotides, which are organic molecules that serve as the monomer units to form DNA or RNA. With the development of DNA origami, it is possible through bottom-up fabrication process to assemble strands of DNA and form different 2D-3D nanostructures. These structures may be used as drug carriers. For example, Douglas et al. [2012] designed a DNA nanorobot capable of transporting and delivering molecular payloads such as gold nanoparticles to cells.

Virus-like nanoparticles They are made of capsid proteins (protein shell of a virus which encloses the genetic material of the virus), without the virus genetic material to avoid virulence. They may be used for immunotherapy, on melanoma for example. They may also express therapeutic proteins, once in target cells.

Protein-based nanoparticles Proteins show good chemical compatibility with non-organic NPs and peptide chains are used as building blocks. One limit is that it is challenging to predict the 3D structure of assembled peptide chains, although it is essential for the protein functionality.

Carbon NMs These types of NPs have unusual properties. It includes carbon nanocage, or carbon nano-tubes which are made of graphite sheets rolled into cylinders. However, their low solubility limit their use, and they must be functionalized to increase their bioavailability (Raju et al. [2015]).

Inorganic based NPs Inorganic NPs offer many possibilities as they have electronic, optical and magnetic properties that may be used for many applications. They may include metallic NPs such as gold, copper or silver NPs or non-metallic NPs such as silica NPs. In particular, gold NPs are interesting for, among others, their high stability and ease of preparation, which allows ease chemical binding to bio-conjugates. Magnetic NPs, made of iron, nickel or cobalt for instance, are also of interest. Semi-conductor quantum dots (QDs) are small (2 to 10 nm) NPs with semiconducting properties. All of these NPs may be good candidates for bio-conjugation with furtive agents, targeting bio-molecules or fluorescent agents.

The next section lists some of the applications developed with these NPs for new strategies to fight cancer.

2.3.4. Main applications

In the field of cancer applications, and as introduced previously in section 2.2, NPs may be used as therapeutic, preventive and diagnosis agent. Some examples are listed thereafter.

NPs as drug delivery agents Drug delivery is by far the main application of NPs in cancerology. The size of NPs make them an ideal drug carrier, as previously discussed. Drug carriers must meet a few requirements: (1) effective binding and carrying of the drug, (2) stability when in circulation, (3) biocompatibility in the body, (4) accumulation preferably in target cells while avoiding healthy cells, (5) release of drugs once in the cancer cell (Raju et al. [2015]). NPs may be used for encapsulation of anticancer chemotherapeutics, immunotherapeutics or nucleic acids. They can improve some drugs solubility and thus their bioavailability. They can hence be used to improve existing anti-cancer compounds. Their small size and high surface to volume ratio enables to tight drugs to the surface or encapsulate it inside carriers which, once reaching the tumour degrade and release the drug. As previously discussed, the use of NP carriers can increase differential in biodistribution through the EPR effect or *via* cell-targeting. Compared to standard chemotherapeutics, they usually result in lower toxicity. They also have the ability to deliver poorly soluble cancer therapeutic, such as taxanes. These NPs might be designed to release the drug once in contact with a tumour-specific stimuli: for instance in solid tumours the extracellular pH is more acidic than the systemic pH, thus the drug might be released only in acidic condition. The particular tumour micro-environment can be used for triggering the release of drugs.

Most of previously listed NPs may be used as nanocarriers. The prominent ones are liposomes and polymer-based nanoformulations, which are available in clinical use. In a review, Sanna et al. [2014] reported 6 clinically approved NP-combined chemotherapeutics for cancer and many more under clinical investigation. For instance, Doxil^{TM}, the NP formulation of doxorubicin based on PEGylated liposomes previously discussed, has lower dose-limiting toxicity than doxorubicin, the chemo-agent. It has a circulation half-life of 2-3 days *vs* less than 5 minutes for doxorubicin alone. Abraxane^{TM} is an albumin-based formulation of paclitaxel (which is a mitotic inhibitor) approved by the FDA in 2005 and has higher therapeutic efficacy against breast cancer than the traditional formulation of paclitaxel. It has shown higher tumour response rates, and longer times to tumour progression in patients with metastatic breast cancer. More recently (2007), a micelle based formulation of paclitaxel was approved in Korea. Mesoporous silica NPs, whose size might be in the nanometre range or in the micrometre range, can effectively transport drugs. Metal NPs could be also used for drug delivery, as they have the ability to easily bind to biomolecules. Molecular targeted NPs have achieved impressive clinical results (Wang et al. [2012]). Polymeric NPs or metallic NPs are well suited for targeting therapy. For instance, targeted polymeric nanoformulation based on RNA A10-aptamer, which is overexpressed on the surface of prostate cancers or neovasculature of many solid tumours, has been approved for clinical use (Sanna et al. [2014]).

However, such strategies have also had failures. For instance, liposomal based encapsulation has faced limits. Cisplatin is a platinum based product and belonging to the alkylator class of chemo-agents, which prevent the strands of the double helix of DNA to link as they should, thus affecting the ability of the cancer cell to multiply. Liposomal NP formulations of cisplatin were tested but most of them have failed to demonstrate efficacy in clinical trials, due to a poor release of cisplatin from liposomes. In general, among other limits, these formulations face problems of controlled drug release and stability. Regarding metallic NPs, they induce toxicity due to their accumulation in some organs such as the liver, and therefore their applications have remained mostly at preclinical stage.

NPs as cancer prevention agents Virus like NPs are used as preventive cancer vaccines, with the use of anti-hepatitis B virus (HBV) to prevent HBV-associated hepatocellular carci-

noma, and anti-human papilomavirus (HPV) to prevent HPV-associated cervical carcinoma (Doll et al. [2013]). They also may be used as biomarkers for early detection of cancer cells and monitoring disease progression (Hull et al. [2014]). For instance, cancer cells can be detected by immuno-targeting by conjugating antibody-GNPs with antigens that are overexpressed in cancer cells. It was applied in the detection of prostate-specific antigen using GNPs. The use of NPs for *in vitro* diagnosis is particularly interesting as the lower concentration limit of detection is around the femtomolar (10^{-15} M) (Wang and Tepper [2014]).

NPs as cancer prevention agents Virus like NPs are used as preventive cancer vaccines, with the use of anti-hepatitis B virus (HBV) to prevent HBV-associated hepatocellular carcinoma, and anti-human papilomavirus (HPV) to prevent HPV-associated cervical carcinoma (Doll et al. [2013]). They also may be used as biomarkers for early detection of cancer cells and monitoring disease progression (Hull et al. [2014]). For instance, cancer cells can be detected by immuno-targeting by conjugating antibody-GNPs with antigens that are overexpressed in cancer cells. It was applied in the detection of prostate-specific antigen using GNPs. The use of NPs for *in vitro* diagnosis is particularly interesting as the lower concentration limit of detection is around the femtomolar (10^{-15} M) (Wang and Tepper [2014]).

NPs as imaging agents Superparamagnetic iron oxide nanoparticles (SPIONs) are iron oxide NPs that possess superparamagnetic properties that are not present in other iron oxide materials. When accumulating inside tumours, these NPs have made a strong impact on medical diagnosis with, among other advantages, improved sensitivity compared to traditional MRI. They have been applied in particular in lymph node mapping or lymph node metastasis detection. GNPs have also interesting properties that make them good contrasting agents. Besides, fluorescent agents may be combined to various types of NPs. QDs have been engineered to have specific fluorescent emission properties. The dendrimer polyamidoamine (PAMAM) has also been used as imaging agent, by conjugation with fluorescein isothiocyanate. Carbon nanotubes were applied for x-ray imaging, resulting in better resolution, lower radiation dose and smaller sized equipment (Wang and Tepper [2014]).

NPs as trigger-agents An external stimuli, such as light, heat, ultrasound or a magnetic field, might be used to trigger the therapeutic potential of NPs, as illustrated on Fig. 2.2 C. This may further improve the drug delivery system. For instance, micelle-based drug release may be regulated by external stimuli. Gold nanocages containing doxorubicin covered with a polymer showed that, under near-infrared light, the absorption of the light by gold caused the polymer to collapse, thus releasing the doxorubicin (Raju et al. [2015]). However, this strategy might have drawbacks. Due to the low release of cisplastin from liposomes, another formulation with a built-in drug release trigger was tested. It showed significant renal toxicities, terminating the clinical trial in phase I (Wang et al. [2012]). These types of drugs are under development, and efforts are made to improve the stimuli-responsiveness of these carriers. External stimuli might also consist of exposing NP-loaded tumour to near-infrared radiation or radiofrequency fields, to induce hyperthermic cytotoxicity resulting in tumour ablation. Laser hyperthermia also known as photothermal therapy, may be done using carbon-based NMs, or metallic NPs. The temperature that is locally applied to get hyperthermia is up to 42 °C (Wicki et al. [2015]). Most of malignant tumour cells are more susceptible to elevated temperatures than most normal cells: at 43 °C, they are lethally injured when most of normal cells can recover (Friberg and Nyström [2015]). Additionally, magnetic NPs may be controlled using powerful magnetic field in the target tumour area, and be applied for hyperthermia. Photosensitizing QDs produce radicals upon absorption of visible light. Finally, in the area of medical radiation, heavy-Z NPs have shown promising radiosensitizing effects, which will be discussed in details in Chapter 3.

Multi-modal nanoplatform As opposed to single-tasked NPs that were previously mentioned, a new generation of NPs is currently entering clinical development. Due to the versatility of NMs, NPs may conjugate all of the aforementioned applications in one agent, thus creating the notion

of nanoplatforms. Multifunctional NPs have the ability to perform several tasks at once, such as drug delivery, stimuli systems, imaging or multi-targeting. Theranostic (**thera**py + diag**nostic**) agents are an emerging type of multifunctional nanomedicine, that provide both the diagnosis and treatment within the same formulation (Wicki et al. [2015]). They can monitor the accumulation of the drug in the site, visualize its biodistribution, quantify the amount of drug released and assess therapeutic efficacy. It holds promises for personalized medicine, or may be handy to deal with tumour heterogeneity. Theranostic agents may be use for image-guided analysis of the EPR effect, and thus better control the heterogeneity of the tumour during treatment. There are several theranostic agents in preclinical and some in clinical development (Wicki et al. [2015]). The concept of nanoplatform is illustrated on Fig. 2.3: the NP contains a core as the foundation, to which are attached furtive agents to escape the RES, targeting ligands to specifically bind to cancer cells, and theragnostic agents to allow controlled diffusion of the drug and monitoring at the same time. These new platforms might in particular help against cancer heterogeneity. Note that it is also possible to combine therapeutic modes. For instance, GNPs are a good tool for a combination of phototermal therapy and radiosensitization.

2.4. Challenges in nanomedicine

Although thousands of studies have proven NP-based cancer therapeutic to be effective both *in vitro* and *in vivo*, only a few of them have successfully entered in clinical trials. As summarized by Wicki et al. [2015], the remaining challenges may be divided into 4 points:

Characterization of the product The full physico-chemical characterization of the final product is challenging. In particular, the variability in NP structure, size, composition, surface properties, porosity, charge and aggregation behaviour should be controlled with care, as even a small change in one of these properties might drastically alter the biocompatibility, toxicology and *in vivo* outcomes. Besides, experimental conditions under which the characterization is performed should be representative of the real *in vivo* conditions. In particular, as discussed later, NPs may interact with biological fluids (blood serum) or biomolecules, which may change their aggregation behaviour. Consequently, toxicity that has not been predicted under *in vitro* conditions might unexpectedly occur under *in vivo* conditions. This challenges the transition to clinical routine, and only a few drugs make it all through the four clinical trial phases. The FDA approval rate for all oncology drugs is only around 5 % and estimated to be lower for NP-based therapeutics in cancerology due to additional obstacles that standard cancer drugs do not face (Raju et al. [2015]).

Toxicity With the development of NPs in nanomedicine comes the question of potential toxicity. The toxicity of manufactured NMs, especially under chronic administration, is a major concern. In particular, the choice of materials, their stability *in vivo*, their pharmacokinetic, biodistribution, potential long term retention in vital organs and associated long-term toxicity must be analysed with care for the safe use of nanomedicine. In particular, when reaching the blood stream, NPs can be too large for renal clearance and tend to accumulate in the liver, spleen and bone marrow, which may have long term side effects. Many studies have reported that NPs accumulate in the reticuloendothelial system due to phagocytosis by Kupffer cells, resulting in liver damages (Akhter et al. [2013]). Current knowledge of NPs safety in clinical use is still in its infancy (Akhter et al. [2013]). Mechanisms of action are various and depend on the type of NPs. Their large surface to volume ratio promotes interaction of NPs with the biological system. The consequence is that NPs may affect biological behaviours at the cellular, subcellular and protein level (Nel et al. [2006]). This particular point will be further discussed in chapter 4. Additionally, facing an increasing use of NMs not only for medical use but also in industrial large-scale production areas, toxicity towards the environment is a concern. The monitoring of such objects and the effect of their exposure is to be studied. While a full description of the different toxicological pathways of NMs is beyond the scope of this work, this is a crucial consideration for safe and perennial

translation of NPs from the laboratory *in vitro* experiment to clinical routine.

Regulation With the emergence of this new type of drugs comes the need for potential new regulations. European Technology Platform on Nanomedicine intends to set up a European Nano-Characterisation Laboratory. In USA, the FDA collaborates with the Nanotechnology Characterization Laboratory to facilitate the full characterization and safety issues of these new products. A standardization of the characterization methods is required for a more efficient transition of nano-objects to clinical use (Krug and Wick [2011]).

Manufacturing While the production of NMs in laboratories allow the conception of complex nano-assemblies, the production of these products when transitioning to industry is challenging and inevitable for clinical routine use. The scale up of NPs demands a robust, scalable and continuous process for efficient NP formulation. The complexity of the designed NPs might be a problem when it comes to costs, and might dissuade pharmaceutical companies from taking large-scale production (Sanna et al. [2014]).

2.5. Summary

Nanoparticles (NPs) are commonly defined as objects whose three external dimensions are within 1-100 nm. Due to their small size, they display unique properties. Synthetic NPs are objects that are manufactured intentionally to take benefit of such properties. They have been applied in many fields on an industrial level. In particular, the field of nanomedicine aims at using NPs for the diagnosis and treatment of diseases at the molecular level. A lot of researches in nanomedicine have been dedicated to cancer applications, with the study of a great variety of NPs. Cancer cells may proliferate quickly, forming a tumour that have abnormal vasculature with very large junctions (up to few hundreds of nanometers) compared to normal vessel junctions (5-10 nm), and a defected lymphatic drainage. This facilitates the extravasion of macromolecules, such as NPs, in the tumour interstitial space. This passive targeting is known as the Enhanced Permeation and Retention (EPR) effect. When the NPs are injected intravenously, the EPR effect may be optimised by maximising the life-time of NPs in the blood. To that end, molecules such as polyethylene glycol (PEG) can be used to prevent the recognition and early elimination of NPs by the immune system. In addition, active targeting may also be applied to further favour the tumour accumulation of NPs. Molecules that bin specifically to tumour cells or the tumour microenvironment are attached to the surface of NPs, to increase the ratio of tumour to normal tissue NP concentration. This tumour accumulation has been used for different strategies. Some NPs were used as drug delivery carriers, for instance to improve the delivery of chemo-agents. Other NPs have been proposed as imaging agents, either as contrast agents (MRI, X-rays) or as fluorescent agents. Finally, NPs may be used as trigger-agents. Once localised in the tumour, an external stimuli (light/radiation, heat, ultrasound or magnetic field) is used to trigger the therapeutic potential of NPs. This induce, for instance, hyperthermia or the production of toxic chemical species, resulting in the death of cancer cells. The use of high-Z NPs in radiation therapy are part of this category, as further discussed in the next chapter. The emergence of nanomedicine brings many challenges that are specific to the size and complexity of these new objects. A full characterization of their physico-chemical properties remains challenging. The toxicity is also a central question. These two questions demand a regulation with the establishment of standard methods to evaluate the NPs properties. One last challenge is the industrial manufacturing, that demands a robust method to ensure the reproducibility of NPs.

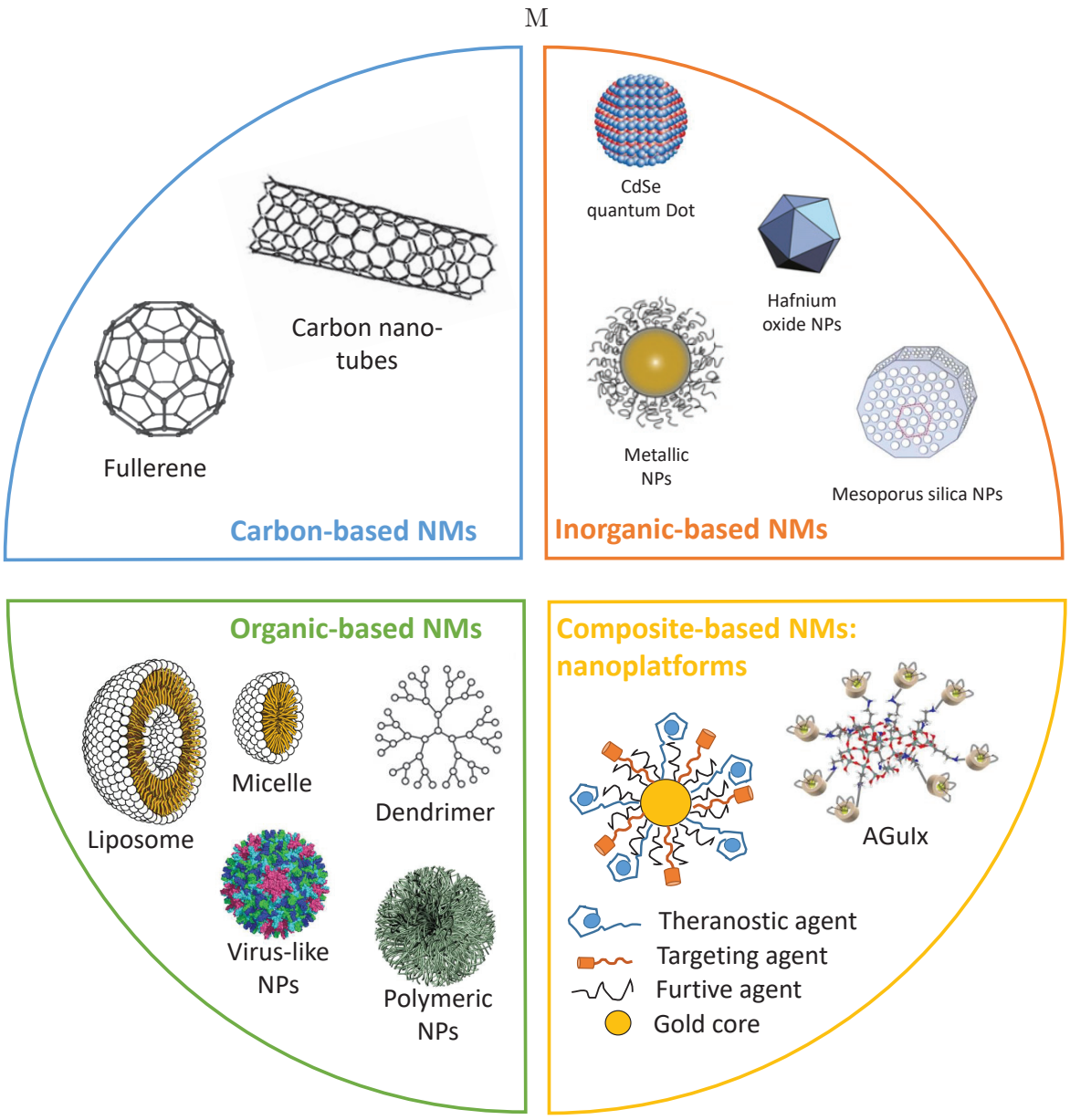

Figure 2.3.: Examples of different nanoparticles used in cancer applications, adapted from Doll et al., Sanna et al. [2013, 2014].

3. Radiotherapy

Contents

Along with surgery and chemotherapy, radiation therapy is the most important modality used in cancer treatment with $\sim$ 50 % of the patients receiving radiation therapy during their treatment, although it accounts for only approximately 5 % of the total cost of cancer care (Baskar et al. [2012]). Radiation therapy may either be used for palliative or curative treatment, contributing towards 40 % of curative treatment (Baskar et al. [2012]). It may also be combined with other modalities (chemotherapy, surgery or immunotherapy). For instance, neoadjuvant therapy consists in irradiating the tumour before surgery to shrink it, while adjuvant therapy destroys microscopic tumour cells that may have been left post surgery. Depending on the source, the treatment is categorised either as internal or external radiation therapy. The former may use liquid sources (systemic therapy, such as radioactive iodine based therapy for thyroid cancer or targeted radionuclide therapy) or solid sources (brachytherapy). To note, the use of NPs combined with radionuclides is under investigation (Lai et al. [2017]), but beyond the scope of this work. Regarding external radiation therapy, most of the current machines use photon beams. The following section introduces the basic mechanisms radiation therapy relies on.

3.1. Mechanisms of action of radiations

3.1.1. Direct *vs* indirect action of radiation

Radiation therapy uses the ability of radiation to penetrate through matter and in particular the human body. When particles travel through cells, they deposit energy by interacting with atoms or molecules of the cell's medium. The energy deposited may induce the destruction of cellular molecules or generate chemical species toxic to the cell, which further induce the death of the cell. The deoxyribonucleic acid (DNA) is usually considered as the main cellular target of radiations. Its destruction may be induced by physical or chemical mechanisms, usually categorized as direct and indirect effects of the radiations.

The direct action is usually referred to as the direct ionization/excitation of the target, thus eventually leading to irreversible damages. Direct actions are believed to dominate for particles having a high Linear Energy Transfer (LET), such as ions.

The indirect actions of radiations are due to the interaction of radiations with other atoms and molecules that induce the creation of reactive chemical species. These chemical species are mostly created by the interaction of radiation with water, as cells are constituted of 80 % of water on average (Hall et al. [2006]). This is known as the water radiolysis. A cascade of chemical reactions lead to the creation of reactive oxygen species (ROS) (such as hydroxyl radicals $^{\bullet}OH$ or hydrogen peroxide H_2O_2) and reactive nitric species (RNS), that eventually attack molecules of the cell. Most of these species have very short life-time. For example, it is estimated that the hydroxyl radical has a life-time of 10^{-9} s in cells (Hall et al. [2006]).

Both mechanisms occur at a very short time scale following the interaction of a radiation with an atom (e.g. primary interaction). Direct radiation damage is initiated in the range of 10^{-14} - 10^{-12} s following the interaction of radiation with an atom, with the breaking of S-H, O-H, N-H and C-H bonds. Indirect damages by radiolytic products start at 10^{-12} s, with thiol depletion and further bond breaking (C-C and C-N). In comparison, biological consequences of direct and indirect actions occur at much longer time. While by 1 ms after the primary interaction, the repair processes are initiated, biological consequences of irradiation may appear minutes, hours or even years following the irradiation. In the next section, the main cellular conditions influencing the lethality of radiation is described.

3.1.2. Radiosensitivity

The radiosensitivity of a cell is defined as its relative susceptibility to the effect of ionizing radiation. There is a great variation of the radio-sensitivity depending on the cell line, and depending whether cells are healthy or cancerous. For instance, the more differentiated cells are, the less they multiply thus making them more radioresistant. The ability of the cell to repair damages is also fundamental in radiosensitivity. Besides, both the cell-cycle and level of oxygen affect the radiosensitivity, as further discussed. To note, genetic diseases may also induce a particular radiosensitivity or radioresistance, but this is beyond the scope of this work.

Cell-cycle During its life-time, the cell undergoes different metabolic reactions that form the cell-cycle and lead to the replication of chromosomes and cell division. As displayed on Fig. 3.1, a cell-cycle is made of 4 successive steps (Gap 1 (G_1), Synthesis (S), Gap 2 (G_2) and Mitosis (M)) during which the cell is more or less radiosensitive.

The first 3 phases (G_1, S and G_2) are part of the interphase and are consecutive to the cell division. During these phases the cell takes up nutrients in order to be capable of dividing again, and makes a copy of DNA. It occupies typically 91 % of the total time of the cell cycle. The G_1

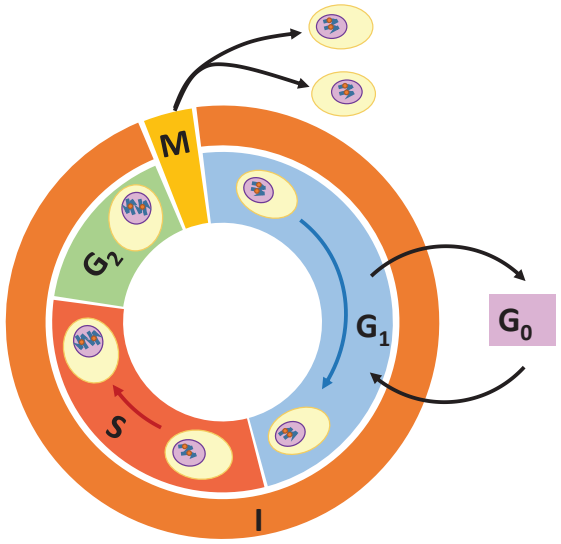

State	Phase	Description	RS
Resting	Gap 0 (G_0)	The cell left the cell cycle and stopped dividing	- -
Inter-phase	Gap 1 (G_1)	Growth phase Increase of proteins, number of organelles	- - +
	Synthesis (S)	Rapid synthesis and replication of DNA and histones	+ -
	Gap 2 (G_2)	Preparation for mitosis and cell division	+ +
Cell division	Mitosis (M)	Relatively short period during which the cell divide	+ + +

Time

Figure 3.1.: The different phases of cell cycle, their function and their radio-sensitivity (RS).

phase is the first phase during which the cell increases in size, copies organelles and synthesize proteins it will need for the next phase. The biosynthetic activities are considerably increased with respect to previous phase. Its duration varies from one cell type to another. It is normally a period of radio-resistance, which declines towards the S phase. The S phase is the phase during which DNA (in form of chromosomes) is duplicated. The radio-sensitivity decreases towards the end on this phase. The G_2 phase is the second phase of cellular growth, during which the cell increases proteins and organelles and begins to organize its content in preparation for mitosis. It is almost as sensitive as the mitotic phase. The division occurs during the mitosis, leading to the creation of two daughter-cells. It is the most radio-sensitive phase of the cell cycle, but also the shortest (about 1h). Cells may exit G_1 phase and enter a resting state, the G_0 phase. This phase is permanent for some cells, but may also go back to the G_1 phase.

Each of these steps are tightly controlled by the cell and essential to conserve its integrity. The movement of cell cycle is driven by cyclin-dependent kinases (CDKs), which phosphorylate other proteins to initiate progression through the cycle. Many checkpoints control the integrity of the cell before further proceeding in the cell cycle. As further discussed, DNA damages often lead to arrest at cell cycle checkpoints. In particular, the S phase arrest enables repairs of the radiation-induced damages before they are permanently fixed by DNA replication into irreparable chromosomal breaks.

Oxygen level In biological media, organic radicals ($R^\bullet$) that are created following irradiation rapidly react with O_2, creating peroxyl radicals ($RO_2^\bullet$). They further form ROOH by interacting with other surrounding molecules, causing a permanent fixation of the damages. This cascade of events relies on the presence of oxygen. Therefore cells that are lacking oxygen are usually radioresistant. This is of clinical relevance as, as previously mentioned, parts of the tumour might lack oxygen supplies due to poor tumour vascularisation, in particular in the inner part of the tumour. The ratio of doses administered under hypoxic to normoxic conditions to reach the same biological effect is called the oxygen enhancement ratio (OER). For sparsely ionizing radiation, the OER is usually around 3 for doses larger than about 2 Gy, and about 2 for lower doses. Only small amount of oxygen is required for radiosensitization: 0.5 % of oxygen results in a radiosensitivity halfway between hypoxia and full oxygenation. Note that the oxygen level has

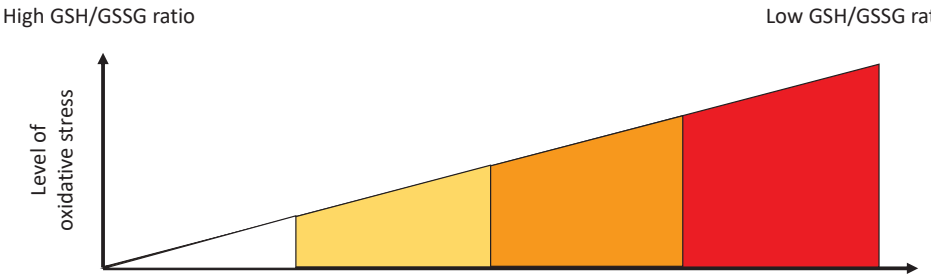

Response pathways	Normal	Anti-oxidant defense	Inflammation	Cytotoxicity
Signaling pathway		Nrf-2	MAP Kinase NF-kB cascade	Mitochondrial permeability transition pore
Genetic response		Anti-oxidant response element	AP-1 NF-kB	N/A
Outcome		Phase II enzyme	Cytokines Chemokines	Apoptosis

Figure 3.2.: Response to oxidative stress depending on the ratio of GSH/GSSG, adapted from Nel et al. [2006]. N/A means not applicable.

different consequences depending on the cell cycle stage the cell is in. Besides, the oxygen effect is much more pronounced for sparsely ionizing radiations such as X-rays or γ-rays than for ions (Colliaux et al., Colliaux et al. [2011, 2015]).

3.1.3. Oxidative stress and molecular consequence

Oxidative stress plays a central role in radiation-induced damages. It is important to note that the production of ROS occurs naturally in cells. For example, the mitochondrial ROS are the largest contribution of natural ROS (Simonet [2018]) and are produced through the mitochondrial electron transport chain. The nicotinamide adenine dinucleotide phosphate (NADPH) oxidase is a membrane-bound enzyme that catalyses the production of superoxide ($O_2^{\bullet -}$). Cells constantly adjust their level of ROS to maintain a physiological level that is harmless to its constituents. Cellular pathways that are activated by ROS are not always deleterious. Besides, in many cancers, ROS upregulate some pathways which increase proliferation, promote survival, alter metabolisms and increase cellular mobility (Simonet [2018]). Any damages to constituents involved in these pathways may induce a deregulation of the complex mechanisms affecting the level of ROS production, and trigger an additional burst of oxidative stress.

As ROS are naturally present, cells have mechanisms (cellular antioxidants) to handle oxidative stress and maintain a normal intra-cellular balance. The superoxide dismutase (SOD) converts highly reactive superoxide radicals into less reactive peroxide radicals (H_2O_2). H_2O_2 may be further destroyed by peroxiredoxins (Prx) and thioredoxin (Trx) to form water, or react with monomeric glutathione (GSH) to form water and glutathione disulfite (GSSG) (Arora et al., Colliaux et al. [2012, 2011]).

As mentioned in section 3.1.1, the products of water radiolysis induce the production of both ROS and RNS. For instance, it has been reported that physiological concentration of H_2O_2 was comprised between 10^{-8} - 10^{-7} M, while a 2 Gy irradiation would produce 10^{-7} M of H_2O_2 (Reisz et al. [2014]). In addition to a chemical primary boost, ROS and RNS may further increase at longer time scales (tens of second following irradiation) through indirect mechanisms. Immediately

after the irradiation, the antioxidant supply becomes compromised, leading for example to an increased level of GSSG. As displayed on Fig. 3.2, the ratio of GSH/GSSG in the cell might trigger different cellular pathways, in an effort to handle the oxidative burst. Under normal conditions, more than 95 % of GSH in the cell is reduced and thus the ratio is high. At low oxidative stress (the ratio increases), phase II anti-oxidant enzymes are induced via transcriptional activation of the antioxidant response element by Nrf-2 to restore cellular homeostasis. At intermediate oxidative stress, activation of MAPL and NF-κB cascades induce pro-inflammatory responses. At high oxidative stress, the apoptosis (programmed cell death) is triggered. Depletion of GSH can induce oxidative stress without the intervention of ROS.

During irradiation, direct and indirect production of ROS disrupt the cellular redox balance, inducing efficient modification of small molecules such as nucleic acids, lipids or proteins, that further damage cell organelles. Nucleic acid modification leads to DNA damages, which has long been considered as the primary mechanism responsible for the genotoxic effect of radiations. Lipids constitute the cell membranes and are estimated to be about 5 nm thick (the membrane is made of a double layer of lipids). Radiation generates lipid peroxidation that may induce membrane permeability, disruption of ion gradients and affect other transmembrane processes. Lipids of the organelle membranes may also undergo peroxidation. Recently, with improvement of technologies, it has been possible to also study the effect of irradiation on proteins, and how their alteration may impact the cellular fate. Impact of irradiation (IR) on the proteome (the ensemble of proteins that constitute the cell) was long underestimated, but is now accepted to affect cellular processes. Proteins may be oxidized or reduced, and the profiling of protein expression changes in response to IR. Its consequences at cellular scale is an active area in research (Reisz et al. [2014]).

In the next section, the consequence of these molecular damages at the cellular level are explored.

3.1.4. DNA as the target

DNA structure DNA is believed to be the main radiation target and its damages induce cell killing, carcinogenesis and mutations. DNA is a large molecule made of two strands that are held together by hydrogen bonds between bases, which carries the genetic information the cell uses to grow, develop, reproduce, etc. Each strand is an alternation of sugar (deoxyribose) and phosphate groups, to which are attached four types of bases (adenine, cytosine, thymine and guanine). The width of a DNA strand is about 2 nm. Although any molecule (proteins, enzymes, etc.) of the cell might get ionized by IR, most of them have multiple copies, limiting the consequences of their damage. In contrast, DNA has only two copies and a limited turnover. The consequence of its damage might therefore be serious or lethal to the cell (Wouters and Begg [2009]). Under normal conditions, healthy cells may undergo DNA damages, and thus they have developed mechanisms to face genotoxic risks.

DNA damages During an irradiation, a large number of DNA lesions are produced, which may or not be repaired. There are many types of DNA lesions and their severity varies. The ones most commonly studied in radiobiology are DNA single-strand breaks (SSBs) and DNA double-strand breaks (DSBs). The former one consists of phospho-sugar bond breakage of one strand, while the later one consists of the breakage of the bond of both breaks on sites close to each others. On average, after a 1 Gy irradiation of a cell with X-rays, one may find approximately 10^5 ionizations, 40 DNA double-strand breaks (DSBs) and 1 000 DNA single-strand breaks (SSBs) (Hall et al. [2006]). SSBs are usually easily repaired (within one hours) and have thus little impact of cells viability. DSBs are believed to be the most important lesions produced by radiations in chromosomes. Besides, the number of unrepaired DSBs 24 hours after IR, also known as residual DSBs, correlates well with radiation lethality. They increase when cells are irradiated with higher LET particles due to denser ionization clusters, compared to low LET radiation.

DNA repair The DNA damage response is a complex and coordinated system, made of many signalling pathways (Wouters and Begg [2009]). This may be divided into two parts: the sensors of DNA damage and the effectors of damage response.

- During the sensing of damages, lesions are detected by sensor proteins. A large number of proteins, such as ATM (Ataxia Telangiectasia Mutates) and ATR (Ataxia Telangiectasia RAD3 Related) belonging to the kinase group, are recruited and bind to the DNA damage site. This region eventually form a *foci* which may be detected by the use of microscope. For instance, the detection of γH2AX, the phosphorylated form of the histone H2AX, is a highly sensitive method for detecting the presence and/or repair of DSBs. This occurs within 15-30 minutes post irradiation. Then, the information is transmitted to effector pathways: phosphorylated proteins active various downstream effectors.

- During the effector part, three main effector pathways may be activated which together determine the fate of the cell.

  1. Programmed cell death. The protein group p53-MDM2 are both phosphorylated by ATM, destabilizing their interaction, leading to the up-regulation of many target genes of p53, among which the pro-apoptotic genes BAX and PUMA.
  2. Activation of cell-cycle checkpoints by inhibition of the cyclin-CDK complex. This temporary blocks the progress of cells through the cell cycle. For instance, activation of p53 inhibits the G1 cyclin-CDK, preventing from entering the S phase of the cycle. Likewise, irradiation may slow the progression through during S phase, prevent entry into mitosis during early G2, or induce accumulation of cells into the G2 phase. These checkpoints may affect the radiosensitivity of cells to multiple (fractionated) doses, as it induces a redistribution of the cell cycle. Note that tumour cells may miss some of these checkpoints due to genetic mutations.
  3. DNA repair. Sensor proteins may also initiate DNA repair, in which case the cell stops other activities such as transcription or cell-cycle progression. Each lesion type has its repairing pathway: the single-strand breaks repair (SSBR) for SSBs, and the homologous recombination (HR) and non-homologous end-joining (NHEJ) for DSBs. HR uses homologous undamaged DNA to repair the DSB. The whole process lasts up to 6 hours or more to complete. NHEJ takes less time but is less accurate as it is often associated with small DNA deletions or insertions. As HR requires a homologous chromosome, it is rare or absent in G1 where there is no sister chromatid. Mutations or deletions on genes involved in SSBR, HR or NHEJ lead to increased radiosensitivity.

3.1.5. Beyond DNA damage

The mechanisms involved in radiation-induced cellular injury and death remain incompletely understood (Persson et al. [2005]). The DNA-centric approach has been questioned due to divergences existing between cell killing and DNA damages in some cell-death pathways. This has led to the emergence of a new category of responses, namely non-targeted responses, in which biological effects are not directly related to the amount of energy deposited in the DNA of cells. The first paragraph is an example of such a divergence, while the other paragraphs give some insights on radiation effects on other cellular components, at either molecular or organelle scale.

Bystander effect Despite many evidences showing the correlation between DNA damages and cellular lethality, sophisticated experiments have shown that mutations can be induced by α-particles which pass through the cytoplasm and never touch the nucleus. This was first observed with irradiation of cells with high LET α-particles. While less than 1 % of irradiated cell nuclei were estimated to have been traversed by particles, 30 % of the cells showed an increase in sister chromatid exchanges. This was also observed using soft X ray microbeams. Besides, a number

of experiments have shown that cell death can occur in cells that have not been exposed to IR, but are in contact with neighbour cells that have been irradiated. This indirect effect is known as Bystander effect, which encompasses a less understood type of cell death. Studies have suggested that irradiated cells secrete factors that can damage non-irradiated cells. Cytokines such as tumour necrosis factor α or interleukin 8, ROS such as hydrogen peroxide or superoxide anions or miRNA (micro-ribonucleic acid) might be involved in the process. The Bystander effect may trigger many pathways: altered gene expression, damage in the DNA, cell proliferation alterations, cell death or changes in the translation process in non-irradiated cells (Rosa et al. [2017]).

Mitochondria damages On an organelle level, mitochondria may be considered as a direct intracellular target of ionizing radiations. Mitochondria are essential to human cells as they produce the energy the cell needs, using among other dioxygen. A singularity of these organelles is that mitochondria have their own DNA. They are also involved in multiple other tasks making them central organelles affecting the fate of cells. In cancer cells, their function might be altered. For instance, some cancer cells upregulate alternative anaerobic ways of creating energy, thus making them hypoxic-resistant. Mitochondria are also considered as a suicidal weapon that can be activated under stress. They control apoptosis via regulating the translocation of pro-apoptotic proteins from the mitochondrial intermediate space to the cytosol. However, cancer cells overexpress anti-apoptotic proteins, and thus are more resistant to apoptosis. Mitochondria also play a major role in the regulation of oxidative stress. While under normal physiological conditions or in cancerous cells a continuous amount of ROS is produced, their concentration greatly increases after irradiation and products of lipid peroxidation accumulate. Thus, alteration in the mitochondria are frequently observed. These altered mitochondria may further release their ROS causing additional damages or trigger apoptosis. Damages to mitochondrial DNA may also be deleterious (Simonet [2018]).

Lysosome damages Lysosomes are the main digestive organelles of the cells. They make up about 5 % of the intracellular volume and have different sizes and morphology (Canton and Battaglia [2012]). While lysosomes have long been considered as 'garbage disposal units', recent findings have shown that cancer cell death could be triggered by the release of lysosomal enzymes such as cathepsins. Although it was believed for long that the break of lysosomes was a late consequence of necrotic death, some studies have suggested that early lysosome damages could occur at early stage during cell death. Lysosomal membrane permeabilization (LMP) could be fatal by releasing the lysosome contents into the cytosol. During irradiation, the number and volume of lysosomes increase along with their enzymatic activity. Lysosomal enzymes have been observed in the cytosol and the extracellular fluid (Somosy [2000]). It was suggested that the production of H_2O_2 during irradiation inside lysosomes, or their accumulation inside lysosomes by diffusion from the cytosol, could trigger Fenton like reactions as lysosomes contain redox-active iron, thus generating $^{\bullet}OH$ that would induce lysosomial membrane rupture. By exposing Jurkat T-cells to H_2O_2, Antunes et al. [2001] showed that concentrations of cytosolic H_2O_2 from 0.7 to 3 µM (corresponding to $\approx$ 2 - 20 µM extracellular H_2O_2 under steady-state conditions) were sufficient to induce lysosomal rupture. The release of lysosomal content (redox-active iron, or hydrolytic enzymes) could trigger autophagy and necrosis. It could also trigger apoptosis, as observed by Antunes et al. [2001], potentially by causing mitochondrial outer membrane permeabilization (Biswas and Torchilin [2014]). Additionally, the released redox-active iron could relocate to the nuclear and mitochondrial DNA, thus making the cell more radiosensitive after a second irradiation as it was observed by Persson et al. [2005].

Cellular membranes On a molecular level, irradiation could impact cellular membranes. An alteration of the amount and/or distribution of the negatively charged membrane components on cell membranes post irradiation was observed (Somosy [2000]). The cellular membrane damages may also impact the number and/or response of several receptors. Although controversial, studies suggested that energy deposited in cell membranes only could trigger apoptosis (Prise et al. [2005]). Besides, membrane lipid peroxidation increases its permeability, which may re-

sult in cells inability to maintain ionic homeostatis (Simonet [2018]). The involvement of the membrane to radiation response has come back into considerations (Prise et al. [2005]).

Other cellular targets The Endoplasmic Reticulum (ER) plays an essential role in protein synthesis, folding, trafficking and dynamic calcium homeostasis. Activation of caspase-8-mediated apoptotic pathway occurs in response to the ER stress. ER lumen is a major site of Ca^{2+} storage, the release of which promotes cleavage of caspase-8 and initiates ER stress- induced apoptosis. It has been observed on some cell lines that irradiation caused ER stress (Simonet [2018]). The cytoskeleton may also be impacted by cell IR with a disorganization of actin network and disruption of intermediate filaments (Somosy [2000]).

3.1.6. Cell death

In radiobiology, cell death is usually assessed by determining clonogenic survival, *i.e.* the ability of a cell to proliferate after irradiation. It hence includes any process that leads to the permanent loss of clonogenic capacity. However, cell death under irradiation may be generated through many pathways and at different times. There are many mechanisms leading to cell death, which all have molecular and morphological distinctions. These pathways are differentially activated in different tissue types and are frequently altered in cancer.

- **Apoptosis.** It is a programmed cell death that is activated either by the cell itself when undergoing stress or by signals generated externally. During mitosis, cellular contents are fragmented into many membrane-enclosed apoptotic bodies which are, *in vivo*, taken up by phagocytes. The molecules involved can be divided into the sensors, which make the decision to initiate apoptosis, and the effectors which are carrying out the decision. It may be triggered by DNA damages through the p53-mediated pathways that upregulate the proapoptotic protein BAX. However, other cellular components may initiate apoptosis. Caspase 8 is an example of apoptotic sensor, which normally activates upon the binding of an extracellular ligand to a cell death membrane receptor, such as the tumour necrosis factor (TNF). Caspase 9 is another example, and its activation is controlled in large part by the balance of pro- and anti-apoptotic proteins that reside in or near the mitochondria. After irradiation, this balanced can be tipped in favour of apoptosis.

- **Autophagy.** Meaning self-eating, it designates a process in which cells digest parts of their cytoplasm components using lysosomes. The understanding of autophagy is still an active area. It may be activated in response to growth factors or starvation. While this may help survival under harsh conditions, it can also lead to a distinct form of programmed cell death. The signals for the induction of autophagy after irradiation are still unclear, but it may imply the stress of endoplasmic reticulum and the redox imbalance (Stagni et al. [2018]).

- **Senescence.** Senescence designates cells that have lost permanently their ability to divide, but maintain their activity. After irradition, cellular senescence prevents proliferation and thus contributes to tumour recovery.

- **Necrosis.** It is usually considered to be an uncontrollable, irreversible and chaotic form of cell death, under extremely unfavourable cellular conditions. However, more recently, some studies have suggested that it may be regulated. In particular, cell stress including oxidative stress, calcium levels and p53 activation have been shown to influence lysosomal membrane permeability, leading to intracellular acidification and release of various enzymes that promote necrosis.

- **Mitotic catastrophe.** This type of cell death designates cells that fail to complete mitosis correctly, due to entry of cells into mitosis with unrepaired or misrepaired DNA damage.

This is frequently the case of irradiated cells. They show a particular morphology, including chromosome aberrations, micronuclei, etc. These cells may lose their replicative ability simply from a physical inability to replicate and separate the genetic material correctly. It may also trigger the aforementioned cellular death pathways, which are in this case a secondary consequence of cell irradiation. Several checkpoints in G2 and throughout mitosis may prevent mitotic catastrophe.

All these types of cell death and their occurrence upon irradiation strongly depend on the cell type. For instance, the pro and anti-apoptotic balance is extremely dependent on the cell line, thus apoptosis varies depending on the irradiated cell. Besides, genes regulating apoptosis of cancer cells are generally altered. The dose of irradiation might also be a decisive factor for the type of cell death. The form of cell death may influence the rate at which cells die and thus the tumour regression. In a small minority of cell types, cell death may occur within hours post irradiation. It is limited to cells that proliferate rapidly, and cancers such as lymphomas are particularly responsive to irradiation. However, this type of cell death is rarely observed in solid tumours. The vast majority of cells (cancerous or normal) usually undergo late post-mitotic cell death. Cells may undergo many replications before they cease proliferation. Thus, most of cells have the time to activate both cell-cycle checkpoints and repair pathways. The signal for cell death does not directly arise from radiation-induced damages, but is rather the consequences of failure to properly complete mitosis.

3.2. Experimental assessment of radiation effects

3.2.1. Experimental assays

The goal of radiation therapy is not necessarily to kill cancerous cells, but to stop their proliferation. While 100 Gy is usually necessary to destroy cell function in non-proliferating systems, the mean lethal dose for loss of proliferative capacity is usually less than 2 Gy (Hall et al. [2006]). Clonogenic assays aim at measuring the ability of clonogenic cells to produce a sizeable colony of descendants. They have formed the basis of cellular response to radiation. The experiment consists of keeping single-cell suspension of tumour cells irradiated or not (control) under identical conditions and, after a given time of incubation (1 to 2 weeks), scoring the colonies. Any colony that reaches less than 50 cells (which represents 5 or 6 generations) is not accounted for, as they are considered to have lost their ability to proliferate. The control cells enable to calculate the plating efficiency (PE) and the final surviving fraction is given by:

$$\text{Surviving fraction} = \frac{\text{Colonies counted for irradiated cells}}{\text{Cells seeded} \times \text{PE}} \tag{3.1}$$

Other experimental measurements may also be performed. The 3-(4,5 dimethythiazol-2-yl)-2,5-diphenyl tetrazolium bromide (MTT) is a colorimetric assay that estimates cell metabolic activity based on the enzymatic reduction of tetrazodium dye, and thus reflects the number of viable cells. As mentioned previously, it is possible to measure DNA damage directly by the detection of γH2AX. Recently, additional assays have been used to assess protein expression, or the type of death cells undergo, in order to better understand the fundamental mechanisms of cell death upon irradiation.

3.2.2. Describing the relationship between cell survival and radiation dose

Cell survival is usually given in % and represented using a semi-logarithmic scale. Under low LET irradiation, the curve usually starts out straight on the semi-log scale, with a finite initial slope

(i.e. the surviving fraction is an exponential function of the dose). Then, at higher doses, the curve tends to bend for a dose range of a few grays. Eventually at very high doses, the survival curve often straighten again. Descriptive models are used in radiobiology research to provide a framework in which to analyse and compare data, and are further detailed elsewhere (Joiner [2009]). Many models have been developed, but the mostly used one is the Linear Quadratic Model. The shape of cell survival curve is fitted by,

$$S(D) = \exp(-\alpha D - \beta D^2). \tag{3.2}$$

The shape of the curve is determined by the α/β ratio. The use of the LQ model is widespread in both experimental and clinical radiobiology. Several interpretations of the α and β coefficients have been made. One common interpretation is that the α parameter represents the formation of complex lethal DNA damage while the β parameters represent sub-lethal damages. This is supported by the fact that, upon ions irradiation, the β parameter tends to 0, and this type of beam is well known for inducing complex lethal damages. Another idea is that the linear component ($\exp(-\alpha D)$) might result from singe-track events while the quadratic component ($\exp(-\beta D^2)$) might result from two-track events, which is supported by studies showing that the survival of cells at low dose rate tends to become straight. Another completely different interpretation suggested that α would represent recognized but non-repaired damages while β would represent non-recognized, thus non-repaired damages (Bodgi and Foray [2016]). This model represents well cell survival response to dose within clinical (< 6 Gy) range, with the exception of very low doses (< 1 Gy).

3.3. Limits of radiation therapy and strategies

A major limit of radiations is the lack of selectivity towards tumour tissues. As the particle beam travels through the body, energy may be deposited inside healthy tissues, potentially damaging healthy cells and inducing undesired size effects. Additionally, one may face tumour resistance and recurrence. As previously discussed, tumours are usually extremely heterogeneous with a hypoxic region that is usually extremely radioresistant. Besides, some tumour cells may be located farther away from the site of radiation and hence might receive a lower dose (Kwatra et al. [2013]). Thus, radiotherapy faces challenges: the delivery of enough dose to the tumour to effectively kill or inactivate cancer cells and avoid recurrence, while being able to preserve surrounding tissues, especially the ones from organs at risk. Different techniques may be used to improve this therapeutic ratio and are discussed thereafter.

Fractionation A common approach is the use of fractionation, which consists in delivering dose to the tumour during successive sessions. This is based on the capacity of normal cells to handle better sublethal damage repair than cancer cells. As they proliferate slower, they have more time to repair the damages before undergoing division. A typical radiation therapy treatment consists of daily fractions from 1.5 to 3 Gy for several weeks (Baskar et al. [2012]).

3D conformal therapy With improvement of imaging modalities, delivery systems and software, the focus of dose inside the tumour has become more achievable. 3D conformal radiotherapy is based on CT imaging to accurately localize the tumour, thus allowing an optimum beam placement and shielding to maximize the dose to the tumour while sparing organs at risk. By varying the angle of incidence of the beam, it is possible to focus the dose inside the tumour and minimize the dose to healthy tissues. Intensity modulated radiation therapy (IMRT) is based on inverse planning software and computer-controlled intensity-modulation of multiple radiation beams and allows improvements in the therapeutic ratio for several tumour sites. Compared to 3D conformal radiotherapy, it is based on smaller beams, whose intensity may be changed to give higher doses in some parts of the tumour. Image-guide radiotherapy (IGRT) is a type of IMRT that uses

imaging during the treatment to detect potential tumour's size and position changes, and adapt the treatment if needed. At last, stereotactic body radiation therapy consists of delivery high individual doses of radiation over only a few treatments to ablate small well defined primary tumours.

Hadrontherapy Another possibility is to switch from photon-based irradiation to other types of particles, such as ions (protons or carbon ions), better known as hadrontherapy (Durante et al., Kamada et al., Schardt et al. [2017, 2015, 2010]). Ions have unique physical and radiobiological properties. They can penetrate through tissues with little diffusion, and lead to a maximum energy deposition at the end of their path, a phenomenon known as the Bragg peak (Karger and Peschke [2017]). This allows a precise definition of the specific region to be irradiated. Additionally, ions deposit their energy in a more heterogeneous way than photons, generating dense tracks that are highly lethal when traversing a sensitive biological target. They generate damages that are less repairable by the cell, inducing a higher radiobiological effectiveness than photons.

Radiosensitization and radioprotection While the aforementioned techniques have greatly improved the therapeutic ratio, they face issues due to limited dose delivery, organs at risk located near the tumour, or cells located on moving organs. A last possible strategy to improve radiation treatment is the use of radiosensitizing or radioprotector agents. Usually, a prerequisite is to preferentially accumulate these agents within the tumour (radiosensitizers) or the healthy tissues (radioprotector) to increase the differential response between cancer cells and normal cells. The former emphasizes the response of cancer cells to the radiation treatment, by either making them more radiosensible or by reversing the radioresistance of some cancer cells. Many strategies can be adopted based on the radiation therapy mechanisms explained previously. For example, modulating the DNA damage response by blocking cancer cells DNA repair mechanisms was proposed. Another way is to modulate cell cycle checkpoints, which may block cells in a phase, inducing eventually a failure in DNA repair and thus induction of cell death. The use of radiosensitizing agents by targeting radioresistance may be applied as cancer cells have biological pathways that make them more resistant upon irradiation. One example is the protein survivin, which is overexpressed in many cancer cells. Despite their interesting properties, only a few of these agents have made it in pre-clinical studies in combination with radiation therapy. They lack cancer selectivity and thus face toxicity issues (Simonet [2018]).

Nanomedicine and radiation therapy Despite its constant improvement, radiotherapy may still fail at eradicating the tumour and efforts are still required to improve the therapeutic ratio. NPs are a new emerging type of agent that may be utilized in combination with radiation therapy. As mentioned in chapter 2, NPs have shown good capability for passive or active targeting of cancer cells. Thus, NPs may be used as nanocarriers to improve the delivery of chemical substances that make cancer cells more radiosensitive, or use NPs to deliver chemotherapeutic substances and thus combine radiation therapy with chemotherapy. Another approach is to use high-Z NPs which, when combined with radiation therapy, have shown experimental potential capabilities to act as a contrast agent and increase the local dose deposition. There are also cumulating evidences that these types of NPs may also trigger chemical and biological mechanisms that induce radiosensitizing effects, as further discussed in the coming section.

3.4. Nanoparticles in radiation therapy

3.4.1. Discovery of the effect

With the rise of nanomedicine, the application of NPs to radiation therapy has been investigated for the last 20 years (Douglass et al. [2013]). The first idea was to use high-Z NPs as a physical contrast agent with kilovoltage photons. The photo-electric effect cross section varies $\propto Z^n/E^3$,

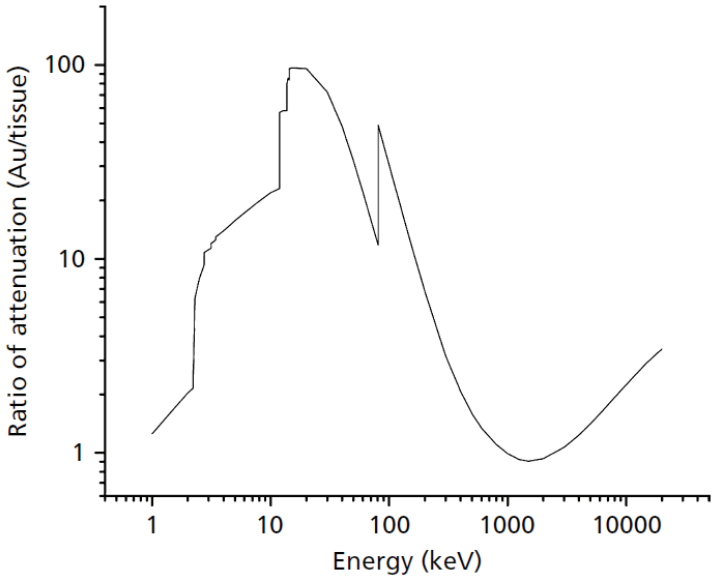

Figure 3.3.: Ratio of photon attenuation (in g·cm^2) in gold and in tissues. A factor of nearly 100 is obtained at 20 keV. Taken from Hainfeld et al. [2008].

where E is the energy of the photon, where Z is the atomic number of the material the photon is propagating in and n varies from 4 to 5 depending on the value of E (Cooper et al. [2014]). Thus, tumours loaded with high-Z materials absorb more photons compared to tissues and more dose is deposited. This is illustrated by Fig. 3.3, which compares photon attenuation in gold and tissues as a function of the photon energy. When calculating the ratio, a peak of 100 is obtained at $\sim$ 20 keV. The use of high-Z materials to enhance dose absorption is not new, and the investigation began in the late 1940s (Douglass et al. [2013]). Iodine was for instance discovered to behave like a contrast agent for X-rays. However, accumulation of high-Z material inside the tumour has always been challenging *in vivo*.

The emergence of nanomedicine with high-Z agents in radiation therapy started with the use of gold microspheres by Herold et al. [2000]. Gold microspheres were suspended in cells *in vitro* or injected in tumours *in vivo*, and irradiated with kilovoltage X-rays and Cs-137 beams. *In vitro*, authors reached dose ratios for 10 % survival with *vs* without microspheres ranging from 1.36 to 1.54, while preliminary *in vivo* results showed a modest effect with an extremely heterogeneous distribution of microspheres. A few years later, the use of NPs *in vivo* was proposed by Hainfeld et al. [2004], which overcame the problem of heterogeneity. Mice bearing subcutaneous EMT-6 mammary carcinomas received a single intravenous injection of 1.9 nm diameter GNP with concentrations up to 2.7 g of gold per kg body weight, reaching 7 mg of gold per g in tumours. Imaging showed a high accumulation of GNPs in the tumour due to leaky vasculature. Two minutes post injection, mice were irradiated once with 250 kVp x-rays at 5 Gy·min^{-1}. Mice tumours showed an important decrease of the tumour volume one month post-treatment compared to irradiation only, for an irradiation at 30 Gy. For an irradiation at 26 Gy, the one year survival of mice who received only irradiation was 20 %, while mice receiving 1.35 or 2.7 g Au/kg before radiation showed 50 % and 86 % one year survival. Due to the short time lapse between injection and irradiation, most of NPs were located in the blood, and as tumours are extremely vascularized (at least in the periphery), GNPs acted as an anti-angiogenic therapy. This first study showed promising 'proof-of-principle' results, and in particular overcame previous issues faced with contrast agent with regard to tumour accumulation. This study paved the way towards a new application of NPs.

3.4.2. Emerging mechanisms

Many studies followed both *in vivo* and *in vitro*, with GNPs but also other high-Z materials. These studies enabled to evidence different mechanisms of actions that are listed thereafter.

Global dose enhancement As previously mentioned, a first effect is the increase of the macroscopic dose. Monte Carlo simulations predict that, for tissue loaded with 0.5 - 1 % by weight of gold, one may achieve a dose enhancement factor of about 2 when using conventional 80 - 140 kVp X-ray tube sources. In clinical applications, the use of keV photons are limited to superficial tumours due to low penetration (half length of the order of cm). Therefore, the use of GNPs was also tested in the MeV energy range. *In vitro* experiments showed significant effects, despite the fact that no particular contrast is observed between gold and tissue photon absorption (Butterworth et al. [2013]). This was a first evidence showing that the dose enhancement might not be enough to explain the extent of the biological effect. Besides, many *in vitro* experimental results showed an enhancement of cell death that was beyond what was expected with the physical dose enhancement, even for keV photon energies. Other mechanisms were thus investigated.

Local dose enhancement Additionally to this macroscopic increase, it was quickly suggested that Auger electrons might be responsible for local dense clusters of ionization that might be more lethal to cells, similarly to what is observed in hadrontherapy (Kobayashi et al. [2010]). When a high-Z atom is ionized, a vacancy is created on the shell from which the electron is ejected. Dense materials such as gold have many atomic shells, and if the electron is ejected from a deep shell, the atom is left in a highly unstable state. During the consecutive desexcitation process, electrons from outer-shells 'fall' into the vacancy, and the extra-energy coming from the difference of binding energies between the two shells may expel an additional electron or a fluorescence photon. The new created vacancy may result in additional electron ejection, until vacancies reach the surface of the atom, thus leading to a cascade of secondary electrons. For gold, we calculated that an average of 11 electrons were ejected after the ionization of the K-shell. Auger electrons have typically a low energy (< 10 keV), and thus a short range in water. They thus generate a local dense boost of dose deposition and radical species in the vicinity of NPs.

The use of photon activation technique (PAT) was suggested nearly 3 decades ago. Tuning photon energy just above the K-shell of phosphorus (2 145.5 eV), which is highly present inside DNA, showed enhanced DNA SSB and DSB in plasmid DNA and an enhanced cell killing effect *in vitro* (Kobayashi et al. [2010]). This was also achievable by incorporating high Z atoms inside DNA. However, these effects highly depend on the intra-cellular localization of the high-Z agent, with a lower efficiency if located out of the nucleus, although some effects were observed when localized in the cytoplasm.

Chemical and biological effects A recurrent divergence between theoretical calculations and the biological experiments have focused attention on potential alternative mechanisms that do not rely directly on physical mechanisms. Eventually, it was suggested that NPs may act as radiosensitizers through chemical and biological pathways, as further discussed in chapter 5. In the review by Butterworth et al. [2013], it was suggested that oxidative stress is a central mechanism of GNP radiosensitization. Elevated level of ROS has been reported for many GNPs *in vitro*, although the precise mechanism by which NPs induce oxidative stress remains to be elucidated.

Conclusion As pointed by Her et al. [2017], it has become evident that NPs may have a role in the physical, chemical and biological phases of the mechanisms of irradiated biological tissues. However, the contribution of each step remains to be fully elucidated.

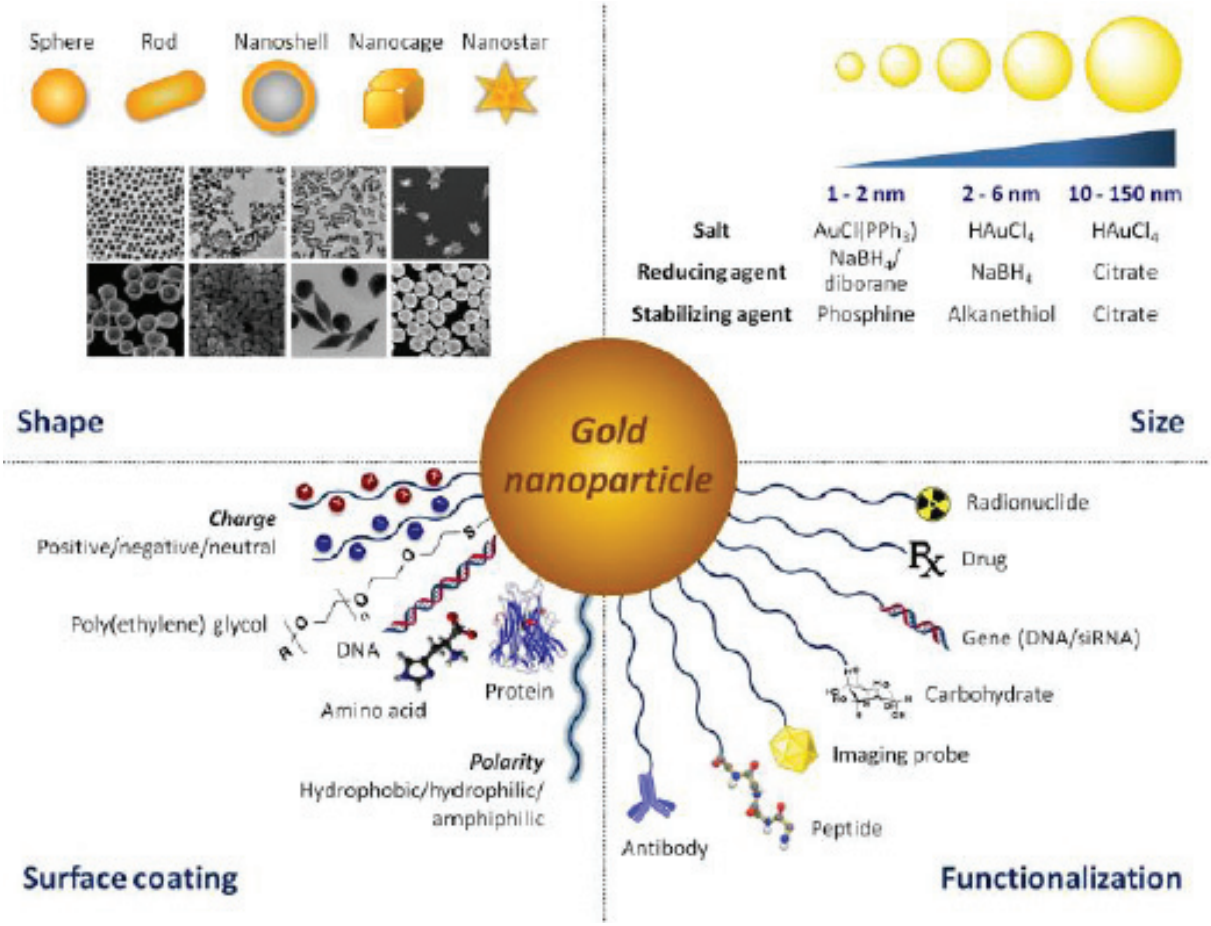

Figure 3.4.: GNPs properties, taken from Her et al. [2017].

3.4.3. Which NPs for radiosensitization

Many types of NPs have been used in radiosensitizing strategies. The review by Brun and Sicard-Roselli [2016] studied a total of 80 research articles published from 2008 to 2016 dealing with cellular experiments of radiosensitization by nanomaterials. Gold (Z=79) based NPs represented a total of 62.5 % of the NPs, and spherical gold a total of 53 %. It was followed by gadolinium (Z=64) based NPs (11 %) and silver (Z=47) based (6 %) NPs. Other elements included bismuth (Z=83), platinum (Z=78), hafnium (Z=72), cerium (Z=58), cadmium (Z=48), selenium (Z=34), iron (Z=26), titanium (Z=22), silicon (Z=14) and carbon (Z=6). Gadolinium (Gd) has been used for the design of NPs due to its properties that allow a visualization in magnetic resonance imaging, thus making GdNPs an ideal theranostic tool. GdNPs in combination with radiation therapy have made it all the way to clinical trials, as further discussed in section 3.4.5. Silver based NPs were also used in this context, showing similar response to that of GNPs. Metal oxide based NPs have also been tested with a successful application of hafnium oxide based NPs all the way to clinical trial. Superparamagnetic iron oxide nanoparticles were also tested, and have shown to enhance the radiation induced DNA damage by catalyzing the ROS production. Non-metal based NPs were also tested, such as aminosilanized oxidized silicon NPs, or nanocrystals of underivatized fullerene C_{60}. Given the very large amount of available data for GNPs compared to other NPs, we decided to focus on this material. The advantages and properties of GNPs are further discussed in the next subsection.

3.4.4. The case of GNPs

GNPs have many advantages (Subiel et al. [2016]). GNPs are often referenced as relatively easy and inexpensive to synthesize within a variety of sizes and easily functionalized, as illustrated on Fig. 3.4. Besides, it has often been reported as biocompatible and with low toxicity, although there has been debates on this last point, due to small size specificities. They are thus extremely useful for contrast imaging, drug delivery or NP-based radiation therapy enhancement (Butterworth et al. [2013]). Besides, they constitute an ideal nanoplatform which may be used for multiple modalities.

Synthesis There are many methods used to synthesize NPs that can be classified into two categories: the top down strategies which take large bulk materials and rely on physical methods to break them down into NPs, and bottom-up strategies which go from atomic elements to form NPs based on chemical methods. GNPs synthesis is relatively easy. It can use both physical and chemical techniques, but commonly relies on chemical techniques. The general concept consists in using metal salts (example: chloroauric acid $HAu(III)Cl_4$), also known as gold precursor (Mikami et al. [2013]) dissolved in an appropriate solvent. When put in contact, they form NPs through chemical reduction steps using a reducing agent such as $NaBH_4$ (Ju-Nam and Lead, Mikami et al. [2008, 2013]). As the aggregation is quick, a crucial step is to know when to stop it by using a stabilizing agent. Ligand molecules such as citrate can be used to stop bulk formation and result in GNPs of different sizes depending on the ligand used. Sodium citrate results in GNP of size between 10-150 nm , while alkanethiols (alkane = tree structure in which all the carbon-carbon bonds are single + thiol = R-SH) results in GNP of size between 2-6 nm. Optimization of this method allows a good size control. Once synthesized in a colloid form, NPs usually require a stabilization to avoid aggregation. The use of gold allows easy functionalization of the NP. The binding of molecules may be achieved by a direct physical adsorption of native ligands, chemical attachment of their thiolated derivatives or by the use of intermediate linkers (Khlebtsov and Dykman [2011]). The most robust stabilizers used to attach oligonucleotides (short DNA or RNA molecules), peptides and PEGs are thiolate ligands, as a strong bond is formed between the soft Au acid and the soft thiolate base. Multifunctionalization for drug delivery is possible. As reported in the review by Brun and Sicard-Roselli [2016], the nature of NPs coating in the context of NP radiosensitization is extremely variable, and listed below:

- Small molecules (thioglucose, tiopronin, cysteamine)
- Polymers (mainly thiolated-PEG, but also PVA)
- DNA fragments
- Proteins and peptides (TAT, RCG, pHLIP with/without PEG)
- Ligands of specific receptors (folate, goserelin, trastuzumab, panitumumab).

Physical properties GNPs demonstrate unique physical properties due to their size. Under an electromagnetic field, a resonant coherent oscillation of the free electrons occur at the surface of the NP if the size is smaller than the light wavelength. This resonance, called surface plasmon resonance, is a key property. Plasmon absorption and scattering (the former dominating for NPs smaller than 20 nm) occurring in the NP can be used for spectroscopic techniques. The position of the peak depends on the surrounding environment of the NP: the temperature, solvent and ligands that might be attached to it. Typically, GNPs that are stabilized with citrate are red colloidal solutions with a peak of absorption at 550 nm. When interacting with natural organic macromolecules, the maximum is shifted toward lower wavelength (Daniel and Astruc [2004]). The effect is also dependent on the size of the NP, and sharply decreases with decreasing diameter. When the NP is smaller than 3 nm, quantum effects tend to dominate: the NP starts behaving as a molecule depicted by molecular orbitals, and it is better to talk about clusters than NPs.

Chemical properties Although bulk gold is well known for being chemically inactive, gold NPs have been reported to have intrinsic chemical reactions that are specific to their small dimension. In particular, very small GNPs (3-5 nm of diameter) are particularly catalytically active, can induce oxidation of chemical species, and react with chemical species such as CO or oxygen (Daniel and Astruc [2004]). Density functional theory calculation with extra-small gold particles in vacuum (Au_{10} clusters) showed that these species can bind to the surface of GNPs due to its structure. While surface gold atoms usually have many neighbours when the metal is in its bulk form (the coordination number is 7), small particles are constituted of corners which can have gold atoms with a coordination number as low as 3 (Hvolbæk et al. [2007]). The binding energy decreases with the coordination numbers, thus allowing bonding of GNPs with chemical species that would not be energetically allowed in its bulk form. These chemical properties are strongly dependent on the GNP size.

GNP in the clinic Two intraveneous preparations have already been clinically investigated, however it was not in the context of radiosensitization. AurImmune^{TM} (NCT00356980 and NCT00436410) started a clinical trial in 2006 (early phase 1) and 2007 (phase 1), and both phases were completed. These gold based NPs are targeted with the tumour necrosis factor, which may stimulate the immune system in different ways and stop tumour cells from growing. AuroLase^{TM} (NCT01679470, NCT00848042 and NCT02680535) are GNPs developed also for cancer applications, and are silica NPs covered with a thin layer of gold. They are used for photothermal therapy.

3.4.5. Preclinical and clinical evaluation of radiosensitizing NPs

3.4.5.1. Preclinical investigation with GNPs

Additional pre-clinical evidences of the radiosensitizing effect of GNPs followed the one by Hainfeld et al. [2004]. The 1.9 nm GNPs were tested on mice bearing SCCVII squamous cell carcinoma tumours, injecting intravenously 1.9 g/kg before irradiating with 42 Gy using a 68 keV X-ray machine (Hainfeld et al. [2010]). The irradiation was performed $\sim$ 1 min post-injection, when the blood gold levels were $\sim$ 70 % of their initial peak value and tumour levels were $\sim$ 7 mg/g of gold. The tumour took 43 % longer time to double in volume, compared with radiation-only treated mice. The authors showed an energy dependence as irradiating with 157 keV photons led to only 7 % extension in tumour growth delay. Hainfeld et al. [2013] worked with a tumour model mimicking aggressive human gliobastoma, using non-functionalized 11 nm GNPs. The NPs were injected 15 h prior to irradiation, and accumulated within the brain tumour at a ratio of 19:1 (tumour:normal brain tissue). Following a 30 Gy irradiation, long-term survival ($>$ 365 days) of untreated mice was equal to 0 %, as they died within 23 days. For irradiation only, the survival was extended by animals were all dead by 150 days, resulting in a long term survival of 0 %. The use of 4 g/kg in combination with radiation resulted in one year survival of 50 % of the mice.

The use of vectors was tested *in vivo* by Chattopadhyay et al. [2013], by conjugating 30 nm GNPs with the human epidermal growth factor receptor-2 (HER-2) to target breast cancer. Mice bearing subcutaneous MDA-MB-361 xenografts were treated with a single dose of 11 Gy with 100 kVp X-rays, post intra-tumoural injection of GNPs ($\approx$ 0.8 mg of Au). They observed a regression of the tumour by 46 % compared to treatment with radiation only (16 % increase in tumour volume) for a period of 120 days.

Chang et al. [2008] used GNPs as a radiosensitizer/contrast agent for electron irradiation. Using a B16F10 (melanoma) tumour-bearing mouse model and 1 g/kg of 13 nm GNPs, they showed an *in vivo* radiosensitizing effect for a single dose irradiation of 25 Gy administered 24 h post GNP injection, both in terms of tumour control and mean survival. Kim et al. [2010] proposed to use GNP in combination with proton irradiation, based on the Particle-Induced X-ray Emission

(PIXE) effect. The mice received GNP injections at 300 mg/kg body weight via the tail vein. 20 days post proton irradiation, a tumour volume reduction of 90 % was obtained, while it was of 18 % for the irradiation only.

Zhang et al. [2012] studied the effect of PEG-GNPs on tumour mice with a U14 tumour model (cervical cancer cells). They tested GNPs of different sizes (4.8, 12.1, 27.3 and 46.6 nm). *In vitro* tests showed that 12.1 and 27.3 nm GNPs had a stronger radiosensitizing effect. The GNPs were injected *via* intraperitoneal injection, followed by a 5 Gy γ rays (^{136}Cs at 662 keV). The tumour volume was measured and authors obtained a significant effect, in particular for 12.1 nm GNPs, while 46.6 nm showed little effect. The small GNPs could rapidly diffuse throughout the tumour matrix, and accumulated in the tumour at high concentration ($\sim$ 250 µg/kg). Larger ones could only stay near the vasculature. However, small GNPs mostly accumulated in the liver ($\sim$ 2800 µg/kg), causing subsequent damages. In another work (Zhang et al. [2014]), the same authors proposed the use of ultrasmall gold nanoclusters Au_{25} ($<$ 2 nm), coated with a glutathione (biocompatible) ligand. Due to their size, these NPs are easily cleared out of the body by the kidney, minimizing potential toxicity. They obtained a gold concentration of $\sim$ 1.4 µg/g of tumour. 20 days following a 5 Gy γ rays (^{136}Cs at 662 keV), they obtained a tumour volume decrease that was enhanced by 35 % as compared to irradiation alone.

Three studies investigated the use of GNPs for glioma (brain cancer). Due to limited dose that can be safely delivered and the blood-brain barrier that limits the delivery of systemic anticancer agents, these types of tumour have a very poor prognosis. Joh et al. [2013] studied the use of PEGylated GNPs (12 nm gold core) in combination with radiation therapy both *in vitro* and *in vivo*. Following *in vitro* confirmation that the GNPs could induce an increase in cell death (4 Gy for a 150 kVp irradiation), mice were administered IV GNPs 48 h before receiving a 20 Gy irradiation (175 kVp). Compared to irradiation alone, they obtained a delayed tumour growth and improved survival. Bobyk et al. [2013] used 15 nm GNPs with intracerebral delivery at a concentration of 50 mg·mL^{-1}. It was followed by low energy irradiation (88 keV) at 15 Gy, and showed an increase in cell survival of rats compared to irradiation alone. Chen et al. [2015] proposed the use of Bovine Serum Albumin (BSA)-capped GNPs ($\sim$ 18 nm in size) for gliobastoma tumour radiation therapy. For *in vitro* 160 kVp irradiation, they obtained enhanced DNA DSB (0.5 and 2 h following the irradiation), and enhanced cell apoptosis for U87 cells. *In vivo*, the rats were intravenously treated with BSA-GNPs (250 µL, 1.3 mg·mL^{-1}), and irradiated 2 h and 24 h following injection. Both resulted in similar decrease of tumour growth, but significant amount of GNPs was found in the liver.

Wolfe et al. [2015] studied the radiosensitization of prostate cancers *in vitro* and *in vivo* using goserelin-conjugated gold nanorods. They obtained radiosensitization properties for megavoltage radiation. Finally, McQuade et al. [2015] proposed to use a multifunctional nanoplatform for imaging, radiotherapy and prediction of therapeutic response. They developed a micelle nanoparticle loaded with gold and superparamagnetic iron oxide nanoparticles. When injected intravenously, they accumulated in the tumour and enabled magnetic resonance imaging of the tumour. Irradiation enabled a 90-day survival of 71 %, compared to 25 % for mice treated with radiation alone.

Despite the large amount of proof-of-concept studies of the radiosensitizing effect of GNPs, none of these particles have yet made it to clinical trials.

3.4.5.2. Clinical investigation

While GNPs have not yet been approved for clinical investigation, NPs based on other materials have successfully been investigated during pre-clinical phase and are now undergoing clinical trial. The search of 'Nanoparticle' + 'Cancer' + 'Radiotherapy' gave a total of 32 studies on the database

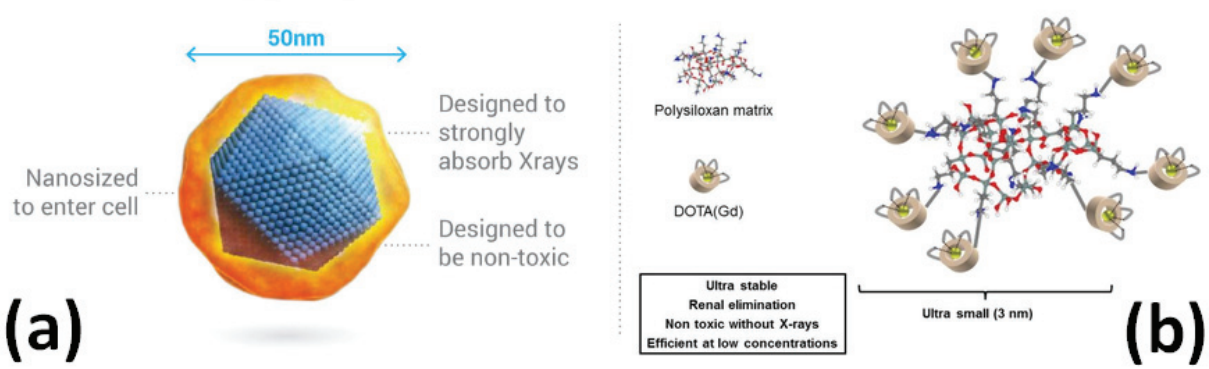

Figure 3.5.: Two high-Z NPs in clinical trials designed to enhance radiotherapy. On the left the product from Nanobiotix, based on hafnium oxide and on the right the product from NHTheraguix, based on gadolinium atoms.

ClinicalTrials[1], all of which first posted after 2007. Among them, 25 were conducted in US centres and 7 in Europe centres, among which 6 in French centres. Apart from heat ablation of tumours, or drug delivery of chemo-sensitizers, two main NPs are used for their high-Z properties.

The nanoparticle NBTXR3 is a 50 nm NP made of Hafnium-Oxide (HfO2, Z=72 for hafnium) core with negatively charged surface coating (see Fig. 3.5 (a)). The first published work by Maggiorella et al. [2012] studied the effect of NBTXR3 injected directly in the tumour at 64 mg·mL^{-1}, followed by an irradiation with a ^{60}Co source. They studied the biodistribution of the NP both at the tumour scale and the cellular scale. At tumoural scale, they found that the time of residence of the NPs was at least 14 days after the injection. At cellular scale, they found large clusters of NPs contained in cytoplasmic endosomes, responsible for high dose spikes. *In vitro* clonogenic assays showed an increased cell death in presence of NBTXR3. *In vivo* experiments showed anti-tumour activities in terms of survival, tumour-specific growth delay and local control both in mesenchymal and epithelial human tumour xenografted models. No toxicity was observed, and the NBTXR3 crystal structured remained unchanged after long-term residence *in vivo*. Following theoretical, *in vitro* and *in vivo* investigations on mesenchymal and epithelial cells (Maggiorella et al. [2012]) but also numerous other cell lines including glioblastoma (Marill et al. [2014]), these NPs were successfully taken to clinical trial. A clinical stage pharmaceutical company Nanobiotix[2] was created for its clinical development and commercialization, whose head-quarter is located in Paris. A total of 8 studies are registered on ClinicalTrials, starting from 2011. The first clinical investigation was done on adult soft tissue sarcoma, rare cancers that develop in different types of soft tissues. These cancers are usually treated by radiotherapy followed by surgery in Europe. During the first phase they evaluated the pre-operative efficacy and the safety of NBTXR3. They obtained a pathological complete response rate of 16.1 % with the radioenhancer compared to 7.9 % without. On April the 4th, NBTXR3 obtained the CE mark for the treatment of locally-advanced soft tissue sarcoma. Due to its mode of action, NBTXR3 is eligible for many other types of cancer. It is currently in clinical trial for head and neck cancer (in Taiwan, USA and France), for patients having locally advanced squamous cell carcinoma of the oral cavity or oropharynx and facing limited treatment options. They obtained promising results during the phase I/II trial regarding local control of the tumour, and obtained authorization to commence phase II/III in the USA. It is also investigated in combination with anti-PD-1 antibodies in lung and head and neck cancer patients (in the USA), for liver cancers (in France), locally advanced rectal cancer (in combination with chemotherapy, in Taiwan), head and neck cancer in combination with chemotherapy (in Taiwan) and prostate adenocarcinoma (in USA).

AGuIX^{TM} is another NP based on the use of gadolinium as a high Z component, which also led

[1] www.clinicaltrials.gov
[2] www.nanobiotix.com

to the creation of a clinical stage pharmaceutical company, NHTheraguix[3]. Gadolinium is a good contrast agent for MRI, however free gadolinium ions cannot be used as they are highly toxic in humans. They may however be chelated with molecules such as DOTA (detraxetan) or DTPA (pentetic acid), which allows a good stability of non-toxic complexes. As displayed in Fig. 3.5 (b), AGuIX^{TM} is a very small NP (hydrodynamic diameter smaller that 5 nm), with a core made of a polysiloxane matrix, mainly composed of silicon (grey), oxygen (red) and nitrogen (blue). DOTA/DTPA molecules (brown) are attached to the core and used to chelate gadolinium atoms. Each NP contains on average 10 atoms of gadolinium, and the NP has a slightly positive zeta potential. These NPs were tested *in vitro* and *in vivo*, and an overview of the results is available in the thesis work of Simonet [2018]. After ten years of academic research, the first in men clinical trial started in 2016 in Grenoble, for brain metastasis (NCT02820454). Another clinical trial started in October 2017 for gynecologic cancer (NCT03308604). Other clinical trials are under way, for potential application to Head and Neck cancer as well as on glioblastoma and lung cancer. Studies are currently undergoing to create the next generation of AGuIX.

3.5. Summary

Along with surgery and chemotherapy, radiation therapy constitutes the most common modality with ~ 50 % of the patients receiving radiation therapy during their cancer treatment. Radiation therapy uses the ability of ionising radiations to penetrate through the human body and reach the tumour. When interacting with atoms and molecules of cancerous cells, radiations deposit energy that may ionise atoms of vital biomolecules, further inducing the break of chemical bonds and, as a consequence, the destruction of these biomolecules (direct action). Radiations may also generate toxic chemical species, in particular by ionising and exciting water molecules that constitute the cells (indirect action). This further triggers oxidative stress, which plays a central role radiation-induced damages. Both mechanisms may result in cell death through different mechanisms (apoptosis, autophagy, senescence, necrosis or mitotic catastrophe). DNA is often referred as a key radiation-damageable target. DNA double strand breaks are believed to be the most severe lesions produced by radiations, as they are complex to repair. Besides, sophisticated experiments have demonstrated that mutations can be induced by radiations that only passed through the cytoplasm. These studies suggest that damages to cellular organelles such as mitochondria, lysosomes or cellular membranes, may also play a role in radiation-induced cell death. Additionally, experiments have demonstrated that non-irradiation cells undergo cell-death when in contact with irradiated cells (Bystander effect), possibly through the secretion of chemical signals or molecules. The propensity of cells to die following irradiation depends on many factors. In particular, the level of oxygen and the phase of the cell cycle are two key parameters that determine the radiosensitivity of a cell.

A major limit of radiations is the lack of selectivity towards tumour tissues, compared to healthy tissues. Irradiation of healthy tissues may induce severe side effects, which limit the maximum dose that can be delivered to the tumour. Besides, solid tumours are usually very heterogeneous with a hypoxic region in the inner-part that is extremely radioresistant. Delivering enough dose to the tumour to effectively kill or inactivate cancer cells and avoid recurrence, while sparing surrounding healthy tissues, remains challenging. Many techniques may be used to improve the therapeutic window, among which the use of radiosensitizing agents. When accumulated in the tumour, these agents aim at amplifying the destructive effect of the dose.

With the rise of nanomedicine, it was first suggested in 2004[115] that gold NPs (GNPs) may be used as a contrast agent with kVp photons. This pioneering study demonstrated that GNPs were particularly effective *in vivo*, with mice receiving GNPs in addition to X-rays having a 1 year survival of 80 %, against 20 % for mice receiving radiation only. Many *in vitro* and *in vivo* studies followed these very encouraging results, with NPs made of gold or other high-Z elements. Two

[3] www.nhtheraguix.com

NPs, made of hafnium or gadolinium, made it to clinical trials. Hafnium NPs were granted the CE mark for the treatment of locally-advanced soft tissue sarcoma, April the 4th 2019. These experimental studies, in addition to theoretical (simulation studies) enabled to identify several mechanisms that may explain the effect. Low-energy (keV) photons have a higher probability to interact with high-Z atoms, compared to soft-tissues (mostly constituted of water). This results in a global higher dose deposition throughout the entire tumour. Besides, when ionised, high-Z atoms undergo a desexcitation process that release a cascade of secondary electrons (Auger electrons). It was often suggested that this cascade results in a dense energy deposition in the vicinity of GNPs, that may be particularly efficient at destroying sensitive biomolecules. Finally, *in vitro* studies have shown growing evidences that complex chemical and biological mechanisms may further increase the effect, as further developed in chapter 5. These mechanisms highly depend on the NP biodistribution. This point is therefore discussed in the next chapter.

4. The journey of nanoparticles in the living

Contents

This chapter is an overview of the interaction of NPs from the molecular scale to the *in vivo* scale. It aims at better understanding GNP biodistribution and toxicity mechanisms, which are both key concepts for an optimized and safe use of GNP radiosensitization. In particular, in the scope of this work, an understanding of the interaction of GNPs with cells is mandatory when it comes to biophysical modelling of the system GNP + cell.

4.1. NPs interaction at the molecular scale

4.1.1. NP chemical reactivity

NPs usually have an inherent chemical reactivity, that increases with increasing surface to volume ratio, as illustrated by Fig. 4.1 (right). As previously discussed, when the size of the NP decreases, the surface area increases and allows a greater proportion of its atoms or molecules to be displayed on the surface. These surface atoms have unusual properties compared to bulk materials and induce specific chemical reactions. These reactions may be relevant when studying radiation therapy combined with GNPs. For instance, some NMs have been reported to react with reactive oxygen species and convert less reactive oxidants such as H_2O_2 or superoxide molecules into more reactive radicals such as $^{\bullet}OH$ (Fu et al., He et al. [2014, 2013]). Additionally, metallic based NPs may release ions in their vicinity, thus catalysing production of hydroxyl radicals from H_2O_2 in a Fenton-like reaction. These reactions are extremely dependent on the surface composition and shape of NPs, or on the surrounding medium properties (He et al. [2013]). Some of the chemical reactions that may occur at the surface of the NP are illustrated in Fig. 4.1.

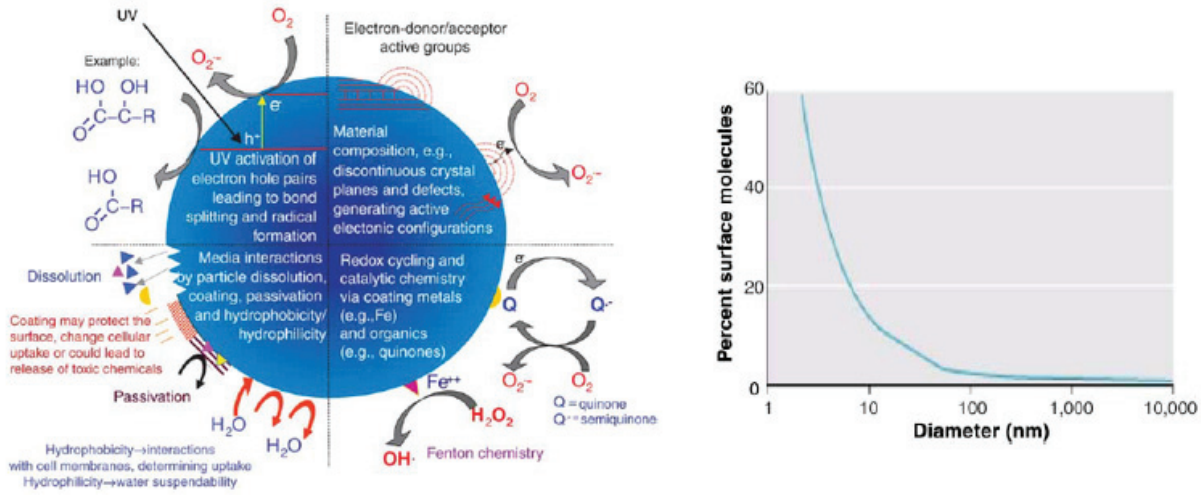

Figure 4.1.: (Left) Examples of mechanisms by which NMs interact with the surrounding molecules, illustrating the importance of material composition, electronic structure, bonded surface species, surface coatings, solubility and interactions with other external factors (e.g. light activation). (Right) Inverse relationship between particle size and number of surface expressed molecules/atoms, expressed in % of molecules/atoms in the NP. Taken from Nel et al. [2006].

Note that, as further discussed in this thesis, this chemical reactivity makes any measurements difficult, due to potential interaction between the NP and the probe. Most experimental measurements rely on indirect methods. Possible physico-chemical interference between the NPs and the probe can lead to the generation of unreliable data and conflicting results, as pointed out in the review by Tournebize et al. [2013]. Typically, in cell free measurement of free radicals, spectrophotometry based techniques might be a problem, due to the particular optical properties of NPs. Likewise, fluorescence intensity of probes can significantly decrease in presence of metallic NPs, giving a biased impression of signal loss only due to the presence of NPs. It was recommended to use two methods of measurement for one type of biological endpoint to avoid biased results (Krug and Wick [2011]).

4.1.2. NP interaction with biomolecules

Additionally to the spontaneous generation of ROS, the binding of NPs with biomolecules may generate toxic species. For example, Jia et al. [2008] studied the release of nitric oxide (NO) following the interaction of GNPs with S-nitrosothiols (RSNO) molecules in blood serum. Using 13 nm GNPs at various concentrations (10 to 80 µM), they found the NO is detectable directly after addition of GNPs and that it increases with GNP concentration. Nitric oxide may further react with superoxide and produce peroxynitrite ($ONOO^-$) species, which are harmful to the cell. It was also shown that NPs can bind to biomolecules involved in the oxidative stress regulation, such as TrxR1 (Liu et al., Penninckx et al., Penninckx et al. [2014, 2018, 2019]) or glutathion (Mateo et al. [2014]). For 10 nm amino-PEG functionalized GNPs, it was shown that a good correlation existed between cell response to radiation and residual TrxR activity level (Penninckx et al. [2019]), suggesting a central role of the cellular detoxification system. This example emphasises the strong need to better understand the interaction of NPs at molecular level, to have a full picture of the potential origins of the NP radiosensitizing effect.

4.1.3. The protein corona

As seen in Chapter 2, the gold standard for a NP journey in the human body is, once injected in the bloodstream, to circulate before reaching the target tissue (Corbo et al. [2016]). Ideally, when reaching the target, a ligand attached on the NP surface recognizes its specific receptor expressed

in cells of the target tissue, and the drug is released in a controlled manner. While in theory the concept is simple, it is harder to put it in practice. When in contact with a biological fluid, NPs interact with surrounding biomolecules - mainly proteins, but potentially sugars, nucleic acids and lipids - forming a biomolecular corona and giving NPs their "biological identity" (Brun and Sicard-Roselli, Polo et al. [2014, 2017]). The protein corona quickly covers the entire NP surface through hydrophobic and electrostatic interactions (Canton and Battaglia [2012]). There are evidences indicating that a strong correlation would exist between the nature of the protein corona (PC) and the cellular uptake of NPs, both *in vitro* and *in vivo*, thus making the understanding of protein-NPs interaction crucial. The analysis of the PC content is difficult, as the measurement perturbs it (Brun and Sicard-Roselli [2014]). The question on its composition, stability, and influence on NPs fate in biological systems is currently of high interest and a challenging question. The gap between *in vitro* applications and their translation to clinical trial is believed to be partly due to the lack of understanding of the biological identity of NPs.

Consequences of the PC corona are large. The PC could impact targeting strategies, although its influence is still controversial. The PC may also impact the toxicology of NPs, although reports appear yet contradictory. In some cases, it may reduce toxicity. For example, positively charged NPs can perturb the continuity of plasma membrane due to their interaction with the negatively charged surface of the cell, leading to cell membrane disruption and eventually cell death. The presence of the PC may mask the charge and thus reduce the toxicity. A delayed toxicity could be due to the PC degradation inside lysosomes: once the PC is digested, the NP is exposed and damages the lysosome. Toxicity could also be triggered by modification of proteins on the NP surface, due to protein unfolding or protein aggregates. Unfolded proteins may have altered signalling, and thus generate biological activities leading to inflammation and macrophage activation. PC also opens perspectives on the development of nanomedicine: the concept of "personalized protein corona" has been introduced as a way to engineer patient-specific and disease-specific NPs for safer clinical applications.

4.2. *In vitro* fate of NPs

4.2.1. Cellular trafficking

Endocytosis is a fundamental process in which eukaryotic cells internalize molecules and macromolecules through the deformation of the membrane and generation of membrane-bound carriers, known as vesicles. As eukaryotic cells are multi-compartmented, these vesicles play a role in the trafficking of molecules from the extracellular space to the cytosol to specific target organelles, and thus enable the exchange of many isolated biochemical information. This process is an active process that demands energy from the cell. It is the primary route bacteria and viruses use to enter cells. As illustrated on Fig. 4.2, the endocytotic mechanism is usually divided into two categories: phagocytosis (i.e., cell eating) and the pinocytosis (i.e., cell drinking). The former is limited to a few specialised cells that are part of our immune system, while the later concerns most of eukaryotic cells. In this second class, different sub-categories classify the mechanisms (Canton and Battaglia [2012]), the most studied one being the receptor-mediated endocytosis (or clathrin-mediated endocytosis). All these mechanisms usually go through common steps: the specific binding of the cargo (i.e., the molecule to internalize) on the cell surface and the plasma membrane wrapping and pinching off, resulting in the formation of a vesicle. Once the vesicle is detached from the membrane, it delivers its content to other subcellular compartments or ends up in lysosomes for degradation, where the pH is maintained around 4.5-5 (Canton and Battaglia [2012]). Ultimately, the cargo may leave cells through exocytosis, which is also an energy-dependent process (Chithrani et al. [2010]). In some cells, a process called transcytosis enables the transport of macromolecular cargo from one side of a cell to the other side vesicles. It is a crucial mechanism for multicellular organisms to control the transport of material between different tissues. Endothelial cells, which are cells that constitute the wall of blood vessels, is

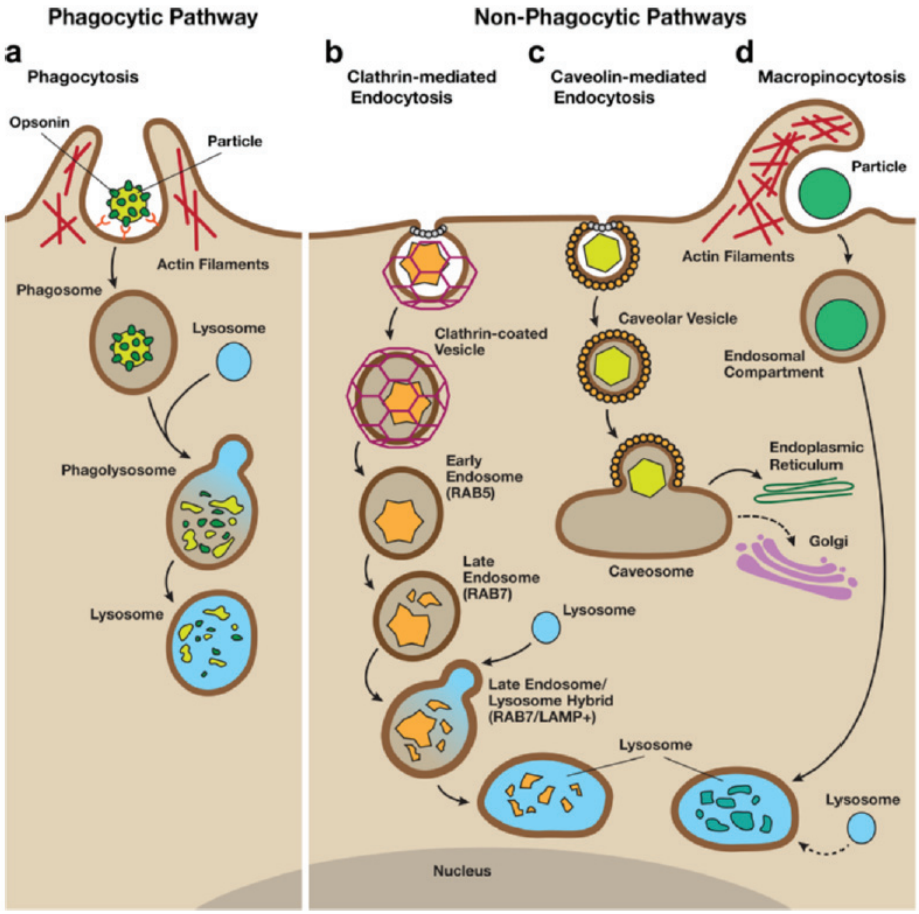

Figure 4.2.: Cellular endocytosis pathways illustrated, taken from Stern et al. [2012].

one type of cell that uses this process. The understanding of all these processes is crucial for pharmacokinetics and NPs toxicology (Canton and Battaglia [2012]).

The numerous studies of NPs uptake by cells showed that one cannot define a unique cellular uptake mechanism for NP: it may occur via active recognition of the NP or passive processes (diffusion, penetration, adhesive interaction). Due to their very small size, NPs can enter cells the same way proteins and molecules do. NPs can also induce deformation and even complete invagination of the membrane due to physical interaction between the curved NP and the phospholipidic membrane. The mechanisms depend on the NP properties, the experimental conditions and therefore the NP environment and the NP target cell (its type, normal *vs* cancer cells, etc.). As previously mentioned, the composition of the PC could greatly impact the internalization of NPs. Besides, the use of specific ligands could trigger preferentially a given internalization pathway, that may target a specific organelle. Strategies to escape endosomes can be developed, depending on the application the NP was designed for. However, most of the endocytic routes of NMs cellular uptake converge towards lysosomal entrapment, making lysosomes the most common intracellular site of NP sequestration and degradation (Stern et al. [2012]). The accumulation of NPs inside lysosomal compartments might have side effects.

4.2.2. Parameters governing NP trafficking

Parameters governing NP trafficking have been studied with *in vitro* experiments. Such experiments consist of mixing GNPs with the extra-cellular medium and leave it in contact with cells for a given time of incubation. The study by Chithrani et al. [2010] suggested that GNPs were

mostly internalized through receptor-mediated endocytosis, following the adsorption of serum proteins onto GNPs. As expected, NP trafficking depends on many parameters: the experimental conditions, the nature of the NP studied and the biological system studied.

4.2.2.1. Influence of NP design on the uptake

Size A major dependence of the NP uptake is the size of the NP. Chithrani et al. [2006] observed a dependence on the GNP diameter: the cellular uptake was greater for 50 nm citrate-capped GNP, compared to 14 and 74 nm GNPs. They found the same trend for transferrin-coated GNPs, and it was in particular independent on the cell type (Chithrani and Chan [2007]). Gao et al. [2005] theoretically calculated that the optimum radius for receptor-mediated endocytosis is about 25 nm. Small nanoparticles do not trigger the production of enough free energy when receipted on the membrane to wrap completely the NP, and must be clustered together to get inside the cell. For larger GNPs, the wrapping time is slower because of the slower reception diffusion kinetics. The shortest internalization time of 20 minutes was calculated for 50 nm diameter GNPs.

Shape For cellular interaction, the shape of the NP is as important as its size. The curvature of the NP could have a critical effect of its internalization. The nature of the cell could also display selectivity towards the shape of NPs to internalize. This dependence was used to design NPs shaped in order to limit the uptake by the immune system, thus improving the blood circulation time and consequent therapeutic effects. Chithrani et al. [2006] showed that the GNP uptake is less efficient for nanorods compared to spherical GNPs. As nanorods have a larger area bound to the cell, it reduces the available sites.

Surface charge The surface chemistry of the NP affects its interaction with the surrounding. Neutral and anionic NPs are much less efficiently internalized by cells than cationic ones, due to the high affinity of species with negatively charged proteoglycans, a protein expressed on the surface of most cells. Different internalization pathways may be activated depending on the charge of the NP. For example, computational calculation showed that passive membrane translocation was favoured for neutral or sightly cationic NPs while highly cationic NPs went though endocytosis-mediated uptake (da Rocha et al. [2013]). However, positively charged NPs have been associated with mitochondrial damage and apoptosis, while anionic NPs have been reported to be less toxic. This was experimentally observed by Kong et al. [2007], with a higher uptake of cysteamine GNPs (positively charged) than thio-glucose GNPs or TGS-GNPs (neutral).

Surface coating Although connected to surface chemistry, surface coating might be particularly important. GNPs pre-coated with one protein showed lower uptake than serum coated GNPs. This is a result of the number of different proteins present on the surface: if they are coated with only one protein, the receptors on cells quickly saturate. If NPs are functionalized, they might trigger alternative endocytosis pathways.

Surface topology Additionally to the surface chemistry, the topology of the NP might affect its uptake. This was already observed in viruses. Only recently, the nanotechnologies have allowed sufficient control of NP design to allow such studies. It has been observed that, depending on their surface motifs, NPs could enter cells via different routes.

Mechanical properties At last, the stiffness of NPs can also change the mode of internalization: stiffer NPs can achieve full wrapping more easily.

4.2.2.2. Influence of experimental conditions on the uptake

Time of incubation The time of incubation and the concentration of NPs used in the media can greatly impact the final intra-cellular uptake. Regardless of the NP characteristics, or cell lines,

many studies have reported an increase of NP uptake with increasing time of incubation within few hours, before reaching a plateau (Chithrani and Chan, Chithrani et al., Coulter et al., Khoshgard et al., Song et al. [2007, 2006, 2012, 2014, 2013]). Other studies obtained first a sharp increase of the cellular uptake within first few hours, before slowly decreasing (Cui et al., Cui et al., Geng et al., Roa et al., Song et al. [2013, 2014, 2011, 2009, 2013]).

Extra-cellular concentration The GNP extra-cellular concentration used during incubation impacts the final intra-cellular concentration reached. For a given time of incubation, the intracellular uptake usually increases with increasing extra-cellular concentrations, and eventually reaches a plateau (Chithrani et al., Cui et al., Jain et al., Liu et al., Liu et al. [2006, 2014, 2011, 2008, 2015]). This saturation was attributed to the saturation of receptor mediated endocytosis, since uptake of these GNPs was shown to be mediated by nonspecific adsorption of serum proteins onto the GNPs (Chithrani et al. [2006]).

Extra-cellular medium As discussed previously, following the contact between GNPs and a biological fluid (such as the serum for *in vitro* experiments), GNPs usually get covered in proteins, forming the PC. Consequently, GNPs may be internalized through receptor-mediated endocytosis, by the binding of the PC with receptors located on the surface of the cell. Therefore, the nature of the extra-cellular medium and in particular the nature of the serum (fetal bovine serum *vs* human serum) may impact intra-cellular uptake, as the proteins that are present are not the same. For example, Chithrani et al. [2006] showed that the number of transferrin-coated GNPs that entered cells was 3 times less than citrate-GNP, which adsorbed proteins of the serum.

Level of oxygen The level of oxygen has shown to impact NP uptake (Cui et al., Jain et al. [2014, 2014]), with a strong decrease of GNPs uptake with lower oxygen level. For instance, Jain et al. [2014] showed that DU145, MDA-MB-231 and L132 cells had a relative uptake of 0.29, 0.53 and 0.56 for hypoxic cells compared to aerobic cells (0.1 % vs 21 % level of oxygen). They hypothesized that this lower uptake was due to a lower production of energy for hypoxic cells, which is mandatory for receptor mediated endocytosis. Besides, increased level of lactic acid (produced in anaerobic metabolism) alters cellular pH, which could in turn change aggregation potential of GNPs.

4.2.2.3. Influence of biological system on the uptake

At last, GNP uptake is also very dependent on the biological system studied, and hence varies with the cell line used. Chithrani and Chan [2007] showed for example that transferrin-coated GNPs had an uptake half-life of 1.19 h for 14 nm GNPs on HeLa cells, 2.02 hours for SNB19 cells and 2.45 h for STO cells. Interestingly, Geng et al. [2011] showed that a normal ovarian cell line had a 10 times lower uptake than a cancer ovarian cell line using glucose-capped GNPs. Note that many factors are not taken into account in static *in vitro* experiments, which might change the uptake of GNPs by cells. For example, whether the GNP is in a static or dynamic system (for example in the blood stream) could greatly impact the final uptake ability of cells.

4.3. The *in vivo* fate of nanoparticles

The biodistribution of NPs is in the human body is a complex topic. It depends on multiple parameters: NP design, mode of administration, dose of administration, animal model, etc. The goal of this section is not to give an exhaustive list of reported biodistributions but rather to identify key concepts in the *in vivo* fate of NPs: dose administered, key targeted organs, intratumoural concentration, clearance and toxicity. There has been many studies on the *in vivo* fate of NPs on animal models, some of which are reviewed in Her et al., Khlebtsov and Dykman, Schuemann et al. [2017, 2011, 2016] for the case of GNPs.

Injection NPs may be injected inside the body in different ways, among which inhalation, oral administration, intravenous injection (IV), intra-tumoural injection (IT) or dermal exposure. In clinical trials (AGuIx and NBTXR3), IV and IT injections are used.

Circulation Once in the bloodstream or tumour interstitium, NPs are in contact with the complex biological environment, and interact with biomolecules, resulting in the protein corona formation (Her et al. [2017]). The blood plasma is the extracellular matrix of blood cells and makes up about 55 % of the body's total blood. It is essentially made of water (95 %), but also contains dissolved proteins. The most common ones are albumins (55 %), globulins (38 %) and fibrinogen (7 %). The interaction may result in aggregation of non-stabilized NPs, which may modify tumoural or cellular uptake but also adverse events such as blockage of blood vessels.

Tumour accumulation Once in the blood stream and stable, NPs must have sufficient life time to reach tumour and accumulate. The clearance of NPs plays a major role. It must be slow enough to achieve tumour accumulation, but yet prevent healthy tissue accumulation and adverse toxic effects. In particular, NPs should avoid sequestration by the reticuloendothelial system (RES), composed of phagocytic cells, macrophages resident in the spleen, lymph nodes and liver. Resident macrophages in the RES act as filters to eliminate NPs (similar in size to bacteria and viruses) from the body (Schuemann et al. [2016]). The circulatory half-lives of NPs are usually complex and depend mostly on the particle size and preparation, with NPs often cleared out of blood within 24h. The uniformity of the distribution increases with decreasing GNP size. Smaller NPs are usually also found in kidneys and are capable of accumulating in the brain, thus penetrating the blood-brain barrier. The shape of the NP also impact its *in vivo* fate. Elongated NPs are more likely to localize along the blood vessel wall, resulting in a greater probability of extravasation through vascular fenestration into the tumour interstitium. As a consequence, rods have shown greater accumulation inside the tumour. Note that *in vivo*, the dynamic of the medium might result in significantly different results compared to *in vitro* experiments.

Tumour diffusion Once reaching the tumour, given long enough circulation time, the size of NP significantly affects how NPs interact with tumour capillarities, with typical cut-off size of the pores up to 400 nm. NPs size thus greatly influence how NPs achieve intratumoural diffusion (Ngwa et al. [2014]). NPs must penetrate the tumour interstitium in order to achieve homogeneous distribution. A good penetration is required to reach hypoxic cells that are generally distant from the vasculature. Larger NPs tend to accumulate in the vasculature while smaller diffuse more deeply throughout the tumour achieving a more homogeneous distribution. Few *in vivo* studies showed that active targeting was efficiently achieving a better tumoural accumulation. For example, GNP targeted with the tumour necrosis factor-alpha showed to accumulate inside tumours. However, in general, the magnitude of tumour-specific accumulation achieved with active targeting is less than an order of magnitude greater than with passive targeting.

Clearance and toxicity The final step of NP life in the human body is its clearance, which is strongly correlated with NP *in vivo* chronic toxicity. Small NPs (< 7 nm) are generally eliminated via renal clearance within few minutes post IV injection, while large NPs (10 -100 nm) accumulate in the liver and spleen via opsonization followed by recognition by the RES. NPs reside in Kupffer cells in the liver for a period of time ranging from days to even months following intravenous injection, often demonstrating slow hepatic elimination. This may result in long term toxic adverse side effects. As previously mentioned, this depends on the coating. For example, Schuemann et al. [2016] studied the biodistribution of 5 nm GNPs having a coating made of either short PEG chains of 750 Da or long PEG chains 10 000 Da). The authors found that for the former, 95 % were located in the RES within 1h post IV, while for the later, 90 % remained in the blood stream for long PEG chains. The toxicology may depend on many parameters, with a major one being the concentration of GNPs. .

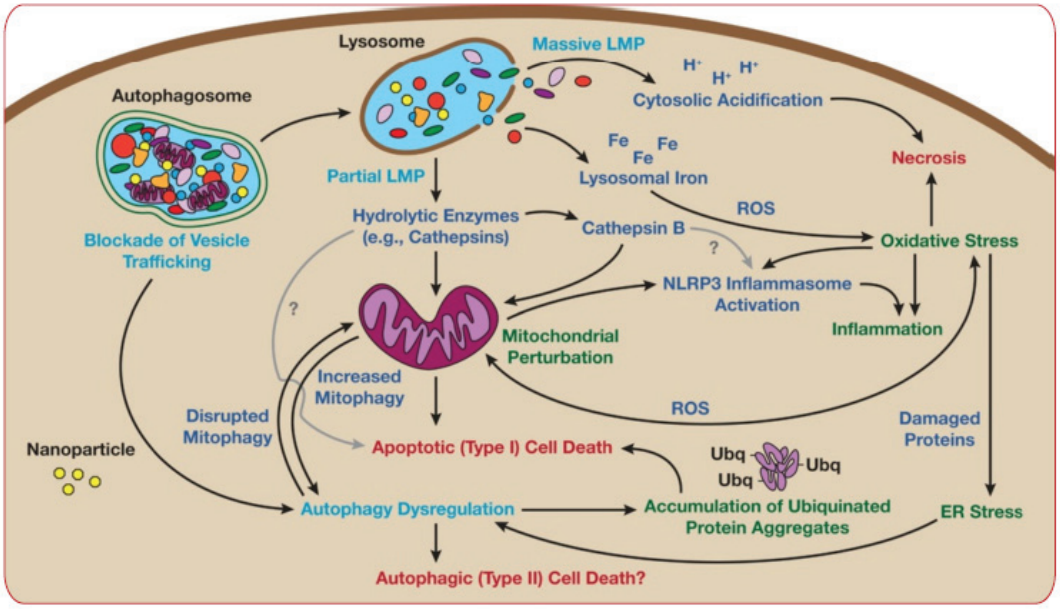

Figure 4.3.: Possible pathways of nanomaterial toxicity, taken from Stern et al. [2012]. LMP: lysosome membrane permeabilization.

Conclusion On a full body scale, NP delivery is highly complex and faces additional challenges compared to a cellular, *in vitro* scale. A meticulous characterization of physico-chemical GNP properties, along with their biodistribution and pharmacokinetics are mandatory.

4.4. Consequence on NP toxicity

As seen in the previous sections, NPs can be very reactive, and thus by interacting both at sub-cellular and cellular scales, they may cause harm to cells. The potential mechanisms are numerous: spontaneous generation of toxic chemical species, direct interaction with biomolecules causing altered signalling cascades, interaction with organelles, etc. On a large scale, NPs may cause inflammation, DNA mutations or alteration of the cell cycle without necessarily NPs located within the nucleus, mitochondrial perturbation or ultimately cell death (Krug and Wick, Nel et al., Unfried et al. [2011, 2006, 2007]).

Modes of action include increased production of reactive oxygen species as a central drive. Various mechanisms may be at the origin of their overproduction, either direct through NPs surface reactivity or indirect through physical interaction of NPs with cellular components such as Thioredoxin Reductase 1 (TrxR1) or GSH that prevent the cell from activating anti-oxidant mechanisms. ROS accumulation leads to the destruction of cellular components such as DNA, RNA or proteins. As previously mentioned, NPs usually interact with proteins causing them to unfold, and either inactivate or denature them.The accumulation of unfolded proteins may induce interference in enzyme functions but may also cause endoplasmic reticulum stress. The underlying mechanisms of oxidative stress generation and inflammation remain to be fully elucidated, and the cause *vs* consequence of each mechanism is not easily differentiated.

In the review by Stern et al. [2012], different complex cellular toxicity pathways have been identified for NPs, which are summarized in Fig. 4.3. They suggest that biopersistant nanomaterials (NMs) cause lysosomal dysfunctions, playing an important role in NP toxicity which could result in some of the aforementioned consequences, such as (indirect) ROS induction and inflammation. Among lysosomal dysfunctions, the lysosome membrane permeabilization (LMP) is a recognized

cell death mechanism that can result in mitochondrial membrane damages through various mechanisms, among which lysosomal-iron mediated oxidative stress or release of cathepsins or other lysosomal hydrolases. Massive LMP can cause cytosolic acidification and necrosis. Lysosomal perturbation has been observed for many types of NPs, including small negatively charged GNPs (Tedesco et al. [2010]).

Additionally, Stern et al. [2012] also suggests that NMs can cause autophagy dysfunction. The autophagy process is the fusion of autophagosomes with lysosomes, forming double membrane-structures called autolysosomes, which result in the breakdown of encapsulated materials to components that are then available for the cell (Stern et al. [2012]). Its dysfunction can be provoked by either an excessive autophagy induction or blockade of autophagy flux. In the former case, it may be induced by an oxidative stress generated by the accumulation of damaged proteins, and subsequent endoplasmic reticulum stress, or by mitochondrial damage. In the later case, they may alter autophagic signalling pathways. It results in autophagosome accumulation, potentially leading to aptosis or autophagy cell death. These dysfunctional mechanisms can originate from lysosomal overload, which disrupt lysosomal fusion with other cellular compartments. The disruption of the cytoskeleton could also be a cause, as the autophagy and lysosomal compartments rely on it for cellular tracking. Indeed, some NPs have shown a particular affinity to actin (proteins that form microfilaments) and may bind to it. Despite many references indicating gold as a biocompatible, safe material, GNPs were associated with many toxic behaviours, as further discussed in chapter 5.

4.5. Summary

As discussed in Chapter 2, NPs are smaller than a human cell, and may be as large as some vital molecules such as DNA or proteins. NPs can thus potentially interact with biomolecules, penetrate inside cells or induce side effects. These multi-scale interactions determine the amount of NPs that are accumulated in the targeted cells, but also the toxicity they may generate, overall determining the treatment efficacy.

On a molecular scale, NPs usually have an inherent chemical reactivity. They may react with chemical species or biomolecules and catalyse the production of toxic chemical species such as radicals. The chemical reactivity of GNPs may also have consequences on their biodistribution. Specifically, when in contact with a biological environment, NPs that have no coating naturally react with proteins of the medium to form a protein corona (PC) that gives the NP its “biological identity”. There are many experimental evidences showing that the nature of the PC influences the cellular uptake of the NPs. Such interactions may also cover ligands attached to the NPs and perturb targeting strategies.

After a potential cover-up of proteins, NPs may eventually get in contact with external membranes of cells, that further leads to internalization. The endocytosis of NPs occur through different pathways, usually through the formation of a vesicle. Once internalized, the vesicle content is delivered to sub-cellular compartments or - mostly in the case of NPs - ends up in lysosomes for degradation. There are many parameters that may influence the NP trafficking in the cell: the size of the NP, its shape, its surface properties, but also experimental conditions such as the time of incubation or incubation concentration, or the biological system considered. For instance, the nature of the medium, and specifically the proteins it contains, determines the composition of the protein corona, that further plays a role in the amount of NPs that are internalized.

On a full body scale, the picture is more complex and a homogeneous accumulation of NPs inside the tumour remains challenging. The biodistribution in the different organs depend on the injection method (intra-tumour *vs* intravenous for instance). If injected in the bloodstream, NPs usually get covered with proteins. They must have a long enough time of life in the bloodstream

to enable accumulation in the tumour. In particular, they must avoid the reticuloendothelial system, in charge of eliminating foreign bodies out of the system. The size of the NPs plays a large role in the diffusion throughout the tumour. It also affects how the NPs will be eliminated, with small NPs ($< \sim$7 nm) being eliminated through renal clearance, while large NPs tend to accumulate inside the liver, potentially raising toxicity issues.

This multi-scale interaction has consequences in terms of toxicity. Interaction of NPs with biomolecules of cells, such as antioxidants, may perturb the ROS balance of the cell and induce oxidative stress. Besides, unfolded proteins or aggregates, a consequence of the PC formation, may also induce adverse side effects. This may trigger complex cellular mechanisms that may further cause inflammation, alteration of signalling cascades, etc., that ultimately can lead to cell death and, on a full body scale, long term side effects.

5. Gold nanoparticles in radiotherapy – Experimental studies

Contents

As previously stated, the radiosensitizing effect of GNPs may originate from physical, chemical, and biophysical mechanisms. A clear view of the implication of each step is yet challenging. A wide range of experimental systems have been investigated, resulting in a large variation of the biological outcomes. Different, sometimes conflicting results have been reported, making a clear identification of the mechanisms difficult. This chapter gives an overview of experimental results for the irradiation of GNPs in water (section 5.1), in combination with biomolecules (section 5.2), and *in vitro* (section 5.3). Thus, each section has an increasing level of the complexity of the studied system. The goal is to have an overview of the extent of the effect, how it varies with the parameters, and the proposed biological mechanisms. Having a global view of the possible mechanisms, including biological ones, is primordial to interpret the simulation results.

5.1. *In solution:* Colloidal GNP and ROS production

5.1.1. Experimental measurement of radical species

The measurement of radical species (R) requires the use of scavengers (S) as they are very unstable and quickly react. Once the scavengers reacted with the chemical species, the final products have particular properties that are measurable through different techniques, such as fluorescence or electron paramagnetic resonance spectroscopy. A good probe is a scavenger that reacts with only

one particular radical, and leads to a signal that is measurable even at low concentration. The final measurable product is ideally obtained with a direct reaction between the scavenger and the radical, but may also be obtained after a cascade of secondary reactions. The reaction between the scavenger and the radical may lead to one unique measurable product or many products among which one is measurable. For a pulsed irradiation, it is possible to obtain relative radical yields produced at a given time t following the irradiation, or the absolute radical yields when calibrating with standard referential quantities (Baldacchino et al. [2009]).

When measuring free radicals in presence of GNPs, the choice of the probe is critical. As pointed out in section 4.1, cautions must be taken. Fluorescence signals can be quenched by NPs, and it is advised to remove them from solution by precipitation followed by a centrifugation or a filtration step before the fluorescence measurement (Tournebize et al. [2013]). It is also essential to verify a possible interaction between NPs and the probe that would modify, for instance, the reaction constant or the regioselectivity of the probe, leading to biased results. As a direct consequence, it is preferable to obtain the final measurable product through a direct chemical reaction between the radical and the probe, without any intermediate steps in order to prevent from having potential interference between NPs and intermediate product. It is also important to point out that, according to the experimental set-up, the type of measured enhancement is not necessarily the same. The enhancement can be induced by the increased absorption of X-rays by high-Z NPs (such as metal) but also by catalytic properties of NPs (Davidson and Guo [2015]). These mechanisms (physical enhancement and chemical enhancement) coexist, interfere and convolute in most experiments to result in a total measured enhancement, and it is *a priori* difficult to separate one mechanism to another.

For colloidal GNPs, two probes were used to measure $^{\bullet}$OH: the coumarin (Cheng et al., Davidson and Guo, Davidson and Guo, Gilles et al., Gilles et al., Sicard-Roselli et al. [2012, 2014, 2015, 2014, 2018, 2014]) and the spin trap BMPO (5-tert-butoxycarbonyl 5-methyl-1-pyrroline N-oxide) (Chang et al. [2016]). In this thesis, a special focus on the coumarin assay was decided, mainly because more data are available. As the experimental conditions are an essential information to understand the measure, a brief description of these probes is given thereafter.

5.1.2. The coumarin assay

5.1.2.1. Description in pure water

Two groups (Cheng et al., Davidson and Guo, Davidson and Guo [2012, 2014, 2015], and Gilles et al., Gilles et al., Sicard-Roselli et al. [2014, 2018, 2014]) measured the formation of $^{\bullet}$OH in the presence of GNP using respectively coumarin-3-carboxylic acid (3CCA) and coumarin (C). This molecule scavenges $^{\bullet}$OH to form, among various products, 7-hydroxy-coumarin (7OH-3CCA or 7OH-C), a fluorescent chemical species (maximum fluorescence for an excitation at 456 nm).

In the absence of GNPs, the coumarin assay enables to detect quantities down to 30 nM of hydroxyl radicals (Sicard-Roselli et al. [2014]). The reaction between $^{\bullet}$OH and coumarin is considered pseudo first order (Baldacchino et al. [2009]), and the constant of reaction with $^{\bullet}$OH was reported to be comprised between $k = 5.6 \times 10^9$ $M^{-1}s^{-1}$ and $k = 1.05 \times 10^{10}$ $M^{-1}s^{-1}$ (Baldacchino et al., C. et al., Cheng et al., Sicard-Roselli et al. [2009, 2018, 2012, 2014]). Obtaining 7OH-C/7OH-3CCA after the reaction with $^{\bullet}$OH is not direct as shown in Fig. 5.1. There are many intermediate reactions, intermediate products, and various final products detectable through chromatography (6OH-C, 7OH-C, 8OH-C, 5OH-C, 3OH-C and 4 OH-C) (Louit et al. [2005]). In pure water, under aerated conditions and in the absence of any other scavengers, Baldacchino et al. [2009] found that 5.6 nmol·$J^{-1}$of 7OH-3CCA represented 100 nmol·$J^{-1}$of $^{\bullet}$OH (i.e., ratio of 5.6 %), in close agreement with Newton and Milligan [2006] who found a ratio of 4.7 %. There has been reports of dependence on the yield of 7OH-3CCA/7OH-C according to the dose rate (Collins et al., Louit

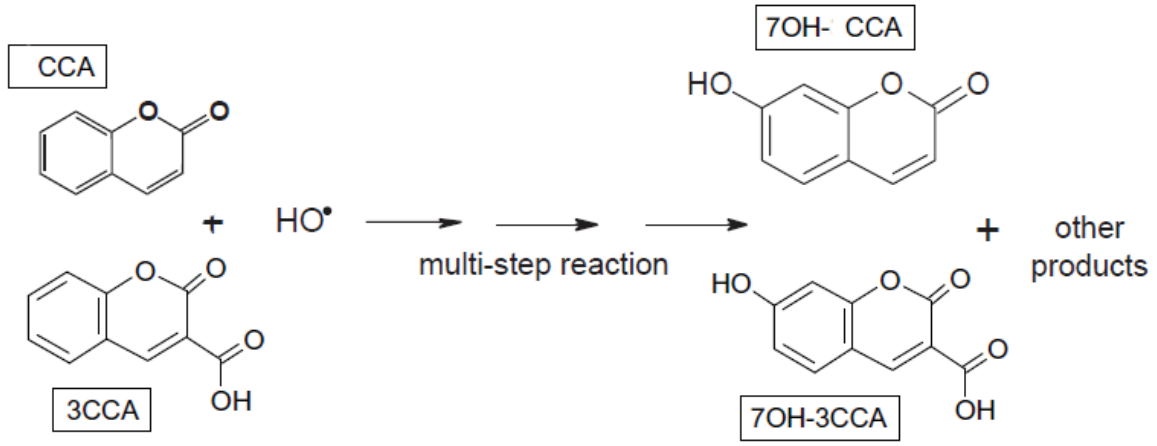

Figure 5.1.: Chemical reaction between C/3CCA and •OH to form 7OH-C/7OH-3CCA, adapted from Baldacchino et al., Louit et al. [2009, 2005].

et al. [1994, 2005]). They attributed this decrease to metal impurities (presence of Fe, Cr, Zn, Al, Mg and Ca by few ppm). The Fenton reaction, that occurs in presence of metal impurities, has a slow reaction constant (76 $M^{-1}s^{-1}$), and thus is favoured at low dose rate. It is also important to note that the reaction depends on experimental conditions and in particular on the amount of dissolved gases such as O_2 in water (Collins et al., Louit et al. [1994, 2005]).

5.1.2.2. Interference between coumarin and GNPs

In the thesis work of Gilles [2015], evidences of possible interactions between coumarin and GNPs were reported. First, a decrease of the fluorescence signal was observed after irradiation if the NP was incubated in the solution for a time larger than 40 s. This decrease was no longer visible when the NP was covered by molecules for functionalization, nor under saturated oxygen atmosphere. It was thus suggested that this decrease could be due to a surface effect, possibly linked to a covering of the NP with O_2 molecules, and in particular radiative or non radiative energy transfer from the 7OH-C to the NP. Additionally, the regioselectivity of the chemical reaction between coumarin and •OH changed in presence of GNPs. This change depended on the atmosphere conditions and the coating of the NP. The regioselectivity change was however the same within the range of studied GNP concentration. Finally, a possible covering of the GNP with coumarin molecules was reported. The amount of adsorbed coumarin was measured by mixing GNPs and coumarin, and by measuring the amount of coumarin left in solution after removing GNPs from the solution. The removal of GNPs was either directly applied by centrifugation, or by adding salts (NaCl) to first induce precipitation followed by centrifugation. For 0.5 mM of coumarin (concentration used for the measure of •OH), the number of coumarin molecules adsorbed per GNP was measured, for GNP concentration varying from 0 to 10 nM. Fig. 5.2 shows the proportion of coumarin in the solution that is adsorbed on the surface of GNPs. There is first an increase that tends toward a limit value of either ~ 3 to ~ 5 % depending on the measurement technique.

5.1.2.3. Results

Group University of California The different results of the group from the University of California are summarized in Tab. 5.1. In all studies, the enhancement factor (EF) was defined as the fluorescence signal with NP divided by the fluorescence signal without NP minus 1 (0 for no enhancement, 1 for 100 % enhancement).

Davidson and Guo [2014] measured the relative physical enhancement of radical production in presence of GNPs. To remove any possible chemical interference of the GNP with the probe,

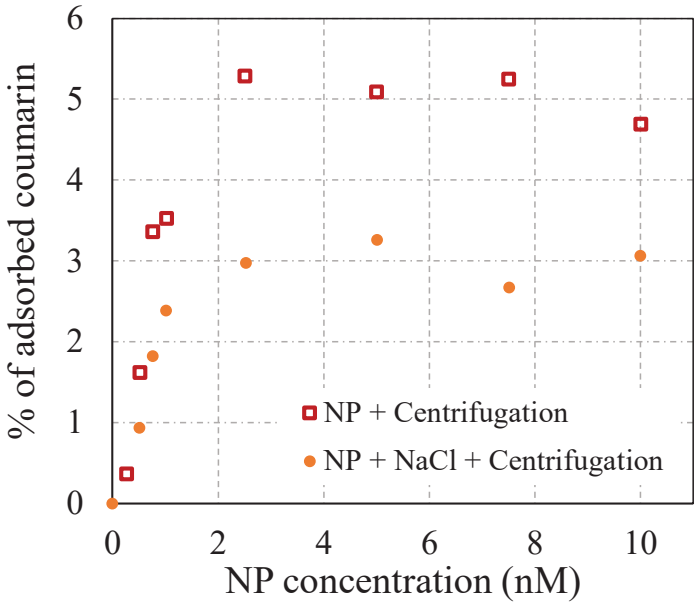

Figure 5.2.: Proportion of coumarin adsorbed on the surface of GNPs as a function of the GNP concentration, for a coumarin concentration of 0.5 mM. The data were taken from Gilles [2015].

they used SiO_2 covered GNPs. They obtained an enhancement normalized to the concentration of GNPs of 0.103 $(mg/mL)^{-1}$, which is close to their theoretical prediction based on the increase of dose deposition. The enhancement depended on the beam filter and therefore the energy of the photons. Unfiltered X-rays contain much more low (< 40 keV) X-rays photons, energies at which the contrast between water-photon and gold-photon cross sections is not optimal, reducing in turn the enhancement. As shown in the Tab. 5.1, the enhancement changed when varying the GNP size or coating. They attributed this change to a chemical enhancement additionally to the physical enhancement. They concluded that while large, coated NPs that prevent chemical enhancement can improve radiotherapy efficiency with *a priori* known, controlled mechanisms, smaller uncoated NP effects could be dominated by chemical effects that are yet not understood.

A second work by Cheng et al. [2012] focused on the chemical enhancement using uncoated GNPs. The chemical enhancement varied from 0 to 60 % for increasing GNP concentration. As illustrated in Tab. 5.1 for a 7 nm GNP, it strongly depended on the size of the GNP, the material, the coating and the dose rate. Finally, they also tested various scavengers such as sodium azide (NaN_3) to scavenge singlet oxygen, SOD to scavenge superoxide $O_2^{\bullet -}$ and sodium nitrate to scavenge solvated electrons. Only SOD resulted in a change, and induced a quenching of the enhancement, thus suggesting an implication of $O_2^{\bullet -}$ in the enhancement. As illustrated by Fig. 5.3, Cheng et al. [2012] hypothesized that weakly electronegative metal surfaces free of oxides (such as GNP or platinum NP) combined with $O_2^{\bullet -}$ are mandatory for a chemical enhancement. $O_2^{\bullet -}$ are mandatory to make NPs anionic, allowing 3CAA-OH$^\bullet$ to react on the surface and form 7OH-3CCA. They proposed that the NP coupled with a superoxide could react with 3CAA-OH$^\bullet$, to form 7OH-3CCA. An alternative would be that the NP coupled with a superoxide could enhance the reaction between a O_2 molecule and 3CAA-OH$^\bullet$ to form 7OH-3CCA. They excluded the possibility of superoxide conversion to $^\bullet$OH by the GNP. Davidson and Guo [2015] studied the combined effect of physical and chemical enhancement. They combined two NPs for the study: SiO_2@GNP, which was shown by Davidson and Guo [2014] to induce a physical enhancement, and hydroxymethal phosponium chloride (THPC)-coated GNP of 2.3 nm for the chemical enhancement. They found that the relative enhancement was 4.9-fold with SiO_2@GNP alone (75 mg·mL^{-1}) and 2.1-fold for THPC@GNP alone (0.2 mg·mL^{-1}). The enhancement was 18-fold when both were combined. Combining two NPs thus is a clear advantage in terms of chemical effect.

Ref.	Beam energy	NP	Probe	Sample	Enhancement
75	120 kVp + 0.127 mm Cu filter	(1) SiO_2@GNP (core 88 nm, coating 20 nm) (2) SiO_2@GNP (8 nm) (3) PEG@GNP (8 nm)	3-CCA fluorometry ($^{\bullet}OH$)	10 mM 3-CCA + phosphate buffer or DMSO, aerated solution	(1) 0.103 $(mg/mL)^{-1}$ (2) 0.116 $(mg/mL)^{-1}$ (3) 0.156 $(mg/mL)^{-1}$
51	100 kVp (Filter NS) or microfocus X-ray source 3.3 Gy min^{-1} + 6 to 40 Gy min^{-1}	7 nm GNP	3-CCA fluorometry ($^{\bullet}OH$)	1 mM 3-CCA + 5 mM DMSO, aerated solution	GNP concentration variation: at 3 Gy min^{-1}, max: 0.6 Beam rate variation: from 0.6 to a saturation of 2 (20 Gy min^{-1})
76	120 kVp with thin Cu filter 2.3 Gy min^{-1}	SiO_2@GNP (core 88 nm, coating 20 nm) + THPC@GNP (2.3 nm)	3-CCA fluorometry ($^{\bullet}OH$)	20 mM of 3-CCA + 100 mM of DMSO	4.9 for 75 mg/mL SiO_2@GNP alone 2.1 for 0.2 mg/mL THPC@GNP alone 18 for both combined

Table 5.1.: Main results of colloidal irradiation with different NPs of the group from University of California, probes and beam parameters. References: Davidson and Guo [2014][75], Cheng et al. [2012][51], Davidson and Guo [2015][76]. NS* = not specified.

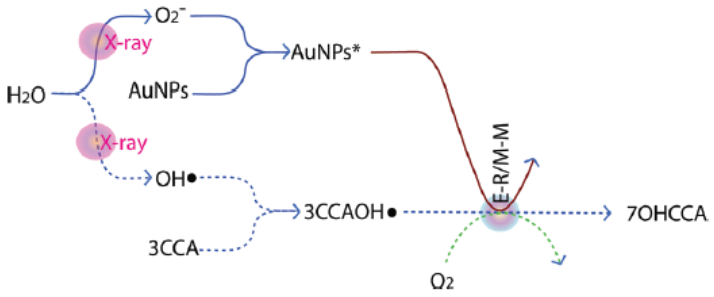

Figure 5.3.: Mechanisms proposed by Cheng et al. [2012] for the chemical enhancement of fluorescent coumarin detection for irradiated colloidal GNP solution. Taken from Cheng et al. [2012].

Group University Paris-Sud Because of the interferences between GNPs and coumarin, the Group from the University Paris-Sud (Gilles et al., Gilles et al., Sicard-Roselli et al. [2014, 2018, 2014]) applied a scaling coefficient in presence of GNPs for the conversion of the 7OH-C yield into $^{\bullet}OH$ yield, to ensure an absolute measurement of $^{\bullet}OH$. The coefficient was set to reach the radiolytic yield of $^{\bullet}OH$ in the absence of GNPs (i.e., 200 nmol·J^{-1}) when the concentration of GNPs tends towards 0 nM. The final enhancement of $^{\bullet}OH$ was defined as the yield of $^{\bullet}OH$ obtained with GNPs, to that of the yield without GNPs (i.e., 200 nmol·J^{-1}). Thus, for low GNP concentrations, the enhancement was, by definition, equal to 1. It is interesting to note that with this approach, 6 nmol·J^{-1} of 7OH-C gave 200 nmol·J^{-1} of $^{\bullet}OH$, leading to a ratio of 3.1 %. In pure water, as previously mentioned, it was found to be $\sim$ 5 %. By definition, this enhancement is therefore different than the one defined by the Group from University of California.

Using uncoated ("naked") GNPs, Sicard-Roselli et al. [2014] first showed that for a fixed concentration of NPs, the fluorescence yield linearly increased with the dose. The slope of the data provided the G-value (in nmol·J^{-1}), which was then obtained as a function of the GNP concentration (up to 6 nM). The G value of $^{\bullet}OH$ linearly increased with the concentration of GNPs up to 2 nM, after which there was a slow down in the slope that then reached a plateau. For GNP con-

	N_2	Air	Oxygen	Air + 0.1 % NaCl
		X-ray		
$^{\bullet}OH$	1812 ± 136	965 ± 48	174 ± 28	390 ± 34
e^-_{aq}	1539 ± 368			
EF_{max}	4.5	3.2	1.7	2.2
		γ-ray		
$^{\bullet}OH$	2474 ± 82	1356 ± 54	287 ± 18	
e^-_{aq}	2445 ± 406			

Table 5.2.: Slope (in nmol/J/(nM of GNP)) of $^{\bullet}OH$ and e^-_{aq} under different atmosphere conditions, obtained by Gilles et al. [2018]. The slopes are valid up to 0.3 nM, after which a plateau is reached. EF_{max} is the maximum enhancement factor when the plateau is reached at ≈ 1 nM of GNP, valid for both chemical species.

centrations below 2 nM, a slope of 221 nmol·J^{-1}/(nM of GNP) was obtained. They pointed out that a pure physical effect would only lead to a slope of 5 nmol/J/(nM of GNP), and is thus not sufficient to explain the extent of the effect. In a second study, Gilles et al. [2014] showed that this slope strongly depended on the surface properties of GNPs. It decreased with increasing number of atoms attached on the surface. When introducing DNA in the solution, the enhancement of DNA damages was about twice lower than the $^{\bullet}OH$ enhancement. They pointed out the fact that enhancement factors are particularly low when GNPs are covered with albumin, which could be a problem given that GNP are covered with a protein corona in biological fluids. However, many authors have reported *in vitro* effects despite high molecular weight coating, suggesting that the radiosensitization could imply different mechanisms. In their last recent paper, Gilles et al. [2018] determined the production of solvated electrons additionally to $^{\bullet}OH$ with uncoated GNPs, using different atmosphere conditions. Introducing N_2O atmosphere enables the detection of solvated electrons through the reaction, $e^-_{aq} + N_2O + H_2O \rightarrow {}^{\bullet}OH + {}^{-}OH + N_2$. They also measured the enhancement with a MeV photon source (against keV in the previous works), to study the impact of the photon energy. As previously observed, they found that the first part of the curve (0 - 0.3 nM) was linear and sharply increased for all atmospheres. It was followed by a slowing down in the slope before reaching a plateau at ∼ 1 nM. The slopes were different according to the atmosphere conditions and are given in Tab. 5.2. In addition to previous finding, they found similar efficiency for γ-rays, for which there is no increase of energy absorption coefficient in gold. They concluded that the GNP/water interface plays a key role. To verify their hypothesis, they added salts in the solution, which interacted with GNPs and are believed to modify the interaction of water at the GNP surface. They found a decrease of the measured yields, which testified a perturbation of the whole process.

5.2. *In solution*: Colloidal GNP and biomolecules

As pointed out by Her et al. [2017], the study of the effect of NPs on molecular targets such as DNA plasmid enables to assess the radiation-induced molecular damage in the absence of cellular biological response to radiation. Although it might not be representative to what happens on a cellular level, it provides a good first insight of the effect of NPs on a sensitive cellular target, while removing the complexity of cellular mechanisms. This section gives an overview of the experimental data of irradiation of either DNA plasmid or protein in a colloidal GNP solution. The objective is to give a first insight on the effect of GNP on molecular targets, and how the different parameters governing GNP radiosensitizing effects might influence the results. As pointed out by Brun and Sicard-Roselli [2016], experimental conditions and measured metrics might be crucial when studying the extent of the effect. Hence, Tab. 5.3 provides technical details to define the system as precisely as possible. Inter-comparison of the data must be taken with care, as the system might be completely different from one experiment to another.

It should be noted that a few studies (Huang et al., Xiao et al., Yao et al., Zheng and Sanche, Zheng et al., Zheng et al. [2013, 2011, 2015, 2009, 2008, 2008]) have reported results for electron irradiation of dried DNA+GNP samples. Although these results are interesting, they are far away from *in vitro* and *in vivo* experimental conditions. The water medium and chemical interaction of radical species might be crucial in the radiosensitizing effect of GNPs and misrepresented for lyophilized samples. Thus, only studies set up in an aqueous environment were reported.

5.2.1. Plasmid DNA damages

Plasmid DNA is a useful tool to study the effect of ionizing radiation because damage causes a topological change in the DNA that can be determined by agarose gel electrophoresis. When supercoiled (SC) plasmid DNA (scDNA) has a break in one strand, the molecule adopts a change in its structure to an open circular form (OC, or relaxed form). When the break occurs in both strands of the DNA (typically within 10 base pair of each other, which represents about 3 nm), the structure of the molecule becomes linear (L). The amount of DNA in the linear form is usually much lower than the amount of DNA in the other forms, especially at low dose. Note that, according to the reference, experimental values greatly varied even without GNP, partly due to the sensitivity of the results to the chemical environment (Butterworth et al. [2008]).

5.2.1.1. scDNA-GNPs complexes

Two experiments (Carter et al., Foley et al. [2007, 2005]) studied DNA damages for scDNA-GNP complexes. In both, the enhancement was defined as the ratio of DNA SSB in presence of GNPs to that without GNP. At 1 Gy, Foley et al. [2005] obtained 50 % of scNDA in relaxed/circular form in presence of GNPs, against 25 % in absence. The enhancement was maximum at this dose (0.5 - 2 Gy). At higher doses, most of the scDNA was in its relaxed form even without GNPs, thus decreasing the ratio down to 1. Carter et al. [2007] reported a distance between the GNPs and DNA lower than 2 nm. $^{\bullet}$OH scavengers (TRIS) at different concentrations were used. In absence of scavengers, no enhancement effect was observed when comparing irradiation with and without GNPs, as SSBs were dominated by reactions with $^{\bullet}$OH coming from the surrounding irradiated aqueous solution. When the concentration increased up to around 100 mM, the enhancement peaked at a value of 150 %. All the $^{\bullet}$OH from long range background irradiation were scavenged and only locally produced ($\leq$ 5nm) $^{\bullet}$OH could react. This peak was associated to the locally produced Auger electrons. Then when TRIS concentration kept increasing, as the $^{\bullet}$OH from short distances were scavenged too, no effect was observable anymore. It was concluded that additional DNA damages coming from GNPs were caused mostly by low energy electrons, and that the range of action was about 5 nm. The two experiments are hardly comparable, due to experimental conditions that varied a lot from one to the other. Though, surprisingly, the extend of the effect was close, with a maximum of 2.1 for Foley et al. [2005] *vs* 1.5 for Carter et al. [2007], despite the first experiment reporting 100 GNP per scDNA *vs* 10 GNP per scDNA for the second one.

5.2.1.2. Negatively charged GNPs

The e1xperiments using negatively-charged GNPs reported no particular attachment of GNPs to scDNA. Brun et al. [2009] aimed at studying the radiosensitizing effect as a function of the beam energy, GNP size and GNP concentration. When studying the impact of GNP concentration, they found a linear increase of the enhancement with increasing gold concentration. Using a fixed GNP concentration of 1 nM, they studied the impact of the GNP size. Note that 1 nM of 8.1 nm of GNP represents 0.003 mg/mL (of gold), 1 nM of 20.2 nm GNPs 0.05 mg/mL, 1 nM of 37.5 nm GNP 0.3 mg/mL and 1 nM of 91.7 nm GNP 4.7 mg/mL. They found that the enhancement increased linearly with the diameter of the GNP. Regarding the energy of photons, they found two maxima around 30 and 50 keV of equivalent energy. However, the standard deviation was

Reference	Beam	Dose	Medium	NP	Molecule	NP/Molecule Distribution	NP:Molecule ratio	Biological measurement	Maximum enhancement	Additional information
DNA in solution										
GNP-scDNA complexes - Enhancement definition: ratio of damages with GNP to that without GNP										
Exp. 1[92]	Photons 100 kVp	0 to 8 Gy 0.5 Gy/min	Aqueous	TMA-C_{12}GNP 10/15 ligands per NP 5.6 ± 1.7 nm Positively charged	scDNA 500 nm long 1.5 nm diameter	Bound to DNA	100:1 200 ng scDNA	SSB by agarose gels	200 % at 2 Gy	At 1 Gy, 50 % of scDNA in circular form for NP-DNA against 25 % without NP. Enhancement ratio decreases with increasing radiation
Exp. 2[45]	Photon 100 kVp	100 Gy?	Aqueous solution 100 ng of scDNA in 5 μL of water + 10 μl of NP solution (or water for control) + 5 μL of different TRIS concentration solutions Final DNA concentration 10 ng/μl	3-nm NP ethidium-based intercalating ligand (ligand per NP < 10) and charge-neutral surfactants	scDNA 500 nm long 1.5 nm diameter	Bound to DNA Average distance < 2 nm	10:1	SSB by agarose gel	Up to 1.50	Damages are effective within 5 nm away from GNP. In presence of surfactants alone, no change in yields observed.
Negatively charged GNP- Enhancement definition: ratio of slope of damages as a function of the dose of irradiation										
Exp. 3[38]	Photon 160 kVp (Av. energy 80.7 keV)	0 to 1000 Gy 14.3 Gy/min	Aqueous solution with 2 types of buffer: - TE buffer (10 mM Tris, 1 mM EDTA, pH 7.5) - PBS (137 mM NaCl, 10 mM PO4, 2.7 mM KCl) + DMSO added to investigate free radical scavenger effect	30 nm silver NP 1.5 μm GNP 5 nm GNP 20 nm GNP	5.4 kbp DNA (pCDNA3.1)	Not provided	NP 50 μg/L 500 ng of DNA	SSB and DSB (in $Gy^{-1}.Da^{-1}$) by agarose gel	**TE Buffer** **No NP**: SSB 1 DSB 1 **1.5 μm**: SSB: 1.41, DSB 1.12 **20 nm**: SSB : 2.12, DSB 1 **5 nm**: SSB : 2.29, DSB 1.25 **Silver**: SSB : 1.41, DSB 1.03 **PBS** **No NP**: SSB 100 DSB 48 (compared to Tris) **5 nm**: SSB 0.21, DSB 0.33	Without NP, increase of SSB/DSB when replacing TE buffer with PBS buffer but ineffective with NP.
Exp. 4[37]	X-ray av. energy 14.8 keV, 24.4 keV, 29.8 keV, 42.4 keV, 49 keV, 70.1 keV	2-3 Gy/min 0 - 5 Gy	TE buffer (10 mM Tris, 1 mM EDTA, pH 8) and desalted	8.1 nm GNP 20.2 nm GNP 37.5 nm GNP 91.7 nm AuNP Negatively charged	pGEM-3Zf(-) DNA (negatively charged, 3197 bp)	No strong interaction reported	DNA: 5 nM GNP: 0 to 5 nM 1:10 1:2 1:1	SSB with agarose gel (% SC)	**Concentration** (49 keV, 37.5 nm): linearly increases, max at 5 nM (1:1), reaches ≈ 3.3 **Size** (1:5, 49 keV): linearly increases with diameter, max at 90 nm ≈ 3 **Energy** (1:1, 37.5 nm): Two maxima around 30 and 50 keV reaching ≈ 3-3.5	Samples exposed at 15 cm from source in a treatment cylinder of 2.5 cm of diameter
Exp. 5[193]	(1) Mono- energetic: 8 to 60 keV (2) Mono- energetic: 30 to 80	(1) 0-50 Gy 195 Gy/s	DNA prepared in TE buffer (10 mM Tris, 1 mM EDTA, pH 8) (1) TE buffer diluted with water (0.25 mM Tris) (2) 2 μg/mL of DNA 1600 μg/mL of GNP	(1) 11 nm (2) 37.5 nm	(1) pcDNA3.1 (5400 bp) (2) pUC18 (2686 base pairs)	No strong interaction reported	(1) 1 per 4 plasmid (1 per 21 600 bp) (2) 1 per 640 pb	SSB (poor results with DSB) with agarose gel	Maxima around 20-30 and 50-60 keV reaching 1.3	Concentration of gold always < 1% by mass (2) In treatment cylinder (see above)
	160 kVp (Av. energy 78 keV)	Up to 500 Gy	Same as (1), with different Tris concentrations (0.25 mM to 5 mM)	11 nm GNP	pcDNA3.1 (5400 bp)	No interaction reported	1 per 4 plasmid	SSB with agarose gel	From 1.5 at 0.25 mM down to 1.25 at 1 mM and ≈ 1 at 5 mM	Decrease as function of TE concentration. Enhancement quenched by high concentration of scavengers. Effect conducted by radical species production.
Protein										
Exp. 6[36]	^{60}Co (1.3 MeV) + X-ray source (Av. energy 8 keV, 24.4 keV and 49 keV)	Up to 340 Gy, X-ray source 2 Gy/min	10 mM phosphate buffer pH 7 Protein concentration 16.5×10^{-6} mol/L	GNPs Radius 37.5 ± 5.6 nm Negatively charge	Human centrin 2 (Hscen2) Small acidic protein (172 amino-acids) Can play a role in DNA repair. Highly sensitive to oxidizing radicals. Size 6 nm × 3 nm.	Interaction through electrostatic forces. At least 500 Hscen2 per NP	2×10^{-5} 1×10^{-4} 2×10^{-4}	Visualization of damages with SDS-PAGE (gels) + HPLC (liquid chromatography) Quantification with HPLC	**At 8 keV** 2×10^{-5}: 1.22 1×10^{-4}: 1.15 2×10^{-4}: 1.48 **At 2 $\times$ 10^{-4}** 8 keV : 1.17 (Inconsistent with above) 24.4 keV : 1.13 49 keV : 1.30	Damages could be missing due to technique of measurements Enhancement obtained by dividing the slopes of the damage=f(dose) function

Table 5.3.: Overview of experimental set-up and enhancement of bio-molecule damages in presence of GNPs, reported in the literature. *bp = base-pair

rather large, making it difficult to clearly conclude. In the same spirit, McMahon et al. [2011] studied the impact of the beam energy with an addition of 2 sets of independent experiments. They obtained a similar trend as reported by Brun et al. [2009], with a local minimum at 40 keV and two maxima around 20-30 keV and 50-55 keV.

Butterworth et al. [2008] tested the impact of the chemical environment on the scDNA damages in presence of GNPs. The amount of damages was mostly linear with the dose, and a linear fit was done to obtain the slope, defined as the yield of plasmid damage (in $Gy^{-1}{\cdot}Da^{-1}$). When using a TE (Tris-EDTA) buffer, they obtained SSB yield enhancement as high as 2.29 for 5 nm GNPs, and as high as 1.25 for DSB yield enhancement. When replacing the TE buffer by PBS, in the absence of GNPs the number of SSBs was multiplied by 100, while the number of DSBs was multiplied by 48. This displays the protective effect of Tris, which is know to scavenge hydroxyl radicals. Surprisingly, when comparing the yield with PBS and with *vs* without GNP, the yield was lower in presence of 5 nm GNPs (enhancement of 0.21). McMahon et al. [2011] also tested the impact of the chemical environment. For varying Tris-EDTA concentrations (0.25 mM to 5 mM), the authors found that the enhancement dropped from 1.5 at 0.25 mM down to $\sim$ 1.25 at 1 mM, and down to nearly 1 at 5 mM of TE. McMahon et al. [2011] concluded that the dose enhancement due to the presence of GNP could not explain the enhancement measured. In particular, 0.01 mg/mL of gold only increased the dose of $\sim$ 0.1 %, while they obtained much larger enhancement of DNA damages, suggesting a complex mechanism. A precise knowledge of the geometrical characteristics of the system, in particular the distance between GNPs and DNA plasmids is required to conclude whether, in particular, Auger electrons and subsequent radical species could be partly responsible for the enhancement as observed for DNA-GNP complexes, or if another process such as a catalytic process would be at the origin of the effect.

5.2.2. Protein damage and biomolecular corona

Brun et al. [2009] studied the effect of GNPs on the protein Hscen2 (human centrin 2) damages under photon irradiation in colloidal solution. These proteins have been reported to be involved in the process of DNA repair and are highly sensitive to oxidizing radicals. The measurement of the protein degradation relies on the separation of the protein and damaged pieces by the size (SDS-PAGE or HPLC, gels or liquid chromatography). When adding GNPs, bounding between proteins and GNPs occur through electrostatic and Van der Waals interactions, which are detectable through spectroscopy and flocculation tests. Although the quantification of the number of proteins per GNP is unknown, the flocculation test showed that at least 500 molecules of Hscen2 were adsorbed per GNP. Despite the very low NP/protein ratio (2×10^{-5} to 2×10^{-4}), they reported significant effects when irradiating under low energy X-rays. $^{\bullet}$OH or aqueous electrons coming from the GNP, and in particular low-energy Auger electrons, could be responsible for the attack of proteins adsorbed on the surface, as observed for DNA-GNP complexes.

5.3. *In vitro*

The experimental *in vitro* radiosensitizing effect of GNPs is often expressed as a ratio of two measurable experimental quantities, that are obtained with *vs* without NP under irradiation. As stated by Retif et al. [2016], this ratio depends on many parameters (cell, GNP, beam, etc.). The experimental set up, as previously discussed, may greatly affect the NP uptake, and thus their biodistribution. The type of cells significantly change the effect as well. The biological endpoint itself is also crucial. In an effort to compare quantities with a fully described system, the experimental results were classified in a set of tables (Tab. A.1 to A.9 of Appendix A.1). In these tables, the data are ordered for a given type of NP. They may be used at any time to have a full description of the studied system.

5.3.1. Quantification of cellular uptake

In Tab. A.1 to A.9, the extracellular concentration used in each experiment was systematically specified (in nM and mg of gold/mL) along with the time of incubation. Note that concentrations had to be sometimes calculated from the data provided in the paper. When available the intracellular number of GNP, and the weight of gold internalized per cell were indicated. As most of the time, intracellular concentrations were either given in number of GNPs/cell or pg/cell, the second one was calculated based on the average gold core size that was provided in the paper (for TEM imaging), to enable a consistent cross-checking. When authors specified if the extracellular medium containing GNPs was removed before irradiation, it was indicated in the tables. This last point is actually potentially crucial, as later discussed.

The intra-cellular weight of gold was found to be extremely variable. Under normal oxygenation, the lowest intra-cellular weight that was reported was 0.042 pg/cell, and it reached more than 100 pg/cell. However, only AuroVist^{TM} GNPs and tiopronin GNPs reached very large concentrations (> 12.3 pg) and it was often accompanied with cytotoxic effects. An exception is to be noted for folic acid 4ATP-GNP, which reached concentrations as high as 44 pg/cell without any reported cytotoxic effects. The intra-cellular gold weight was extremely dependent on the cell line, time of incubation, extra-cellular incubation concentration, and type of GNPs.

The volumes of the cells are mandatory to convert gold weight to intra-cellular gold concentration (in mg·mL^{-1}). However, in most of the studies, these values were not provided. This makes the determination of intracellular gold concentration impossible for most experimental studies, as the variation of cell volumes is very large. This is illustrated by the study of Lechtman, Lechtman et al. [2013, 2013]: 6.19 pg/cell of GNPs for PC-3 cell line represented only 0.84 mg/mL of gold per cell, while 2.78 pg/cell of GNPs for SK-BR-3 cell line represented 1.19 mg/mL. This lack of experimental data makes the assessment of the radiosensitizing effect particularly difficult, as these data are required in particular to study dosimetric quantities at nanoscale.

5.3.2. Biodistribution

Many authors have performed TEM images of cells containing GNPs to get the biodistribution of NPs. Regardless of the GNP surface coating, cell line or oxygenation condition, the vast majority of the studies found that GNPs, once internalized, were located within membrane-coated vesicles (endosomes/lysosomes). The analysis of the TEM images showed that the size of these lysosomes varied, with diameters reported from 150 nm to a few thousands of nm. As previously discussed in Chapter 4, the accumulation of GNPs within lysosomes is a time dependent process. Images of Bobyk et al. [2013] showed that, while originally GNPs were contained in relatively small dispersed vesicles, they eventually accumulated in larger lysosomes. This is consistent with the trafficking of vacuoles that tends toward their fusion with lysosomes.

When the GNPs were very small (AuroVist^{TM} or 2.7 nm tiopronin-GNPs), the GNPs appeared particularly densely packed in clusters in the lysosomes. Large clusters, up to a few hundreds of nm in diameter, could be reached. Zhang et al. [2012] reported that PEG-GNPs formed larger clusters of 35-60 nm in size. When the size of the GNP increased, the number of GNP per vesicle appeared to decrease. The number of GNPs per vesicles was rarely investigated, nor the number of clusters per cell. For modelling purposes, Retif et al. [2016] estimated about 10 clusters of radius 250 nm containing 100 GNP of size 20 nm and only about 9 clusters of 50 nm GNPs. Jeynes et al. [2014] reported a much larger amount of vesicles (135 of size varying from 150 to 350 nm) each containing between 30 to 100 GNPs per vesicle.

A few authors reported that the vesicles accumulated in the perinuclear region. In particular, McQuaid et al. [2016] measured a peak of localisation of the GNPs at 500 nm from the nu-

clear membrane, for MDA-MB-231 cells incubated with AuroVist^{TM} GNPs. Marginally, Song et al. [2013] found glucose-capped GNPs in the nucleus and mitochondria, while Zhu et al. [2015] found citrate-capped GNPs in the mitochondria. One study achieved efficient nuclear targeting with a specific functionalization of the GNP.

5.3.3. Quantification of the radiosensitizing effect with the clonogenic assay

5.3.3.1. Biological endpoint

The characterization of the radiosensitizing effect of GNPs greatly depends on the biological endpoint chosen, and the lack of standardization is a major obstacle for intercomparison of results (Subiel et al. [2016]). When studying the radiosensitizing effect of GNPs with clonogenic assays, the final radiosensitizing effect is defined as the ratio of a biological endpoint (e.g., ratio of doses, ratio of surviving fractions, etc.) without and with GNPs. There are many possible biological endpoints, and the extent of the effect differs depending on which one is chosen. Throughout the different papers studied, extremely variable ways of defining this ratio were found: the radiosensitizing effect was evaluated either with a ratio of surviving fractions (SF) for a fixed dose or a ratio of dose for a fixed cell survival. The radiosensitizing effect was also studied with the α/β parameters of the LQ model, or with the ratio of Mean Inactivation Dose (MID) (integral of the surviving fraction curve). These different quantities are not directly comparable to each other. As an illustration, let us take the case for which $\alpha_{NP} = 0.3$ Gy^{-1}, $\beta_{NP} = 0.05$ Gy^{-1}; and $\alpha_{Cont} = 0.1$ Gy^{-1} (e.g. α for control, without NP), $\beta_{Cont} = 0.02$ Gy^{-1} (Bobyk [2010]). The ratio of MID is $\sim$ 2. The ratio of doses is 3 for SF of 0.9 % and 1.9 for SF of 0.1 %. The ratio of survival fractions is 1.7 for fixed dose of 2 Gy, and 2.8 for fixed dose of 4 Gy.

Thus, to offer some clarity, and in order to compare more rigorously the enhancement ratio from one experiment to another, we separated each of these types of enhancement in Tab. A.1 to A.9 and, when possible (i.e. when α and β parameters were available) calculated some of them. In this section, a ratio of doses is referred to as the dose enhancement ratio (DER), and a ratio of survival fractions as the survival enhancement ratio (SER). Given the very large variety of results, only the most commonly found quantities were calculated, i.e. the SER at 2 and 4 Gy, the DER at a SF of 0.1 and 0.9 and the MID ratio. These quantities calculated with the LQ model were put in italic to identify them from the ones provided by the paper.

5.3.3.2. Impact of the GNP intra-cellular concentration

The impact of GNP intra-cellular concentration on the final radiosensitizing effect has surprisingly not been much studied. On the one hand, a few studies showed that an increased gold concentration induced an increased radiosensitization effect Cui et al., Kong et al. [2014, 2007]. By varying the time of incubation or the extra-cellular concentration, Cui et al. [2014] obtained intra-cellular concentrations of gold varying from 8.6 to 100.1 pg/cell, for (2.7 nm) tiopronin GNPs in MDA-MB-231 cells. As displayed on Fig. 5.4, there is a visible trend showing an increase of the SER at 4 Gy with increasing cellular concentrations. In this study, tiopronin GNPs achieved a very high uptake compared to other GNPs. We may thus expect a significant physical dose enhancement, that could explain the trend we observe. A significant toxicity was reported for high intra-cellular concentration. Additionally, many authors (Chattopadhyay et al., Jeynes et al., Khoshgard et al., Zhu et al. [2013, 2014, 2014, 2015]) showed that functionalizing the GNPs lead to higher cellular uptake, and further lead to higher radiosensitizing effects despite similar GNPs intracellular biodistribution. On the other hand, Chithrani et al. [2010] obtained a higher massic concentration of gold for 74 nm GNPs (12.3 pg/cell) but it showed a lower DER for a survival of 0.1 than 50 nm GNPs (7.58 pg/cell). The DER appeared to be linearly correlated with the number of GNPs per cell, rather than the massic gold concentration. Similarly, Lechtman, Lechtman et al. [2013, 2013] showed that despite achieving a lower gold intracellular uptake

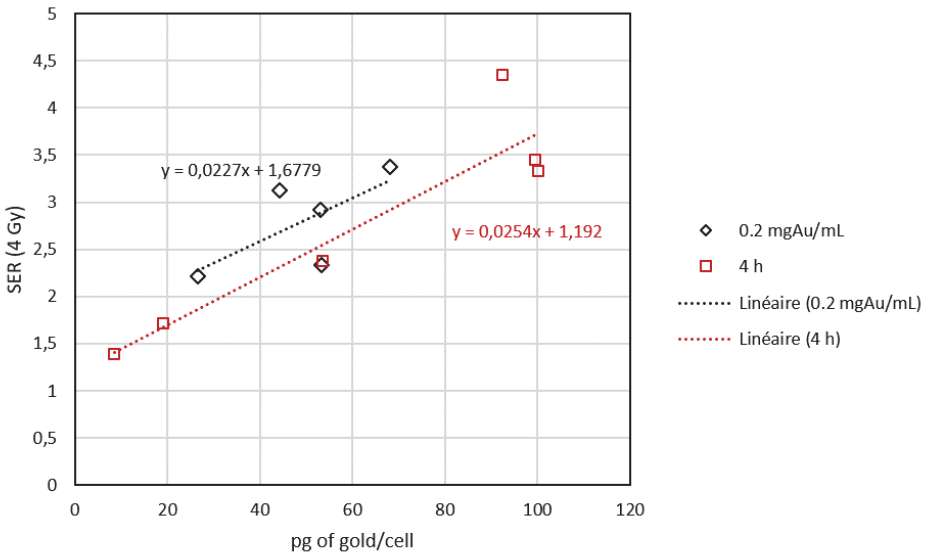

Figure 5.4.: SER at 4 Gy as a function of the intra-cellular gold concentration, for MDA-MB-231 cells irradiated with a 225 kVp irradiator. Two sets of data are presented (1) 0.2 mgAu/mL are a set of data for which cells were incubated with a constant extra-cellular concentration of gold, for a time varying from 1 h to 24 h, (2) 4 h are a set of data for which cells were incubated with a constant time of 4 h, and extra-cellular concentrations varying from 0.04 mgAu/mL up to 0.8 mgAu/mL. All the data were taken from Cui et al. [2014].

(30 nm : 0.84 mg/mL, 5 nm : 0.38 mg/mL), 5 nm PEG-GNPs had a higher MID ratio (1.36) than 30 nm PEG-GNPs (1.21). The number of GNPs per cell was much higher for 5 nm GNPs (2.15×10^6) than 30 nm GNPs (2.27×10^4). As previously explained, it was shown that larger GNPs resulted in a lower number of clusters than for small GNPs (Retif et al. [2016]). Thus, the radiosensitizing effect may depend on the number of clusters that are formed at the time of irradiation, rather than the actual massic gold concentration or the number of GNPs per cell. This requires further systematic investigation to be confirmed.

5.3.3.3. Impact of extra-cellular GNP biodistribution

A couple of papers (Bobyk et al., Cui et al. [2013, 2014]) studied the impact of the presence or absence of GNPs in the extra-cellular medium prior to irradiation, both at keV photon irradiation. In the study by Bobyk et al. [2013], F98 cells were either mixed with the medium containing 10 mg·mL^{-1} of 1.9 nm and 15 nm AuroVist^{TM} just before irradiation, or pre-incubated, before washing the medium containing the GNPs. Thus in the first case the GNPs were mostly only in the extra-cellular region while in the second case they were mostly only in the intra-cellular region. Under these conditions, the authors found that the effect was more important when GNPs were located in the extra-cellular area. In the study by Cui et al. [2014], MDA-MB-231 cells were irradiated with a medium containing 0.4 mg·mL^{-1} of 2.7 nm tiopronin-GNPs (1) with an incubation of 4 h and not removing the medium prior to IR, (2) with an incubation time of 4 h and removing the medium prior to IR and (3) without an incubation and the medium was added just prior to IR. Note that after a 4 h incubation period, approximately 5 % of the total amount of gold was inside the cells while 95 % remained in the extra-cellular medium. The intra-cellular concentration reached about 93 pg per cell. In this case, the conclusion appeared opposite to that of Bobyk et al. [2013]. Removing the extra-cellular medium prior to irradiation did not yield a significant difference compared when the GNPs were incubated (1 and 2). However, without incubation prior to irradiation, no significant radiosensitizing effect was observed (3). The apparent opposite conclusions could be explainable by the difference of extra-cellular concentration used. While the first one used 10 mg·mL^{-1} of gold, the second one used only 0.4 mg·mL^{-1}. In

the first case, a significant macroscopic physical dose enhancement occurs while in the second one, the physical dose enhancement will be negligible. These findings suggest that efficient delivery of AuNPs into target cells is crucial for full exploitation of their radiosensitization effects if the gold concentration is low.

5.3.3.4. Impact of intra-cellular GNP biodistribution

The vast majority of studies found GNPs within vesicles inside the cytoplasm. However, Yang et al. [2014] compared the radiosensitizing effect of BSA-peptide GNPs *vs* non-targeted GNPs on HeLa cells. The targeted GNPs managed to reach the nucleus of the cells, and a higher intracellular uptake. The sensitizing effect was estimated for a fixed dose of irradiation of 2 Gy. They found that while non-targeted GNPs reached a SER of 1.26 at 2 Gy, targeted-GNPs reached a SER of 4.4. This was associated with an increase of DNA-DSB at 24 h. This suggests that targeted GNPs could have a great impact on the radiosensitizing effect. While they did not perform a clonogenic assay but a MTT assay (a colorimetric assay that estimates cell metabolic activity based on the enzymatic reduction of tetrazodium dye), Kong et al., Kong et al. [2007, 2008] tested Glu-GNPs and AET-GNPs on MCF-7 cells. The former were mostly internalized while the later were mostly localized on the cell membrane. For a same number of GNPs per cell for both Glu-GNPs and AET-GNPs,[160] showed that cells treated with Glu-GNP and X-ray irradiation (200 kVp, 10 Gy) had a lower cell viability 48 h post irradiation than cells treated with AET-GNPs and X-ray. Optimizing the GNP biodistribution could therefore greatly impacts the radiosensitizing effect: internalization of GNPs appears to reach higher effects, even more when targeting the nucleus.

5.3.3.5. Impact of the cell line

Few studies have shown that the cell line considered definitely impacts the extent of the radiosensitizing effect. For instance, for AuroVist^{TM} GNPs, Butterworth et al. [2010] showed a great difference of the radiosensitizing effect depending on the cell line studied, despite identical experimental conditions. One reason of these disparities could be the ability of cells to internalize GNPs. Jain et al. [2011] showed a correlation between, intracellular concentrations of MDA-MB-231, DU145 and L132 cells and the SER at 4 Gy for AuroVist^{TM} GNPs. However, Jain et al. [2011] also showed that the radiosensitizing effect was not systematically significant despite established cellular uptake. Another interesting result was established by Kong et al. [2008] with an MTT assay. Using Glu-GNP and two cell lines MCF-7 and MCF-10A (non malignant), they found that despite similar the intracellular concentration, they did not have the same cell viability at 220 kVp (40 % *vs* 75 %). This was not observed when using AET-GNPs: both cells had the same viability. Coulter et al. [2013] concluded that the disparities between the radiation sensitivity of different tumour cell lines, despite continuity between all other variables, suggest complex biological responses.

5.3.3.6. Impact of the beam type and energy

A few studies focused on the dependence of the effect with regard to the photon energy in the keV range, with either a synchrotron (Rahman et al. [2014]) or a kVp irradiator (Chithrani et al., Khoshgard et al., Lechtman, Rahman et al. [2010, 2014, 2013, 2009]). Chithrani et al. [2010] showed that increasing the energy (105 kVp, 220 kVp and 662 keV) decreased the radiosensitizing effect. Likewise, Lechtman [2013] showed that irradiating with a 100 kVp photon source (average energy 33 keV) resulted in a higher effect compared to a 300 kVp photon source (average energy 100 keV). Investigating more in details in the 20-100 keV range, Rahman et al. [2014] used BAEC cells incubated with AuroVist^{TM} and irradiated with a monochromatic source. They found a first peak around 40-60 keV. It was followed by a drop at 70 keV, before increasing again at 81 keV, just after the K-shell threshold. These findings suggest that there is definitely a dependence

of the effect depending on the photon energy. Rahman et al. [2014] obtained maxima that are consistent with the predicted photon-cross section enhancement between gold and soft tissue. Thus, for those experiments, at least part of the effect is due to a physical effect. Such effect is expected to strongly correlate with the concentration of GNPs, both intra- and extra-cellular.

As many clinical beams operate under MeV energies, many authors investigated the effect of GNPs under MeV photon irradiation. At these energies, the ratio of photon attenuation in gold over tissues is close to 1 (see Fig. 3.3), and thus no physical dose enhancement is expected. Despite these predictions, many authors[55,104,134,148,160] have reported a radiosensitizing effect. This suggests that either chemical or biological mechanisms are partly responsible of the effect. However, in all the studies, the effect was reported smaller compared to keV photon irradiation. These mechanisms might therefore add up.

A few authors investigated the possible radiosensitizing effect of GNPs for electron (Jain et al., Rahman et al. [2011, 2009]), proton (Li et al. [2016]) or carbon ion (Kaur et al., Liu et al. [2013, 2015]) irradiation. Modest but yet significant radiosensitizing effects were often obtained, which were though reported lower than for keV photon irradiation. Mechanisms of ion irradiation in combination with GNPs are not yet fully understood, and are under investigation. A review with additional details is available elsewhere (Lacombe et al. [2017]).

5.3.3.7. Effect of oxygenation

Two papers (Cui et al., Jain et al. [2014, 2014]) studied the effect of oxygen level on the radiosensitizing effect of GNPs. As discussed in chapter 3, the level of oxygen is known to affect cell radiosensitivity. In each case, the protocol was different, but both used the MDA-MB-231 cell line, and keV photon irradiation. The physiological oxygen level of normal tissues is commonly in the range 3.5 to 6 % but is often below 2.5 % in cancer tissues.

Both obtained a lower cellular uptake of GNPs when cells were under hypoxic conditions. Jain et al. [2014] suggested that this was due to lack of energy, as endocytosis is an energy dependent process. In an anaerobic process, glycolysis generates less energy. At 1 % oxygen, Jain et al. [2014] obtained roughly the same intra-cellular concentrations as for oxic condition. Jain et al. [2014] obtained a significant radiosensitizing effect under normal and 1 % oxygen level for MDA-MB-231 cells. They obtained no significant radiosensitization in MDA-MB-231 cells under 0.1 % oxygen level, despite a lower but still significant internalization of GNPs. Cui et al. [2014] studied the effect of chronic *vs* acute hypoxia. These conditions are meant to reproduce the conditions in solid tumours where some cells may undergo acute hypoxia due to cycles of hypoxia and reoxygenation over minutes to hours, or chronic hypoxia due to cell proliferation and increasing distance from blood vasculature. They obtained a greater radiosensitizing effect in cells under oxio, followed by chronic and then acute hypoxia. Compared to the other study, they found that hypoxic conditions did not limit the efficacy of GNPs.

5.3.3.8. Effect of NPs geometry

While GdNPs will not be studied in this thesis, the experimental work from Delorme, Taupin [2013, 2013] provides additional interesting information on the impact of the NP geometry on the radiosensitizing effect. The experiment was done with spherical GdNPs (hydrodynamic diameter 2.5 nm) and a contrast product (Magnevist^{TM}, i.e. a small molecule) to study the impact of the gadolinium geometry on cell survival (NP vs molecule). TEM images showed that GdNPs tend to aggregate on the cellular membrane rather than in the cytoplasm, while the Magnevist^{TM} was overall rather homogeneously distributed. The results showed that an increase of the effect occurred at the photo-electric threshold of gadolinium (51 keV) suggesting that part of the effect was physical. The Magnevist^{TM} was overall less efficient than the GdNPs. For the contrast agent,

no effect was observed at high energies (^{60}Co irradiation), while effects were obtained for all conditions when using GdNPs. In line with the previous observations, this work suggested that an additional biological effect could be responsible for the observed efficiency of GdNPs that would sum on top of the physical effect due to the increase of the dose. The thesis work of Taupin [2013] showed in particular that when incubating F98 cells with GdNPs, they tend to accumulate in the G2/M phase (57 % compared to control), which is a phase where cell DNA is dense and less likely to repair, thus more radiosensitive. Additionally, it was suggested that potential inhomogeneities in the dose deposition at sub-cellular scale, "hot spots" close to biological targets, could be responsible for an increase in the biological effectiveness of GdNPs (see chapter 6).

5.3.4. Emerging mechanisms

5.3.4.1. ROS

The perturbation of intra-cellular ROS concentrations and subsequent oxidative stress was often associated with natural toxicity of GNPs, and was observed even without radiation (Butterworth et al., Coulter et al., Cui et al., Rosa et al., Taggart et al. [2010, 2012, 2013, 2017, 2016]). Butterworth et al. [2013] indicated that oxidative stress directly produced by GNPs may be due to the interaction of GNPs with cellular molecules such as glutathione, or biological processes induced by GNP uptake such as stress of the Endoplasmic Reticulum (ER). ER stress has been validated as a potential mechanism of oxidative stress, ultimately resulting in apoptotic and necrotic cell death. When irradiating the cells in presence of GNPs, depletion of GSH, or inhibition of thioredoxin reductase 1 (TrxR1) activity (regulator of cellular redox environment in mammalian cells) may also cause increased cell death (Her et al. [2017]). Penninckx et al., Penninckx et al. [2018, 2019] found a good correlation between the level of activity of TrxR1 and the extent of the radiosensitizing effect. However, a few studies have also shown that NPs may act as anti-oxidants, depending on the surface properties of NPs (Butterworth et al. [2013]).

5.3.4.2. Cell cycle

Many studies investigated the impact of GNPs on cell cycle regulation, as some cell cycle phases are more radiosensitive than others. Studies reported conflicting results. On the one hand, many authors reported alteration in the cell cycle. Geng et al., Roa et al., Wang et al., Zhu et al. [2011, 2009, 2015, 2015] observed an increase of cells in the G2/M phase and a decrease in the G0/G1 phase (with or without irradiation). Roa et al. [2009] reported that this was accompanied by a decreased expression of p53 and cyclin A, which are believed to be necessary for progression through the S phase and G2-M transition, and an increased expression of cyclin B1 and E which are G1-S transition key regulators. Authors concluded that Glu-GNPs triggered activation of the CDK kinases leading to cell cycle acceleration the G0/G1 phase and accumulation in the G2/M phase. On the other hand, other authors reported no change in the cell cycle (Butterworth et al., Cui et al., Jain et al., Liu et al. [2010, 2014, 2011, 2015]. Cell cycle alteration in presence of GNPs appear to strongly depend on the type of GNP and/or the cell type. The accumulation was sensitive on whether or not the cell was irradiated before the measurement.

5.3.4.3. DNA damages

Many groups measured DNA damages by measuring the foci γH2AX or 53BP1, either 30 minutes or 24 h post irradiation. While the former indicate early DNA damages before any repair process, the latter indicate residual DNA damages that cells did not manage to repair. The results are summarized in Tab. 5.4. Increased DNA damages were observed without irradiation for the toxic AuroVist^{TM} GNPs, but not for non-toxic GNPs. Under irradiation, some authors found increased DNA damages both at 1 h and 24 h (Chithrani et al., Taggart et al. [2010, 2014]), but it was dependent on the cell line (Taggart et al. [2014]). It was suggested that early damage increase

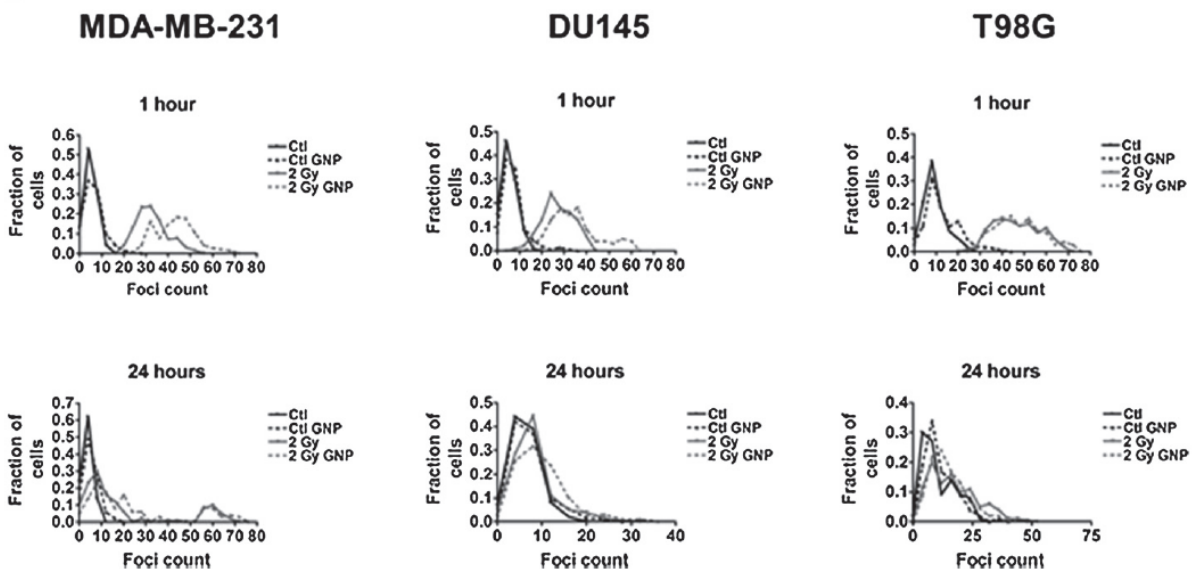

Figure 5.5.: Distribution of 53BP1 foci (1 h and 24 h post irradiation) in MDA-MB-231, DU-145 and T98G cells treated with 1.9 nm GNPs at 0.5 mg/mL for 24 h prior to irradiation. Ctl (control): no IR, no GNP; Ctl CNP: no IR with GNP; 2 Gy: 2 Gy IR, no GNP; 2 Gy GNP: 2 Gy IR with GNP. Taken from Taggart et al. [2014].

would be linked to the presence of NPs in the perinuclear region (Rosa et al. [2017]). Others reported increase of late damages only (Cui et al., Yasui et al. [2014, 2014]). As pointed by Brun and Sicard-Roselli [2016], this could indicate a DNA repair mechanism impairment. A precise knowledge of the GNPs concentrations would be necessary to conclude whether some of the damages are directly correlated to a dose increase, or if this is due to indirect cellular pathways, such as DNA damage impairment or oxidative stress consequent to other biological events. Interestingly, Taggart Taggart et al. [2014] also determined the distribution of foci numbers per cell, to determine if there was an overall increase in the levels of DNA damage across the population or if only a subset of population showed significant increase in DNA damage (see Fig. 5.5). They concluded that the increased DNA damage following treatment with GNPs alone is a result of a small shift in the observed levels of DNA damage within the whole cell population, while the increased levels of DNA damage post irradiation were a result of a cell population subset with greatly amplified levels of DNA damage, rather than the whole population. They pointed out that this could be a result of oxidative stress, and further investigated the effect of GNPs on mitochondria, as discussed in next section.

5.3.4.4. Other biological targets

Mitochondria As pointed by Jain et al. [2011], there are evidences pointing out the fact that mitochondrial damages may contribute to the cytotoxic effect of radiation. Few studies focused on the potential implication of mitochondrial damages in cell death, for AuroVist^{TM} GNPs. Taggart et al. [2014] showed that GNPs alone significantly altered the mitochondria membrane polarization and mitochondrial oxidation. Membrane depolarisation may be caused by the presence of free radicals, high intracellular calcium concentrations or stress of the endoplasmic reticulum. Taggart et al. [2016] suggested a mechanism. The protein disulphide isomerase (PDI) is an enzyme that catalyses the creation and cleavage of disulphide bonds in folding proteins in the ER. With the presence of GNPs nearby the surface of cells, the PDI reduces thiolated surface of GNPs, resulting in PDI oxidation. Oxidized PDI further required reduction by glutathione. This reduction reaction led to the oxidation of glutathione (GSH $\rightarrow$ GSSG). A recurrent repetition of this process may result in depletion of cellular antioxidant glutathione, inducing a cellular redox imbalance and hence an oxidative stress which may cause mitochondrial membrane depolarisation.

Ref.	NP	Beam	Cell line	Intracellular concentration	Early DNA damages	Late DNA damages
134	AuroVist^{TM} 1.9 nm GNP	160 kVp 1 Gy	MDA-MB-231	≈ 4 µg/mL 96 nM	53BP1 foci No significant difference	53BP1 foci No significant difference
66,262	AuroVist^{TM} 1.9 nm GNP	No IR	MDA-MB-231	1.3×10^8 GNP/cell 9.01 pg 6.9 mg/mL	53BP1 foci With GNP ≈ 4.6*** Control ≈ 3.6 1.3 fold increase	53BP1 foci With GNP ≈ 3.8 Control ≈ 2.6 1.5 fold increase
66,262	AuroVist^{TM} 1.9 nm GNP	225 kVp 2 Gy	MDA-MB-231	1.3×10^8 GNP/cell 9.01 pg 6.9 mg/mL	53BP1 foci With GNP ≈ 41.5** Control ≈ 30.8 1.3 fold increase	53BP1 foci With GNP ≈ 11.8** Control ≈ 8.0 1.5 fold increase
66,262	AuroVist^{TM} 1.9 nm GNP	No IR	DU145	1.6×10^8 GNP/cell 11.1 pg 8.4 mg/mL	53BP1 foci With GNP ≈ 6.1*** Control ≈ 4.1 1.5 fold increase	53BP1 foci With GNP ≈ 5.6* Control ≈ 4.6 1.2 fold increase
66,262	AuroVist^{TM} 1.9 nm GNP	225 kVp 2 Gy	DU145	1.6×10^8 GNP/cell 11.1 pg 8.4 mg/mL	53BP1 foci With GNP ≈ 33.3*** Control ≈ 25.6 1.3 fold increase	53BP1 foci With GNP ≈ 8.3** Control ≈ 6.9 1.2 fold increase
66,262	AuroVist^{TM} 1.9 nm GNP	No IR	T98G		53BP1 foci With GNP ≈ 11.1*** Control ≈ 7.0 1.6 fold increase	53BP1 foci With GNP ≈ 10.0 Control ≈ 9.0 1.1 fold increase
66,262	AuroVist^{TM} 1.9 nm GNP	225 kVp 2 Gy	T98G		53BP1 foci With GNP ≈ 50.1*** Control ≈ 44.6 1.1 fold increase	53BP1 foci With GNP ≈ 13.1* Control ≈ 15.1 0.87 fold increase
68	Tiopronin-GNP 2.7 nm	No IR	MDA-MB-231	92.7 pg	γH2AX With GNP 6.5 Control 6.0 1.1 fold increase	γH2AX With GNP 6.3 Control 5.8 1.1 fold increase
68	Tiopronin-GNP 2.7 nm	225 kVp 2 Gy	MDA-MB-231	92.7 pg 4.66×10^8 GNP/cell	γH2AX With GNP 32.3 Control 32.0 1.0 fold increase	γH2AX With GNP 14.0* Control 10.3 1.3 fold increase
68	Tiopronin-GNP 2.7 nm	225 kVp 4 Gy	MDA-MB-231	92.7 pg 4.66×10^8 GNP/cell	γH2AX With GNP 64.7 Control 63.2 1.0 fold increase	γH2AX With GNP 34.8* Control 23.2 1.5 fold increase
55	Citric-acid stabilized GNP 50 nm	220 kVp 4 Gy	HeLa	≈ 6000 NP/cell 7.58 pg	γH2AX With GNP 83 Control 45 1.8 fold increase 53BP1 With GNP 65 Control 43 1.5 fold increase	γH2AX With GNP 26 Control 20 1.3 fold increase 53BP1 With GNP 18 Control 13 1.4 fold increase
55	Citric-acid stabilized GNP 50 nm	6 MV 4 Gy	HeLa	≈ 6000 NP/cell 7.58 pg	γH2AX With GNP 40 Control 25 53BP1 With GNP 40 Control 22	γH2AX With GNP 20 Control 7 2.9 fold increase 53BP1 With GNP 13 Control 10 1.3 fold increase
179	PEG-GNP 6.1 ± 1.9 nm	160 kVp (E_{av} 73 keV) 2 Gy	EMT-6		Increased γ-H2AX	
179	PEG-GNP 6.1 ± 1.9 nm	Cu-Kα_1 (8.048 keV) 2 Gy	EMT-6		Increased γ-H2AX	
43,49	HER-2 GNP 30 nm	100 kVp (E_{av} 33 keV) 0.5 Gy	MDA-MB-361	7.7×10^3 GNP/cell (2.10 pg)	γH2AX foci With GNP 2.0 Control 0.6 3.3-fold increase	
43,49	PEG-GNP 30 nm	100 kVp (E_{av} 33 keV) 0.5 Gy	MDA-MB-361	1.0×10^3 GNP/cell (0.27 pg)	γH2AX foci With GNP 1.0 Control 0.6 1.7-fold increase	
285	BSA-peptide GNP, 14 nm	225 kVp 2 Gy	HeLa		γH2AX Increased foci number	
296	Galactose PEG-GNP 20 nm (core)	6 MV 0.5 Gy	HepG2	2.2×10^4 GNP/cell 1.78 pg	γH2AX With GNP 21.4 Control 2.5 8.6-fold increase**	
296	Citrate-capped GNP 20 nm (core)	6 MV 0.5 Gy	HepG2	8.2×10^3 GNP/cell 0.66 pg	γH2AX With GNP 11.1 Control 2.5 4.5-fold increase*	

Table 5.4.: Table of early (30 min or 1 h) and late (24 h) DNA damages measured with/without GNP. All the results are provided in foci per nucleus, except for Chattopadhyay et al. [2013] who provided a number of foci per nuclear area. References: Jain et al. [2011][134], Coulter et al., Taggart et al. [2012, 2014][66,262], Cui et al. [2014][68], Chithrani et al. [2010][55], Liu et al. [2010][179], Cai et al., Chattopadhyay et al. [2013, 2013][43,49], Yang et al. [2014][285], Zhu et al. [2015][296].

The potential accumulation of ROS could also be at the origin of DNA damages. Additionally, Wang et al. [2013] found deregulation of pro-apoptotic proteins in presence of Glu-GNPs, which could indicate that those GNPs could trigger apoptosis through mitochondrial pathway. Zhu et al. [2015], who studied citrate-capped GNPs and Gal-PEG-GNPs, were the only ones to detect GNPs in mitochondria. They found in addition that GNPs induced a higher expression of intracellular apoptotic molecules and an inhibition of the expression of anti-apoptic proteins. Recently, Ghita et al. [2017] investigated 1.9 nm Aurovist^{TM} radiosensitization mechanisms using microbeam irradiation (energy 278 eV) of MDA-MB-231 and AG01522 cells, either irradiating the nucleus only or the cytoplasm only. Their findings suggest a role of the mitochondria in the increased cell death observed with GNPs. However, whether this mechanism applies to other GNPs remains an open question.

ER and Golgi apparatus Some authors reported co-localization with the ER and the Golgi apparatus, which could also constitute an interesting target(Chang et al., Yasui et al. [2008, 2014]). The ER stress results from accumulation of misfolded/unfolded proteins and activates the Unfolded Protein Response. It is a complex cellular response that includes the exacerbation of defective proteins degradation. A consequence is that the protein Rad51 may be down-regulated, and thus induce an impairment of DNA repair (Brun and Sicard-Roselli [2016]).

Cellular membrane Some NPs were found mostly on the cell membrane (Kong et al., Kong et al. [2007, 2008]), and some authors pointed out that many GNPs may be located outside of the cells (Cui et al. [2014])), thus nearby the membrane. However, in the set of studies, there was no investigation on potential cell membrane damages. Brun and Sicard-Roselli [2014] pointed the fact that cell membranes could be one of the targets inducing, through complex cellular signalling, cell death in presence of GNPs.

Lysosome Jain et al. [2014] was the only one to suggest lysosomes as a potential target. As seen in chapter 3, the partial destruction of lysosomal membrane could lead to adverse side effects, and be induced by the irradiation of cells containing GNPs that are all located in vesicles.

5.4. Summary

From *in solution* experiment to *in vitro* experiments, the radiosensitizing effect of GNPs may originate from complex mechanisms that are yet not fully elucidated. There are many evidences comforting toward a radiosensitizing effect that is more complex than a simple increase of energy deposition. The irradiation of GNP colloidal solution with either scavengers or biomolecules indicated that chemical effects should be considered for the radiosensitizing effect of GNPs. Scavengers may be used to measure the production of free radicals. Two research groups[51,75,76,109,110,251] investigated the production of hydroxyl radicals when irradiating a colloidal solution of GNPs mixed coumarin molecules. The coumarin molecule may react with $^{\bullet}$OH and, through a multi-step reaction, produces, among many products, a fluorescent molecule. Experimental measurements showed that the fluorescent signals were much higher than their theoretical dosimetric calculations. While both groups had different interpretation of the discrepancy between theoretical and experimental results, they both pointed out the fact that GNPs were chemically active. Further work is required to better understand the origin of these effects, and whether it may translate into an *in vitro* effect.

The irradiation of biomolecules in a GNP colloidal solution enabled to quantify the amount of molecular damages in the absence of a cellular response. One may distinguish two types of experimental systems: (1) DNA-GNPs complexes and protein-GNPs aggregates, in which case the biomolecule was located on the surface of the GNP, and (2) solutions of DNA molecules and GNPs, in which case the distance between GNPs and biomolecules was unclear. For the former system, a close proximity between the GNPs and the biomolecules enabled a very high increase

of biomolecule damages, despite a low concentration of the biomolecules[36,45,92]. For the latter, it was shown that the amount of DNA damages had a dependence on the beam energy and size and concentration of GNPs[37,38,193]. Both types of systems reported that the chemical environment appeared to be a key point with regard to biomolecule damages, and in particular the scavenging ability of the solution. However, given the multiple parameters and the extreme sensitivity of the enhancement with regard to experimental conditions, it is yet hard to conclude on the extent of this chemical effect, in particular for more complex systems such as *in vitro* experiments.

Compared to *in solution* experimental results, *in vitro* experiments depicted an even more complex picture, with results that were not always in agreement from one experiment to another. The very large variability of the parameters made a clear identification of the mechanisms difficult. It may also be the cause of the variability of the results, as illustrated by Fig. 5.6 and Fig. 5.7. α and β parameters experimentally obtained are reported on Fig. 5.6, with (in black) or without GNP (in red). Additionally, the Relative Biological Effectiveness (RBE) obtained at 2 Gy (i.e., 2 Gy divided by the dose required in presence of GNPs necessary to obtain the same survival obtained without GNP at 2 Gy) is displayed on Fig. 5.7, along with the experimental conditions. While many authors reported a significant increase of the α parameter when the radiosensitizing effect was significant, the results are less obvious for the β parameter, with no systematic trend. Such variation results in a great variation of the RBE, as shown on Fig. 5.7. No systematic trend was obtained, even for identical cell lines. Despite this variability, a few main conclusions can be drawn. A dependence of photon energy was observed, confirming that part of the effect for *in vitro* system is driven by physical mechanisms (provided a high enough GNP concentration). However, an increase of the macroscopic dose was not sufficient to explain the whole effect, and many other mechanisms were suggested: cellular detoxification system alteration, cell cycle alteration, DNA repair impairment, ER stress, alterations of organelles such as mitochondria, or lysosomes. These mechanisms can be impacted by experimental conditions and the nature of GNPs. A unified mechanism, that would be the cause of the variety of the results, remains to be found. Brun and Sicard-Roselli [2016] also suggested that, given the variety of existing NPs, probably not only one mechanism is at the origin of the radiosensitization. Better quantifying the impact of early, radiation induced, mechanisms (e.g. direct and indirect effects of radiation with GNP) on biological outcomes (e.g. cell survival or biomolecule damage) could help to better understand each situation and whether a pure physico-chemical effect is sufficient to explain the outcome, or if more complex biological pathways are at the origin of the radiosensitization. This is the objective of theoretical studies, as further developed in the next chapter.

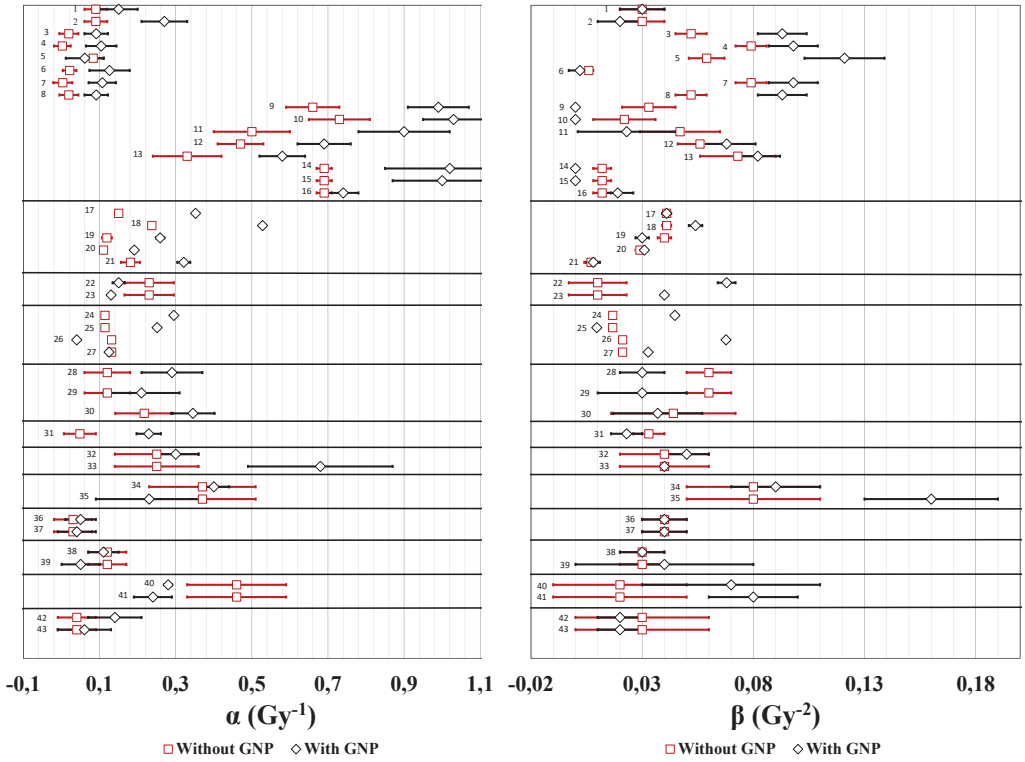

Figure 5.6.: Summary of α and β parameters with (black) or without (red) obtained for various *in vitro* experiments.

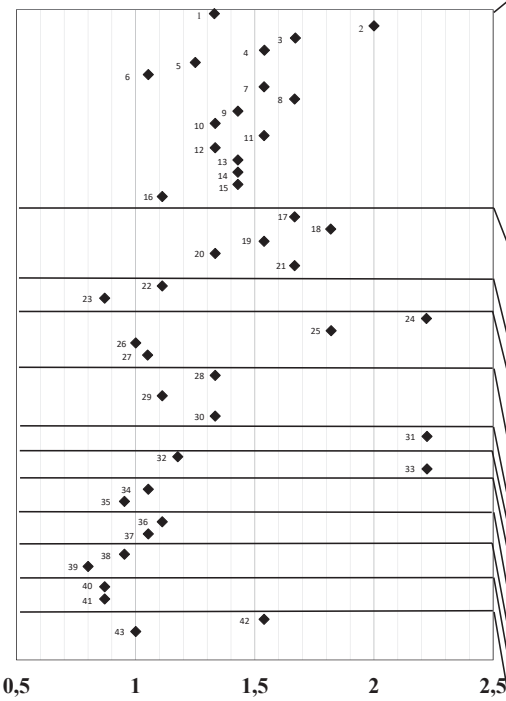

	Cell	Ref.	GNP	C.	T.	E.	Comment
1	MDA-	Butterworth 2010	1,9 nm AuroVist	0,01 mg/mL	1 h	160 kVp	
2	MB-231			0,1 mg/mL			
3		Jain 2011	1,9 nm AuroVist	0,5 mg/mL	24 h	160 kVp	
4						6 MV	
5						15 MV	
6		Jain 2014	1,9 nm AuroVist	0,5 mg/mL	24 h	160 kVp	Hypoxia 0,1 %
7							Hypoxia 1 %
8							Normoxia
9		Cui 2014	Tio-pronin	0,25 mg/mL	1 h	225 kVp	
10					4 h		
11					8 h		
12					16 h		
13					24 h		
14				0,5 mg/mL	4 h	225 kVp	Extra-cell not removed
15					4 h		Extra-cell removed
16					0 h		Extra-cell not removed
			50 nm Citric-acid				
17	HeLa	Chithrani 2010	GNP	0,01 mg/mL	27 h	220 kVp	
18						105 kVp	
19						137Cs	
20						6 MV	
21		Kaur 2013	5 - 9 nm Glu-GNP	7 mg/mL	6 h	60 Co	
22	MDA-	Chattopadhyay 2013	30 nm HER-2 GNP	2,4 mg/mL	Overnight	100 kVp	
23	MB-361		30 nm PEG-GNP				
24	F98	Bobyk 2013 (Thesis)	1,9 nm AuroVist	10 mg/mL	0 h	50 keV	Only extra-cell
25					24 h	50 keV	Only intra-cell
26			15 nm AuroVist	10 mg/mL	0 h	50 keV	Only extra-cell
27					3 h 40	50 keV	Only intra-cell
28	PC-3	Butterworth 2010	1,9 nm AuroVist	0,01 mg/mL	1 h	160 kVp	
29				0,1 mg/mL			
30		Lechtman 2013	30 nm PEG-GNP	2 mg/mL	24 h	300 kVp	
31	RT112	Jeynes 2014	50 nm FBS-GNP	0,0055 mg/mL	4 h	250 kVp	
32	AGO-	Butterworth 2010	1,9 nm AuroVist	0,01 mg/mL	1 h	160 kVp	
33	1552B			0,1 mg/mL			
34	ASTRO	Butterworth 2010	1,9 nm AuroVist	0,01 mg/mL	1 h	160 kVp	
35				0,1 mg/mL			
36	DU145	Butterworth 2010	1,9 nm AuroVist	0,01 mg/mL	1 h	160 kVp	
37				0,1 mg/mL			
38	L132	Butterworth 2010	1,9 nm AuroVist	0,01 mg/mL	1 h	160 kVp	
39				0,1 mg/mL			
40	MCF-7	Butterworth 2010	1,9 nm AuroVist	0,01 mg/mL	1 h	160 kVp	
41				0,1 mg/mL			
42	T98G	Butterworth 2010	1,9 nm AuroVist	0,01 mg/mL	1 h	160 kVp	
43				0,1 mg/mL			

Figure 5.7.: Summary of RBE at 2 Gy obtained for various *in vitro* experiments. Experimental conditions are also provided, i.e., the cell line, the GNP type, the extra-cellular incubation concentration (C.), the time of incubation (T.) and the voltage or type of photon source (E.). Some experiments[26,68] removed the extra-cellular medium containing GNPs prior to irradiation to replace it with fresh medium, as specified in the comments.

6. Gold nanoparticles in radiotherapy - Simulation studies

Contents

This chapter is dedicated to Monte Carlo studies of the radiosensitizing effect of high-Z NP, and in particular GNP. It is organized based on the scale at which the study was performed, and decomposed in 4 parts. The first section describes results on the tumour (macroscopic) scale, and present some potential applications in clinical case. The second part presents simulation results on microscopic scale, with studies at cell or sub-cellular (organelle) scale (typically lysosome, nucleus or mitochondria). The third part focuses on the nanoscopic scale. The last part focuses on biological endpoints, such as the calculation of cell survival or sub-cellular damages. This chapter focuses in particular on photon irradiation.

6.1. Macroscopic scale

Macroscopic dose enhancement A first suggestion to explain the radiosensitizing effect of GNPs relied on the high energy absorption coefficient of keV photons for gold, compared to

Reference	MC code	Beam	Geometry Phantom	Tumor Depth	Tumor Size	GNP Size	GNP Concentration	MDEF
Cho [2005]	BEAMnrc/ DOSXYZnrc	Ext., 140 kVp (4×4 cm^2, av. 57.9 keV) Int., ^{192}Ir (395 keV) Ext., 4/6 MV (4×4 cm^2)	$30 \times 30 \times 30$ cm^3	0.053 cm N/A 3.5 cm	$1 \times 1 \times 0.15$ cm^3 Sphere (R=3.5 cm) $2.4 \times 2.4 \times 3.5$ cm^3	N/A	7, 18, 30 mg·mL^{-1}	3.8 to 5.601 Up to 1.3 1.01-1.03
Cho et al. [2009]	MCNP5	Int., ^{125}I Int., 50 kVp Int., ^{169}Y	Sphere (R=30 cm)	N/A N/A 3.5 cm	Sphere (R=1.5 cm)	N/A	7, 18 mg·mL^{-1}	Up to 3 Up to 2.6 Up to 2.1
Zhang et al. [2009]	Geant4.8	Int., ^{192}Ir (parallel, 380 keV)	Sphere (R=40 mm)	10 mm	$1 \times 1 \times 1$ cm^3	N/A 100 nm	$\sim$ 100 mg·mL^{-1} $\sim$ 100 mg·mL^{-1}	36 % 28 %
Montenegro et al. [2009]	Geant4.9	Ext., 68 keV (D=3 mm) Ext., 82 keV (D=3 mm)	$15 \times 5 \times 5$ cm^3	10 cm 10 cm	$2 \times 5 \times 5$ cm^3	N/A	5 mg·mL^{-1} to 50 mg·mL^{-1}	$\sim$ 11 throughout tumour From 1 to $\sim$ 11
Van den Heuvel et al. [2010]	MCNPX	110 kVp plane source adjacent to the gold slab	Tank filled with water	5 cm	1 mm thick slab	N/A	From 0 to 100 mg·mL^{-1}	Up to 13
Mesbahi et al. [2013]	MCNPX	Ext., 50 keV to 120 keV Ext., 50 keV to 120 keV Ext., ^{6}0Co and 6/18 MV	$20 \times 20 \times 20$ cm^3	Surface Surface 2 cm	$1 \times 1 \times 1$ cm^3	D=30, 50 and 100 nm	7 mg·mL^{-1} 18 mg/g 7+18 mg/g	1.4 to 2.1, optimum at 90 keV 2. to 3.7, optimum at 90 keV < 1.01-1.03
Amato et al. [2013]	Geant4	Ext., 6 MV (2×2 cm^2)	$20 \times 20 \times 20$ cm^3	1.1 cm 5 cm 10 cm	$2 \times 2 \times 2$ cm^3	N/A	2 mg·mL^{-1} to 100 mg·mL^{-1}	1.0021 to 1.1823, linear 1.0019 to 1.1383, linear 1.0025 to 1.1433, linear
Amato et al. [2013]	Geant4	Ext., 150 kVp (mean 55 keV)	$8 \times 8 \times 12$ cm	0 cm 1.5 cm 3 cm 5 cm	$2 \times 2 \times 1$	N/A	10 to 200 mg·mL^{-1} (with different GNP biodistributions)	Max. from 2 to 12 Max. from 2 to 11 Max. from 2 to 13 Max. from 2 to 16

Table 6.1.: Ratio of dose enhancement in presence of gold nanoparticles in the tumour (modelled as an atomic homogeneous gold/water structure) for different phantom and tumour geometries. Brachytherapy sources are noted as internal. The tumour depth represents the tumour distance to the surface when irradiating with an external beam or the distance to the source when irradiating with a brachytherapy source, if the source is not placed directly inside the tumour (noted NA). The DEF is averaged over the whole tumour. D refers as diameter and R as radius. N/A stands for Non Applicable.

water, resulting in a higher dose deposition where the GNPs are located. Historically, the first simulation study to understand the radiosensitizing effect of GNPs was done by Cho [2005]. Many studies (Amato et al., Amato et al., Cho, Cho et al., Koger and Kirkby, Mesbahi et al., Montenegro et al., Van den Heuvel et al., Zhang et al. [2013, 2013, 2005, 2009, 2016, 2013, 2009, 2010, 2009]) have then focused on the macroscopic dose enhancement achievable inside the tumour, which depends on (1) the energy of the photons and the beam geometry (internal vs external beams), (2) the geometry of the phantom, the depth and size of the tumour and (3) the concentration of GNPs. The results of some studies are reported in Tab. 6.1. Globally, the different studies are consistent: in the keV range significant dose enhancement can be reached both for external beams and brachytherapy sources. The Macroscopic Dose Enhancement Ratio (MDER, ratio of the macroscopic dose deposited in the tumour with to without GNPs) is then highly sensitive to the concentration of GNPs: for example, for an external irradiation at 140 kVp (mean energy 57.9 keV), Cho [2005] reported MDER from 3.8 to 5.6 for concentrations from 7 to 30 mg·mL^{-1}. GNPs are hence particularly effective for keV energies, where the photoelectric effect dominates in gold. This requires however a sufficient concentration of GNPs and a good contrast between healthy and cancer tissues. For photon energies varying in the range 10-100 keV, we calculated that the different studies provided an increase of a few percents up to 40 % per mg·mL^{-1} of GNPs. It dropped to $\sim$ 1 % or less per mg·mL^{-1} for photon energies of few hundreds of keV. When increasing the energy of the beam up to MeV energies, the dose enhancement is dramatically decreased: at these energies, the mass absorption coefficient has little difference between gold and water. For example, Cho [2005] reported a MDEF of only 1.01-1.03 for an external 4/6 MV irradiation and a tumour at 3.5 cm. Large concentrations of GNPs that might not be clinically feasible are necessary to obtain a significant MDER.

Beam fluence Many authors (Cho et al., Martinov and Thomson, Montenegro et al. [2009, 2017, 2009]) have reported a change in the beam fluence when introducing gold nanoparticles inside a tumour, especially at low energy. This may result in an inhomogeneous dose deposition inside the tumour, which should be considered for practical clinical case to avoid cold dose spots at a deep depth. Consequently, it may also induce a lower dose deposition to healthy tissues at deeper depths after the tumour.

Atomic mixtures *vs* geometric nanoparticles Originally, the MC simulations considered an atomic mixture of gold atom and water molecules to model a tumour doped with GNPs. As pointed out by Zhang et al. [2009], approximating GNPs inside the tumour as an atomic mixture of gold and water can result in inaccuracies in the dose estimation: some of the energy is absorbed by the GNPs, resulting in an lower average dose deposition in the medium outside the NPs. However, modelling gold nanospheres can be extremely challenging when considering macroscopic geometries. Due to the very small size of the nanoparticles compared to the size of the irradiated volumes, the number of geometries to simulation is extremely large and the computing time becomes quickly prohibitive. The first study to estimate the dose discrepancy between an atomic gold-water mixture and a NP-water mixture was done by Zhang et al. [2009], where they simulated a 1 cm^3 cubic volume filled with 100 mg·mL^{-1} of 100 nm diameter GNPs, using the MC toolkit Geant4.8. A total of $\sim 10^{13}$ spheres were simulated to fill the volume, which was then irradiated by an isotropic ^{192}Ir brachytherapy source placed 10 mm away from the GNP-doped volume. They found that assimilating GNPs as atoms overestimated the dose by 16 %. In line with this observation, Martinov and Thomson [2017] found MDER that globally decreased with the size of the GNP. Koger and Kirkby [2016] proposed a method to calculate the dose deposition using a uniform atomic mixture and convert it to a dose deposition with GNPs by calculating converting coefficients as a function of the photon beam energy.

Clinical applications A few clinical treatment planning were studied, based on the increase of macroscopic dose. Overall, different interesting techniques can be developed, based on either internal (brachytherapy) or external irradiation, to achieve an increase of the physical dose inside the tumour site and better restrict the dose within the tumour. One of the first studies reported

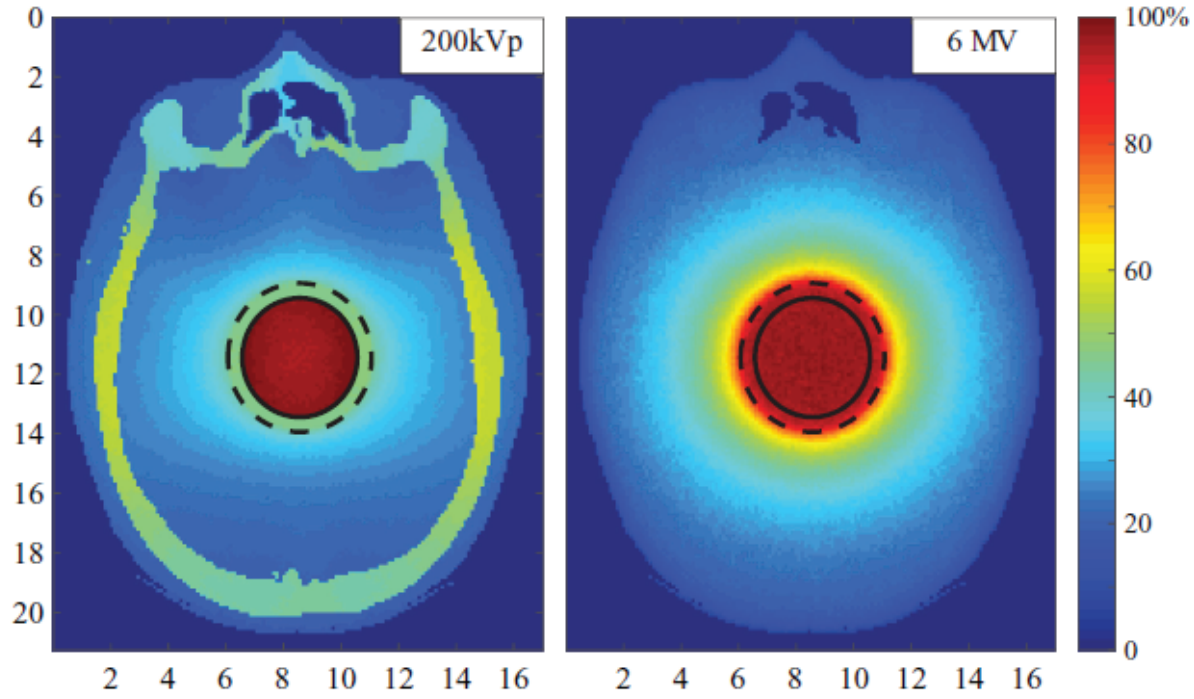

Figure 6.1.: Figure taken from Koger and Kirkby [2016] illustrates the dose irradiation difference for an ARC therapy delivery at 200 kVp (left) with a tumour filled with 10 mg/g of GNPs, or a conventional 6 MV therapy on the right. The tumour size was 2 cm of radius placed a the centre. The Axis values are in centimetres. Both distributions were scored along the central axis of the beam at the centre of the tumour.

was done by McMahon et al. [2008], to investigate the potential physical dose enhancement when using a contrast agent made of gold. Asadi et al. [2015] proposed a treatment for a human eye choroidal melanoma and calculated the dose using a real human eye geometry with a ^{125}I brachytherapy source. High gold concentration enabled to reduce the time of irradiation by increasing the dose to the tumour, and reduced the dose to healthy tissues. However, this model did not account for the potential diffusion inside healthy tissues. As such, the use of brachytherapy sources combined with GNP might be limited in practice: the GNP half-life (a few days) is usually rather low compared to the dose rate of brachytherapy sources and the time of irradiation therefore required (Cho et al. [2009]). Martinov and Thomson, Sinha et al. [2017, 2015] studied the dose deposition for a brachytherapy source considering different sources (^{125}I, ^{103}Pd and ^{131}Cs) and gold nanoparticles for prostate cancer. The idea was to combine the implant with a polymer film embedded with GNPs on the inter-seed spacers (Martinov and Thomson [2017]). Garnica-Garza, Koger and Kirkby, Tu et al. [2010, 2016, 2013] have suggested to use GNPs with ARC therapy, for prostate cancer (Garnica-Garza [2010]) or brain cancer (Koger and Kirkby [2016]). The latter is illustrated on Fig. 6.1. Koger and Kirkby [2016] showed that up to 16 % more dose was achievable inside the tumour while sparing the surrounding tissues. Besides, the dose was more contained within the tumour in presence of GNPs. However, the inconvenience of the technique was the increase in dose delivery to the skull bones due to the low energy irradiation at 200 kVp compared to 6 MV.

6.2. Microscopic scale: from the cellular to the sub-cellular scale

Studies have suggested that a heterogeneity of the dose deposition at cellular and sub-cellular scale could be responsible for biological effects that are higher than those predicted by a macroscopic dose enhancement. Thus, many authors have also studied the dose deposition at the microscopic

scale.

6.2.1. Average dose deposition inside sub-cellular compartments

A few studies (Delorme [2013],Douglass et al. [2013], Cai et al. [2013], Retif et al. [2016]) have focused on the average dose achieved inside different cellular compartments such as the membrane, cytoplasm or nucleus.

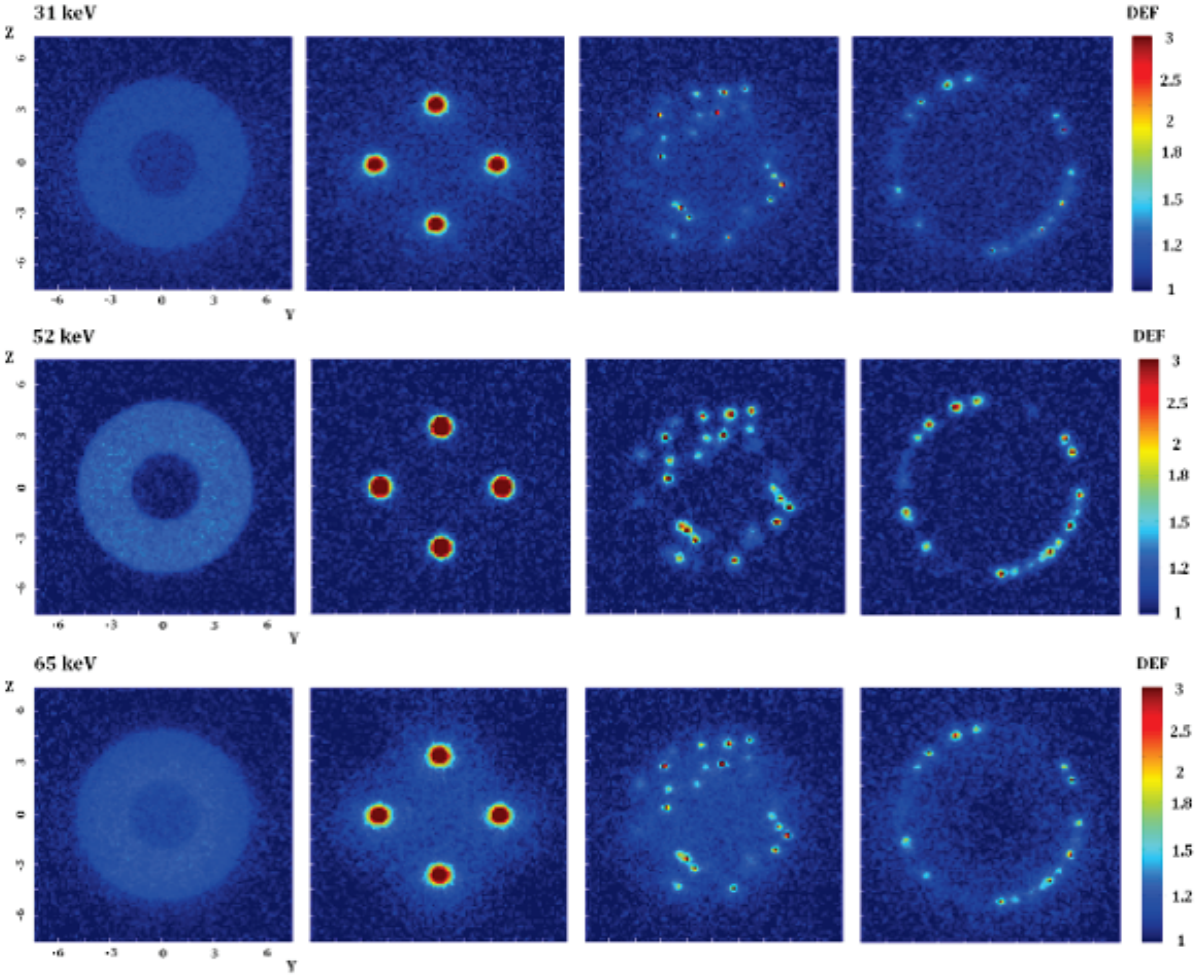

Figure 6.2.: Figure taken from Delorme [2013] displaying DER in the YZ plan at x=0, pour different energies (31 keV, 52 keV, 65 keV) and 4 conditions of gadolinium biodistribution, all equivalent to a mass concentration of 2 mg·mL^{-1}. From left to right, the biodistributions are: (1) in form of a contrast agent (i.e., atomic mixture) in the cytoplasm, (2) GdNPs inside lysosomes, (3) GdNPs randomly distributed inside the cytoplasm, or (4) GdNPs on the membrane. The YZ axis scale is in µm.

Delorme [2013] In line with the biological measurements reported in chapter 5, section 5.3.3.8 (Taupin [2013]), Delorme [2013] studied the heterogeneity of the dose deposition at cellular scale depending on the size of the nanoparticles, their geometry (i.e. contrast agent *vs* spherical NPs) and their biodistribution. The dose was calculated in different cellular compartments (in the cytoplasm, nucleus and external cellular membrane) to estimate the µDER (e.g. dose enhancement ratios at microscale). The aim was to find existing correlations between experimental cell survivals and physical predictions, for keV photon and ^{60}Co irradiation. The work was based on GdNPs but the general conclusions are independent on the material.

In particular, different intra-cellular biodistributions were modelled, considering either contrast agents (i.e., atomic mixture) (1) or spherical NPs (100 nm diameter) clustered in lysosomes (2),

homogeneously distributed in the cytoplasm (3) or fixed on the surface of the cell (4). This is illustrated on Fig. 6.2. For these 4 biodistributions, the same mass of gadolinium was used, equivalent of 2 mg·mL^{-1} for the contrast agent. Contrast agents predicted no effect for MeV irradiation with the ^{60}Co source irradiation, as theoretically and experimentally predicted, and a good correlation was obtained in the keV range between experimental and simulation results. When GdNPs were randomly distributed inside the cytoplasm, there was only a little difference observed for cytoplasmic µDER compared to an atomic mixture, with a decrease due to energy absorption inside GdNPs. The cytoplasmic µDER was the highest for the homogeneous distribution, and decreased when the GdNPs were contained inside lysosomes due to an additional energy loss in the GdNPs. It was even lower when GdNPs were located on the membrane, as part of the energy was lost in the extra-cellular medium. The nucleus µDER decreased if the GdNPs were located on the membrane. Finally, the membrane µDER was much higher when GdNPs were accumulated on the membrane, reaching nearly 1.45 at 58 keV compared to $\sim$ 1.12 for the other conditions. When comparing the variation of the different µDER with regard to the photon energy, only the membrane µDER could reproduced the trends observed experimentally. As most of the GdNPs experimentally accumulated on the membrane, it appeared to be a good target to consider. When considering the full 3D dose deposition rather than just average doses in cellular compartments, as displayed in Fig. 6.2, the heterogeneity of the dose deposition is striking. When GdNPs are contained in vesicles, the dose deposition is particularly important, within 700 nm from the centre of the lysosome, with a ratio of doses reaching a maximum 3 inside lysosomes. Such an increase of the dose deposition could lead to the destruction of the lysosome.

Douglass et al. [2013] In the study by Douglass et al. [2013], 2 GNPs simulation scenarii were set up using the MC simulation Geant4: a single 400 nm diameter gold cluster randomly distributed in the cytoplasm (based on experimental conditions measured by Zhang et al. [2009]) or a 300 nm gold layer around the nucleus of the cell (based on experimental conditions by Liu et al. [2008]). The cells were irradiated with a 80 kVp photon beam or a 6 MV photon beam. A total of 840 elliptical cells (representing typically human keratinocytes) were modelled with semi-major axis length randomised between 9 to 13 µm, with random orientations, to form a cubic tumour of side length 0.40 mm. The cubic geometry was placed inside a volume of water to ensure electronic build up (1 mm depth). The dose deposition was calculated for 5 regions (cytoplasm, membrane, nucleus, reticulum endoplasmic and nucleolus). They observed no difference for the first scenario, and high µDERs in the second case. In particular, they showed that the DERs were an order of magnitude higher for low energy compared to 6 MV. They also showed that Auger electrons had a statistically insignificant effect on the dose deposition. The increase was mostly due to additional photoelectrons. Note that for this study, the amount of gold used in both conditions was very different. In terms of concentration per cell, assuming a spherical cell of radius 13 µm (largest semi-axis), the first scenario represented $\sim$ 0.07 mg·mL^{-1} of gold, while the second represented $\sim$ 78.5 mg·mL^{-1}. This large difference could explain why in the first case there is no increase of the observed DER.

Cai et al. [2013] Another study of average dose deposition inside different sub-cellular compartments was proposed by Cai et al. [2013]. Using the MC code MCNP 5, they modelled a human breast cancer cell (MDA-MB-361) as a sphere of radius 9.3 µm with a centred nucleus of radius 6.3 µm. They also considered 2 extra-cellular compartments: the surface of the cell which was modelled as a concentric shell of thickness 0.1 µm, and the extra-cellular space which was taken as a concentric shell of inner radius equal to 9.4 µm and outer radius 11 µm. Three different cellular geometries were considered: a single cell contained inside a cube of tissue of length 0.24 cm, a monolayer of cells to reproduce the irradiation of cells inside wells or a cube of cells of length 0.24 cm. The cells were irradiated with keV X-rays, while different GNP sizes were investigated. In each simulation, one of the compartment was filled with GNPs at varying concentrations (from 2.01 $\times 10^4$ to 8 $\times 10^5$ GNPs distributed per compartment). They calculated the nuclear dose enhancement factor (NDER) and the cytoplasm dose enhancement factor (CDER). For a concentration of 2.01 $\times 10^5$ 30 nm GNPs per cell located in the nucleus (i.e., estimated

local nuclear concentration of $\sim$ 50 mg·mL^{-1}), they showed that the NDER could be as high as 3.4. Overall at this scale, both the NDER and CDER strongly depended on the photon energy, but also their biodistribution. The NDER and CDER both increased with increasing number of cells and increasing number of GNPs. This model was used to test it against experimental data (Chattopadhyay et al. [2013]) and they found that the NDER of a monolayer of cells was better to describe the experimental observations.

Retif et al. [2016] Retif et al. [2016] proposed an *in vitro* method to assess the radiation-enhancing capacity of different NPs. They based their MC modelling using TEM/ICP-OES spectroscopy to quantify the biodistribution of *in vitro* GNPs (or iron NPs). If the absolute increase of the mean dose to the cell appeared not sufficient to explain the biological extent observed experimentally, they however could reproduce the trends regarding the efficacy of 3 distinct NPs. In particular, they showed that data of the biodistribution of the NPs (number of NPs and their distribution within the cell) was necessary in order to reproduce accurately the trend of the radiosensitizing effect.

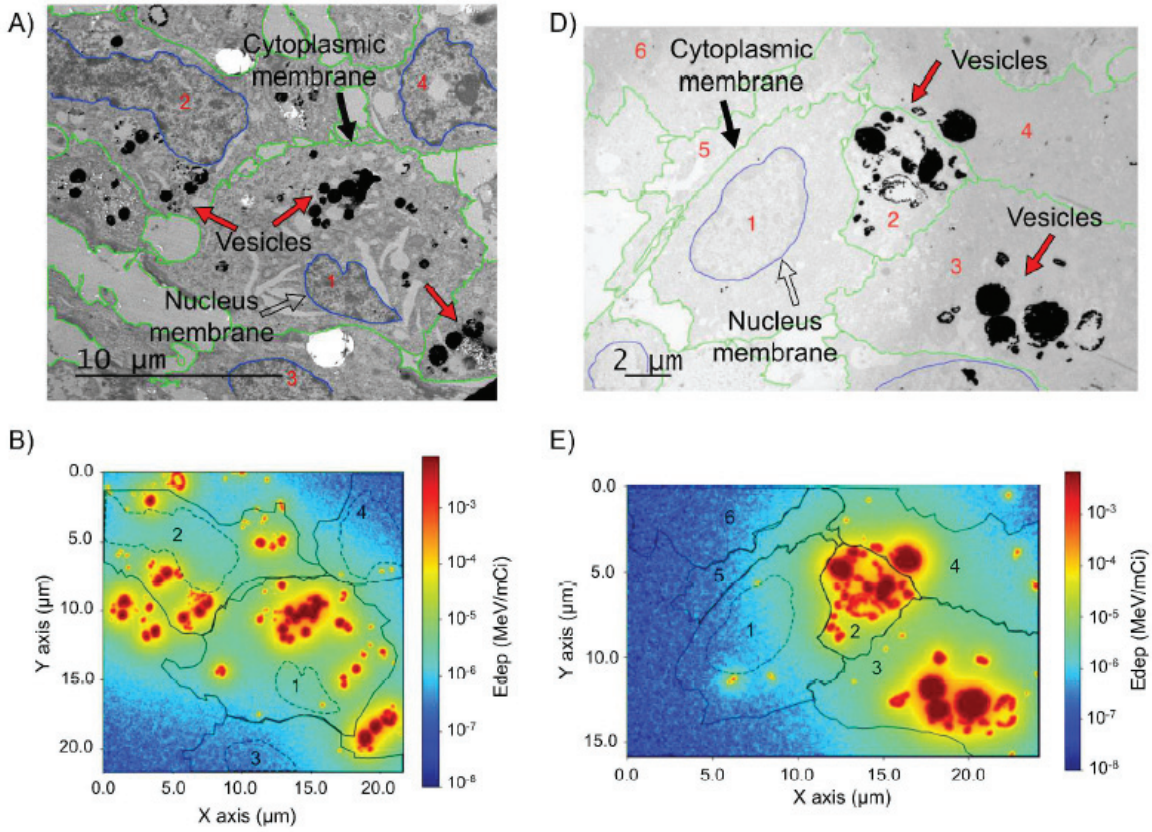

Figure 6.3.: Figure taken from Laprise-Pelletier et al. [2018] illustrating the dose inhomogeneity at cellular scale following the injection of radioactive (^{103}Pd) GNPs in a prostate cancer. The biodistributions were obtained at 24 h and 8 days following the intratumoral injection.

Laprise-Pelletier et al. [2018] Laprise-Pelletier et al. [2018] injected intratumoral low-dose rate radioactive (^{103}Pd) GNPs in prostate cancer tumours grown in a murine model. Their distribution was visualized by computed tomography *in vivo*, and transmission electron and optical microscopy *ex vivo* at 2 h, 24 h and 8 days following the injection. These data were used to model the dose deposition both at tumour scale and sub-cellular scale, using a MC simulation. More than 80 % of the GNPs remained in the tumour. At 2 h, most of NPs were located very close to the injection site, within 100 µm. At 24 h, it diffused up to 350 µm from the needle site. At tumour scale, Laprise-Pelletier et al. [2018] modelled the GNPs as a sphere of 1 mm radius, with a local NPs concentration of 68.9 mg·mL^{-1}. They obtained a macroscopic dose profile that was limited to a

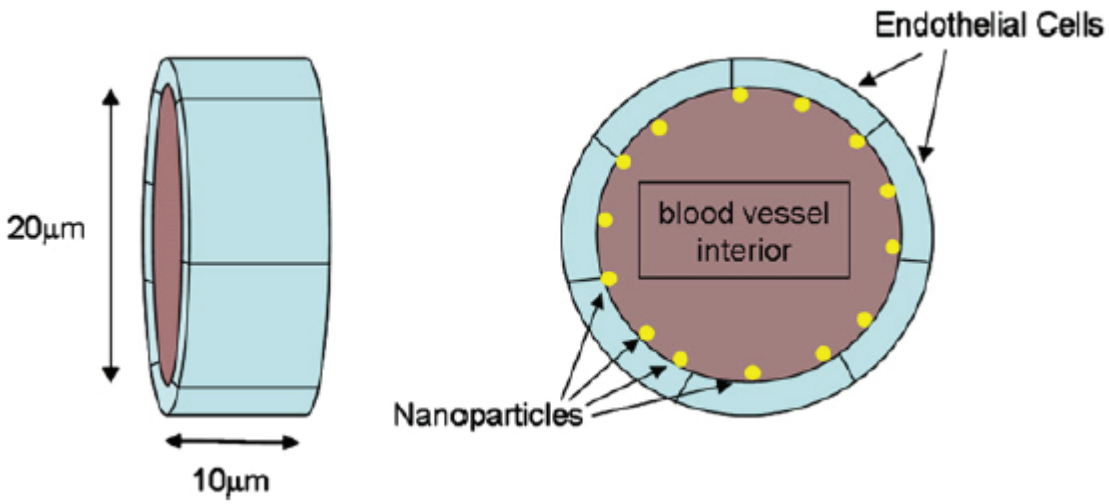

Figure 6.4.: Geometry considered by Berbeco et al. [2011] to calculate dose enhancement factors to endothetial cells. Figure taken from Berbeco et al. [2011].

much smaller area than standard low-dose rate radioactive sources. The authors suggested that this could help reach a better precision of the treatment. At sub-cellular scale, similarly to what has been reported by Bobyk et al. [2013], GNPs were accumulating in vesicles whose size increased when the post-injection time increased. At 8 days following the injection, they found no GNPs in the extra-cellular matrix. As illustrated in Fig. 6.3, maps of doses (normalized to the activity) based on intra-cellular GNP biodistributions 24 h and 8 days after the injection showed that the dose distribution was highly inhomogeneous, both intra and inter cells. Peaks of dose were mostly located around the GNPs, restricted to vesicles. A comparative study of the dose maps with or without a NP gold coating showed that the enhancement of dose due to gold was consecutively restricted to those vesicle, and could reach a factor of 25 at the surface of the vesicles. Only a small fraction was deposited within the nucleus, and authors concluded that therapeutic efficacy seemed driven by indirect mechanisms, such as ROS production.

6.2.2. Average dose enhancement to endothelial cells

When combining irradiation of the tumour with GNPs 2 min after the injection, Hainfeld et al. [2004] have reported that subcutaneous EMT-6 mammary carcinoma tumour became haemorrhagic before shrinking, indicating catastrophic endothelial cell damages. Preclinical studies have indicated that combining various tumour vascular disrupting agents (VDAs) with radiotherapy results in consequent improvements in cancer treatment (Ngwa et al. [2012]). It was even reported that the combination of VDAs and radiation could eliminate poorly oxygenated and hence radioresistant cells. GNPs could be a good VDAs agent, especially if targeted to the inner wall of the vasculature. To estimate this potential vasculature disruption enhancement, a few dosimetry studies have in particular focused on the dose enhancement in endothelial cells using analytical calculation (based on the Cole energy loss formula, Berbeco et al., Ngwa et al., Ngwa et al. [2011, 2010, 2012]) or Monte Carlo simulation (Amato et al., Lin et al. [2013, 2015]).

As observed previously for macroscopic DER, the dose enhancement that could be reached inside endothelial cells depended on the energy of the source (Berbeco et al., Ngwa et al., Ngwa et al. [2011, 2010, 2012]), the geometry of the endothelial cells considered (Ngwa et al., Ngwa et al. [2010, 2012]), the geometry and depth of the tumour considered (Berbeco et al. [2011]) and the GNP biodistribution and concentration (Amato et al., Lin et al. [2013, 2015]). For instance, considering a vessel surrounded by tumoural tissues and GNPs that were either restricted to the vessels or diffused throughout the tumour, Amato et al. [2013] found sharp gradients of

DER that were strongly related to the GNPs concentration. When all the GNPs were inside the vasculature, they found a DER of 9.3 (140 mg·mL^{-1}, with photon irradiation at 150 kVp) inside the vessel while there was no effect in the tumour. They concluded that limited GNP diffusion range was desirable to boost the radiation dose and therapeutic effect in tumour microvasculature while sparing surrounding viable tissue. Berbeco et al. [2011] reported that the cellular DERs were more important (8 to 16 times higher) than reported before for macroscopic DER, due to local high concentration of NPs. Indeed, GNP concentrations were estimated based on the *in vivo* study of Hainfeld et al. [2004]. Authors estimated that the GNP concentration throughout the tumour was 7 mg·mL^{-1}, which was further used to estimate dosimetric enhancement to the tumour (Cho [2005]). Considering that the vasculature represents about 5 % of the tumour volume, then if none of the GNPs had time to diffuse throughout the tumour and were therefore restricted to the vasculature, a local concentration of 140 mg·mL^{-1} would be reached.

Overall, a significant dose enhancement can be achieved to endothelial cells, especially if the NPs are located on the surface of the cells. To limit the NPs to the vasculature, two methods are possible: by passive targeting, large NPs (100 nm diameter) may be used to accumulate the NPs inside the vasculature instead of the tumour. Otherwise, active targeting may be done by using cell-specific targeting of NPs by multivalent attachment of small molecules. For a better contrast between the vessels and healthy tissue, the diffusion of GNPs inside the tumour should be avoided. While this technique is more efficient for low energy keV photons, they could also be used for MeV and proton irradiation, especially for targeted GNPs.

6.3. Nanoscopic scale: around the GNP

A few studies (Carter et al., Incerti et al., Jones et al., Lechtman et al., Leung et al., Lin et al., Van den Heuvel et al. [2007, 2016, 2010, 2011, 2011, 2014, 2010]) have focused on the electron emission characteristics and its associated dose deposition at nanometric scale when irradiating gold NP or gold slabs. The rate of NP ionization per sent Gy is useful to determine the number of GNPs that are ionized inside a given volume (Lechtman et al. [2011]). Other interesting metrics were also studied. One can either study the energy distribution of ejected electrons (Incerti et al. [2016]), the range of emitted electrons (Lechtman et al., Leung et al. [2011, 2011]) or the dose deposited in the vicinity of the NP compared to a theoretical sphere of water (Jones et al., Lin et al. [2010, 2014]).

6.3.1. Average energy conversion per photoelectric effect in the NP

For an ionized GNP, Lechtman et al. [2011] studied the percentage of energy converted into (1) energy internally absorbed in the GNP; (2) Auger electrons (outside the NP); (3) X-rays and (4) photo-electron (outside the NP). It was investigated for different photon sources (^{103}Pd (20-23 keV), ^{125}I (22.1-35.5 keV), ^{169}Yb (49.5-307 keV), 300 kVp (average energy 100 keV), ^{192}Ir (296-608 keV) and 6 MV (average energy 2 MeV)) and different sizes of GNPs (1.9 nm, 5 nm, 30 nm and 100 nm). It should be noted that, in this study, only the photoelectric effect was considered.

1. When the average energy of the source increased, or the size of the NP decreased, the energy internally absorbed inside the NP decreased. Taking the extreme cases, the energy internally absorbed inside the NP for ^{103}Pd was 4.65 % for the 1.9 nm GNP, and 25 % for the largest. For the most energetic source (6 MV), the energy internally absorbed was 0.91 % for the smallest GNP and 4.38 % for the 100 nm GNP.

2. The internally absorbed energy mostly arose from Auger electrons. Hence, the amount of energy converted into Auger electrons decreased when the size of the NP increased. It also decreased when the energy of the source increased: the photo-electron energy increased while the energy of Auger electrons remained quite constant after the K-edge. Hence, for

^{103}Pd source, 32 % to 19 % of the energy was converted into Auger electrons for 1.9 nm and 100 nm GNPs. It dropped at 11 % to 7 % for ^{169}Yb and remained below 9 % for other sources.

3. Energy converted into X-rays was constant for a given source, as the photons were not absorbed by the GNP. It increased from $\sim$ 14 % for ^{103}Pd to $\sim$ 42 % for 300 kVp (beyond the K-edge), and then decreased to about 23-24 % for higher energy sources.

4. The energy converted into a photo-electron was the most important part regardless of the energy. It decreased when the energy of the source decreased, or when the size of the GNP increased. For example, for the ^{103}Pd source, it went from 49 % for 1.9 nm GNPs to 42 % for the 100 nm GNPs. It became relatively constant for higher energies, at $\sim$ 70 %, except for a drop around the K-edge.

To conclude, the photo-electron carried most of the energy following an ionisation. The energy loss within the NP was mostly negligible, except at low energy for large NPs. Except at really low energy (20 keV), Auger electrons represented a very small amount of the total energy, around $\sim$ 4 %.

6.3.2. Ionization rate per NP per Gy

The rate of ionization of one GNP is highly dependent on the size of the NP and the energy of the source. Lechtman et al. [2011] calculated the GNP ionization rate for different sources at a tissue depth of 1 cm (brachytherapy sources) or 5 cm (external sources), for a 2 Gy irradiation. For a fixed size of 1.9 nm, the ionization rate (per 2 Gy per NP for the photoelectric effect only) varied from 7.38×10^{-6} at 20.6 keV (^{103}Pd) down to 6.43×10^{-9} at 1861 keV (6 MV). For a fixed source (^{103}Pd), the ionization rate varied from 7.38×10^{-6} for a 1.9 nm GNP up to 1.08 for a 100 nm GNP. If the ionization rate was highly dependent of the size of the NP, it was however independent of the gold mass concentration. Lin et al. [2015] reported ionization rates per Gy for a 50 nm GNP for different irradiation particles. For proton spread out Bragg peaks taken at different depth (12.7 cm range in water and 7 cm modulation), the rate was nearly constant and equal to $\sim 7 \times 10^{-4}$, of the same order of magnitude as for a pristine Bragg peak (proton energy 100 MeV). For a 6 MV photon irradiation, the rate was 4.9×10^{-4} at 100 % percentage depth dose (few mm) and increased with increasing depth, reaching 1.0×10^{-3} at 50 % depth dose ($\sim$ 20 cm).

To conclude, for photon irradiation, the ionization rate was higher in the keV range compared to MeV. The variation of the GNP diameter from 1.9 nm up to 100 nm induced a variation of the ionization rate that covered nearly 6 orders of magnitude. This is consistent with the variation of the number of atoms, that is proportional to the volume of the GNP. For high photon energies (MeV), the ionization rate dropped compared to keV. It was higher when the GNP was located deeper due to a relative higher low energy contribution in the photon spectrum.

6.3.3. Energy spectra of electrons emitted out of GNPs

Leung et al. [2011] calculated mean energies of electrons emitted out of GNPs. For 50 kVp, 250 kVp, ^{60}Co or 6 MV beams, they found mean energies of 6.82 keV, 20.2 keV, 450 keV and 230 keV for 2 nm GNPs and 11.77 keV, 37.2 keV, 454 keV and 386 keV for 100 nm GNPs. Detailed spectra of electrons emitted out of a GNP were calculated by Incerti et al. [2016]. The GNP was put in vacuum and irradiated by a beam of photons (or protons) of diameter equal to the diameter of GNP. The spectra were normalized per incident particle. An example of such distribution, obtained with our Monte Carlo simulation is displayed in Fig. 6.5 and compared to Geant4 results for a photon irradiation. The distribution peaks a low energies ($\leq$ 1 keV), and

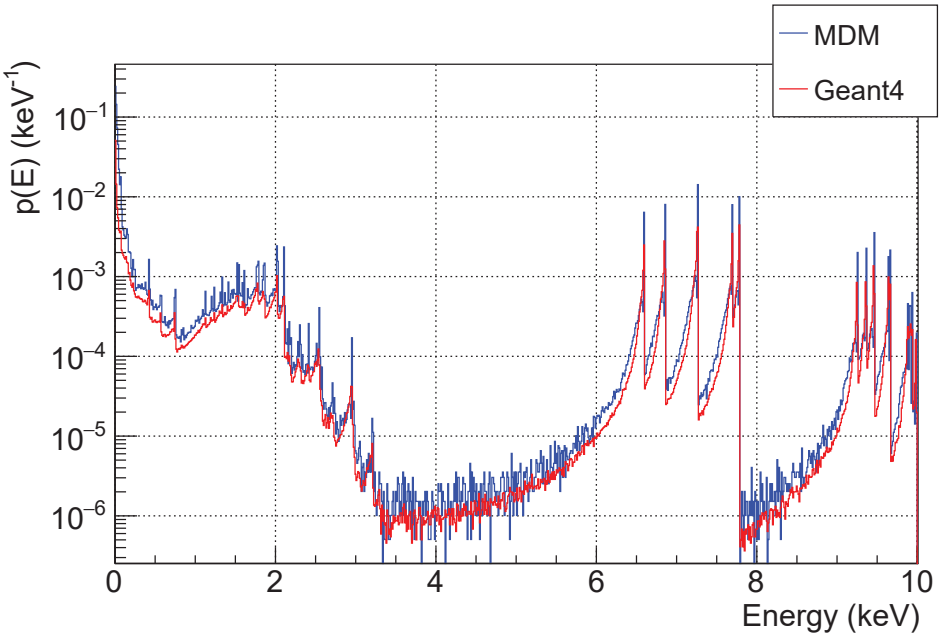

Figure 6.5.: Energy distribution of electrons emitted out of a 5 nm GNP, normalized to the number of incident 10 keV photons. In blue, the results from the MC code MDM (see chapter 8), in red the results from the MC code Geant4.

around 2 keV due to secondary Auger electron cascades. Beyond 2 keV, other peaks up to the energy of the incoming photon are due to photo-electrons. When the photon energy was equal to 100 keV, a plateau was observable due to Compton scattering. McMahon et al. [2011] studied the number of Auger electron emitted out of nanoparticles, and found that it greatly depended on the size of the NP. Most of Auger electrons had energy below 10 keV, and mostly below 1 keV. As a consequence, their range in gold is of the order of a few nanometres. The Auger electron emission out of the NP thus greatly depended on the distance from the NP surface from which the initial vacancy was generated.

6.3.4. Effective range of electrons emitted out of GNPs

Lechtman et al., Leung et al. [2011, 2011] studied the range of emitted electrons to compare it with the size of a cell, for different sources. Lechtman et al. [2011] calculated the distribution of electrons ranges, normalized per photoelectric event. Results are displayed in Fig. 6.6. While low energy irradiation of GNPs generates electrons that can travel up to about 10 µm (^{103}Pd), the maximum range increases with the energy of the beam. For example, for the ^{192}Ir source, emitted electrons may travel up to 2 000 µm. Regardless of the photon source, the intensity of low range ($\leq$ 100 nm) was more important for small nanoparticles. This was due to the absorption of low energy electrons when the NP is large.

6.3.5. Dose deposition

Different studies were followed considering either the dose deposition in concentric shells around GNPs as a function of the distance to the NP (Carter et al., Lin et al., Lin et al., McMahon et al., McMahon et al. [2007, 2014, 2015, 2011, 2011]), referred as the radial dose, or in cubic voxels (Zygmanski et al. [2013]).

Carter et al. [2007] calculated the radial dose coming from the "GNP contribution", i.e., the radial dose induced following an interaction between a photon and a GNP. This GNP radial dose was

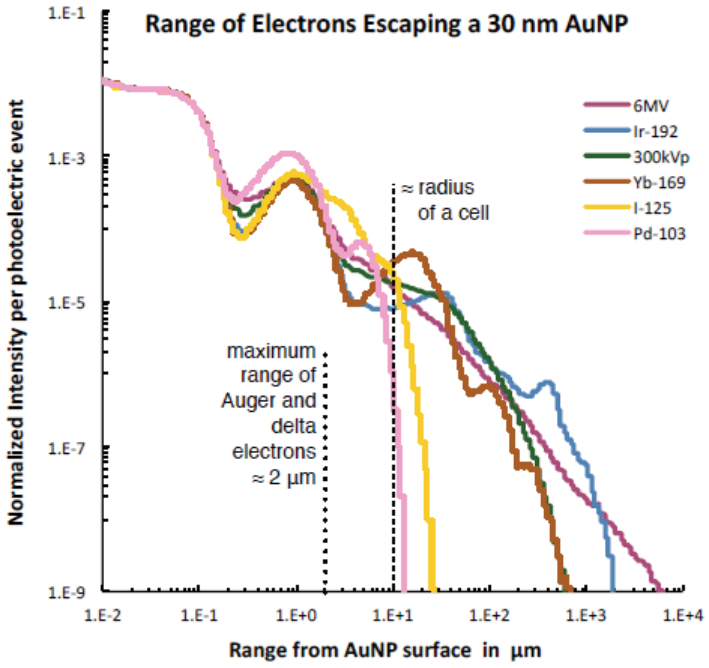

Figure 6.6.: Range distribution of the electrons ejected out of an ionized GNP. Figure taken from Lechtman et al. [2011].

normalized per GNP per Gy. It fell below the "background dose" (i.e., the dose induced by the interaction of photons with water molecules, equal to 1 Gy) beyond a distance of 5 nm from a 3 nm GNP surface for an irradiation at 100 kVp.

In the work by McMahon et al. [2011], the radial dose per ionization event in the GNP was calculated for different sizes of GNPs at 40 keV. The energy deposition was broken down in sub-contributions (Auger or photo-electron). McMahon et al. [2011] observed a boost from 0 to 150 nm due to Auger electrons which quickly dropped, while the energy deposited by photo-electrons in this range was minor. Radial doses per ionization reached up to 100 000 Gy on the surface of the GNP regardless of the size of the NP. This very high dose spike was often used as a figure of merit, to denote a "local dose inhomogeneity" compared to the background macroscopic dose deposition. Note that, however, when normalized to the probability of hitting the GNP as done in the work by Carter et al. [2007], the radial dose dropped significantly, resulting in average boost per GNP on the surface that are equal to 0.2, 6.8 and 11.1 Gy per prescribed Gy for a 2 nm, 20 nm and 50 nm GNP. This last figure of merit (radial dose around GNP per prescribed Gy) is much relevant (in respect to the same dose per GNP ionization) when comparing with the macroscopic "background" dose (i.e. 1 Gy). Moreover it is worth to note that these values are consistent with the dose calculated in the 2D maps previously presented (e.g. Figure 6.2).

Lin et al. [2014] studied the radial dose for different sources (protons, MeV photons and keV photons), normalized per incident particle or per MeV absorbed and compared it to theoretical water NPs. The concept is illustrated on Fig. 6.7. The DER was defined as the ratio of the radial dose obtained per incident particle for GNP, divided by the radial dose for WNP. It is very different compared to other macroscopic and microscopic DERs previously discussed, as it does not account for the concentration of GNPs nor the contribution of the background. For monoenergetic proton beams, they found relatively similar DER, and it went from 5.8 on the surface of the NP up to 15 at 10 µm for proton energies of 10 MeV. In particular, the authors found that activating Auger cascade resulted only in 1.5 % difference in dose. Unlike monoenergetic beams, SOBP beams contained secondary particles like neutrons, electrons and photons. The DER was found to be

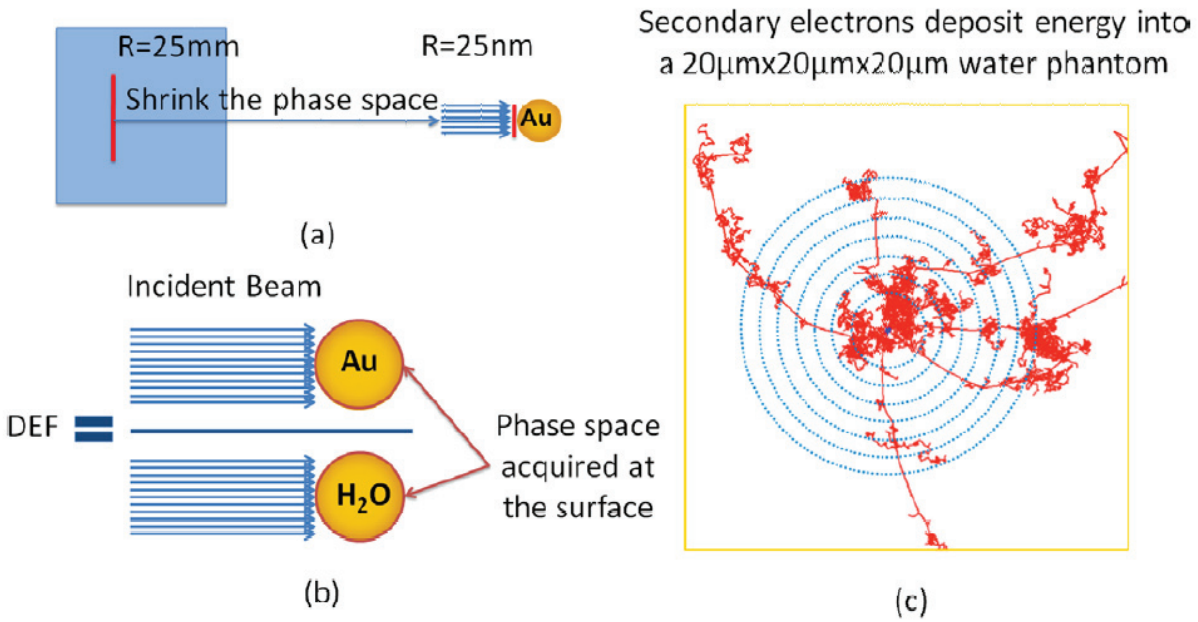

Figure 6.7.: Dose Enhancement Factor defined at the NP scale. Figure taken from Lin et al. [2014].

quite independent of the depth (difference of dose below 30 %) and secondary particles did not significantly contributed to the radial dose (below 1 %). For monoenergetic keV photon beams, they found that the DER was highly dependent on the energy. It was of the order of 10^3 on the surface for 50 keV, and 15 times higher for 50 keV than 250 keV. At 50 keV, a sudden increase was obtained around 1 µm due to the drop of the radial dose for WNP. Finally, they found that, when the radial dose was normalized per MeV irradiation, results were very similar (within 15 %) for all types of sources.

6.3.6. Clusters *vs* single GNPs

A few studies (Gadoue et al., Zygmanski et al. [2018, 2013]) investigated the effect of GNP aggregation on the dose deposition, as many experimental work have reported aggregates of GNPs when internalized or on the surface of the cell. Zygmanski et al. [2013] studied planar cluster of GNPs (which could correspond to accumulation of GNPs on the cell surface). The cluster size was set at 2×2 µm^2. The distance between GNPs varied, thus increasing the number of GNPs contained in the cluster proportionally to the square of the distance. The dose was recorded along the central axis in 100 nm length voxels. GNPs were cubical, with a length of 100 nm. The DER was defined as the ratio of the average dose inside the voxel with GNPs, divided by the average dose in the same voxel without GNPs. If the distance between GNPs were larger than 450 nm, the DER tends to be same as isolated GNPs (about 10 on the surface). For an extreme case of a distance between GNPs of 50 nm, then the DER increased and was about 24 on the surface. For packed clusters, the DER also increased at longer distances. While the DER tends to 1 at 250 nm for isolated GNP, it remained around 5 at 2000 nm when the distance between GNPs was equal to 50 nm. These observations were obtained regardless of the photon energy, and were more important for lower energies (20 keV *vs* 100 keV).

Gadoue et al. [2018] studied the impact of clusters as a function of the geometry and size of the cluster, using a deterministic computation method. They studied the DER (defined as the ratio of the dose with to that without GNPs) for 120 kVp and 6.5 MV photon beams. They studied clusters containing up to 4 GNPs, and different geometries for each cluster (linear or packed). They found that agglomerates have two types of dose enhancement: a smooth peripheral enhancement characterized by iso-DERs and isolated hotspots. Both are illustrated in Fig. 6.8.

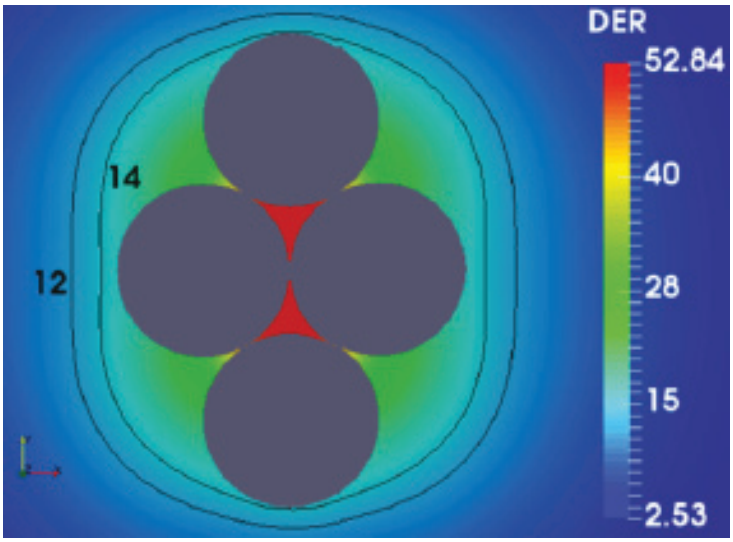

Figure 6.8.: Example of DER obtained by Gadoue et al. [2018], for a 120 kVp irradiation and a cluster of 4 50 nm GNPs. Taken from Gadoue et al. [2018].

For kVp irradiation, the authors found an iso-DER of 11.6 for a single 50 nm GNP, while it varied between 12.6 to 14 for packed GNPs. For MV, iso-DERs were of the order of 1.05. Additionally, they found that the geometry of the GNP clusters did not change significantly the DER at long distances (500 nm, 1 µm and 2 µm), but the DER increased with increasing cluster size. They found very high values of the DER in the hotspot areas, up to 52.84.

6.3.7. Chemical modelling

Similarly to the radial DER reported by Lin et al. [2014], Tran et al. [2016] reported chemical species radial distribution for GNPs or theoretical WNPs irradiated by a beam of protons, using the simulation toolkit Geant4-DNA. Only the interaction of the primary beam with the NPs were considered. Consequently, only the chemical species produced by the interaction of secondary particle emitted out of the NPs with surrounding water molecules were taken into account. The study was done for proton beam energies varying from 2 to 170 MeV, and a GNP radius of 50 nm. They obtained radiolysis radial profiles that were very similar to that of the radial dose profile.

6.4. Biological endpoints

6.4.1. Sub-cellular damages

In order to translate the dose increase into biological endpoints, different studies modelled biological targets and evaluated the dose deposition inside the targets. He and Chow, Sotiropoulos et al., Xie et al. [2016, 2017, 2015] studied dose deposition or damages in DNA fragments, and Kirkby and Ghasroddashti, McNamara et al. [2015, 2016] studied the impact of GNPs on the dose deposition inside mitochondria.

6.4.1.1. DNA damage

Using the MC code PARTRAC, Xie et al. [2015] studied the increase of DNA SSB and DSB induced by GNPs inside a cell under keV X-ray irradiation (simulation conditions are summarized in Tab. 6.2). Different GNP sizes, concentrations and biodistributions (on the cell surface, in the cytoplasm or on the nucleus membrane) were investigated. They found that the yield of SSB was larger than that of DSB by a factor of 20 under all conditions. For a fixed number of GNPs,

Reference	Code	Beam source	Beam geometry	System geometry	GNP diameter	GNP distribution	GNP concentration	Equivalent cellular concentration (mg·mL^{-1})*	Main metrics	Main results	Experimental data
DNA damage											
Xie et al. [2015]	PARTRAC	X-ray source 60, 80, 100, 150 and 200 kVp	Planar source at 50 µm from cell	Spherical cell, diameter 30 µm Spherical nucleus, diameter 10 µm DNA in chromatin form	2, 14, 50, 74, and 100 nm	(1) On nucleus surface (2) On a virtual surface in cytoplasm (20 µm diameter) (3) On cell surface	(1) Fixed number (1000 GNPs) (2) Fixed gold mass	(1) 14 nm: 2 $\times 10^{-3}$ 50 nm: 0.1 100 nm: 0.7 (2) 0.2	DNA SSB + DNA DSB	Enhancement only if GNP on nucleus surface Optimal: 100 nm GNPs, 60 kVp	×
He and Chow [2016]	GEANT4-DNA (v10.2)	X-ray source 50, 100, 150 and 200 keV	At 200 nm from GNP Diameter twice that of GNP	Cubic of side 1 µm DNA on right hand side of the GNP at 30, 80 or 130 nm	30, 50 and 100 nm	GNP in the center	Single GNP	×	Dose enhancement to the DNA with over without GNP	Optimum DER = 3.7, at 150 kVp for DNA at 30 nm, GNP of 100 nm	×
Sotiropoulos et al. [2017]	GEANT4-DNA (v10.2)	Proton source 1, 10 and 50 MeV	Protons enter geometry from ellipsoidal surface (half-axes 15 µm × 12 µm) At 7 µm from nucleus	Ellipsoidal cell (half axis 13 × 10 × 5 µm^3) Ellipsoidal nucleus (half axis 11.83 × 8.52 × 3 µm^3) In a water box (32 × 26 × 16 µm^3)	12, 30 and 60 nm	Homogeneously in cytoplasm or in lysosomes	12 nm: 5.9 $\times 10^5$ to 3.5 $\times 10^7$ 30 nm: 3.8 $\times 10^4$ to 2.3 $\times 10^6$ 60 nm: 4.7 $\times 10^3$ to 2.8 $\times 10^5$	3.8 to 228	SSB and DSB	No enhancement	×
Mitochondria damage											
McNamara et al. [2016]	GEANT4 (v10.1)	X-ray source 10-50 keV	Planar source at 10 µm from cell centre Field size 12 × 12 μm^2	Spherical cell (diameter 11.5 µm) Composition: (1) water (2) Realistic homogeneous cell (50 % water, 50 % measured) (3) Realistic in compartments: 40 % centred spherical nucleus + 11 % ellipsoid mitochondria	Atomic mixture	(1 + 2) whole cell (3) in cytosol	1 % by mass	10 for (1+2) and 4 for (3)	Energy deposition + number of ionisations (whole cell + compartments)	If photon energy ≥ 45 keV, number of ionizations and energy deposition is the same as liquid water 1 % of gold increases energy deposition by 1.1, 2.1 and 1.7 for 10, 30 and 50 keV	Measure of cell and organelles composition for JURKAT cells
Kirkby and Ghasroddashti [2015]	PENELOPE	Photon source at 1.5 cm, 6 MV (1.44 MeV/1.02 MeV) ^{60}Co (1.09 MeV), 300 kVp (124 keV) 200 kVp (79.1 keV) 125 kVp (54.7 keV) 90 kVp (47.5 keV)	Planar source Field size 10 × 10 cm^2	Ellipsoidal mitochondria (2 semi-axis (1) varying from 200 to 500 nm + (2) 500 nm) Outer-membrane + inter-membrane space + inner folded-membrane Contained in a larger volume of water	13 nm	On the surface of the mitochondria at 0 or 26 nm to account for coating	0 to 6000 per mitochondria	0.024	Dose enhancement in (1) the mitochondria, (2) the membrane (3) 13 nm side voxels	DER over whole mitochondria from 1.1 to 1.6 for kVp sources and less than 1.01 for MV sources for referential experimental results Membrane DER of 2.3 for 90 kVp Max voxel DER of 8.2 for 90 kVp	Distribution by Karataş et al. [2009] 13 nm GNPs 565 GNP per mitochondria with 13 nm coating
Biophysical models											
McMahon et al. [2011]	Geant4 + LEM	160 kVp + Monoenergetic	Planar source at 200 µm	MDA-MB-231 $\alpha = 0.019$, $\beta = 0.052$ α/β ratio: 0.37 Gy Volume not specified	2 to 50 nm	Homogeneously inside the cell	0.5 mg·mL^{-1}	0.5	RBE(2 Gy) Survival 0:8 Gy MID	RBE(2Gy) 40 keV, ∼ 2.05 (2 nm), 1.7 (5 nm), 1.45 (10 nm) 1.17 (40 nm) RBE(2Gy), 20 nm ∼ from 1.4 to 1.1 (20 keV to 80 keV) then 1.35 to 1.05 (up to 140 keV) MID(0:7 Gy) with NP = 2.36 without NP = 3.68, Ratio = 1.56	From Jain et al. [2011] 160 kVp, 1.9 nm Cell survival
McMahon et al. [2011]	Geant4 + LEM	Photons 6 MV + 15 MV	Planar source, 5 cm diameter beam, 5 cm depth	MDA-MB-231 6 MV: α/β ratio: 0.025 $\alpha = 0.002$, $\beta = 0.079$, 15 MV: α/β ratio: 1.08, $\alpha = 0.077$ $\beta = 0.071$ Volume not specified	2 nm	Homogeneously	1.3 × 10^8 GNP intracellular	34 (Estimated with volume measured by Lin et al. [2015])	Survival 0:8 Gy MID	6 MV: $\alpha = 0.11$, $\beta = 0.080$ 15 MV: $\alpha = 0.17$, $\beta = 0.072$ 6 MV: MID(0:6Gy) Without NP 3.11, with NP 2.52, Ratio 1.24 15 MV: MID(0:7 Gy) Without NP 2.83, with NP 2.36, Ratio 1.18	From Jain et al. [2011] 6 MV: Ratio 1.29 15 MV: Ratio 1.16
Lin et al. [2015]	Geant4 + LEM	(1) 150+250 kVp (2) 6 MV photons (3) Proton 100 MeV at Bragg peak (4) SOBP (12.7 cm range + 7 cm modulation)	Depth: (1) ∼ 1 mm, (2) Few mm + ∼ 80 mm + ∼ 175 mm (3) ∼ 75 mm (4) ∼ 75-100 mm	MDA-MB-231 Cylindrical cell (Thickness 2 µm, Diameter 13.5 µm) Nucleus diameter 8 µm Media thickness 2.5 µm $\alpha = 0.019$, $\beta = 0.052$ (same for any IR), DU145, α/β ratio = 2 $\alpha = 0.13$, $\beta = 0.022$, Brain tissue, α/β ratio = 6 $\alpha = 0.1$, $\beta = 0.05$	2, 10, 20 and 50 nm	(c1) Nucleus only (c2) Homogeneous in cell (c3) Cytoplasm only (c4) Extracellular only	10 nM to 10 µM	50 nm 1 µm = 761	Survival (0:8 Gy) MID (ratio normalized to X-ray MID)	50 nm GNP, Protons (SOBP), 1 µM SOBP: (c1) 1.81, (c2) 1.33, (c3) 1.018 (c4) 1.0001 BP: (c1) 1.93, (c2) 1.33, (c3) 1.016, (c4) 1.00 50 nm, kVp, 100 nM 150 kVp: (c1) 5.97, (c2) 4.88, (c3) 1.77, (c4) 1.08 250 kVp: (c1) 5.74, (c2) 4.04, (c3) 1.56, (c4) 1.06 50 nm GNP, 6 MV, 1 µM PDD100: (c1) 4.35 (c2) 2.59 (c3) 1.08 (c4) 1.004 PDD80: (c1) 5.78 (c2) 4.32 (c3) 1.14 (c4) 1.006 PDD50: (c1) 5.89 (c2) 4.74 (c3) 1.16 (c4) 1.008	×
Lechtman et al. [2013]	MCNP, PENELOPE, LEM	Photons 300 kVp (Av. 100 keV)	4 mm depth	PC-3, α/β ratio = 4.9 $\alpha = 0.217$, $\beta = 0.044$ Spherical, cell radius 13.1 µm Nucleus radius 8.2 µm Media thickness 147 µm	30 nm	Homogeneously distributed in compartments, nothing in nucleus, 2 mg·mL^{-1} extracellular media, cytoplasm 0.84 mg·mL^{-1}			Survival (0:8 Gy) α and β MID	With GNP: $\alpha = 0.315$, $\beta = 0.045$ MID with GNP: 2.13, Ratio 1.20	With GNP $\alpha = 0.345$, $\beta = 0.037$ MID with GNP: 2.11, Ratio 1.21
Lechtman [2013]	MCNP, PENELOPE, LEM	Photon 300 kVp + 100 kVp	4 mm depth	PC-3 (see above) SK-BR-3, α/β ratio = 7.8 $\alpha = 0.274$, $\beta = 0.035$ Cell radius 9.3 µm Nucleus radius 6.3 µm Media thickness 147 µm	5 and 30 nm	Homogeneously distributed in compartments, nothing in nucleus (c1) PC-3, 30 nm, extra-cellular 2 mg·mL^{-1}, cytoplasm 0.84 mg·mL^{-1}, (c2) PC-3, 5 nm, extra-cellular 2 mg·mL^{-1}, cytoplasm 0.38 mg·mL^{-1} (c3) SK-BR-3, 30 nm, extra-cellular 0.2 mg·mL^{-1}, cytoplasm 0.14 mg·mL^{-1} (c4) SK-BR-3, 30 nm, extra-cellular 2 mg·mL^{-1}, cytoplasm 1.19 mg·mL^{-1}			Survival MID or RBE (2 Gy)	(c1) 100 kVp, Ratio MID 1.52 (c2) 300 kVp, RBE(2Gy) 1.21 (c3) 300 kVp, RBE(2Gy) 1.05 (c4) 300 kVp, RBE(2Gy) 1.40	(c1) 100 kVp, Ratio MID 1.51 (c2) 300 kVp, Ratio MID 1.36 (c3) 300 kVp, RBE(2Gy) 1.05 (c4) 300 kVp, RBE(2Gy) 1.37

Table 6.2.: Summary of different simulation studies, towards calculating a biological endpoint (sub-cellular damage or cell survival). The cellular concentrations are calculated by dividing the total number of GNPs included in the simulation over the volume of the whole cell.

the most effective conditions to induce DNA damages were the 60 kVp beam combined with the 100 nm GNP (largest). For fixed gold mass, smaller GNPs were more effective. Significant DNA damage enhancement was only reached when GNPs were located on the surface of the nucleus: for example, they found a DNA damage enhancement of 1.14 for 100 nm GNPs (fixed mass), while when located elsewhere the enhancement was only of 1.01. SSB and DSB enhancements were both very close. Compared to the nucleus dose enhancement (e.g. ratio of the dose deposited in the nucleus with to without GNPs), they found smaller DNA damage enhancements. They attributed it to the DNA distribution inside the nucleus, which does not occupy 100 % of the volume.

McQuaid et al. [2016] combined images of GNP biodistribution and MC simulation to predict the DNA damages. Using MDA-MB-231 cell line incubated with 0.5 mg·mL^{-1} of GNPs, they obtained intra-cellular concentrations of 7 mg·mL^{-1}. The GNPs were found predominantly in the cytoplasmic regions with an accumulation in the perinuclear protoplasm region. The gold intensity peaked at 0.5 µm from the nucleus surface and decreased with increasing distance from the nuclear membrane. The cells were irradiated with photons of energy ranging from 10 to 60 keV. Nuclei foci were measured by γ-H2AX phosphorylation 1 h following irradiation. The nuclear damage enhancement peaked at $\sim$ 50 keV and decreased for energy above and below. The authors constructed a model considering that the photo-electron emitted out of a GNP deposited their energy in a sphere whose radius was determined according to the photo-electron maximum range in water. The overlapping between this sphere and the nucleus was used to determine the amount of DNA damages. The model reproduced a peak around 40 keV and roughly matched the trend of early DNA-damage. They concluded that early DNA damages were better represented by long-range photo-electrons, compared to Auger-electrons.

Finally, Sotiropoulos et al. [2017] studied the SSB/DSB enhancement induced by GNPs for proton irradiation. They reported concentrations of 7 mg·mL^{-1} inside the cytoplasm, which represents a total cellular concentration of 3.8 mg·mL^{-1} (see Tab. 6.2). They showed that, under clinically relevant concentrations and irradiation doses, there was no additional DNA SSB/DSB induced by GNPs, even when the GNPs are directly contained inside the chromosomal territory. Indeed, the number and range of electrons produced were not insufficient to create measurable effects due to a small interaction probability of protons with GNPs. As a small number of protons are needed to deliver a clinically relevant dose, the geometrical interaction probability of a proton with a GNP is expected to be extremely low. They therefore suggested that another mechanism was responsible for the GNPs effectiveness under ion irradiation.

6.4.1.2. Mitochondrial damages

As discussed in Chapter 3 and 5, there are growing experimental evidences which suggest that the mitochondrion may be a particularly important radiation target outside the nucleus (McNamara et al. [2016]). Given the cytoplasmic localisation of GNPs and some reports of GNPs attaching to mitochondria (Kirkby and Ghasroddashti [2015]), Kirkby and Ghasroddashti, McNamara et al. [2015, 2016] have estimated mitochondrial damages.

Kirkby and Ghasroddashti [2015] studied the energy deposition inside mitochondria (with water composition) and the dose enhancement in different mitochondrial compartments. They modelled a realistic distribution of 13 nm GNPs on the surface of the membrane based on the study by Karataş et al. [2009]. They studied the impact of GNPs on the dose deposition inside different compartments (whole mitochondria, membrane or voxels), according to the number or distribution of GNPs, the thickness of the GNP coating, the photon energy, the geometry of the mitochondria. When 565 GNPs were distributed on the mitochondria surface, they found mitochondrial DER varying from 1.1 to 1.6 for kVp sources and less than 1.01 for MV sources. Changing the size of the mitochondria varied the DER up to 14 % for low energy sources, while changing the coating

thickness varied the DER up to 7 %. When averaging over the outer membrane, the membrane DER was equal to 2.3 for 90 kVp. When studying DER at a voxel scale (representing the local heterogeneity of the dose deposition), it reached up to 8.2 for kVp sources, and increased if GNPs were clustered together. The voxel DER reached up to 30.7 when the number of GNPs was increased up to 6000. This high DER could lead to membrane rupture or at least perturbation of its functionality. The authors pointed out that they neglected other GNPs located in the cytoplasm, which could increase the total background dose.

McNamara et al. [2016] calculated energy deposition and number of ionisation inside mitochondria (and nucleus) using either a homogeneous cell with a realistic measured composition or with sub-compartments, whose composition were also based on measurements. The mean ionisation energy was 78 eV for liquid water (69 when accounting for separate atomic elements) while it was around 68-69 eV when considering experimental compositions (composed of 29 to 33 % of carbon). For cells with a homogeneous concentration (including gold), they found that, when adding 1 % by mass of gold in the whole cell, the total number of ionizations and the energy deposition increased by a factor of 1.1, 2.1 and 1.7 for 10, 30 and 50 keV photons. To compare, it increased by a factor of 2.6 for pure water at 30 keV. When considering separate compartments, and adding gold in the cytosol, the energy deposition was increased by 32 % for mitochondria and by 13 % for nucleus.

6.4.2. Cell survival and biophysical models

Biophysical models aim at calculating cell survival upon irradiation, often based on dosimetric quantities. The goal of this section is to give a summarize of results obtained with the Local Effect Model (LEM), to predict cell survival in the presence of GNPs. This model was used to study the variation of cell survival with regard to the beam particle or energy (Lechtman and Pignol, Lechtman et al., Lin et al. [2017, 2013, 2015]), the GNP biodistribution (Lechtman and Pignol, Lin et al. [2017, 2015]), the GNP size (Lechtman and Pignol, Lechtman et al., Lin et al. [2017, 2013, 2015]), the GNP material (McMahon et al. [2016]) or the cell morphology (Sung et al. [2017]).

6.4.2.1. Description of the Local Effect Model (LEM)

As the profile of GNP dose deposition showed inhomogeneities similar to what can be observed in hadrontherapy (McMahon et al. [2011]), many studies (Lechtman and Pignol, Lechtman et al., Lin et al., McMahon et al., McMahon et al. [2017, 2013, 2015, 2011, 2011]) used the LEM, which was originally developed in the context of hadrontherapy.

In case of photon irradiation, the surviving fraction of cells to a dose D is given by:

$$S(D) = \exp(-n_{\text{lethal}}(D)) \tag{6.1}$$

where $n_{\text{lethal}}(D)$ is the number of lethal events is characterized by the quadratic model:

$$n_{\text{lethal}}(D) = \alpha D + \beta D^2 \tag{6.2}$$

where α and β are parameters which depend on the cell line.

Instead of calculating a dose averaged over the whole cell volume, the LEM calculates the probability of damage occurring at each point within a cell based on the local dose at that point. Hence, the number of lethal events reads,

$$n_{\text{lethal}}(D) = \int_{V_{\text{sensitive}}} v(D_{\text{local}}) \mathrm{d}V \tag{6.3}$$

where $V_{\text{sensitive}}$ is the volume of the sensitive target, usually taken as the nucleus, and

$$v(D_{\text{local}}) = \begin{cases} \frac{\alpha D_{\text{local}} + \beta D_{\text{local}}^2}{V_{\text{sensitive}}}, & \text{if } D_{\text{local}} \leq D_t \\ v(D_t) + \frac{S_{\max}(D_{\text{local}} - D_t)}{V_{target}}, & \text{if } D_{\text{local}} > D_t, \text{ and } S_{\max} = \alpha + 2\beta D_t \end{cases} \tag{6.4}$$

where $S_{\max}$ is a threshold which is determined empirically. The final results depend on this threshold, on the α and β parameters determined experimentally, and on the sensitive volume selected. As further discussed in Chapter 13, it also depends on the chosen local dose representation. The different implementations of the local dose are discussed in the next section.

6.4.2.2. Dosimetric approaches

Different approaches of the LEM have been implemented, that were based on different representation of the local dose.

Lin et al., McMahon et al., McMahon et al., McMahon et al., Sung et al. [2015, 2011, 2011, 2016, 2017] implemented the model using the radial dose. The authors calculated the radial dose around one GNP following an ionization event. The number of ionized GNPs was calculated per Gy, to obtain the total number of ionized GNPs in the cell, depending on the GNP concentration. The background dose, resulting from the interaction of the beam with the surrounding water molecules, was added as a uniform background dose. In the first version (McMahon et al., McMahon et al., McMahon et al. [2011, 2011, 2016]), the sensitive volume was reported to be the whole cell volume. Besides, there was no mention of the use of a dose threshold D_t. In the latest version (Lin et al., Sung et al. [2015, 2017]), the sensitive volume was set equal to the cell nucleus. The threshold was set at 20 Gy for MDA-MB-231 cells. The final number of lethal events was calculated as being the sum of the number of lethal events for a uniform irradiation, using Eq. 6.2, in addition to the number of lethal events induced by ionized GNPs using Eq. 6.3.

In the studies by Lechtman, Lechtman and Pignol, Lechtman et al. [2013, 2017, 2013], the dose following an ionization event in a GNP was scored in nanovoxels ($20 \times 20 \times 20$ nm^3) track by track after calculating the number of ionized GNP for a given concentration. For the background, the dose was assumed to be homogeneously distributed within the sensitive volume. The sensitive target was set to be the nucleus. The threshold was set at 23.9 Gy for PC-3 and 38.7 for SK-BR-3. The final number of lethal events was calculated by integrating over the whole cell nucleus using Eq. 6.3.

It should be pointed out that, although the same model is used with two approaches, the results are hardly comparable with each other. The concentration, energy of the beam and cell lines are very different from one study to another. The metrics were not always the same (Mean Inactivation Dose (MID), α and β, cell survival or Relative Biological Effectiveness (RBE)).

6.4.2.3. Results for keV photon irradiation

Lechtman et al. [2013] found results for a 300 kVp irradiation (average energy 100 keV) and PC-3 (prostate) cancer cells ($\alpha/\beta = 4.9$). Using measured intra- and extra-cellular concentrations, they found a MID ratio of 1.20 with their approach, against 1.21 for experiment. They compared it to a standard macroscopic model based on the macroscopic dose enhancement and the linear

quadratic model,

$$S = \exp(-[\alpha(D') + \beta(D')^2])) \tag{6.5}$$

where D' is the dose obtained in presence of GNPs, for a dose of irradiation D. With this approach, they found a MID ratio of 1.07, thus concluding that a nanoscale dose deposition is mandatory for survival prediction. Using the same cell line, they found a MID ratio of 1.52 for 100 kVp (against 1.51 for experiment), showing an increased effect at lower energies.

McMahon et al. [2011] studied MDA-MB-231 cancer cells (α/β = 0.37 Gy) irradiated with a 160 kVp source. It should be noted that in their first calculation, McMahon et al. [2011] used a concentration of 0.5 mg·mL^{-1}, which is the media extra-cellular concentration used in the referential experiment (Jain et al. [2011]). For a 160 kVp irradiation, they found a MID ratio of 1.56, which is close to results from Lechtman et al. [2013]. They also calculated Relative Biological Effectiveness (RBE) at 2 Gy for monoenergetic beams, i.e., 2 Gy divided by the dose required to achieve the same survival than that at 2 Gy without GNPs. It varied from 1.4 to 1.1 for a GNP diameter of 20 nm and an energy varying from 20 keV to 80 keV, and 1.35 to 1.05 for energies varying up to 140 keV.

Using substantially larger concentrations (100 nM of 50 nm GNP, i.e., $\sim$ 76 mg·mL^{-1}), Lin et al. [2015] found a significant MID ratio for 150 and 250 kVp. For a homogeneous concentration in the cytoplasm, they found a MID ratio of 1.77 at 150 kVp and 1.56 at 250 kVp, thus finding higher effects for lower energies.

6.4.2.4. Results for MeV photon irradiation

McMahon et al. [2011] calculated MID ratio for a 6 MV and a 15 MV irradiation at 5 cm depth in water. Compared to the study for keV photon irradiation (McMahon et al. [2011]), although based the same referential experiment (Jain et al. [2011]), McMahon et al. [2011] used a concentration of 1.3 $\times$ 10^8 GNP per cell, rather than the incubation concentration. This number was based on an experimental measurement of the average number of GNPs per cell. Based on the MDA-MB-231 volume measurements from Lin et al. [2015], it represents an intracellular concentration of $\sim$ 34 mg·mL^{-1}. Therefore, for this calculation, the GNP concentration was 68 times higher than that used for the keV calculation, although it was based on the same experimental work. For a homogeneous distribution inside the cell, they found a significant MID ratio of 1.24 at 6 MV and 1.18 at 15 MV, which is close to experimental results and lower than keV irradiation. Similarly, Lin et al. [2015] calculated MID ratio for a 6 MV irradiation at different depth. For a uniform concentration in the cytoplasm only (1 µm of 50 nm GNPs, i.e., $\sim$ 761 mg·mL^{-1}), they found a MID ratio of 1.08 at the first depth (few mm), 1.14 at $\sim$ 8 cm and 1.16 at $\sim$ 17.5 cm. When homogeneously distributed in the cell, it went up to 2.59, 4.32 and 4.74. Therefore, when the GNPs are located deeper, the effect was found to be more important. It remained however lower than the effect for keV irradiation. Note that the concentration used by Lin et al. [2015] are extremely high compared to reported intra-cellular concentrations.

6.4.2.5. Results for proton irradiation

Lin et al. [2015] also studied the effect of proton irradiation. However, they used α and β parameters calculated for keV irradiation when applying Eq. 6.3. Effects were found to be much lower than that of keV and MeV photon irradiation. For a GNP concentration of 1 µM and modelling a proton SOBP, the MID ratio reached only 1.018 when GNPs were contained inside the cytoplasm, and 1.33 if they were distributed throughout the whole cell.

6.4.2.6. Influence of GNP distribution

For PC-3 cells, Lechtman [2013] applied the LEM for different GNP biodistributions, for photon irradiation at either 100 or 300 kVp. Fixing the concentration at 2 mg·mL^{-1}, they studied the effect of GNPs localisation, located either (1) in the extra-cellular media only, (2) in the extra-cellular media and the cell cytoplasm, or (3) in the extra-cellular media, cell cytoplasm and cell nucleus (= sensitive volume). They found a MID ratio of 1.34 when GNPs were located only in the media, and 2.56 if they were located in the media, cytoplasm and nucleus (1.9 nm GNPs irradiated at 100 kVp). Besides, they noted that the impact of the localisation was much more pronounced for an irradiation at 100 kVp than at 300 kVp.

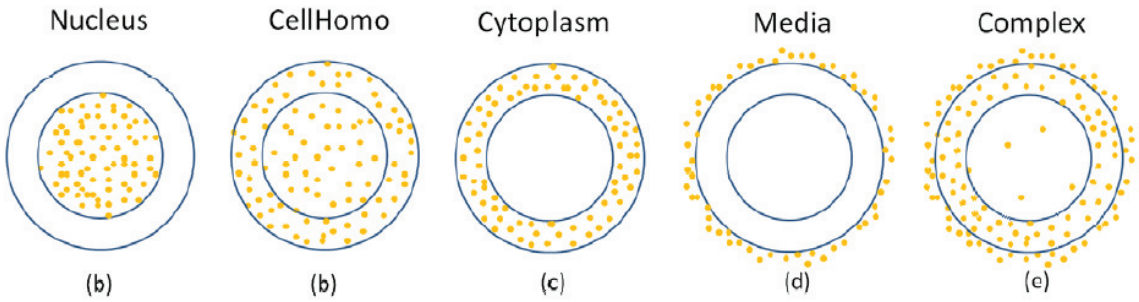

Figure 6.9.: Biodistribution considered by Lin et al. [2015] to study the impact on cell survival with the LEM (nucleus as the sensitive volume). Figure taken from Lin et al. [2014].

Lin et al. [2015] also studied the impact of GNP biodistributions, using the ones reported on Fig. 6.9. It should be pointed out that for some of the distributions, there are no GNPs in the surrounding media, compared to Lechtman [2013] who studied effects with GNPs systematically in the media. While they found a significant MID ratio when GNPs were contained in the volume or throughout the whole cell (5.97 and 4.88 respectively at 100 kVp), they found a much lower MID ratio if GNPs were located in the cytoplasm only (1.77) and if they are located in the extra-cellular media (1.08). This dependence of the radiosensitization was true regardless of the type of beam.

Overall, both authors reported significant effects if GNPs were inside the nucleus. However, while Lechtman [2013] found significant results if GNPs were located only in the media for kVp irradiation, Lin et al. [2015] found much lower effects in this configuration. As further discussed in chapter 13, this may be a consequence of the difference in dosimetric approaches.

6.4.3. Towards photon radiotherapy treatment planning with high Z nanoparticle radiosensitization agents

Recently, Brown and Currell, Brown et al. [2017, 2018] proposed a theoretical framework to predict the radiosensitization of GNPs at different concentrations, based on *in vitro* data obtained for one concentration. As demonstrated by Brown and Currell [2017] based on the Local Effect Model, the survival fraction in presence of a concentration C of GNPs and for a dose of irradiation D reads,

$$\mathrm{SF}(C,D) = \exp\left(-\left(\alpha_\mathrm{U} + \frac{C}{C_0}\Delta\alpha\right)D - \left(\beta_\mathrm{U} + \frac{C}{C_0}\Delta\beta\right)D^2\right), \tag{6.6}$$

where α_U and β_U are the parameters obtained for a reference irradiation without GNP, and $\Delta\alpha = \alpha_\mathrm{tot}(C_0) - \alpha_\mathrm{U}$ (likewise for $\Delta\beta$), where $\alpha_\mathrm{tot}(C_0)$ is the parameter obtained in presence of

a concentration C_0 of GNPs. A benchmark with results of Rahman et al. [2009] (and PhD work of the same author) was performed. The experiment consisted of irradiating BAEC cells under kVp photon irradiation (80 kVp, 100 kVp and 150 kVp), using different concentrations of 1.9 nm GNPs. Using one set of experimental measurements at one concentration of GNPs (1 mM, e.g. $\sim$ 42 mg·mL^{-1}), they could accurately reproduce cell survival experimentally obtained at other GNP concentrations (0.25 mM and 0.5 mM).

Their framework was further applied to estimate the impact of high Z NPs in breast cancer for MV photon radiotherapy, modelling an adult female phantom (Brown et al. [2018]). The tumour was doped with 0.5 mg·mL^{-1} of 1.9 nm GNPs. The parameters of their framework was based on the study by Jain et al. [2011], who obtained significantly higher α and β parameters in presence of GNPs for MDA-MB-231 cells. While less than 1 % difference of dose was obtained when adding GNPs, an increased of biological effectiveness was calculated in the tumour. For average values of α/β parameters obtained in the study by Jain et al. [2011], they found that conventional radiotherapy treatment approach would require a 33 % increase in radiation exposure to reach the same effects. Although a more realistic GNP *in vivo* distribution is required, this study illustrates the potential benefit of GNPs for a clinical scenario, based on experimental *in vitro* measurements accounting for the biological effectiveness of GNPs.

6.5. Summary

Monte Carlo simulations have extensively been used to study the GNP radiosensitization mechanisms at multiple scales. Early simulations at the macroscopic scale enabled to evaluate the extent of GNP dose deposition increase at the tumour scale. A significant increase of the dose deposition could be reached, provided sufficient gold concentration and a beam energy below $\sim$ 500 keV, for which photon-gold interaction cross sections remain significantly higher than photon-water interaction cross sections. This increase was highly sensitive to both the photon energy and GNP concentration. For photon energies in the energy range 10-100 keV, studies found an increase of a few percents up to 40 % per mg·mL^{-1} of gold. This enhancement decreased to $\sim$ 1 % per mg·mL^{-1} of gold for photon energies of a few hundreds of keV, before going below 1 % per mg·mL^{-1} of gold in the MeV range. It was suggested to use GNPs as a dose amplifier for different treatments (human eye choroidal melanoma, prostate cancer, brain cancer) with both external radiation therapy or brachytherapy sources.

Due to experimental evidences incompatible with theoretical predictions (such as a radiosensitization observed at MeV irradiation), it was suggested a local Auger electrons emission inducing a boost of the dose in the vicinity of the GNP could be responsible for an increase in cell death. Therefore, MC studies at the sub-cellular scale were performed to quantify this inhomogeneity. Dose enhancement ratios varied a lot in the different compartments of the cell (nucleus, cytoplasm), depending on the GNP local biodistribution and concentration, and the energy of the photons. However, such variation remained consistent with the results obtained at the tumour scale. For instance, Cai et al. [2013] reported a nuclear dose enhancement factor of 3.5 for a GNP concentration of $\sim$ 50 mg·mL^{-1} in the nucleus (photons at 15 keV). This translates into an increase of $\sim$ 5 % per mg·mL^{-1} of GNPs, in the same range to what was obtained at the tumour scale. Besides, based on experimental biodistributions, 2D maps of the average dose distribution throughout the cell showed that high dose spikes were obtained near GNPs, either in lysosomes or on the cell membrane, depending on where GNPs accumulated. A few studies also evidenced that an accumulation of GNPs in the vessels of the tumour, following an intravenous injection, might induce a high boost of dose deposition inside endothelial cells, that leads to vascular disruption. Vasculature dose enhancement ratios reached high values, as high as 9.3 for a local concentration of 140 mg·mL^{-1} for instance (Amato et al. [2013]). These predictions remained consistent with those predicted at the tumour scale, with an increase of $\sim$ 6 % per mg·mL^{-1} of GNPs. Such studies highlight the consequences of multi-scale heterogeneity of GNP concentration, with the

induction of "hot spots" in large biological targets such as vessels, or smaller ones such as cellular organelles (lysosomes) or membranes. The destruction of the vasculature, or sub-cellular targets may result in increased biological effects.

On a nanometric scale, many authors used MC simulations to characterize photon-GNP interaction processes, both in terms of electronic emission or probability of interacting with the particles of the beam. The electronic emission around a GNP was further used to estimate the radial dose distribution around one GNP. The radial dose was often used to compare the efficiency of different beams (keV *vs* MeV photons, photons *vs* ions), but also to compare gold material against water material.

Several studies used MC simulations to estimate dose deposition inside biological targets, such as DNA or mitochondria, to investigate whether significant damages could be reached. Overall, it appeared that an increase in DNA damages, higher than the one predicted by the macroscopic dose, was inconsistent with the fact that GNPs were located outside of the nucleus. However, one study suggested that photo-electron could be at the origin of an increase of early DNA damages. Finally, the Local Effect Model was used to translate the dose profiles at sub-cellular scale into cell death. It was shown that the LEM could reproduce some cell survival curves obtained experimentally. It was concluded that the dose boost induced by Auger electrons in the vicinity of GNPs was responsible for the increased cell-death, compared to a pure macroscopic approach. This model was further used to investigate the influence of various parameters on the cell survival, such as the GNP biodistribution, concentration, size or material.

7. Rationale of this Ph.D work

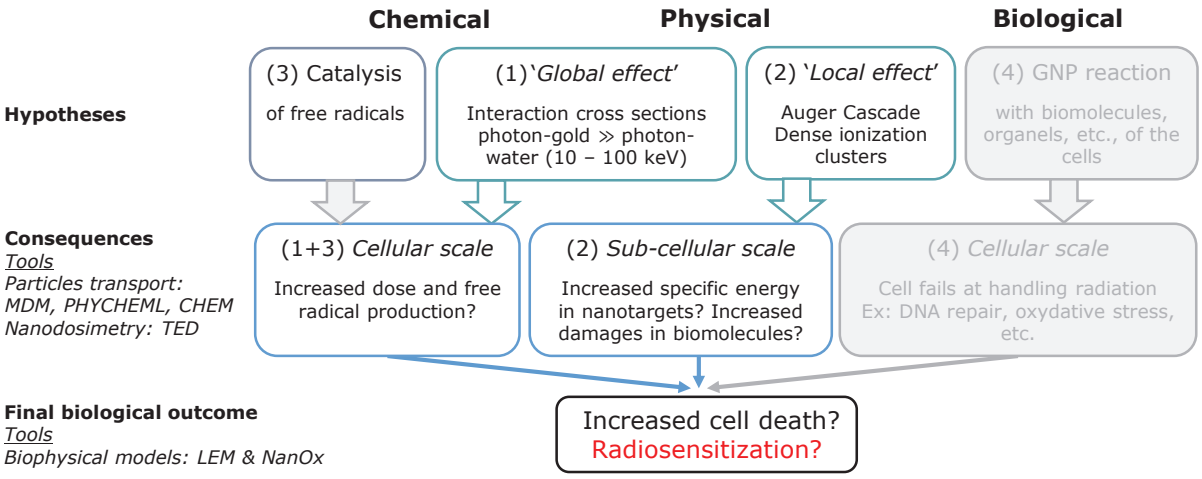

Figure 7.1.: List of mechanisms that may be responsible for GNP radiosensitization. Only mechanisms (1), (2) and (3) were considered in this work.

The extensive study of experimental and simulation studies presented in Chapter 2 to Chapter 6 allows to identify and classify four general mechanisms that may be responsible for the radiosensitizing properties of GNPs. These mechanisms are summarized in Fig. 7.1. First, a 'global effect' (1) of GNPs originates from higher cross sections between photon and gold compared to photon and water, leading at a cellular scale to an increase of the dose and free radical production. GNPs may also induce a 'local effect' (2), due to the emission of low-energy Auger electrons, creating dense ionization clusters that may be particularly efficient at destroying biological nanotargets. Some *in silico* studies also suggested that GNPs may have catalytic properties (3) that would in turn generate additional radical species following the irradiation. Finally, biological mechanisms (4), such as an impairment of DNA repair or of the cellular detoxification system, could be responsible for an additional radiosensitizing effect, that would lead to cells failing at handling the radiation stress. In the scope of this work, and as illustrated in Fig. 7.1, we propose to study only the mechanisms (1), (2) and (3), based on modelling tools. Monte Carlo simulations were required to model these 3 mechanisms, in order to compute the distribution of excited/ionized water molecules at the physical stage and distribution of chemical species. The tool Transfer Energy Distribution (TED) was used to compute efficiently the specific energy distribution. For the final calculations of cell survival, we used two approaches: the Local Effect Model and the NanOx model. Compared to what has been previously done and as further detailed in the coming sections, we propose some improvements, some alternatives and some novelties. In particular, we propose to use improved Monte Carlo simulations for the transport of electrons in gold. We propose to study the specific energy distribution as an alternative to the radial distribution to better characterize the local effects, considering a quantity closer to biological endpoints such as DNA damages. We also propose to perform studies of chemical species production, which has never been done for low-energy photon irradiation of colloidal GNP. Finally, we propose to calculate cell survival with the biophysical model NanOx as an alternative to the LEM, which has never been done for GNP-enhanced radiation therapy.

7.1. Physical modelling

7.1.1. Limits of existing Monte Carlo toolkits

As discussed in details through Part I, further work is still required to better understand and quantify the origin of the radiosensitizing effect, in particular at an early stage. Regarding the physical aspects, a lot has been done as detailed in chapter 6. However, the results of the simulation presented were based on Monte Carlo tools that were not accurate for the tracking of electrons below $\sim$ 1 keV, with energy cuts usually around 250 eV. While this is sufficient when studying dose deposition at a macroscopic scale, this may induce inaccuracy in the energy deposition around GNPs at the nanometric scale. This was recently discussed in the work by Sakata et al. [2018]. In 2016, a model of low-energy electron tracking in gold was implemented in the MC simulation toolkit Geant4-DNA[238]. This model, in addition to the standard one used in the MC studies presented in chapter 6, was further used to study 2D profiles of energy deposition around GNPs. It was shown that in the nanometre range (in a radius of 150 nm around the GNP), these dose profiles depended on the physics models. This study illustrates the need of an accurate transport of electrons inside gold. At the beginning of this project, no open source codes existed that provided such models. Therefore, before the beginning of my Ph.D work, A. Ipatov started implementing models of electron transport in gold, during a post-doctoral position at the IPNL, in our "in house" MC toolkit MDM. The first part of this Ph.D work was to finalise and validate these models. The results are presented in chapter 8. Once validated, this MC toolkit, which also enables an accurate tracking of electrons in water and provides the possibility to model radiolysis in water, was further used to quantify physical and chemical quantities.

7.1.2. Use and limits of average dose at the nanometric scale

As discussed in chapter 6, a lot of studies focused on the average energy deposition around GNPs, in particular at the nanometric scale. However, it is worth mentioning that the use of average doses at the nanometric scale is questionable, especially when it is further used to estimate biological damages, in particular in biophysical models. The choice of representation of the dose deposition at the nanoscale, used to predict the fate of a cell in biophysical models, may have consequences regarding cell survival predictions. As discussed in section 6.4.2, the use of energy deposition at the nanometric scale coupled to the Local Effect Model (LEM) was previously used to calculate the number of lethal events in the presence of GNPs. In the first implementation[176,192,193], the energy deposition was divided into two sub-contributions: the NPs contribution and the background contribution. The former corresponds to interaction of the photon beam with the NP, including or not secondary particles from water that interact with the NP. The NP contribution was calculated using the radial dose around the NP. The radial dose around one NP was calculated, first per ionization, and then normalized per delivered Gray to water. The background contribution corresponds to dose deposition due to interaction of the beam with water only, excluding any interaction of the electronic cascade with the NP. It was represented by a uniform background dose, corresponding to the prescribed dose to water.

As it has already been pointed out by Beuve *et al.*[20,22], averaging over spherical concentric shells raises a problem since the volume increases as a function of the square of the radius, diluting the cluster effect inherent to inhomogeneous dose deposition. This point is illustrated on Fig. 7.2, representing a schematic situation where a GNP is hit by a photon inducing a cluster of ionization represented by small dots. From a biological point of view, representing the biological target as a nanotarget, if this cluster is located on the nanotarget, the distance of the cluster from the NP should not change the energy deposition in this target. When introducing the concept of radial dose, in Fig. 7.2a, for a concentric shell containing the cluster, located at d_1 from the GNP surface, with a thickness of Δd and a dose deposition of E_0, the radial dose is $\propto \frac{E_0}{d_1^2}$. The probability of having this energy deposition is 100 %. On the contrary, in Fig. 7.2c, when introducing a

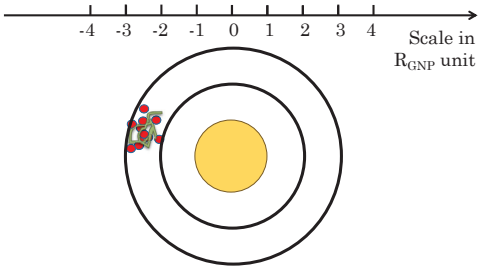

(a) Calculation of the radial dose, **at** $d_1 = R_{\mathrm{NP}} + \frac{\Delta d}{2}$ from the GNP surface. The **radial dose** $D_1 \propto E_0/d_1^2$, is constant over the shell, and $D_1 \approx$ 2000 Gy.

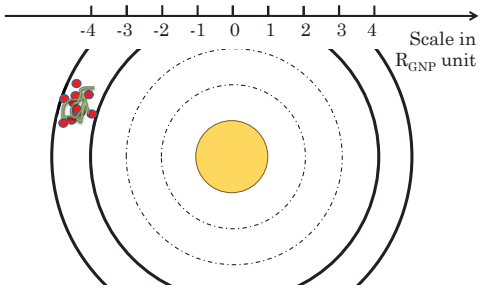

(b) Calculation of the radial dose, **at** $d_2 = 3R_{\mathrm{NP}} + \frac{\Delta d}{2}$ from the GNP surface. The **radial dose** $D_2 \propto E_0/d_2^2$, is constant over the shell, and $D_2 \approx$ 600 Gy.

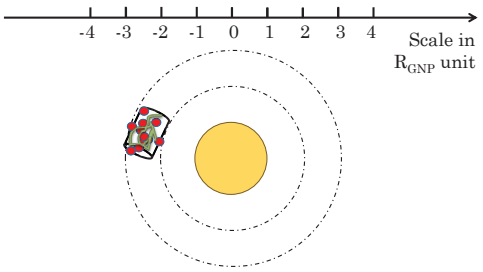

(c) Calculation of the energy deposition in a cylindrical **nanotarget** of diameter Δd and thickness Δd, located **at** $d_1 = R_{\mathrm{NP}} + \frac{\Delta d}{2}$ from the GNP surface. The **energy deposition per unit mass varies from 0 to** $\frac{E_0}{m_{\mathrm{t}}}$, is highly fluctuating, and is comprised between 0 to 50 000 Gy.

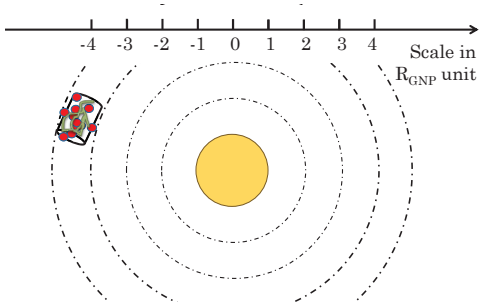

(d) Calculation of the energy deposition in a cylindrical **nanotarget** of diameter Δd and thickness Δd, located **at** $d_2 = 3R_{\mathrm{NP}} + \frac{\Delta d}{2}$ from the GNP surface. The **energy deposition per unit mass varies from 0 to** $\frac{E_0}{m_{\mathrm{t}}}$, is highly fluctuating, and is comprised between 0 to 50 000 Gy.

Figure 7.2.: Illustration of the limits of radial dose when working at the nanometric scale. Each yellow disk represents a GNP, each cylinder a nanometric target and each set of dots energy transfer points of a cluster. E_0 represents the total energy deposition induced by the cluster. Each concentric shell represented here has a thickness of Δd. d_1 and d_2 represent the distance between the shell or the target centre and the GNP surface. In this specific example, $R_{\mathrm{NP}} = 10$ nm, $\Delta d = 10$ nm, and $E_0 = 1$ keV.

nanotarget of fixed volume and mass m_{t} located at d_1 from the GNP surface, the energy deposited inside the target is most of the time equal to zero, but may reach a maximum value of $\frac{E_0}{m_{\mathrm{t}}}$, when the target contains the whole cluster. The range covered by the energy deposition in this nanotarget is huge: from 0 to $\approx$ 50 000 Gy. Concerning the dependence with regard to the distance to the GNP, in Fig. 7.2b and Fig. 7.2d where the same cluster is located further away ($d_2 > d_1$), the probability of hitting the target decreases but the dose deposition range remains identical for nanotargets, resulting in similar biological damages. On the contrary, the radial dose decreases by a factor of $\frac{d_1^2}{d_2^2}$, thus dramatically diluting the potential cluster effect. For any effect scaling with the energy deposition, both radial dose and nanodosimetry would be equivalent. However, considering that the lethality of the biological induced effect depends on the energy deposition in a non-linear way, working with mean quantities instead of energy distributions may be less appropriate.

In line with this discussion, Lechtman *et al.*[169,171] calculated the energy deposition in cubic nanometric voxels of size 20 × 20 × 20 nm^3 for the NP contribution: a track was generated for each ionized NP and the energy deposition was scored in nanovoxels. Thus, the radial dose limitations were overcome, and the NP contribution was better represented with regard to biological endpoints such as nanotargets. However, for the background, the dose was assumed to be homo-

geneously distributed over the volume, as it was the case with the previous approach, leading to a uniform background.

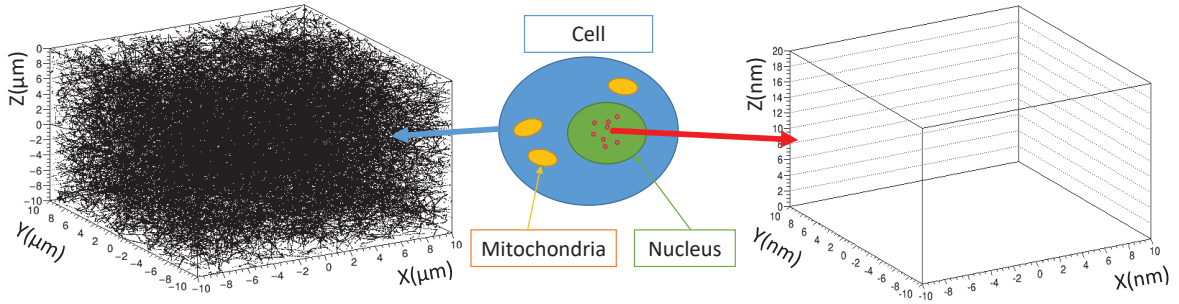

(a) Target ≈ cell:
≈ 100 % of hit targets per delivered Gy
The dose varies by ≈ ± 10 %

(b) Target ≈ DNA DSB:
≈ 0.06 % of hit targets per delivered Gy
The dose varies from 0 to ≈ 50 000 Gy
In the present illustration, the dose in null.

Figure 7.3.: Illustration of the limits of homogeneous background dose when working on nanometric scale. The illustration corresponds to photon irradiation.

The assumption that the background is uniform at a nanometric scale is far from the reality, even for sparsely ionizing radiations. Let us consider Fig. 7.3 displaying all the energy transfer events (ionizations, excitations) induced in a volume as large as (a) a cell (micrometric scale) or (b) a DNA target (nanometric scale) for a 1 Gy irradiation. Whereas a cell receives a dose of $\approx 1 \pm 0.1$ Gy, the probability that a DNA fragment receives any energy deposition is only of ≈ 0.06 % for a 1 Gy irradiation. This is due to the stochastic nature of photon interaction on a nanometric scale[20], which is illustrated by the empty box on the right hand side of Fig. 7.3.

To conclude, despite the fact that the energy deposited inside the nanotargets per mass unit is on average equal to the macroscopic dose of irradiation, the fluctuation of the energy deposition inside the target covers several orders of magnitude. Again, most of the time the nanotarget is spared and receives no energy at all, while only a few times it receives enough energy to potentially lead to a biological damage. Even sparsely ionizing radiation such as photons deposit energy in a quite heterogeneous way at nanoscale[20,23]. Therefore, one needs to go one step further by considering the energy deposition distribution for both the NP contribution and the background contribution. This is the goal of the chapter 9 of this Ph.D.

7.2. Chemical modelling

As seen in chapter 6, not much has been done yet regarding the prediction of free radicals production in presence of GNPs. As discussed in details in chapter 5, it has often been suggested that chemical mechanisms could be partly responsible for the radiosensitizing effect of GNPs. We therefore propose to investigate, in Part III, how the presence of GNPs modifies radiolytic yields, for low-energy photon irradiation. Our Monte Carlo simulation was used to investigate such a production at the macroscopic scale for a concentration of GNPs and at the nanometric scale around one GNP. We wished to study whether, for example, Auger electrons could increase the production of H_2O_2, due to the production of dense ionisation clusters. We also used our MC simulation and analytical approaches to understand the experimental observations reported in section 5.1 of chapter 5.

7.3. Biophysical modelling

In line with the discussion about the representation of the dose deposition at the nanometric scale, we implemented the LEM, using the different representations of the dose deposition at the

nanoscale proposed in the literature (i.e., consideration of a macroscopic dose for the background contribution, and radial dose *vs* nanovoxels dose for the GNP contribution). A paradox of the LEM approach is that it uses a macroscopic description of the relation between the prescribed dose and the cell survival (i.e., the Linear Quadratic Model), to calculate cell survival using a partial nanometric representation of the dose. We therefore propose in this thesis to study how the choice of representation of the energy deposition impacts the predictions of the LEM, and therefore the conclusion that can be drawn. We also propose to implement the biophysical model NanOx to estimate cell survival in the presence of GNPs. Compared to the LEM, NanOx uses a fully stochastic representation of the energy deposition at the nanoscale (i.e., the specific energy distribution) to calculate a number of lethal events. These results are presented in the chapter 13 of this thesis.

Part II.

Physical modelling: Monte Carlo simulation of low-energy electron transport in gold, and its application for the calculation of specific energy distribution in the vicinity of gold nanoparticles

8. Monte Carlo simulation of low-energy electrons in metals - Benchmarking of electron gold interaction

Authors: Floriane Poignant[a], Andrei Ipatov[c], Oleg Chakchir[c], Pierre-Jean Lartaud[a], Étienne Testa[a], Benoit Gervais[b], Michaël Beuve[a]

(a) Univ Lyon, Université Claude Bernard Lyon 1, CNRS/IN2P3, Institut de Physique Nucléaire de Lyon, 69622 Villeurbanne, France.

(b) CIMAP, unité mixte CEA-CNRS-ENSICAEN-UCBN 6252 BP 5133, F-14070 Caen, Cedex 05, France

(c) St.Petersburg National Research Academic University RAS, 194021 St.Petersburg, Russia

This chapter presents the models implemented in MDM for the transport of low-energy electron in gold. It also presents the benchmark that was performed to validate these models. This chapter was submitted as an article to the European Physical Journal Plus and is currently under review. Results were presented at the international conferences MCMA (2017, Napoli, oral presentation), CIRLAF13 (2017, Lyon, oral presentation), ARGENT (2018, Paris, oral presentation), and the national conference CLARA (2016/2017, Lyon, oral and poster).

Abstract

Transport of electrons through matter is used for many applications. Some of them need models that are together efficient in terms of computing time and sufficiently accurate over a wide range of electron energy. With respect to existing simulation it is desirable to consider relatively low-energy electrons, which control the electron emission yield. This is for instance the requirement for applications related to radiochemistry and radiotherapy enhanced by metallic nanoparticles. We have implemented a physical model for electron transport down to low energy in solid metallic media that meets both of the aforementioned requirements. In particular, this model accounts for both bulk and surface collective excitation. The main goal of this paper is to present the theoretical framework of our Monte Carlo simulation MDM, its application to gold metal and an extensive comparison with available data for gold-foil irradiated by electron beams, for projectile energies ranging from a few eV to 90 keV. In particular, we calculated secondary electron emission to assess the accuracy of the MDM code at energies below 50 eV. A close agreement with experiment is obtained for a large range of energy for various quantities related to electron transport

and emission, even though the backward emission yields of low-energy electron is systematically underestimated. Nevertheless, the accuracy and efficiency of the MDM simulation are appropriate for nanoscale applications such as nanodosimetry or the evaluation of free radical production in presence of gold nanoparticles, which demand high statistics with limited computing resources.

8.1. Introduction

Monte Carlo (MC) simulations are used in many research fields, such as high energy physics, astrophysics, solid state physics, medical physics, nuclear physics, etc. The main advantage of this approach is to allow the use of synthetic cross section kernels to solve a rather complex transport problem. There is a wide choice of Monte Carlo toolkits available[1,28,30,248], and most of them are applicable in a very broad energy range, from keV to MeV or even TeV particle energies. However, the codes for low-energy electron transport are scarce. In this context, the LQD code[106] is a Monte Carlo simulation, which performs an event-by-event tracking of electrons and ions. It was originally developed in the context of radiochemistry to estimate the production of radicals by the interaction of swift heavy ions with liquid water[105]. It was later modified to consider various heterogeneous domains, which has led to the emergence of a new branch MDM, i.e. for MeDiuM. This new version of the code was used to study the radiolysis of water confined in porous silica[214], or recently to calculate W-values, which is the mean energy required to generate an ion pair, a quantity widely used in medical physics[266].

In the past decade, there has been a growing interest in the study of dose enhancement by nanoparticles in radiotherapy. The Geant4-DNA code[19] was used to investigate the micro/nanodosimetry around gold nanoparticles[175,176,191]. Most of 'standard' MC simulations for similar applications (Geant4[1], Penelope[248], MCNP[30], Partrac[96]) are based on atomic models, which can be inaccurate for electron energies below 1 keV in gold. These models do not account for any solid state effects, such as collective excitations of valence electrons, which may play an important role in the process of energy loss for low-energy electrons, especially in the case of nanoscale objects. Recently, a collective excitation model was proposed for Geant4-DNA[238,239], and it was shown that different physical models produced significantly different dose profiles around gold nanoparticles embedded in water[239]. Thus, an adequate description of transport of these slow electrons in metallic nanoparticles is essential to reproduce an accurate dose deposition around the nanoparticle.

The description of low-energy electron transport is definitely a formidable challenge, which should in principle be addressed by quantum many-body concepts and methods. While desirable, such an approach is computationally out of reach, and we must derive some *ad hoc* procedures to simulate low-energy electron emission. Following numerous authors in this field, we shall adopt here a trajectory model that may be regarded as a rough approximation, but which should be sufficient to reproduce the major trends of electron emission in the whole energy range. Our goal is to obtain a simulation that is a compromise between accuracy and computational efficiency. To address these issues, we have extended the MDM code for the description of electron transport inside metallic media, and benchmarked this simulation with experimental data obtained for gold material.

The aim of this article is to present the simulation framework, describing the different types of interactions of electrons with metallic media that differ from previous work[238]. Additionally, the results of electron transport simulation in gold are presented in the energy range from a few eV up to 90 keV. We investigated in particular secondary electron emission, to assess the reliability of the results at energies below 50 eV, which has not been done yet in this context[238]. This gives some insights on the accuracy for nanodosimetry calculations, which is one of the aimed

applications of this MC simulation. Section 8.2 describes the energy conventions adopted here for metallic media. Section 8.3 summarizes the electron-metal interaction processes implemented in the code and explains how MDM combines a 'solid state' model with an 'atomic' model for electron collisions with metallic target. Sections 8.4 to 8.8 give the results of the benchmark using data available in the literature. The final section 8.9 summarizes our conclusions.

8.2. Energy and potential conventions

As the MDM code simulates the travel of a charged particle through different types of media, it is essential to define a potential reference to provide a coherent absolute energy tracking of the particle when it changes medium. At glancing angles, when a particle is moving from one medium to another, it must have enough energy to penetrate through the potential barrier. Regarding excited electrons, their potential is decomposed in a mesoscopic part and a microscopic one[21]. We describe the evolution process of an electron as its motion in the mesoscopic potential V_0, accounting for the collisions associated to the microscopic interactions. V_0 represents the mean electrostatic potential experienced by an excited electron in a given medium. Therefore, its total energy is equal to the sum of its kinetic energy and the mesoscopic potential energy,

$$U = \frac{1}{2}mv^2 + qV_0, \tag{8.1}$$

with q the charge of the electron, v its velocity and m its mass. It should be noted that, in a general case, effective electron masses may differ in different media, but in the current study we take it equal to the free electron mass, $m = m_e$. The density of states of the ejected electrons is taken as parabolic, setting the energy at the bottom equals to V_0. This mesoscopic potential is defined as a convolution of the electrostatic potential, with a shape defined at a mesoscopic scale. This latter is expected large, compared to the scale of the microscopic potential fluctuations, but smaller than the dimension of the macroscopic object. Here, it is assumed to be uniform in a given medium, and the value is chosen so that the vacuum potential is zero. Practically, this corresponds to a standard definition for most of the particle transport codes. When an electron moves from one medium to another medium or to vacuum through the surface barrier, the total energy of the particle should be conserved. Consequently, as soon as the mesoscopic potential changes, the momentum of the particle changes as well.

The representation of the electronic state depends on the binding energy. For the inner shells, an atomic-like description is used but a dispersion in the binding energy is added, when necessary, to account for solid state effects. For the innermost shells, this effect is small and may be safely neglected. For the outer shells, the band structure is simply modelled by a uniform density of states between an upper and lower energy. However, a DOS fitted by a linear combination of Gaussians may be used as well. The possible temperature effects are disregarded.

The definitions of energy levels for metals are depicted in Fig.8.1. For gold, u_{Fermi} is set at -0.169 a.u.[7]. V_0 was taken as -0.369 a.u., which corresponds to $u_{\text{Fermi}} - E_{\text{Fermi}}$, where E_{Fermi} is the Fermi energy in the Sommerfeld model.

Such a definition enables a coherent tracking of electrons when changing medium, by considering the potential energy change. As illustrated on Fig. 8.2, when an electron is moving from a medium 1 to a medium 2, it experiences the potential barrier given by $V_{0,1\to2} = V_{0,2} - V_{0,1}$. Let us consider the normal component of the kinetic energy, $E_{\text{kin},1,\perp} = p_{1,\perp}^2/2m$, where $p_{1,\perp}^2 = (\vec{p}_1 \cdot \vec{n})^2$, $\vec{n}$ the normal vector to the surface. When it is lower than the surface potential barrier $V_{0,1\to2}$, the electron is reflected without any energy loss, and the normal momentum projection only changes sign, $p_{1,\perp} \to -p_{1,\perp}$. Otherwise, the electron is transmitted and crosses the surface barrier. Its

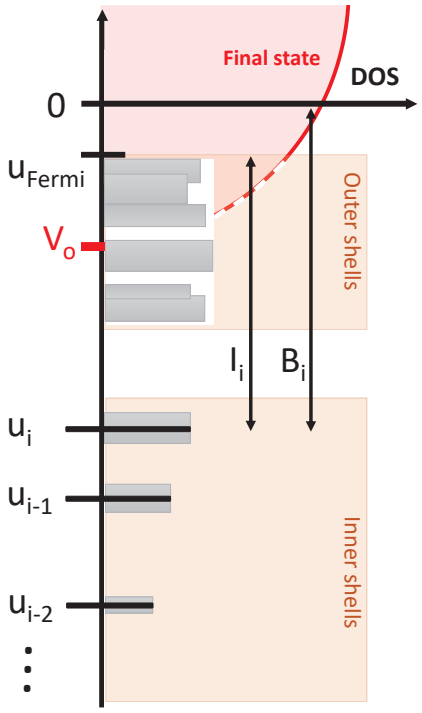

Figure 8.1.: Energy diagram for metal, as adopted in our simulation. $v_{\text{vacuum}} = 0$ is the vacuum reference potential. u_{Fermi} is the Fermi energy, defined as the highest occupied electronic level in the ground state. In our convention, it corresponds to the work function taken with opposite sign. u_i is the energy of the bound level i. $I_i = u_{\text{Fermi}} - u_i$ is the energy necessary to promote the electron from level i to the Fermi level, and $B_i = u_{\text{vacuum}} - u_i$, is the energy necessary to promote it to vacuum.

new kinetic energy and the normal momentum projection are given by $E_{\text{kin},2} = E_{\text{kin},1} - V_{0,1\to2}$ and $p_{2,\perp} = \sqrt{p_{1,\perp}^2 - 2mV_{0,1\to2}}$, respectively. In practice, these definitions (i.e. mesoscopic potential and potential barrier) are similar to the internal potential and surface barrier defined in various other MC simulations, applied in particular to scanning electron microscopes[151,250].

8.3. Electron-gold interactions

This section gives an overview of our models for elastic scattering (section 8.3.1), inelastic scattering (section 8.3.2), and vacancy decay (i.e. Auger cascade, section 8.3.3). In the next sections, all formulas are given in the system of atomic units, $\hbar = |e| = m_e = 1$, except when otherwise stated.

8.3.1. Elastic scattering

In MDM, the elastic scattering is described with two models, depending on the momentum transfer. When the momentum transfer is relatively high (more than a few eV), we assume that the elastic scattering results from an interaction of the electron with a single atom. It is predominant for an energy larger than a few eV. On the contrary, when the momentum transfer is low, i.e. comparable to the momenta of the lattice oscillation modes, the momentum transfer is better described by a phonon excitation model. For electrons with very low energies, phonon absorption competes with phonon emission during the electron thermalization. Note that in this benchmarking, the electron-phonon interaction does not significantly affect the electron emission from gold, as the work function is about 5 eV[7]. However it plays a role in slowing down electrons inside the metal and may be important in a situation where the external medium is not vacuum but another metal or solid insulator. To provide the adequate transition from one model to the other,

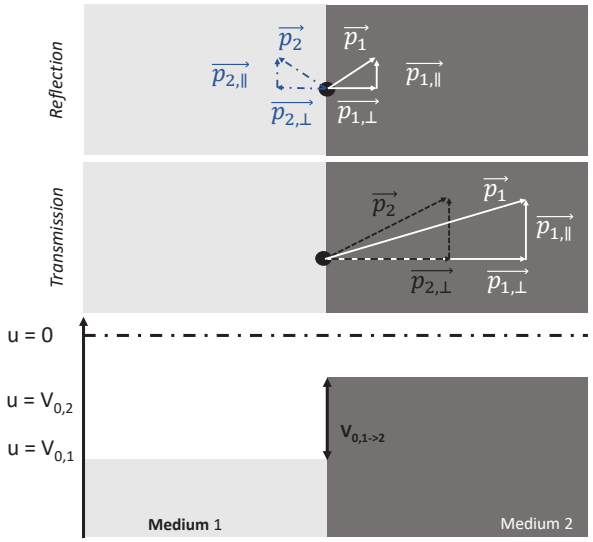

Figure 8.2.: Electron crossing the surface from one medium to another: $\vec{p}$ is the momentum of the electron crossing the surface, $\vec{n}$ is the normal vector to the surface, $V_{0,1}$ and $V_{0,2}$ are the mesoscopic potentials in media 1 and 2, respectively. In the upper part of the figure, two cases are depicted: reflection on the left and transmission on the right.

a momentum transfer cut-off q_{cut} is introduced in the code. If the transferred momentum $q > q_{\text{cut}}$, the 'atomic' elastic scattering model is used. On the contrary, if $q \leq q_{\text{cut}}$, the electron-phonon description is chosen. To be consistent with this choice, the elastic scattering cross section is set to zero for low momentum transfer in the 'atomic' description. We do not take into account any structure factor for the scattering of electrons. This might play a role for low-energy electron penetration into the target. However, the significance of this effect is difficult to assess.

8.3.1.1. High momentum transfer – electron scattering on an isolated atom

Although the elastic scattering of high-energy electrons leads neither to energy loss nor to the generation of secondary electrons, this process has a significant effect on the projected mean range for these electrons. Our model of elastic scattering is based on the differential cross sections (DCS) and the total cross sections (TCS), calculated by the ELSEPA[240] code. The elastic scattering cross sections are obtained using the partial-wave quantum-mechanical approach in static-field approximation. The effective electron-atom interaction is described by means of an optical-model potential, consisting of several components. For our simulations, we have accounted for the electrostatic, exchange, correlation-polarization and absorption potentials, while the long-range polarization potential was neglected. For the electrostatic potential, the point nucleus nuclear charge distribution model was used with a numerical Dirac-Fock (DF) electron distribution. Some solid state effects are accounted for by using a muffin-tin option with a gold radius of 0.144 nm. We tentatively extended the calculation down to very low energies (< 50 eV), though its accuracy is difficult to assess. To get an idea of the sensitivity of the cross section to the muffin-tin radius R_{MT}, we also calculated it by changing the muffin-tin radius value by 10 % (see section 8.4).

8.3.1.2. Low momentum transfer – electron-phonon interaction

In our simulations we restrict ourselves to acoustic phonons in gold medium. The inverse mean free path (IMFP) calculation of phonon emission and absorption follows the work by Del Fatti *et al.*[77]. The IMFP for phonon emission is given in Eq. 8.2,

$$\lambda_{\mathrm{em}}^{-1} = \frac{\tau_{\mathrm{em}}^{-1}}{v}, \tag{8.2}$$

where v is the velocity of incoming electron, and τ_{em}^{-1}, the probability of phonon emission per unit of time, is given by Eq. 8.3:

$$\tau_{\mathrm{em}}^{-1} = \tau_0^{-1} \int_{q_{\mathrm{min}}}^{q_{\mathrm{max}}} \frac{q^3}{v\omega}(n_{\mathrm{ph}} + 1)dq, \tag{8.3}$$

where $q_{\mathrm{min}} = 0$ and $q_{\mathrm{max}} = \mathrm{MIN}(2v, q_{\mathrm{cut}})$ with $q_{\mathrm{cut}} = 0.583$ a.u., ω is the energy loss and q the transferred momentum. ω and q are linked together by the dispersion relation $\omega = c_{\mathrm{s}}q$, where $c_{\mathrm{s}} = 9.25 \times 10^{-04}$ a.u. is the sound velocity in gold[77]. The magnitude, τ_0^{-1}, reads,

$$\tau_0^{-1} = \frac{3v_{\mathrm{acc}}^2}{4\pi M_{\mathrm{Au}}}, \tag{8.4}$$

where $v_{\mathrm{acc}} = 0.07852$ a.u. is the acoustic deformation potential amplitude and $M_{\mathrm{Au}} = 197$ g/mol is the gold molar mass. Finally, the phonon population, n_{ph}, introduced in Eq. 8.3, is given by,

$$n_{\mathrm{ph}} = \frac{1}{e^{\beta\omega} - 1} \tag{8.5}$$

with $\beta = 1/(k_{\mathrm{B}}T)$, k_{B} the Boltzman constant and T the temperature set at 300 Kelvins. Likewise, the phonon absorption cross section is given by Eq. 8.6:

$$\lambda_{\mathrm{ab}}^{-1} = \frac{\tau_{\mathrm{ab}}^{-1}}{v}, \tag{8.6}$$

where τ_{ab}^{-1} is given by Eq. 8.7:

$$\tau_{\mathrm{ab}}^{-1} = \tau_0^{-1} \int_{q_{\mathrm{min}}}^{q_{\mathrm{max}}} \frac{q^3}{v\omega} n_{\mathrm{ph}} dq. \tag{8.7}$$

8.3.2. Inelastic scattering

To describe the excitation and secondary electron emission in solid metals, we distinguish two types of electrons: the deeply bound electrons (core-electrons), and the weakly bound electrons (valence and conduction electrons). Excitation of deeply bound electrons from inner atomic shells is assumed to be a monoelectronic process associated to a large momentum transfer. For such momentum and energy transfer, the screening by the outer shell electrons is negligible, and the solid is well represented by a collection of non interacting atoms. This process may thus be described as an interaction of a projectile with an isolated atom. On the contrary, low momentum and energy transfer are associated to considerable redistribution of the oscillator strength, and the excitation of weakly-bound electrons has to be described as a collective process. Such excitation modes are not localized in the vicinity of a single lattice atom and may be characterized as plasmon excitations, whose properties may be described using the dielectric formalism[79,233]. As a result, a combination of two distinct models is used in MDM: an 'atomic' model for core-electrons and a 'solid state' model for valence and conduction electrons.

8.3.2.1. Core-ionization: an 'atomic' model

The calculation of the total cross section (TCS) and the energy differential cross section (DCS) for core ionization was done using the Binary-Encounter-Bethe (BEB) model developed by Kim *et al.*[153]. It gathers two approaches: the binary-encounter theory which accounts for hard collisions and a simple version of the dipole model, which accounts for soft collisions. The full description of the model is available elsewhere[106,153]. A relativistic extension of the model is available in the work by Kim *et al.*[154], which will be implemented in MDM in the future. The parameters that were used in our calculations for gold are presented in Appendix B.5. In our model, the binding energy of an electron is defined as $B_{\text{Kim}} = B + V_0$. Therefore, considering the Pauli exclusion principle, the minimal energy to eject a bound electron is $u_{\text{Fermi}} - u_i = -W + B$, where W is the work function. This way, the electron-impact ionization cross sections depend on the choice of the mesoscopic potential V_0. To sample the ejection angle of an emitted electron and the diffusion angle of a primary electron in the lab frame, the model proposed by Grosswendt *et al.*[113] is used. The full description is available elsewhere[106].

8.3.2.2. Infinite medium: collective excitation in bulk

The interaction of a projectile with the medium weakly bound electrons is described following the work by Ritchie *et al.*[233]. The doubly differential inverse mean free path (doubly DIMFP), $\frac{d^2\lambda_{b,\infty}^{-1}}{d\omega dq}$, reads:

$$\frac{d^2\lambda_{b,\infty}^{-1}}{d\omega dq} = \frac{1}{\pi E_{kin,1}} \frac{1}{q} \Im\left\{\frac{-1}{\varepsilon(q,\omega)}\right\}. \tag{8.8}$$

Here ω is the projectile energy loss, $E_{kin,1}$ is the kinetic energy of the projectile, $\varepsilon(q,\omega)$ is the dielectric function. The integration limits over the momentum transfer, q, in Eq. (8.8) are defined by the relation:

$$q_{\pm} = v_1 \pm \sqrt{v_1^2 - 2\omega}. \tag{8.9}$$

By integrating Eq. (8.8) over ω from 0 to $\omega_{\max} = E_{\text{kin},1} + qV_0 - u_{\text{Fermi}}$, we obtain the inelastic mean free path λ. Note that $qV_0 \leq 0$. To calculate the total cross section we need the dielectric function. A common approach is to represent it in the optical limit case, $\varepsilon(q = 0, \omega)$, using a parametric expression. Following the method by Tougaard *et al.*[267] and Ritchie *et al.*[233] , the optical energy loss function is expanded into a sum of several terms of the Drude-type energy loss function. Then, for the general case $q > 0$, the dielectric function is extended as it was proposed by Ashley *et al*[11,12]. The detailed description of the method which we use to calculate the differential inverse mean free path (DIMFP) is given in Appendix B.1. For gold, we used a set of 9 Lorenzian profiles[62] to reproduce the data measured by Wehenkel *et al.*[277]. Each mode i has an associated amplitude A_i, a bulk resonance energy $\omega_{b,i}$ and a full width at half maximum γ_i. The numerical values of the fitting parameters are given in Tab. B.1 of Appendix B.4.

8.3.2.3. Finite medium: collective excitation at surface

The model described in the previous subsection is valid in the case of an infinite material. When an interface is introduced, the discontinuity of the material induces a break in the translation symmetry perpendicular to the surface plane. In principle, a dielectric function that depends on the distance to the surface, the energy ω and the transverse momentum should be defined.

However the introduction of such formalism in a Monte Carlo code would lead to a severe increase of computing time. We therefore followed a more phenomenological approach. As it was shown by Ritchie *et al.*[234], introducing a surface has the following consequences.

- An attenuation of the probability to excite the medium at a given bulk excitation mode of energy ω_b in the vicinity of the surface. This phenomenon is called the *Begrenzung effect* and is explained by the fact that the oscillator strength of the bulk excitation modes decreases in the vicinity of the surface. In our model this effect is taken into account by decreasing the bulk cross section near the surface;

- A new type of excitation modes, resulting in an additional energy loss at a frequency $\omega_s = \omega_b/\sqrt{1+\varepsilon_m}$, where ε_m is the dielectric constant of the surrounding medium, and ω_b the corresponding bulk excitation energy.

Introducing the surface excitation modes may have an impact on the overall energy loss and on emission of secondary electrons. As there is a significant shift towards lower energy loss near the surface, the secondary electrons get less energy and their chance to escape the medium becomes lower. On the contrary, the primary electron energy loss spectrum is shifted towards smaller energies in the vicinity of the surface. The balance between these two effects determines the amount of electrons emitted outwards the metallic medium. This effect may have consequences in macroscopic solids, but it becomes even more important in small finite structures, like nanoparticles, where the surface/volume ratio increases.

The dielectric function approach was successfully applied to different metals such as aluminium or gold[79]. However, surface plasmons have only scarcely been implemented in Monte Carlo simulations to simulate electron transport in gold[241]. As the cross section depends on the position of the particle with respect to the surface, the general theory becomes rather complicated to apply in a Monte Carlo simulation, as it becomes computationally cumbersome[241]. In our work a few simplifying hypothesis were made:

- the electron gold interaction is neglected when the electron is located out of the material;

- the probability of interacting with a surface mode at a given depth in the material follows an exponential dependence with a characteristic depth z_{eff}[216,237];

- each bulk mode is associated to its own surface mode, of resonance energy $\omega_s = \frac{\omega_b}{\sqrt{1+\epsilon_m}}$[221]. In the specific case where the external medium is vacuum, it reads $\omega_s = \frac{\omega_b}{\sqrt{2}}$.

The corresponding cross sections for the surface modes were calculated using the dielectric function as it is done for bulk modes, simply replacing ω_b with ω_s. To account for the exponential increase of the probability for excitation of surface modes and its associated decrease of the interaction of an electron with bulk modes, the bulk and surface mean free paths were defined as follows:

$$\lambda_{b,i}^{-1} = \lambda_{b,\infty,i}^{-1}\left(1 - \exp\left(\frac{-z}{z_{\text{eff},i}}\right)\right), \tag{8.10}$$

$$\lambda_{s,i}^{-1} = \lambda_{s,\infty,i}^{-1}\exp\left(\frac{-z}{z_{\text{eff},i}}\right). \tag{8.11}$$

Here, z is the distance to the nearest surface and $z_{\text{eff},i}$ is the characteristic depth of the 'i'-th

mode. As it was pointed out by Pauly *et al.*[216], there are various suggestions for determination of $z_{\text{eff},i}$. Taking into account that the impact of z_{eff} is not critical for the total energy loss, we follow[237]:

$$z_{\text{eff},i} = \frac{v}{\omega_{s,i}}, \tag{8.12}$$

where $\omega_{s,i}$ is the resonance energy of the surface mode i, v is the electron velocity. The parametrization of $\lambda^{-1}_{s,\infty,i}$ is deduced from the parametrization of $\lambda^{-1}_{b,\infty,i}$ described in the previous section, using the same parameters A_i, γ_i and by substitution $\omega_{b,i} \to \frac{\omega_{b,i}}{\sqrt{2}} = \omega_{s,i}$, as it is given in appendix B.4.

In our simulations we have to define the distance to the closest surface z. If one assumes only a single planar surface in a macroscopic semi-infinite solid, the shortest distance to the surface is easily determined. In case of a foil with its thickness of the order of magnitude of z_{eff}, both surfaces are taken into account. Typically, for 50 eV electrons, $z_{\text{eff},i}$ may be maximum of the order of 1 nm for the mode with the lowest resonance energy. The detail of the MC position dependent mean free path is provided in Appendix B.2. The influence of surface modes on the cross section, yields and energy spectra are discussed in the section 8.3.2.4.

8.3.2.4. Relaxation of collective excitation

Each collective excitation is assumed to relax through the creation of one single electron-hole pair. The probability to eject an electron from a bound orbital i to a free state of momentum $\mathbf{v}$ for a given momentum exchange $\mathbf{q}$ and an energy loss ω is proportional to the square of transition matrix element:

$$|f_{i,\mathbf{v}}(\mathbf{q})|^2 = \left|\langle i|\, e^{i\mathbf{q}\cdot\mathbf{r}}\, |\mathbf{v}\rangle\right|^2 \tag{8.13}$$

To proceed further, we assume an impulse approximation for a hydrogenic target model. We thus assume that the continuum state is a plane wave of momentum $\mathbf{v}$ and the bound orbital i is a spherically symmetric s wave, which is given a hydrogenic functional form, *i.e.* $\langle \mathbf{r}|i\rangle = \phi_i(\mathbf{r}) = e^{-\alpha_i r}$. We define the effective charge $\alpha_i = \sqrt{-2u_i}$, where u_i is the binding energy of an electron in the orbital i. In the impulse approximation, the form factor $f_{i,\mathbf{v}}(\mathbf{q})$ reduces thus within an inessential constant factor to $\hat{\phi}_i(\mathbf{p})$, the Fourier transform of the orbital $\phi_i(\mathbf{r})$ taken at $\mathbf{p} = \mathbf{q} - \mathbf{v}$. The hydrogenic approximation allows us to obtain $\hat{\phi}_i(\mathbf{p})$ analytically.

We compute for each allowed level i the probability P_i to eject an electron with momentum v in the direction θ defined as the angle between the momentum transferred to the electron $\mathbf{q}$ and the ejected electron momentum $\mathbf{v}$ and for an azimuthal angle ϕ around the direction of $\mathbf{q}$.

We have:

$$\frac{d^3P_i}{v^2 dv d\cos\theta d\phi} \propto \left|\hat{\phi}_i(\mathbf{p})\right|^2 \delta(E_v - I_i - \omega) \tag{8.14}$$

where $E_v = v^2/2 + V_0$ is the kinetic energy of the ejected electron in the uniform potential of the target V_0 and $I_i = u_i - u_{\text{Fermi}}$. The integration over v and ϕ is straightforward and gives us the probability to eject the electron along the direction defined by θ for a given orbital i. Using the above hydrogenic assumption, we obtain:

$$\frac{dP_i}{d\cos\theta} \propto \frac{2\pi\alpha_i v}{(\alpha_i^2 + v^2 + q^2 + 2vq\cos\theta)^2} \tag{8.15}$$

and

$$P_i \propto \frac{4\pi\alpha_i v}{(\alpha_i^2 + p_+^2)(\alpha_i^2 + p_-^2)} \tag{8.16}$$

where $p_\pm = v^2 + q^2 \pm 2vq$. The above probability Eq. 8.16 is obtained for a discrete energy level characterized by its binding energy u_i. In our model such a level can be degenerated according to the occupation of level i by the bound electrons of the target and the probability needs to be weighted by this occupation number n_i. For the valence band of the target, the band width should be accounted for, in principle by integrating over the binding energy for a given density of state. We avoid such an integration by considering for a given band of levels one single energy taken as the average energy of the band, assuming a uniform density of state. In other words, the above probability is used with a parameter α_i equal to the average binding energy of the band and for the corresponding occupation of the band. Of course, the kinetic energy of the ejected electron should be above the Fermi level. This constrains the available bound energy levels i to those such like $u_{\text{Fermi}} - u_i < \omega$. It is thus a simple matter to sample the energy level i from the known allowed probabilities $n_i P_i$, after normalization to all the contributing energy levels.

Once i is known, the direction of emission is obtained by sampling the cosine of the angle θ from equation 8.15 followed by the composition with the direction of $\mathbf{q}$ in the lab frame. The Fig. 8.3 shows the angular distribution of the ejected electron with respect to the direction of $\mathbf{q}$. It displays the influence of the parameters α, q and $E = v^2/2$, the kinetic energy of the ejected electron. In Fig. 8.3a, α was taken equal to 0.74 a.u., which corresponds to the value of the valence band for gold. When the transferred momentum q decreases, the angular distribution tends to be more and more uniform. For high momentum transfer on the contrary, the secondary electron is emitted in forward direction. For a fixed momentum transfer and fixed α, an increase of the incoming electron energy leads to a more uniform distribution as well. Finally, when α increases, *i.e.* when the electron is emitted from a deeper orbital, the distribution becomes more and more isotropic, as observed in Fig. 8.3b.

8.3.2.5. From 'atomic' model to collective excitations

It is difficult to define a clear criteria to distinguish between an 'atomic' model with bound electrons and a 'solid state' model with nearly free electrons. Commonly, the interaction with the less-bound electrons is described by the dielectric formalism, while the BEB model is appropriate for deep-shell electrons. However, the electrons from external shells with binding energies around 100 eV may not be adequately described by any of these models. The number of electrons included in the collective effect description was set to obtain a good description of the dielectric function. For gold, the corresponding sum of the oscillator strength leads to 17.3 electrons, and includes the atomic orbitals 4f, 5s, 5p, 5d, and 6s. The sum of all accounted electrons in both descriptions should be equal to the total number of electrons per atom in the target. Therefore, we introduce a dual description of the intermediate 4f and 5s shells, by introducing a correction coefficient c according to:

$$N_{\text{tot}} = \sum_{i\in I_1} n_{e,i} + \sum_{i\in I_2} c n_{e,i} + \sum_{j\in I_3} \frac{A_j}{4\pi n_a} \tag{8.17}$$

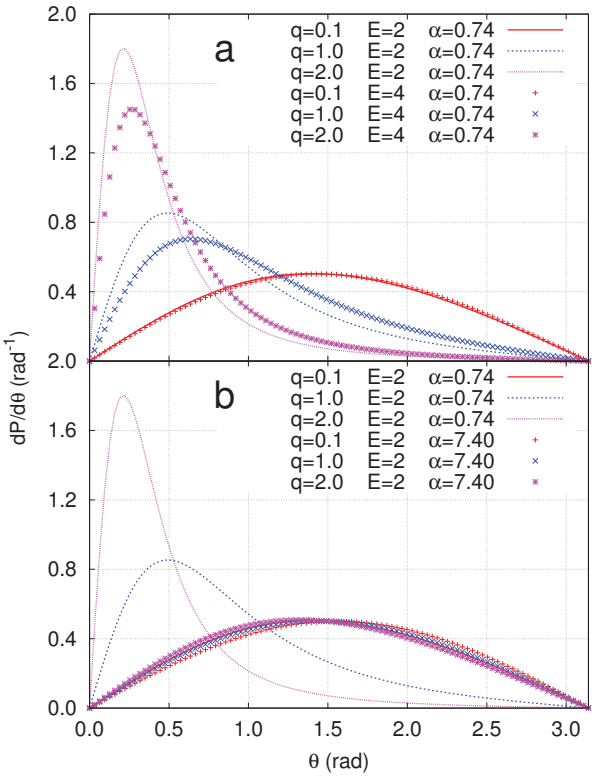

Figure 8.3.: Distribution of secondary electron emission angle θ with respect to the momentum exchange direction. The influence of kinetic energy of the ejected electron (E) (resp. effective charge α) on θ sampling is displayed on Fig. 8.3a (resp. Fig. 8.3b) for several q values. All values are given in a.u.

where the intervals I_1, I_2, I_3 are defined as $I_1 = [1s, 2s, 2p, .., 4d]$, $I_2 = [4f, 5s]$, and I_3 includes the fitted peaks of the bulk excitation spectrum of the energy loss function. $n_{e,i}$ is the number of electrons in the atomic shell i, A_j - the corresponding amplitude of the j-th mode, as it is given in Tab. B.1 and n_a the number of atoms per unit volume. The values for gold medium are given in appendices B.5 and B.4.

8.3.3. Vacancy decay and Auger cascade

In MDM, the simulation of relaxation of the electronic excitation associated to hole creation is based on the use of recombination probabilities taken from the Evaluated Atomic Data Library (EADL)[219], which describes the bound-to-bound radiative and non-radiative transitions for a given ionization event. In the present work, the fluorescence photons are not tracked. This is not essential for the present study limited to relatively low electron energies, for which the inner-shell ionization is very limited and because the outer-shell relaxation is dominated by non-radiative relaxation.

The energies provided by the EADL database are strictly valid for singly ionized atoms, while for gold, Auger cascades often lead to multiple holes configuration. The transition energies associated to such multiply ionized configurations are different from the transition energies of the singly ionized configuration, and this leads to a broadening of the Auger peaks[161]. Instead of taking into account explicitly this complex effect, we simply introduced a sampling of the binding energy of the level from which the Auger electrons originate. For the sake of simplicity we associated to each level an energy broadening, which was adjusted to match roughly the experimental width of the Auger peaks. The broadening was obtained by sampling a Gaussian distribution of binding

energy with the desired width, as given in in Tab. B.2 of Appendix B.5. We emphasis that such a broadening does not change the number of Auger electron and has no influence of the total number secondary electrons. The effect of the broadening will be shown in section 8.8.

The input data file of MDM was arranged as a table, each line representing one transition. For each transition, the corresponding probability P_{EADL}, the nature of emitted particle particle index (either electron or photon), its energy and the hole configuration after transition are given. It should be noted that the entire cascade is taken into account for every initial vacancy. We treat hole recombination through a recursive algorithm with increasing shell energy (i.e. decreasing binding energy). To account for the evolution of shell population during the cascade process, we apply the following probability scaling to P_{EADL},

$$\begin{cases} P(i) = P_{\mathrm{EADL}}(i)\frac{n_i}{n_{i,0}}, & \text{for fluorescence} \\ P(i) = P_{\mathrm{EADL}}(i)\frac{n_i}{n_{i,0}}\frac{n_i-1}{n_{i,0}-1}, & \text{for Koster-Cronig} \\ P(i,j) = P_{\mathrm{EADL}}(i,j)\frac{n_i}{n_{i,0}}\frac{n_j}{n_{j,0}}, & \text{for Auger} \end{cases} \tag{8.18}$$

where i, j are the shell(s) the recombination electrons are taken from, n_i and n_j the associated population updated along the cascade process, $n_{i,0}, n_{j,0}$ are the corresponding shell occupation for the neutral atom, i.e. number of electrons n_{e^-} in shells i and j as defined in Tab. B.2. In the case of a gold atom, a total number of 1622 transitions is considered. Typically, if an electron is ejected from a deep shell, such as $2s^2$, an average number of 13 Auger electrons is ejected. For intermediate shells such as $4d^{10}$, an average number of 4 Auger electrons is ejected.

8.4. Cross sections of electron interaction with gold target

8.4.1. Elastic scattering cross sections

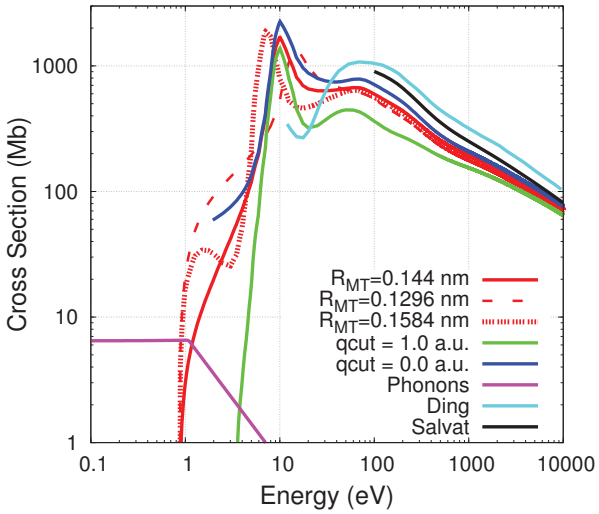

Figure 8.4.: Elastic scattering cross section as a function of electron kinetic energy. MDM results are presented for 3 different muffin-tin radius R_{MT}, for $q_{\mathrm{cut}} = 0.5$ a.u. (red lines), and for different cut-off values q_{cut} with $R_{\mathrm{MT}} = 0.144$ nm. They are compared with theoretical studies[80,189].

The total elastic scattering cross section on isolated gold atoms is shown in Fig. 8.4 for different choices of q_{cut} and R_{MT} (see section 8.3.1), as well as the electron-phonon interaction cross section. The probability of electron-phonon interaction dominates only at very low energies ($<$ 1eV). As it is expected, when q_{cut} increases, the elastic cross section reduces for small energies. For $q_{\mathrm{cut}} =$

0.5 a.u., the impact is mainly observable at low energies. However, when $q_{\text{cut}} = 1$ a.u., there is a clear decrease of the total cross section for the energies up to 1000 eV, with a difference of a factor of 2 at 100 eV. The final cut-off set up was $q_{\text{cut}} = 0.5$ a.u., which roughly corresponds to the size of an atom in the position space.

We have checked the sensitivity of the elastic scattering cross section by varying the muffin-tin radius by ± 10 % and keeping q_{cut}=0.5 a.u.. The corresponding cross sections are depicted by the red dashed line in Fig. 8.4. The cross section changes are observable mostly at low energies, i.e. below 100 eV. There is a shift of the peak, from ≈ 20 eV for R_{MT} =0.1296 nm to ≈ 7 eV for R_{MT} =0.1584 nm. We further investigate the role of these changes on the backward yields and energy distribution. However we do not observe much changes regarding electron emission. The secondary electron yields change by ≈ 10 % when the projectile energy is around 100-200 eV. Regarding the energy distribution reported in Fig. 8.16, the changes are limited to energy lower than 30 eV and do not exceed 10 %. Such a result may be understood by considering the nature of low-energy electron transport. In this energy range, elastic collisions are rather isotropic and the electron transport is dominated by multiple scattering. As a result, the details of each collisions are not critical for the electron yields we are interested in.

The results obtained using the atomic model for elastic cross section were compared with the data by Salvat *et al.*[189] and Ding. *et al*[80]. Our cross section obtained with ELSEPA is visibly lower than the results given by Salvat *et al.*[189] (referential database results). This difference may be attributed to our inclusion of the muffin-tin option to account for condensed matter effect. Ding *et al.*[80] find a globally higher elastic cross section at energies above 100 eV. Besides, they also observe an important valley around 20 eV. This structure is not well pronounced in the cross section calculated in our model, but tends to be more noticeable when q_{cut} increases. The differential cross section $\frac{d\sigma}{d\omega}$ was compared to another theoretical study by Czyzewski *et al.*[71] at a projectile energy of 100 eV and to experimental results from Reichert *et al.*[228]. The excellent agreement between our simulation and the experimental data is shown in the appendix B.3.

8.4.2. Core ionization

The core ionization cross sections are important for high energy collisions with lattice atoms. Our analysis shows that the BEB model underestimates the cross section with respect to experimental values for energies larger than 100 keV. This may be explained by the fact that in the current version, our BEB model does not take into account relativistic effects, which play an important role at high energies. Relativistic effects will be considered in a future work[154]. However, the impact of uncertainty on the core ionization has limited influence for our benchmark, because transport is dominated by interactions with the outermost shells.

8.4.3. Bulk and surface collective modes

As it was previously mentioned, the cross sections of surface modes in the present work were calculated for a gold-vacuum interface, as experimental systems for which data are available consist of thin slab of gold put in vacuum. Cross sections were calculated assuming a single planar surface with a semi-infinite gold-vacuum geometry, with several distances of the projectile to the surface: $z = 0.01$, $z = 0.1$, $z = 1$, $z = 10$ and $z = 100$ a.u.. Fig. 8.5.a (respectively Fig. 8.5.b) shows the variation of the cross section as a function of the projectile energy, for bulk modes only (respectively surface modes only). Results are as expected. As the distance to the surface increases, the probability to excite a bulk mode dominates while the contribution of surface modes becomes negligible. When $z = 1$ a.u., the IMFP associated to surface modes dominates the bulk IMFP. For $z = 10$ a.u. however, the surface IMFP is dominated by the bulk IMFP for energy below 100 eV. Regarding the transition from bulk to surface modes, it takes place in a rather thin layer. For $z > 100$ a.u., i.e. a few nm, the bulk mode dominates because the characteristic depth

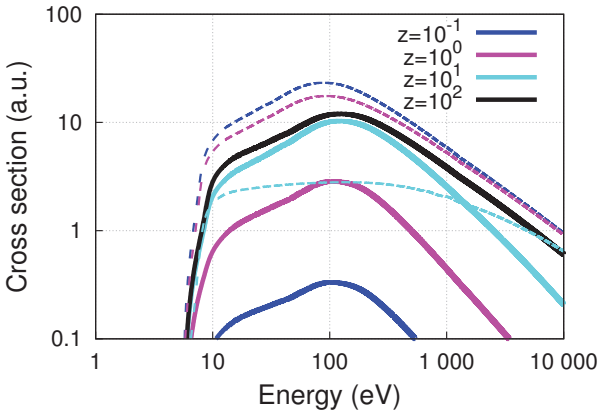

Figure 8.5.: Bulk (solid line) and surface (dashed line) plasmon cross sections versus electron energy for different depth from the surface z (in atomic units).

z_{eff} is small. For keV energies, z_{eff} increase up to a dozen of nanometers for the mode with the lowest energy, but for the other modes it remains of the order of a few nm. Finally, it is interesting to note that the maximum of the surface IMFP is higher than the maximum of bulk IMFP. This is explained by the redshift of the surface resonance energy by a factor of $\sqrt{2}$ with respect to the bulk energy. Adding surface modes thus impacts the total inelastic cross section in the close vicinity of the surface, which gives a large contribution to secondary electron emission.

8.4.4. Total cross section

Fig. 8.6 shows the different cross sections for the various types of interactions, calculated in the energy range from 0 keV to 90 keV. The cross sections based on dielectric formalism are represented for a z value much larger than z_{eff} (i.e. bulk excitations). For energies below 1 eV, only electron-phonon interaction can lead to particle thermalization. Atomic elastic scattering is predominant for energies above 1 eV. Regarding inelastic interactions, the cross sections based on dielectric model dominate in the whole energy range. Although they do not individually lead to large energy loss, the larger number of interactions lead to a large contribution to the cumulated energy loss. As expected, the core-ionization cross sections starts only at energy higher than 100 eV, where the cut-off between the 'solid state' and 'atomic' model was defined.

8.4.5. Inelastic mean free path

Fig. 8.7 represents the inelastic mean free path for gold, accounting only for the bulk modes (solid red line) or only for surface modes (black dashed line), in comparison with the results from literature. Theoretical results are plotted with solid lines and experimental data are shown by discrete points. It must be kept in mind that IMFP are not directly measurable quantities, in contrast with electron emission yield. The experimental values presented here are thus dependent on the model used to extract them. For energies above 1000 eV, MDM results are comparable to what is found in literature in case only bulk plasmons are accounted for. It shows the same trend as other studies[80,100] and falls within the cloud of experimental data. Around the valley at 100 eV, it is also quite close to the values obtained in other theoretical studies, but a bit higher than the experimental data. For low energies (<100 eV), the IMFP is slightly shifted towards the lower energies, but is still close to experiment and other theoretical results. It should be noted that the results in this energy range may be highly sensitive to the actual value of V_0. Using a deeper V_0 value reduces the difference between the experiment and our model, for the lowest energy part. However, as discussed later, changing the V_0 value has also a significant impact on electron emission.

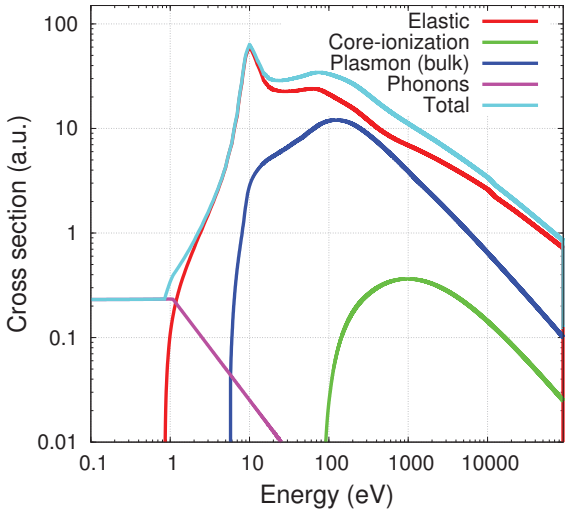

Figure 8.6.: MDM cross sections for the different processes (core-ionization, bulk plasmon, phonons, elastic and total) as a function of the projectile energy.

8.5. Simulation set up for the benchmarking study

To check the reliability of our theoretical models and validate the Monte Carlo simulation, a set of benchmarks was performed with available experimental and theoretical results. The next sections give a comparison of primary and secondary electron yields, energy distributions and elastic peak angular distribution with experiments. The experimental measurements consisted of irradiating a gold foil in vacuum with an electron beam, and collecting backward and forward emitted electrons. The energy and angle of incidence of the incoming beam, and the thickness of the gold target may be varied to investigate the behaviour of the escaping electrons and to compare it with simulation results. The electron yield is defined as the number of backward or forward electrons divided by the number of electrons impinging the foil surface. Among the electrons escaping the foil, one distinguishes primary electrons (i.e. coming from the incident beam) and secondary electrons (generated by the medium irradiation). Secondary electrons initially occupy the valence and core energy levels of the target, and have been excited by impact of the primary electron, up to an energy sufficient to escape from the material. As it is impossible to distinguish whether the electron comes from the primary beam or from the irradiated medium, the primary electrons are defined as electrons with energies above 50 eV and secondary electrons with energies below 50 eV, respectively[229]. Although some of the secondary electrons escape the sample with energies greater than 50 eV, this threshold is a good experimental criteria to separate secondary and primary electrons. The backscattered elastic peak represents all the electrons that undergo an elastic scattering in the metal and are backscattered without energy loss. In the next sections, the simulations were performed turning on and off the surface modes to show the influence they have on the results.

8.6. Backscattered elastic peak

The study of the backscattered elastic peak gives good indications on the quality of the differential elastic cross section. In Fig. 8.8, we present the relative intensity $I(\alpha) \propto \frac{d\sigma}{\sin\alpha d\alpha}$, for a given scattering angle α as a function of incident electron energy, where α is defined as the angle between the normal vector to the surface $\vec{n}$ and the direction of emission of the reflected electron $\vec{v}$. MDM results were normalized to the maximum of the experimental results, and compared to experimental and theoretical data from Jablonski *et al.*[133]. Our results are very close to the experimental data in the whole energy range considered here. It provides a better agreement with

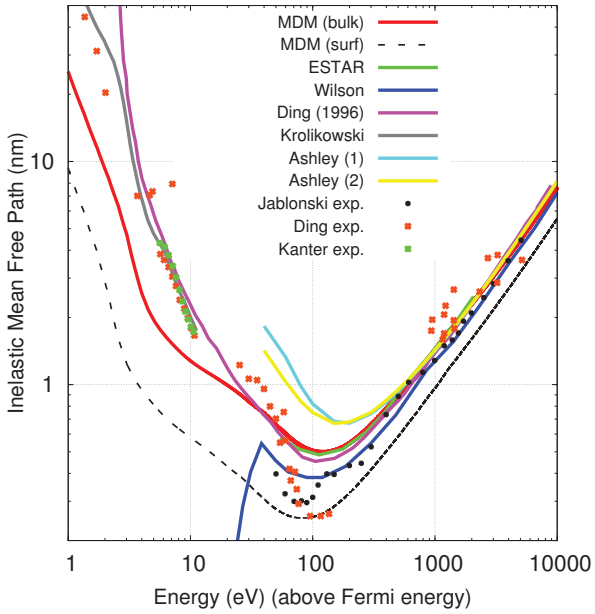

Figure 8.7.: Inelastic mean free path as a function of electron energy. MDM results are represented in solid red line ($z = 1 \times 10^{10}$ a.u., i.e. bulk plasmon cross sections dominate over surface plasmon cross sections) and dashed grey line ($z = 1 \times 10^{-10}$ a.u., i.e. surface plasmon cross sections dominate over bulk plasmon cross sections). The values referred to 'Ding' and the set of experimental data were taken from Ding *et al.*[80], 'Jablonski' from Jablonski *et al.*[131], 'Wilson' from Wilson *et al.*[100], 'Kanter' and 'Krolikowski' from Kanter *et al.*[145], and 'Ashley' from Ashley *et al.*[11,12].

experiment than the simulation by Jablonski *et al.*[133] at large angles for $E > 50$ eV.

Similar experiments were done in the work by Jablonski *et al.*[132] to measure the angular distribution of elastically backscattered electrons. The results show the intensity $I(\alpha)$ of the elastic scattering peak according to the reflection angle α. The calculations were performed accounting for the experimental angular resolution $\Delta\alpha = \pm 4.1$ degrees. The results of simulation, shown in Fig. 8.9, were normalized to the local maximum peak around 45-60 eV, as the measurements did not provide absolute values. Again, there is a good agreement between experimental data and our numerical results, despite a small deviation with respect to the distribution by Jablonski *et al.*[132] at small angles of emission (i.e. maximal backscattering), which is magnified by the $\sin^{-1}(\alpha)$ factor.

8.7. Electron emission yields

8.7.1. Comparison with experimental yields by Reimer *et al.*

Our simulation results were compared with the experimental data from Reimer *et al.*[229]. The simulations were performed for various energies of primary electrons. The incident electronic beam was approximated as a point like beam, directed normally to the surface. The gold layer was surrounded by vacuum, and each transmitted or backscattered electron was recorded and distinguished as primary or secondary electrons depending on the energy cut-off equal to 50 eV. To achieve a meaningful statistics, a total number of 50 000 electrons were sent for each energy and layer thickness. The results with and without surface modes are represented in Fig. 8.10.

The primary electron yields are in excellent agreement with the experimental data, both for transmission and backscattering processes. Moreover, the surface modes do not have any influence

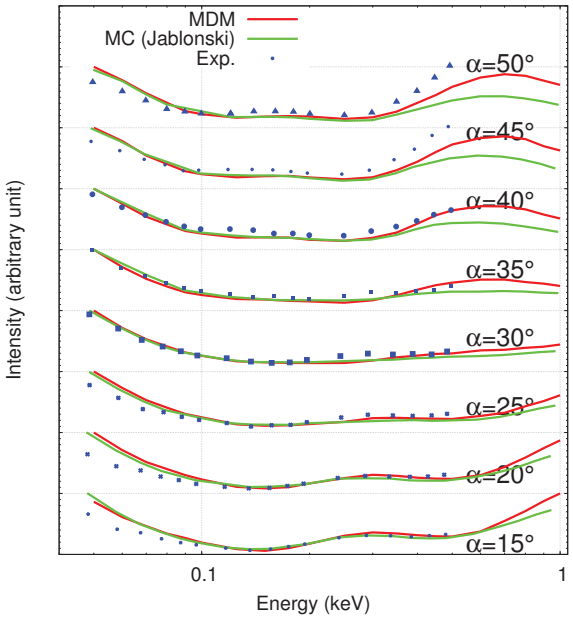

Figure 8.8.: Elastic scattering intensity as a function of the energy of the incident electron beam, for different angles of detection α. Red solid line: MDM simulation. Green solid line: Jablonski[133] (simulation). Blue dots: Jablonski *et al.*[133] (experimental).

on the primary electron yields. For large thickness, the region in which the surface plasmons can be excited is negligible compared to the thickness of the foil. Therefore, surface plasmons play a minor role. We may expect a more important role for lower thickness. However, the primary yield is dominated by elastic diffusion and hard collisions.

Regarding the secondary electrons, the yield of the forward emitted electrons is close to experimental results. The forward yield is overestimated when only bulk modes are activated, especially for low primary energy and thin thickness. However, accounting for the surface excitation modes tends to decrease the yield for thin foils and improves the agreement with experiment. This may be explained by two reasons. First, the cross sections of the surface modes are higher than that of the bulk modes, which increases the probability of low-energy secondary electrons to lose a part of their energy. Second, the surface modes dominate near the medium border, where the produced secondary electrons have more chances to escape from the medium. As a result, with increase of the energy loss caused by the surface modes, the secondary electrons are less likely to leave the sample. When the sample becomes thicker, the contribution of surface modes decreases, and both yields, with and without surface modes, asymptotically approach the same limit, which is close to experimental value.

A systematic underestimation of the backscattered secondary electrons is noticeable. It was found that the backward emission yield is very sensitive to the sampling of the energy level from which the secondary electron is ejected, especially for shells $5d$ and $6s$. If we systematically choose the highest possible energy level, u_{up}, instead of a random energy distribution between u_{up} and u_{min}, the number of backward secondary electrons strongly increases. This effect has already been observed by Ding *et al.*[81], whose results are shown in Fig. 8.12 in the next subsection. However, it has the direct consequence of increasing the number of forward secondary electrons. A reasonable compromise was to set the upper electron band width (which includes $5d^{10}$ and $6s^1$) equal to 0.2 a.u. Alternatively, the situation may probably be improved by more accurate parametrization of the energy loss function for $q \neq 0$ and improving the plasmon annihilation. More work is necessary, with different materials, to understand better this discrepancy.

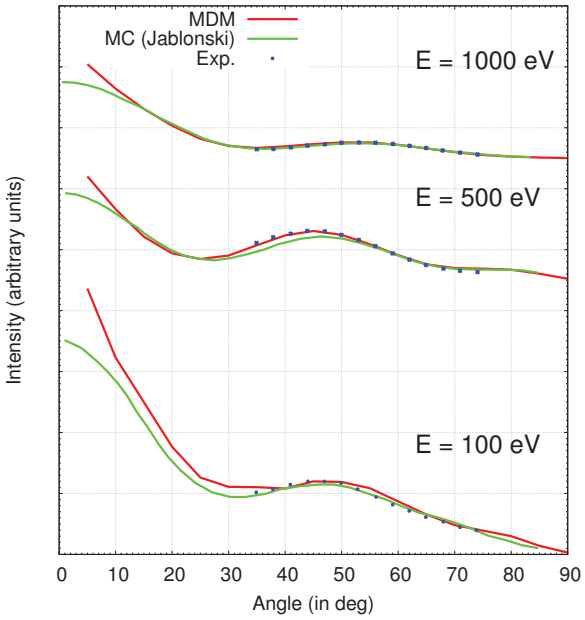

Figure 8.9.: Elastic scattering intensity (arbitrary units) as function of the electron emission angle, for different electron energies. Red solid line: MDM simulation. Green solid line: Jablonski[132] (simulation). Blue dots, Jablonski *et al.*[132] (experimental).

8.7.2. Influence of incident angle on backscattering

In the experimental study reported in the work by Neubert *et al.*[209], the incidence angle of the electron beam was varied. The primary electron beam energy was set at 30 keV. Fig. 8.11.a (respectively Fig. 8.11.b) shows the primary electron backscattering yield, i.e. electrons having energies above 50 eV, as a function of the gold film thickness for different incident angles (respectively the backscattering yield as a function of the incidence angle for different layer thickness). On Fig.8.11.a, we added the results from Reimer *et al.*[229] obtained for a similar energy value (32.4 keV) to demonstrate the good consistency of the results for two distinct experiments. The simulation results were obtained with surface modes on.

The simulation results by MDM are in excellent agreement with experimental data in all range of incident angles and foil thickness. It is worth mentioning that the lowest foil thickness considered was equal to 58 µg/cm^2, which corresponds to 26 nm for gold. This agreement gives a good confidence in the modelling of elastic scattering but also the inelastic collisions for this energy.

8.7.3. Backscattering coefficient

The experimental backscattering coefficient is obtained when the thickness of the gold foil is large enough so that no electrons are transmitted. Many experimental results are available. It is worth mentioning that for energies above 2 keV, when approaching the plateau, the experimental results for backscattering coefficient vary from 0.45 to 0.5. As it was pointed out by Belhaj *et al.*[184], it is important to clean the sample: if the surface is oxidized, the coefficient tends to be underestimated for gold, which could explain the variability of experimental data. Results were compared with experimental data for primary electron beam energy varying from 0.1 to 90 keV.

The plots presented in Fig. 8.12.a confirm the good agreement between the simulated backscattering coefficient and the experimental data, up to an energy of 80 keV, after which there's a visible drop due to the fact that relativistic effects are not included in the simulation. Again, an introduction of surface modes does not impact the results, even at low irradiation energy (100

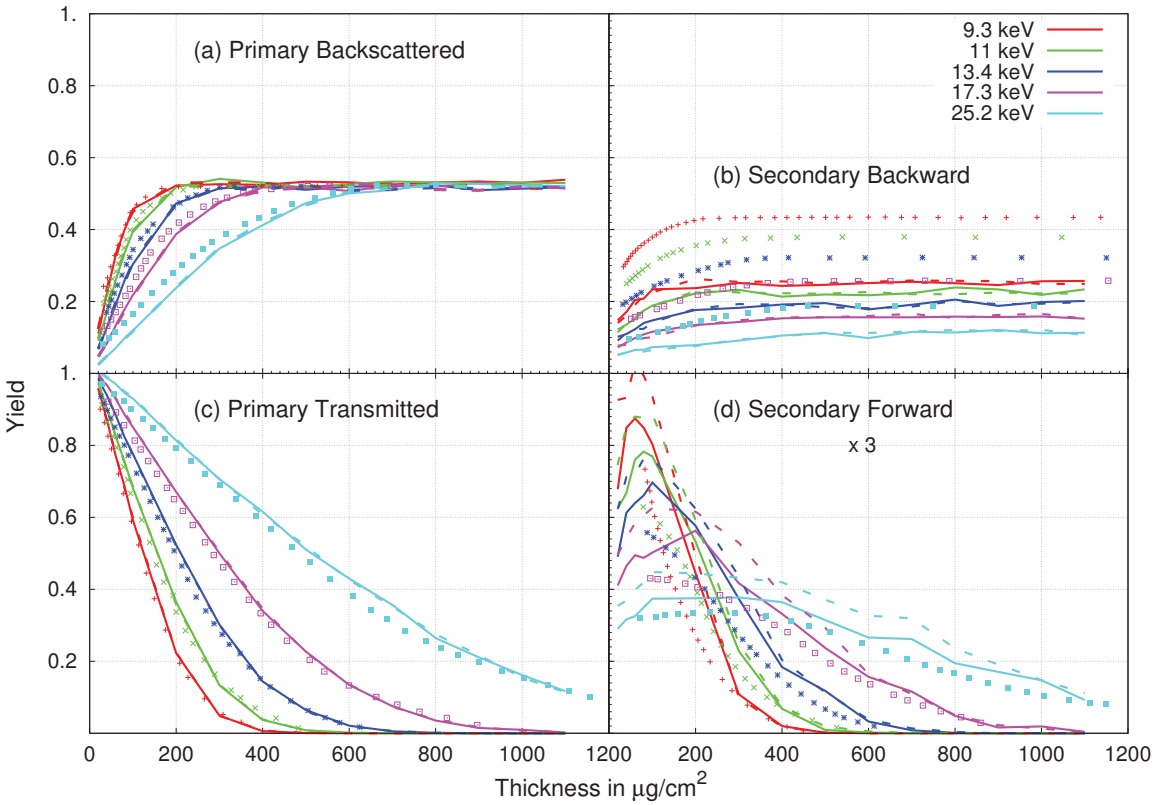

Figure 8.10.: Electron yields (primary and secondary) as a function of the foil thickness. Secondary forward electron yields were magnified by a factor of 3 for a better visualization. Experimental data (points) were taken from Reimer *et al.*[229]. MDM simulation results were obtained both with (solid line) and without (dashed line) surface excitations.

eV). Our simulation was done for two cut-off energies (0 and 100 eV), in order to estimate the impact of this cut-off and to compare with Penelope predictions[249]. Although this energy cut-off does not impact the yield for primary electron energies above 5 keV, there is a visible difference at lower energies. This leads to the conclusion that the contribution of low energy electrons (50 eV $<$ E $<$100 eV) must be taken into account, even for keV incident energies, to get accurate results.

Fig. 8.12.b shows backward secondary emission. As it was already seen in the previous subsection, this yield is systematically underestimated. For thick foils and low energies, the surface modes tend to give a higher secondary electron yield, but it still remains underestimated. Many possible reasons could explain this underestimation: a possible uncertainty regarding V_0, an inaccuracy of the model used for elastic scattering at low energies, an uncertainty in electronic density of states, to which the secondary electron emission is very sensitive, and the hydrogenic model used for the plasmon annihilation. The low energy electron backward yield is sensitive to the choice of the mesoscopic potential V_0. We tried to reduce its value to recover the very low backward energy yield but it was found that an attempt to correct the value of V_0 results in a too large forward secondary yield for higher impact energies, meaning that the problem cannot be fixed only that way. Besides, it should be noted that the experimental results from Gomati *et al.*[88] were obtained for samples that were either cleaned or not before irradiation. Cleaning of the sample increases the yield by nearly a factor of two. More experimental results for a wider range of energies would be necessary to validate the experimental data, as it is very sensitive to the experimental set-up, in particular to the impurities on the surface and surface charging effects.

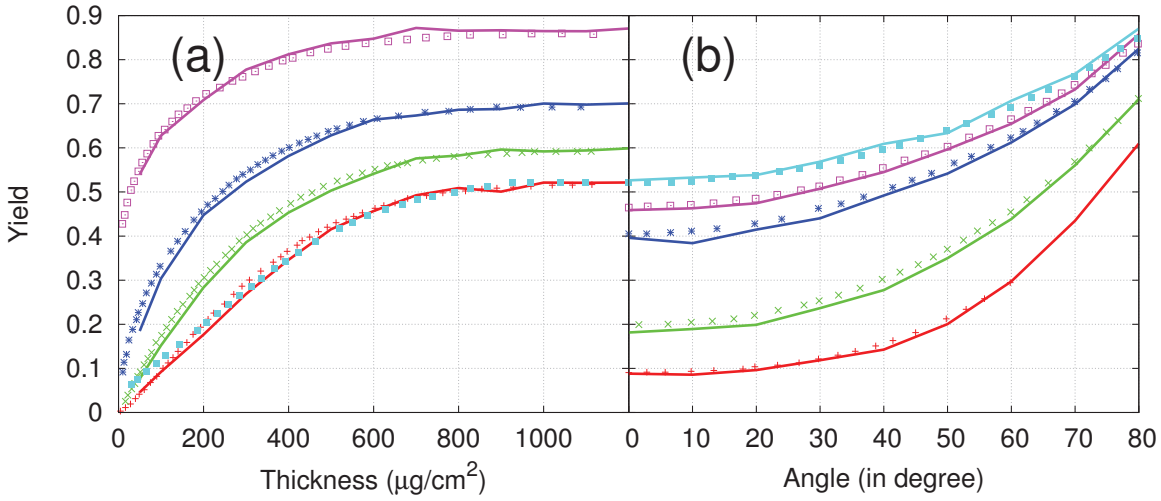

Figure 8.11.: Comparison of experimental data (points) with MDM simulation results (solid lines) (a) Primary backscattering yield as a function of the thickness of the gold foil, for various angles of incidence. All the experimental results are taken from Neubert *et al.*[209] (energy 30 keV), except for the light blue dot which are taken from Reimer *et al.*[229] (energy 32.4 keV). Angles correspond to 0, 40, 60 and 80 ° from bottom to top; (b) The primary backscattering yield as a function of the incidence angle, for various thickness. Experimental results are taken from Neubert *et al.*[209]. Thickness are 98, 198, 461, 603 and 1110 µg/cm^2 from bottom to top.

8.7.4. Irradiation with low-energy electrons

We base our analysis on the experimental results obtained by Belhaj *et al.*[184]. The incident low-energy electron beam was directed normally to the sample surface. For our simulation, different situations were considered: with and without account of surface excitation modes and without account of secondary electrons in the simulation.

Similarly to the situation with high-energy incident electrons, a systematic underestimation of the backward electron yield by a factor of at least 2 was observed at low energy. Only very few secondary electrons are emitted, thus having a limited impact on the yield. This greatly reduces the impact of surface plasmons. It is remarkable that the experimental yield for the primary electron energies slightly below the work function of gold is close to unity. At these energies, it is not possible to have, at one time, after a collision, a secondary and the primary electron with energies larger than the vacuum level. That is to say the yield can not possibly be larger than 1. Instead, because of the transport and the diffusion of both primary and secondary electrons, the yield is expected to be lower. Therefore, the experimental value close to 1 is in the energy range [0-25] eV is puzzling. On the other hand, for elastic collision, our approach does not take into account any structure factor of the solid, and it is likely that this effect is important for the penetration of low energy electrons into the metallic media. This does not mean that the transport cross section inside the material is qualitatively incorrect, but rather that additional effects intrinsic to wave penetration in the foil should be taken into account to simulate accurately the experiment.

8.7.5. Transmission yield

As there is a significant fluctuation of the measured yields depending on the experimental set up, the simulated transmission yield was compared with several experimental data sets to check the consistency of experimental results and to validate the simulation approach in a wide energy range. A set of numerical and experimental results is shown in Fig. 8.14.a and 8.14.b.

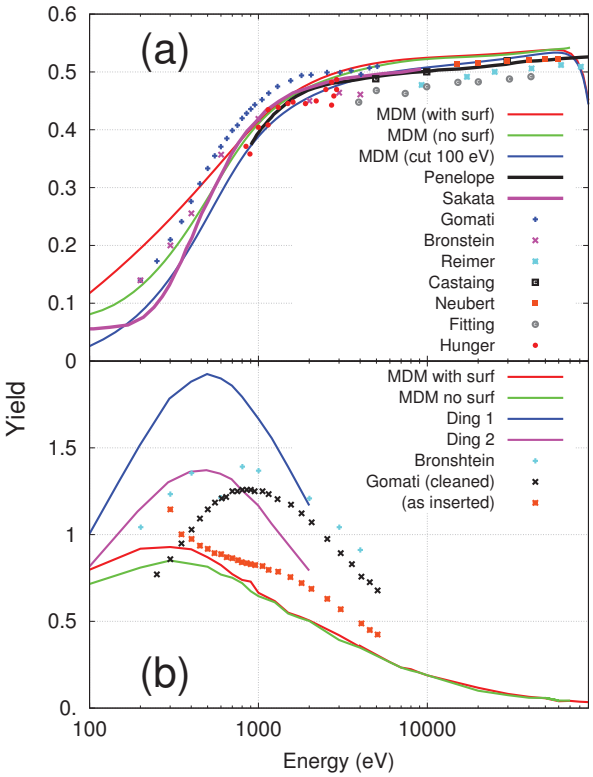

Figure 8.12.: Theoretical (lines) and experimental (points) backscattered primary electron yield (panel a) and secondary backward electron yield (panel b) as a function of the projectile energy, for a thick gold foil. The blue line in panel a represents MDM results with an energy cutoff set at 100 eV as used for the MC simulation Penelope in Sempau *et al.*[249] ('Penelope'). Other data are taken from Gomati *et al.*[88] ('Gomati'), Bronstein *et al.*[31] ('Bronstein'), Reimer *et al.*[229] ('Reimer'), Castaing *et al.*[46] ('Castaing'), Neubert *et al.*[209] ('Neubert'), Fitting *et al.*[91] ('Fitting'), Hunger *et al.*[128] ('Hunger'), Sakata *et al.*[238] ('Sakata'). On Fig. 8.12.b, data were taken from Ding *et al.*[81] ('Ding1' + 'Ding2'), Bronstein *et al.*[31] ('Bronstein'), Gomati *et al.*[88] ('Gomati (cleaned)' or '(as inserted)').

Similarly to the case of backscattered yield, there is a systematic underestimation of the transmitted yield by Penelope code[249] in comparison to MDM results, which comes from the choice of the low-energy cut-off at 100 eV. The experimental data by Al-Ahmad *et al.*[3] tends to overestimate the transmission yield with respect to results of the other measurements. This is probably the reason of the large difference on Fig. 8.14.b between the experimental and numerical results. However, one should note that the qualitative behaviour of the energy dependence of the yield is the same for the simulation and the experiment.

8.7.6. Conclusion on electron emission yields

Primary electron yields obtained using the MDM simulation are in good agreement with experimental data, both in transmission and backscattering cases, for different incident angles and different values of the foil thickness. Concerning the role of the surface excitation modes, it was found that they practically do not impact the result for primary electrons. The backscattered secondary electron yields are found to be underestimated in comparison with experimental data, for any thickness or energy values. For incident electron energies above 1 keV, surface modes do not impact the results, while for lower energies, addition of the surface modes tends to slightly increase the secondary electron yield for thick samples. The calculated transmitted yields of secondary electrons are in good agreement with experiments in the wide range of parameters, though

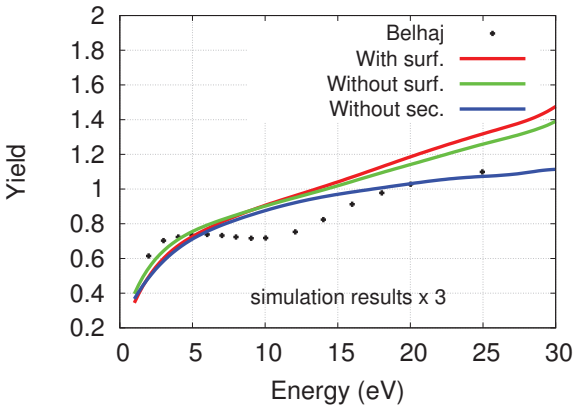

Figure 8.13.: Backscattered electron yield as a function of the projectile energy. Experimental data (points) are from Belhaj *et al.*[184]. Note that MDM simulations (lines) were magnified by a factor 3 for the sake of clarity. Red line: full simulation; green line: simulation without surface plasmon; blue line: simulation without secondary.

for very thin foils ($\leq$ 300 µg/cm^2) the simulated yield is slightly overestimated. In that case, an addition of the surface modes leads to reduced yield and improves the agreement of the results with experimental data. In our approach, the energy loss by surface plasmon excitation when the electron is in the close vicinity of the surface out of the medium was not included. This is certainly a source of additional electron emission which might be responsible for some of the observed difference with the experiment.

8.8. Energy distribution of emitted electrons

All the simulated spectra of backward and forward electrons were normalized to represent the energy distribution per one incoming electron. As experimental spectra are essentially in relative scale, we normalized them to the integral of the simulation spectra.

8.8.1. Energy distribution of backward electron emission

The doubly differential yields with respect to electron emission energy and angle is definitely a very stringent benchmark for our simulation. It is thus desirable to compare our simulated spectra to data available in the literature. We shall consider here the simulated results obtained by Ding *et al.*[82] by means of a MC simulation quite similar to ours. This work forms a rather complete set of simulated data and has been applied to other materials. We shall also compare our results to the experiments performed by Goto and coworkers[82,111,263], which provides the most complete set of experimental data, and also to the reference spectrum published by Seah and Smith[247].

All simulated spectra are normalized to represent the distribution per one incoming electron, per unit of solid angle and energy. A total of 1×10^8 incident electrons are used in our simulation. Electrons were shot with either a normal incidence with regard to the surface of the sample[82,263], or at 30 angular degrees to the normal surface[247]. The detection angle for emitted electron was chosen equal to 42.3 $\pm$ 6 angular degrees with respect to the normal to the surface (Goto and coworkers[82,263]), or at 0 $\pm$ 6 angular degree (Seah *et al.*[247]). Each spectrum was convolved by a Gaussian profile with a standard deviation equal to the experimental energy resolution (0.24 %) and normalized to the histogram bin width and the solid angle. To check the influence of the binding energy distribution in Auger spectra and the contribution of surface modes, the simulations were performed with or without accounting for surface modes, and with or without accounting for binding energy distribution in Auger cascade simulation.

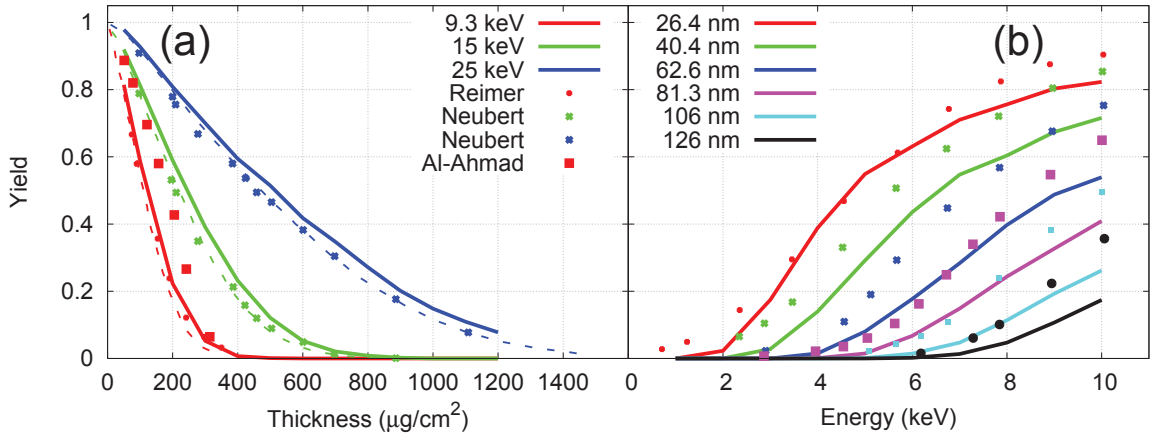

Figure 8.14.: Panel a: transmitted primary electron yield versus thickness, for different incident energies. MDM (solid lines); PENELOPE (dashed lines): Sempau *et al.*[249] ('Penelope'). Experiment (points): Reimer *et al.*[229] ('Reimer'), Neubert *et al.*[209] ('Neubert'), and Al-Ahmad *et al.*[3] ('Al-Ahmad'). Panel b: transmitted primary electron yield versus energy, for foil thickness. MDM (solid lines); Experiment (points): Al-Ahmad *et al.*[3].

Regarding the comparison with experimental spectra, it is important to keep in mind that obtaining good quality experimental spectra is an extremely difficult task. The main reason is that the transmission and detection efficiency of the spectrometer are difficult to obtain accurately[247]. Moreover, for a given energy selection, there is always a background due to secondary electron generated inside the analyser by high-energy electrons. We believe that experimentalists take great care of such effects, but they are intrinsically difficult to analyse and no information were given regarding their significance. The problem is probably not severe for sufficiently high energy of the emitted electron. In a paper dedicated to the transmission analysis of a cylindrical mirror analyser (CMA)[4], it was shown that the ratio between the current delivered by a mini-electron gun located at the entrance of the CMA and the detected current reaches a constant value for energies beyond 200 eV approximately. This means that the experiment is certainly reliable above this energy, where the spectrum is not subject to deformation inherent to the detection apparatus. For energy below this value, on the contrary, it is difficult to estimate the actual detection efficiency of the spectrometer, and the comparison between our results and those published by Goto and coworkers should be considered as a limited qualitative comparison. We also compare our simulation with the reference spectrum published by Seah and Smith[247]. According to these authors, their spectrum is corrected from transmission and detection efficiency.

The experiment and simulation results are shown in Fig. 8.15 for an incident electron energy of 5 keV and in Fig. 8.16 for an incident electron energy of 0.5 keV. Note that the experimental spectra are given in relative scale. We normalized them to the integral of the simulation spectra to perform the comparison. According to common practice in Auger Electron Spectroscopy, the spectra are weighted by the secondary electron energy.

Considering the 5 keV results, we first note that the agreement between both experiments is excellent. The change of incidence angle from 0 to 30 degrees has a negligible effect on the spectral shape, as it can be observed in the Fig. 8.15. The solid angle impacts the intensity of the spectrum, with a higher intensity for a detection angle normal to the surface. The consistency of the experimental results obtained with two different spectrometers suggests that the detection efficiency quoted in the previous paragraph regarding Goto's results below 200 eV, is probably not overwhelming.

The agreement between the experiments and both simulations is excellent for energies above 2

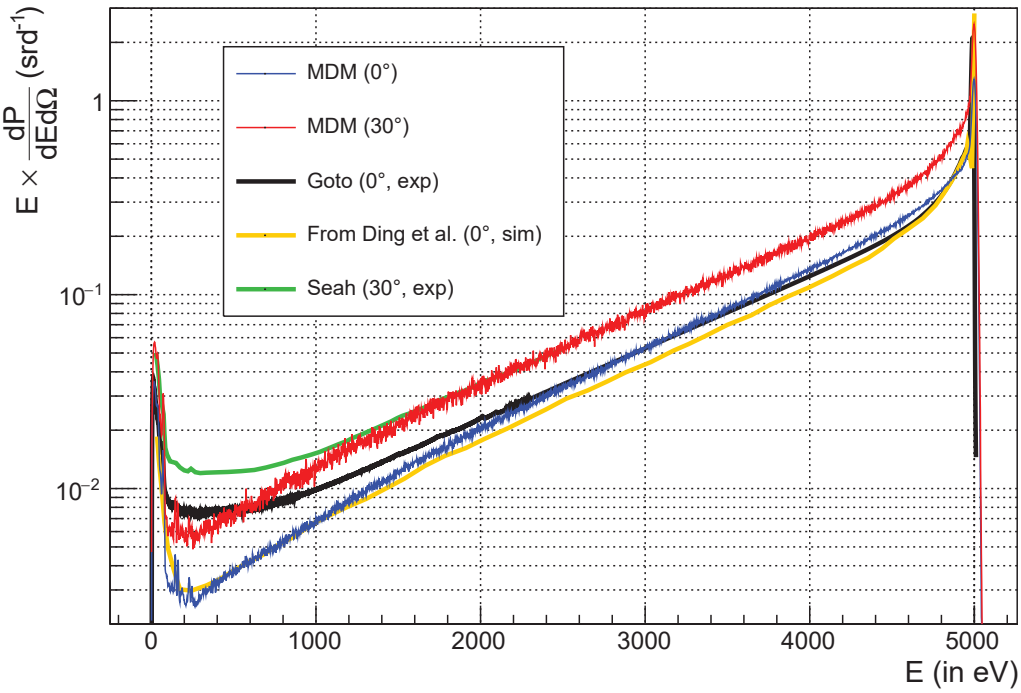

Figure 8.15.: Energy distribution of backward emitted electrons from a thick gold target, for a projectile energy of 5 keV, (1) for a normal incidence and a detection solid angle of 42.3 ± 6 degrees ("MDM 0°") and (2) for at 30 ° incidence with respect to the normal surface and a detection solid angle of 0 ± 6 degrees ("MDM 30°"). Experimental results are taken from Goto *et al.*[263] and from Seah *et al.*[247]. The other simulation result was taken from Ding *et al.*[82].

keV. It is interesting to note that both our simulation and the one by Ding[82] underestimate the electron emission between 0.1 and 1.0 keV. The main difference between both simulations is the account for the Auger process and the surface plasmon excitation in our work. The surface plasmon excitation plays only a minor role at 5 keV, but the influence of the Auger process can be observed around 200 eV in Fig. 8.15. As shown in a previous experimental work[111], we obtain a good reproduction of the Auger structures NOO at 140 and 236 eV (which may also be visualized in Fig 8.16), and the OVV structure at 65 eV. Our spectrum does not display clearly the MNN Auger peaks at 2011 and 2097 eV. In this energy range, experimental peaks have a rather small intensity. It is thus difficult to conclude whether this is due to an underestimated intensity or the noise that prevents from visualizing the peaks.

Considering now the secondary electron emission below 100 eV, we obtain a fair agreement between our simulation and the experiment. In doing this comparison, it must be kept in mind that the experimental spectrum area was normalized to the simulation area. Therefore, the comparison is sensitive to the renormalization factor. We notice in the previous section that our simulation underestimate the backward emission below 50 eV by a factor 2 approximately at 5 keV (see Fig. 8.12). A higher emission of low-energy electrons would globally shift upward the experimental spectra, thus enhancing the differences between experiment and simulation. Nevertheless, the agreement regarding the spectral shape would still be fair.

Considering now the 0.5 keV results, we observe also a global agreement between simulation and experiment. We have only one experiment at this energy. However, it was obtained with the same apparatus as for the 5 keV results reported above, and our confidence is the same. We notice in Fig. 8.16 a similar underestimation by our simulation of the experimental spectral

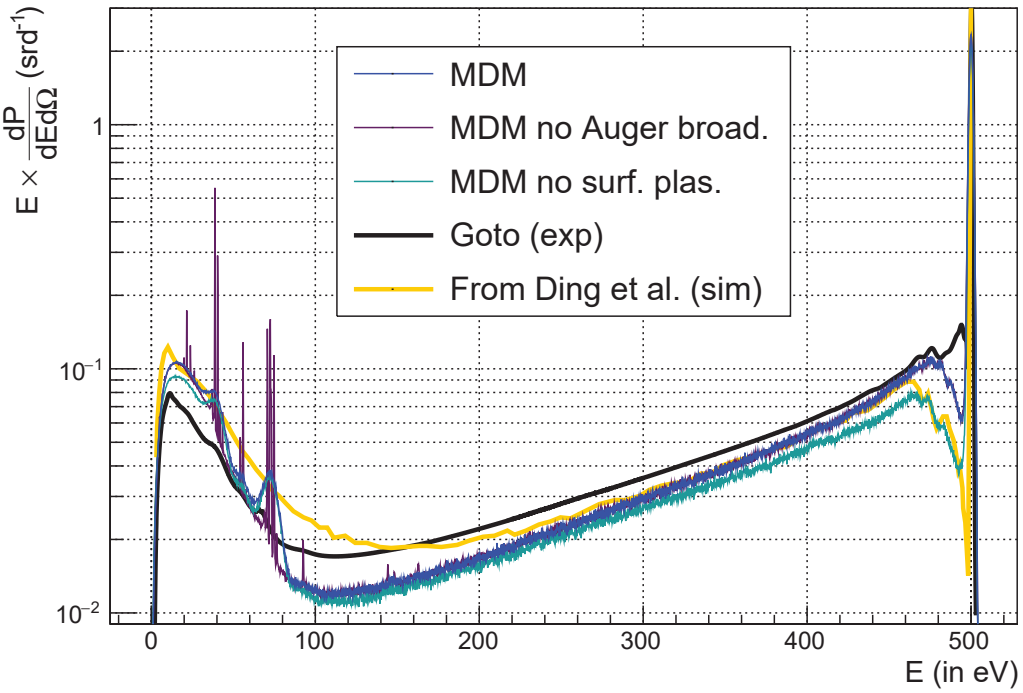

Figure 8.16.: Same as Fig. 8.15 for a projectile energy of 0.5 keV. Experimental results are taken from Goto *et al.*[263]. The other simulation result was taken from Ding *et al.*[82]. In our simulation, the Auger electron broadening is either accounted for ("MDM") or not ("MDM no Auger broad.") and the significance of the surface plasmon process is analysed by removing it ("MDM no surf. plas.").

intensity between 100 and 200 eV. The simulation by Ding *et al.* performs better in that respect. Both simulations overestimate slightly the low-energy electron emission, but the normalization factor applied to the experimental spectrum is quite uncertain and no definitive conclusion can be reached regarding the accuracy of the simulation.

With respect to the 5 keV results, this lower energy spectrum exhibits more details related to surface plasmon and Auger emission, which can be analysed in the simulation by adding or removing them. Adding an energy distribution in the decay of Auger electrons allows us to reproduce the Auger peaks much more accurately. One should note that several groups of Auger peaks in our spectrum appear too intense, especially the group of narrow lines around 70 eV. However, this apparent overestimation is most likely due to an underestimation of the backward electron yield, as it was shown in the yield section. Increasing the relative contribution of low energy electrons would relatively reduce the peaks intensity.

When surface effects are not accounted for, there is a reduction of intensity at small energy losses associated to a reduction of the emission of low-energy electron. The lack of surface excitation is also clearly visible in the simulation by Ding *et al.* at small energy losses. This effect is much more significant at 0.5 keV than at 5 keV. The surface specific interactions are only partially included in our simulation. In particular the emission induced by a particle moving in the close vicinity of the surface out of the material is neglected. This lack of surface mode excitation is visible in our simulation for small energy losses. A comparison of our simulation results with the electron energy loss spectroscopy measurements by Hagelin *et al.*[114] (not shown here) confirms that the probability of low energy loss was underestimated. In order to analyse the possible reason of this underestimation, we tentatively added an extra excitation line in the optical spectrum at the energy of 0.11 a.u. (3 eV). It was possible to reproduce the shape of the spectrum by tuning the

amplitude of this mode. However, it strongly impacts the production of secondary electrons by greatly reducing the number of electrons able to escape the sample. We conclude that additional experimental energy loss data with various well-defined values of thickness and for $q \neq 0$, would be extremely useful to better understand this region and to improve the theoretical model.

8.8.2. Energy distribution of transmitted electrons

A total of 2×10^9 primary electrons were sent to obtain Fig. 8.17. As in the experiment by Wehenkel *et al.*[277], the foil thickness was set at 22 nm, and the electron beam energy to 35 keV. The transmitted particles were collected within an acceptance angle of 0 ± 5 mrad. Most of the transmitted electrons have only one interaction on their path through the foil. For each transmitted electron, the number of interactions of each type was recorded to account for the contributions of the surface modes, bulk modes, core ionization, double inelastic interaction and triple inelastic interaction. The final energy loss spectrum is shown in Fig. 8.17 from 0 to 120 eV. The results of the simulations were normalized to the number of incoming electrons and the histogram was converted to a double differential spectrum by taking into account for the solid angle and the histogram bin width (0.25 eV). The experimental spectrum was normalized to the integral of the whole simulation spectrum.

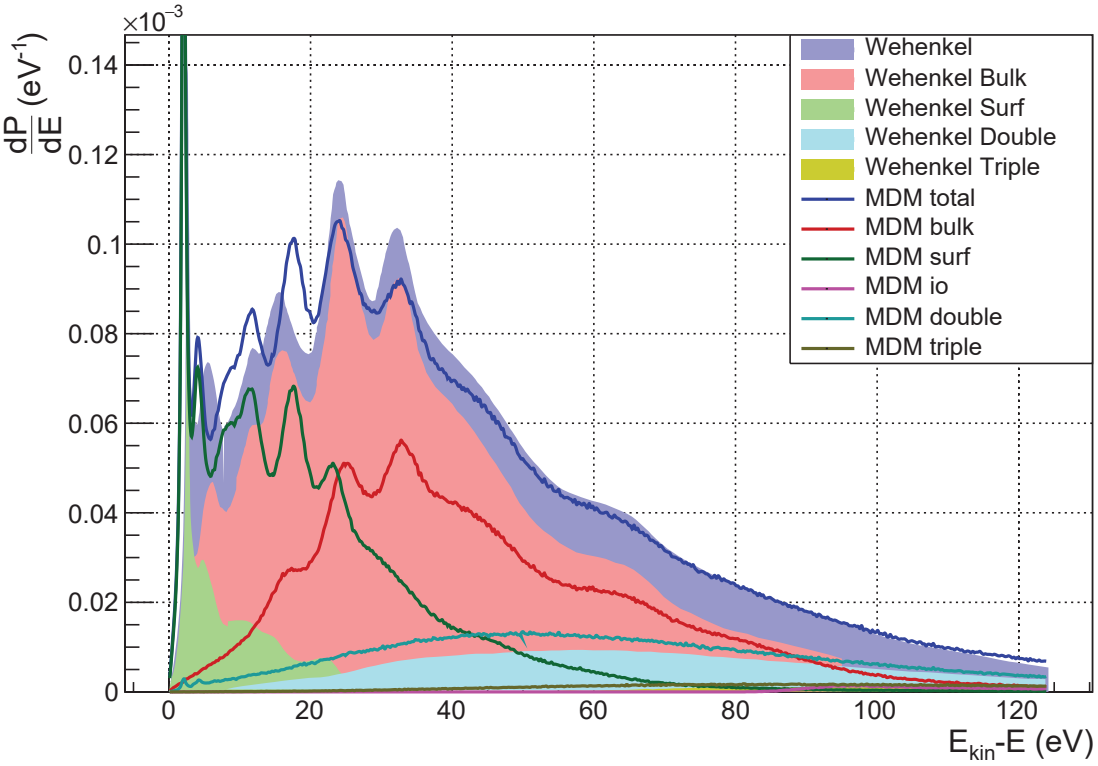

Figure 8.17.: Transmitted electron energy loss distribution for a gold film thickness 20 nm and a primary electron beam energy 35 keV. MDM results are shown by lines, experimental data[277] by filled plots.

In Fig. 8.17, one can see that the simulation results are in very good agreement with experimental data in the energy range of 40-120 eV. The two peaks around 25 and 35 eV are also well reproduced. However, the peaks at lower energies are slightly redshifted, and the simulation intensity slightly differs from the experimental data. This shift may be explained by the difference of the contribution of the surface modes between the experiment and our simulation. It is difficult, however, to conclude whether the discrepancy in the estimation of the surface effect contribution results from limitations of our theoretical model based on the macroscopic dielectric function of

the media, or from the analysis used in the work by Wehenkel *et al.*[277] to estimate the contribution of surface effects in the experiment. More experimental measurements with different values of the foil thickness would help to better separate the bulk and surface contribution.

8.9. Conclusion and outlook

We presented the theoretical framework of the MDM Monte Carlo simulation for transport of non-relativistic electrons down to low energy in metallic media. The approach is based on a model which includes solid state effects in metal and medium interface. The surface excitation were taken into account explicitly by means of a simple position-dependent cross sections.

We performed a thorough benchmark of our model for the case of gold with available theoretical and experimental data in the literature. We emphasis that numerous aspects of electron emission were consistently reproduced with one single model of electron transport. It was demonstrated that our results are in good agreement with experimental data both for electron yields and energy loss spectra. Primary electron yields demonstrate an excellent agreement. Energy spectrum of transmitted electrons also reproduces the experimental dependence with reasonable accuracy. However, the yield of backward secondary electrons is systematically underestimated. Applying a rescaling of the cross sections for low energy modes, or changing the average mesoscopic potential V_0 alone, which defines the surface potential barrier, did not fix the problem.

The discrepancy with experimental data might be due to the quadratic extension of the dielectric function for $q \neq 0$ and in the domain of low energy loss ω. However the success of HREELS simulation for Aluminum target with a parameterization of the dielectric function similar to the one used here[241] suggests that this is probably not a strong source of discrepancy. Additional experimental data would be useful to better understand and improve the theoretical results in this region. However, the energy loss by surface plasmon excitation when the electron is in the close vicinity of the surface out of the medium was not included in our simulation. This may be a source of additional backward electron emission, and including it in our model may improve the agreement with experimental results[278]. Besides, additional comparison with other metallic targets are in progress.

Nevertheless, the results of our study demonstrates the possibility to use the model in various research fields, in particular transport of electrons in nano-objects, which requires an explicit description of the transport of low-energy electrons. In particular, we expect reliable results for nanodosimetry applications in the context of gold nanoparticle enhanced radiation therapy. We emphasise that this model may be easily implemented in a MC simulation, introducing bulk/surface excitations and IMFP depending upon the position of the electron while remaining computationally efficient. This is essential in order to achieve reasonable calculation time for such applications. Besides, it is noteworthy that our simulation can also be used together with physico-chemical tools to investigate the production of radical species induced by gold nanoparticles in water.

The presented study opens wide perspectives in further development. An influence of the collective excitation on the electron emission processes from irradiated nanoparticles surrounded by water medium could be investigated. Moreover, the models constitute a solid basis to extend the simulation to other metallic materials such as platinum or silver, which are also used for nanoparticle radiosensitizing effects. We also intend to extend the MDM simulation towards higher energies by taking into account relativistic effects for electron transport.

8.10. Acknowledgement

This work was supported by the LABEX PRIMES (ANR-11-LABX-0063) of Université de Lyon, within the program "Investissements d'Avenir" (ANR-11-IDEX-0007) operated by the French Na-

tional Research Agency (ANR). Financial support received from INCa-ITMO (No. PC201307-BIOHYDRA) within the Programme Plan Cancer 2009-2013 (Inserm) and the Conseil Régional de Basse-Normandie is gratefully acknowledged. This work has been supported by the Fondation ARC pour la recherche sur le cancer.

9. Nanodosimetry study of the radiosensitizing effect of gold nanoparticles in radiotherapy

Authors: Floriane Poignant[a], Caterina Monini[a], Étienne Testa[a], Michaël Beuve[a]

(a) Univ Lyon, Université Claude Bernard Lyon 1, CNRS/IN2P3, Institut de Physique Nucléaire de Lyon, 69622 Villeurbanne, France.

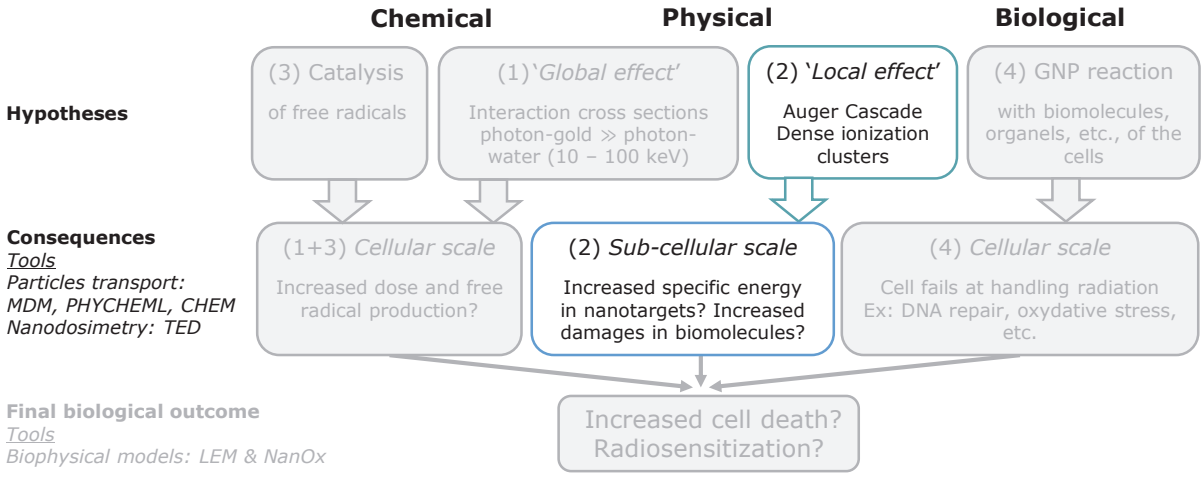

Figure 9.1.: List of mechanisms that may be responsible for GNP radiosensitization. This chapter focuses on the local effects.

In chapter 8, the Monte Carlo simulation MDM for the transport of electron in gold was validated down to a few eV. This benchmark, in combination with models for the transport of electron in water down to meV which were validated a decade ago[106], allowed us to be confident on the prediction of dose deposition at the nanoscale. This chapter presents the results of the specific energy distribution obtained in nanotargets located near a GNP, based on the Monte Carlo simulation MDM. Following the classification of mechanisms responsible for GNP radiosensitizing properties introduced in Chapter 7 and as illustrated in Fig. 9.1, this work enables to better characterize the local effects. Compared to previous work, we propose to study a quantity that is closer to biological endpoints such as damages in biomolecules. This chapter was submitted to the Medical Physics journal. However, reviewers requested for the results of the previous chapter (electron transport in gold) to be published in order to be able to evaluate the reliability of our MC approach. It will therefore be resubmitted as soon as the previous chapter has been published. Results were presented at the international conferences Nanotech (2017, Paris, oral presentation), MCMA (2017, Napoli, oral presentation), CIRLAF13 (2017, Lyon, oral presentation), ARGENT (2018, Paris, oral presentation), ICRR (2019, Manchester, oral presentation) and the national

conference CLARA (2018, Lyon, poster).

Abstract

Purpose: For the past two decades, high-Z nanoparticles (NPs) have been of high interest to improve the therapeutic outcomes of radiation therapy. They have demonstrated interesting radiosensitizing properties that may originate from a local dose increase, within few hundreds of nanometers around the NP. So far, Monte Carlo (MC) simulations have been used to evaluate this dose heterogeneity, by calculating average energy deposition at the nanoscale. However, as biological effects and in particular cellular lethal events do not scale with average energy deposition at such a scale, one needs to go beyond average quantities and account for the stochastic nature of energy deposition in cellular targets such as DNA or cell membrane. Therefore, to further understand the radiosensitizing properties of high-Z NPs, we calculated the probability distribution of the specific energy (restricted to ionization and excitation events) in the vicinity gold NPs (GNPs), for 20-90 keV photon irradiation. **Methods:** This nanodosimetric study was based on a Monte Carlo simulation which was accurate for electron transport down to low energy, both in water and gold. We emphasize that the computation time of such quantities is prohibitive without several numerical optimizations, which allowed us to gain five orders of magnitude. We introduced a new quantity, namely the probability enhancement ratio (PER), by estimating the probability of having the restricted specific energy larger than a threshold z_0 in comparison with pure water. **Results:** Our calculations showed that the PER varied a lot with the GNP radius, the photon energy, z_0 and the distance of the GNP to the nanotarget. The highest PER was 95 when the nanotarget was located at 5 nm from the GNP surface, for a photon energy of 20 keV, a threshold of 20 kGy, and a radius of 50 nm. This enhancement occurred in the vicinity of GNPs, as, beyond 200 nm and for the optimal case (largest GNP at 20 keV), it went below 1.5. **Conclusions:** PER allows to study the impact of nanoparticles on energy deposition at nanoscale. It accounts for the stochastic nature of energy deposition at nanoscale and seems better adapted than mean dose deposition to describe the formation of biological damage. Such calculations will be used with biophysical models to convert PER into enhancement of lethal cellular events.

9.1. Introduction

The use of nanoparticles (NPs) for medical applications has faced a growing interest with the emergence of nanotechnologies. Due to their unique properties, NPs may be used as nanoplatforms for many applications. Among them, the use of NPs as theranostics agents is of high interest. Over 50% of cancer patients have to undergo radiation treatments[35], the limitation of which is their lack of discrimination between the tumour tissues and healthy tissues. The maximum dose delivered to the tumour is in particular limited by the side effects induced by dose deposition to healthy tissues. The use of radiosensitizers enhances the dose effect upon irradiation via the injection of a product, which migrates preferentially inside cancer cells by passive or active targeting. The pioneering *in vivo* study[115] showed that gold NPs (GNPs) could be used as radiosensitizers. In this work, 86 % of mice with EMT-6 carcinomas and irradiated with external 250 kVp X-rays survived over 1 year when being injected 7 (mg of Au)/(g of tissue) of gold NPs solution, against 20 % when irradiated without GNPs. These very encouraging results were followed by many *in vitro* and *in vivo* experiments[124]. At the same time, many simulation studies were performed

to investigate the mechanisms and optimize the parameters governing the radiosensitization of NPs[245], both for external beam or brachytherapy sources.

At an early stage, physical effects relying on the interaction of ionizing radiation with NPs are expected to trigger the radiosensitizing effect. On a macroscopic and microscopic scale, the high density of the NP material increases the probability of keV photons interaction, leading to an increase of the microscopic and macroscopic dose deposition through the photoelectric effect[170]. Early studies estimated macroscopic dose enhancement in tumours[56,57]. Although they showed an increase of the dose, it was not always sufficient to explain the extent of the biological effect, in particular given the *in vitro* cellular concentrations of GNPs obtained experimentally[171].

As macroscopic quantities were insufficient to explain biological observations, it was suggested that a local inhomogeneity of the dose distribution could be responsible for an enhanced biological effect, similar to the biological enhancement in hadrontherapy with light ions[191]. Once ionized, high-Z atoms of NPs undergo a relaxation process that creates a cascade of secondary low energy electrons, known as the Auger cascade. These electrons may escape NPs, leading to an increase in energy deposition in the vicinity of the NP within a range of a few hundreds of nanometres[40]. By creating dense clusters of ionization in cellular molecules, this may induce the destruction of sensitive biological targets located near the NP, potentially fatal to the cell. Hence, macrodosimetry studies were followed by dosimetry studies at micro and nanoscale studies, to better account for dose inhomogeneities. Microdosimetry works[17,43,85,142,166,211,212] found high dose inhomogeneities, confirming the possible change of biological effectiveness of radiation in presence of GNPs. At nanoscale, studies of the radial dose around GNPs evidenced a high deposition in the vicinity of the NP[122,122,155,155,169,171,177,191,195,297].

So far, those studies of energy deposition at nanoscale in presence of NPs were based on *average* energy deposition in nanovolumes. While such quantities may evidence the heterogeneity of energy deposition at nanoscale, they do not account for the substantial fluctuation of the energy deposition inside cellular nanotargets (i.e. targets of dimensions of the order of a few nanometres up to a few tens of nanometres). Indeed, typical nanometric cellular targets, such as DNA fragments or cellular membranes, experience tremendous fluctuations in energy deposition. When a cell is irradiated at 1 Gy by a monoenergetic beam of low-energy photons (tens of keV), one cellular component, of dimensions of the order of 10 nm, has a probability of receiving an energy deposition of only $\sim 4 \times 10^{-4}$. As a consequence, from a biological point of view, the dose deposition at such a scale is most of the time equal to 0 Gy, but may be as high as tens of kGy. Average dose fails at accounting for such fluctuation. This may be a limit when such quantities are used in biophysical models to further predict cell-death, since at nanoscale the biological response (e.g. the lethal events due to the destruction of cellular nanotargets) is not linear with the energy deposition[23,202,204]. To better characterize such a fluctuation, the concept of nanodosimetry is mandatory. Thus, the distribution of the specific energy, defined as the energy deposited inside a nanotarget (see section 9.2), enables to account for the variation of the energy deposition at nanoscale, and is more appropriate to determine lethal cellular events than average dose. To our knowledge, no study of the impact of GNPs on such distribution has been performed yet, most probably due to the computing challenges such calculations bring.

In this work, we therefore calculated the distribution of the energy deposition in nanotargets in the presence of GNPs. Our calculations were performed for one GNP in a water volume irradiated by a large photon irradiation field. We aim at further clarifying the impact of GNPs at nanoscale, by understanding how the presence of a NP impacts the distribution of energy deposition in nanotargets located in the vicinity of the NP: are such cellular targets more likely to receive energy, and in particular a very high amount of energy? These calculations were performed for 4 cases of GNP radii (5 nm, 12.5 nm, 25 nm and 50 nm) and various values of photon energy (from 20 keV to 90 keV), to investigate the optimum to reach the highest effect, from a nanotarget point of view. We stress out that calculating specific energy distributions, as opposed to average dose, is

challenging. As we are calculating a distribution inside nanotargets, obtaining statistically good results requires massive computing resources together with developing highly efficient algorithms in order to minimize computing times.

This paper is organized as follows. Section 9.2 briefly describes the Monte Carlo simulation we used and the concept of restricted specific energy. A MC simulation valid for the transport of both high (keV) and low (eV) energy electron within GNPs was used to ensure an accurate dose deposition profile. Section 9.3 shows the results of our nanodosimetry calculation. Section 9.4 discusses the results obtained, and compares them with studies existing in the literature. Finally, the paper concludes in section 9.5 on the potential use and perspectives of our work.

9.2. Materials and Methods

9.2.1. System

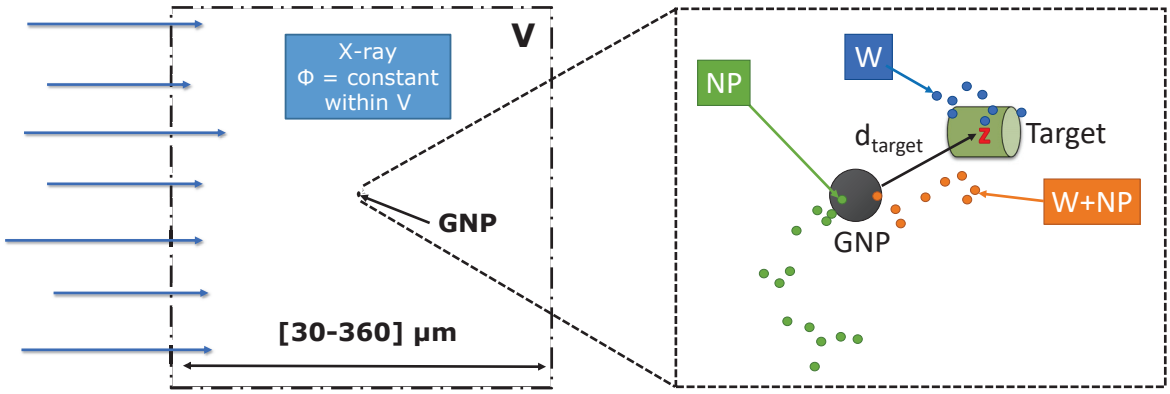

Figure 9.2.: Schematic view of the system considered for nanodosimetry calculations. On the left: Φ represents the fluence of the beam, and is set constant within the volume of interest V.. On the right: the nanotarget, shown as a green cylinder, may represent any sensitive biological target impacted by the irradiation: a fragment of DNA, of a cell membrane or of an organelle, a protein, etc. z is the restricted specific energy inside the nanotarget. The dose deposition was split into different sub-contributions (W, W+NP, NP). The arrow points at the original photon impact location, and all the circles are energy transfer points (i.e. excited or ionized atoms of gold or molecules of water) created by the interaction of secondary electrons with the medium (water or gold). Note that this is not at scale, as tracks after a photon irradiation may be much larger than the GNP.

The goal of this work is to calculate the impact of a NP on the probability distribution of energy deposition inside a nanotarget, under low-energy photon irradiation. To that purpose, we modelled a single NP in a large volume of water irradiated by a beam of monoenergetic photons. The system designed for our simulation is sketched in Fig. 9.2. We considered an infinite volume of water. Then, we defined a volume of interest V of water (cube of 30-360 µm sizes), containing one NP placed at the centre of the volume. The fluence of the photon beam remained constant within this volume of interest. We assumed that the GNP was placed at a position where the system was at charge equilibrium. The half size of V was chosen to be larger than the maximum range of the most energetic photo-electron in water. Assuming that the fluence remained unchanged in V was reasonable as long as the volume dimensions of the system remained small compared to the photon's mean free path. For the smallest beam energy (i.e. 20 keV), the mean free path of photons in water is about 1 cm, which is much larger than the volume of interest considered (30 µm side at 20 keV). This volume was irradiated with a macroscopic reference dose D in water without GNP. The contribution of the dose deposition was split into 3 components, as shown in Fig. 9.2.

1. (W) the case where a photon interacted with water and did not lead to secondary particles interacting with the GNP,

2. (W+NP) the case where a photon interacted with water and led to at least one secondary particle interacting with the GNP,

3. (NP) the case where the photon directly interacted with the GNP.

All the results are given for an irradiation dose D in water set at 1 Gy. A total of 4 radii of NPs (5 nm, 12.5 nm, 25 nm and 50 nm) and energies from 20 to 90 keV were chosen to systematically study the impact of the NP size and photon energy on the nanodosimetry. The half length of the volume of interest hence varied between 15 µm at 20 keV and up to 160 µm at 90 keV. The nanotarget was set to be a cylinder of height and radius equal to 10 nm, oriented along the beam axis. The nanotarget medium was assimilated to water, and did not account for the biological composition which might differ from water molecules. This choice is common in micro/nanodosimetry, and is justified by the equivalence of cell medium to water. The energy deposition inside the nanotarget was calculated for a distance d_{target} of the nanotarget from the GNP surface. To characterize the influence of this parameter, the centre of the target was taken as the target coordinates. The volume around the GNP was decomposed in concentric shells of width Δd. d_{target} represented the discrete distances between the GNP surface and the centre of the shell. Any target whose coordinate was comprised within $d_{\text{target}} \pm 0.5\Delta d$ was therefore contributing to the specific energy distribution at d_{target}. By definition, results were always normalized per target located inside the given sub-volume. To avoid overlapping issues between the NP and the nanotarget, d_{target} varied from 5 nm to 199 nm and was incremented by 2 nm from one value to the next.

9.2.2. Monte Carlo simulation

9.2.2.1. Photon irradiation

As seen in the previous section, the geometry of the system allowed us to consider that the fluence of photons remained unchanged both in direction and energy spectrum over the volume of interest V. Moreover, we limited our study to a situation where the volume of interest was placed in condition of charged particle equilibrium, but as close as possible to the source. Thus the beam was considered monoenergetic in V. These considerations simplified the simulation, since photons did not require an explicit tracking. Photon interactions were homogeneously distributed in water and in the GNP. As the total cross section was larger for gold material than water, the interaction density was larger. Only the photoelectric effect and the Compton effect were taken into account as, at these energies, they are predominant. The photoelectric cross sections were taken from the database[18]. In our simulation, the angular distribution of the ejected photoelectron was assumed to be isotropic. For the Compton effect, the cross section was calculated using the differential cross section based on the Klein-Nishina formula[172].

9.2.2.2. Electron-gold interaction

We recently implemented a physical model for electron transport down to low energy in solid metallic media. According to the transferred momentum, elastic scattering is described through a single-atom potential[240] or with creation of phonons[77]. Inelastic collisions were described as atomic-like processes[153] for inner-shell electrons, and through a dielectric formalism for outer-shell electrons[233]. A full description of the models implemented and the results of the benchmark are given in the chapter 8.

9.2.2.3. Electron-water interaction

The models used for electron-water interaction are described elsewhere[70,106]. In short, inelastic collisions were described using the model developed by Kim *et al.*[153] for ionization, by Cobut *et al.*[58] for excitation of the water molecule into the a1b1 or b1a1 electronic state, and by Richardson *at al.*[232] for double ionization. The angular distributions of electrons after an ionizing collision were modelled based on the work by Grosswendt *et al.*[113]. Elastic collisions of electrons were based on the work by Michaud *et al.*[200]. Inelastic collisions associated with vibrational excitation of water molecule cross sections were based on the measurement in amorphous ice by Michaud *et al.*[199] and Cobut *et al.*[58] and enhanced by 15 % to account for the liquid state and improve the comparison with experimental decay of solvated electrons[15,207]. Finally, attachment cross sections were adjusted to reproduce the yield of molecular hydrogen measured by Pastina *et al.*[215].

9.2.2.4. Auger and fluorescence processes

The whole Auger cascade was taken into account for every initial vacancy, based on the EADL library. In the case of the gold atom, a total number of 1622 transitions were considered. As pointed out previously, photons were not tracked, hence fluorescence photons from gold atom desexcitation were considered as lost energy and did not lead to additional energy deposition in the volume. Although these photons might carry a large amount of the initial photon energy after a GNP ionization, especially for the K-shell ionization, most of these fluorescence photons had an energy larger than 10 keV. Hence, their mean free path in water was larger than the dimensions of the volume of interest, meaning their contribution to the local dose deposition was negligible. This was already pointed out by Lechtman *et al.*[170], who concluded that X-rays emitted through fluorescence have a range too long to contribute to the local dose enhancement.

9.2.2.5. Water-gold interface

The change of mesoscopic potential energies when an electron changes medium was taken into account. The kinetic energy of the electron was modified when crossing the water-GNP interface, on the basis of the difference of the media's respective potential energies. The mesoscopic (e.g. internal[151]) potential energy of water was -1.30 eV with regard to the vacuum potential (set to zero), and the one of gold was -10.04 eV. Hence, when an electron moved from gold to water, it lost 8.74 eV of kinetic energy (see Appendix C for the conventions).

9.2.3. Calculated quantities

9.2.3.1. Restricted specific energy distribution: definition

After the irradiation of a volume of water containing one GNP with photons, MC outputs consisted of the spatial distribution of all low-energy electrons and ionized or excited water molecules. Each of these events was represented by an energy-transfer point of coordinate r_i and energy ϵ_i, located where the event i occurred. The excitation energies considered for the different types of interaction processes i are summarized in Tab. 9.1.

The specific energy z in a nanotarget of mass m_t is defined as the energy deposited in the nanotarget, divided by its mass:

$$z = \frac{1}{m_t} \sum_{i, r_i \in \text{target}} \epsilon_i \tag{9.1}$$

with ϵ_i the energy from a single transfer point of coordinates r_i contained within the nanotarget.

Stored energy (eV)	State	Process
1.3	N/A	Aqueous electron attachment
8.4	a1b1	Water molecule excitation
10.1	b1a1	
12	1b1	Ionization of the different electronic shells
14.7	2a1	
16.6	1b2	
32.4	1a1	
539.7	1s	

Table 9.1.: Summary of deposited energies following a given interaction process[70]. Indicated ionization values are central values as we considered a broadening of the binding energy around a central value[106]. The energy stored for multi-ionizations (due to Auger decay or double ionization) is calculated by summing the binding energies associated with each hole. N/A = Not Applicable.

In this study, we considered only a fraction of the events. All the energy transfers that may lead to events relevant for the biological effects of radiation (e.g. ionizations, part of the electron attachment process and dissociative excitations) were taken into account, while the ones that simply caused the heating of the medium were disregarded. Therefore, the energy dissipated in molecular vibrations ($\approx$ 17-18 % of the average deposited energy), part of the attachment process ($\approx$ 1 % of the average deposited energy) and geminate recombinations were not considered in energy deposition. Therefore, on average, we find,

$$< z >= \eta D \tag{9.2}$$

with $\eta = 81.5 \pm 0.5$ %. We use the term "restricted specific energy" to denote z[69]. When considering microscopic and nanoscopic scales, the fluctuations are extremely important. Therefore, the distribution of the restricted specific energy $S(z)$ was computed :

$$S(z) = \frac{\mathrm{d}P}{\mathrm{d}z}(z) \tag{9.3}$$

This quantity represents the probability density of the restricted specific energy s. Introducing $\vec{r}$ the distance between the centre of the GNP and the centre of the target, we defined $S(\vec{r}, z)$ the probability density of restricted specific energy z for a target located at $\vec{r}$. As the distance d_{target} of the target to the NP surface is an important parameter, we defined the spectra $S(d_{\text{target}}, z)$ as the average of $S(\vec{r}, z)$ over a concentric shell,

$$S(d_{target}, z) = \int\limits_{\vec{r} \in Sph(r)} \frac{S(\vec{r}, z)\mathrm{d}s}{4\pi r^2} \tag{9.4}$$

where $Sph(r)$ is the surface of a sphere centred around the GNP, and of radius $r = d_{\text{target}} + R_{\text{GNP}}$. The optimization consisting of calculating the restricted specific energy for the different sub-contributions detailed in section 9.2.1 is detailed in the Appendix C.

9.2.3.2. Restricted specific energy distribution: calculation

The histograms of the restricted specific energy distribution were derived from the restricted specific energy z in N nanotargets within the volume V and for many irradiation configurations. The total volume of the nanotargets was chosen smaller than the total volume V. The resulting histogram of specific energy was converted into a distribution of the restricted specific energy, or probability density function, as follows:

$$S(z) = \frac{\partial P}{\partial z}(z) = \frac{1}{N}\frac{N_k}{\Delta z_k}, \qquad \text{for } z \in \left[z_k - \frac{\Delta z_k}{2}, z_k + \frac{\Delta z_k}{2}\right]. \tag{9.5}$$

N_k is the number of nanotargets receiving a restricted specific energy value $z_k \pm \frac{\Delta z_k}{2}$, where Δz_k is the binning width. In our study, the histograms were computed for a restricted specific energy ranging from 10 Gy to 100 000 Gy. A logarithmic binning was used, corresponding to a relative accuracy of 0.04 %. The integral of the distribution over the whole range of specific energies represents the probability P_{hit} of having an energy deposition inside a nanotarget strictly larger than 0, while $1 - P_{\text{hit}}$ represents the probability that a nanotarget receives no energy.

9.2.3.3. Integrated restricted specific energy

From a biological point of view, one expects that the larger the specific energy is, the more complex and lethal the damages inside the nanotarget for the cell. Therefore, the probability of having a specific energy larger than a threshold z_0 is an relevant observable, and z_0 appears as an index of severity. This threshold effect was highlighted by the biophysical model NanOx, which describes part of the lethal events by a local lethal event function (see section 9.4 for more details). The locality is described at a nanometric scale, and this function displays a step-like function with a threshold. Thus, let us introduce the probability of having a restricted specific energy larger than a threshold z_0,

$$P(d_{\text{target}}, z \geq z_0) = \int_{z_0}^{\infty} \frac{\mathrm{d}P}{\mathrm{d}z}(d_{\text{target}}, z)\mathrm{d}z, \quad \text{(resp.} \quad P(z \geq z_0) = \int_{z_0}^{\infty} \frac{\mathrm{d}P}{\mathrm{d}z}(z)\mathrm{d}z) \tag{9.6}$$

in presence of a GNP and with pure water (respectively). We then define a probability enhancement ratio, $R(d_{\text{target}}, z > z_0)$ of the two quantities,

$$R(d_{\text{target}}, z \geq z_0) = \frac{P(d_{\text{target}}, z \geq z_0)}{P(z \geq z_0)}. \tag{9.7}$$

9.2.3.4. Statistical uncertainty

The determination of statistical uncertainty is made difficult by the multiple biasing methods used. In order to achieve statistically good results with such potentially high computing time-consuming processes, we had to limit the number of simulations performed and the number of cases to be studied. The calculations were performed 4 times independently for the case of $E_{\text{photon}} = 50$ keV and $R_{\text{GNP}} = 5$ nm of diameter. The smallest diameter was chosen, for which the smallest shell volumes might result in the lowest number of events in a given shell, and thus a lower statistics. The standard deviation of integrated probabilities was found to be between approximately 1 % to 3 %, depending on the threshold ($< 20\,000$ Gy) and the distance from the GNP surface.

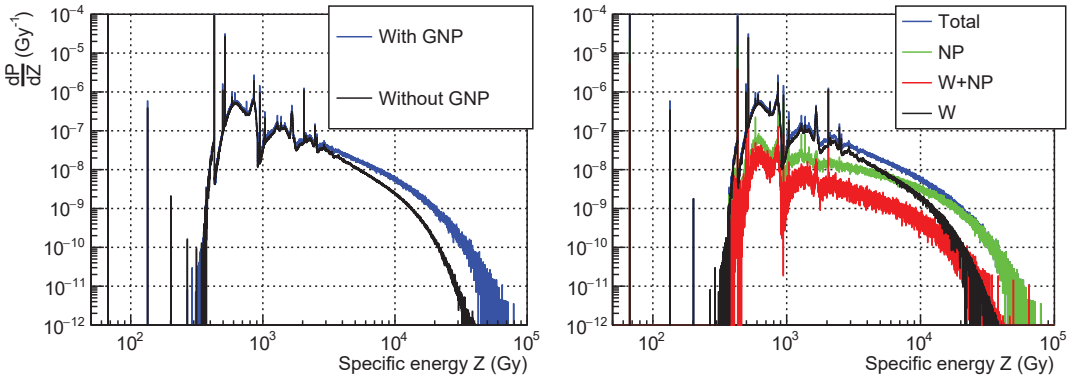

Figure 9.3.: Restricted specific energy distribution (Gy^{-1}) for an irradiation of 1 Gy in water at 50 keV and a GNP radius set at 5 nm. The nanotarget was located on the surface of the GNP. On the left, the results with or without GNP, and on the right, the results with GNP broken down in the 3 sub-contributions.

9.3. Results

9.3.1. Restricted specific energy distribution

The results are all displayed for an irradiation dose D of 1 Gy. As a consequence, the average restricted specific energy in the nanotargets is equal to about 0.82 Gy.

9.3.1.1. Water and GNP contributions

We investigated the contributions to the probability distribution of the restricted specific energy according to the type of tracks. Fig. 9.3 displays the restricted specific energy distribution obtained for an irradiation dose of 1 Gy with 50 keV photons in a volume of pure water (without GNP) and in presence of a GNP with a 5 nm radius. For the latter case we consider a distance of 5 nm between the target and the surface of the GNP. The restricted specific energy distribution is also broken down into sub-contributions coming from the different track types, as explained in Fig. 9.2, namely: NP which designates the case where a photon directly interacts with the GNP, W where a photon interacts in water, leading to secondary particles that do not interact with the GNP, and W+NP where a photon interacts with water leading to at least one secondary particle interacting with the GNP. Overall, there is a higher probability of having high restricted specific energy ($\geq$ 10 000 Gy) inside the nanotarget in presence of a GNP as opposed to without GNP. The major impact of GNPs is due to the NP contribution for targets close to the surface, as the W+NP contribution appears rather small. These observations were the same for any energy or size of GNPs. Hence, for this range of energies, the enhancement effect is induced by electrons leaving a GNP after a direct photon ionization.

By definition, the two spectra 'Without GNP' and 'W' with GNPs should differ. One could expect them to be similar in shape, but different in global intensity due to the probability that a track generated near the GNP would interact with the GNP, decreasing then the W contribution. However, the two spectra appear to be very similar. Thus, the presence of GNPs does not modify the W contribution significantly, which may roughly be modeled as a pure water contribution.

9.3.1.2. Parameters influencing the restricted specific energy distribution

Fig. 9.4 shows the restricted specific energy distributions for 4 distances d_{target} for 1 Gy of irradiation D in water. The parameters influencing the restricted specific energy distribution are: (1)

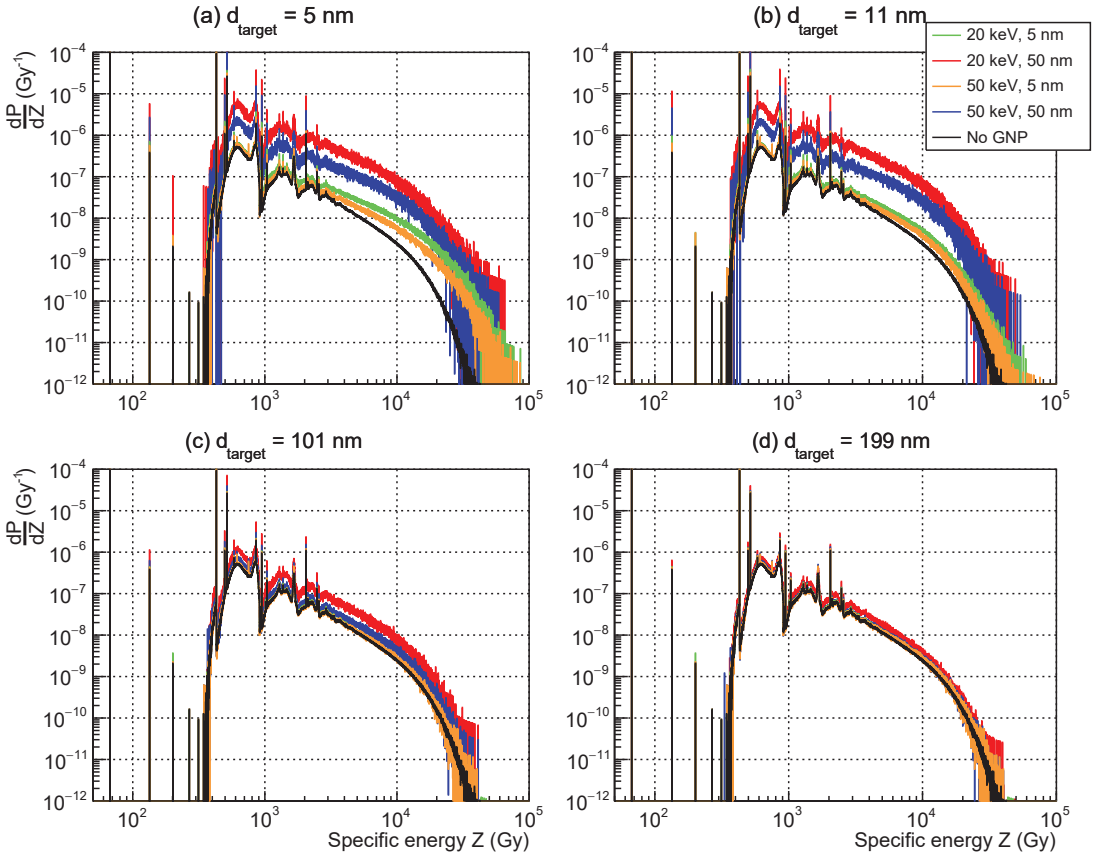

Figure 9.4.: Restricted specific energy distribution (Gy^{-1}) for 4 distances of the target to the GNP surface (a) 5 nm, (b) 11 nm, (c) 101 nm, (d) 199 nm. Each chart displays the results for 2 energies (20 keV and 50 keV), 2 radii (5 nm and 50 nm) and 1 Gy irradiation.

the distance of the target to the GNP surface (d_{target}), (2) the radius of the GNP (R_{GNP}), (3) the energy of the photons (E_{photon}).

Nanotarget-GNP distance When the nanotarget is on the surface of the GNP or close to it ($<$ 20 nm) there is a clear enhancement, due to the GNP, in the probability of hitting the nanotarget for large GNPs. Moreover, when the nanotarget is on the surface of the GNP, there is also an enhancement in the probability of having high specific energy for small GNPs. When the distance increases, there is a rapid decrease of the GNP effect. At about 20 nm, the effect is already negligible for the smallest GNPs, while for the largest one the effect remains noticeable up to about 200 nm. This shows that the enhancement of restricted specific energy distribution of nanotargets is extremely local, and rapidly negligible compared to the surrounding contribution coming from the irradiation of water molecules. 200 nm corresponds to the range of electrons of energies around 3 keV[93]. Based on the electron spectra (see Appendix C), these low ($\leq$ 3 keV) electrons are mostly generated by Auger cascades, except for the 20 keV photon irradiation, where the photo-electron also contributes to low energy electron emission.

GNP size As previously said, the smaller the NP, the smaller the range of action. Thus, the enhancement depends on the size of the GNP. For small GNPs (5 nm), there is only an increase of probability of having very large ($>$ 10 000 Gy) energy deposition. For larger GNPs (50 nm), the major effect is an amplification of the amplitude, leading to a global increase of the probability of hitting the nanotarget, both for low and large restricted specific energy deposition (see Appendix C for the origin of this effect).

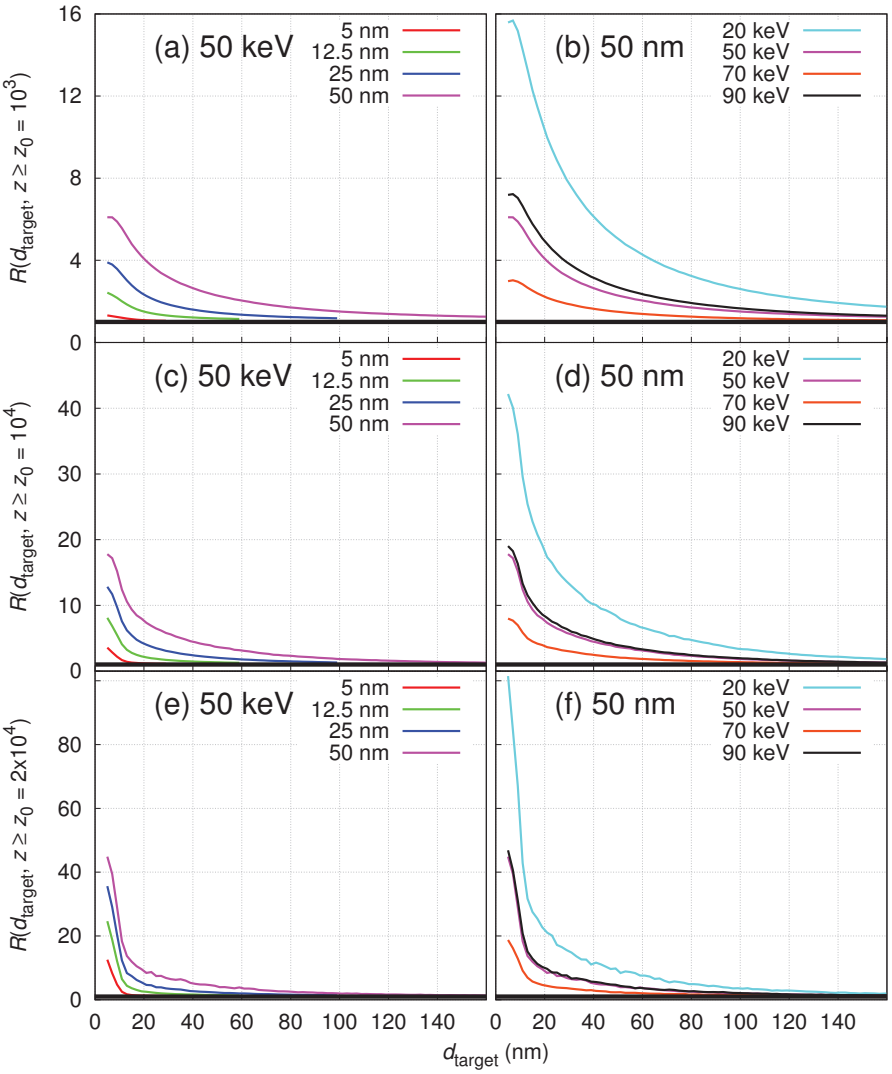

Figure 9.5.: $R(d_{\text{target}}, z \geq z_0) = P(d_{\text{target}}, z \geq z_0)/P(z \geq z_0)$, as a function of d_{target}. Charts 9.5 (a), (c), (e) display cases for fixed energy of 50 keV, and 4 GNP radii (5 nm, 12.5 nm, 25 nm and 50 nm). Charts 9.5 (b), (d), (f) display cases for fixed radius of 50 nm, and 4 energies (20 keV, 50 keV, 70 keV and 90 keV). The black horizontal line represents the value 1.

Photon energy The bigger the GNP, the larger the influence of the photon energy is. Small GNPs show almost the same results for all photon energies (not displayed here). For larger GNPs, the restricted specific energy intensity globally decreases when the photon energy varies from 20 keV to 80 keV, before showing a small increase at 90 keV when the K-edge is reached. Again, this trend is explained by electron emission from GNPs (see Appendix C). It should be noted that these trends are different from macroscopic trends: for 1 Gy and a fixed mass concentration of GNPs, the average dose deposition in water is smaller at 20 keV than at 50 keV, due to energy absorption inside the GNP.

9.3.2. Integrated specific energies

The probability enhancement ratio, $R(d_{\text{target}}, z \geq z_0)$, is displayed in Fig. 9.5 for various values of the GNP radius and of the photon energy. Note that this ratio tends to 1 when d_{target} increases. Different thresholds were chosen: $z_0 = 10^3$ Gy, $z_0 = 10^4$ Gy and $z_0 = 2 \times 10^4$ Gy corresponding respectively to an energy deposition in nanotargets of 20 eV, 196 eV and 392 eV. The former is

Photon energy	20 keV		50 keV		70 keV		90 keV	
R_{GNP}	5 nm	50 nm	5 nm	50 nm	5 nm	50 nm	5 nm	50 nm
$z_0 = 1$ kGy	9 nm	191 nm	NA	97 nm	NA	47 nm	NA	113 nm
$z_0 = 10$ kGy	17 nm	199 nm	11 nm	127 nm	11 nm	83 nm	13 nm	133 nm
$z_0 = 20$ kGy	19 nm	195 nm	15 nm	127 nm	13 nm	85 nm	15 nm	135 nm

Table 9.2.: Table of range values $d_{\mathrm{target}}(R = 1.5)$ for which R is lower than 1.5. NA = Non applicable, i.e. the ratio is lower than 1.5 for any distance.

typically the mean energy necessary to induce the ionization of one water molecule. Therefore, it may correspond to a simple damage, while the others may represent more complex damages. In pure water, $P(z > 1 \times 10^3)$ is of the order of 4×10^{-4}, $P(z > 1 \times 10^4)$ is of the order of 9×10^{-6} and $P(z > 2 \times 10^4)$ is of the order of 5×10^{-7}. Therefore, $P(d_{\mathrm{target}} = 5\ \mathrm{nm}, z \geq z_0)$ is equal to 6.2×10^{-3} for $z_0 = 10^3$ Gy, 3.8×10^{-4} for $z_0 = 10^4$ Gy and 5.1×10^{-5} for $z_0 = 2 \times 10^4$ Gy.

We observe that the higher the threshold, the higher the ratio, meaning GNPs are very effective at depositing high specific energies compared to pure water. The highest ratios were obtained for a photon energy of 20 keV, and a GNP radius of 50 nm, regardless of z_0. Under these conditions, the ratio goes up to nearly 16 at 5 nm from the GNP surface for a threshold of 1 kGy. It increases to about 40 when the threshold is 10 kGy and to 95 when the threshold is 20 kGy.

Tab. 9.2 displays the range ($d_{\mathrm{target}}(R = 1.5)$) for which the ratio R becomes lower than 1.5, for different photon energies and GNP sizes. When z_0 increases, the range of action usually increases noticeably. For instance, for $E_{\mathrm{photon}} = 20$ keV and $R_{\mathrm{GNP}} = 5$ nm, $d_{\mathrm{target}}(R = 1.5)$ increases from 9 nm for $z_0 = 1$ kGy to 19 nm for $z_0 = 20$ kGy. This is due to the presence of Auger electrons which induce local clusters that are very effective at depositing locally high energy. When the GNP radius increases, $d_{\mathrm{target}}(R = 1.5)$ increases. For $E_{\mathrm{photon}} = 20$ keV and for $z_0 = 20$ kGy, it goes from 19 nm to 195 nm for GNP radii of 5 nm and 50 nm respectively. The probability of having an energy deposition in one nanotarget at a distance r from the GNP centre ($r = R_{\mathrm{GNP}} + d_{\mathrm{target}}$) decreases since the solid angle scale with $1/r^2$. However, when the GNP radius increases, this decrease is compensated by an increasing probability of photon interaction in the GNP. The latter is proportional to R^3_{GNP}.

When the energy of the primary photon increases, $d_{\mathrm{target}}(R = 1.5)$ decreases due to the decrease of the photon-gold interaction cross section and a higher energy of the photo-electron which contributes to a lower concentration of energy deposition. An exception is noticeable at 90 keV, for which one may observe higher $d_{\mathrm{target}}(R = 1.5)$ with respect to a 70 keV photon irradiation. This is due to the gold K-edge and associated increase of the photon-gold cross section, along with a decrease of the photo-electron energy. However, it remains lower than the $d_{\mathrm{target}}(R = 1.5)$ at 20 keV, since the photo-electron energy remains higher, the cross section is lower, and there is a loss of the energy due to a higher fluorescence emission (see Appendix C).

Overall, the range of action has a maximum value of 199 nm for 20 keV, 50 nm and $z_0 = 10$ kGy. This range strongly depends on the GNP size, but also, to a lesser extent, on the photon energy. Again, we observe that the optimization cannot be found independently for a fixed radius of GNP or a fixed photon energy, but for an optimized combination of both of them.

9.4. Discussion

We studied the impact of a GNP embedded in a water volume irradiated with keV photons on the probability distribution of the restricted specific energy inside nanotargets. As mentioned in section 9.2, this quantity corresponds to the energy imparted to the medium via ionization, electron attachment and excitation processes, leading to molecule dissociation. More precisely,

we performed a systematic study on the influence of (1) the NP size, (2) the photon energy and (3) the distance between the GNP and the nanotarget. In this study, the target was a cylinder of radius and height set to 10 nm[204], oriented along the beam axis. This orientation was not critical as the nanotargets were very small compared to the length of electron tracks. The size of the nanotarget was chosen to model potential lethal damages, such as DNA double strand breaks (DSB). The DNA helix is about 2.2-2.6 nm wide, and a DSB is approximately 6 to 13 nm long[171]. Besides, hydroxyl radicals are considered the key reactants in DNA sub-lethal damage[96] and characterized by a very high production rate. Their diffusion is of the order of 4 nm within DNA molecules[90]. Hence, the nanotarget dimensions appeared as a good choice to account for direct (ionization of DNA) and indirect (chemical reaction of $^{\bullet}$OH) local damages, as well as for potential cluster effects. It should be noted that although this dimension was chosen in relation with DNA targets, it may be applied to other targets such as membrane portion (whose thickness is about 7-10 nm for lysosome membranes[246]) or small proteins.

Our results showed that GNP enhanced the probability of obtaining high values of restricted specific energy in nanotargets, compared to a pure volume of water. It comes mostly from Auger electrons emitted from the GNP but also from the photo-electron in some cases. This enhancement depends on the photon energy for 3 reasons. First, the probability of photon-gold interaction varies with increasing photon energy. Second, the photo-electron energy increases with increasing photon energy, which in turn deposits less energy in the vicinity of the GNP, with an exception at 90 keV due to the gold K-edge. Last, there is a loss of local energy deposition due to high fluorescence emission at 90 keV. This enhancement also greatly depends on the radius of the GNP and is higher for larger GNPs. However, the enhancement does not scale with the volume of the GNP due to energy absorption in the NP. The optimum cannot be obtained for an isolated energy or radius, but for a combination of both. In our case, the highest enhancement was obtained for an energy of 20 keV and a radius of 50 nm. The enhancement also depends on the chosen endpoint. When comparing the probability of having a specific energy greater than a threshold z_0 with and without GNP, we found that the ratio of probabilities was greatly impacted by the value of z_0. For 20 keV and 50 nm, it varied from 16 for $z_0 = 1$ kGy to 95 for $z_0 = 20$ kGy for the nanotarget located at 5 nm from the GNP surface.

The thresholds were chosen in the light of the NanOx biophysical model[69,202,204]. This recent model aims at predicting cell survival after particles irradiation, originally with ions in the context of hadrontherapy. The goal is to calculate the mean cell survival probability when irradiating with a given dose D. The main postulate is that cell survival may be expressed in terms of two separate components: one related to local lethal events defined at nanometric scale inducing direct cell killing, and one related to non-local events representing the accumulation and/or the interaction, at the microscopic cellular scale, of sub-lethal damages in different cellular structures and oxidative stress. The local lethal events are deduced from an "effective lethal function" derived *via* a data-driven method. It may be expressed as follows,

$$F(z) = \frac{h}{2}\left[1 + \mathrm{erf}\left(\frac{z - z_0}{\sigma}\right)\right] \tag{9.8}$$

z_0 appears as a threshold in restricted specific energy, above which the nanotarget damage induces efficiently cell death. σ is the width of the increase, and h the level of the response attesting the function's saturation. These parameters are determined through the fitting of experimental $\alpha(LET)$ data[204], and are specific to a given cell line. For the cell lines HSG, V79 and CHO-K1, z_0 was respectively 15, 22 and 14 kGy. We thus used the two thresholds $z_0 = 10$ kGy and $z_0 = 20$ kGy, additionally to 1 kGy (e.g. 20 eV), which typically represents the mean energy necessary to induce the ionization of one water molecule. The research presented in this paper was developed towards investigating whether the number of local lethal events could be increased in presence of

GNPs, i.e. to check if the modification of restricted specific energy distribution in nanotargets could result in the observed increase of cell death. Our findings show that the addition of GNPs increases the probability of having the restricted specific energy larger than z_0 and could, in the framework of NanOx, increase the number of lethal local damages. However, any critical damages to a biological nanotarget induced by a physical effect coming from Auger electrons would occur only if the nanotarget is located near the GNP. Indeed, we observed that the ratio of probabilities decreased to 1.5 for a distance of 200 nm from the GNP surface for R_{GNP} = 50 nm and E_{photon} = 20 keV. This range is consistent with previous report [40].

Our finding appears consistent with the theoretical study of Xie *et al.* [283]. The authors simulated the enhancement of DNA Single Strand Break (SSB) and Double Strand Break (DSB) in a cell containing either a fixed mass (0.2 mg/g) or a fixed number of 100 nm diameter GNPs located outside the nucleus, irradiated by X-ray photons with a 60 kVp beam (average energy 38 keV), using the MC toolkit PARTRAC [96]. They found that an enhancement was only possible when GNPs were located on the nucleus surface and that there was no enhancement on DNA target damages in other configurations (on the cell surface, or inside the cytoplasm). Given our calculated ranges, we expect similar effects: if the GNPs are too far away from the sensitive volume (e.g. the nucleus [283]), then we do not expect any particular enhancement besides the one coming from the macroscopic dose increase.

However, our results differ from those of He *et al.* [122]. Authors investigated the *average* energy deposited in a DNA fragment, that was located at different distances to a NP surface. They modeled the irradiation of a system NP + DNA with a mono-energetic photon source located at 200 nm from the NP and opposite to the DNA fragment with regard to the NP position. The beam diameter was set to be twice that of the GNP. The dose enhancement ratio was defined as the *average* energy deposited in the DNA fragment with NP to the *average* energy deposited in the DNA fragment without NP. It was calculated for different beam energies, NP sizes and distances between the NP and DNA fragment. For E_{photon} = 50 keV and a distance varying from 30 nm up to 130 nm, they found a dose enhancement ratio decreasing from 2.9 to 2.6 for R_{GNP} = 50 nm, and from 2.4 to 2.3 for R_{GNP} = 25 nm. We find probability enhancement ratios that varied much more abruptly with regards to the NP-nanotarget distance. Besides, our ratios fall below 2 for distances beyond 100 nm for E_{photon} = 50 keV. Such differences arise from 2 distinct reasons. First, the definition of the ratios are different. In particular, our ratios were highly dependent on the energy threshold. Second, the system of our work is placed in a large field irradiation (compared to the size of the NP and the nanotargets), whereas He *et al.* [122] considered a narrow beam. Such an approach, with an unrealistic beam geometry, might induce biased results with regard to the dosimetric scoring [297], and may further explain the difference of results. In particular, it may explain the reason why their ratio remains high at larger distances.

Altogether, our work, compared to previous work, highlights the importance of considering a large irradiation field for the system modelled, as previously stated [297]. It also highlights the need to account for the stochastic distribution of the energy rather than the average energy to translate local energy deposition into meaningful biological outcomes. The lethality associated to damage of molecules (such as DNA) highly depends on the amount of actual energy deposited in or around it, and not on the mean value.

9.5. Conclusions

In this paper, we calculated the probability distribution of restricted specific energy in nanotargets around a GNP. The GNP was embedded in a water volume irradiated by photons with energies varying from 20 to 90 keV. We showed that the GNP significantly enhanced the probability to deposit high amount of energy in nanotargets. Quantitatively, we observed an increase of the probability of having a specific energy larger than a threshold z_0 compared with pure water. This

enhancement of probabilities depends on the photon energy and increases with GNP size. It also depends on the chosen threshold value: the larger the threshold, the higher the enhancement, showing the capacity of GNPs to induce severe damages. Among the calculated values, it was maximum for a threshold z_0 of 20 kGy, a GNP radius of 50 nm and a photon energy of 20 keV, and equal to 95 for a nanotarget located at 5 nm from the GNP surface. However, this enhancement was found to occur in the vicinity of GNPs, as beyond 200 nm, it became lower than 1.5. These calculations shed some light on how the presence of GNPs may impact the damage severity and probability for biological nanotargets. Among many perspectives, these results could be coupled with the NanOx model to estimate the effect of GNPs for different scenarios in terms of cell killing enhancement. In a future work, we will also estimate the production of free radicals in the presence of NPs, as they may play a large role in the radiosensitizing effect of NPs[35,124].

Part III.

Chemical modelling: quantification of free radical production in irradiated colloidal gold nanoparticle solution, and comparison to an experimental *in silico* study

10. Monte Carlo study of the free radical production under keV photon irradiation in the presence of gold nanoparticles. Part I: macroscopic scale.

Authors: Floriane Poignant[a], Hela Charfi[a], Chen-Hui Chan[c], Elise Dumont[c], David Loffreda[c], Étienne Testa[a], Benoit Gervais[b], Michaël Beuve[a]

(a) Univ Lyon, Université Claude Bernard Lyon 1, CNRS/IN2P3, Institut de Physique Nucléaire de Lyon, 69622 Villeurbanne, France.

(b) CIMAP, unité mixte CEA-CNRS-ENSICAEN-UCBN 6252 BP 5133, F-14070 Caen, Cedex 05, France

(c) Univ Lyon, Ens de Lyon, CNRS UMR 5182, Université Claude Bernard Lyon 1, Laboratoire de Chimie, F-69342 Lyon, France

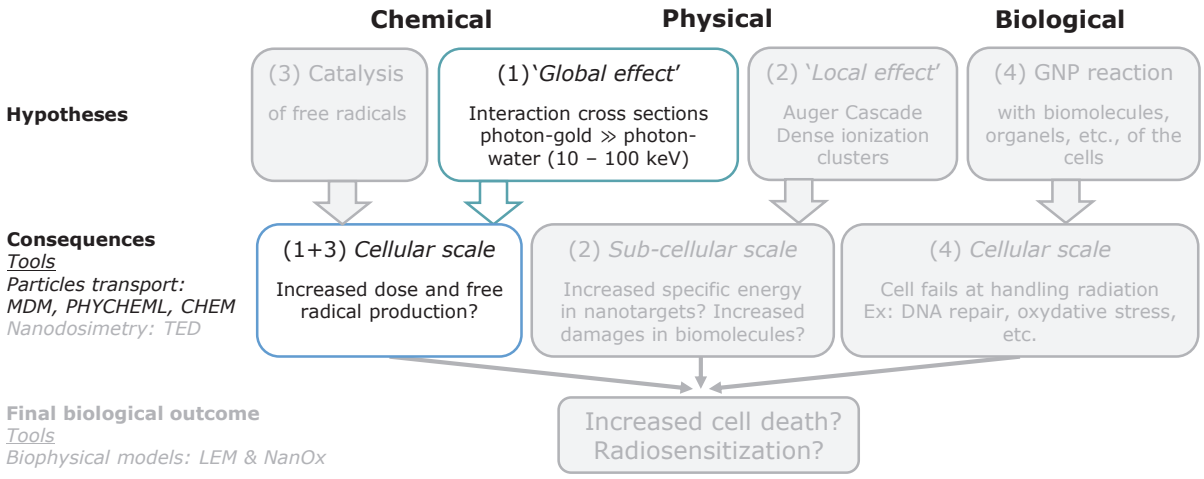

Figure 10.1.: List of mechanisms that may be responsible for GNP radiosensitization. This chapter focuses on the global effects.

Following the validation of our Monte Carlo approach in chapter 8 for the transport of electrons in gold, and the study of the 'local effects' in chapter 9 (see Fig. 10.1 for the different mechanisms as introduced in chapter 7), the next stage was to investigate the 'global effects'. Previous works have focused on the dose deposition at the cellular scale. In this work, we propose to focus on the primary chemical yields at the cellular scale, and therefore characterize the 'global effects' in

terms of chemical yields rather than energy deposition. The idea was to see whether there would be a 'fingerprint' due to the presence of GNPs, such as an overproduction of H_2O_2 due to Auger electrons. This work was done using the package of Monte Carlo tools MDM/PHYCHEM/CHEM, as introduced in chapter 1. This chapter will be submitted as an article once the review by the different co-authors is completed. Results were presented at the international conference MCMA (2017, Napoli, oral presentation), CIRLAF13 (2017, Lyon, oral presentation), ARGENT (2018, Paris, oral presentation), ICRR (2019, Manchester, oral presentation) and the national conference CLARA (2018, Lyon, poster).

Abstract

The use of gold nanoparticles to enhance radiation therapy has been of high interest for the past two decades. While theoretical studies have mostly focused on the physical mechanisms and the dose enhancement, the ones regarding the production of free radicals are scarce. In this work, we therefore investigated the production of free radicals ($^{\bullet}OH$ and H_2O_2) in presence of GNPs, at macro/microscale, induced by 20-90 keV monoenergetic photons. This study was based on a Monte Carlo simulation which enables electron transport down to low energy, both in water and gold. We obtained, for a gold concentration of 1 mg·mL^{-1}, average chemical enhancement that varied from 6 to 14 %, depending mostly on the photon energy but also, to a lesser extent, the chemical species, size of the GNP and time after the primary photon interaction. This enhancement was strongly correlated to the dose deposition enhancement, although not strictly proportional.

10.1. Introduction

The use of nanoparticles (NPs) in cancer therapy has been of high interest since the pioneering work of Hainfeld *et al.*[115], demonstrating the efficacy of the combination of injected gold nanoparticles (GNPs) with X-ray irradiation for mice with EMT-6 carcinoma tumours. The mechanisms of NP enhanced radiotherapy may originate from complex physical, physico-chemical, chemical and biological steps which depend on many parameters, such as the composition of the NP, the energy of the irradiation beam, and the biological system[124]. The relative contribution of these different steps, and the connection between them, still needs to be clarified[35]. As the time scale and spatial scale involved in the early mechanisms are very small, a clear experimental identification of the origin of the effect is not straightforward and remains under investigation. In this context, theoretical approaches, such as Monte Carlo (MC) simulations, may help to better understand how early physical and chemical stages could impact a biological system and lead, for instance, to an increase in cell death.

Many MC studies have focused on the physical stage, to study the dose deposition at different scales. NPs that are made of high-Z materials such as metals are more efficient at absorbing low energy (keV) X-rays. For energies up to $\sim$ 500 keV, the photo-electric effect dominates in metals, resulting in a particularly high probability of photon-metal interaction compared to photon-water interaction, and consequently an increase in the macroscopic (tumour) dose deposition[6,56,57,157,158,190,198,206,253,288]. In particular, studies showed that a significant dose enhancement may occur when the concentration of GNP inside the tumour is high enough. For example, 7 mg gold/g tumour could result in a dose enhancement as high as 110 % for 140 kVp and 70 % for I-125 gamma rays[245]. Strategies were discussed to use GNPs as contrast agents for human eye choroidal

melanoma[10], prostate cancer brachytherapy[187], ARC therapy applied to brain tumours[158] or as a tumour vascular disrupting agents (VDAs)[5,17,177,211,212]. Another study suggested the use of radioactive low-dose rate GNPs, to improve the current low-dose rate brachytherapy strategies[166].

However, MC studies on the chemical stage are scarce. *In solution* irradiation experiments with colloidal GNPs[47,51,75,76,109,110,251] or in presence of bio-molecules[36–38,45,92,192] put in light the importance of the chemical stage. In particular, the use of plasmid DNA evidenced that the enhancement of DNA single strand breaks (SSBs) was dependent on the energy of the incident photon in the keV range[37,192], the concentration of GNPs[37], the chemical environment of the solution and in particular its scavenging ability[38,45,192], and the proximity between the GNPs and the biomolecules[36,45]. Whether it is directly produced by the interaction of radiations with GNPs, or indirectly by the interaction of the GNPs with cellular components, large increase of ROS production was also measured with *in vitro* probes for cells irradiated in presence of GNPs, compared to cells irradiated alone[104,138]. Overproduction of free radicals during water radiolysis induce an oxidative stress which may results in cells failing to maintain normal physiological redox-regulated functions[99]. Dramatic effects, such as oxidative modification of proteins, lipid peroxidation, DNA-strand break, etc.[99], result in cell death.

As pointed by Her *et al.*[124] in a recent review, the chemical stage has yet not been fully investigated. Whereas there has been many MC studies on the physical step, to our knowledge only one MC study has been conducted on the chemical enhancement for GNP-enhanced protontherapy[269], although it was suggested to be a crucial step that may connect the physical effect to the biological consequences[35,166]. In particular, no systematic study of free radical production has been performed for GNP-enhanced radiotherapy in the range of keV photon energies. The goal of this work is thus to investigate, in a systematic way, the impact of GNPs on the production of free radicals for keV photon irradiation in water. As most of the probes of the aforementioned studies measured either hydroxyl radicals ($^{\bullet}OH$) and hydrogen peroxide (H_2O_2), this study focused on these two species. To calculate these chemical yields, we implemented a MC simulation in order to reproduce the physical, physico-chemical and chemical steps at short time. Our MC tool models the interaction of photons with GNPs and surrounding water and tracks secondary electrons and chemical radiolysis products up to 1 µs. We aim, in particular, to estimate how the physical step and the increase of dose deposition affect the chemical radiolytic yield, at macroscopic and microscopic scales.

This paper is organized as follows. In section 10.2, the MC tool and system considered are presented. Section 10.3 displays the different results: the average dose deposition and the radical species production are studied, on a macroscopic scale, as a function of different parameters (photon energy, time after the primary photon interaction, size of the GNP and type of chemical species). In particular, the correlation between dose deposition and free radical production is investigated. Section 10.4 discusses the results, with regard to theoretical and experimental results available in the literature, before concluding in section 10.5.

10.2. Material and methods

10.2.1. System

A. System definition The goal of this study is to calculate the yield Y_X of chemical species X in nmol·J^{-1}, for a given concentration C_{NP} of NPs contained in water, irradiated by a beam of monoenergetic low energy photons. The yield was calculated for various times t after a photon irradiation, with t shorter than 1 µs. The system considered for the calculation is described in Fig. 10.2. We considered an infinite volume of water. We defined a volume of interest V of water, containing a concentration C_{NP} of NPs homogeneously distributed in the volume. We assumed that the concentration C_{NP} was low enough so that the irradiation of one GNP did not influence

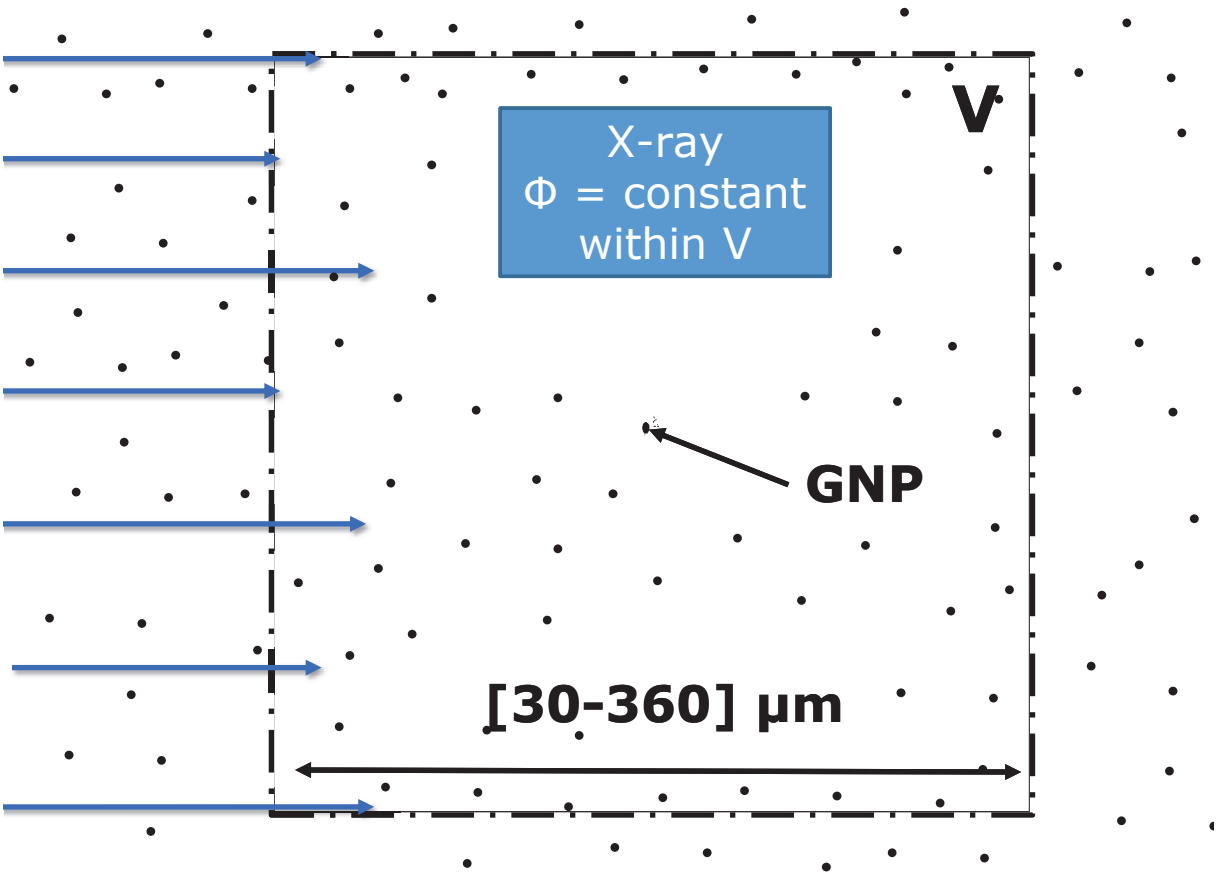

Figure 10.2.: Schematic view of the systems considered for radical species calculation. Φ represents the fluence of the beam, and is set constant within the volume of interest V. The GNPs represented by small dots have a concentration C_{NP} and are homogeneously distributed.

the energy deposition around another. The fluence of the photon beam remained constant within this volume of interest. We assumed that the volume V was placed at a position where the system was at charge equilibrium, but as close as possible to the source. For each photon energy, the half length of V was chosen to be larger than the maximum range of the most energetic photo-electron in water. Assuming that the fluence remained unchanged in V was reasonable as long as the dimensions of the volume of interest V remained small compared to the photon's mean free path. For the lowest beam energy (i.e. 20 keV), the mean free path of photons in water is about 1 cm, which is much larger than the volume of interest considered (30 µm side at 20 keV). This volume was irradiated with a macroscopic referential dose D in water without GNP.

A total of 4 radii of NPs (5 nm, 12.5 nm, 25 nm and 50 nm) and energies from 20 to 90 keV were chosen to systematically study the impact of the NP size and photon energy on chemical species yields. The volume of interest's half length hence varied between 15 µm at 20 keV and up to 160 µm at 90 keV. The different calculations were systematically performed for a dose D of 1 Gy, and at a GNP concentration of 1 mg·mL^{-1}. This concentration is in the range of reported *in solution* and *in vitro* experimental concentrations (see section 10.4). For comparison with the results from the literature, we reported different quantities in Tab. 10.1. The concentrations are provided in nM and in number of GNP·cm^{-3} for the different GNP sizes that we investigated. We also reported the minimum and maximum number and proportion of GNP ionized (provided they are singly ionized) for 1 Gy of irradiation in a cubic volume of length equal to 10 µm (typical dimension of a cell). For a fixed dose and fixed mass concentration of GNPs, this number depends only on the energy of the incident beam. The minimum number of GNP ionized was equal to

R_{GNP}	5 nm	12.5 nm	25 nm	50 nm
GNP concentration in mg·mL^{-1}	1			
GNP concentration in nM	164	10	1.3	0.16
GNP concentration in NP·cm^{-3}	9.9×10^{13}	6.3×10^{12}	7.9×10^{11}	9.9×10^{10}
Average distance between 2 GNPs (nm)	216	541	1080	2160
	Cellular volume : cube of $10 \times 10 \times 10$ µm^3			
Number of GNPs	$\sim$ 100 000	$\sim$ 6 000	$\sim$ 800	$\sim$ 100
f_{mn} (%)	0.01	0.1	0.77	6.15
f_{max} (%)	0.05	0.71	5.66	45.28
n_{mn}	6			
n_{max}	45			
Ratio volume GNP over volume water	$\sim 5 \times 10^{-5}$			

Table 10.1.: Concentration of GNP for different metrics and different particle size. f_{mn} and f_{max} are the minimum and maximum proportion of ionized GNPs for 1 Gy, in %, corresponding respectively to energies of 80 keV and 20 keV respectively. Likewise, n_{mn} and n_{max} are the minimum and maximum number of GNPs ionized in a $10 \times 10 \times 10$ µm^3 volume. The average distance between two GNPs was calculated assuming that GNPs are homogeneously distributed in a cubic network.

6 for 80 keV and the maximum was equal to 45 for 20 keV. Note that the proportion of GNPs ionized is extremely small for 5 nm GNPs, while it is close to 50 % for 1 Gy at 20 keV for the largest GNPs.

B. Nomenclature Tab. 10.2 refers the different quantities defined for this work, related to dosimetry, energy, yields and GNPs. These quantities are introduced further throughout this paper.

10.2.2. Monte Carlo simulation for dosimetry and water radiolysis

The irradiation of a volume of water containing GNPs at a concentration C_{NP} may be modelled by 3 distinctive steps. During the physical stage, particles travelling through the media deposit energy, which may be simulated to calculate dosimetric quantities. This physical step is followed by a physico-chemical and a chemical step leading to the creation of many highly reactive chemical species. In particular, water radiolysis produces four reactive species and two molecular products in significant quantities: the hydrated electron e^-_{aq}, the hydrated proton (H^+ or H_3O^+), the hydrogen atom ($H^\bullet$), the hydroxyl radical ($^\bullet OH$), the molecular dihydrogen (H_2) and the hydrogen peroxide (H_2O_2)[222]. At the physical stage and the beginning of the chemical stage, the track structure is highly inhomogeneous. Hence the chemical reactions cannot be described by simple first or second order kinetic equations ([98]). Thus, at short time, Monte Carlo (MC) techniques are required to calculate chemical yields as a function of the time. A full description of the MC models and constant of chemical reactions are available elsewhere ([60,106], and Chapter 8), and are briefly presented in this section.

10.2.2.1. Physical stage

The physical stage occurs from 10^{-18} to 10^{-15} second after each primary interaction of the beam photons. At the end of this stage, the water molecules may be either excited (H_2O^*) or ionized

	Track type i	
$i = 1$ or W	The primary photon interacts in water, and does not lead to secondary electrons interacting with a GNP	N/A
$i = 2$ or W+NP	The primary photon interacts in water, and leads to at least one secondary electron interacting with a GNP	N/A
$i = 3$ or NP	The primary photon interacts in a GNP	N/A
D_i or Y_i	Sub-contributions of the calculated quantities (dose or yields) of track type i are denoted with an index i (i = 1, 2 or 3)	Gy or nmol·J^{-1}
	GNP	
C_{NP}	Concentration of GNP in solution	NP·cm^{-3} or mg·mL^{-1}
R_{NP}	Radius of the GNP	nm
	Dosimetry	
D	Prescribed dose of irradiation in the absence of GNP	Gy
$D_{\mathrm{res},0}$	Restricted dose deposited, in the absence of GNP	Gy
η_0	Fraction of D deposited in water: $D_{\mathrm{res},0} = \eta_0 D$, $\eta_0 \sim 82\%$	No unit
D_{res}	Total dose deposited for a concentration C_{NP} of GNPs	Gy
$D_{\mathrm{res},C_{\mathrm{NP}}}$	Additional dose deposition per mg·mL^{-1} of GNPs.	Gy·(mg·mL^{-1})$^{-1}$
η'	Fraction of D deposited in water due to GNPs, normalized per dose and C_{NP}	(mg·mL^{-1})$^{-1}$
	$\eta = \eta_0 + C_{\mathrm{NP}}\eta'$	
	Energy	
E_{photon}	Primary photon energy	keV
E_{trans}	Energy the photon transfers to the medium, i.e. part of its energy for Compton scattering	keV
$E_{\mathrm{res,W}}$	Total restricted energy deposited in water	keV
E_{NP}	Energy deposited inside the GNP or self-absorbed energy	keV
E_{th}	Energy loss by heating of water	keV
E_{fluo}	Energy lost by fluorescence when GNP emits fluorescent photons	keV
	$E_{\mathrm{trans}} = E_{\mathrm{NP}} + E_{\mathrm{res,W}} + E_{\mathrm{th}} + E_{\mathrm{fluo}}$	
	Number of chemical species	
$R_X(D)$	Number of chemical species for a dose D, and a concentration C_{NP} of GNPs in V	Number of species
	Yield of chemical species	
$Y_{X,0}$	Total yield of a given species X in the absence of GNPs	nmol·J^{-1}
Y_X	Total yield of a given species X for a concentration C_{NP} of GNPs	nmol·J^{-1}
Y'_X	Additional yield of a given chemical species X per mg·mL^{-1} of GNPs	nmol·J^{-1}·(mg·mL^{-1})$^{-1}$
	$Y_X = Y_{X,0} + C_{\mathrm{NP}} Y'_X$	

Table 10.2.: Nomenclature for the different variables, their definition and their unit (if applicable), introduced throughout this work.

(H_2O^+, H_2O^{2+} and H_2O^-), and the medium contains thermalized electrons (e^-_{th}). Our model[106] consisted of an event-by-event tracking of particles in the different media (water or gold). The energy deposited inside GNPs was considered as lost energy, and vacancies or electrons that were

contained within GNPs were no longer tracked at the end of this step. The next paragraphs give a brief overview of the interactions considered for photons and electrons with the media of interest (water and gold).

A. Photons As seen in section 10.2.1, the geometry of the system allowed us to consider that the flux of photons remained unchanged both in direction and energy spectrum over the volume of interest V. Thus the beam was considered monoenergetic in V. These considerations simplified the simulation, since photons did not require an explicit tracking. Photon interactions were homogeneously distributed in water and in GNPs. As the total cross section was larger for gold material than water, the interaction density was larger. Only the photoelectric effect and the Compton effect were taken into account as, at these energies, they are predominant.

B. Electron-gold interaction We recently implemented physical models for electron transport down to low energy in solid metallic media. Our approach accounted for electron scattering using a separation of the interaction events depending upon the momentum or the energy loss. Collisions leading to high value of momentum transfer were described as an elastic diffusion process on an isolated atom[240], while collisions implying low momentum transfer were described as interactions with phonons[77]. Likewise, inner-shell electron-impact excitations were described as atomic-like processes using the binary encounter-Bethe model[153]. On the contrary, the interaction with outer-shell electrons were based on solid state formalism, for which the properties of the media are described by a macroscopic dielectric function[233] (collective excitation). A thorough benchmarking was performed for gold-electron interaction for energies ranging from a few eV up to 90 keV. A full description of the models implemented and the results of the benchmarking are described in the Chapter 8. It should be noted that, for this study, surface plasmons were not accounted for.

C. Electron-water interaction The models used for electron-water interaction are listed elsewhere[106]. Briefly, inelastic collisions were described using the model developed by Kim *et al.*[153] for ionization, by Cobut *et al.*[58] for excitation of the water molecule into the a1b1 or b1a1 electronic state, and by Richardson *at al.*[232] for double ionization. The angular distributions of electrons after an ionizing collision were modelled based on the work by Grosswendt *et al.*[113]. Elastic collisions of electrons were based on the work by Michaud *et al.*[200]. The cross sections of inelastic collisions associated with vibrational excitation of water molecules were based on the measurement in amorphous ice by Michaud *et al.*[199], and Cobut *et al.*[58] and enhanced by 15 % to account for the liquid state and improve the comparison with experimental decay of solvated electrons[15,207]. Finally, attachment cross sections were adjusted to reproduce the yield of molecular hydrogen measured by Pastina *et al.*[215].

D. Water-gold interface As described in Chapters 8 and 9, materials were described by a mesoscopic potential in which the ejected electrons moved. The change of the mesoscopic potential when an electron changes medium was taken into account. The kinetic energy of the electron was modified when crossing the water-GNP interface, on the basis of the difference of the media's respective mesoscopic potentials (-1.30 eV for water and -10.04 eV for gold, with respect to vacuum set at zero). Hence, when an electron moved from gold to water, it lost 8.74 eV of kinetic energy. The conventions adopted for both media are given in Chapter 9.

E. Electron-hole recombination The MC simulation dealt with electron-hole recombination differently according to the binding energy of the initial vacancy. For gold, for binding energies lower than -61 eV ($5p^6$ shell), both Auger cascade and fluorescence photons were accounted for. The whole Auger cascade was taken into account for each initial vacancy, based on the EADL library. A total number of 1622 transitions were thus considered. As pointed out previously, photons were not tracked, hence fluorescence photons from gold atom desexcitation were considered as lost energy and did not lead to additional energy deposition in the volume. Although these

photons might carry a large amount of the initial photon energy after a GNP ionization, especially for the K-shell ionization (see Appendix D.3), most of these fluorescence photons had an energy larger than 10 keV. Hence, their mean free path in water was larger than the dimensions of the volume of interest, meaning their contribution to the chemical yield was negligible. As previously mentioned, the mean free path of photons in water is about 1 cm at 20 keV, and under experimental conditions that we discuss in section 10.4, the samples are thin compared to the attenuation length of the radiation[251]. For instance, in the experimental work by Gilles *et al.*[110], the volume of the irradiated samples was 120 µL, indicating a small photon beam attenuation. Besides, fluorescence photons were only generated consecutively to a gold-photon interaction, which in proportion reduced their overall impact. For binding energies higher than -61 eV, the holes were discarded as we expect that this recombination does not contribute to additional radicals in water.

For water, only Auger process for the 1*s* hole recombination was considered. The fluorescence can be neglected. The recombination of other vacancies was taken into account when the electron cascade led to thermalized electrons[214], resulting in an excited water molecule. The ejected electrons were either solvated, or recombined with holes before ionized water molecules dissociate.

10.2.2.2. Physico-chemical stage in water

This stage models the relaxation of water molecules leading to the production of primary chemical species, occurring from 10^{-15} to 10^{-12} s after the interaction of a photon with the media. The molecules may dissociate, in which case the two products were generated at a given distance from one to another to account for their kinetic energy. The orientation and direction of the molecules were assumed to be isotropic. Electrons polarized water molecules to form aqueous electrons. The different branch rates of each molecular rearrangement are provided in Tab. 10.3[106]. They were not influenced by the presence of the GNP. At the end of this stage, the following chemical species were produced: e^-_{aq}, H_3O^+, $^\bullet OH$, $^\bullet H$, H_2, and O, with a majority of e^-_{aq}, H_3O^+ and $^\bullet OH$. The atomic oxygen was either at a fundamental state ($O(^3P)$) or an excited state ($O(^1D)$). Note that chemical species did not diffuse during this stage.

H_2O^+	$\overset{H_2O}{\rightarrow}$	$^\bullet OH + H_3O^+$	100%	$d_{OH-H_3O^+} = 0.30$
$H_2O^*(A^1B_1)$	$\rightarrow$	H_2O	30%	
	$\rightarrow$	$^\bullet OH +^\bullet H$	70%	$d_{OH-H} = 0.80$
$H_2O^*(B^1A_1)$	$\rightarrow$	$H_2O^+ + e^-$	25%	
	$\rightarrow$	H_2O	22.5%	
	$\rightarrow$	$^\bullet OH +^\bullet H$	40.95%	$d_{OH-H} = 0.80$
	$\rightarrow$	$O + 2^\bullet H$	6.30%	$d_{O-H} = 0.80$
	$\rightarrow$	$O(^1D) + H_2$	5.25%	$d_{O-H_2} = 0.36$
$H_2O^+ + e^-$	$\rightarrow$	H_2O	40%	
	$\rightarrow$	$^\bullet OH +^\bullet H$	30%	$d_{OH-H} = 0.80$
	$\rightarrow$	$O + 2^\bullet H$	15.6%	$d_{O-H} = 0.80$
	$\rightarrow$	$O(^1D) + H_2$	14.4%	$d_{O-H_2} = 0.36$
H_2O^-	$\overset{H_2O}{\rightarrow}$	$H_2 + OH^- +^\bullet OH$	100%	
H_2O^{2+}	$\rightarrow H^+ + OH^+$	$\overset{H_2O}{\rightarrow} 2H_3O^+ + O$	29%	$d_{H^+-OH^+} = 1.20$
	$\rightarrow H^+ +^\bullet H + OH^+$	$\overset{H_2O}{\rightarrow} 2H_3O^+ +^\bullet H +^\bullet OH + O$	16%	$d_{H^+-O^+} = 1.20$ $d_{H-O^+} = 0.80$
	$\rightarrow H^+ + H^+ + O$	$\overset{H_2O}{\rightarrow} 2H_3O^+ + O$	55%	$d_{O-H^+} = 1.20$

Table 10.3.: Single event dissociation channels used for simulation of the physico-chemical stage in liquid water. Distance between the fragments are given in nanometres.

10.2.2.3. Chemical stage in water

At 10^{-12} s, the primary chemical species start the diffusion and may react with each other. Our simulation tracked all chemical species up to 10^{-6} s. At the end of the chemical stage, the so-called steady state is reached and the radiolytic yields reach asymptotic values[98,106]. Our method used to calculate the yields was developed by Gervais *et al.*[106]. The full procedure is described elsewhere[59,60]. Briefly, this model was inspired by the IRT method, i.e., the reactions are treated independently by pairs of reactants. However, while IRT method treats the reactions according to a sampling of reaction times, we sampled the reaction probabilities, which fastened the calculation. The probabilities were calculated based on the work by Green *et al.*[112]. For this method to be accurate, the time interval δt must be small enough so that the probability of having a chemical product reacting more than once is negligible. This time interval δt was increased with the time ($\delta t = \frac{t}{20}$), as the probability of having more than one reaction decreased due to the homogenization of the species. The diffusion process during each time step was sampled according to standard law of diffusion, taking into account the diffusion coefficients of each species (see Tab. 10.4). As for the IRT method, a time zero stage was simulated to take account for the overlapping of the species at the end of the physico-chemical stage. The constants of reaction, diffusion time, reaction radii, types of reaction and time zero probabilities of the reactions were taken from the work by Frongillo *et al.*[98]. More than fifty reactions were possible, and are listed elsewhere[60]. When two species reacted with each other, different types of reactions may occur, which are listed below:

- *Diffusion controlled reactions.* For the fully controlled diffusion reaction, a reaction occurred as soon as the distance between two species was lower than the reaction radius.
- *Partly diffusion controlled reactions.* When two species met, there was a chance they might not interact together and escape from the reaction. A parameter, known as the reaction velocity v_r, characterized the reaction probability.
- *Charged species reactions.* The Coulomb potential induced by the charged particles played a role in the efficiency of the reaction. Usually, it consisted of an additional terms in the probability calculations from the previous types of reactions.
- *Spin reactions.* The spins of the reactive species must be anti-parallel for the reaction to occur. Aqueous electrons and atomic hydrogens were controlled by diffusion but their spin had to be anti-parallel for the reaction to occur. The spin was randomly sampled and the probability for the spin to change during a time δt obeyed an exponential law.

Generally, it is possible to add a solute in the pure water to study, for example, the impact of the pH, the impact of oxygen in aerated conditions[60], the impact of scavengers, or the impact of antioxidants, which are naturally present in cells[59]. The presence of dioxygen, for instance, scavenge aqueous electrons to produce $O_2^{\bullet -}$ and $^\bullet H$ to produce $HO_2^\bullet$, while some scavengers may react with hydroxyl radicals. This is, however, beyond the scope of this work. Note that, during this stage, interaction of chemical species with the GNP were not considered.

10.2.2.4. Chemical species and reactions of interest

In this work, we focused on the production of $^\bullet OH$ and H_2O_2. $^\bullet OH$ is mainly produced at the physico-chemical stage, through the desexcitation of excited water molecules H_2O^* and ionized molecules H_2O^+. $^\bullet OH$ is the main source of H_2O_2 production, through the recombination process,

$$
\begin{array}{lcll}
^\bullet OH + ^\bullet OH & \rightarrow & H_2O_2 & \text{R1} \\
H^\bullet + ^\bullet OH & \rightarrow & HO_2^\bullet & \text{R2} \\
e^-_{aq} + ^\bullet OH & \rightarrow & OH^- & \text{R3}
\end{array}
$$

Species	Diffusion coefficient (10^{-9} m^2.s^{-1})	Charge	Spin	Radii (nm)
e_{aq}	4.9	-1	1	0.5
H_3O^+	9.46	1	0	0.25
$^\bullet OH$	2.2	0	0	0.22
$^\bullet H$	7.0	0	1	0.19
H_2	4.8	0	0	0.14
H_2O_2	2.3	0	0	0.21
OH^-	5.3	-1	0	0.33
O_2	2.4	0	0	0.17
O_2^-	1.75	-1	0	0.22
HO_2^-	1.4	-1	0	0.25
HO_2	2.3	0	0	0.21

Table 10.4.: Main chemical species properties.

10.2.3. Calculated quantities

We calculated average dose deposition and chemical yields in the volume V, for a concentration C_{NP} of GNPs under keV photon irradiation. Our approach was valid provided that (1) the probability of chemical species coming from two distinct tracks to react together was negligible and (2) the presence of GNPs did not influence the track coming from the ionization of another GNP (see section 10.4 for more details).

10.2.3.1. Chemical species yield in water

The chemical species production was split into 3 contributions as previously done Chapter 9. These contributions are displayed in Fig. 10.3, and consisted of 3 situations: the situation (W) where a photon interacted with water and did not lead to secondary particles interacting with the GNP, the situation (W+NP) where a photon interacted with water and led to at least one secondary particle interacting with the GNP and the situation (NP) where the photon directly interacted with the GNP. They are referred to as (1,2,3), corresponding respectively to (W,W+NP,NP). Defining $R_X(D)$ the mean number of radical species X produced in a volume V for a dose of irradiation D, we decomposed $R_X(D)$ as the sum of the 3 contributions,

$$R_X(D) = R_{X,1}(D) + R_{X,2}(D) + R_{X,3}(D) \tag{10.1}$$

Given our hypotheses, it was possible to decompose the production of chemical species for a given irradiation dose D as the sum of the chemical species produced by isolated tracks. The introduction of the GNP concentration is explicitly explained in Appendix D.1. Each of the contributions was then decomposed as a linear combination of single-track chemical species,

$$R_X(D) = n_1(D)R^1_{X,1} + n_2(D)R^1_{X,2} + n_3(D)R^1_{X,3}, \tag{10.2}$$

where $n_1(D)$ and $n_2(D)$ are the mean number of photon interactions in water for a given prescribed dose D in the water volume, respectively without and with an interaction of a secondary electron with the GNP at the physical stage, and $n_3(D)$ is the mean number of photon interactions in the GNPs for a given prescribed dose D in water. This results in the following system,

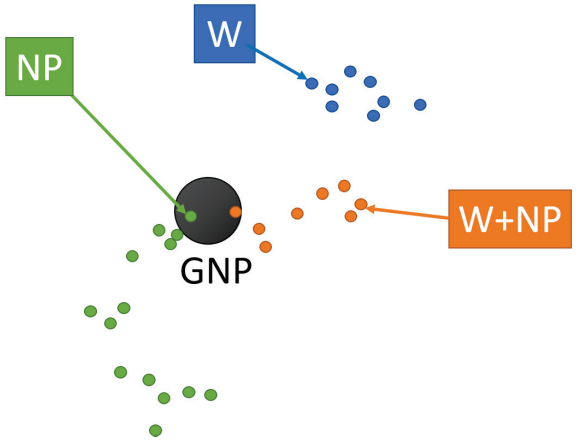

Figure 10.3.: Schematic view of the system considered for radical species calculation. The yield is split in different sub-contributions : (W) the photons interact with water and do not lead to secondary particles interacting with the GNP, (W+NP) the photons interact with water and lead to at least one secondary particle interacting with the GNP, (NP) the photons directly interact with the GNP. The arrow points at the original photon impact localization, and all the circles are transfer points (i.e. excited or ionized atoms of gold or molecules of water) created by the interaction of secondary electrons with the medium (water or gold).

$$\begin{cases} n_1(D) = n_2(D) = F(D)\sigma_{\mathrm{W}}\rho_{\mathrm{W}}V(1 - C_{\mathrm{NP}}V_{\mathrm{NP}}) \\ n_3(D) = F(D)\sigma_{\mathrm{NP}}\rho_{\mathrm{NP}}VC_{\mathrm{NP}}V_{\mathrm{NP}} \end{cases} \tag{10.3}$$

with Φ the fluence of incoming photons in particle cm^{-2} which is linear with the dose D, V the total volume in cm^3, V_{NP} the volume of one nanoparticle in cm^3, C_{NP} the GNP concentration in $\mathrm{NP{\cdot}cm}^{-3}$, σ_x the total cross section for photon-interaction in the medium x in $\mathrm{cm}^2{\cdot}\mathrm{g}^{-1}$, ρ_x the density of the medium x in $\mathrm{g{\cdot}cm}^{-3}$.

Each number of chemical species $R^1_{X,i}$ is now given per primary photon interaction,

$$R^1_{X,\mathrm{i}} = \sum_{t \in T_{\mathrm{i}}} \frac{\sigma^t}{\sigma_{\mathrm{i}}} R^t_X \quad \text{with } i \in [1,2,3] \tag{10.4}$$

with T_1, T_2 and T_3 subsets of tracks generated by single photon interaction corresponding respectively to the contributions W, W+NP and NP, σ^t the cross section for a photon interaction that leads to a track t and $\sum_{t \in T_{\mathrm{i}}} \frac{\sigma^t}{\sigma_{\mathrm{i}}} = 1$, and R^t is the number of chemical species of track t. Note that t includes, at the physical stage, not only the ejected primary electron and the secondary electronic cascade, but also the Auger cascade. The results were expressed as a number of chemical species produced. By definition, the number of species was proportional to the dose D, and the effect of GNPs proportional to C_{NP}. To have a yield Y_X in $\mathrm{nmol{\cdot}J}^{-1}$, the conversion was done as follows,

$$Y_X = f(D)R_X(D) \tag{10.5}$$

with, expressed in $\mathrm{nmol{\cdot}J}^{-1}(\mathrm{species})^{-1}$, is independent of the species, and reads,

$$f(D) = \frac{10^{12}}{DV \times \rho_W \times N_a} \tag{10.6}$$

with N_a the Avogadro number. Note that, as the chemical species number was proportional to D, the resulting yields are independent of the dose D.

10.2.3.2. Energy deposition in water

After irradiating a volume of water containing C_{NP} GNPs, dosimetric outputs consisted in the spatial distribution of all low-energy electrons and ionized or excited water molecules. Each of these events was represented by an energy-transfer point of coordinate r_i and energy ϵ_i, located where the event i occurred. The energies accounted for the different types of interaction processes i in water are summarized in Tab. 10.5.

	Ionization				
State	1a1	2a1	1b2	3a1	1b1
Energy stored (eV)	62	32.4	16.6	14.7	11.97
	Excitation		Attachment	Double ionization	
State	a1b1	b1a1			
Energy stored (eV)	8.38	10.1	1.31	40	

Table 10.5.: Summary of the excitation energies stored in water, following a given interaction process in water, as defined in Ref.[70]. It should be noted that for the ionization of the deepest water shell, the final stored energy is the energy after the desexcitation of the water molecule through the Auger process.

For the volume V_{W} of water ($V_{\mathrm{W}} = V(1 - C_{\mathrm{NP}}V_{\mathrm{NP}})$), the final dose deposition is[70],

$$D_{\mathrm{res}} = \frac{1}{m_{\mathrm{W}}} \sum_{i=1}^{M} \epsilon_i \tag{10.7}$$

where m_{W} is the mass of the volume V_{W}, ϵ_i is the energy associated with the transfer point i of coordinates r_i and M is the total number of transfer points contained in V_{W}. In this study, all the energy transfers that may lead to events relevant for the biological effects of radiation (i.e. ionizations, dissociative excitations and attached electrons) were taken into account, while the ones that simply caused the heating of the medium were disregarded. Since we considered neither the energy dissipated in molecular vibrations ($\sim$ 17 % of the deposited energy), nor part of the attachment process ($\sim$ 1 % of the deposited energy) and nor part of geminate recombinations, the energy stored per unit of mass when irradiating a homogeneous volume of water represented on average $\eta_0 = 82$ % of the macroscopic dose (D) lost in that volume. To avoid any confusion, we referred to this quantity as "the restricted dose" $D_{\mathrm{res},0}$.The track-by-track method, previously introduced for the calculation of the average yield of chemical species, was also applied for the calculation of the dose deposition. In particular, we found,

$$D_{\mathrm{res}}(D) = \sum_i n_i(D) D^1_{\mathrm{res},i} \quad \text{with } i \in [1,2,3] \tag{10.8}$$

with $D^1_{\mathrm{res},i}$ the restricted energy deposition for the track type i, defined similarly as to Eq. 10.4,

$$D^1_{\mathrm{res},i} = \sum_{t \in T_\mathrm{i}} \frac{\sigma^t}{\sigma_\mathrm{i}} D^t_\mathrm{res} \quad \text{with } i \in [1,2,3] \tag{10.9}$$

10.2.3.3. Dose-yield correlation

To study the correlation between the dose deposition and the induced chemical species, we defined,

$$Y_X = Y_{X,0} + C_\mathrm{NP} Y_{X,C_\mathrm{NP}} \tag{10.10}$$

where Y_X is the radiolytic yield (in nmol·J^{-1}) of the chemical species X produced per unit of dose, $Y_{X,0}$ is the radiolytic yield of a chemical species in the absence of a GNP and Y_{X,C_NP} is the additional chemical species production generated by GNPs, per unit of dose and GNP concentration, in nmol·J^{-1}(mg·mL^{-1})$^{-1}$. Likewise, the restricted dose normalized to the prescribed dose D, reads,

$$\eta = \eta_0 + C_\mathrm{NP} \eta' \tag{10.11}$$

and $\eta' = X_\mathrm{NP}\eta_0$ is the additional restricted dose generated by GNPs, per unit of dose and GNP concentration, in (mg·mL^{-1} of GNP)$^{-1}$.

10.2.3.4. Statistical uncertainty

For the contribution i and the chemical species X, associated with N_i the number of tracks of type i simulated, the standard deviation $\sigma_{R_{X,i}(D)}$ of the number of chemical species $R_{X,i}(D)$ is,

$$\sigma_{R_{X,i}(D)} = \sqrt{\frac{1}{N_i} \sum_{t=1}^{N_i} \left(n_i(D) \frac{\sigma^t}{\sigma_\mathrm{i}} R^t_X - R_{X,i}(D) \right)^2} \tag{10.12}$$

The final statistical uncertainty, for the number of chemical species, reads,

$$\sigma_{R_X(D)} = \sqrt{\left(\frac{\sigma_{R_{X,1}}}{\sqrt{N_1}}\right)^2 + \left(\frac{\sigma_{R_{X,2}}}{\sqrt{N_2}}\right)^2 + \left(\frac{\sigma_{R_{X,3}}}{\sqrt{N_3}}\right)^2} \tag{10.13}$$

Similar uncertainties were obtained for the energy deposition, the yields and radial quantities. Each results were displayed with error bars that were set to $\pm\, \sigma_{R_X}$.

10.3. Results

10.3.1. Energy deposition

Fig. 10.4 represents different macroscopic dosimetric quantities for 1 mg·mL^{-1} of GNPs and for a prescribed dose $D = 1$ Gy. On Fig.10.4 (a) the restricted dose is given in Gy and for 4 GNP radii and pure water. The relative increase of the restricted dose with regard to pure water is

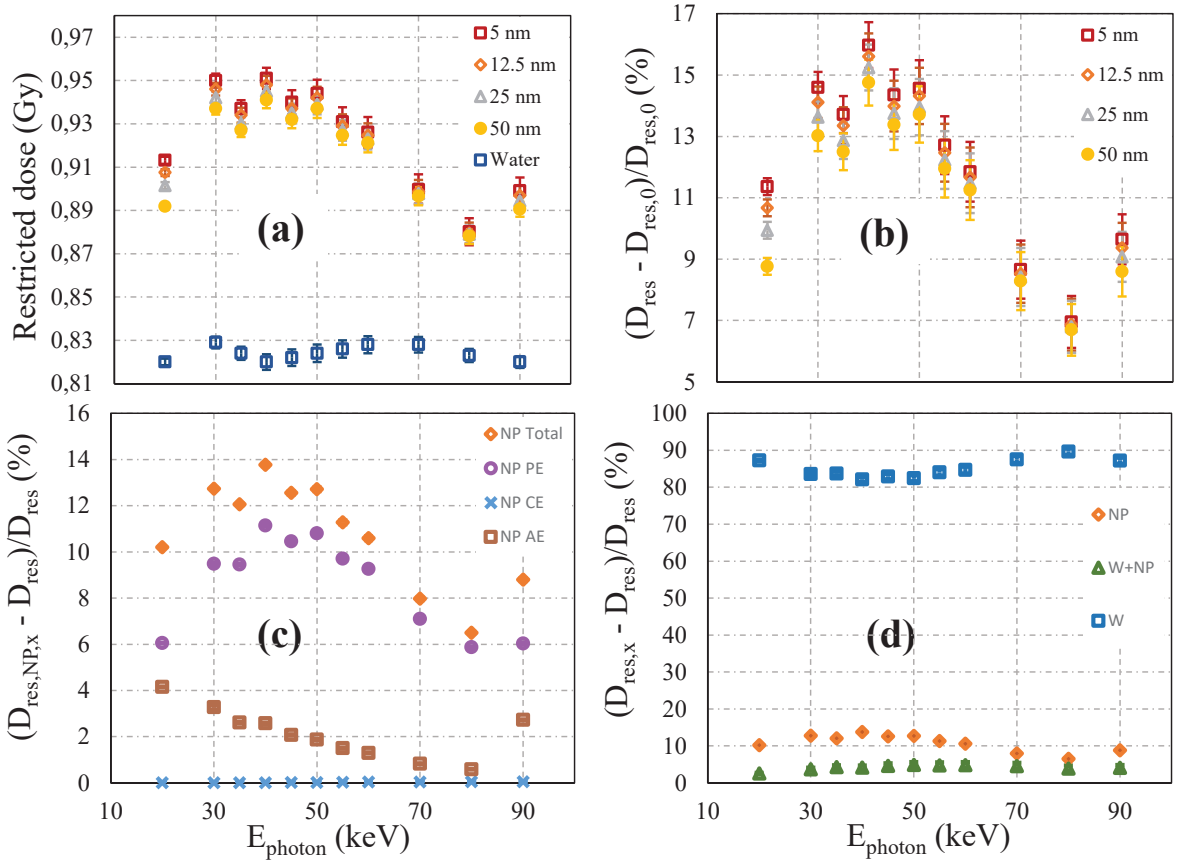

Figure 10.4.: Restricted dose D_{res} (with NP) and $D_{\text{res},0}$ (a), relative increase of D_{res} with regard to $D_{\text{res},0}$ (b) and relative sub-contributions (c) and (d), as a function of the photon energy E_{photon}, for C_{NP} = 1 mg·mL^{-1} and a prescribed dose to water D = 1 Gy. Fig.10.4 (a) represents the absolute restricted dose D_{res} (in Gy) for 4 GNP radii R_{NP} and for pure water, and Fig.10.4 (b) the associated relative increase of D_{res} in presence of GNP for 4 GNP radii R_{NP} with regard to the dose deposited ($D_{\text{res},0}$) in pure water (in %). Fig.10.4 (c) and (d) gives relative sub-contributions to the total restricted dose for R_{NP} = 5 nm. Fig.10.4 (c) gives the contribution from track type t_{NP} (i.e. direct ionization of the GNP by the photon), broken down according to the processes that lead to the primary photo-electron: PE for photo-electron, CE for Compton electron and AE for Auger electron. Fig.10.4 (d) gives the different track types contributions.

displayed on Fig.10.4 (b). The increase of the dose due to GNPs is between $\sim$ 6 % up to $\sim$ 16 % depending on the photon primary energy. For energy larger than 20 keV, there is an increase of the dose deposition with increasing photon energy, as the photo-electron energy is higher and leads to less energy deposition within the GNP. Then, the relative increase goes down to 6 % at 80 keV as the photon cross section ratio decreases. The maximum is reached around 40-50 keV. At 90 keV, there is small increase of the restricted dose due to the K-shell and associated increase of the photo-electric cross section of gold. It can be noted that the increase is relatively independent of the radius, except for low energy photons, in which case the energy deposited in the GNP is significantly more important for large GNPs. At 20 keV, the energy deposited inside the GNP represents $\sim$ 25 % of E_{trans} (the energy of the photons transmitted to the medium) for 50 nm GNPs, and $\sim$ 5 % for 5 nm GNPs as seen in Fig. D.2 of Appendix D.3. It decreases down to less than 10 % for all radii beyond 40 keV.

Fig. 10.4 (d) represents the relative contribution of the restricted dose deposition induced by all the different track types t_{NP}, $t_{\text{NP+W}}$ and t_{W}, as defined in section 10.2.3.1, with regard to the total restricted dose. The contribution t_{W} dominates at this concentration of GNP, while t_{NP} only contributes to $\sim$ 5 to $\sim$ 15 % of the total dose deposition. As defined by our system, this contribu-

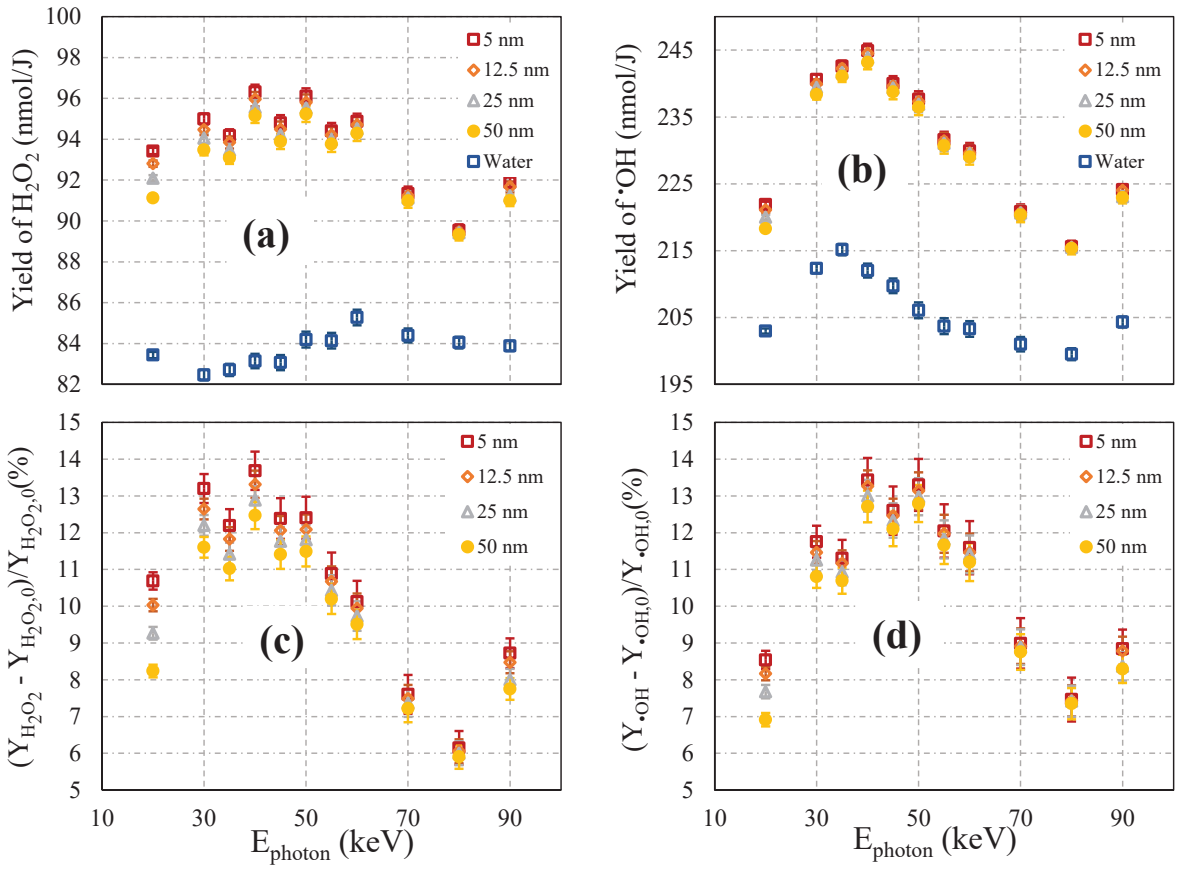

Figure 10.5.: H_2O_2 and $^{\bullet}$OH yield dependence upon primary photon energy for different R_{GNP} and pure water at 1×10^{-6} s. The GNP concentration C_{GNP} was set at 1 mg·mL^{-1}. On top, yields are in nmol·J^{-1} while on the bottom, relative enhancements with regard to the yield in the absence of GNPs are in %.

tion is linear with the GNP concentration. Besides, it is interesting to note that the contribution t_{W+NP} is very low, thus showing that electrons generated by photon-water interactions deposit their energy relatively independently of the GNP at this concentration. Moreover, it does not induce much energy loss due to the absorption of energy by GNPs. Thus, on a macroscopic scale, at these photon energies, the contribution coming from photon interaction with water (t_{W+NP} + t_W) can be replaced by a contribution coming from an infinite volume of water where there are no GNPs.

Fig. 10.4 (c) focuses on the contribution of track type t_{NP}, for a 5 nm GNP, with regard to the total restricted dose. The contribution is broken down into 3 different sub-contributions: the dose deposition coming from secondary particles excited by the initial photo-electron (NP PE), the dose deposition coming from secondary particles excited by the initial Auger cascade after ionization of the GNP (NP AE) and the dose deposition coming from secondary particles excited by primary Compton electrons in the GNP (NP CE). At this energy the contribution of Compton electrons is negligible. While Auger electrons are responsible for local effects near the GNP (see Chapter 9), they contribute to only < 1 % up to a maximum of 4 % of the total restricted dose deposition at 1 mg·mL^{-1}.

10.3.2. Chemical yields in water

10.3.2.1. Photon energy dependence of radiolytic yields

Fig. 10.5 displays the absolute ((a) and (b)) and relative to pure water ((c) and (d)) yields of H_2O_2 and $^\bullet$OH at 10^{-6} s, as a function of the primary photon energy (in keV), for a GNP concentration of 1 mg·mL^{-1}, for different R_{GNP}.

In the absence of GNPs, there is a small fluctuation of the chemical yields depending on the photon energy. From 20 to 35 keV, $^\bullet$OH yield increases from 203.0 ± 0.4 nmol·J^{-1} up to 215.2 ± 0.8 nmol·J^{-1}. At these energies, the photo-electric effect remains non negligible and as the photo-electron energy increases ionizations in tracks are less dense and favour the accumulation of $^\bullet$OH. Then, as the photo-electric cross section decreases from 40 to 80 keV, and the Compton effect starts dominating, the photo-electron energy distribution is impacted and small, dense ionizations in tracks are produced leading to more $^\bullet$OH recombination, thus reducing its yield down to 199.5 ± 0.9 nmol·J^{-1} and increasing H_2O_2 production. Then, as the photon energy increases, the primary electron energy tends to be higher on average, thus leading to the production of sparser ionizations in tracks and favoring back $^\bullet$OH yields.

Regarding the yields in the presence of GNPs, both H_2O_2 and $^\bullet$OH yields follow similar trends with regard to the photon primary energy variation and behave alike the restricted dose: there is first an increase of the yield enhancement from ∼ 11 to ∼ 14 % for H_2O_2 and ∼ 8 to ∼ 14 % for $^\bullet$OH, when the photon energy increases from 20 to 40-50 keV. Then, the enhancement decreases down to ∼ 6 % for H_2O_2 and ∼ 7.5 % for $^\bullet$OH, when the photon energy increases to 80 keV. At 90 keV, both enhancements increase back to ∼ 8-9 %. Interestingly, the enhancements are sightly different depending on the chemical species. In particular, H_2O_2 is favoured at lower photon energies while $^\bullet$OH is favoured at higher energies. This is explained by the photo-electron energy dependency of the chemical yields as displayed in Appendix D.2. When the primary photon energy and thus photo-electron energy is low (from 20 to 35 keV), ionizations in tracks are denser and thus recombination becomes more important, leading to a higher H_2O_2 yield.

It may also be noted that, just as for the restricted dose enhancement, the radius of the GNP does not impact much the radiolytic enhancement. Although, at 20 keV, the enhancement significantly varies from ∼ 9 to ∼ 12 % with decreasing radius, this difference becomes negligible at higher energies. This is due to energy absorption within the GNP, which decreases with increasing photon energy (see Fig. D.2 of Appendix D.3).

10.3.2.2. Time dependence of radiolytic yields

Fig. 10.6 (panels (a) and (b)) displays the absolute yields of H_2O_2 and $^\bullet$OH (in nmol·J^{-1}) as a function of the time (in s) for different photon energies and a concentration of 1 mg·mL^{-1} of 5 nm GNPs, or without GNP ("water"). At very short time, H_2O_2 yield highly increases due to spurs and a high recombination of $^\bullet$OH, both with and without GNP, regardless of the photon energy. Then it increases with a lower slope and reaches a saturation at ∼ 10^{-8} s, followed by a very light decrease up to 10^{-6} s, due to its reaction with e^-_{aq} and, to a lesser extent, with $^-$OH. The yield of $^\bullet$OH decreases regularly without showing any particular structure at 10^{-8} s. This indicates that the decrease of $^\bullet$OH is not dominated by the production of H_2O_2. Indeed, in this time interval, the reaction $^\bullet$OH + e^-_{aq} dominates. For both chemical species, the variation of the yield with time is very similar regardless of the photon energy, with a higher increase of the yield with regard to the yield in pure water at 50 keV as previously stated.

Fig.10.6 (panels (c) and (d)) displays the relative enhancement of H_2O_2 and $^\bullet$OH as a function of the photon energy, for a 5 nm GNP at 1 mg·mL^{-1}, for 3 different times (1 ps, 1 ns and 1 µs).

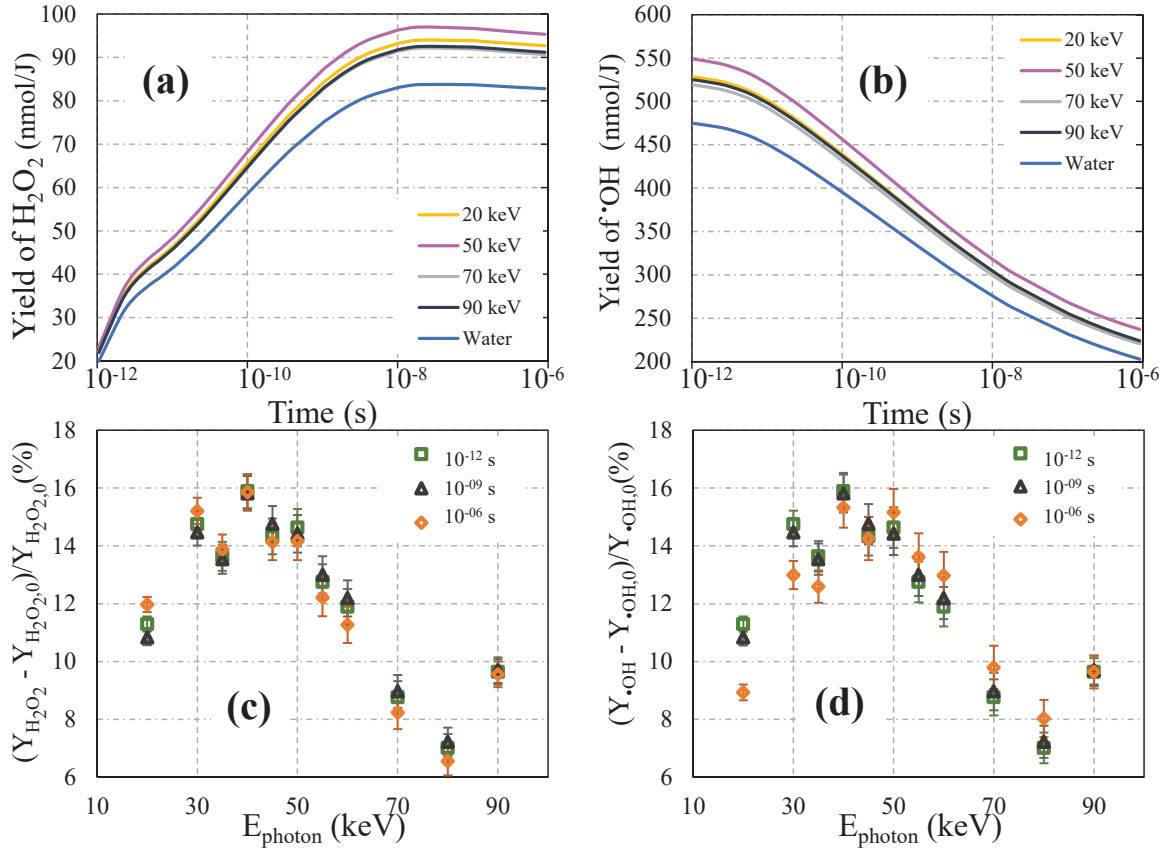

Figure 10.6.: On Fig.10.6 (a) and (b),$Y_{H_2O_2}$ and $Y_{•OH}$ yields (in nmol·J^{-1}) as a function of time (in second) for different photon primary energies for R_{NP} = 5 nm, and in pure water ($Y_{H_2O_2,0}$ and $Y_{•OH,0}$, photon energy 20 keV). On Fig.10.6 (c) and (d), H_2O_2 and •OH relative yield increase (in %) with regard to the yield in water in the absence of GNPs, as a function of the primary photon energy for R_{GNP} = 5 nm, for different times. The GNP concentration C_{GNP} was set at 1 mg·mL^{-1}.

Regardless of the time and chemical species, the chemical yield enhancements are very similar. Only small variations are observable, in particular at 20 keV for the •OH enhancement, which is lower at 10^{-6} s compared to other times. These results were observed for other sizes of NPs.

10.3.3. Dose-yield correlation

Fig. 10.7 (a) and (b) display the GNP contribution to the chemical yield, Y'_X, in nmol·J^{-1}(mg·mL^{-1})$^{-1}$, as a function of η', following Eq. 10.10 and Eq. 10.11. Results are displayed for various radii at 10^{-6} s, and for each radius the results are given for various E_{photon}. The sets of data for a fixed photon energy show the impact of the GNP radius. For fixed E_{photon}, each set of data appears linear. A linear fit provided correlation coefficients larger than 0.85 for •OH and larger than 0.95 for H_2O_2. On average, the slope was equal to 158 nmol·J^{-1} for •OH, with a standard deviation of 50 nmol·J^{-1}, and equal to 112 nmol·J^{-1} for H_2O_2, with a standard deviation of 34 nmol·J^{-1}. Besides, the set of data corresponding to lower photon energies, with the exception of 90 keV, showed a larger range of values for η' and Y'_X. This dispersion is due to the increase of energy loss within the GNP, which is more important when the primary photon energy is lower. Consequently, data with lower η' correspond to larger radii, within a set of data for fixed E_{photon}. Note that, for a fixed radius, and as shown previously in Fig. 10.4, data for high η' correspond to photon energies from 30 - 60 keV.

Overall, Fig. 10.7 (a) and (b) show that the increase of H_2O_2 and •OH yields due to the GNP are nearly linear with η', with the exception of low photon energies (20 - 35 keV). This may

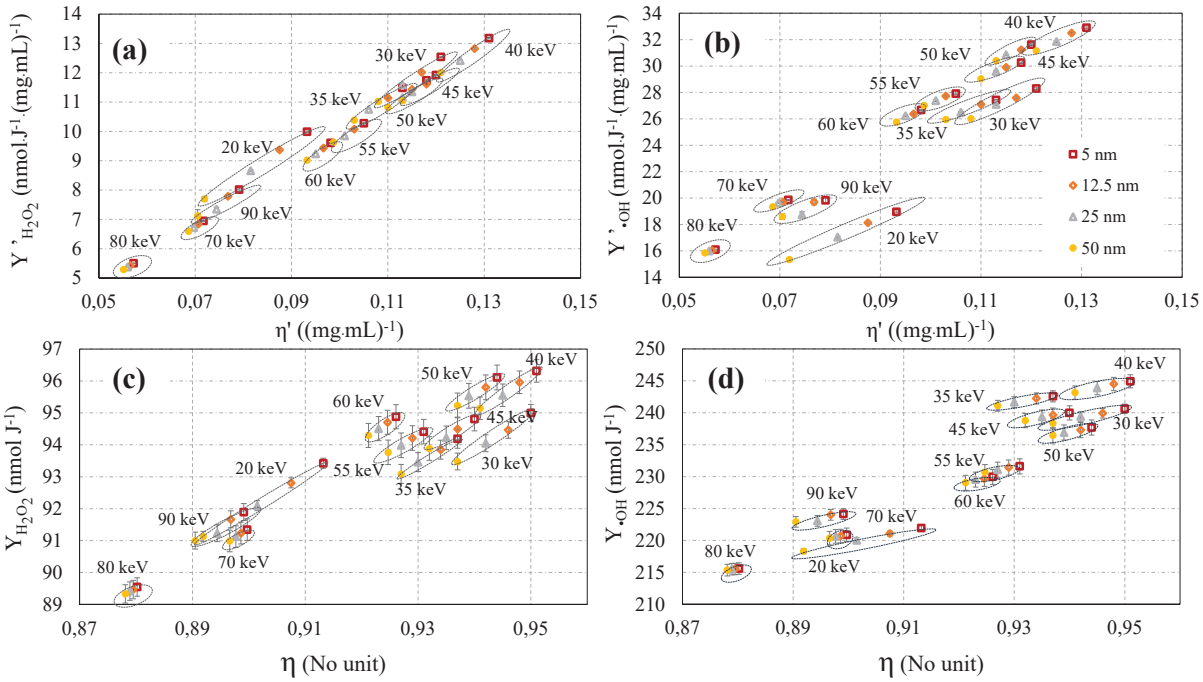

Figure 10.7.: Chemical yields of H_2O_2 and $^{\bullet}OH$ as a function of η' (panels (a) and (b)) or η (panels (c) and (d), for various GNP radii and photon energies, at 10^{-6} s. On panels (a) and (b), only the GNP contribution is displayed, Y'_X in nmol·J^{-1}(mg·mL^{-1})$^{-1}$. On panels (c) and (d), the total yields are displayed.

be explained by the variation of the primary photo-electron energy, and the dependence of both chemical species yields according to the electron energy, as displayed in Fig. D.1 of Appendix D.2: for E_{photon} = 20 keV, the primary electron energy is mainly comprised between 5.7 to 8 keV. At such energy, the yield of $^{\bullet}OH$ considerably drops, while the yield of H_2O_2 increases, compared to higher electron energies. Besides, the variation is more important for $^{\bullet}OH$ than H_2O_2, resulting in a more apparent variation for $^{\bullet}OH$ in Fig. 10.7. For photon energy ranging from 30 keV to 80 keV, the energy of the photo-electron increases, reaching $\sim$ 16 keV for E_{photon} = 30 keV and > 20 keV for larger photon energies. In this range of electron energies, the yields of both chemical species are more steady, thus resulting in the linear trend in Fig. 10.7. Note that, for E_{photon} = 90 keV, the photo-electron energy is on average equal to 9 keV.

Fig. 10.7 (c) and (d) show the yields of H_2O_2 (c) and $^{\bullet}OH$ (d) as a function of η, with the same parameters as for panels (a) and (b). We observe similar correlation with R_{NP} as for previous panels, and again the yields for large η correspond to mid photon energies (30 to 60 keV). However, the global correlation is more complex than previously, and H_2O_2 and $^{\bullet}OH$ yields do not strictly linearly increase with η, due to the dependence on the photon energy for both W and NP contributions. However, the dispersion of the yield for a fixed η remains modest. For instance, at η = 0.94, it varies from $\sim$ 94 to $\sim$ 96 nmol·J^{-1} for H_2O_2 and from $\sim$ 237 to $\sim$ 243 nmol·J^{-1} for $^{\bullet}OH$.

10.4. Discussion

In this work, we investigated the radical species (H_2O_2 and $^{\bullet}OH$) production for a concentration C_{NP} of GNPs in water under keV photon irradiation, using a MC simulation we developed. The variation of this quantity was systematically studied with regard to the photon energy (20 to 90 keV), the time following the primary photon interaction (10^{-12} to 10^{-6} s), and the NP radius (5 to 50 nm). We also calculated the restricted energy deposition, i.e. the energy corresponding

to the events: ionizations, dissociative excitations and attached electrons. Beyond the study of radical species production at macroscopic (cell) scale in the presence of GNPs, we correlated the enhancement of radical species production with the enhancement of the energy deposition.

In the context of NP enhanced-radiation therapy, MC simulations have been used to calculate energy deposition at tumour scale[6,56,57,157,158,190,198,206,253,288], and both at cellular and sub-cellular scale[43,85,142,155,195]. Both keV and MeV photon energies were investigated[191,193], and hadrontherapy combined with NPs were also studied[177]. However, the study of radical species production in presence of NPs has yet hardly been investigated. To our knowledge, one study investigated the production of radiolysis species for protontherapy combined with NPs[269]. In this study, the proton beam was directly shot from the entrance surface of the GNP, and radial distribution of chemical species were compared with the radial distribution of chemical species of a theoretical NP made of water.

Instead, in the present study, we investigated the production of chemical species under photon irradiation, and adopted a macroscopic approach, i.e. we calculated the average production of chemical species in a volume V of water containing a concentration C_{NP} of GNPs. Such calculations would be time prohibitive without several optimizations and simplifications. In our approach, we defined a system that would be applicable for *in solution* (i.e. colloidal GNPs) experiments, and to some extent to *in vitro* experiments. In particular, we considered that the probability that chemical species coming from two distinct tracks to react together was negligible. For *in solution* experiments, this condition may be experimentally reached as long as the dose remains low, or that the medium renewal is sufficient. This condition is easily obtained for standard experiment conditions (i.e. up to a maximum of few hundreds of Gy min^{-1}, and for doses of maximum a few dozens of Gy). For *in vitro* experiments, chemical species are quickly scavenged after their production. Typically, in a nucleus environment, the scavenging capacity of hydroxyl radicals was estimated at $\sim 4 \times 10^8$ s^{-1} [95]. Therefore, chemical species of one track react before they have the time to react with the primary radicals of another track. Though, note that the radicals produced by a photon interaction could react with a biomolecule produced or impact by the radicals produced by a precedent photon interaction. Extrapolations of results obtained from *in solution* system needs caution.

We also neglected the interaction between radical species and the GNP. This assumption was reasonable as the time of observation after the primary photon interaction was below 10^{-6} s, thus limiting the diffusion of chemical species. Besides, due to the complexity of *in vitro* systems, some compromises were mandatory in order to achieve reasonable computation time. In particular, we limited our study to low GNP concentration. In this work, results were applied to 1 $\mathrm{mg{\cdot}mL^{-1}}$. This concentration is in the range of reported colloidal GNP-water solution concentrations[110,251], and experimental *in vitro* intra-cellular concentrations[169,171,231]. The resulting ratio of the total volume of GNP divided by the total volume of water remained low (typically 4×10^{-5} at 1 $\mathrm{mg{\cdot}mL^{-1}}$). We also assumed that the GNPs were distributed homogeneously. Note that many *in vitro* experiments reported clusters of GNPs. These situations might be roughly represented by large GNPs. These two conditions (concentration and homogeneity) ensured that the dose deposition around one GNP was not influenced by the presence of another. These assumptions, which represent a typical *in solution* experiment[38,45,92,109,110,192,251], enabled to calculate the yields of radicals as a function of the NP concentration. Our calculations were performed for keV photons in the energy range 20-90 keV. Due to the high photon-gold photon-water cross section ratio, the effects are expected to be maximized at such energies. Besides, many *in solution*[36–38,45,47,51,75,76,92,109,110,192,251] and *in vitro*[26,39,55,68,134,135,226] investigations were done in this energy range.

For 1 $\mathrm{mg{\cdot}mL^{-1}}$ of gold, we obtained a relative dose increase which varied from $\sim$ 6 to $\sim$ 16 %, depending mostly on the photon energy but also, to a lesser extent, on the GNP radius for the lowest photon energies. This increase is due to the higher photon-gold interaction cross section compared to water, and most of the energy was deposited by the photo-electron, while

the contribution of Auger electrons overall remained below 4 %. These values are consistent with what has been reported in the literature. For instance, Lechtman *et al.*[170] reported that, for 5-100 nm diameter GNPs and a monoenergetic source of Pd-103 (20.48 keV), $\sim$ 6-8 mg·mL^{-1} of GNPs would be required to double the dose. In comparison, at 20 keV, we find that 8.8-11 mg·mL^{-1} would be necessary to double the dose deposition for 10-100 nm diameter GNPs. In another work[56], a dose enhancement factor of 3.8 to 5.6 was reported for an atomic mixture of gold-water, and gold concentrations varying from 7 to 30 mg·mL^{-1}, at 140 kVp (mean energy 57.9 keV). For our smallest GNP and an energy of 60 keV, we find enhancement ratios from 1.8 to 4.6 for 7-30 mg·mL^{-1}, which is sightly lower. This difference is partly due to the energy absorption within the GNP, which cannot be reproduced with an atomic mixture. This difference may also arise from the difference of physical models. Recently, Martinov *et al*[187] found, for a uniform mixture of 20-100 nm diameter GNPs and water, an enhancement ratio of 3.1 and 2.7 at 20 mg·mL^{-1}, 20 keV. In comparison, for a 100 nm GNP, we reached a dose increase of 2.8.

The chemical yields obtained showed that, as expected, the yield of $^{\bullet}$OH decreased with the time after the primary photon interaction varying from 10^{-12} s to 10^{-6} s, while the yield of H_2O_2 increased. Interestingly, both contributions coming from photon interacting with water, and photon interacting with gold atoms, reached yields that depended on the photon energy. We obtained chemical yield enhancements that were close to the dose increase. At 1 mg·mL^{-1} of gold, it varied from $\sim$ 11 to $\sim$ 14 % for H_2O_2 and $\sim$ 8 to $\sim$ 14 % for $^{\bullet}$OH, when the photon energy increases from 20 to 40-50 keV. Then, the enhancement decreased down to $\sim$ 6 % for H_2O_2 and $\sim$ 7.5 % for $^{\bullet}$OH, when the photon energy increased to 80 keV. At 90 keV, both enhancements increase back to $\sim$ 8-9 %. Interestingly, the chemical enhancements were slightly different depending on the chemical species: H_2O_2 was slightly over-produced compared to $^{\bullet}$OH for low energies by a few percents, while the situation was reversed for higher energies. These enhancements mostly depended on the photon energy, similarly to the dose enhancement, and to a lesser extent with the GNP radius and the time after primary photon interaction. As expected, the highest yields were obtained for the smallest NPs, as the energy lost in the NP was minimized.

Finally, a correlation between the yields of $^{\bullet}$OH and H_2O_2 and the dose deposition was investigated. The increase of chemical yields were not strictly linear with the increase of the dose deposition. However, the variation of chemical species for a fixed dose deposition remained very modest, i.e. less than 3 %. Regarding the contribution of the GNPs (i.e. the photon interacts with a gold atom), the increase of the chemical yield appeared linear with the increase of the energy deposition coming from GNPs, both for H_2O_2 and $^{\bullet}$OH, with the exception of low photon energies. Such behaviour was expected as the chemical species that are produce directly derive from the dose deposition in water.

These simulations did not account for a potential catalytic effect of the GNP that was suggested in some experimental studies that investigated the production of $^{\bullet}$OH for a colloidal solution irradiated by keV photons[110,251]. Our simulation could not reproduce the particularly high radiolytic enhancement obtained for low GNP mass concentrations, and further work is still required to better understand the origin of such effect. In a future work, we will study the different scenarios that might explain this discrepancy, and investigate the potential interaction between radiolytic chemical products and GNPs.

Despite a gap between our simplified system and an *in vitro* system, these results may provide further insights on the origin of the effect of GNP radiosensitization, in particular on the primary chemical stage, which has not been much investigated yet[35,124]. In cells, $^{\bullet}$OH is well known to be extremely reactive and induce irreversible damages, while H_2O_2 may diffuse on longer distances, and eventually react with cellular components. *In vitro* measurement of chemical species are not necessarily direct measurements of the primary chemical yield. In cells, amplification phenomena may occur due to complex biological mechanisms. However, a comparison of our simple system, with an experimental study comparing oxidative stress with *vs* without GNP, could help evidence

whether the GNP has an effect on the oxidative stress.

A study showed an increase of ROS production with GNPs when irradiating cells, as compared to without GNPs[104]. The authors used a fluorescent dye that measured ROS production (CM-H2-DCFDA) in SK-OV-3 cells. In the absence of GNPs, they obtained a 5.1-fold increase of the signal when irradiating with 8 Gy using a 90 kVp photon irradiator compared to without irradiation. They obtained a 8.3-fold increase of the signal in the presence of 14 nm thio-glucose GNPs. This led to a ratio with/without GNPs, $R = (8.3 - 1)/(5.1 - 1) = 1.75$. Although the incubation concentration they used was low (5 nM, i.e. 0.1 mg/mL), cells may reach a very high intra-cellular concentration, and they obtained a total of $\sim 1.6 \times 10^5$ GNPs per cell, which corresponds to ~ 4 pg/cell. Although the average volume of the cells is not provided, immortal cells have been reported to have a volume comprised between 0.5 to 4 $\times$ 10^{-9} cm[31]. Thus, intra-cellular concentration may be comprised from 1 to 8 mg·mL. Given this range of concentration, we find an enhancement that would vary from 1.06 (1 mg·mL and $E_{\text{photon}} = 70$ keV) to 2.12 (8 mg·mL and $E_{\text{photon}} = 50$ keV), a rather large range which includes the experimental enhancement. For a firm conclusion on whether primary chemical processes are sufficient to explain their measurements, additional information, mainly the average cellular volume and the energy spectrum of the photon beam, would be mandatory.

Overall, we found that macroscopic radiolytic yields are expected to be of the same order of magnitude as the dose increase. Note that, at this scale, we did not observed a particularly high H_2O_2 radiolytic yield, despite the dense clusters of Auger cascade that may favour $^{\bullet}$OH conversion. Some experimental *in vitro* studies reported that the dose increase was not always sufficient to explain the extent of the biological effects[135,171,191], suggesting other mechanisms. Theoretical calculations suggested that a local increase of the energy deposition in the vicinity of the NP would be responsible for the biological consequences[191]. In line with this suggestion, our next study investigates the local production of radical species around one GNP. The overproduction of radical species might attack cellular targets in the vicinity of the NP, which could result in a complex series of biological events. In addition, some studies reported ROS increase or decrease in the presence of GNPs, and without irradiation[40], that depended on the cell line and time of incubation. This suggests complex interactions between the GNPs and biological components, that trigger an oxidative stress independently from an irradiation. Other studies suggested that the deleterious effect of oxidative stress could be due to an indirect effect of GNPs, by interacting with cellular molecules thus decreasing the cellular detoxification system[41,217]. Therefore, one may distinguish three mechanisms: (1) enhanced chemical effects due to the increase of the number of primary chemical species induced by the presence of GNPs under irradiation, (2) local effect triggering a series of complex biological events, or (3) indirect chemical effects, that impacts the response of cells to radiation. This may be for instance related to a decreased cellular detoxification system. It is yet difficult to draw a general conclusion on which one dominates. This may be dependent on many parameters, in particular the intra-cellular concentration of GNPs, but also the characteristics of the GNP, or the cell line.

10.5. Conclusion

In this paper, we calculated free radical yields in presence of GNPs and under low keV photon irradiation, at macro/microscale, with a focus on $^{\bullet}$OH and H_2O_2 production. The aim was to investigate the impact of GNPs on water radiolysis and to systematically study the influence of various parameters, namely the photon energy (20 to 90 keV), the GNP radius (5 to 50 nm) and the time post-irradiation during the chemical phase (from 10^{-12} s to 10^{-6} s). We obtained, on a macro/microscopic (cell) scale, a yield enhancement comprised between 6 to 14 % for 1 mg·mL^{-1} of gold, that varied mostly with the photon energy and was maximum at 40-50 keV. Variations of the yields of a few percent were obtained with regard to the other parameters (GNP size,

[1] book.bionumbers.org/how-big-is-a-human-cell/

time after the primary photon interaction, and type of chemical species). This enhancement was strongly correlated with the dose deposition enhancement, although not strictly linear. These results enables to better quantify the amount of primary radicals produced for low-energy photon irradiation. Perspectives are wide. In a next study, we will focus on the chemical species yields on a nanometric scale around one GNP, for low-energy (keV) photons. Besides, coupled with the nanodosimetry results obtained in a previous study, these results will be used in the NanOx model to estimate the effect of GNPs for different scenarios in terms of cell killing.

11. Monte Carlo study of the free radical production under keV photon irradiation in the presence of gold nanoparticles. Part II: nanometric scale.

Authors: Floriane Poignant[a], Hela Charfi[a], Chen-Hui Chan[c], Elise Dumont[c], David Loffreda[c], Étienne Testa[a], Benoit Gervais[b], Michaël Beuve[a]

(a) Univ Lyon, Université Claude Bernard Lyon 1, CNRS/IN2P3, Institut de Physique Nucléaire de Lyon, 69622 Villeurbanne, France.

(b) CIMAP, unité mixte CEA-CNRS-ENSICAEN-UCBN 6252 BP 5133, F-14070 Caen, Cedex 05, France

(c) Univ Lyon, Ens de Lyon, CNRS UMR 5182, Université Claude Bernard Lyon 1, Laboratoire de Chimie, F-69342 Lyon, France

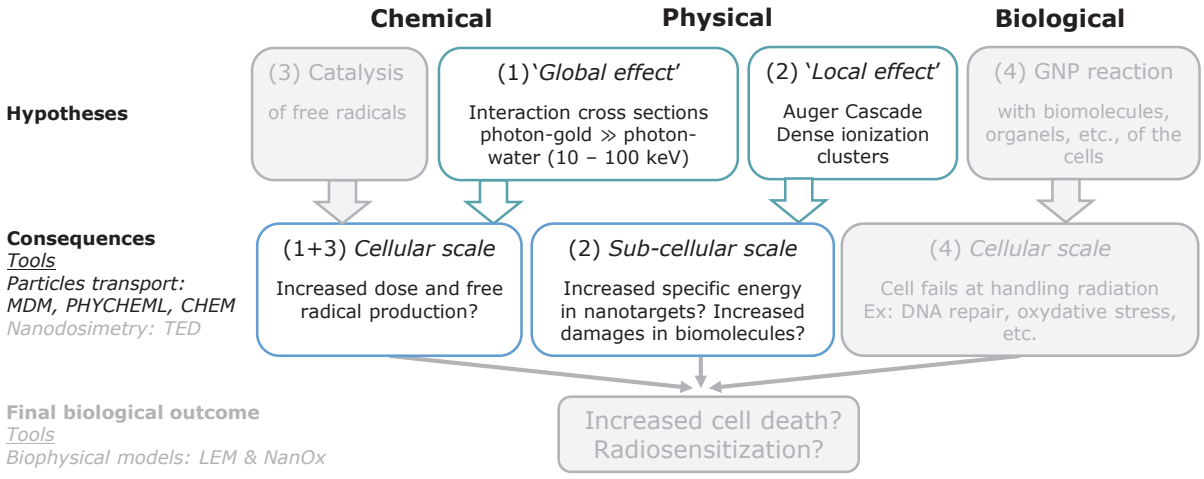

Figure 11.1.: List of mechanisms that may be responsible for GNP radiosensitization. This chapter focuses on both the global and local effects.

In chapter 10, we obtained primary chemical enhancement at the cellular scale that were mostly identical to the dose enhancement. In particular, Auger electrons did not induce an overproduction of H_2O_2, as the total amount of energy deposition it represented was too small to induce a visible effect. We wished to see whether, near the GNP, where the majority of Auger electrons deposit their energy, we would obtain more significant differences. This chapter therefore presents

the average number of chemical species produced following a GNP ionization, and their radial distribution. It was compared to the same results obtained for a theoretical nanoparticle made of water to have a reference to compare to. Following the classification of mechanisms responsible for GNP radiosensitizing properties introduced in Chapter 7 and as illustrated in Fig. 11.1, this work enables to better characterize both the global and the local effects. Indeed, quantification of the production of chemical species near the GNP enables to better understand the consequence of Auger electrons, while quantification of the production of chemical species far away from the GNP (up to thousands of nm) enables to better understand the impact of the photoelectric effect on the production of radicals throughout the entire cell. This chapter will be submitted as an article once the review by the different co-authors is completed.

Abstract

For the past two decades, gold nanoparticles (GNPs) have been investigated as a radiosensitizer agent for radiation therapy. Many theoretical studies have shown that GNPs increase the dose deposition for keV photon irradiation, both at macro and nanoscale, due in particular to a high photon-gold interaction probability. However, theoretical studies on the production of free radicals with GNPs are scarce. We studied the production of radiolysis chemical products ($^{\bullet}OH$ and H_2O_2) following an ionization event induced by a 20-90 keV photon in a nanoparticle (NP) made of either gold or water (WNP). This study was based on a Monte Carlo simulation which provides accurate electron transport down to low energy, both in water and gold. Radial concentrations show a large boost of chemical species concentration near the NP surface with values of the order of mM at 10^{-12} s after the primary photon interaction, followed by a decrease as the distance to the NP increases. However, somewhat surprisingly, this local boost was due to geometrical considerations, i.e., small volumes near the NP surface, independently of the NP material (water or gold). Indeed, compared to water, gold material showed on average a higher number of chemical species produced following an ionization, but these chemical species were produced mostly far away from the NP. To further characterize this local chemical boost, we estimated the concentration of chemical species reached in a target containing the NP following an ionization event. For targets of size of the order of 100 nm, this concentration was not necessarily higher for GNPs compared to WNPs. This means that Auger-electrons did not induce a particularly high boost of chemical species concentrations in the vicinity of the NP, compared to WNP. In conclusion, the local effect of GNPs is not to induce a higher effect near the GNP following an ionization, but rather to increase the chances of having this event to occur, due to a high probability of photon-gold interaction compared to water-photon interaction.

11.1. Introduction

Over the past two decades, the use of high-Z nanoparticles (NPs) have been of high interest due to their radiosensitizing properties. Several pre-clinical studies have shown the efficiency of gold NPs (GNPs) to enhance the effect of radiation therapy, in particular when using low energy (keV) X-rays[115,124]. The mechanisms of NP enhanced radiotherapy may originate from complex physical, physico-chemical, chemical and biological stages. The relative contribution of each stage remains under investigation[35]. Theoretical approaches, such as Monte Carlo (MC) simulations, may help to better understand how early physical and chemical stages could impact a biological system and lead, for instance, to an increase in cell death.

MC studies have shown that a significant increase of the dose deposition may be reached provided a sufficient concentration of GNPs, for keV X-rays. At such energies, the photo-electric effect dominates for high-Z materials and induce a high photon-NP atoms interaction probability, compared to biological tissues[56,57]. Other MC studies have suggested that heterogeneity of the dose deposition in the vicinity of NPs may further contribute to the enhancement, due to the release of low-energy electrons. Following a photo-ionization of a metallic NP, desexcitation processes result in the emission of a cascade of secondary electrons called Auger cascade. This boost would be responsible for a high energy deposition in the vicinity of the GNP, and has often been associated with GNP efficiency, by presumably inducing an increased biological effectiveness similar to that observed in hadrontherapy[56,57,171,191,193].

While there has been many MC studies on the physical stage and dose deposition, simulation studies of the chemical stage are scarce[269]. In particular, the impact of GNPs on water radiolysis has hardly been investigated, although it was suggested to be a crucial step that may connect the physical effect to the biological consequences[35]. In Chapter 10, we studied, on a macroscopic scale, the impact of GNPs on free radical yields for 20-90 keV photon irradiation. We showed that for a GNP concentration of 1 mg·mL, the increase of yields corresponded to the macroscopic dose enhancement. Yields were found to mostly depend on the photon energy and, to a lesser extent, on the time after the primary photon interaction, the NP radius and the type of chemical species. As MC studies on nanometric scale pointed out the importance of dose heterogeneity and, in particular, the high energy deposition in the vicinity of the GNP, we wished to focus, in this study, on the production of chemical species at the nanoscale. In particular we searched for any boost of radical production near the GNP and potential enhancement of radical recombination in regions of high radical concentration.

The goal of this work was thus to investigate, in a systematic way, the production of free radicals for keV photon irradiation in water around one GNP, following an ionization event. It was compared to the production of chemical species following an ionization event in a NP made of water (WNP), to study the specificity of gold material. We focused in particular on the production of hydroxyl radicals ($^{\bullet}OH$) and hydrogen peroxide (H_2O_2). To calculate these chemical species production, we implemented a MC simulation in order to reproduce the physical, physico-chemical and chemical steps at short time, e.g. up 1 µs following the ionization event. Various photon energies (20-90 keV) and GNP radii (5-50 nm) were investigated, to study their impact on the free radicals production.

This paper is organized as follows. In section 11.2, the MC tool and system considered are presented. Section 11.3 present the results. We studied in particular the radial distribution of the chemical species, both in terms of number of chemical species and concentration. Section 11.4 discusses the results before concluding in section 11.5.

11.2. Material and methods

11.2.1. System

The system considered for the calculation is described in Fig. 11.2. We defined a GNP placed at the centre of a volume of V filled with liquid water. For each photon energy, the half length of V was chosen to be larger than the maximum range of the most energetic photo-electron in water. The half length of the volume of interest hence varied between 15 µm at 20 keV and up to 160 µm at 90 keV. The GNP was ionized by a photon whose energy varied from 20 to 90 keV. A total of 4 radii of NPs (5 nm, 12.5 nm, 25 nm and 50 nm) and were chosen to systematically study the impact of the NP size on chemical species yields. To compared the specificity of gold material, the calculation was also performed for a hypothetical spherical NP made of water (WNP).

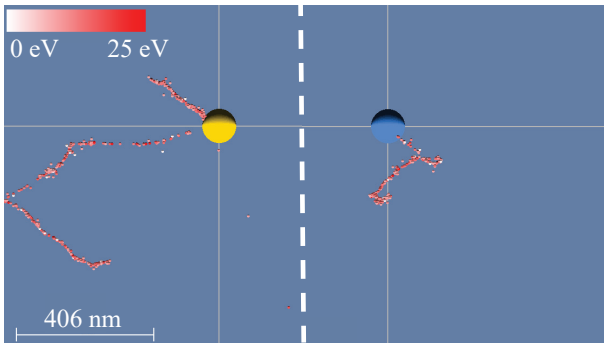

Figure 11.2.: View of the system zoomed around a WNP (right) or a GNP (left). Red-white dots represent energy-transfer points produced at the end of the physical stage, following the ionization of a NP. Note that this is an example for E_{photon} =90 keV and R_{NP} = 50 nm, and it is not representative of all the cases investigated.

11.2.2. Monte Carlo simulation for water radiolysis

We investigated in Chapter 10 the yields of free radicals in presence of GNPs under keV photon irradiation on a macroscopic scale, where the full description of the MC models is available. In short, 3 consecutive stages were mandatory to calculate the yield of chemical species. First, the physical stage occurred from 10^{-18} to 10^{-15} s after the primary photon interaction. Our model consisted of an event-by-event tracking of particles in the different media (water or gold). Photons were not explicitly tracked, and we only considered the photoelectric effect and the Compton scattering as they dominate at the photon energies investigated. The tracking of electrons were based on models whose description may be found elsewhere (see the work by Gervais *et al.*[106] and chapters 8 and 10). At the end of the physical stage, the water molecule may be found either excited (H_2O^*) or ionized (H_2O^+, H_2O^{2+} and H_2O^-), and the medium contained thermalized electrons (e_{th}). Any electrons in GNP for which the energy was to low to cross the surface of GNP were not longer tracked, as they did not lead to additional water molecule excitation or ionization.

This stage was followed by a physico-chemical stage (from 10^{-15} to 10^{-12} s), during which the medium (i.e. water) relaxes, leading to the production of primary chemical species. The different branching ratios of each molecular rearrangement are described elsewhere[106]. At the end of this stage, the outcome consisted of spatial distribution of chemical species: e^-_{aq}, H_3O^+, $^\bullet OH$, $^\bullet H$, H_2, ^-OH and O, with a majority of e^-_{aq}, H_3O^+ and $^\bullet OH$. The atomic oxygen was either at a fundamental state ($O(^3P)$) or at excited state ($O(^1D)$). Finally, at 10^{-12} s after the primary interaction, the chemical phase began and the primary chemical species diffused and interacted with each other. In our simulation, this phase was simulated up to 10^{-6} s. The method used to calculate the yields and optimize the computing time, as well as the list of standard chemical reactions of water radiolysis, are available elsewhere and will not be discussed in this paper[59,60,106]. More than 50 chemical reactions were possible.

11.2.2.1. Chemical species and reactions of interest

In this work, we focused on the production of $^\bullet OH$ and H_2O_2. $^\bullet OH$ is mainly produced at the physico-chemical stage, through the desexcitation of excited water molecules H_2O^* and ionized molecules H_2O^+. $^\bullet OH$ is the main source of H_2O_2 production, through the recombination process,

$$^\bullet OH + {}^\bullet OH \rightarrow H_2O_2$$

This reaction is mostly in competition with the reactions,

$$\mathrm{H} + {}^{\bullet}\mathrm{OH} \rightarrow \mathrm{H_2O}\ \mathrm{e^-_{aq}} + {}^{\bullet}\mathrm{OH} \rightarrow {}^{-}\mathrm{OH}.$$

11.2.3. Calculated quantities

We calculated 4 different quantities to characterize the distribution of chemical species around one NP. (1) We calculated the mean number of chemical species following one ionization event in the NP, differential in the radial distance $\frac{\partial R^1_X}{\partial r}$. (2) We defined the radial concentration of the chemical species X, as the concentration of X averaged over the spherical shell of radius r, thickness δr and centred around the GNP. This quantity is related to the previous one through the equation,

$$C_{r,X}(r) = \frac{1}{4\pi r^2 \delta r} \int_r^{r+\delta r} \frac{\partial R^1_X}{\partial r} \mathrm{d}r. \tag{11.1}$$

(3) We then defined the normalized cumulative radial distribution of the number of chemical species X per singly-ionized NP,

$$K_X(r) = \frac{1}{R^1_X} \int_{R_{\mathrm{NP}}}^{r} \frac{\partial R^1_X}{\partial r} \mathrm{d}r. \tag{11.2}$$

Note that $K_X(r)$ is normalized to 1 for r large. Finally, we calculated (4) the concentration per ionized NP, averaged over a spherical shell centred on the NP and limited by the NP surface and the radial distance r,

$$C_{sph,X}(r) = \int_{R_{\mathrm{NP}}}^{r} \frac{\frac{\partial R^1_X}{\partial r}}{\frac{4}{3}\pi(r^3 - R^3_{\mathrm{NP}})} \mathrm{d}r. \tag{11.3}$$

11.3. Results

This section presents the results of the chemical species production following a single ionization event either in a GNP or a WNP. The dependence on the following parameters are presented: (1) material of the NP (e.g. GNP or WNP), (2) photon energy E_{photon}, (3) size of the NP R_{NP}, (4) time following the ionization event t and (5) nature of the chemical species (e.g. ${}^{\bullet}\mathrm{OH}$ and $\mathrm{H_2O_2}$). In section 11.3.1 we show the average number of chemical species created following an ionization event in a GNP or a WNP. In section 11.3.2, 11.3.3 and 11.3.4 we present the radial distribution of chemical species with the different quantities introduced in section 11.2. Even if the absolute numbers of ${}^{\bullet}\mathrm{OH}$ and $\mathrm{H_2O_2}$ differ, the distributions are similar for both chemical species. Therefore, we chose to focus on ${}^{\bullet}\mathrm{OH}$ in a majority of the results.

11.3.1. Average number of chemical species per NP ionization

Tab. 11.1 gives the average number of chemical species ($R^1_{{}^{\bullet}\mathrm{OH}}$ and $R^1_{\mathrm{H_2O_2}}$) for one single ionization of GNP/WNP, for various E_{photon}, $R_{\mathrm{NP}} = 5$ or 50 nm, and both at 10^{-12} and 10^{-6} s. For the smallest GNPs, the number of ${}^{\bullet}\mathrm{OH}$ produced at 10^{-12} s varies from 721 ($E_{\mathrm{photon}} = 20$ keV), up to 2912 ($E_{\mathrm{photon}} = 70$ keV), due to an increase of the photo-electron energy. It then drops at

	10^{-12} s				10^{-6} s			
	$^{\bullet}$OH		H_2O_2		$^{\bullet}$OH		H_2O_2	
Energy	GNP	WNP	GNP	WNP	GNP	WNP	GNP	WNP
	R_{NP} = 5 nm							
20 keV	721	673	33	28	256	288	135	118
50 keV	2070	460	81	20	934	198	350	81
70 keV	2912	501	112	21	1385	211	482	88
90 keV	1560	618	63	25	671	264	270	108
	R_{NP} = 50 nm							
20 keV	571	674	25	28	212	288	107	118
50 keV	1960	455	76	19	906	196	329	80
70 keV	2820	500	107	21	1365	211	462	88
90 keV	1401	617	56	26	625	263	239	108

Table 11.1.: Average number of chemical species produced per GNP/WNP ionization for different times, photon energies and GNP radii. The statistical uncertainty was < 1 %.

E_{photon} = 90 keV, as there is a high fluorescence emission probability. This drop is due to the fact that we considered fluorescent photons as a lost energy in our modelled system. If the GNP is embedded in a volume of water larger than the photon mean free path, the photon would deposit its energy in the volume, but most of the time far away from the ionized GNP. The number of chemical species decreases with increasing GNP radius due to the energy loss in the GNP. This is particular visible at 20 keV: at 10^{-12} s, the number of $^{\bullet}$OH decreases from 721 to 571 when the radius of the GNP increases from 5 nm to 50 nm. The same trends are observed with H_2O_2.

For WNP, the number of chemical species is hardly impacted by the NP size. The number of chemical species, at fixed time, first decreases from 20 keV to 50 keV, before increasing again. The first drop is due to the fact that, at 20 keV, the photo-electric effect remains non-negligible, in which case all the photon energy is deposited. As the Compton effect becomes dominant, only part of the photon energy is deposited leading, on average, to a lower number of chemical species per ionization. This is then compensated by the increased photon energy and increased average primary electron energy.

The number of chemical species generated per NP ionization is systematically higher for GNPs than WNPs, with two exceptions. For E_{photon} = 20 keV and R_{NP} = 50 nm, the number of chemical species for GNPs in below that of WNP, due to a particularly high energy absorption within the GNP. At 10^{-6} s, E_{photon} = 20keV, and R_{NP} = 5 nm, the number of $^{\bullet}$OH for GNP is also below that of WNP, while it is not the case of H_2O_2. This denotes the fact that in this specific case, the recombination of $^{\bullet}$OH is particularly important, leading to a high number of H_2O_2. The largest difference between GNPs and WNPs is obtained at 70 keV. This is expected, as the predominant interaction in water is the Compton interaction. In this case, the photon does not transmit its entire energy during the interaction. In comparison, photo-electric interaction in gold dominates within the whole energy range.

11.3.2. Radial concentration

Fig. 11.3 shows the radial concentration $C_{r,X}(r)$ of the chemical species X following an ionization event in the NP, as a function of the distance to the NP surface $x = r - R_{NP}$. Results are displayed for GNP for various photon energies (panel (a)), various times following the ionization event (panel (b)) and various GNP sizes (panel (c)). Panel (d) compares the results of GNP and WNP, for various photon energies.

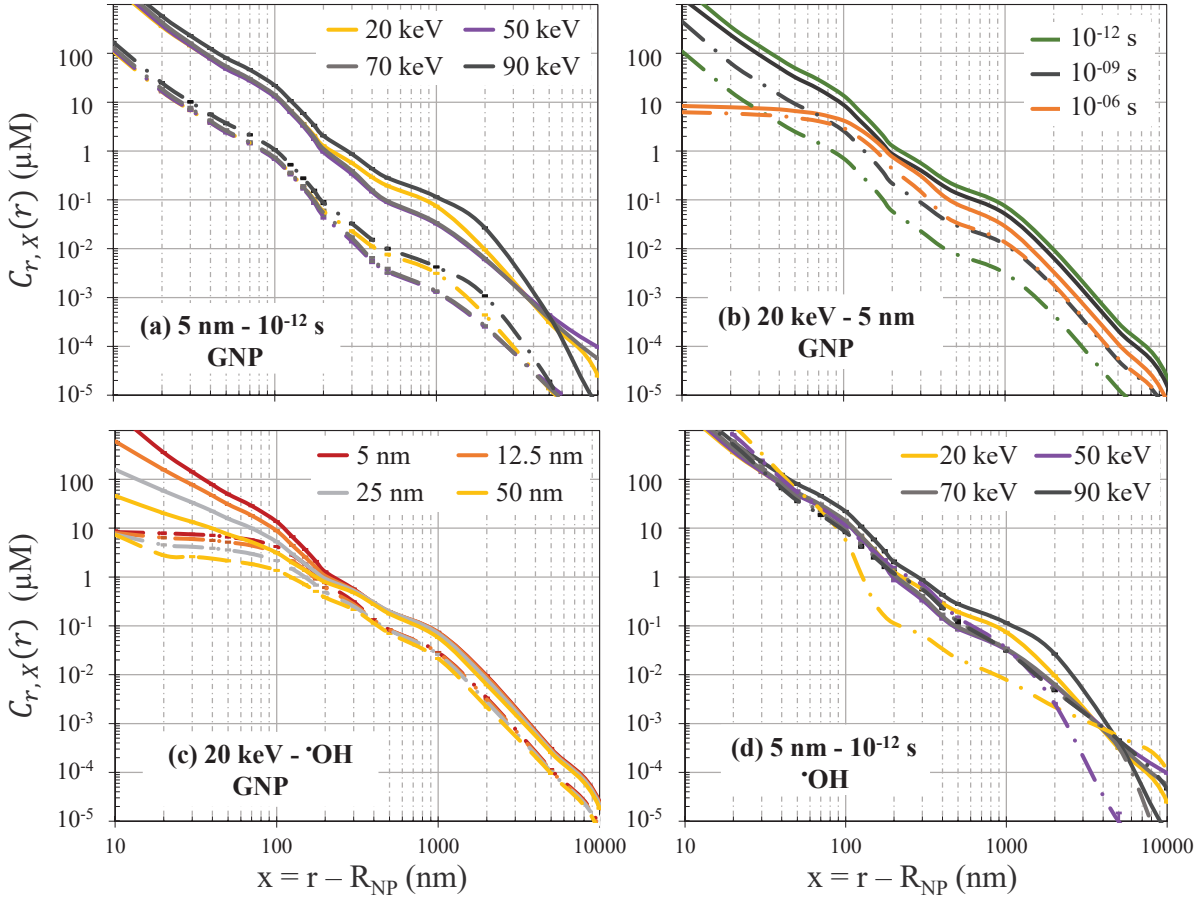

Figure 11.3.: Radial concentration $C_{r,X}(r)$ of the chemical species X as a function of x. In panels (a), (b) and (c) results are given for a GNP. Panel (a) and (b): solid line is $^{\bullet}$OH and dashed line H_2O_2. Panel (c): solid line is for $t = 10^{-12}$ s and dashed line is for $t = 10^{-6}$ s. Panel (d): solid line shows results for a GNP and dashed line for a WNP.

As panel (a) indicates, at $t = 10^{-12}$ s, the profile for the concentration $C_{r,X}(r)$ shows a peak near the ionization event (i.e., at small distance from the NP surface) with values of the order of mM at 10^{-12} s, and a severe drop for higher values of r. This decrease is proportional to $1/r^2$ and is due to the high increase of the volume when r increases. Such tendency is similar regardless of the photon energy, both at 10^{-12} s and 10^{-6} s (not shown here). This distribution is not specific to the material, as WNP shows the same tendency (see panel (d)). This high boost of concentration at the surface of the NP is not surprising, as it is located near the primary event. Besides, both $^{\bullet}$OH and H_2O_2 display similar radial concentration but with different amplitudes. As shown on panel (b), radial concentration of $^{\bullet}$OH decreases with increasing t over the whole r range, while overall it increases for H_2O_2. An exception is noticeable for $x < 200$ nm. For both chemical species, $C_{r,X}(r)$ drops from 10^{-12} to 10^{-6} s due to the diffusion process, which is of the order of 100 nm.

As seen in panel (c), R_{NP} impacts $C_{r,X}(r)$ below 200 nm, regardless of the photon energy, time t, chemical species or material. In this range, the radial concentration drops when the size of the NP increases. It arises from two reasons: for both WNP and GNP, the number of species was normalized to the volume of the shell. For a fixed x, the size of the shell considered increases with increasing GNP radius. The difference of shell volumes is, in proportion, more important when x is small and explains why both the GNP and WNP show a decrease of $C_{r,X}(r)$ for $x < 200$ nm. In addition, the decrease of $C_{r,X}(r)$ for GNPs is also due to an absorption of a part of the energy when the NP is ionized, as observed in the previous section. Mostly low-energy Auger electrons

are absorbed within the NP and therefore mostly impacts $C_{r,X}(r)$ at small x.

Finally, as shown in panel (d), the relative difference of $C_{r,X}(r)$ between WNP and GNP depends on the photon energy and the range of x considered. While $C_{r,X}(r)$ is dominated by high concentration near the NP and a decrease due to increasing distance from the position of the ionization, we observe small structures that appear around 100 nm and 1000 nm, and differences at long range that differ depending on the photon energy. These structures may be due to particular events such as the Auger cascade, but are difficult to analyse with $C_{r,X}(r)$. The Auger process and the cascade of chemical species that are produced consecutively, are distributed along a path that is rather linear. As radial concentrations decrease in $1/r^2$, the analysis of these specific structures is difficult. In the next section, we will focus on the number of chemical species normalized to the thickness of the shell rather than its volume, to better visualize these particular structures.

11.3.3. Radial distribution of the number of chemical species

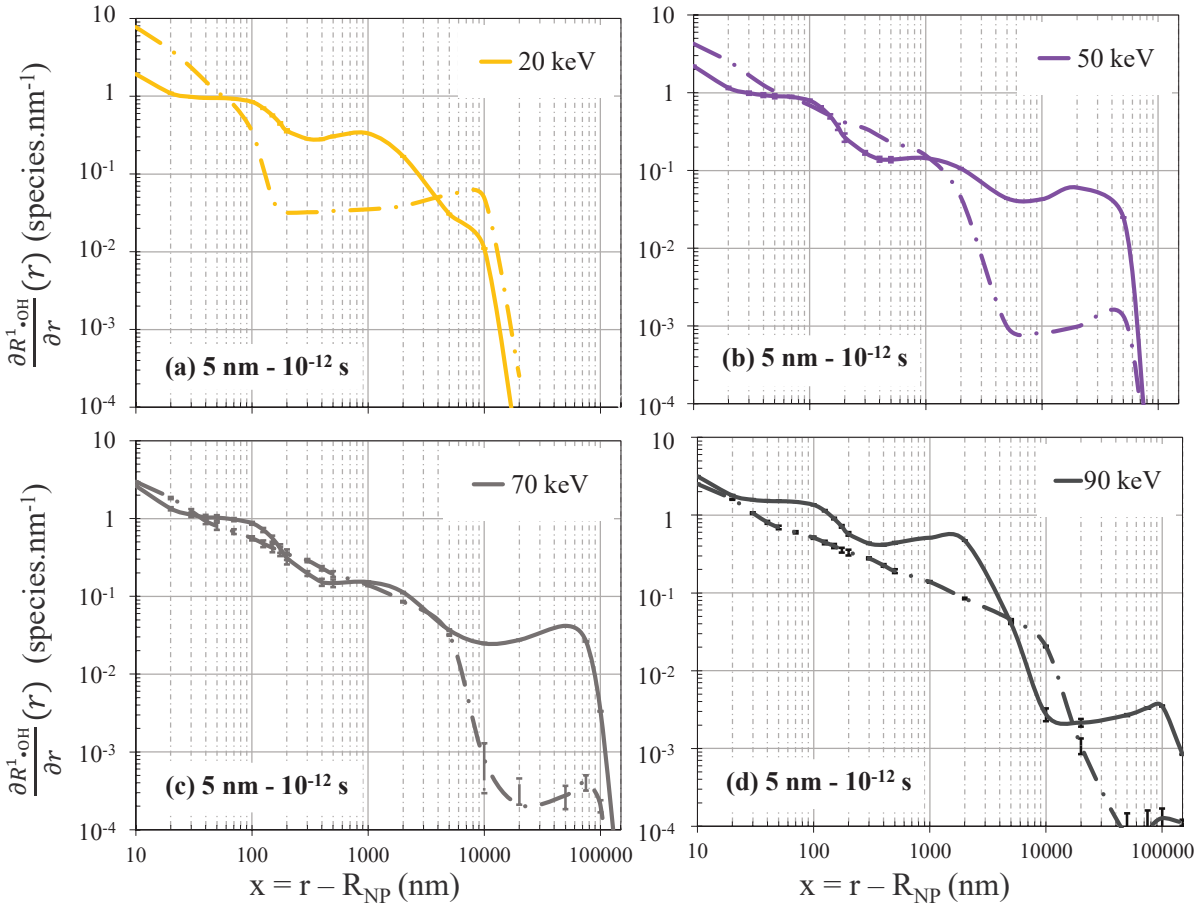

Figure 11.4.: Radial differential distribution of the number of chemical species $\frac{\partial R^1_{\bullet OH}}{\partial r}$ as a function of x. In each panel, results are given for a GNP (solid line) and a WNP (dashed line). Results are displayed for E_{photon} varying from 20 to 90 keV. $R_{\text{NP}} = 5$ nm, and $t = 10^{-12}$ s.

Fig. 11.4 displays the differential radial distribution of the number of chemical species $^{\bullet}$OH, $\frac{\partial R^1_{\bullet OH}}{\partial r}$, as a function of the distance to the NP surface x. This quantity enables to better visualize the dependence of the distribution of chemical species according to the photon energy, both for WNP and GNP.

For GNP, a peak is visible around $x = 100$ nm and 1000 nm, regardless of the photon energy, which corresponds to the end of the Auger electron path. Auger electrons are emitted with an energy that is mostly below 2 keV, which corresponds to ranges lower than ~ 160 nm. Some Auger

h

Atomic shell	K			L			≥ M		
E_{photon}	P.	E.	R.	P.	E.	R.	P.	E.	R.
20 keV	0	-	-	77	6-8	0.9-1.5	23	> 17	5.3-7.4
50 keV	0	-	-	77	17-18	5.3-6	23	> 47	35-42
70 keV	0	-	-	77	56-58	49-53	23	> 67	68-74
90 keV	77	9	1.8	16	76-78	88-92	7	> 87	> 111

Table 11.2.: Probability (P. in %) of ionizing the shell K,L or above, photo-electron energy (E. in keV) and range of the photo-electron in water (R. in µm) following an ionization event in gold with a photon of energy E_{photon}.

electrons are also be emitted with an energy comprised between 6-10 keV which corresponds to a range in water around 1000-2000 nm. Other peaks for large x are visible, and correspond to the end of photo-electron path. As shown in Tab. 11.2, these photo-electrons have different energies depending on the photon energy and the shell from which the electron is ejected. This phenomenon is particularly visible for $E_{\text{photon}} = 90$ keV. As the probability to ionize the K-shell is very high, many photo-electrons are ejected with an energy around 9 keV. These electrons therefore contribute to the boost of the number of chemical species observed around 1000 nm. Tab. 11.2 also explains the reason why $\frac{\partial R^1_{\bullet OH}}{\partial r}$ decreases: the photo-electrons that go the furthest away from the NP correspond to outer-shells (≥ M shell), which have a lower probability to be ionized.

For WNP, the progressive decrease of $\frac{\partial R^1_{\bullet OH}}{\partial r}$ is related to the energy distribution of Compton electrons. An exception is noticeable for 20 keV: as the photo-electric effect remains non-negligible, the radial distribution of chemical species is a combination of the radial distribution following a photo-electric event, for which the photo-electron has an energy $\sim$ 19.5 keV, and the radial distribution following a Compton event.

When comparing GNP and WNP, the first striking fact is that $\frac{\partial R^1_{\bullet OH}}{\partial r}$ remains higher at longer distances ($x > \sim$ 10 000 nm) for GNP. This is explained by the fact that, on average, the Compton-electron has an energy that is lower than a photo-electron. On the contrary, at very small distance ($x < 50$ nm), the number of chemical species is equivalent or even higher for WNP. This is particularly true at 20 keV, and due to the fact that Compton electrons may have very small energies, leading to a large number of chemical species produced near the surface. The boost of Auger electrons around 100 nm gives a higher number of chemical species for GNP than WNP, with ratios of GNP radial distribution over WNP radial distribution going from 1.3 for $E_{\text{photon}} = 50$ keV, up to 3 for 90 keV.

These observations are further confirmed by Fig. 11.5. It shows the relative cumulative number of chemical species as a function of the distance to the NP surface x. In other words, it represents the amount of chemical species that are located at a distance smaller than x from the NP surface. Similar structures and ranges are obtained as observed on Fig. 11.4. It is interesting to note that very low-energy Auger electrons represent only a very small fraction (< 15 %) of the total number of chemical species produced after a gold ionization. The large majority of chemical species are produced by the photo-electron, especially when the photon energy is large. Therefore, the Auger boost observed on Fig. 11.4 concerns only a minority of the total number of chemical species.

11.3.4. Spherical concentration

The spherical concentration per ionized GNP (in µM) is displayed on Fig. 11.6 as a function of the thickness of the shell. This quantity represents the concentration of chemical species a volume

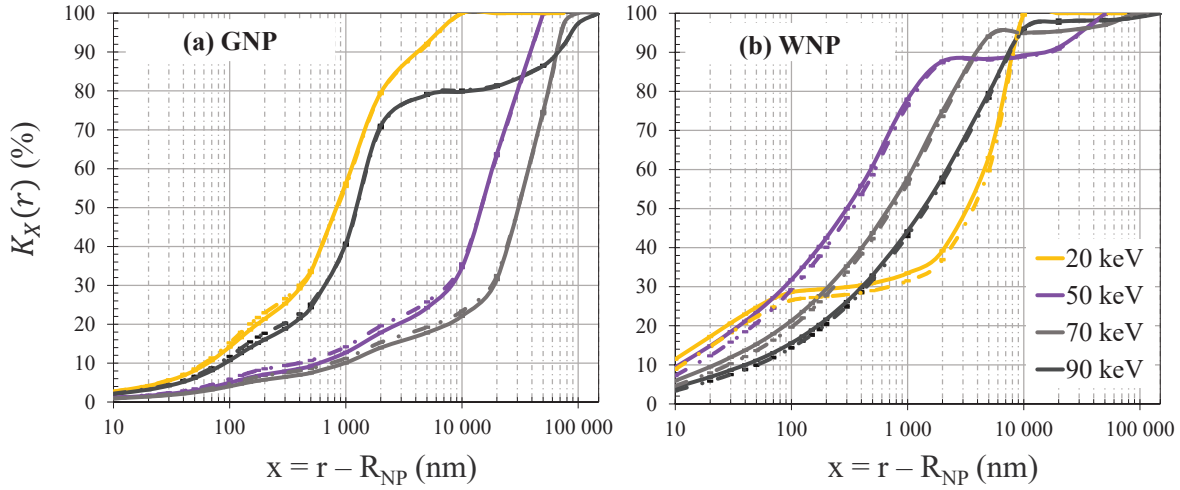

Figure 11.5.: Cumulative number of chemical species X, $K_X(r)$ ($^\bullet$OH in solid line and H_2O_2 in dashed line), as a function of x. Results are displayed for E_{photon} varying from 20 to 90 keV. Panel (a): GNP, panel (b): WNP. $R_{\text{NP}} = 5$ nm, and $t = 10^{-12}$ s.

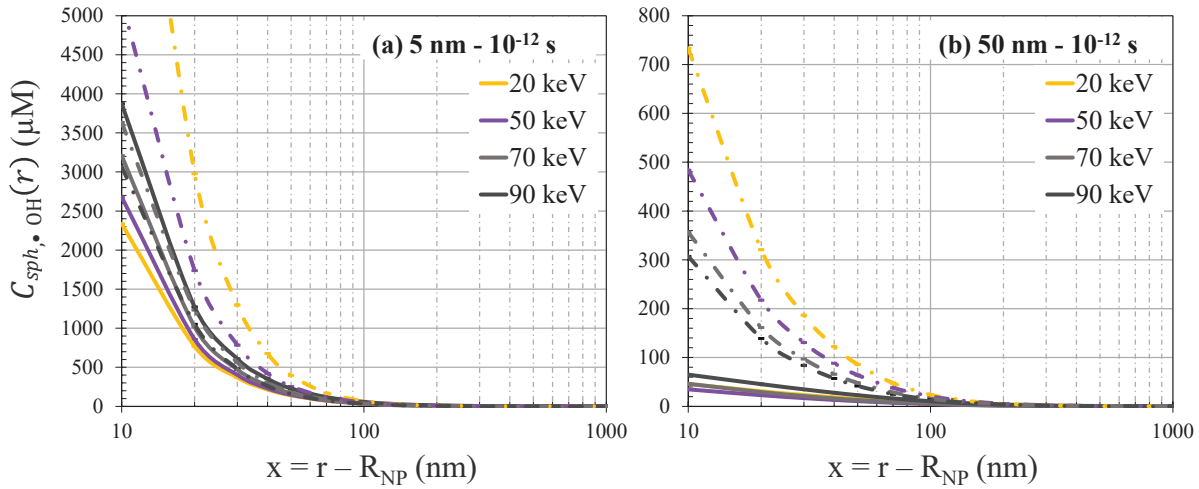

Figure 11.6.: Spherical concentration $S_{\bullet\text{OH}}(r)$ around an ionized NP a function of x, which represents the thickness of the concentric shell. Solid line: GNP. Dashed line: WNP. Both results are displayed for $t = 10^{-12}$ s, and panel (a) for $R_{\text{NP}} = 5$ nm, panel (b) for $R_{\text{NP}} = 50$ nm.

containing a GNP experiences in case of a GNP ionization, according to the size of the volume (e.g. the radius of the volume is r).

As previously observed, a small volume ($x = 10$ nm) containing a GNP experiences a large boost of chemical species concentration, due to the proximity of the ionization event. For small GNPs, $^\bullet$OH concentration is as high as a few mM at 10^{-12} s, and it decreases down to a few dozens of µM for the largest NP. When the time increases, this concentration drops down to a few µM due to the diffusion of chemical species, and the recombination of $^\bullet$OH. For larger volumes, the concentration of $^\bullet$OH also decreases, down to tens of µM for $x = 100$ nm, hundreds of nM for $x = 1000$ nm and of the order of 0.1 nM for $x = 10\,000$ nm.

Tab. 11.3 displays the relative difference of spherical concentration of GNP to that of WNP,

$$\frac{C_{sph,X,\mathrm{GNP}}(r) - C_{sph,X,\mathrm{WNP}}(r)}{C_{sph,X,\mathrm{WNP}}(r)}, \tag{11.4}$$

in %, for $^{\bullet}$OH species, at $t = 10^{-12}$ s, and for the two extrema sizes of NPs investigated. The same trends were observed for H_2O_2 or higher times. As previously observed, for $R_{\mathrm{NP}} = 5$ nm, the spherical concentration of WNPs for small volumes (10 and 100 nm thick) are higher than that of GNP, when the photon energy is equal to 20 or 50 keV. On the contrary, it is higher for GNP if the photon energy is equal to 70 or 90 keV. However, when the size of the NP increases, due to non negligible energy loss in the GNP, the relative difference of concentrations become negative for small volumes, regardless of the photon energy. When the considered volume increases ($x = 1000$ nm), the concentration for GNPs tends to be higher than that of WNP for small GNPs, but it depends on the size of the GNP. For very large volume thickness (10 µm), the concentrations are higher for GNPs, with one exception ($E_{\mathrm{photon}} = 20$ keV and $R_{\mathrm{NP}} = 50$ nm). This translates the fact that, on average, GNPs generate more chemical species than WNP following an ionization event.

X	10 nm	100 nm	1 000 nm	10 000 nm	100 000
$t = 10^{-6}$ s - $R_{\mathrm{NP}} = 5$ nm					
20 keV	-68	-65	50	-11	-11
50 keV	-60	-57	-40	78	370
70 keV	-21	-26	-14	38	555
90 keV	9	21	130	109	150
$t = 10^{-6}$ s - $R_{\mathrm{NP}} = 50$ nm					
20 keV	-85	-77	32	-27	-27
50 keV	-88	-83	-56	64	362
70 keV	-78	-71	-38	20	547
90 keV	-51	-30	134	94	134

Table 11.3.: Relative difference of spherical $^{\bullet}$OH concentration in a X nm thick shell around a nanoparticle in %.

11.4. Discussion

In this work, we investigated the production and distribution of radical species following an ionization by keV photons of a GNP embedded in a volume of water. Different quantities were calculated: the differential radial concentration of chemical species, the radial distribution of the number of chemical species and the spherical concentration of chemical species. We focused in particular on the chemical species $^{\bullet}$OH and H_2O_2. The variation of these quantities were systematically studied with regard to the photon energy (20 to 90 keV), the time following the beginning of the irradiation (10^{-12} to 10^{-6} s), and the NP radius (5 to 50 nm). In order to study the specificity of gold material, the calculation was also performed for a hypothetical NP made of water. The goal of this work was to study at a nanometric scale the impact of the presence of GNPs on the radical species production. In particular, it aimed at studying the Auger cascade specificity emitted in the vicinity of the GNP.

Radial concentrations showed a high boost near the NP surface which rapidly decreased when the distance to the NP increased. This distribution was due to a bias between the original position of the ionization event and the distance from which the concentration was calculated. As a consequence, both GNPs and WNPs showed very similar radial concentration profiles, and in particular high concentrations near the NP surface. This boost sharply decreased when the time following the ionization event increased, due both to the diffusion of chemical species and their

reaction. This trend was already observed before[269].

Different specificities were obtained for gold compare to water:

(1) We observed that, on average, an ionization in a GNP produced more chemical species than an ionization event in a WNP, as a photo-electron caries more energy than a Compton electron, the later dominating water-photon interactions at the energy investigated. Besides, as photo-electrons are more energetic, GNP radial concentrations remained higher at very long distances compared to that of WNPs.

(2) Chemical species produced by the interaction of Auger-electrons with water molecules following an ionization event in GNPs, represented only a very small proportion of the total number of chemical species. It induced a minor boost of the differential radial concentration around 100 nm and 1000 nm, that was however relatively small when comparing to the concentration of chemical species for WNPs.

(3) Both $^{\bullet}OH$ and H_2O_2 had very similar distributions. In particular, H_2O_2 was not particularly higher due to Auger electrons, as one may have expected. Indeed, high LET radiations are known to favour the production of H_2O_2, as they produce dense clusters of ionization that favour the recombination of $^{\bullet}OH$. However, the proportion of Auger-electrons was too small to induce a significant boost of H_2O_2.

(4) As spherical concentrations showed, the concentration of chemical species was not necessarily higher for GNP compared to WNP near the ionization event (within few hundreds of nm), despite the Auger electron cascade. This was particularly true for large GNPs, for which the absorption of the low-energy electrons within the GNP showed a drop of the number of chemical species near the surface. Therefore, a cellular target located near an ionized GNP does not benefit from a higher concentration of chemical species, compared to the ionization of water. It only benefits from a higher occurrence of this event, as gold-photon interaction has a higher cross section than water-photon interaction at these energies. In other words, the major effect of gold is not to induce a high boost of concentration of chemical species compared to water, but to make the probability of an ionization event to happen more likely.

The spherical concentration of chemical species may be used to estimate the chemical boost cellular components may experience when containing internalized GNPs. Typically, a thickness of 10 nm may represent the dimension of a membrane, a DNA Double Strand Break (DSB) or a histone; a thickness of 100 nm may represent the dimensions of an organelle (mitochondria, lysosome); a thickness of 1000 nm may represent the dimensions of a large organelle (large lysosome) or a chromosome; a thickness of 10 000 nm may represent a nucleus. Note that biological media contain many scavenger elements. They may also catalyse complex reactions inducing an additional boost of chemical species production. Our calculation may therefore only characterize the primary chemical events at very short time following an ionization event. As *in vitro* data showed, GNPs often appear clustered together in vesicles[26,53,55,138,231], which could roughly be represented by large GNPs. As our calculation showed, large GNPs decrease the number of chemical species following an ionization event, especially in the vicinity of the NP. At first sight, it thus appears less advantageous to have aggregates rather than isolated GNPs. However, if NPs accumulate in a specific zone of the cell, an accumulation of damages may occur near the NP, due to a high probability of photon-gold interaction. Such accumulation might be deleterious for the cell. In particular, when internalized, NPs are often localized within lysosomes. Our calculation may help provide useful information on the amount of chemical species primarily produced within these vesicles. The accumulation of the chemical species $^{\bullet}OH$ in lysosomes that are produced in the vicinity of the NP could attack lysosomial membranes. Besides, lysosomes contain iron, and the H_2O_2 that are produced near the GNP could be converted back to $^{\bullet}OH$ through a Fenton

reaction, and thus further attack the lysosomal membrane[8]. The release of lysosomal content (redox-active iron, or hydrolytic enzymes) could trigger several biological events eventually leading to cell death[8,24].

In this study, we did not consider any possible catalysis events at the surface of the GNP. Irradiation of colloidal solution containing GNPs suggested that a larger amount of $^{\bullet}$OH could be produced than predicted by theoretical calculation[110,251]. The mechanisms behind these measurements will be investigated in a future work.

11.5. Conclusion

In this paper, we investigated the production and distribution of chemical species following the ionization of a GNP embedded in water by 20-90 keV photons. Results were compared to the one for a NP made of water, to study the specificity of gold material. Our calculation showed a large production of chemical species near the GNP that was not specific to the gold material but mostly due to the spatial correlation between the ionization in the NP and the region where the chemical species were observed, i.e. around the NP. While a minor boost of chemical species production was noticeable around 100 nm and 1000 nm from the GNP surface due to Auger electrons, these boosts were mostly insufficient to generate a significant increase of the chemical species concentration for a small regions (of the order of 100 nm) around the ionized GNP, compared to the case of an ionized WNP. This suggests that the impact of Auger-electron in the vicinity of GNPs is minor. The local effect of GNPs is therefore not to induce a higher number of chemical species near the GNP following an ionization (compared to a water ionization), but rather to increase the chances of having this ionization, due to a high probability of photon-gold interaction compared to water-photon interaction.

12. Theoretical investigation on the origin of the coumarin fluorescence enhancement under photon irradiation for colloidal gold nanoparticle solution

Authors: Floriane Poignant[a], Chen-Hui Chan[c], Elise Dumont[c], David Loffreda[c], Étienne Testa[a], Benoit Gervais[b], Michaël Beuve[a]

(a) Univ Lyon, Université Claude Bernard Lyon 1, CNRS/IN2P3, Institut de Physique Nucléaire de Lyon, 69622 Villeurbanne, France.

(b) CIMAP, unité mixte CEA-CNRS-ENSICAEN-UCBN 6252 BP 5133, F-14070 Caen, Cedex 05, France

(c) Univ Lyon, Ens de Lyon, CNRS UMR 5182, Université Claude Bernard Lyon 1, Laboratoire de Chimie, F-69342 Lyon, France

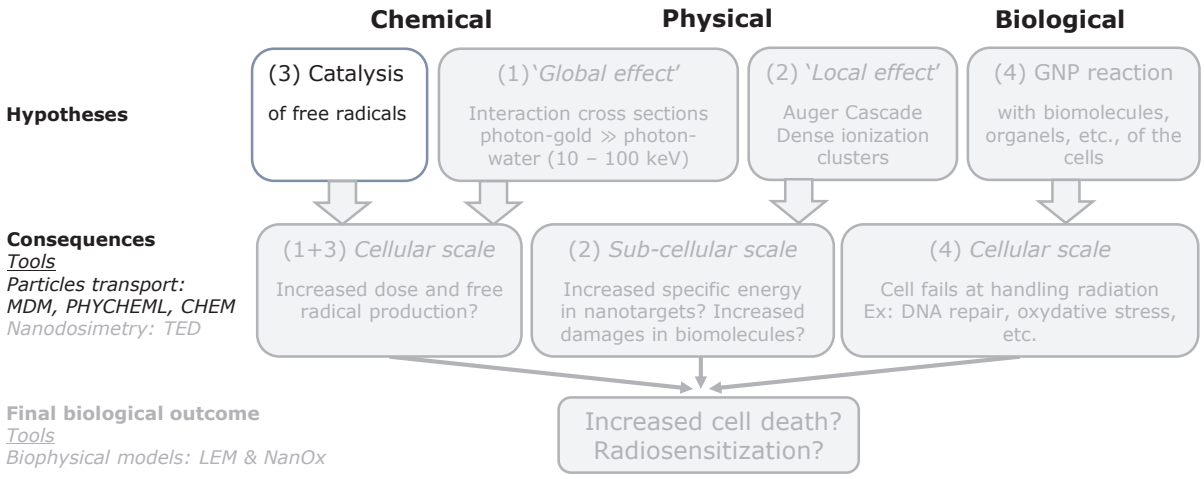

Figure 12.1.: List of mechanisms that may be responsible for GNP radiosensitization. This chapter focuses on potential catalytic properties of GNP to overproduce radicals.

Chapters 10 and 11 showed that GNPs did not induce an overproduction of primary hydroxyl radical yields higher than the dose enhancement would predict. It remained impossible to explain the unexpectedly high fluorescent yields that were experimentally obtained following the irradiation of a colloidal solution of GNPs mixed with coumarin molecules, used to measure hydroxyl radical yields[109,110,251]. Using the same Monte Carlo *in silico* approach developed in chapters 10 and

11, and analytical methods, this chapter presents the study of different scenarios to explain the experimental results. Following the classification of mechanisms responsible for GNP radiosensitizing properties introduced in Chapter 7 and as illustrated in Fig. 12.1, this work enables to investigate potential catalytic properties of GNPs. At the end of the chapter, an explanation is proposed to explain the high fluorescent yield obtained by experimental works. This chapter will be submitted as an article once the review by the different co-authors is completed.

Abstract

Over the past two decades, gold nanoparticles (GNPs) have been studied for their radiosensitizing properties. Among the possible origins of this effect, GNPs are believed to enhance radiation therapy through chemical mechanisms. In particular, they may enhance the production of radical species. Colloidal solutions of GNPs combined with scavengers may be used to measure such a chemical enhancement. In particular, the coumarin molecule has been used to measure the production of $^{\bullet}$OH for a colloidal GNP solution irradiated by X-rays. When reacting with $^{\bullet}$OH, coumarin molecules undergo a series of chemical reactions that lead, among many products, to the production of a fluorescent molecule. Experimental studies have shown unexpectedly high fluorescent yields for irradiated GNP colloidal solutions, whose origins are yet not understood. In this study, we propose a theoretical approach based on Monte Carlo and analytical tools, to test the different scenarios that have been suggested in the literature. Investigating four scenarios, we show that only one could reproduce experimental results. This scenario suggests that the high fluorescent yield is obtained due to interference between a coumarin intermediate by-product and the GNPs, rather than an overproduction of $^{\bullet}$OH.

12.1. Introduction

The use of high-Z nanoparticles (NPs) in cancer radiation therapy has demonstrated its efficacy on many biological systems, from *in vitro* to *in vivo* experiments[35,124]. The identification of the origin of the radiosensitizing effect of NPs is challenging, due to the complexity and variability of the experimental systems and the many parameters that may impact the outcome. This new therapy may rely on complex physical, chemical and biological mechanisms[124]. At low-energy (keV), photons have a higher probability to interact with the NP atoms through the photoelectric effect, compared to biological tissues. This results in a higher dose deposition[56,57], and consequently a higher production of free radicals (such as $^{\bullet}$OH) that are toxic for cells (see chapters 10 and 11). While two NPs have made it to clinical trial, there is a need to better quantify the physical and chemical steps and their consequence on a biological level to optimize this treatment and allow a safe transition to clinical routine[35]. As physical and chemical mechanisms occur at very short time and spatial scale, a direct experimental measurement is challenging. Although they do not represent the complexity of cellular *in vitro* experiments nor potential interaction between NPs and cellular components, experimental measurements of the radical species produced in NP colloidal solutions may help to better understand the early mechanisms and in particular the production of toxic radical species. Recently, many *in solution* irradiation experiments with colloidal gold NPs (GNPs)[47,51,75,76,109,110,251] put in light the potential importance of this chemical step. As further developed in the section 12.2, some experiments reported unexpectedly high measurements of the fluorescent signal of a coumarin by-product produced from the reaction of a $^{\bullet}$OH species with a coumarin molecule. This enhancement can not be explained by a pure energy deposition

enhancement, and its origin remains unknown. In this study, we propose to investigate different scenarios that could explain this enhancement, with Monte Carlo (MC) simulations and analytical methods.

This paper is organized as follows. Section 12.2 presents an overview of experimental results of colloidal GNP solution irradiation mixed with coumarin molecules. The different scenarios we propose to investigate to explain the unexpected high fluorescent yield are introduced. In section 12.3, we present the different tools used for our calculation. Section 12.4 presents, for each scenario, the approximations and results and discuss their validity with regard to experimental results. Finally, we conclude in section 12.5 on a plausible scenario.

12.2. Overview of the experimental results

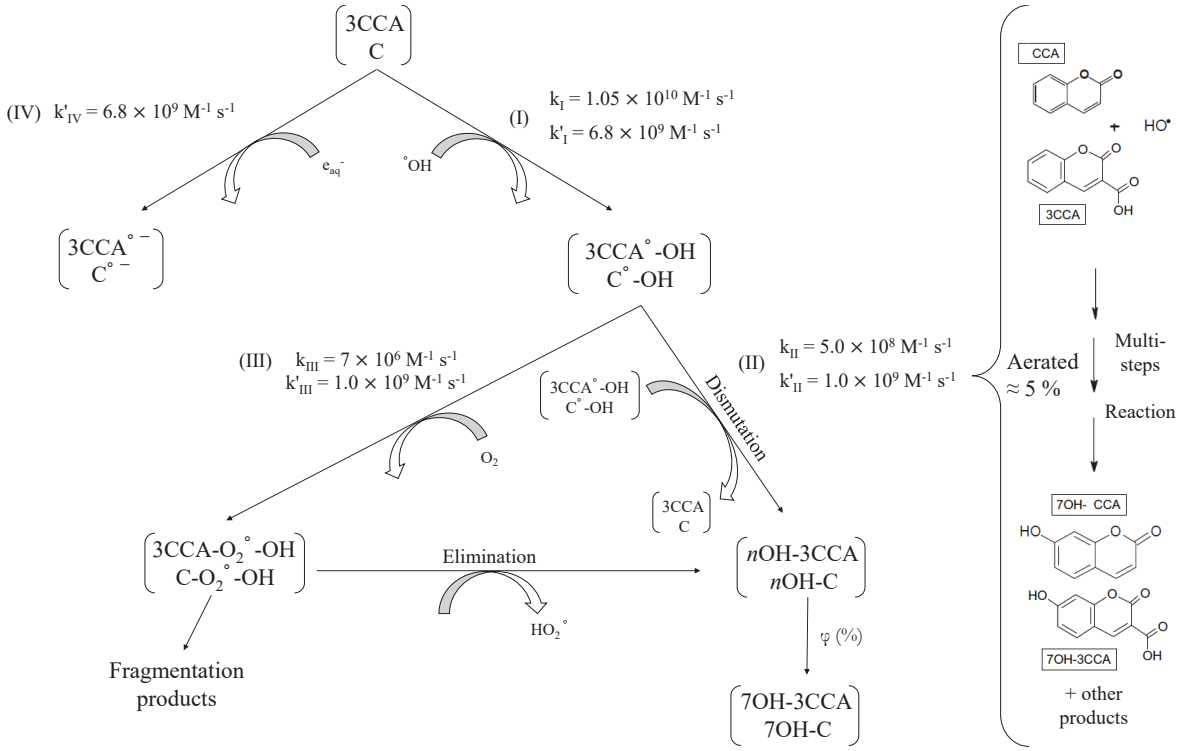

Figure 12.2.: Detailed scheme of reaction and conversion from C/3CCA + •OH to 7OH-C/7OH-3CCA adapted from[14,108,183,284]. The reaction constants are: $k_{\mathrm{I}} = 1.05 \times 10^{10}$ M^{-1} s^{-1}/$k'_{\mathrm{I}} = 6.8 \times 10^{9}$ M^{-1} s^{-1}; $k_{\mathrm{II}} = 5 \times 10^{8}$ M^{-1} s^{-1}/$k'_{\mathrm{II}} = 1.0 \times 10^{9}$ M^{-1} s^{-1}; $k_{\mathrm{III}} = 7 \times 10^{6}$ M^{-1} s^{-1}/$k'_{\mathrm{III}} = 1.0 \times 10^{9}$ M^{-1} s^{-1}.

Reference	GNP	Energy	Dose rate	Maximum time of irradiation
Sicard *et al.*[251]	32.5 nm	20 keV	12 Gy · s^{-1}	15 s
Gilles *et al.*[108,110]	32.5 nm	17.5 keV	0.33 Gy · s^{-1}	40 s
Cheng *et al.*[51]	3, 7 and 30 nm	100 kVp	0.055 Gy · s^{-1}	30 min

Table 12.1.: Conditions in the different experiments of GNP colloidal solution irradiation with coumarin. The maximum time of irradiation was calculated with the maximum dose delivered and the dose rate[110,251]. Note that Gilles *et al.* did not use a mono-energetic beam and the average energy is provided.

The experimental measurement of free radicals may be done by direct measurement with a pulsed beam or indirect measurement by the scavenger method[284]. In the present context, two research groups have focused on the measurement of radiolysis products in colloidal solutions of

GNPs, from University Paris-Sud[109,110,251] and from University of California[47,51,75,76] by indirect measurement with scavengers. The experimental main parameters are provided in Tab. 12.1. The measurements were done with coumarin (C) molecules[109,110,251], 3-carboxylic acid coumarin (3CCA) molecules[51,75,76], or with the spin trap BMPO[47]. In this work, we focused on the results obtained with C and 3CCA, and will equally refer to these similar molecules as Cou.

The Cou molecule reacts with $^{\bullet}$OH to form, among many products (5OH-Cou, 7OH-Cou, 5/8OH-Cou, etc.), a fluorescent molecule (7OH-Cou). The reaction that leads to the production of this fluorescent molecule is a multi-step reaction as illustrated in Fig. 12.2. The coumarin assay enables to detect quantities down to 30 nM of hydroxyl radicals[251]. The reaction between $^{\bullet}$OH and coumarin is considered pseudo first order[14], and the constant of reaction with $^{\bullet}$OH was reported to be comprised between 5.6×10^9 M^{-1} s^{-1} and 1.05×10^{10} M^{-1} s^{-1} [14,42,51,251]. In pure water, under aerated conditions and in the absence of any other scavengers, Baldacchino *et al.*[14] found that 5.6 nmol $\cdot$ J^{-1} of 7OH-3CCA represented 100 nmol $\cdot$ J^{-1} of $^{\bullet}$OH (i.e., ratio of 5.6 %), in close agreement with Newton *et al.*[210] who found a ratio of 4.7 %. There has been reports of dependence on the yield of 7OH-3CCA/7OH-C according to the dose rate[61,183]. This dependence was attributed to metal impurities. The Fenton reaction, that decomposes H_2O_2 into $^{\bullet}$OH, occurs in presence of metal impurities and has a slow reaction constant (76 $M^{-1}s^{-1}$). It is thus favoured at low dose rate. It is also important to note that the reaction between Cou and $^{\bullet}$OH depends on the amount of dissolved gases such as O_2 in water[61,108,183]. For instance, Gilles *et al.*[108] found similar 7OH-C yields for air, O_2-saturated and N_2O conditions, while it was doubled for N_2O atmosphere and divided by two for N_2 atmosphere (i.e. no oxygen).

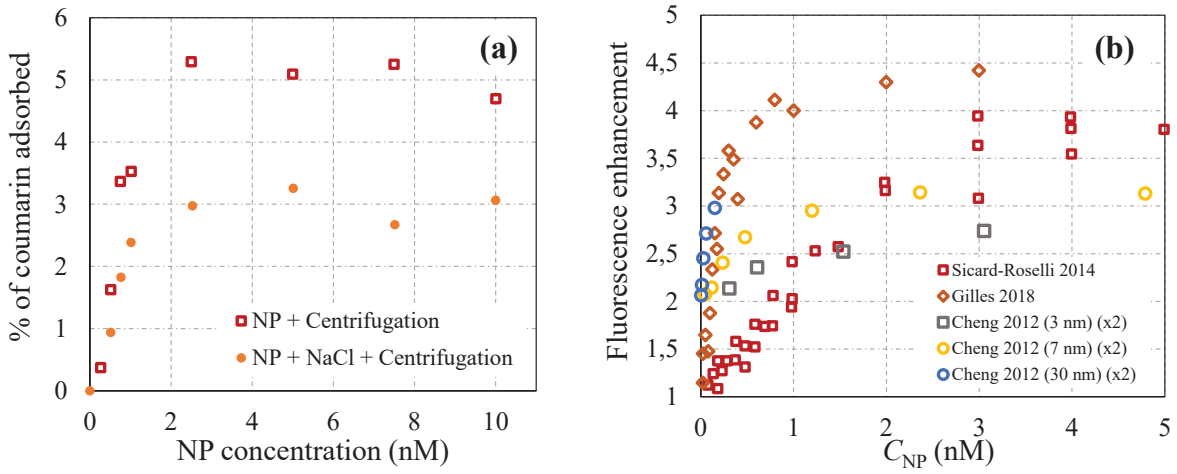

Figure 12.3.: Experimental data obtained from the literature. Panel (a) Proportion of coumarin adsorbed on the surface of GNPs as a function of the GNP concentration, for a coumarin concentration of 0.5 mM. The data were taken from *Gilles*[108]. Panel (b) Enhancement of 7OH-Cou measured with regard to a solution of Cou/water without GNPs, as defined in[51]. Note that the results from Cheng *et al.*[51] by a factor of 2 to account for the difference of enhancement definition. The experiments presented were performed under aerated condition.

It is worth mentioning that the determination of radical species yields in presence of NPs is not straightforward, partly due to the possible interference between NPs and the probe or its byproducts. In the present context, there has been several evidences of interactions between NPs and Cou. For instance, 7OH-C fluorescence signal is sensitive to the experimental protocol, as reported by Sicard *et al.*[251]. Besides, some of the Cou molecules in solution were found to be adsorbed on the surface of the NP, as shown in Fig. 12.3 (a). For 0.5 mM of Cou in solution, Gilles[108] measured the amount of Cou molecules that was adsorbed on the NPs, by removing the NPs by centrifugation with or without preliminary adding NaCl into the solution to aggregate the NPs, and then measuring the amount of Cou molecules left in solution. The amount of Cou that was on the surface of the NPs increased from 0 to $\sim$ 1 nM of GNPs, before reaching a limit

value of 3 or 5 % of the Cou present in solution, depending on the method of measurement. In this work, we differentiate the coumarin in solution to the coumarin adsorbed on the GNP surface by the names Cou_{sol} and Cou_{surf} respectively. The authors also evidenced that the proportion of 7OH-C with regards to other hydroxy-coumarin byproducts was impacted by the presence of NPs. This change of regioselectivity varied with atmosphere conditions. Finally, they found that the amount of 7OH-C when the concentration of NP was close to 0 was equal to ~ 4 nmol $\cdot$ J^{-1}. The coumarin concentration used in these experiments enabled to measure a $^{\bullet}$OH yield at $\sim 10^{-6}$ s, which corresponds to 200 nmol $\cdot$ J^{-1}. Therefore, for a similar irradiation of Cou solution without NP, one may expect a yield of 7OH-C of ~ 10 nmol $\cdot$ J^{-1} provided a conversion factor of 5 %[284]. In turns, the fluorescent signal was divided by a factor of nearly 2 compared to a solution without GNPs.

For these many reasons, in some of the experiments[109,110,251], a scaling of the $^{\bullet}$OH yield in presence of GNPs was applied to reach the radiolytic yield of $^{\bullet}$OH in the absence of GNPs (i.e. 200 nmol $\cdot$ J^{-1}) when the concentration of GNPs was close to 0 nM. Thus, for low GNP concentrations, the enhancement was, by definition, equal to 1. This scaling was not applied for the other experiments[47,51,75,76], and the raw fluorescent signals with/without GNPs were compared to deduce an enhancement. We thus may expect a factor of ~ 2 between these two sets of experiments.

While the protocols slightly differed depending on the research group, they both found a large enhancement of the fluorescence signal for non-coated (naked) GNPs under low-energy photon irradiation (see Tab. 12.1 for experimental conditions). As displayed in Fig. 12.3 (b), this was characterized by a sharp increase of the enhancement before reaching a plateau for a GNP concentration around 1 nM. Interestingly, this enhancement followed the same trend as in Fig. 12.3 (a). The maximum enhancement was different depending on the protocol. While Cheng *et al.* obtained a maximum enhancement of 1.6[51], the University of Paris-Sud group obtained a maximum enhancement of ~ 4[110,251] for aerated condition. This difference most likely arises from the difference of protocol, and the difference of enhancement definition. However, despite the variation of the extent of the effect, this enhancement can not be explained by a pure physical enhancement, as the GNP concentration was too low. This is illustrated in Tab. 12.2, showing our theoretical predictions of dose enhancement based on previous work (see chapter 10), compared to some of the experimental results obtained with the Cou probe[251]. The difference in enhancement obtained is particularly striking at 5 nM, as dosimetric results predict an enhancement of ~ 1.1, while experimental data give an enhancement of 3.8. While the physical enhancement depends on the energy of the photons, the maximum that may be obtained is 16 % at 1 mg$\cdot$ mL^{-1} for 50 keV, which remains insufficient to explain the extent of the effect for all the experimental data.

Additionally, Gilles *et al.*[110] found that an enhancement of the same order of magnitude is produced under MeV irradiation, although no enhancement is predicted by physical mechanisms. A similar shape of the enhancement curve was obtained, whatever the atmosphere conditions, but with different plateau values. For instance, the presence of oxygen impacted the maximum enhancement, going from 320 % with air down to 170 % with oxygen-saturated condition[110]. Both groups found that this high enhancement disappeared when adding a coating on the surface of the GNP[75,109]. They also reported a variation of the enhancement with the dose rate. The influence of salts, which reduced the amount of Cou adsorbed on the surface of the NP (see Fig. 12.3 (a)) also reduced the enhancement, and in particular reduced the plateau value down to 220 %[110] (aerated condition).

It was concluded that the enhancement was dominated by chemical effects rather than physical mechanisms for naked GNPs. Different interpretations of the mechanism behind these measurements were proposed, that relied on the implication of the GNP-solution interface. On the one hand, Gilles *et al.*[110] concluded that this enhancement may be induced by additional production of $^{\bullet}$OH, due to surface properties of GNPs. Although bulk gold is well known for being chemically

nM	0.5	0.75	2.5	5	7.5	10
mg·mL^{-1}	0.10	0.15	0.50	1.0	1.5	2.0
Dose enhancement	1.01	1.015	1.05	1.1	1.15	1.20
Experimental enhancement[251]	1.5	1.8	N/A	3.8	N/A	N/A

Table 12.2.: Concentration of GNP for a 16 nm radius GNP, and associated dose enhancement expected from our MC simulation, *vs* experimental enhancement[251]. The dose enhancement was obtained due to a higher cross-section of gold-photon interaction, compared to water-photon interaction.

inactive, GNPs have been reported to have intrinsic chemical reactions that are specific to their small dimension. Gilles *et al.* suggested that the GNPs induce a particular organization of water molecules that favors its radiolytic dissociation, leading to higher quantities of radicals than expected. They also proposed that radiolysis products, such as H_2O_2, may react with NPs to form $^{\bullet}$OH, leading to additional fluorescence signal. On the other hand, Cheng *et al.*[51] concluded that it was due to an interference between the GNPs and an intermediate product of the probe ($CCA^{\bullet} - OH$), resulting in an enhanced signal. They suggested that the combination of $C^{\bullet -}$ with GNPs make NPs anionic, allowing $CCA^{\bullet} - OH$ to react on the surface of the NP to form 7OH-3CCA.

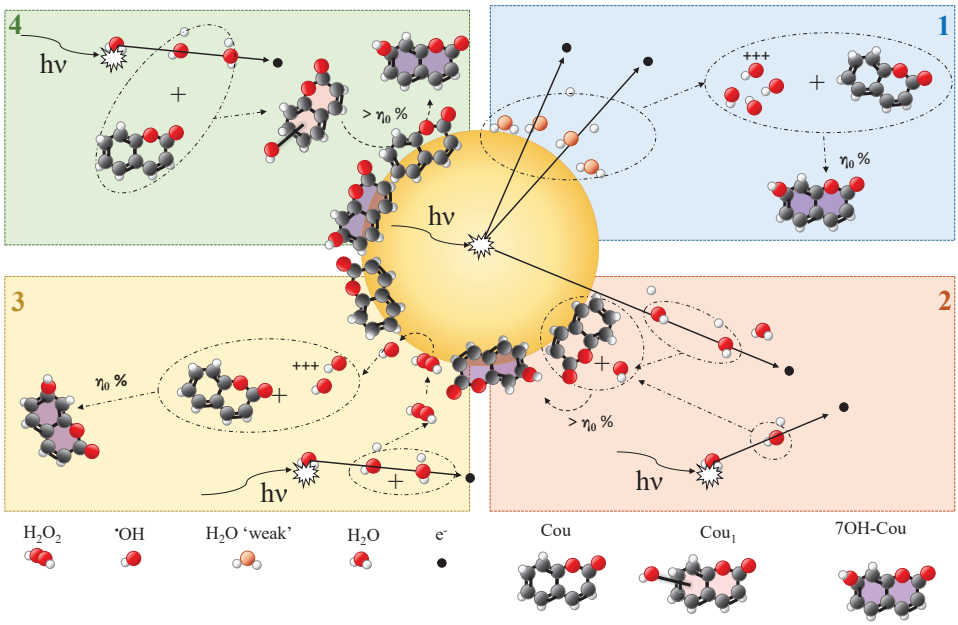

Figure 12.4.: Schematic diagrams of the hypothetical pathways involved in the enhancement of the fluorescent signal of 7OH-C/7OH-CCA for the irradiation of a solution of colloidal GNPs. (1) Water molecules adsorbed on the surface of the NP have weakened bonds and thus require less energy to break, leading to an increase of $^{\bullet}$OH, and consequently of the fluorescence signal. (2) $^{\bullet}$OH produced following an interaction between a photon and the NP or a photon and a water molecule, reacts with a coumarin molecule located on the surface of the NP. The amount of 7OH-C/7OH-3CCA produced after the different steps (see Fig. 12.2) is higher than for a coumarin molecule in water, which leads to an increase of the fluorescent signal. (3) H_2O_2 molecules that are produced during water radiolysis react on the surface of the NP through a Fenton-like reaction, increasing the amount of $^{\bullet}$OH. It reacts either with a coumarin molecule in solution or on the surface of the NP, and consequently increases the fluorescent signal. (4) A by-product of coumarin molecules ($C^{\bullet}$-OH/$3CCA^{\bullet}$-OH) interacts with the NP on which coumarin molecules are adsorbed and leads to a higher amount of 7OH-C/7OH-CCA compared to the other isomers than in pure water.

As the underlying mechanisms of this chemical enhancement remain unclear, we investigated the proposed scenarios with theoretical calculations. A total of 4 scenarios, based on experimental

evidences and suggestions of the authors of the studies, were investigated and confronted against experimental data (see Fig. 12.4). They all involved somehow the surface of the NP, and are summarized through the following questions:

1. Could a decrease of energy required to dissociate water molecules adsorbed on the NP surface increase the production of $^{\bullet}$OH and explain the increase of the fluorescence signal?

2. Could $^{\bullet}$OH preferentially reacts with the coumarin molecules located on the NP surface, which would in turn produce a higher amount of 7OH-C/7OH-3CCA compared to a coumarin molecule in solution, due to a higher conversion rate into a fluorescent product?

3. Could H_2O_2 react on the surface of the NP through a Fenton-like reaction and produce additional $^{\bullet}$OH that would explain the increase of the fluorescence signal?

4. Could coumarin molecule by-products react with NPs or coumarin on the NP surface, and in turn favor the production of 7OH-C/7OH-3CCA compared to its isomers?

12.3. Material and methods

12.3.1. System

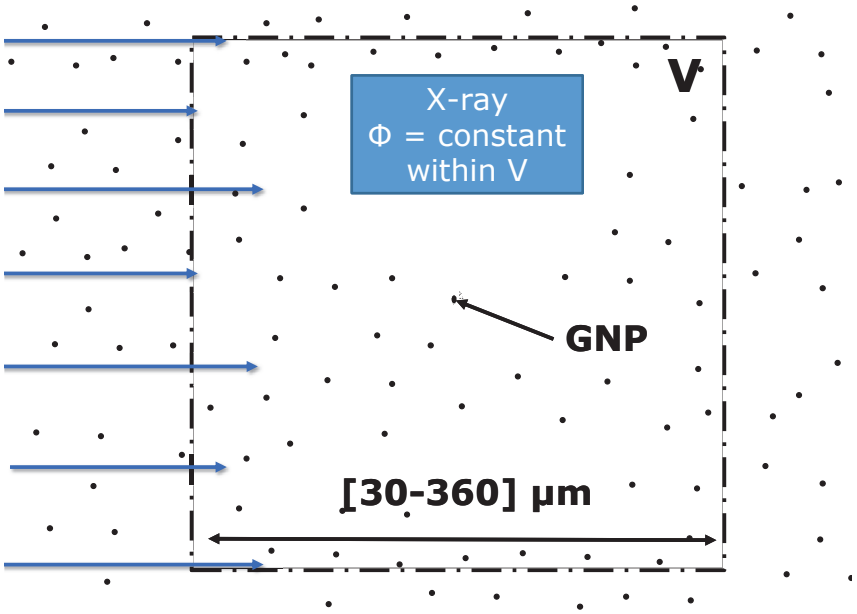

Figure 12.5.: Schematic view of the system considered for radical species calculation. Φ represents the fluence of the beam, and is set constant within the volume of interest V. The GNPs represented by small dots have a concentration C_{NP} and are homogeneously distributed.

The goal of this study is to calculate the yield Y_X of radical species X in nmol $\cdot$ J^{-1} and their reaction rate with Cou molecules, for a given concentration C_{NP} of NPs mixed with Cou molecules, under keV photon irradiation. The yield of the chemical species X produced in water may be related to the concentration of the species $[X]$, by the relation $[X] = DY_X$. The yields were calculated for various times t after the beginning of irradiation. The system considered for the calculation is described by Fig. 12.5. In order to estimate the production of these chemical species, we defined a system that would be applicable for *in solution* (i.e. colloidal GNPs) experiments. In these experiments, the samples were thin compared to the attenuation length of the radiation[251]. In our simulation, we considered an infinite volume of water containing a concentration C_{NP} of

NPs, distributed throughout the volume. We defined a volume of interest V of water, within which the fluence of the photons is constant. The half length of V was chosen to be larger than the maximum range of the most energetic photo-electron in water. We limited our study to low GNP concentrations (< 10 mg $\cdot$ mL^{-1}), which is in the range of the experimental conditions of the studies we investigated[109,110,251]. The resulting ratio of the total volume of GNP divided by the total volume of water remained low ($< 10^{-4}$). Besides, we assumed that the GNPs were distributed homogeneously. These two conditions (concentration and homogeneity) ensured that the irradiation of one GNP did not influence the energy deposition around another. The Cou molecules were homogeneously distributed in V. We also modelled the Cou molecules adsorbed on the surface of the GNPs. We tested 3 atmosphere conditions and therefore accounted for the presence of oxygen by adding a homogeneous concentration of O_2 in solution[59]. The dioxygen concentrations were taken from experimental measurements[108] and are summarised in Tab. 12.3. The goal of this study was not to investigate the effect of photon energy nor the size of the NPs. We thus fixed the GNP radius at 16 nm and the photon energy at 20 keV, which corresponds to the experimental conditions from Sicard *et al.*[251] and is close to other studies[109,110]. The Cou concentration was fixed at 0.5 mM[109,110,251]. The yields for a time $< 10^{-6}$ s were calculated with a MC simulation, while the yields at longer time were investigated with analytical models. The next sections describe our MC approach and our analytical models.

Atmosphere	N_2	Air	100 % O_2
O_2 in solution	90 µM	460 µM	1 740 µM

Table 12.3.: Concentration of oxygen in solution, according to the atmosphere conditions. Taken from Gilles[108].

12.3.2. Monte carlo simulation of water radiolysis

12.3.2.1. General procedure

We previously investigated the yields of free radicals in presence of GNPs under keV photon irradiation (see chapter 10 and 11), where the full description of the MC models is available. Briefly, 3 consecutive steps were mandatory to calculate the yield of chemical species. First, the physical stage occurred from 10^{-18} to 10^{-15} s after the primary photon interaction. Our model consists in an event-by-event tracking of particles in the different media (water or gold). Photons were not explicitly tracked, and we only considered the photoelectric effect and the Compton scattering as they dominate at the photon energies investigated. The tracking of electrons were based on models that allowed accurate transport down to low energy both in water (meV) and gold (eV). The description of these models may be found in chapter 8 and elsewhere[106]. During this stage, the amount of energy deposition may be obtained. At the end of the physical stage, the water molecule may be either excited (H_2O^*) or ionized (H_2O^+, H_2O^{2+} and H_2O^-), and the medium contained thermalized electrons (e_{th}). Any holes or electrons that were produced within the GNP were no longer tracked, as it did not lead to additional water molecule excitation or ionization.

This stage was followed by a physico-chemical stage (from 10^{-15} to 10^{-12} s), during which the medium (i.e. water) relaxes leading the the production of primary chemical species. The different branch rates of each molecular rearrangement are described elsewhere[106]. At the end of this stage, the MC outcome consisted of spatial distribution of chemical species: e^-_{aq}, H_3O^+, $^\bullet OH$, $^\bullet H$, H_2, ^-OH and O, with a majority of e^-_{aq}, H_3O^+ and $^\bullet OH$.

Finally, at 10^{-12} s after the primary interaction, the chemical phase began and the primary chemical species diffused and interacted with each other. In our simulation, this phase was simulated up to 10^{-6} s. At the end of the chemical stage, the so-called steady state was reached and the radiolytic yields (or G-values in molecule per 100 eV of deposited energy) reached asymptotic

values. The method used to calculate the yields and optimize the computing time, and the list of standard chemical reactions of water radiolysis (more than 50 chemical reactions), are available elsewhere and will not be discussed in this paper[59,60,106].

12.3.2.2. Radiolysis with coumarin molecules

To account for the presence of coumarin in the solution, we extended the simulation to introduce Cou molecules and quantify their reaction with radical species. The Cou diffusion coefficient was set equal to $D_{\text{cou}} = 8 \times 10^{-6}$ cm^2 s^{-1} [87] and the reaction radius of the chemical species was equal to 0.25 nm. This was based on the work by Gilles[108] who reported a molecule area of 0.49×0.68 nm^2. Varying the reaction radius showed little consequence on the calculated yields. We considered the following reactions for coumarin molecules or by-products:

$$\begin{array}{lcll} \text{Cou}_{\text{surf}}/\text{Cou}_{\text{sol}} + {}^{\bullet}\text{OH} & \rightarrow & \text{Cou}_1 & k_{\text{I}}/k'_{\text{I}} \quad \text{R1} \\ \text{Cou}_1 + \text{Cou}_1 & \rightarrow & \text{Cou}_2 & k_{\text{II}}/k'_{\text{II}} \quad \text{R2} \\ \text{Cou}_1 + \text{O}_2 & \rightarrow & \text{Cou}_3 & k_{\text{III}}/k'_{\text{III}} \quad \text{R3.} \end{array}$$

They were all diffusion controlled[14,284]. As described in Fig. 12.2, different reaction constants were reported for R1, R2 and R3[108,284]: $k_{\text{I}} = 1.05 \times 10^{10}$ M^{-1} s^{-1}/$k'_{\text{I}} = 6.8 \times 10^9$ M^{-1} s^{-1}; $k_{\text{II}} = 5 \times 10^8$ M^{-1} s^{-1}/$k'_{\text{II}} = 1.0 \times 10^9$ M^{-1} s^{-1}; $k_{\text{III}} = 7 \times 10^6$ M^{-1} s^{-1}/$k'_{\text{III}} = 1.0 \times 10^9$ M^{-1} s^{-1}. We therefore tested both sets of reaction constants. For the reaction R1, $^{\bullet}$OH could react either with coumarin in solution (Cou_{sol}) or with coumarin on the surface of GNPs (Cou_{surf}). To account for both distributions, two distinctive methods were used. For Cou_{surf}, we generated Cou molecules directly on the surface of the NP at the end of the physico-chemical stage. Considering an average molecule diameter of 0.5 nm, the volume around GNPs was divided in sub-shells of thickness 0.5 nm. Using a cubic network with a 0.5 nm mesh, the Cou_{surf} were randomly distributed in the sub-shells, filling up first the closest sub-shell to the NP surface before filling the next sub-shell. As the number of coumarins per NP was dependent of the NP concentration, 6 different configurations were simulated, presented in Tab. 12.4. As seen in section 12.2, the number of Cou_{surf} depended on the method of measurement. We thus chose to use the data which maximized Cou_{surf}, to maximize the reaction between the molecules and the radiolysis products. A maximum of 2 sub-shells were necessary for the maximum number of coumarin molecules per NP (22 000). The measurement uncertainty of the number of coumarin molecules per GNP was reported to be $\sim$ 36 %, which may impact the results of scenario 2 and particularly scenario 4. Note that Gilles[108] reported that the layer thickness of Cou_{surf} was lower than 2 nm, which is consistent with our distribution.

GNP concentration (nM)	Coumarin per NP	Coumarin in sub-shell 1	Coumarin sub-shell 2
0.5	16 000	10 760	5 240
0.75	22 000	10 760	11 240
2.5	10 000	10 000	0
5	5 000	5 000	0
7.5	3 500	3 500	0
10	2 000	2 000	0

Table 12.4.: Number of coumarin molecules per NP, according to the NP concentration, taken from Gilles[108]. Note that the uncertainty of the measurement was reported to be of 36 % for the highest number (22 000). Coumarin concentration: 0.5 mM, $R_{\text{NP}} = 16$ nm.

Regarding Cou molecules that were homogeneously distributed in the solution (Cou_{sol}), we used an approximation that consisted in representing the distribution of Cou molecules as an homogeneous

and inexhaustible reservoir[59,60]. Regardless of the NP size, we approximated a constant coumarin concentration of 0.5 mM in solution[109,110,251]. The decrease up to 5 % of the Cou in solution due to adsorption of the molecules onto the surface of the NP did not yield to any significant difference in the yield of the Cou by-products. The same approach was used to account for the presence of O_2 in the solution. Besides, in some scenarios, GNPs were also introduced in the solution as a chemical species, and modelled as a homogeneous and inexhaustible reservoir. In this case, the diffusion of NPs, which is very slow with respect to the other chemical products, was neglected, and the reaction radius set equal to the radius of the GNP (16 nm).

12.3.3. Analytical approaches

In scenario 3 and 4, the reactions involved occurred at time larger than 10^{-6} s. Therefore, an analytical approach was mandatory.

12.3.3.1. Scenario 3

In the third scenario, we investigated the possible reaction between NPs and H_2O_2 molecules to form $^{\bullet}$OH,

$$\mathrm{NP} + \mathrm{H_2O_2} \rightarrow \mathrm{NP^+} +^- \mathrm{OH} +^{\bullet} \mathrm{OH} \qquad k_{\mathrm{IV}} \qquad \mathrm{R4}$$

Following R4, we considered that every formed $^{\bullet}$OH reacted with a coumarin molecule, resulting in the formation of Cou_1. As the reaction constant between $^{\bullet}$OH and Cou is much larger than the Fenton reaction constant, in our analytical model, we considered this two steps reaction as a one step reaction,

$$\mathrm{H_2O_2} + \mathrm{NP} \overset{\mathrm{Cou}}{\rightarrow} \mathrm{Cou_1} +^+ \mathrm{NP} +^- \mathrm{OH} \qquad k_{\mathrm{V}} \qquad \mathrm{R5}$$

The reactions R1, R2, R3 and R5 were used to calculate the evolution of the different chemical species concentrations,

$$\begin{aligned}
\frac{\mathrm{d}[\mathrm{H_2O_2}]}{\mathrm{d}t} &= \Phi G_{\mathrm{H_2O_2}} - k_{\mathrm{V}}[\mathrm{NP}][\mathrm{H_2O_2}] \\
\frac{\mathrm{d}[\mathrm{Cou_1}]}{\mathrm{d}t} &= \Phi G_{\mathrm{Cou_1}} + k_{\mathrm{V}}[\mathrm{NP}][\mathrm{H_2O_2}] - k_{\mathrm{II}}[\mathrm{Cou_1}]^2 - k_{\mathrm{III}}[\mathrm{Cou_1}][\mathrm{O_2}] \\
\frac{\mathrm{d}[\mathrm{Cou_2}]}{\mathrm{d}t} &= k_{\mathrm{II}}[\mathrm{Cou_1}]^2 + \Phi G_{\mathrm{Cou_2}} \\
\frac{\mathrm{d}[\mathrm{Cou_3}]}{\mathrm{d}t} &= k_{\mathrm{III}}[\mathrm{Cou_1}][\mathrm{O_2}] + \Phi G_{\mathrm{Cou_3}}
\end{aligned} \tag{12.1}$$

where Φ is the dose rate in Gy$\cdot\ s^{-1}$ and G_X is the radiolytic yield of the chemical species X at 10^{-6} s, obtained by a MC simulation.

12.3.3.2. Scenario 4

The final scenario hypothesized a reaction between NPs and coumarin by-products. The following reaction was considered,

$$\mathrm{NP} + \mathrm{Cou_1} \rightarrow \mathrm{NP} + \mathrm{Cou_4} \qquad k_{\mathrm{VI}} \qquad \text{R6.}$$

Similarly to the analytical calculation for the scenario 4, the reactions R1-3 and R6 were used to estimate the evolution of the concentration of by-products,

$$\begin{aligned}
-\frac{\mathrm{d}[\mathrm{Cou_1}]}{\mathrm{d}t} &= k_{\mathrm{II}}[\mathrm{Cou_1}]^2 + k_{\mathrm{III}}[\mathrm{Cou_1}][\mathrm{O_2}] + k_{\mathrm{VI}}[\mathrm{Cou_1}][\mathrm{NP}] - \Phi G_{\mathrm{Cou_1}} \\
\frac{\mathrm{d}[\mathrm{Cou_2}]}{\mathrm{d}t} &= k_{\mathrm{II}}[\mathrm{Cou_1}]^2 + \Phi G_{\mathrm{Cou_2}} \\
\frac{\mathrm{d}[\mathrm{Cou_3}]}{\mathrm{d}t} &= k_{\mathrm{III}}[\mathrm{Cou_1}][\mathrm{O_2}] + \Phi G_{\mathrm{Cou_3}} \\
\frac{\mathrm{d}[\mathrm{Cou_4}]}{\mathrm{d}t} &= k_{\mathrm{VI}}[\mathrm{Cou_1}][\mathrm{NP}] + \Phi G_{\mathrm{Cou_4}}.
\end{aligned} \tag{12.2}$$

12.4. Approximations, results and discussion for each scenario

12.4.1. Scenario 1

12.4.1.1. Description

As described in Fig. 12.4, a first proposed scenario[109,110,251] is that a few layers of structured water molecules display specific properties at the GNP-water interface. The thickness of this hydration layer would be of a few water molecules, i.e., no more than 1 nm. Few authors have shown with DFT calculations that there could be a weakening of H-OH bond resulting in a lower dissociation energy of the water molecules at the surface of clean GNPs. For example, Liu *et al.*[180] calculated that H-OH bond energy decreased from 460 kJ/mol to 255 kJ/mol at the surface of the GNP. This lower dissociation energy could result in the ejection of H molecules with a higher kinetic energy, that could further dissociate another water molecule. Additionally, the binding of water molecules to gold NPs may lower excitation or ionisation energies. Both could lead to an increase of the dissociation of water during the radiolysis process (physical and physico-chemical stage) and thus an efficient production of $^{\bullet}$OH.

12.4.1.2. Calculation and approximations

For this scenario, we estimated the increase of $^{\bullet}$OH for a given shell of hydration s around the GNP. We first calculated the amount of energy deposited in a 1 nm thick shell around one GNP. Only the physical phase of the MC simulation was therefore necessary. The relative increase of $^{\bullet}$OH, $\delta n_{^{\bullet}\mathrm{OH}}$, reads,

$$\delta n_{^{\bullet}\mathrm{OH}} = \frac{E_s C_{\mathrm{NP}}}{E_T} \frac{Y_s(^{\bullet}\mathrm{OH})}{Y(^{\bullet}\mathrm{OH})} \tag{12.3}$$

where $\frac{E_s C_{\mathrm{NP}}}{E_T}$ is the fraction of energy deposited in the hydration shells s, and is proportional to the concentration of GNPs C_{NP}. $\mathrm{Y_s}(^{\bullet}\mathrm{OH})$ is the yield of $^{\bullet}$OH production per energy deposited in pure water, $\mathrm{Y_s}(^{\bullet}\mathrm{OH})$ is the yield of $^{\bullet}$OH production per energy deposited in the shell s in the vicinity of the GNP.

As we do not have experimental data on $\mathrm{Y_s}(^{\bullet}\mathrm{OH})$, we made some hypothesis that maximize the effect. We considered that $\mathrm{Y_s}(^{\bullet}\mathrm{OH}) = \gamma\ W'$. γ represents the increase of $^{\bullet}$OH production

efficiency, which we set as the ratio of H-OH binding energy, on the surface of the GNP *vs* far from the GNP. W' is the average number of ionization or excitation per eV in pure water. A first assumption was to consider that 100 % of the water molecules excited or ionized in the shells s led to the creation of one $^{\bullet}$OH. A second maximization of the effect was the assumption that an electron going through the shell s creates γ times more excitation(s) or ionization(s). In reality, in the excitation/ionisation energy is decreased at the surface of GNPs, electrons will rather create the same amount of excitation or ionization but lose less energy, resulting in more energy deposition further away from the GNP. Besides, we also assumed that the increase of efficiency is obtained regardless the type of process (ionization, excitation, attachment), while the binding energy decrease is only strictly valid for H-OH. Therefore, the approximations should lead to an overestimation of the effect for this scenario.

12.4.1.3. Results, discussion and conclusion

First, the enhancement is, by definition, purely linear with the GNP concentration and can not explain the experimental saturation that was observed. Beyond this linearity issue, we also found values that were extremely small. For a yield of excited/ionized molecules of 5.7 per 100 eV and a ratio of binding energy of 1.8[180], we found $Y_s(^{\bullet}OH) = 10.3$ molecules per 100 eV. At the end of the physico-chemical stage, we found $Y(^{\bullet}OH) = 4.6$ molecules per 100 eV. The final ratio $\frac{E_s C_{NP}}{E_T}$ was very low, varying from 3×10^{-5} at 0.5 nM of GNPs up to 5×10^{-4} at 10 nM of GNPs. Hence, we found a relative increase varying from 7×10^{-3} up to 0.11 % for a shell thickness of 1 nm, which is extremely low compared to the 4-fold experimental enhancement. This very low value is due to the very small amount of energy deposition inside the shells compared to the total amount of energy. To reach a ratio of 100 % a shell thickness of 250 nm would be necessary. Therefore, this scenario can not explain the increase observed in the experimental measurement.

12.4.2. Scenario 2

12.4.2.1. Description

In the second scenario, we wished to test the amount of $^{\bullet}$OH that would react with the coumarin molecules on the NP surface. As illustrated in Fig. 12.2, the fraction of the coumarin molecules that reacted with $^{\bullet}$OH which is converted into a fluorescent molecule is relatively low (conversion facteur of $\sim$ 5 % for a solution of coumarin mixed with water under aerated condition). For keV photon irradiation, the yield of fluorescent coumarin is very low, ~ 10 nmol$\cdot$J^{-1} for an irradiation of 0.5 mM of coumarin solution. Interestingly, in presence of NPs, it reached even lower yields, close to 4 nmol $\cdot$ J^{-1} for a GNP concentration close to 0 nM[251]. An increase in this conversion factor could result in a much higher fluorescent yield. As coumarin molecules were found to be adsorbed on the GNP surface[108], we hypothesized that part of $^{\bullet}$OH molecules would react with these coumarin molecules. Due to a higher conversion factor of these molecules to the fluorescent molecule 7OH-Cou, we could therefore reach an increased fluorescent yield. Such an increase of the conversion factor could be explained by the fact that some positions on the benzene ring may be unavailable, due to the bond with NPs, therefore preventing the formation of some isomers while favouring 7OH-Cou.

12.4.2.2. Calculation and approximations

As $^{\bullet}$OH is mostly consumed by 10^{-6} s after the primary photon interaction, only the MC simulation was mandatory for this scenario. To calculate the yield of $^{\bullet}$OH in the presence of NPs, we used the track-by-track methodology discussed in details in chapter 10. This method assumes that one track does not overlap with the other, which is valid as long as the dose and life time of the chemical species remain low. The yield of chemical species could be decomposed as a linear combination of the yields of individual tracks. In particular, the tracks were decomposed into

two different contributions: the case were a photon primarily interacts with a water molecule (1) and the case were a photon primarily interacts with a gold atom (2). The final yields were thus obtained as a linear combination of the yields obtained for individual tracks of type (1) and (2).

We previously showed that cases where a photon interacted with a water molecule and led to secondary particles that would hit a GNP was minor during the physical stage. For a photon energy of 20 keV and a GNP radius of 12.5 nm, nanodosimetry calculations showed that this type of contribution played a minor role in terms of energy deposition in the vicinity of the NP. As the majority of the $^{\bullet}$OH molecules are scavenged before 1 µs by coumarin molecules, we expect very little diffusion, and thus the amount of $^{\bullet}$OH that reach a NP after a primary photon interaction in water is expected to be minor, with a relative contribution similar to what was obtained for nanodosimetry calculations (see chapter 9). Thus, we only considered that only the $^{\bullet}$OH produced after a GNP ionization (i.e. a track type (2)) could react with Cou_{surf}.

The reaction yield between $^{\bullet}$OH and Cou_{surf} was calculated to estimate the amount of $^{\bullet}$OH that may react with Cou_{surf}, and therefore the amount of fluorescent molecules that could be formed on the surface of GNPs. Different atmosphere conditions (i.e., amount of dissolved O_2) were tested.

12.4.2.3. Results, discussion and conclusion

From 10^{-12} to 10^{-8} s, we found that the $^{\bullet}$OH yield decreased, dominated by reactions with radiolytic products, such as $^{\bullet}$OH or e^-_{aq}. Then, from 10^{-8} to 10^{-6} s, the decrease was dominated by the reaction between $^{\bullet}$OH and $\text{Cou}_{\text{surf}}/\text{Cou}_{\text{sol}}$. During this time interval, the yield of the by-product Cou_1 increased and reached a plateau value at $\sim 10^{-6}$ s. This value depended on the GNP concentration, and to a lesser extent the reaction constant. It reached 239 and 281 nmol$\cdot$J^{-1} for 0.5 and 10 nM of GNPs and $k_{\text{I}} = 1.05 \times 10^{10}$ M^{-1}s^{-1} [108]. Same trends were observed both with and without dissolved O_2. Indeed, the reaction constants of R3 were not high enough to induce a significant reaction between Cou_1 and O_2 molecules in the studied time range.

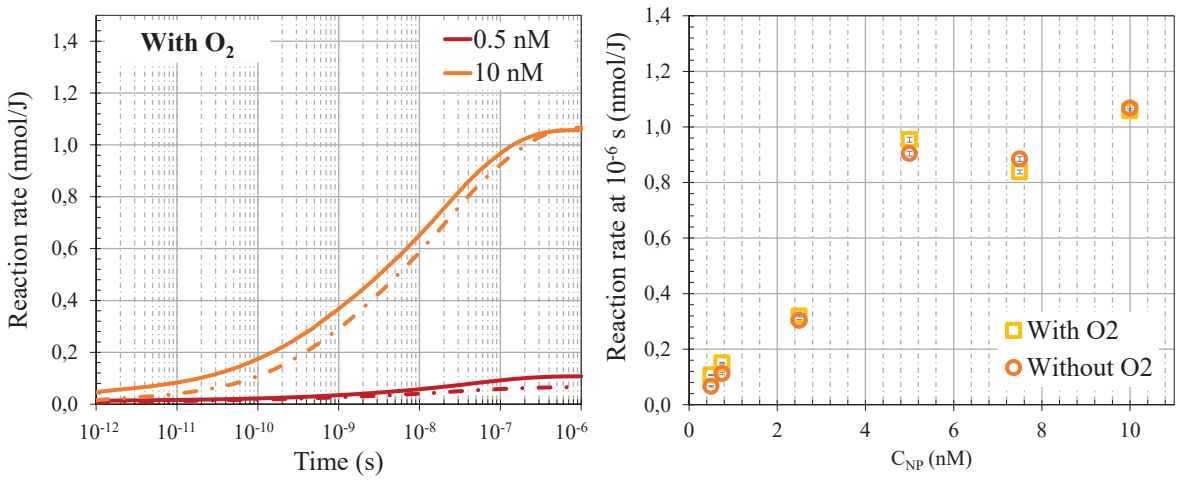

Figure 12.6.: Panel (a). Reaction rate of Cou_{surf} + $^{\bullet}$OH as a function of time after the primary photon interaction. In solid lines the results are for the reaction constants k [108], while in dashed lines the results are for the reaction constants k' [284]. The simulation was performed for a O_2 concentration of 0.27 mmol. Panel (b). Reaction yield of Cou_{surf} + $^{\bullet}$OH at 10^{-6} s (in nmole $\cdot$ J^{-1}), as a function of the GNP concentration (in nM), for the reaction constants k. $R_{\text{NP}} = 16$ nm.

The chemical reaction yield represents the number of occurrence of a given reaction at a given time. The reaction yield between Cou_{surf} and $^{\bullet}$OH is displayed on Fig. 12.6 (a) for 0.5 nM and

10 nM of GNPs. As expected the reaction rate increases with time and is maximum at 10^{-6} s. At this time, the amount of $^{\bullet}$OH that reacts with coumarin on the surface of GNPs reaches a plateau as the yield of $^{\bullet}$OH in solution becomes close to 0. In Fig. 12.6 (b), the reaction yield at 10^{-6} s is displayed as a function of GNPs concentration. It first linearly increases from 0.1 nmol $\cdot$ J^{-1} to $\sim$ 0.9 nmol $\cdot$ J^{-1}, with GNP concentrations increasing from 0.5 up to 2.5 nM. Then, it reaches a saturation for GNP concentrations of 2.5-10 nM. The same results were obtained both with and without O_2 in the solution. This trend appears to be a result of a competition between the increase of GNP concentration and the increase of Cou_{surf} per GNP for $C_{NP} = [0.5 - 0.75]$ nM, followed by a decrease of Cou_{surf} per GNP for $C_{NP} = [0.75 - 10]$ nM.

Despite a trend that appears similar to experimental data, with the reach of a saturation, the yields are low compared to the total yield of Cou_1 formed following the reaction of $^{\bullet}$OH and Cou_{sol}, of the order of 200 nmol $\cdot$ J^{-1} at 10^{-6} s. This modest reaction rate may be explained by the distribution of $^{\bullet}$OH after the primary ionization, as displayed on Fig. E.1, Fig. E.2 and Fig. E.3 of Appendix E.1. The figures show spatial distributions of chemical species at different times (10^{-12}, 10^{-8} and 10^{-6} s) after the primary photon interaction. While an Auger cascade (see panels (c)) may induce a large amount of $^{\bullet}$OH in the vicinity of the GNP, it is not systematically observed (see panels (a)) as the cascade may be self-absorbed within the GNP. Most of the $^{\bullet}$OH molecules remain at distances larger than 100 nm. Thus, they react to form radiolysis products such as H_2O_2 or with Cou_{sol} before having the time to react with Cou_{surf}.

The amount of Cou_1 produced on the surface of the GNP is too low to explain the experimental increase. Even if the GNP increased the rate of 7OH-Cou formation up to 100 % following a reaction between $^{\bullet}$OH and Cou_{sol}, we would reach an additional fluorescent yield of ~ 1 nmol$\cdot$J^{-1}. Compared to the experimental fluorescent yield of ~ 4 nmol$\cdot$J^{-1} observed when the concentration of GNP is close to 0, this is insufficient. A more subsequent number of Cou_{surf} would be necessary to reach higher yields, which seems in contradiction with experimental measurements[108]. To obtain a more significant amount of reactions at the surface of GNPs, the life time of the chemical species must be long enough. In the next two scenarios, we thus investigated two chemical species that remain in solution for a longer time: H_2O_2 and Cou_1.

12.4.3. Scenario 3

12.4.3.1. Description

This third scenario hypothesizes that H_2O_2 molecules would react with metal atoms on the surface of the NP to be converted into $^{\bullet}$OH, further reacting with a coumarin molecule either located on the GNP surface or in solution. H_2O_2 is produced mainly by the reaction $^{\bullet}$OH + $^{\bullet}$OH. It is known to be relatively stable in solution, and may react with metals through a Fenton-like reaction to produce $^{\bullet}$OH[136]. In our case, it may thus diffuse and have a life-time that is long enough to meet and react with a GNP. Depending on the pH conditions, it was experimentally shown that GNPs could decompose H_2O_2 to form $^{\bullet}$OH[123].

12.4.3.2. Calculation and approximations

MC simulations were used to obtain the yield of chemical species at 10^{-6} s necessary for the analytical approach introduced in Eq. 12.1. Reactions R1-R4 were considered for the MC calculation. For the reaction R4, we modelled GNPs as an inexhaustible reservoir. For computing efficiency, the yield of radiolysis species at 10^{-6} s were simulated in pure water, and the increase of radical species due to the presence of GNPs was estimated for one concentration of GNP and scaled for other concentrations through a linear law,

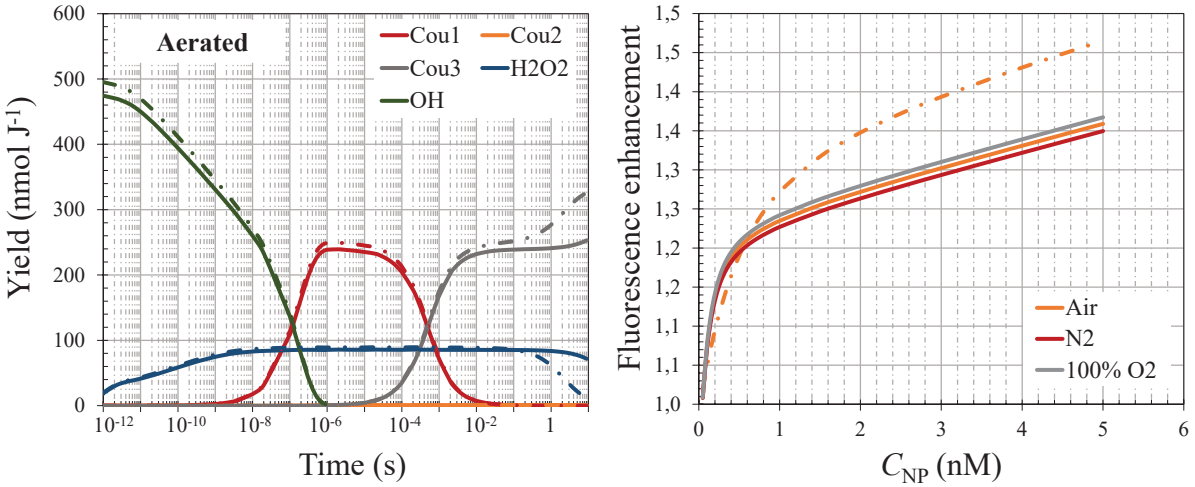

Figure 12.7.: Left: yield of chemical species (in nmol $\cdot$ J^{-1}), as a function of the time after the beginning of the irradiation (in s), obtained under aerated condition and for a dose rate of 0.33 Gy $\cdot$ s^{-1}. Results were obtained with the constants from Gilles *et al.*[108]. In solid line, the results are given for $C_{\mathrm{NP}} = 0.1$ nM while in dashed line they are given for $C_{\mathrm{NP}} = 2$ nM. Right: Fluorescence yield enhancement, as a function of the NP concentration (in nM), for different atmosphere conditions. In solid line, the results are for a dose rate of 0.33 Gy $\cdot$ s^{-1} and a time of irradiation of 40 s[108], and in dashed line the results are for a dose rate of 12 Gy $\cdot$ s^{-1} and a time of irradiation of 15 s[251].

$$R'_X = R_X \times (1 + r_X C_{\mathrm{NP}}) \tag{12.4}$$

where R_X is the number of chemical species X, C_{NP} is the NP concentration in nM and r_X is the number of additional chemical species X due to GNPs, normalized per R_X. For 16 nm GNPs, we found that 1 nM of GNPs induced an increase of 2.2 %.

The fluorescence yields were obtained as follows,

$$Y_{7\mathrm{OH-Cou}} = \eta_0 (Y_{\mathrm{Cou_2}} + Y_{\mathrm{Cou_3}}) \tag{12.5}$$

where η_0 is the conversion rate of $\mathrm{Cou_2}$ and $\mathrm{Cou_3}$ to the fluorescent molecules 7OH-Cou. The final enhancement was,

$$\mathrm{EF} = \frac{Y_{\mathrm{Cou_2}} + Y_{\mathrm{Cou_3}}}{Y_{\mathrm{Cou_2},0} + Y_{\mathrm{Cou_3},0}} \tag{12.6}$$

where $Y_{\mathrm{Cou_2},0}$ and $Y_{\mathrm{Cou_3},0}$ are the concentrations obtained for $C_{\mathrm{NP}} \to 0$ nM. These yields were obtained by a linear fit of the yields for GNP concentrations ranging from 0.1 to 0.3 nM, as it was experimentally done[251]. The constant of reaction k_{V} was used as an adjustment parameter to reproduce experimental measurements.

12.4.3.3. Results, discussion and conclusion

We set the values $\eta_0 = 0.02$, and $k_{\mathrm{V}} = 4 \times 10^8$ M^{-1}s^{-1}. The former was fitted to experimental results under aerated condition, to obtain similar fluorescent yields when $C_{\mathrm{NP}} \to 0$. The latter

was obtained to maximize the slope of the fluorescent yield increase for GNP concentrations in the range 0-0.3 nM. Note that this reaction constant is much larger than reported for standard Fenton reactions, which is around 55 $M \cdot s^{-1}$ [136].

Fig. 12.7, left panel, displays the chemical species yield, as a function of the time after the beginning of irradiation, under aerated conditions. Similar trends were obtained under N_2 and 100 % O_2 conditions. For $t < 10^{-6}$ s, the yield of $^{\bullet}OH$ drops as it is consumed to form, among other products, Cou_1 and H_2O_2. At the same time, the concentration of H_2O_2 increases and reaches a saturation yield of 85.2 $nmol \cdot J^{-1}$. At $t = 10^{-6}$ s, the yield of Cou_1 is maximum. For larger times, it decreases while the yield of Cou_3 increases, reaching a plateau at $\sim 10^{-2}$ s. The yield of Cou_2 remains negligible regardless of the atmosphere condition.

Up to 10^{-2} s, the yields hardly depend on the concentration of NPs. However, beyond $t = 0.1$ s, the yields of Cou_3 and H_2O_2 start varying with regard to the NP concentration, as the reaction between H_2O_2 and NP starts. For $C_{NP} = 0.1$ nM, the yield of H_2O_2 begins to drop at 1 s, consequently increasing the yield of Cou_3 as $^{\bullet}OH$ is formed and reacts with a coumarin molecule. Such a reaction occurs at shorter time for $C_{NP} = 2$ nM, and a drop of H_2O_2 yield is observable at 0.1 s.

The final fluorescent enhancement is displayed on the right panel of Fig. 12.7 for various time of irradiation and dose rates. It displays first a sharp increase with increasing GNP concentration, and then slowly decreases at ~ 1 nM, for a dose rate of 0.33 $Gy \cdot s^{-1}$ (solid line). For $C_{NP} > 1$ nM, the increase is mostly due to the increase of H_2O_2 produced during the radiolysis, due to a higher energy deposition induced by NPs. The enhancement depends on the dose rate. When the dose rate increases from 0.33 to 12 $Gy \cdot s^{-1}$ (dashed line), the enhancement has a slower slope at low GNP concentration. Therefore, it reaches higher values for $C_{NP} > 1$ nM, as the linear fit provides lower values for $Y_{Cou_2,0} + Y_{Cou_3,0}$.

Such a behaviour may appear, at first sight, similar to the enhancements experimentally observed. However, they are inconsistent on several points: first, it is favoured for higher oxygen concentration, which is in contradiction to what has been experimentally observed [108,110]. This is due to the weak dependence of H_2O_2 yield with the level of dissolved O_2. Secondly, there is no saturation for NP concentrations varying from 2 to 5 nM. Finally, and most importantly, the extent of the enhancement reaches a maximum at 1.35 for a dose rate of 0.33 $Gy \cdot s^{-1}$. This is much lower than the experimental enhancements that were as high as ~ 4. This was expected, as the maximum yield of H_2O_2 varied from 80 to 89 $nmol \cdot J^{-1}$ (without NP). If H_2O_2 molecules were all converted into a $^{\bullet}OH$, we could expect a maximum increase of 89 $nmol \cdot J^{-1}$, which is twice lower than the yield measured for $^{\bullet}OH$ in the absence of NPs. Therefore, this scenario can not reconcile with the experimental observations, and in particular can not reproduce the very high enhancements.

12.4.4. Scenario 4

12.4.4.1. Description

The last scenario hypothesized that the coumarin by-product Cou_1, which has a longer life time than hydroxyl radicals, would react with the coumarin molecules located on the surface of the NP and would, in turn, be more efficient at producing the fluorescent 7OH-Cou molecules rather than its isomeres. Such mechanisms could be explained, for instance, by a reaction between Cou_1 and another Cou_1 molecule adsorbed on the NP, leading to a reaction R2. As the Cou_1 is adsorbed, some of the cycle positions for the group OH may be unavailable, leading to more final products with the OH group on position 7.

12.4.4.2. Calculation and approximations

As previously introduced for the scenario 3, both MC and analytic calculations were mandatory. Modelling reactions R1-R3 and R6 with a MC simulation allowed us to obtain, at $t = 10^{-6}$ s, the yields of Cou_1, Cou_2, Cou_3 and Cou_4 necessary for the analytical calculation (see Eq. 12.2). For the reaction R6, we modelled NPs as an inexhaustible reservoir, consistent with our homogeneous kinetics approach. For the reaction constant k_{VI} between Cou_1 and the NP, we hypothesized that it varied with the number of coumarin on the surface of one GNP, Cou_{surf} (see Tab. 12.4). The reaction constant, k_{VI}, thus reads,

$$k_{VI} = k_{VI,max} \frac{Cou_{surf}}{Cou_{surf,max}}. \tag{12.7}$$

We fixed $k_{VI,max}$ at 4×10^{11} $M^{-1}s^{-1}$. For a diffusion-controlled reaction, this corresponds to a reaction radius of $\sim$ 17 nm, which is of the order of the size of the GNP. This value is therefore an upper-limit. The final fluorescent yield reads,

$$Y_{7OH-Cou} = \eta_0(Y_{Cou_2} + Y_{Cou_3}) + \eta_{NP} Y_{Cou_4} \tag{12.8}$$

where η_0 (respectively η_{NP}) is the conversion rate of Cou_2 + Cou_3 (respectively Cou_4) to the fluorescent molecules 7OH-Cou. The final enhancement factor was,

$$EF = \frac{Y_{Cou_2} + Y_{Cou_3}}{Y_{Cou_2,0} + Y_{Cou_3,0}} + \frac{\eta_{NP}}{\eta_0} \frac{Y_{Cou_4}}{(Y_{Cou_2,0} + Y_{Cou_3,0})} \tag{12.9}$$

where $Y_{Cou_2,0}$ and $Y_{Cou_3,0}$ are the concentrations obtained for $C_{NP} \to 0$ nM. This was obtained by a linear fit of the yields for GNP concentrations ranging from 0.1 to 0.3 nM[251]. The conversion rate η_0 was fixed with experimental data, while η_{NP} was a parameter adjusted to reproduce the experimental yield enhancements. We assumed that $\frac{\eta_{NP}}{\eta_0}$ did not depend on the atmosphere condition.

12.4.4.3. Results, discussion and conclusion

Fig. 12.8 displays the yields of Cou_{1-4} and $^{\bullet}OH$ as a function of time after the beginning of irradiation, for a time up to 10 s. Two concentrations of NP are displayed (0.1 nM in dashed line and 2 nM in solid line). The yields are hardly affected by the atmosphere conditions, for a time up to 10^{-6} s. At such a short time, only the reaction R1 is involved, while reactions R2, R3 and R6 occur at a longer time. For $t > 10^{-6}$ s, Cou_1 yield decreases as the reactions R2, R3 and R6 start, leading to an increase of Cou_2, Cou_3 and Cou_4. The decrease of Cou_1, and consequently the formation of its by-products, is dependent both on the NP concentration and the atmosphere conditions.

For a fixed GNP concentration of 0.1 nM, Cou_1 is entirely consumed by O_2 before other reactions could occur. Therefore, the yield of Cou_3 consequently increases and reaches a saturation at $\sim 10^{-3}$ to 10^{-2} s. For larger C_{NP}, the reaction R6 starts being competitive with the reaction R3, lowering the yield of Cou_3 while increasing the yield of Cou_4. The proportion of Cou_3 *vs* Cou_4 highly depends on the concentration of O_2. For a fixed GNP concentration, the yield of Cou_4 highly increases with decreasing dissolved oxygen. The presence of NaCl plays a role on the proportion of Cou_4 produced compared to Cou_3. As the reaction constant k_{VI} depends on the

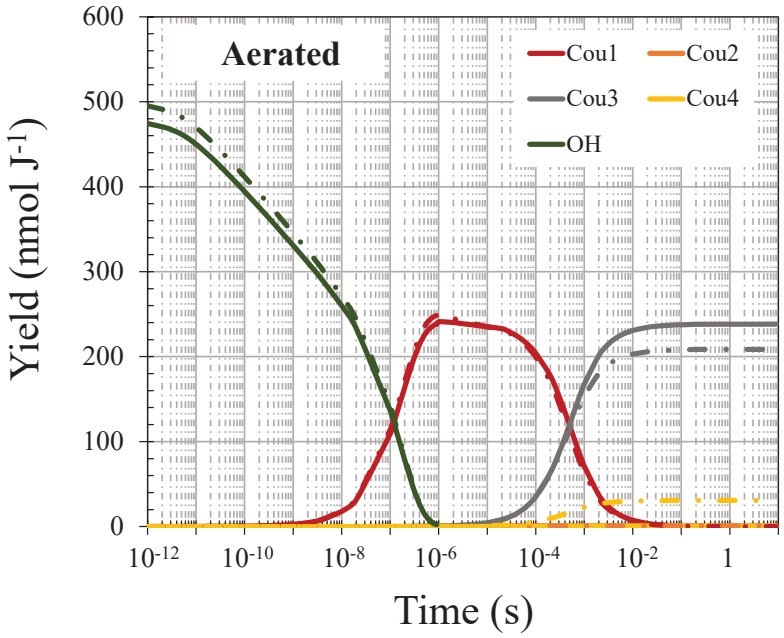

Figure 12.8.: Yield (in nmol $\cdot$ J^{-1}) of chemical species, as a function of the time, in second. In solid line, the results are displayed for a GNP concentration of 0.1 nM, and in dashed lines for a concentration of 2 nM. The dose rate was fixed at 0.33 Gy $\cdot$ s^{-1}.

number of coumarin molecules adsorbed on the NP surface, the reaction R6 was less favoured in presence of NaCl, as the number of Cou_{surf} decreased.

The results of the chemical yields enabled to obtain the fluorescence yield enhancement. On Fig. 12.9, the calculated enhancements are displayed in solid lines as a function of the NP concentration, for different atmosphere conditions. They are compared to experimental yield enhancements[108,251]. To reproduce as much as possible the experimental data of the yield enhancement under the different atmospheric conditions, we set η_{NP} at 0.2.

Overall, we could reproduce the trends experimentally observed, with first a sharp increase of the enhancement for GNP concentrations varying from 0 to 1 nM, and the reach of a saturation for GNP concentrations beyond 2 nM. Such a saturation could be obtained due to the limited amount of Cou_1 species available to interact with NPs. We also qualitatively reproduce the trends with regard to atmosphere conditions. We could reproduce similar increase of the enhancement when changing from aerated atmosphere (see Fig. 12.9 (a)) to N_2 atmosphere (see Fig. 12.9 (b)), due to the lower dissolved O_2 concentration that favoured R6 reaction over R3 reaction. Likewise, under 100 % O_2 atmosphere (see Fig. 12.9 (c)), the enhancement dropped as R3 was more competitive than R6, due to the higher O_2 concentration. When adding NaCl and under aerated condition, we also obtained a drop of the enhancement ratio (see Fig. 12.9 (d)), as previously explained.

The calculated plateau values did not perfectly match the ones obtained experimentally. Increasing the reaction constant k_{VI} by a factor of 10, while reducing η_{NP} enabled to obtain a better match. However, k_{VI} reached a maximum value of 4×10^{12} M^{-1}s^{-1}, corresponding to a reaction radius of $\sim$ 170 nm, which appears too large compared to the size of the chemical species involved. Note that this last scenario main prerequisite is that the coumarin by-product Cou_1 has a life time that is long enough to interact with the GNPs. The results were thus extremely dependent on the constants k_{II} and k_{III}. As previously mentioned, two values were proposed[108,284]. When using the values proposed by Yamashita *et al.*[284], which were considerably higher than the ones proposed by[108] (especially for R3), the life time of Cou_1 was severely impacted. In particular, as $k'_{III} = 10^9$, which is more than 2 orders of magnitude higher than k_{III}, the chemical species

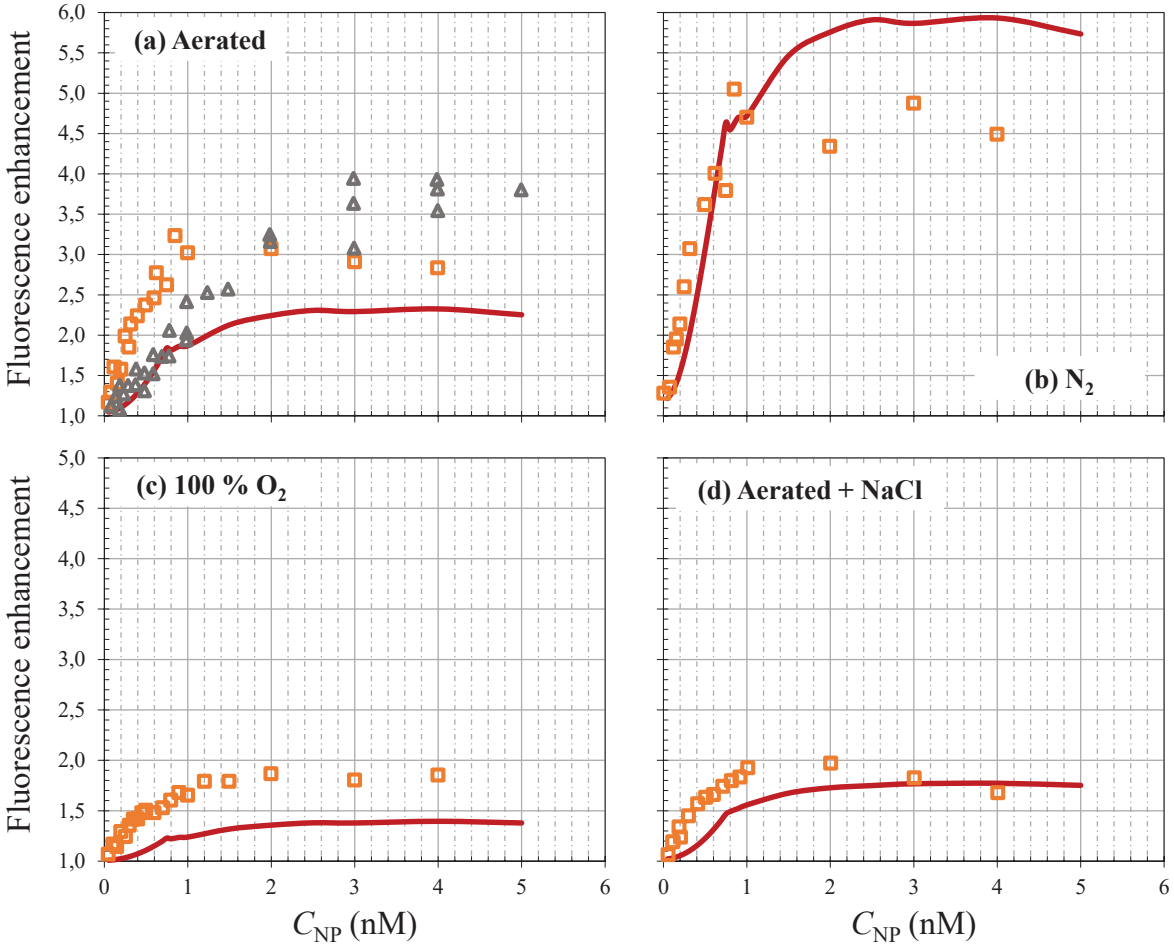

Figure 12.9.: Fluorescence enhancement, as a function of the NP concentration (in nM), for different experimental conditions, obtained using reactions constants from Gilles[108]. The calculation results are displayed in solid lines while the experimental results are displayed in orange squares[108] and grey triangles[251].

Cou_1 reacted much more quickly with O_2. As a consequence, the amount of Cou_1 that reacted with NPs considerably dropped when using the same values k_{VI} and η_0, η_{NP}. To recover the enhancement, the k_{VI} values had to be dramatically increased, along with η_{NP}. While similar enhancements could be obtained compared to the experimental ones for aerated condition, they were much more sensitive to the oxygen concentration. Therefore, the enhancements under N_2 reached higher values than experimentally reported. For a firm conclusion on this scenario, it would therefore be required to precisely know the constant values of the reactions R2 and R3.

In any case, we managed to reproduce the main trends. We may note that this mechanism relies on the presence of coumarin molecules on the surface of the NP. Adding a coating consequently reduces the amount of adsorbed coumarin, and we thus expect this fluorescent yield enhancement to be drastically reduced, as experimentally observed[109]. Finally, this mechanism does not directly depend on the energy of the photons. It is thus compatible with the enhancement observed under MeV photon irradiation[108,110].

12.5. Conclusion

In radiation research, coumarin molecules are used to measure $^{\bullet}OH$ molecules produced during irradiation of a solution[14,183]. When reacting with $^{\bullet}OH$, coumarin molecules undergo a multi-step reaction and form, among many products, a fluorescent molecule, 7OH-Cou. Such a reaction is

not extremely efficient, as the conversion rate between Cou + $^{\bullet}$OH to a fluorescent molecule is only of 5 % under aerated condition. We investigated 4 different scenarios proposed in the literature to explain the very high fluorescence yields observed with coumarin molecules when irradiating a colloidal solution of gold nanoparticles, that could reach up to a 4-fold enhancement[108,110,251]. The first one suggested than a thin layer of water molecules around the NP could have a lowered dissociation energy, leading to an increase of radiolysis products. Such a scenario was found to play a negligible impact on the overall production of $^{\bullet}$OH. In a second scenario, we proposed that $^{\bullet}$OH could react with coumarin molecules adsorbed on the surface of NPs, and form more efficiently the final fluorescent molecule 7OH-Cou. However, the amount of $^{\bullet}$OH molecules that reacted with adsorbed coumarin molecules was too low to reach the experimental enhancement. In the third scenario, we investigated the possibility of a Fenton-like reaction that would convert H_2O_2 molecules into $^{\bullet}$OH molecules, thus increasing the final yield of 7OH-Cou. Again, this scenario reached an enhancement that was much lower than the experimental one. Finally, we suggested that the coumarin by-product resulting from the primary interaction between $^{\bullet}$OH and Cou, would react with coumarin molecules on the NP surface and undergo some interference that would, in turn, increase the efficiency of 7OH-Cou production. This scenario was the only one able to explain the extent of the enhancement experimentally observed. As a conclusion, the scenario 4 could explain the increase of the fluorescent signal. The scenario 3 might add up, and may play a significant role if the conversion efficiency of the $^{\bullet}$OH coming from the decomposition of H_2O_2 into a fluorescent molecule is also increased. To verify these hypothesis, more experimental data would be required. In particular, a clarification of the reaction constants of intermediate coumarin by-products is mandatory as different values were reported in the literature. Besides, a better characterization of the number of coumarin molecules adsorbed on the NP surface, although challenging, would provide significant clarification. At last, a measure of H_2O_2 may help better understand whether a significant decomposition of H_2O_2 occurs.

Part IV.

Biophysical modelling: quantification of cell survival irradiated with keV photons in presence of gold nanoparticles with the NanOx model and the Local Effect Model

13. Theoretical investigation of the radiosensitizing effect of gold nanoparticles with two biophysical models

Authors: Floriane Poignant[a], Caterina Monini[a], Étienne Testa[a], Michaël Beuve[a]

(a) Univ Lyon, Université Claude Bernard Lyon 1, CNRS/IN2P3, Institut de Physique Nucléaire de Lyon, 69622 Villeurbanne, France.

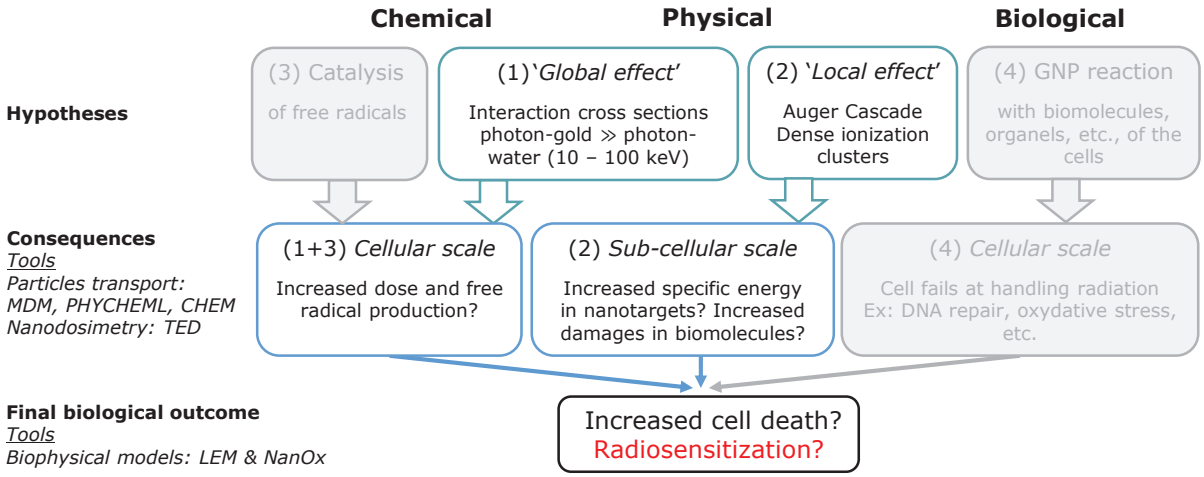

Figure 13.1.: List of mechanisms that may be responsible for GNP radiosensitization. This chapter focuses on cell survival, accounting for the local and global effects.

Chapters 9, 10 and 11 allowed us to quantify the 'local' and 'global' effects of GNPs. Chapter 12 suggested that, at this stage, it is not possible to confirm an overproduction of hydroxyl radicals due to catalytic processes. Therefore, in this chapter, we propose to calculate cell survival solely based on the 'local' and 'global' effects that were previously quantified, as illustrated in Fig. 13.1. This chapter presents cell survival predictions that were obtained for the cell line HSG using the biophysical model NanOx and the Local Effect Model. Results were presented at the international conference ICRR (Manchester, 2019, oral presentation). This chapter will be submitted as an article once the review by the different co-authors is completed.

Abstract

Over the past two decades, gold nanoparticles (GNPs) have been studied for their ability to enhance radiation therapy. When localized in the cancerous cells of the tumour, GNPs may improve the therapeutic outcome of radiation therapy. Different implementations of the Local Effect Model (LEM) have been used to translate the energy deposition at the sub-cellular scale into cell survival, for cells irradiated in presence of GNPs. For keV photon irradiation, these studies have suggested that the biological effectiveness of GNPs arises from two reasons. First, cross section of photon interaction with gold are higher compared to that with biological tissues, resulting in an increase of the macroscopic energy deposition. Second, ionized gold atoms undergo a desexcitation process that generates a burst of low-energy secondary electrons, known as the Auger cascade, that would result in a local dose enhancement in the vicinity of GNPs. In this study, we compared the predictions of the various implementations of the LEM with a unique set of parameters (e.g. cell line, GNP and beam parameters). Cell survival with GNPs was also calculated with the biophysical model NanOx and compared to the LEM predictions for an identical system. We chose a simple, theoretical homogeneous distribution of GNPs, as it has been done in the previous studies. We found the predictions obtained with the various implementations of the LEM to frequently disagree with one another, due to difference of dosimetric approaches. In addition, we found that the NanOx model predicted an increase in cell death that was solely due to the macroscopic increase of the dose deposition. In particular, NanOx predicted no increase of biological effectiveness due to Auger electrons. A much more realistic description of the system is required in order to have predictive biophysical models, both in terms of GNPs biodistribution and sub-cellular nanotargets. Complex biological pathways evidenced by different experimental studies should also be taken under consideration and modelled.

13.1. Introduction

Over the past two decades, gold nanoparticles (GNPs) have demonstrated their ability to enhance radiation therapy both *in vitro*[26,39,55,68,134,135,225,226,261,262] and *in vivo*[26,48,115,117,140,280,290]. Different particle sources have been used, especially photon irradiation. Photon irradiation at keV energies have shown to result in the highest effects[55,134,225,226]. Besides, the use of monoenergetic photon beams of energy varying between 30 to 100 keV in combination with GNPs showed that the extent of the effect depended on the photon energy[226]. Such observations suggest that at least part of the effect originates from physical mechanisms. At such energies, photons have a much higher probability of interacting with gold, compared to soft tissues. This results in a significant increase of the dose deposition, of the order of ~ 6 to ~ 15 % for a gold concentration of 1 mg·mL^{-1}(see chapter 10). In addition, ionized gold atoms undergo desexcitation processes that lead to the emission of a burst of secondary electrons, known as the Auger electrons. These electrons have a short range in water, below ~ 200 nm. Many authors[56,57,191] have suggested that these electrons result in dense ionization clusters that are responsible for an additional increase in cell death, similarly to the relative biological effectiveness observed in hadrontherapy (with ions heavier than protons).

Following these two assumptions, the Local Effect Model (LEM), originally developed to predict cell survival upon ion irradiation, was implemented to reproduce cell survival in presence of GNPs as a function of the prescribed dose[169,171,176,191,193,194]. This model is based on parameters obtained with photon irradiation, and the use of a representation of the energy deposition distribution at sub-cellular scale, often referred to as the local dose D_{local}. When applied to GNP-enhanced radiation therapy, the dose was systematically decomposed as the sum of two contributions: (1) a uniform, macroscopic background dose coming from the interaction of photons with water molecules representing the cell; (2) a heterogeneous, nanoscopic dose (i.e. the local dose) coming from the interaction of photons with gold atoms of the GNPs. Two distinct

methods were proposed to calculate this local dose. In a majority of the studies[176,191,193,194], the local dose resulting from the interaction between GNPs and photons was calculated in concentric shells and expressed as a radial dose as a function of the distance to the NP centre. We will refer to this first approach as the "LEM radial" approach. The second approach[169,171] calculated the dose deposition in nanovoxels of sizes equal to $20 \times 20 \times 20$ nm^3. We will refer to this second approach as the "LEM semi-nano" approach.

The radial approach was used to calculate cell survival of MDA-MB-231 cells under photon irradiation both at keV[191] and MeV[193] energies. Assuming a homogeneous distribution of GNPs throughout the cell, this approach could reproduce experimental cell survival predictions[134]. It was further used to predict cell survival for different GNP biodistributions, concentrations or different particle irradiations[176], and for different GNP materials[194]. The semi-nano approach was used to predict cell survival of PC-3 cells under keV photon irradiation[171], and was further used to study the impact of the photon beam energy and GNP biodistribution on cell survival[169].

While both implementations could reproduce experimental results, no inter-comparison of these methods has yet been reported. Inter-comparison between the different studies is difficult, if not impossible, due to the large variety of parameters used (e.g. different photon beams, cell lines, GNP size, concentration and biodistribution). In this study, we propose to compare these implementations with identical parameters. We also propose a last approach for the LEM, the "LEM full-nano" approach, based on a the "actual" calculation of energy deposition at the nanoscale for both contributions (i.e., ionized GNP atoms and water molecules), therefore without the use of mean dose quantity that cannot represent all the stochastic features of ionizing radiations. In addition and for the first time, we applied the NanOx model[69,202,204] to predict cell survival in presence of GNPs as an alternative to the LEM. The NanOx model predicts cell survival based in particular on the specific energy distribution. The specific energy is defined as the energy scored in targets. By definition, this quantity takes stochastic effects of ionizing radiations into account, on the contrary to mean quantities. In the NanOx model, cell death may be induced by the deposition of energy into a nanotarget, of dimension of the order of ten of nanometre. It therefore integrates a full stochastic, nanoscale energy deposition approach. The NanOx model has shown good results for 3 cell lines in hadrontherapy[202].

In line with previous studies[169,191,193], we chose to model a simple, theoretical situation, where GNPs were homogeneously distributed throughout the cell. For inter-comparison, we used the HSG cell line, as it has shown good results both for the LEM[89,90] and NanOx model[202].

This paper is organized as follows. In section 13.2, we introduce the system studied, the Monte Carlo simulation used to calculate the energy deposition at sub-cellular scale, and the two biophysical models. We then present the results in section 13.3 and discuss them in section 13.4, before concluding in section 13.5.

13.2. Material and methods

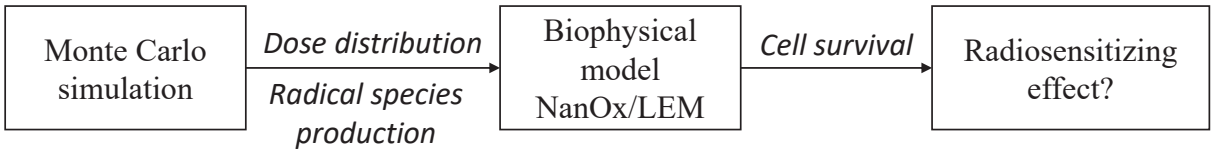

Figure 13.2.: Schematic view of the different steps and data used to calculate the cell survival with different biophysical models.

The goal of this study is to estimate, with two biophysical models, the probability of cell survival to a prescribed dose D in the presence of GNPs and for keV photon irradiation. As displayed

in Fig. 13.2, the prediction of cell survival with biophysical models is carried out in different steps. The distributions of energy deposition per unit mass in the cell is a prerequisite. As previously introduced, this corresponds to the radial dose or the dose deposition in nanovoxels for the LEM applications, and to the specific energy for NanOx. The NanOx model also requires the radiolytic yields of chemical species. Both quantities are obtained by Monte Carlo (MC) simulations. Section 13.2.1 summarizes the different quantities that are used throughout this work. Section 13.2.2 describes the system we defined for this work. Section 13.2.3 describes the MC method we used to calculate both the energy deposition distributions and the radical species production. In section 13.2.4, we introduce the biophysical model NanOx, and its application to nanoparticle-enhanced radiation therapy. Finally, in section 13.2.5, we introduce the LEM, which was used to compare the NanOx prediction.

13.2.1. Nomenclature

Tab. 13.1 summarizes the different notations that will be used in this work.

13.2.2. System

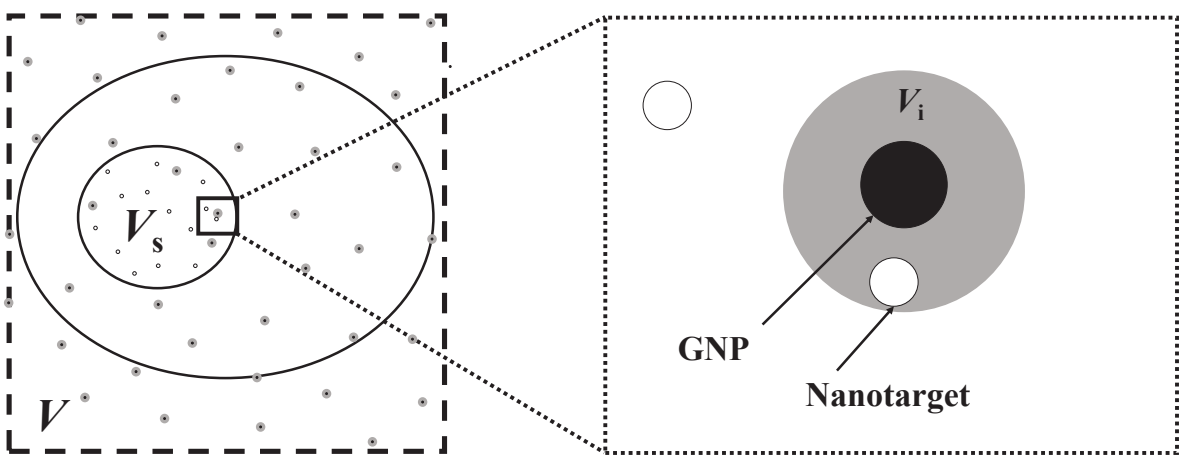

Figure 13.3.: Schematic view (not at scale) of the volumes considered and the biodistribution of gold nanoparticles. The large volume V represents the volume of influence used for MC calculations. The volume V_s is the sensitive volume, modelled as a nucleus in this work. GNPs are represented by black dots and uniformly distributed within V, and the region of interest within which the GNPs have a consequence on local dosimetric quantities is represented by the grey area. The nanotargets modelled in NanOx are represented by white disks.

As illustrated in Fig. 13.3, in the present study, we considered a cell that contained a uniform concentration C_{NP} of GNPs. We set up the sensitive volume V_{s} of the cell as the nucleus. The cell was placed in a cubic volume of influence V, which also contained a uniform concentration C_{NP} of GNPs, and was irradiated by a mono-energetic photon beam. V is defined so that electrons generated outside V do not contribute to energy deposition inside the sensitive volume V_{s}. Therefore, the size of V varied according to the primary photon energy. The half length of the volume was chosen to be larger than the range of the most energetic electron (i.e. $\sim E_{\mathrm{photon}}$ as the primary photon interacts *via* a photoelectric effect in gold). We assumed that V was placed at charge equilibrium, but as close as possible to the source, so that the fluence of the photon beam remained unchanged within V. A total of 4 radii of NPs (5 nm, 12.5 nm, 25 nm and 50 nm) and photon energies from 20 to 90 keV were chosen to systematically study the impact of the NP size and photon energy on cell survival. In this study, C_{NP} was set at 1 mg·mL^{-1}. Usually, *in vitro* experiments do not report intracellular concentrations, but rather the mass of gold per cell. It is usually lower than $\sim$ 10 pg per cell of gold[55,66,134,135,182,261,262], however the actual concentration of gold is hard to assess due to the variability of the cell volume. Different studies reported actual

	GNP quantities	
R_{NP}	Radius of the NP	nm
C_{NP}	Concentration of NPs	$mg{\cdot}mL^{-1}$ or $NP{\cdot}cm^{-3}$
	Volumetric quantities	
V	Volume of influence considered for the irradiation	cm^3
V_s	Sensitive volume of the cell	cm^3
V_i	Volume of interest surrounding a NP within which the local dosimetric quantities (i.e. $d(r)$ or z) are influenced by the presence of the NPs	cm^3
$V_{NP,s}$	Total part of the sensitive volume within which the local dosimetric quantities (i.e. $d(r)$ or z) are influenced by the presence of the NPs $V_{NP,s} = V_s\ C_{NP}\ V_i$	cm^3
$V_{W,s}$	Rest of the sensitive volume within which the local dosimetric quantities (i.e. $d(r)$ or z) are not influenced by the presence of the NPs $V_{W,s} = V_s$ - $V_{NP,s}$	cm^3
V_t	Volume of the nanotarget	cm^3
	Dosimetric quantities	
Global		
D	Prescribed dose in absence of NP	Gy
η	Percentage of the prescribed dose that leads to relevant events for biological targets, i.e. $\eta \sim 81.5$ %	No unit
D'	Macroscopic dose deposited in presence of C_{NP} NPs, for a prescribed dose D	Gy
Z	Restricted specific energy in the micro-volume V_s, without GNPs	Gy
Z'	Restricted specific energy in the micro-volume V_s, with GNPs	Gy
Z_{NP}	Restricted specific energy in the micro-volume $V_{NP,s}$, with GNPs	Gy
Z_W	Restricted specific energy in the micro-volume $V_{W,s}$, with GNPs	Gy
Local		
z	Restricted specific energy in the nano-volume V_t, without GNPs	Gy
$\frac{dP}{dz}(z, D)$	Restricted specific energy distribution without GNP	Gy^{-1}
z'	Restricted specific energy in the nano-volume V_t, with GNPs	Gy
$\frac{dP}{dz'}(z'\|r, D)$	Restricted specific energy distribution with GNP, provided that the nanotarget is located at a radial distance r from the GNP center	Gy^{-1}
$d(r)$	Radial dose around one NP, with r the distance to the NP center	Gy
	Chemical quantities	

Table 13.1.: Nomenclature for the different variables, their definition and their unit (if applicable), introduced throughout this work. z/Z: restricted energy deposition. d/D non-restricted energy deposition.

intra-cellular concentrations that were comprised between 0.1 to 2 mg·mL^{-1} [171], or equal to 7 mg·mL^{-1} [197].

We investigated the HSG cell line, which was already considered for the application of both the NanOx model[202] and the LEM model[89,90] for hadrontherapy. HSG is a human tumour salivary cell line. The reference values of the Linear Quadratic (LQ) parameters α and β are displayed in Tab. 13.2. They correspond to values obtained for a low LET irradiation, e.g. photon irradiation. These values were chosen so that the linear and the quadratic components of a given photon irradiation are the closest to the average over the whole PIDE database[97,204].

	α (Gy^{-1})	β (Gy^{-2})	α/β (Gy)	Survival at 2 Gy
HSG	0.313	0.0615	5.10	0.42

Table 13.2.: Reference values of α and β parameters of the LQ model for low LET irradiation, obtained for HSG cell line[204].

13.2.3. Monte Carlo simulation

A full description of the models used are available elsewhere[60,106] (see chapters 8 and 10) and will be only briefly introduced here. In short, the MC simulation consisted of 3 consecutive steps, during which both the energy deposition and the yield of chemical species were obtained.

Physical stage and energy deposition First, the physical stage occurred from 10^{-18} to 10^{-15} s after the primary photon interaction. Our model consisted of an event-by-event tracking of particles in the different media (water or gold). Photons were not explicitly tracked, and only the photoelectric effect and the Compton scattering were considered as they dominate at the photon energies investigated. The tracking of electrons was based on models that allowed accurate transport down to low energy both in water (meV) and gold (eV). The description of these models may be found elsewhere[106] (see chapter 8). At the end of the physical stage, the water molecules may be either excited (H_2O^*) or ionized (H_2O^+, H_2O^{2+} and H_2O^-), and the medium contained thermalized electrons (e_{th}). Any holes or electrons that were produced within the GNP were not longer tracked, as they did not lead to additional water molecule excitation or ionization. At the end of the physical stage, the spatial distribution of all low-energy electrons and ionized or excited water molecules was obtained. These events were represented by an energy-transfer point of coordinate r_i and energy ϵ_i, located where the event i occurred. An example of such output is represented on Fig. 13.4 for different concentrations of GNPs. In black (resp. red), the transfer points represent events coming from a primary interaction between a photon and a molecule of water (resp. atom of gold). In this work, the black contribution is referred to as the "background" contribution, while the red contribution is referred to as the GNP contribution. The energy per unit mass D deposited in a volume V of mass m was then defined as the sum of all the energies ϵ_i from all the transfer points of coordinates r_i contained in V, divided by m,

$$D = \frac{1}{m} \sum_{r_i \in V} \epsilon_i \tag{13.1}$$

Depending on the biophysical model, different dosimetric approaches were used in terms of type of scored energy. For NanOx application, all the energy transfers that may lead to events relevant for the biological effects of radiation (i.e., ionizations, dissociative excitations and electron attachment) were taken into account, while the ones that simply caused the heating of the medium were disregarded. Therefore, the energy stored per unit of mass when irradiating a homogeneous volume of water represented on average ~ 81.5 % of the macroscopic dose (D) sent to that volume. We denote this factor η. To avoid any confusion, we referred to this quantity as the "restricted"

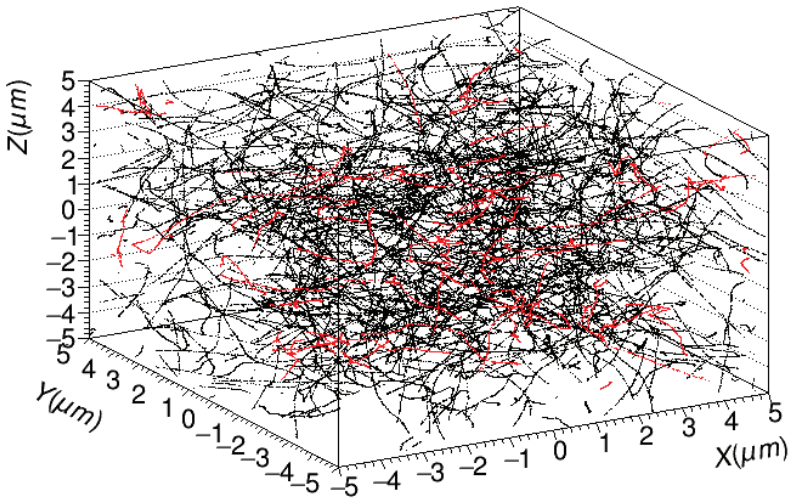

Figure 13.4.: Example of the MC code MDM output at the end of the physical stage. The points represent all the energy transfer points (restricted to ionization, dissociative excitations or electron attachment events) for an irradiation of 1 Gy in a cube of volume $10 \times 10 \times 10$ µm^3, at $E_{\text{photon}} = 20$ keV, $C_{\text{NP}} = 0.1$ mg·mL^{-1}, $R_{\text{NP}} = 5$ nm. In black (resp. red), the transfer points represent events coming from a primary interaction between a photon and a molecule of water (resp. atom of gold).

energy deposition per unit mass. For LEM application, we accounted for the whole energy deposition. As indicated in Tab. 13.1, we refer to restricted or non-restricted energy deposition with different labels. The dosimetric scoring approach also varied in terms of volumes V considered, depending on the biophysical model. This will be further discussed in the sections dedicated to the biophysical models.

Physico-chemical and chemical stage and radiolytic yields The physical stage was followed by a physico-chemical step (from 10^{-15} to 10^{-12} s), during which the medium (i.e. water) relaxes leading to the production of primary chemical species. The different branch rates of each molecular rearrangement are described elsewhere[106]. At the end of this stage, the outcome consisted of spatial distribution of chemical species: e^-_{aq}, H_3O^+, $^\bullet$OH, $^\bullet$H, H_2, $^-$OH and O, with a majority of e^-_{aq}, H_3O^+ and $^\bullet$OH. The atomic oxygen was either at a fundamental state ($O(^3P)$) or and excited state ($O(^1D)$). Finally, at 10^{-12} s after the primary interaction, the chemical phase began and the primary chemical species diffused and interacted with each other. In our simulation, this phase was simulated up to 10^{-6} s. The method used to calculate the yields and optimize the computing time, and the list of more than 50 standard chemical reactions of water radiolysis, are available elsewhere and will not be discussed in this paper[59,60,106] (see chapter 10). During the chemical stage, we obtained the radical species production for a concentration C_{NP} of GNPs (see chapter 10).

13.2.4. NanOx

13.2.4.1. General and brief introduction of the model

NanOx is a theoretical framework aiming at calculating cell survival following a dose of irradiation D, originally developed in the context of hadrontherapy[69,202,204]. Its fundamental premise is that the probability of cell survival to an irradiation depends on two classes of biological events, occurring at different spatial scales: the *local lethal* and *global* events. In the current version, the former class of events is described by a lethal function expressed as a function of the distribution

of the energy deposition per unit mass in nanotargets, defined as the restricted specific energy. The latter class of events is described by a quadratic function of the cellular oxidative stress, estimated through the chemical specific energy[205]. Both quantities are estimated by means of Monte Carlo simulations. Particle tracks are taken into account via the spatial distribution of the energy-transfer points and the physico-chemical events created by K radiation impacts (such configuration is referenced by the index c_K afterwards). NanOx thus includes dose fluctuation both at micrometric and nanometric scales, predicting cell survival probability in terms of an average over all the configurations of radiation impacts and irradiated cells. The mean cell survival probability reads:

$$\overline{S(D)} = \sum_{K=0}^{K=\infty} P(K,D) \cdot \left\langle {}^{c_K}S \right\rangle_{c_K}, \tag{13.2}$$

where $P(K,D)$ is the probability to achieve K impacts with a delivered physical dose D, and $\left\langle {}^{c_K}S \right\rangle_{c_K}$ is the average survival probability over all the configurations c_K. The probability of cell survival is separated into two factors due to the action of the local lethal events (S_{L}) and the action of the global events (S_{G}),

$${}^{c_K}S = {}^{c_K}S_{\mathrm{L}} \times {}^{c_K}S_{\mathrm{G}}. \tag{13.3}$$

The two terms are assumed independent and defined in two sensitive volumes *a priori* different from one to another. Local lethal events are caused by physico-chemical processes localized in nanometric volumes, for which the probability that two distinct tracks deposit energy is negligible, provided standard clinical doses[202]. They may represent a DNA lesion, but could also be extended to other targets such as cell membranes. Global events represent a phenomenon of toxic accumulation, such as the oxidative stress or non severe damages.

Local lethal events Local lethal events are events that may lead on their own to cell death. They are modelled by the inactivation of one among N nanometric targets distributed in a sensitive volume. This inactivation is described by a function of an observable, the restricted specific energy z, calculated by MC tools. z was obtained by scoring the energy deposition inside cylinders of height and radius equal to 10 nm (see chapter 9),

$$z = \frac{1}{m_t} \sum_{i, r_i \in V_t} \epsilon_i \tag{13.4}$$

with V_t the volume of the nanotarget and m_t its mass. We define $\frac{\mathrm{d}P}{\mathrm{d}z}(z,D)$ the distribution of the specific energy z, for a prescribed dose D. Since the target size is defined at the nanometric (local) scale, for the therapeutic doses, the energy deposition in a target essentially comes from one track k only. Assuming that the responses of the local targets are independent, the probability for a cell to survive local lethal events for a given configuration of local targets (c_N) and radiation impacts (c_K), is the probability that no local target is inactivated,

$${}^{c_N,c_K}S_{\mathrm{L}} = \prod_{k=1}^{K} {}^{c_N,c_k}S_{\mathrm{L}} = \prod_{k=1}^{K} \prod_{i=1}^{N} (1 - f({}^{c_i,c_k}z)) \tag{13.5}$$

with f the nanotarget inactivation function, and ${}^{c_i,c_k}z$ the restricted specific energy in the nan-

otarget i with configuration c_i (i.e. position and orientation), after one radiation impact with configuration c_k. Introducing the effective lethal function F, with $F(x) = -N\ln(1 - f(x))$, Eq. 13.5 becomes,

$$ {}^{c_K}S_{\mathrm{L}} = \prod_{k=1}^{K} \exp\left(-\left\langle F({}^{c_i,c_k}z)\right\rangle_{c_i}\right) \tag{13.6} $$

provided that the number of targets N is large, and they are identical and uniformly distributed. $\left\langle F({}^{c_i,c_k}z)\right\rangle_{c_i}$ represents the average of the effective lethal function over all the configurations of local targets. It may be interpreted as an average effective number of local lethal events n^*. In the first version of the model, the effective local lethal function is parametrized with the error-like function,

$$ F(z) = \frac{h}{2}\left[1 + \mathrm{erf}\left(\frac{z - z_0}{\sigma}\right)\right]. \tag{13.7} $$

The parameters z_0 (threshold), σ (width of the increase) and h (height of the response) were obtained via the fit of measured α values of various cell lines for different irradiation beams (see Tab. 13.5 for the HSG cell line).

Global events To model the global events due to oxidative stress in the current version of NanOx, the relative chemical effectiveness, RCE, is introduced. It represents the ratio of chemical radiolytic yields of the considered non-reference radiation (i.e. ion therapy or GNP-enhanced radiation therapy), ${}^{c_K}G$, to that of the reference radiation, G_r,

$$ {}^{c_K}\mathrm{RCE} = \frac{{}^{c_K}G}{G_r} \tag{13.8} $$

In NanOx, the reference radiation is obtained for a ^{60}Co irradiation. These chemical yields were taken as the yield of $^{\bullet}$OH at $T_{\mathrm{RCE}} = 10^{-11}$ s after the primary particle interaction. The concept of chemical specific energy after a configuration of radiation impacts, c_K, is further introduced:

$$ {}^{c_K}\widetilde{Z} = {}^{c_K}\,\mathrm{RCE} \cdot {}^{c_K}\,Z, \tag{13.9} $$

where Z is the restricted specific energy deposited in the sensitive volume V_{s} by K radiation impacts. As the chemical yields are computed for primary reactive chemical species, the tracks may be considered independent for therapeutic doses. In the current version of NanOx, the final survival to global events reads,

$$ {}^{c_K}S_{\mathrm{G}}(\widetilde{Z}) = \exp(-\beta_{\mathrm{G}} \cdot {}^{c_K}\,\widetilde{Z}^2). \tag{13.10} $$

β_{G} is a NanOx parameter determined *via* experimental data (see Tab. 13.5). It was demonstrated that $\beta_{\mathrm{G}} = \frac{\beta}{\eta^2}$ [205], with β the LQ parameter of the cell line (see Tab. 13.2).

13.2.4.2. Photon irradiation without GNP

For an irradiation of cells by a photon beam, several simplifications are applied that derive from the high number of impacts required to obtain a dose D. As previously shown[205], the survival of the cell to a prescribed dose D reads,

$$S(D) = \int_0^\infty S(Z) \cdot \frac{\partial P_D}{\partial Z} \cdot dZ \tag{13.11}$$

$\frac{\partial P_D}{\partial Z}$ the distribution of the specific energy in the sensitive volume V_s, for a macroscopic dose D. As shown elsewhere[203,205], low-LET radiation at therapeutic doses induce a very high number of impacts K. Therefore, the α_L value may be approximated by its average value over all the c_K configurations. Following the simplification that the number of effective local lethal events, n^*, is proportional to Z[203], we then find,

$$S(Z) = S_L(Z) \times S_G(Z) = \exp(-\alpha_L Z - \beta_G Z^2) \tag{13.12}$$

where α_L represents an average effective number of lethal events divided by the restricted specific energy deposited in V_s. It does not depend on the irradiation configuration c_K, and may be obtained using the restricted specific energy distribution in the absence of GNP $\frac{dP}{dz}(z, D)$, and the lethal function $F(z)$,

$$\alpha_L = \frac{1}{\langle Z \rangle} \int_0^\infty \frac{dP}{dz}(z, D) \cdot F(z) \cdot dz \tag{13.13}$$

where $\langle Z \rangle$ is the average restricted specific energy deposited in the volume V_s. Note that α_L was calculated based on the parameters of the lethal function. It is therefore not strictly equal to the reference value α displayed in Tab. 13.2.

13.2.4.3. Photon irradiation with GNPs

Considerations for NP biodistribution As the goal of this study was to obtain NanOx predictions for GNP-enhanced radiation therapy and compare them with the LEM predictions as implemented in the literature, we did not consider the complexity of GNP biodistribution. Realistic biodistributions will be considered in a future work. In the present study, we considered the following simplifications.

- The number of NPs per cell is constant.
- Each NP is identical with a constant radius R_{NP}.
- NPs are uniformly distributed in the volume of influence V, and therefore in the sensitive volume V_s.
- The sensitive volume for local and non-local events were considered identical to the ones used for hadrontherapy, i.e. the nucleus.

As previously introduced in Eq. 13.11 and Eq. 13.12, the survival of cells in presence of NPs reads,

$$S(D) = \int_0^\infty S_L(Z') \times S_G(Z') \cdot \frac{\partial P'_D}{\partial Z'} \cdot dZ' \tag{13.14}$$

where Z' is the microscopic specific energy in V_s in the presence of GNPs. Note that, due to a high probability of gold-photon interaction, we find $\langle Z' \rangle > \langle Z \rangle$.

Local lethal events To calculate the restricted specific energy distribution with GNPs, the sensitive volume was decomposed into two regions (see Fig. 13.3): the region within which the presence of GNPs had no impact on the energy deposition at nanometric scale ($V_\mathrm{W,s}$) and the region within which the presence of GNPs had an impact on such quantities ($V_\mathrm{NP,s}$). When considering only one GNP, the latter region was modelled as a spherical volume centred around the GNP and labelled as the region of interest V_i. This is illustrated on the right side of Fig. 13.3. The NP is represented by a black dot, while V_i is represented by the grey disk. As each NP was identical, this region of interest was the same for any NP. The total volume, contained within V_s, that had an influence on local dosimetric quantities was,

$$V_\mathrm{NP,s} = V_\mathrm{s} C_\mathrm{NP} V_\mathrm{i} \tag{13.15}$$

with C_NP the concentration of NPs. As V_i was small compared to V (radius $\leq$ 200 nm), we neglected any border effect. We therefore obtained $V_\mathrm{W,s} = V_\mathrm{s}$-$V_\mathrm{NP,s}$. The microscopic restricted specific energy in the sub-volumes $V_\mathrm{NP,s}$ and $V_\mathrm{W,s}$, Z_NP and Z_W, were calculated. As we assumed that each NP was identical, we find that $Z_\mathrm{NP} = Z_\mathrm{i}$, with Z_i the average specific energy in the volume V_i. We also have,

$$Z' = \frac{V_\mathrm{NP,s}}{V_\mathrm{s}} Z_\mathrm{NP} + \frac{V_\mathrm{W,s}}{V_\mathrm{s}} Z_\mathrm{W}. \tag{13.16}$$

Then, the distribution of the restricted specific energy was calculated both in $V_\mathrm{NP,s}$ and $V_\mathrm{W,s}$. As previously shown in chapter 9, in the vicinity of the GNP, the distribution of the restricted specific energy may be decomposed as a linear sum of the contribution coming from gold-photon interaction within the GNP, and water-photon interaction. Therefore, in $V_\mathrm{NP,s}$, the distribution of the restricted specific energy, $\frac{\mathrm{d}P}{\mathrm{d}z'}(z'|r, D)$, reads,

$$\frac{\mathrm{d}P}{\mathrm{d}z'}(z'|r, D) = n_\mathrm{W}(D) \frac{\mathrm{d}P_\mathrm{W}}{\mathrm{d}z'}(z') + n_\mathrm{NP}(D) \frac{\mathrm{d}P_\mathrm{NP}}{\mathrm{d}z'}(z'|r) \tag{13.17}$$

where $n_\mathrm{W}(D)$ is the mean number of photon interactions in water for a given prescribed dose D in water, and $n_\mathrm{NP}(D)$ is the mean number of photon interactions with the GNP. Each distribution, $\frac{\mathrm{d}P_\mathrm{W}}{\mathrm{d}z'}(z')$ and $\frac{\mathrm{d}P_\mathrm{NP}}{\mathrm{d}z'}(z'|r)$, is now given per primary photon interaction. For $V_\mathrm{W,s}$, the distribution of the specific energy for C_NP of GNP may be derived from the restricted specific energy in the absence of GNPs as follows,

$$n_\mathrm{W}(D) \frac{\mathrm{d}P_\mathrm{W}}{\mathrm{d}z'}(z') = \frac{D_\mathrm{W}}{D} \frac{\mathrm{d}P}{\mathrm{d}z}(z, D). \tag{13.18}$$

with D the prescribed dose and $D_\mathrm{W} = Z_\mathrm{W}/\eta$. The survival to local events in presence of NPs may be written as follows,

$$S_{\mathrm{L}}(Z') = \exp(-\alpha_{\mathrm{NP,\,L}} \cdot Z_{\mathrm{NP}} - \alpha_{\mathrm{W,\,L}} \cdot Z_{\mathrm{W}}) \tag{13.19}$$

with Z_{NP} and Z_{W} the restricted specific energy in the microscopic volumes $V_{\mathrm{NP,s}}$ and $V_{\mathrm{W,s}}$ respectively. As detailed in Appendix F.1, assuming that the targets were homogeneously distributed in the volume V_{s}, we find,

$$\alpha_{\mathrm{W,\,L}} \sim \frac{V_{\mathrm{W,s}}}{V_{\mathrm{s}}} \cdot \alpha_{\mathrm{L}}. \tag{13.20}$$

The restricted specific energy distribution was calculated in discrete concentric shells of thickness set at 2 nm. We then find,

$$\alpha_{\mathrm{NP,\,L}} \sim \frac{1}{\langle Z_{\mathrm{NP}} \rangle} C_{\mathrm{NP}} V_{\mathrm{s}} \sum_j \int_{z'} \frac{\mathrm{d}P}{\mathrm{d}z'}(z'|j) F(z') \frac{V_j}{V_{\mathrm{s}}} \mathrm{d}z'. \tag{13.21}$$

$\frac{\mathrm{d}P}{\mathrm{d}z}(z|j)$ is the restricted specific energy distribution for each shell j of volume V_j.

Global events As introduced in 13.2.4.1, the survival to global events in presence of GNPs reads,

$$S_G(Z') = \exp(-\beta_{\mathrm{G}} \cdot \mathrm{RCE'} \cdot Z'^2). \tag{13.22}$$

Here, the coefficient RCE' is defined independent of the track configuration c_{K}, and reads,

$$\mathrm{RCE'} = \frac{G'(^{\bullet}\mathrm{OH})}{G(^{\bullet}\mathrm{OH})} \tag{13.23}$$

with $G'(^{\bullet}\mathrm{OH})$ (resp. $G(^{\bullet}\mathrm{OH})$) the chemical yield in presence of GNPs (resp. without GNPs), i.e. the number of molecules $^{\bullet}$OH produced normalized to the deposited energy with GNPs (resp. without GNPs). As shown in chapter 10, the presence of GNPs does not favour particularly any chemical species, on the contrary to what is observed for ions[205]. Therefore, RCE' is close to 1.

13.2.4.4. Application of the model

D (Gy)	$\langle Z \rangle$ (Gy)	σ_Z (Gy)	Ratio %
1	0.816	0.159	19.5
2	1.603	0.217	13.5
4	3.205	0.308	9.6
6	4.815	0.384	7.9
8	6.415	0.434	6.7
10	8.015	0.480	6.0

Table 13.3.: Average microscopic restricted specific energy $\langle Z \rangle$ and standard deviation σ_Z obtained in the sensitive volume V_{s} for a dose of irradiation Z. The ratio $\langle Z \rangle$ over σ_Z is displayed in the last column.

As detailed elsewhere[205], the distributions $\frac{\partial P_D}{\partial Z}$ (resp. $\frac{\partial P'_D}{\partial Z'}$) defined in Eq. 13.11 (resp. Eq. 13.14) may be fitted with a Gaussian law of average value $\langle Z \rangle$ (resp. $\langle Z' \rangle$) and standard deviation σ_Z (resp. $\sigma_{Z'}$), provided that D is high enough, e.g. in the range of clinical dose. In the present study, we limit the dose to 1 Gy $\leq D \leq$ 10 Gy. At the scale of the sensitive volume, we find that the fluctuation of energy deposition is small for photon irradiation, as depicted in Tab. 13.3. In other words, for the Gaussian distribution $\frac{\partial P_D}{\partial Z}$, we find that $\sigma_Z \ll \langle Z \rangle$. Typically, as provided in Tab. 13.3, for a dose of 1 Gy, which is the minimum dose of irradiation we investigate in this work, we obtained a ratio of 19.5 %. For higher doses, the ratio decreases as the number of photon interactions increase. As Tab. 13.4 shows, for $\sigma_Z \ll \langle Z \rangle$, Z hardly fluctuates and the use of its average may directly be applied. Eq. 13.11 and 13.12 are then approximated as follows,

$$S(D) \sim \exp(-\alpha_{\mathrm{L}} \cdot \langle Z \rangle - \beta_{\mathrm{G}} \cdot \langle Z \rangle^2) = \exp(-\alpha_{\mathrm{L}} \cdot \eta D - \beta_{\mathrm{G}} \cdot \eta^2 D^2) \tag{13.24}$$

Tab. 13.4 displays the results of survival for HSG cells at 2 Gy and for a photon energy of 20 keV, applying either Eq. 13.11 ($S(D)$) or Eq. 13.24 ($S_{\mathrm{av}}(D)$), for different values of σ_Z. We find relative differences that are below 1.7 % for the system we consider.

σ_Z	$S(D)$	$S_{\mathrm{av}}(D)$	Rel. diff (%)
10 %	0.3895	0.3878	-0.443
20 %	0.3946	0.3878	-1.717
30 %	0.4021	0.3878	-3.559
40 %	0.4060	0.3878	-4.490

Table 13.4.: HSG cell survival at 2 Gy, for $E_{\mathrm{photon}} = 50$ keV, applying either Eq. 13.11 ($S(D)$) or Eq. 13.24 ($S_{\mathrm{av}}(D)$), assuming a Gaussian distribution of $\frac{\partial P_D}{\partial Z}$ with different values of σ_Z.

Applying the same approximation, the cell survival in presence of GNPs reads,

$$S_{\mathrm{NanOx}}(D) \sim \exp(-\alpha_{\mathrm{W,\,L}} \langle Z_{\mathrm{W}} \rangle - \alpha_{\mathrm{NP,\,L}} \langle Z_{\mathrm{NP}} \rangle - \beta_{\mathrm{G}} \cdot \mathrm{RCE'} \cdot \langle Z' \rangle^2). \tag{13.25}$$

13.2.5. Local Effect Model

13.2.5.1. Photon irradiation without GNP

The Local Effect Model (LEM)[90,244] was also originally developed for hadrontherapy. It was the most often biophysical model adapted for NP-enhanced radiation therapy[169,171,176,191,193]. In case of photon irradiation, the surviving fraction of cells to a dose D is given by:

$$S(D) = \exp(-N_{\mathrm{lethal}}(D)) \tag{13.26}$$

where $N_{\mathrm{lethal}}(D)$ is the number of lethal events, which according to the LQ model, is:

$$N_{\mathrm{lethal}}(D) = \alpha D + \beta D^2 \tag{13.27}$$

where α and β are the LQ parameters determined with experimental data (see Tab. 13.2) which depend on the cell line.

13.2.5.2. Photon irradiation with GNPs

To account for energy deposition inhomogeneities, the LEM calculates the probability of damage occurring at each point within a cell based on the local dose at that point. The number of lethal events reads:

$$N_{\text{lethal}}(D) = \int_{V_\text{s}} v(D_{\text{local}}) \frac{\text{d}V}{V_\text{s}} \tag{13.28}$$

where V_s is the cellular sensitive volume, usually taken as the nucleus, and

$$v(D_{local}) = \begin{cases} \alpha D_{\text{local}} + \beta D_{\text{local}}^2, & \text{if } D_{\text{local}} \leq D_t \\ v(D_t) + S_{\max}(D_{\text{local}} - D_t), & \text{if } D_{\text{local}} > D_t, \text{ and } S_{\max} = \alpha + 2\beta D_t \end{cases} \tag{13.29}$$

where $S_{\max}$ is a threshold which is determined empirically. The final results depend on this threshold, on the α and β obtained experimentally and on the sensitive volume. To compare NanOx prediction to previous published results, we calculated the survival with the LEM for various dosimetric approaches.

LEM radial implementation Following the studies by McMahon *et al.*[176,191,193,194], the radial approach consisted in calculating the number of lethal events based on the radial dose per ionized GNP $d(r)$. $d(r)$, was obtained by calculating the energy deposition within concentric shells centred around the GNP following an ionization event,

$$d(r) = \frac{1}{m_r} \sum_{i, r_i \in V_r} \epsilon_i \tag{13.30}$$

where r is the distance to the NP centre, V_r is the volume of a concentric shell of infinitesimal thickness δr and m_r is its mass. The advantage of this quantity over the restricted specific energy in nanotargets is that it requires less computing resources for the calculation. As previously done[191,193,194], the number of lethal events was decomposed as the sum of the number of lethal events induced by a low LET photon irradiation and the number of lethal events induced by a GNP.

$$S_{\text{LEM radial}}(D) = \exp(N_{\text{lethal,W}}(D) + N_{\text{lethal,NP}}(D)). \tag{13.31}$$

$N_{\text{lethal,W}}$ was calculated with Eq. 13.26. $N_{\text{lethal,NP}}$ was calculated using Eq. 13.29, with D_{local} computed as the radial dose per ionized GNP $d(r)$. The final number of lethal events was therefore proportional to the number of ionized GNPs in V_s.

LEM semi-nano implementation Following the studies by Lechtman *et al.*[169,171], the energy deposition in nanovoxels of the size $20 \times 20 \times 20$ nm^3 was calculated for the GNP contribution in V_s, i.e., for all events following an ionization of a GNP. The sensitive volume was decomposed in nanovoxels. The average number of ionized GNPs in V was calculated, and tracks of ionized GNPs were randomly distributed throughout the volume of interest V. Nanovoxels that received energy were then stored. In any voxel of V_s, the dose was equal to the macroscopic dose of irradiation D, plus the dose deposited by the GNP in the voxel. Eq. 13.29 was applied using this 3D dose

profile. Note that this approach is a semi-nanoscale approach: while the dose deposition induced by the interaction of photons with GNP is calculated at the nanoscale, the dose induced by the interaction of photons with water is calculated at a macroscopic scale.

LEM full-nano implementation In this last approach, we accounted for the dose deposition at the nanoscale both for the GNP contribution and the background contribution. In that case, similarly to what was done for NanOx, the volume was decomposed in 2 sub-regions, $V_{\mathrm{NP,s}}$ and $V_{\mathrm{W,s}}$. The cell survival then reads,

$$S_{\text{LEM full-nano}}(D) = \exp(N_{\text{lethal,full-nano}}(D)), \tag{13.32}$$

with

$$N_{\text{lethal, nano}}(D) = C_{\mathrm{NP}} V_{\mathrm{s}} \sum_j \int_{z'} \frac{\mathrm{d}P}{\mathrm{d}z'}(z'|j) \cdot v\left(\frac{z'}{\eta}\right) \frac{V_j}{V_{\mathrm{s}}} \mathrm{d}z' + \frac{V_{\mathrm{W,s}}}{V_{\mathrm{s}}} \int_z \frac{D_{\mathrm{W}}}{D} \frac{\mathrm{d}P}{\mathrm{d}z}(z, D) v\left(\frac{z}{\eta}\right) \mathrm{d}z. \tag{13.33}$$

13.2.6. Macroscopic approach

A last approach consisted in estimating the cell-survival solely based on the increase of the average microscopic energy deposition per unit mass in V_{s}. The survival reads,

$$S_{\text{macro}}(D) = \exp(-\alpha D' - \beta D'^2), \tag{13.34}$$

with D' the dose deposited in presence of GNPs corresponding to a prescribed dose D (see section 13.2.3). α and β are the LQ parameters sued either for the LEM model (see Eq. 13.27) or the NanOx model (see Eq. 13.24), for low LET photon irradiation without GNP.

13.2.7. Parameters

The different free parameters of the model considered for this study are summarized in Tab. 13.5.

	r_{V_s} (µm)	z_0 (kGy)	σ (Gy)	h ($\times 10^3$)	β_{G} (Gy^{-2})
NanOx	7.0	15.6	549	180	0.0961
	α (Gy^{-1})	β (Gy^{-2})	r_{V_s} (µm)	D_t (Gy)	
LEM	0.313	0.0615	5	30	

Table 13.5.: Parameters set-up for the biophysical models, for the HSG cell line. The NanOx parameters correspond to the ones from Monini *et al.*[204], and the LEM parameters were taken for the LEM version II[89,90]. Both the NanOx and the LEM parameters were obtained through a fit of experimental values.

13.2.8. Metrics of comparison

To summarize, we calculated cell survival to a dose D for HSG cells, using two biophysical models (NanOx and LEM). Both models were used to calculate the cell survival without GNPs, and the cell survival with GNPs solely based on the macroscopic increase of dose deposition. In addition, we calculated cell survival for NanOx and the LEM accounting for energy deposition at the nanoscale. For the LEM, we used 3 approaches: one based on the radial dose for the GNP contribution, one based on a nanodosimetric approach for the GNP contribution and one

based on a full nanodosimetric approach. This resulted in 6 cell survival predictions in presence of GNPs, $S_{\text{macro, NanOx}}(D)$, $S_{\text{NanOx}}(D)$, $S_{\text{macro, LEM}}(D)$, $S_{\text{LEM radial}}(D)$, $S_{\text{LEM semi-nano}}(D)$ and $S_{\text{LEM full-nano}}(D)$. From these cell survivals, we determined the LQ parameters α and β in presence of GNPs. They were further used to estimate the Relative Biological Effectiveness at 2 Gy, defined as follows,

$$\text{RBE}_{2\text{ Gy}} = \frac{2}{D_{\text{GNP}}} \tag{13.35}$$

where D_{GNP} is the dose required in presence of GNP to reach the same survival obtained at 2 Gy in the absence of GNPs.

13.3. Results

13.3.1. Multi-scale energy deposition

This section illustrates the difference obtained for the dosimetric approaches implemented. The figures do not display strictly the same quantities and are not meant to be directly compared to each other. Though, they enable quantitatively to understand the differences between the approaches.

Dosimetric quantities highly depend on the size of the volume considered. When the volumes are microscopic, such as the size of the cell or cell nucleus, the energy deposition per mass unit is of the same order of magnitude compared to the dose of irradiation D. As shown in chapter 10, in presence of GNP we found $D' \sim D + [6 - 17\%]D$, depending mostly on the photon energy, for $C_{\text{NP}} = 1$ mg·mL^{-1}.

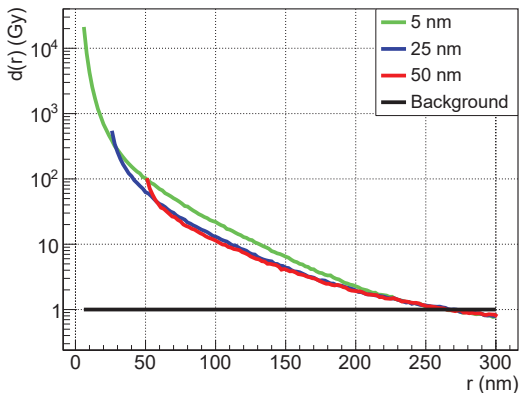

(a) Radial dose $d(r)$ following an ionization event in the GNP, as a function of the distance to the GNP center, r. Results are displayed for different R_{NP}. $E_{\text{photon}} = 20$ keV and $D = 1$ Gy.

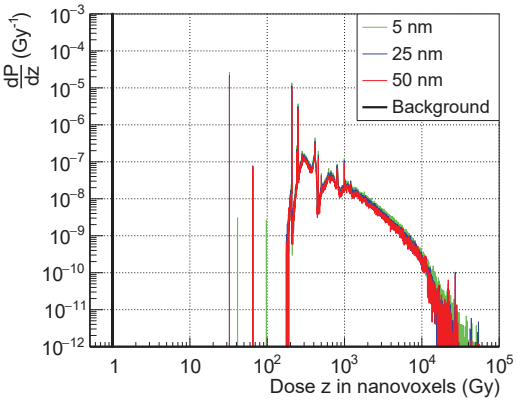

(b) Energy deposition distribution per unit mass in a voxel of size 20 × 20 × 20 nm^3 in V_{s} (HSG). Results are displayed for different R_{NP}. $D = 1$Gy, $C_{\text{NP}} = 1$ mg·mL^{-1}and $E_{\text{photon}} = 20$ keV.

Figure 13.5.: Dosimetric values obtained depending on the LEM implementation.

The radial dose $d(r)$ following a GNP ionization is displayed on Fig. 13.5a. Compared to the macroscopic dose D', $d(r)$ reaches much higher values, up to tens of kGy near the GNP surface. These high values are mostly due to the decrease of the concentric shell volume near the GNP surface. As the distance to the GNP centre r increases, the volume varies proportionally to r^2 and therefore the radial dose drops and becomes lower than the "background" dose (set at 1 Gy in this example) at few hundreds of nm.

Fig. 13.5b displays the distribution of the energy per unit mass scored in nanovoxels of size 20 × 20 × 20 nm^3, following the method by Lechtman *et al.*[169,171]. The irradiation was set at 1 Gy and the volume contained 1 mg·$mL^{-1}$of GNPs. The GNP contribution was scored in the nanovoxels, while the background contribution was taken homogeneous and equal to D in any voxel. As nanovoxel volumes are very small, high values of energy per unit mass are reached for the GNP contribution. We obtained values as high as tens of kGy. The macroscopic description of the background dose induced a peak of high intensity at 1 Gy, resulting in a probability of having 1 Gy in a voxel larger than 99.9 %. This figure illustrates the dual description introduced in this model, and the very different descriptions used for the GNP *vs* background dose contribution.

While this dual approach decreases the computing time required for a full 3D map of the dose deposition inside V_s, it is far from the real energy deposition distribution in the nanovoxels: at the nanoscale, both contributions experience a very large variation of the energy deposition, including the background contribution. This is further illustrated by Fig. 13.3. It shows the variation of the energy deposition inside a nanotarget (∼ in size to the nanovoxels) located near the GNP surface. When a full nanometric approach is implemented, we obtain a specific energy for the background contribution (in black) that has a probability of being larger than 0 Gy of only $\sim 4 \times 10^{-4}$, but that varies from tens of Gy up to tens of kGy.

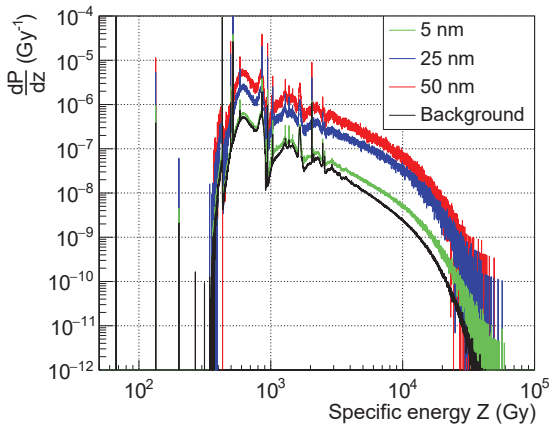

Figure 13.6.: Specific energy distribution in a nanotarget located at 11 nm from a GNP surface. Results are displayed for different R_{NP}. E_{photon} = 20 keV and D = 1 Gy.

13.3.2. Cell survival

An example of cell survival predictions of NanOx and the LEM is displayed on Fig. 13.7, for a photon energy of 20 keV and a GNP concentration of 1 mg·mL^{-1}. Both models have very similar predictions in the absence of GNPs, but slightly differ due to difference of model parametrization.

In presence of GNPs, for E_{photon} = 20 keV, R_{NP} = 5 nm and C_{NP} = 1 mg·mL^{-1}, the macroscopic dose increases by ∼ 11 %. As a consequence, the macroscopic cell survivals ('Macro (NanOx)' and 'Macro (LEM)') show a significant increase in cell death for both models. For nanoscale approaches, we find a very large variation of the cell survival when comparing the different LEM implementations (LEM radial, LEM semi-nano and LEM full-nano). When the implementation is based on the radial dose for the GNP contribution (LEM radial), a small increase in cell killing is obtained compared to the macroscopic approach. Typically, we obtain a cell survival of 0.65 at 1 Gy for the 'Macro' approach, and of 0.62 for the radial approach. The cell survival then considerably drops when the implementation is based on the nanovoxel energy deposition scoring for the GNP contribution (LEM semi-nano). At 1 Gy, it is equal to 0.43. Finally, for a full nanometric energy deposition scoring, the cell survival becomes extremely low (0.01 at 1 Gy)

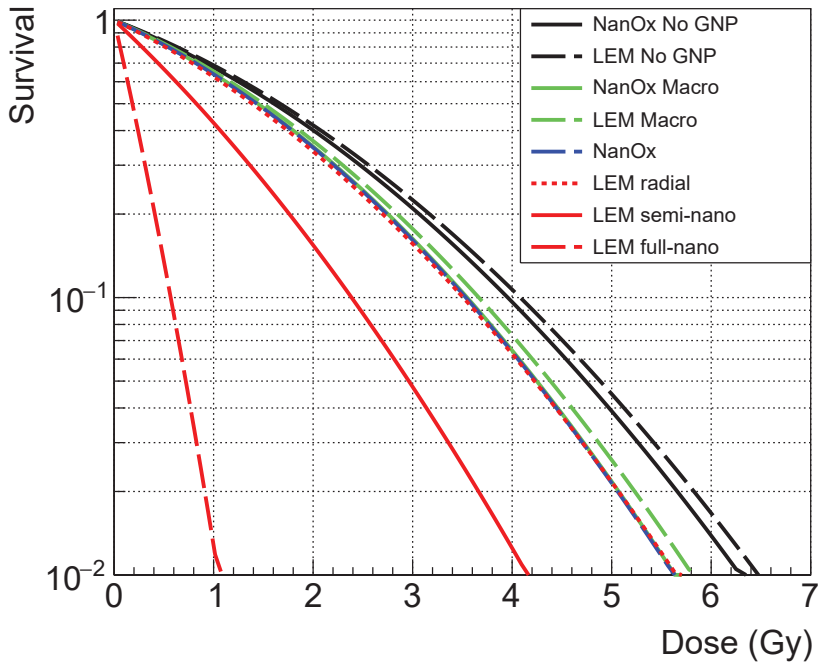

Figure 13.7.: HSG cell survival predictions. $E_{\text{photon}} = 20$ keV, $R_{\text{NP}} = 5$ nm and $C_{\text{NP}} = 1$ mg·mL^{-1}. The NanOx macro, NanOx and LEM radial predictions are superimposed.

and does not display any shoulder any more. Similar trends were obtained, regardless of photon energy or GNP parameters. In comparison, the NanOx predictions obtained are identical to the macroscopic predictions, despite the increase of probability of having high specific energy in the vicinity of GNPs (see Fig. 13.6).

13.3.3. RBE

The RBE at 2 Gy is displayed on Fig. 13.8 as a function of the photon primary energy ($R_{\text{NP}} = 5$ nm and $C_{\text{NP}} = 1$ mg·mL^{-1}). This figure confirms that NanOx does not predict any significant radiosensitizing effect of GNPs, apart from the one caused by the increase of the macroscopic dose deposition. The RBE therefore shows similar dependence with regard to the photon energy, compared to the increase of the macroscopic dose. It varies from 1.06 up to 1.16. The LEM predictions show very different RBE, depending on the implementation. The LEM based on the radial dose shows a minor increase of the RBE compared to macroscopic prediction, increasing for instance up to 1.2 at 20 keV while the macroscopic approach and NanOx reaches 1.1. The LEM based on dose deposition in nanovoxels, indicates a large increase of the RBE, reaching values from 1.5 up to $\sim$ 2.4. For the full nanometric predictions (not shown on the figure), values larger than 8 were obtained. Same trends were obtained with regard to the different LEM implementations, regardless of the GNP size or concentration. However, the amplitude of the RBE strongly depended on the GNP concentration, and was lower when the size of the GNP was larger.

13.4. Discussion

For the past two decades, gold nanoparticles (GNPs) have been studied for their radiosensitizing properties. Biophysical models were applied in order to better understand experimental results and predict cell survival in presence of GNPs. They are used to translate energy deposition at the sub-cellular scale into cell survival prediction. Both the LEM and the NanOx models have

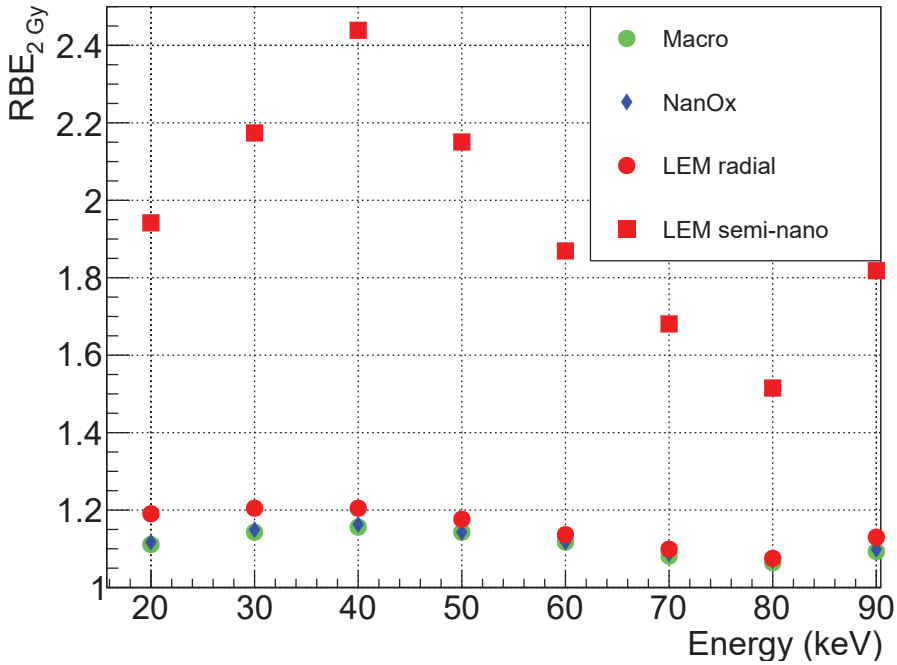

Figure 13.8.: RBE at 2 Gy as a function of the photon primary energy. $R_{\mathrm{NP}} = 5$ nm and $C_{\mathrm{NP}} = 1$ mg·mL^{-1}.

been used for hadrontherapy, and have shown good results for the HSG cell line[89,202]. For GNP-enhanced radiation therapy, only the LEM has yet been applied, in order to investigate whether the macroscopic increase of the dose deposition, in addition to a local boost of the energy deposition near the GNP surface due the Auger electrons, could reproduce experimental cell survival. In this study, both models were used to predict HSG survival in presence of GNPs for keV photon irradiation, and to compare the predictions of both models.

The LEM calculates the number of lethal damages based on the local dose D_{local} (e.g., radial dose in LEM II) throughout the cell's sensitive volume. A lethal function is used to calculate the number of lethal events based on D_{local}. In case of dense ionisation clusters (e.g. ion tracks and presumably Auger cascades), the increase in cell death then arises from the non-linearity of this lethal function, which has a quadratic component. In this study, we implemented 3 methods to calculate the local dose used for the LEM predictions. The first and second ones were based on methods already proposed in the literature[169,171,191]. These methods assumed that energy deposition resulting from the interaction between photons and water molecules representing the cell (the background contribution) could be described by means of a macroscopic, homogeneous, dose deposition. On the contrary, the energy deposition resulting from the interaction between photons and GNP atoms (the GNP contribution) was scored at nanoscale to better account for the heterogeneity of energy deposition induced by Auger cascades. The local dose was either scored in concentric shells around the GNP[191] or in nanovoxels[169,171]. The paradox of this approach is that at nanoscale, even sparsely ionizing radiations such as keV photons deposit energy in a heterogeneous way. Typically, for a 1 Gy irradiation of a volume of water decomposed in nanovoxels (i.e., cube of size ~ 10 nm), the probability of one nanovoxel to receive energy is only $\sim 10^{-4}$. As a consequence, this macroscopic background assumption does not fully account for the stochastic nature of energy deposition at the nanoscale. We therefore proposed a last method that accounted for the energy deposition distribution at the nanoscale for both the background contribution and the GNP contribution. As the LEM assumes that the number of lethal events may be calculated based on the local energy deposition at each point within the cell's sensitive

volume, this last approach is not in contradiction with the LEM basic assumption.

Our results show that the two methods previously implemented have different outcomes when using the same parameters (i.e., HSG cell line, with a homogeneous distribution of GNPs and a threshold D_t based on published LEM data). The radial dose approach gives a lower effect compared to the nanovoxel approach. These differences arise from the different local dose approaches. As the number of lethal events is not linear with the local dose D_{local}, cell survival predictions are very sensitive to both the parameter D_t and the values of D_{local}. Due to geometric considerations, when calculated in concentric shells, the GNP local dose reaches very high values but rapidly decreases as the volume of the shell increases with increasing distance to the GNP centre. In comparison, and as displayed in Fig. 13.5b, the GNP local dose in nanovoxels reaches higher values as the volume of the nanovoxel is constant and small. Consequently, due to the quadratic term of the lethal function, the number of lethal events increases for the semi-nano LEM implementation. This tendency is further confirmed when implementing a fully nanoscale dosimetric approach: very high values of energy deposition per unit mass are reached, and the number of lethal events dramatically increases, leading to RBE values larger than 8.

Such differences may appear surprising, as both approaches implemented in the literature could reproduce experimental data of cell survival for different systems[171,191,193]. However, the good fit between experimental data and theoretical predictions may be explained. In the first study by McMahon *et al.*[191], GNPs were assumed homogeneously distributed throughout the MDA-MB-231 cell at a concentration of 0.5 mg·mL^{-1} (i.e., experimental incubation concentration), and a good fit was found between experimental and theoretical results for keV irradiation. In a second study by the same authors[193], using the same cell line and same experimental work to compare with[134], another intra-cellular concentration of 1.3×10^8 GNP per cell was used. Based on the cell volume measured by the same team[176], this number would correspond roughly to an intra-cellular concentration of $\sim$ 34 mg·mL^{-1}. With this concentration, they could reproduce the experimental cell survival under MeV photon irradiation. In the semi-nano LEM implementation[171], the threshold D_t had no published value for the cell line investigated, and was adjusted so that theoretical predictions would fit the experimental data. For GNPs contained the cytoplasm only, and a threshold value of 23.9 Gy, the authors could reproduce cell survival of PC-3 cells incubated with 30 nm GNPs.

Although these approaches could both reproduce experimental values, some predictions appear to indicate that these approaches display different trends. For instance, the radial and semi-nano LEM implementations were used to investigate the effect of the GNP biodistribution[169,176]. While, based on the radial dose, Lin *et al.*[176] found practically no effect if GNPs were located outside of the cell (irradiation at 250 kVp, $R_{\text{NP}} = 25$ nm and $C_{\text{NP}} = 74$ mg·mL^{-1}), Lechtman *et al.*[169] found a significant effect for such biodistribution, based on the energy deposition in nanovoxels (irradiation at 100 and 300 kVp, $R_{\text{NP}} = 0.95$ and 50 nm and $C_{\text{NP}} = 2$ mg·mL^{-1}). Such differences appear hard to be explained solely based on the difference of parameters, and may be a result of the difference of the LEM implementation. This is consistent with the fact that we found much higher RBE for the semi-nano approach, compared to the radial approach.

In addition to the LEM study for the various implementations, we applied the NanOx model to compare cell survival, using the same conditions with regard to GNPs biodistribution. NanOx calculates the number of lethal events very differently than the LEM model. In particular, it requires the energy deposition per unit mass in nanotargets, defined as the restricted specific energy. Therefore, in NanOx, regardless of the type of beam or, in the present case, regardless of the contribution, the estimation of the number of the local lethal damages is performed using quantities calculated at the nanoscale. To calculate the number of lethal events, the restricted specific energy is used as an input for the effective local lethal function, an error-like function that displays a saturation beyond a given specific energy threshold (set at 15.6 kGy for the HSG cell line). In this study, we assumed a homogeneous distribution of the nanotargets in the sensitive

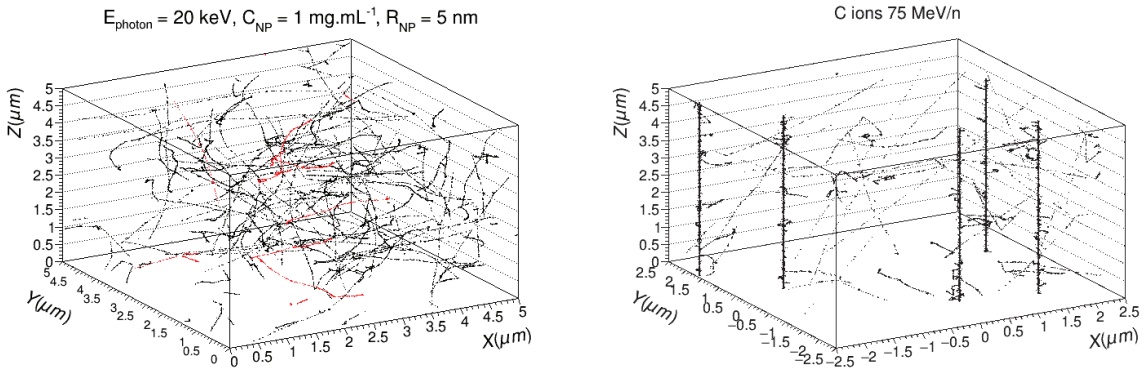

Figure 13.9.: Examples of particle tracks resulting in a dose deposition of $\sim$ 1 Gy in a cubic box with a 5 µm side, for photons in presence of GNPs (left) or for carbon ions (right). On the left, the black (resp. red) transfer points represent events coming from a primary interaction between a photon and a molecule of water (resp. atom of gold). Events were restricted to ionizations, dissociative excitations or electron attachments.

volume. This hypothesis is equivalent to the LEM assumption that the lethal function is uniform throughout the cell's sensitive volume. Under such circumstances, and despite the local increase of the probability of having high specific energy near the GNP surface (see chapter 9), we obtained almost no increase in cell death, except the one due to the increase of the macroscopic dose deposition.

At first sight, these results may appear surprising. GNP-enhanced radiation therapy often predicts higher cell death than the one predicted by a pure macroscopic increase of the dose deposition[134,171]. This increased biological effectiveness was often associated with Auger electrons, and dense ionisation clusters in the vicinity of the GNP. This was often compared to hadrontherapy, as ions are well known to present high ionisation density in the heart of the track and therefore result in a higher amount of sub-cellular lethal damages. However, as Fig. 13.9 illustrates, the actual high ionisation density of Auger electrons is questionable. This figure compares the tracks obtained for 1 Gy photon irradiation with 1 mg·mL^{-1}of GNPs for $E_{\text{photon}} = 20$ keV (left) and the tracks obtained with a 1 Gy ion irradiation with 75 MeV/n carbon ions (right). Tracks resulting from the interaction between photons and GNPs (depicted in red) do not appear qualitatively very different from the tracks resulting from the interaction between photons and water molecules (depicted in black). Compared to the very dense ion track depicted for carbon ions, Auger electrons barely induce any heterogeneity. We calculated that these carbon ions have a RBE of 1.13. These values are much below the ones obtained with the semi-nano LEM implementation, although carbon ions display qualitatively a significantly higher ionisation density. This conclusion appears consistent with the experimental observations. Indeed, if Auger electrons were responsible for the effect, then we would expect an effect as soon as the GNPs are internalized in cells. However, it was observed that despite internalization of GNPs, some cell lines had no radiosensitization[134].

This conclusion brings again the question on why do GNPs sometimes show higher effects than those predicted by a pure macroscopic increase of the dose deposition. There are several possibilities that may explain why the system we studied does not predict additional effects: (1) the assumption of a homogeneous GNP biodistribution in cells, (2) the nature of cellular nanotarget considered and the use of a lethal function that are both DNA damage oriented, (3) the fact that complex biological mechanisms are not considered. First, we considered a homogeneous distribution of the GNPs throughout the cell. This description is far from the reality. Most of *in vitro* experimental images of GNP biodistributions have shown that, when internalized, GNPs are entrapped in large endosomes or lysosomes in the cytoplasm[26,55,66,67,134,135]. In turns, they form dense clusters that appear much larger than isolated GNPs. These agglomerates result in partic-

ularly high average energy deposition in its vicinity[166]. At the nanoscale, this could translate in a higher probability to damage cellular nanotargets located near these agglomerates. This then raises the question regarding the nature and the distribution of cellular nanotargets to consider for GNP-enhanced radiation therapy. In the present study, we assumed that they were homogeneously distributed throughout a sensitive volume modeled as a nucleus. This hypothesis is usually used for biophysical models in hadrontherapy. The nanotargets model DNA fragments distribution throughout a nucleus. The inactivation of a nanotarget then represents complex DNA damages. This DNA centric approach does not seem to be appropriate in the case of GNPs, especially considering that they are not located in the nucleus. Due to their localization, a natural cellular nanotarget could be the lysosome's membrane. If the membrane is disrupted, this could result in the activation of complex biological pathways that would result in adverse side effects for the cell[258]. The close distance between GNPs and lysosome membrane could result in a more significant implication of the Auger effect. Another possibility of improvement for NanOx predictions would be to consider a new lethal function. Indeed, the current one was built considering the DNA as a key damageable cellular nanotarget, which may not be adapted for the GNP-enhanced radiation therapy. At last, another possibility is that this increased biological effectiveness is not induced by physical effects at the nanoscale, but due to complex biological mechanisms. For instance, recent studies[217,218] showed that GNPs released gold ions in the cellular cytosol, that further reacted with thioredoxin reductase. This molecule is involved in the regulation of reactive oxygen species (ROS). As a consequence, GNPs induced a weakening of the cellular detoxification system, which the authors associated to the observed increased sensitivity to radiation. Further studies are required to confirm whether this mechanism is observed with other GNPs. In any case, such mechanisms could be incorporated in the biophysical model NanOx, as NanOx predictions also rely on the global level of oxidative stress.

13.5. Conclusion

We studied the prediction of two biophysical models (the LEM and the NanOx models) of HSG cell survival for keV photon irradiation in the presence of GNPs. We implemented three different approaches of the LEM, among which two were previously reported in the literature. In this theoretical study, we assumed a homogeneous distribution of the GNP throughout the sensitive volume of the cell, as previously done in the literature. We found that the LEM approaches provided different outcomes when using identical input parameters. While the LEM approach predicted an increased RBE that was often attributed to Auger electrons, the implementation of the NanOx model predicted no increase of cell survival, despite the one due to the increase of the macroscopic dose deposition in presence of GNPs. As a consequence, the NanOx model did not predict a increase of biological effectiveness due to Auger electrons. This study suggests that the simplistic approaches currently used to predict cell survival in presence of GNPs must be improved in order to be predictive. In particular, it should account for a more realistic description of the GNP biodistribution, the potential cellular biotargets outside the nucleus and possibly complex biological mechanisms.

Part V.

Conclusion

14. General conclusion

High-Z nanoparticles have been of high interest for the past decades to improve the therapeutic outcomes of radiotherapy. When distributed in the tumour, high-Z NPs amplify the destructive effect of the dose deposited in that tumour. As detailed in Part I of this thesis, the origin of the radiosensitizing effect of high-Z NPs, and more specifically GNPs, remains unclear. Several mechanisms could be responsible for the effect, and may be listed into 3 distinct categories: physical mechanisms, chemical mechanisms and biological mechanisms. The first one originates from a higher cross section of keV photon interaction with high-Z elements as opposed to biological soft tissues, resulting in an increased dose deposition. It is also believed to originate, at the nanoscale, from dense ionisation clusters, due to the emission of Auger electrons. Chemical mechanisms may arise from an increase in free radicals production, deriving from the increase in dose deposition but also potentially from GNP properties. Finally, biological mechanisms would result from the interaction between GNPs and cells, leading to a decrease in cell radioresistance, through for instance a depleted free radicals detoxification system. A better understanding and quantification of each of these steps may help optimize the treatment and ensure a safe transfer towards clinical routine.

In the scope of this thesis, we had three distinct objectives. The first and second goals aimed at quantifying both physical (1) and chemical (2) mechanisms with modelling tools. The third goal was to study the impact of these mechanisms on a biological endpoint, the cell survival, by using biophysical models. In this work, we focused in particular on NPs made of gold, as there are many data available in the literature to compare with the simulation predictions. We also restricted the study for photon energies in the keV range (20 - 90 keV), as we expect to have the highest physical and chemical effects in this range. Part II of this Ph.D work focused on the physical mechanisms, while Part III focused on the chemical mechanisms. Finally, part III focused on the biophysical modelling and the predictions of cell survival.

When studying energy deposition at nanoscale, high-precision tools are mandatory regarding electron transport, in particular at low energy (i.e., from a few eV up to keV). We already had a MC tool to simulate the transport of electrons and chemical species in water (approximated as the cell medium), the MDM code, formerly known as the LQD code. However, at the beginning of this project, high-precision MC tools for the transport of electrons in gold (the nanoparticle medium) were not available in open source at very low energy. In 2013, in the framework of a "physique cancer" project, a collaboration started between the IPNL laboratory, the CIMAP laboratory (Caen) and the LCP laboratory (Paris), that aimed in particular at implementing models for tracking of low-energy electrons in gold. During his post-doc, A. Ipatov implemented these models in our MC simulation toolkit MDM. At the beginning of my Ph.D work, I contributed to the improvement of cross sections (in particular bulk and surface plasmons, and elastic cross sections) and validation of these physical models, as developed in Chapter 8 of Part II. I validated these models with available data from the literature. These experimental works usually consisted of irradiating a foil of gold with an electron beam and of obtaining the yield and energy distribution of the backward and forward electrons. We obtained globally very good yields and energy distributions for both primary and secondary electrons, in a large range of energies. An exception was the yield of backward secondary electrons, which was systematically underestimated. However, these

results were sufficient to obtain accurate results regarding the study of energy deposition around GNPs.

The next stage of the thesis was to investigate the energy deposition around a GNP, as developed in the Chapter 9 of Part II. Various photon energies and gold sizes were systematically studied to investigate the optimum. Compared to previous work (Geant4/Geant4-DNA (e.g. Douglass et al., Lin et al., Lin et al., Lin et al., Retif et al., Zhang et al. [2013, 2014, 2015, 2015, 2016, 2009]) with the exception of the work by Sakata et al., Sakata et al. [2016, 2018], MCNP5/MCNPX (e.g. Cai et al., Cho et al., Lechtman et al., Lechtman et al., Mesbahi et al. [2013, 2009, 2011, 2013, 2013]), PENELOPE (e.g. Koger and Kirkby, Lechtman et al., Lechtman et al. [2016, 2011, 2013]), PARTRAC (e.g. Xie et al. [2015])), we used our MDM MC toolkit that had a better precision regarding electron transport in gold. Besides, we investigated a new dosimetric quantity. Indeed, a majority of the study of energy deposition around a GNP was performed using the radial dose. This quantity shows limitations when translating the energy deposition into meaningful biological outcomes (e.g. DNA double strand break). Instead, we investigated the distribution of the energy deposition inside a nanotarget, defined as the restricted specific energy. The word "restricted" refers to the fact that we only accounted for energy transfers that may lead to events relevant for the biological medium, i.e., ionizations, dissociative excitations and electron attachment. This quantity is more appropriate to further quantify the amount of cellular nanotarget damages. To compute these distributions, considerable optimizations were required in order to achieve reasonable computing time. Once these optimizations were implemented, we obtained probability distribution of specific energy as a function of the distance between the nanotarget and the GNP. We showed (1) a significant increase in the probability of having high specific energy near the GNP and (2) an overall increase in the intensity of the distribution near the GNP surface for large GNPs. We further calculated the probability of having a specific energy larger than a threshold z_0, both with and without GNPs. The ratio of these quantities was obtained as a function of the distance to the GNP surface, which we defined as the probability enhancement ratio (PER). The higher the threshold, the higher the PER, which suggested that the GNP may be particularly effective at inducing complex damages in the nanotarget. The PER dropped when the distance of the nanotarget from the GNP surface increased, and was below 1.5 beyond 200 nm.

During the next stage, we studied the impact of GNPs on the production of radical species at the microscale (Chapter 10) and at the nanoscale, in the vicinity of the GNP (Chapter 11), following keV photon irradiation. To our best knowledge, this is the first study of this kind. In the absence of any catalytic process, the amount of radical species produced at a microscale was correlated to the increase of dose deposition. In particular, we did not observe any print of the Auger electron cascade in terms of radiolytic yields. At the nanoscale, we studied the radial distribution of chemical species per ionization, both for a GNP and a theoretical NP made of water. The latter enabled to compare the specificity of gold material *vs* water material. On average, GNPs produced more radical species per ionization compared to a water nanoparticle (WNP). This was expected, as the photo-electric effect predominates in the keV energy range for gold, whereas the Compton effect mostly dominates for water. As a consequence, the whole energy of the photon is deposited when interacting with gold, while only part of the energy is deposited during a Compton interaction. This higher energy deposition per gold atom ionisation resulted in the production of a higher number of chemical species. However, in the vicinity of the NPs (i.e., for a radial distance up to a few hundreds of nm), the number of chemical species was not systematically higher for GNP compared to WNP, despite the Auger cascade. This observation shows that the local effect of GNPs is not to induce a higher effect (i.e., more chemical species) near the NP but rather to increase the chances of having this effect to occur, due to a higher photon-gold cross section compared to water.

The last chemical study of this thesis focused on the experimental results of the irradiation of a colloidal GNP solution mixed with coumarin. Coumarin molecules react with $^{\bullet}OH$ through a multiple steps reaction. It depends on the amount of O_2 in the solution, and generates several

products, among which one is fluorescent. The rate of production of this fluorescent product is low, with less than 5 % of the $^{\bullet}$OH reacting with the coumarin leading to a fluorescent product. Several experiments showed an unexpectedly high fluorescent yield that cannot be explained by a pure physical effect observed in Chapter 10. Four scenarios proposed in the literature or based on experimental evidences were investigated with MC and analytical tools. The goal was to see whether these scenarios could reproduce the experimental trends observed when irradiating the colloidal solution for various atmosphere conditions or dose rates. Among these scenarios, only one could reproduce the very high fluorescent yield and its variation with regard to atmosphere conditions. This scenario proposed that a coumarin + $^{\bullet}$OH byproduct reacts at the surface of GNPs, which further leads to an increased efficiency at producing a fluorescent product compared to other non-fluorescent products.

Following the study of both physical and chemical effects, the last goal of this Ph.D work was to estimate cell survival based solely on these effects. We wished to estimate whether these effects would be sufficient to explain the radiosensitizing effect of GNPs. Such studies were performed before with the Local Effect Model (LEM), which predicts cell survival based on the local (subcellular) dose in a sensitive volume. It was shown that the LEM could reproduce experimental cell survival in presence of GNPs. The increase in cell death was often attributed to the Auger cascade, that was believed to induce locally dense ionisation clusters, and therefore an increased biological effectiveness. In this Ph.D work, we proposed to use the biophysical model NanOx, and compare it with the various LEM implementations that have been proposed in the literature. NanOx was originally developed in the context of hadrontherapy at the IPNL laboratory. It estimates cell survival based on nanodosimetry and radicals produced by irradiation. For the LEM, we studied two implementations of the LEM, that were proposed in the literature. These approaches represented the dose differently according to its origin. For the energy deposition coming from photons interacting with water molecules (i.e., the cell's medium), the dose deposition was represented on a macroscopic scale. For the energy deposition coming from photons interacting with gold molecules (i.e., the nanoparticle's medium), the dose deposition was represented at the subcellular scale. Two representations of this local dose were proposed: one was based on the radial dose while the other was based on energy scoring in nanovoxels. Therefore, we wished also to study how the scoring of energy deposition per unit mass impacts the cell survival in the LEM framework. In Chapter 13, we therefore studied cell survival prediction for the HSG cell line, both with NanOx and the LEM. We considered a simplistic homogeneous distribution of GNPs throughout the cell, including the sensitive volume, as it has been often done in studies with the LEM. Both implementations of the LEM showed different results, despite identical parameters. This difference was due to the difference of dosimetric approaches of the two implementations. For NanOx, we obtained surprising results: despite the nanodosimetric results obtained in Chapter 9, the cell survival predictions of NanOx showed an increase in cell killing that was only due to the macroscopic increase of dose deposition. Even with GNPs inside the sensitive volume, Auger cascades did not induce any increased biological effectiveness. This comes in contraction with previous studies based on the LEM. Our study suggests that the simplistic approaches currently used to predict cell survival with GNPs must be improved in order to be predictive. In particular, it should account for a more realistic description of the GNP biodistribution, the potential cellular biotargets outside the nucleus and possibly complex biological mechanisms.

During my Ph.D, I also had the chance to collaborate with different teams. First, in the framework of Veronica Tessaro's Ph.D (student at the Instituto de Fisica de Rosario (CONICERT-UNR) in Argentina, in "cotutelle" with our laboratory), our Monte Carlo simulation was used to calculate W-values, which is the mean energy required to generate an ion pair upon the complete slowing down of the ionization radiation. This quantity is widely used in medical physics. I helped her getting familiar with our MC tool, in order to further develop it with ion transport. A collaboration with the team of Elise Dumont, from the ENS Lyon, also started. Their work is based on Density Functional Theory calculations, and they model in particular gold nanoparticles and their interaction with surrounding molecules such as water. The goal of this collaboration

is to further develop chemical modelling of the radiolysis in presence of GNPs, especially at the GNP surface. It also aims at using DFT calculations to calculate quantities that may further improve our MC simulation. Finally, I participated to two EUropean RAdiation DOSimetry (EURADOS) exercises aiming at performing a benchmark of the various MC codes existing, using different quantities. The first exercise aimed at calculating the radial dose around GNPs, both at nanoscale and microscale. The second exercise aimed at calculating the distribution of the number of ionizations in a nanometric target, following the decay of the Auger source ^{125}I. The targets were located at different distances from the source. Both results were presented at the GEANT4 2018 3rd International User Conference at the Physics - Medicine - Biology frontier. The GNP benchmark should lead to a publication in the journal Medica Physica.

The end of this Ph.D work opens many perspectives:

- The physical models implemented with gold could be applied to several other materials such as silver or platinum. Both of these metals are used as radiosensitizers. Provided a thorough benchmark as the one did in Chapter 8, this could be used as a base to compare physical and chemical effects of various materials. For instance, nanodosimetry studies could be done to compare the results obtained with gold *vs* other materials. The physical models could also be improved, for example by accounting for surface plasmons in the medium outside of gold, or by implementing models for nanoparticles specifically. Indeed, surface modes depend on the size or shape of the GNP.

- Regarding Chapter 9, a perspective is to study the specific energy distribution considering a realistic kVp X-ray beam. Besides, studies on the effect of the size (dimensions from 10 to 100 nm) of the nanotarget are ongoing. While not presented in this Ph.D thesis, this work aims at studying, for spherical and cylindrical targets, whether an optimum exists regarding the nanotarget size to obtain the highest effect with a GNP. This may be further used to identify potential biological nanotarget that would be the most sensitive to the presence of GNPs in their neighbourhood.

- For chemical effects (Chapter 10, 11 and 12), the collaboration with the ENS team should help improve the MC simulation. It may also offer new possibilities for GNP surface phenomena modelling, such as catalysis processes.

- There are a lot of perspectives regarding NanOx (Chapter 13). While we did not obtain a significant radiosensitizing effect due to Auger electrons in the current configuration (i.e., homogeneous GNP and nanotargets distribution), different possibilities could change this outcome. First, the presence of clusters of GNPs, if located near a sensitive nanotarget, may increase the probability to generate lethal damages. Since these nanotargets would be preferentially located near the GNP (i.e., < 200 nm), the Auger electrons could play a more significant role. As a consequence, a change in the nanotargets distribution could be considered. Such configuration could be obtained by using an alternative to the DNA-centric approach. Typically, cellular membranes could be considered as a new nanotarget: GNPs are close to lysosome membranes if internalized, or near the extra-cellular membrane if located in the extra-cellular medium. Additionally, a change in the lethal function could also be applied. The NanOx lethal function was built for hadrontherapy application. In hadrontherapy, the main cellular nanotarget that is suspected to be the most critical is the DNA. Since it appears not to be the case for GNP, a new lethal function could be modelled. A last approach could be to explicitly take into account some biological mechanisms that have been evidenced (see chapter 5). For example, a correlation between the weakening of the cellular detoxification system and the radiosensitizing effect of GNPs was observed[217,218]. This could be modelled as NanOx accounts for the cellular oxidative stress.

15. Résumé de thèse

Modélisation physique, chimique et biologique pour la radiothérapie améliorée par les nanoparticules d'or : vers une meilleure compréhension et optimisation de l'effet radiosensibilisant

15.1. Contexte

Les nanosciences ont révolutionné de nombreux domaines. Alors que l'amélioration continue de la technologie a permis de construire des objets reproductibles de plus en plus petits, le domaine de la nanotechnologie devient de plus en plus attractif, en particulier pour les applications médicales. Etant données les possibilités infinies de conception de ces nanomatériaux, ces nouvelles biotechnologies peuvent être appliquées depuis le diagnostique jusqu'au thérapeutique. En particulier, depuis une vingtaine d'années, il a été montré que l'utilisation de nanoparticules à numéro atomique élevé permettrait d'améliorer le potentiel thérapeutique de la radiothérapie.

La radiothérapie est largement utilisée en cancérologie. Jusqu'à 50 % des patients sont concernés durant leur traitement[16]. Grâce à leurs propriétés pénétrantes, les radiations ionisantes peuvent traverser les tissus humains et atteindre les cellules cancéreuses. En interagissant avec les atomes et molécules qui constituent nos cellules, les radiations déposent de l'énergie. Cette énergie peut induire des ionisations et donc rupture de liaisons chimiques, détruisant ainsi des cibles sensibles moléculaires telles que l'ADN, ou peut générer des espèces chimiques toxiques. Ces deux mécanismes peuvent aboutir à la mort de la cellule cancéreuse. Un des principaux défis de la radiothérapie est de maximiser les effets de dose au sein des cellules cancéreuses, tout en épargnant les cellules saines environnantes. Parmi les différentes techniques envisagées, l'utilisation de radiosensibilisants vise à amplifier l'effet destructeur de la dose dans la tumeur, sans aggraver les complications dans les tissus sains. Les nanoparticules à fort-Z (or, gadolinium...) ont démontré expérimentalement leurs effets radio-sensibilisants. L'expérience pionnière de Hainfeld[115] en 2004 a ainsi pu montrer que des souris portant des carcinomes EMT-6 subcutanné, ayant reçu une concentration de solution de nanoparticules d'or de 7 mg Au/g dans la tumeur et une irradiation de 250 kVp de rayon X, survivaient à 86 % sur 1 an, contre 20 % pour une irradiation sans nanoparticules. Suite à cette découverte, de très nombreuses expériences ont suivi, notamment *in vitro* et *in vivo*, afin de mieux comprendre l'origine de cet effet. Une description générale des différents mécanismes mis en évidence grâce à ces travaux expérimentaux sont disponibles dans les 4 premiers chapitres de cette thèse. Ces validations expérimentales ont notamment pu aboutir à quelques essais cliniques, dont un à Grenoble.

Si ces effets sont établis, leur origine est encore mal connue, ce qui ralentit la mise en routine clinique et les pistes d'optimisations. La littérature suggère que des processus physico-chimiques seraient responsables des effets biologiques observés[191]. A basse énergie (keV), les photons du faisceau ont une probabilité d'interaction plus grande avec l'or qu'avec des tissus mous, essentiellement composés d'eau. En confinant les nanoparticules dans la tumeur, cela induit une augmentation de la dose, à travers la tumeur entière. De plus, lorsque les rayonnements ionisants venant du faisceau interagissent avec les nanoparticules, ils créent une cascade d'électrons secondaires appelés électrons Auger. Il a été suggéré que, en se propageant dans la cellule, ces électrons secondaires conduisent à l'augmentation de la dose locale, à échelle nanométrique, et à un "boost" de radicaux libres, espèces chimiques hautement réactives. Cet effet, obtenu à échelle sub-cellulaire, serait responsable de l'augmentation de la mort cellulaire. Bien qu'ils aient des conséquences à échelle du patient, ces mécanismes initiaux se produisent à des échelles de temps extrêmement courtes (de l'ordre de 10^{-18} s) et à des échelles spatiales très petites, de l'ordre de la centaine de nanomètres. Ils ne sont donc pas directement mesurables. La simulation de ces mécanismes peut permettre de mieux les comprendre. Les premières simulations[56], effectuées dans le milieu des années 2000 suivant l'expérience pionnière de Hainfeld[115], ont montré une légère hausse de la dose macroscopique, mais qui est insuffisante pour expliquer les effets biologiques, suggérant que les mécanismes initiaux se produiraient à échelle sub-cellulaire. De plus, de nombreuses études expérimentales ont suggéré que les nanoparticules d'or pourraient ne pas être inertes lorsqu'elles sont en contact avec des cellules. Cela pourrait enclencher des mécanismes biologiques complexes, qui seraient eux aussi responsables de la radiosensibilisation.

15.2. Objectifs

L'objectif de ma thèse s'ancre dans ce contexte et s'articule autour de trois axes scientifiques. Les deux premiers axes consistent à quantifier, à échelle nanométrique, l'impact des nanoparticules d'or sur les processus physiques (1) et chimiques (2) radio-induits par simulation Monte Carlo (MC)[105,106]. Pour cela, la finalisation et validation d'une simulation MC du transport des électrons dans l'or jusqu'à très basse énergie (eV) a été nécessaire. Ce travail de validation fait suite à un projet physique cancer BIOHYDRA, dont l'un des objectifs était de développer une simulation Monte Carlo performante du transport des électrons dans l'or à basse énergie. Le troisième et dernier axe consiste à (3) injecter ces données physico-chimiques dans le modèle biophysique NanOx[70,202,204] et le Local Effect Model (LEM)[89,90], afin de quantifier en terme de mort cellulaire, le bénéfice de ces nanoparticules, basé uniquement sur des effets physico-chimiques. A noter que nous nous concentrons sur les nanoparticules d'or car, pour des raisons historiques, c'est avec ces nanoparticules que le plus grand nombre de résultats expérimentaux a été obtenu.

Par rapport aux travaux les plus proches de ce projet[171,191], nous proposons de:

- Nous appuyer sur des modèles physiques plus précis dans la gamme d'énergie des électrons Auger, supposés en partie responsables de l'effet. La précision des modèles physiques actuellement utilisés dans les simulations, et notamment pour les énergies en dessous du keV (énergie des électrons Auger), peut en effet être remise en question[191], et pourrait amener à sous-estimer la dose locale.
- Produire des spectres de nanodosimétrie plutôt que de s'appuyer sur des doses radiales. La dose radiale représente la dose moyenne (énergie déposée par unité de masse) déposée à une distance donnée de la NP. De par sa définition, elle ne prend pas en compte les variations considérables de la dose déposée dans des nanocibles biologiques (ex : segment d'ADN, membrane mitochondriale...). Pourtant, le spectre de cette dose s'étend sur plus de quatre ordres de grandeur. Cette grandeur est définie comme l'énergie spécifique, dont l'unité est le Gy.
- Etudier l'impact des nanoparticules sur la production de radicaux libres, dans une solution d'or et d'eau ou bien en présence d'un scavenger, la coumarine. Actuellement, une seule

étude a été réalisée avec des simulations Monte Carlo autour d'une nanoparticule d'or, lors d'une irradiation avec des protons[269].

- Utiliser le modèle NanOx et le LEM pour prédire l'effet radiosensibilisant des nanoparticules, grâce aux données de nanodosimétrie et de production de radicaux libres. Actuellement, seul le LEM a été implémenté pour prédire l'effet radiosensibilisant des nanoparticules, qui utilise des données de dépôt de dose à échelle sub-cellulaire[169,171,191,193]. NanOx, par rapport au LEM, utilise la probabilité d'avoir un dépôt d'énergie dans une nanocible, plutôt qu'une dose moyenne. Comme nous le verrons, le choix de représentation des dépôts d'énergie à échelle nanométrique a des conséquences sur les prédictions de survie cellulaire.

15.3. Travail réalisé

15.3.1. Simulation Monte Carlo du transport des électrons dans l'or

Le code Monte Carlo MDM a été historiquement développé dans les années 1990/2000 pour simuler l'interaction des électrons de basse énergie avec l'eau[105,106]. Il a ainsi été testé dans le contexte de l'hadronthérapie et permet de produire des données précises de nanodosimétrie et des rendements chimiques lors de l'irradiation d'ions (protons, carbones). Durant ma première année de thèse j'ai contribué à l'extension de cette simulation MC à l'interaction d'électrons de basse énergie avec l'or et ainsi contribuer à développer des modèles d'excitation collective, des effets de surface et la reproduction complète de la cascade Auger. Les électrons Auger, supposés partiellement responsables de l'effet physique, ont en effet des énergies inférieures à 10 keV, et la plupart du temps inférieures à 1 keV. A cette énergie, leur parcours dans l'or n'est que de quelques nanomètres, et un modèle performant à ces énergies est essentiel pour évaluer la dose aux très petites échelles. Ces modèles ont été validés de manière exhaustive pour des énergies inférieures à 90 keV grâce aux données expérimentales de la littérature. Le dispositif expérimental consiste à irradier une feuille d'or avec un faisceau d'électrons, et à regarder le nombre ou l'énergie des électrons transmis ou rétrodiffusés. Nous avons ainsi pu vérifier que le rendement d'électrons est bien estimé, notamment pour les basses énergies, ce qui nous permet d'être confiants sur la prédiction des rendements radiochimiques par la suite. Nous avons aussi vérifié que la distribution énergétique de ces électrons est bonne, ce qui nous assure une bonne estimation de la dose à petite échelle. Ces résultats font l'objet du Chapitre 8 de cette thèse.

15.3.2. Nanodosimétrie

Une fois la simulation Monte Carlo testée et validée, elle a été utilisée pour calculer la probabilité d'avoir un dépôt d'énergie donné dans une cible de taille nanométrique (i.e. nanocible), au voisinage d'une nanoparticule d'or contenue dans de l'eau, qui modélise le milieu cellulaire. L'énergie déposée dans une nanocible, divisé par sa masse, est définie comme l'énergie spécifique. A noter que, parce que le système doit être proche de la réalité, le volume étudié est grand alors que les grandeurs évaluées se rapportent à des volumes très petits. Nous avons estimé que, dans les meilleures conditions, 500 siècles auraient été nécessaires pour ce calcul sans optimisation. Un travail indispensable a porté sur le développement d'algorithmes performants, ce qui a réduit ce temps de calcul à 2 jours. Nous avons réalisé des calculs pour des énergies de photon variant entre 20 et 90 keV et pour différentes tailles de nanoparticules (5 à 50 nm de rayon). Des spectres de distribution de l'énergie spécifique ont été obtenus en fonction de la distance de la nanocible à la surface de la nanoparticule. Nous avons également calculé la probabilité d'avoir une énergie spécifique supérieure à un seuil. Cette quantité permet de mesurer la complexité du dommage que le dépôt d'énergie permettrait d'induire à la nanocible : plus le seuil est élevé, plus le dommage est complexe et plus les chances d'induire un dommage létal sont élevées. Nous avons obtenu une augmentation de cette probabilité en fonction de la distance à la nanoparticule, par rapport à cette même probabilité dans de l'eau pure. Nous avons obtenu une augmentation de la probabilité d'avoir un très fort dépôt de dose. Ce résultat est particulièrement intéressant, car ce sont ces

forts dépôts de dose qui pourraient être responsables des dégâts les plus létaux pour la cellule. Nous avons obtenu des rapports de probabilité d'autant plus grands que le seuil était élevé, montrant ainsi la capacité de la nanoparticule à induire des dommages importants. En surface de la nanoparticule, ce ratio s'élevait jusqu'à 95 pour une nanoparticule de 50 nm de rayon, une énergie de photon de 20 keV et d'un seuil de 20 kGy. Ce ratio décroit rapidement lorsque la distance à la nanoparticule augmente, et tombe sous la valeur de 1,5 au-delà de 200 nm, quel que soit le système.

15.3.3. Production de radicaux libres en présence de nanoparticules

Les calculs de production de radicaux libres en présence de nanoparticules ont été faits à deux échelle : à une échelle macroscopique en présence d'une concentration C_{NP} de nanoparticules, et à une échelle nanométrique, autours d'une nanoparticule d'or ionisée. Tout comme la nanodosimétrie, ces calculs ont été réalisés pour des énergies de photon variant entre 20 et 90 keV, et pour différentes tailles de nanoparticules. Dans le chapitre 10, nous avons obtenu une augmentation des rendements de $^{\bullet}OH$ et H_2O_2 qui variaient entre 6 et 14 % à échelle macroscopique, pour une concentration de nanoparticule de 1 mg·mL^{-1}. Cette variation dépendait principalement de l'énergie des photons. La variation de la taille des nanoparticules, le temps suivant l'interaction primaires du photon, et le type de l'espèce chimique n'a eu que peu d'influence sur l'augmentation des rendements macroscopiques. Cette augmentation est principalement dû à l'augmentation de la dose macroscopique.

Dans le chapitre 11, nous nous sommes intéressés à la concentration radiale suivant l'ionisation d'une nanoparticule d'or ou d'eau, afin de mieux comprendre les spécificités de l'or en terme de boost chimique. La concentration radiale est calculée en comptant le nombre d'espèces chimiques dans une couronne d'eau centrée sur la nanoparticule, et en divisant ce nombre par le volume de la couronne. Ces concentrations radiales montrent un fort boost en surface de la nanoparticule qui n'est pas spécifique au matériel. Ce boost est essentiellement dû aux considérations géométriques, et en particulier aux petits volume aux abords de la nanoparticule. En moyenne, le nombre d'espèces chimiques produites suivant une ionisation est supérieur pour l'or par rapport à l'eau. Cependant, l'essentiel de ces espèces est produit loin de la nanoparticule d'or. Nous avons également calculé la concentration d'espèces chimiques induites dans une cible sphérique contenant la nanoparticule d'or ou d'eau après son ionisation. Les concentrations atteintes dans des petites cibles (de rayon égal à 100 nm plus le rayon de la nanoparticule) n'étaient pas nécessairement plus grandes pour les nanoparticules d'or que les nanoparticules d'eau. Cela signifie que, malgré le petit boost induit par les électrons Auger, ce boost n'est pas suffisant pour induire une forte concentration d'espèces chimiques aux abords de la nanoparticule d'or ionisée, par rapport à une nanoparticule d'eau ionisée. Cela veut dire que l'effet local des nanoparticules n'est pas d'induire un effet local qualitativement plus important, mais plutôt d'augmenter les chances d'avoir un effet local, en raison de la forte probabilité d'interaction entre l'or et les photons.

Le dernier chapitre (chapitre 12) sur les aspect chimiques porte sur la modélisation de l'irradiation d'une solution de coumarine et de nanoparticules d'or. La coumarine est une molécule qui réagit avec $^{\bullet}OH$ et forme, après plusieurs étapes successives, un ensemble de produits parmi lesquels une molécule fluorescente. La mesure du taux de fluorescence permet ensuite de remonter à la quantité de $^{\bullet}OH$ produit lors de l'irradiation d'une solution. Le taux de conversion entre une molécule de coumarine et $^{\bullet}OH$ en produit fluorescent est bas, d'environs 5 % en absence de nanoparticules. En présence de nanoparticules, des mesures expérimentales[109,110,251] ont montré un taux de fluorescence très important, qui ne peut être expliqué par l'augmentation du nombre de $^{\bullet}OH$ sur de simples considérations dosimétriques. Nous avons étudié quatre scénarios pour expliquer ce taux de fluorescence inattendu. Parmi ces quatre scénarios, un seul permet d'expliquer ce rendement. Ce scénario suggère que la nanoparticule d'or interférerait avec les sous-produits formés durant une des étapes avant la formation du produit final fluorescent. Cela aurait pour

conséquence de modifier le taux de production du produit fluorescent, et de privilégier la formation de cette molécule fluorescente par rapport aux autres.

15.3.4. Prédiction de survie cellulaire avec NanOx

Le chapitre 13, qui est le chapitre final de cette thèse, porte sur l'implémentation du modèle biophysique NanOx pour obtenir des prédictions de survie cellulaire en présence de nanoparticules d'or. Ce modèle a été utilisé en hadronthérapie pour prédire la survie de 3 lignées cellulaires et a obtenu de bons résultats[202]. Ce modèle s'appuie à la fois sur les calculs d'énergie spécifique et sur la production de radicaux libres pour le calcul de la survie cellulaire. Les prédictions de NanOx en présence de nanoparticules d'or ont été comparées à celles du Local Effect Model (LEM), précédemment implémenté dans la littérature. Deux implémentations ont été proposées pour le LEM, lesquelles s'appuient sur différentes approches dosimétriques. Elles ont toutes les deux permis de reproduire des courbes de survie cellulaires en présence de nanoparticules, la première approche pour la lignée MDA-MB-231[191] et la deuxième pour la lignée PC-3[171]. Dans ces études, l'augmentation de la mort cellulaire a été associées à l'hétérogénéités du dépôt d'énergie aux abords de la nanoparticule d'or. Ce travail a donc eu pour objectif de comparer les prédictions des deux implémentations du LEM, ainsi que celles de NanOx, pour un système unique. Nous avons choisi la lignée cellulaire HSG, car elle a montré de bons résultats en hadronthérapie pour le LEM et le modèle NanOx. Nous avons aussi choisi une biodistribution homogène des nanoparticules qui simplifie le système étudié. Ce travail a permis de mettre en évidence plusieurs conclusions. Tout d'abord, les prédictions du LEM sont différentes suivant l'implémentation. Cette différence a pu être associée aux différences d'approches dosimétriques. En effet, les évènements létaux sont calculés via une fonction létale, qui dépend de la dose. Cette fonction létale a une composante quadratique, qui induit une dépendance importante du nombre d'évènements létaux en fonction de façon dont la dose est calculée. Cela questionne l'applicabilité de ces modèles. Par ailleurs, NanOx ne prédit aucun effet dû aux électrons Auger: dans notre modèle, basé sur les mêmes hypothèses que celles du LEM, l'augmentation de la mort cellulaire n'est dû qu'à un effet macroscopique de l'augmentation de la dose. Le boost observé par nos calculs de nanodosimétrie n'était pas suffisant pour induire un effet Auger significatif vis-à-vis de la survie cellulaire. Tandis que les études réalisées avec le LEM ont attribué l'effet des nanoparticules d'or aux électrons Auger et à une forte densité d'ionisation induite, nos résultats suggèrent que cet effet Auger a probablement été surestimé. Des modèles biophysiques beaucoup plus réalistes que ceux existants doivent être mis en places, pour obtenir des résultats prédictifs.

15.4. Ouverture

La fin de ce travail de thèse offre diverses possibilités d'ouverture. Concernant des aspects physiques, notre simulation Monte Carlo pourrait être implémentée pour d'autre types de matériaux tels que le gadolinium ou la platine, tous les deux utilisés comme radiosensibilisants. Par ailleurs, l'étude de l'impact de la taille de nanocibles sur la distribution de l'énergie spécifique en présence de nanoparticules a été commencée. Le travail d'analyse des résultats est en court. Nous souhaitons ainsi voir si une taille de cible optimum existe pour avoir le maximum d'effet. Concernant les aspects de chimie, nous souhaiterions explorer de possibles effets catalytiques qui pourraient éventuellement être implémentés dans notre simulation Monte Carlo. Pour cela, une collaboration avec l'équipe de E. Dumont à l'ENS de Lyon a été entamée. Son équipe travaille sur la modélisation, à échelle atomique, des nanoparticules et de leur interaction avec des molécules en surface. Pour terminer, nos application du modèle NanOx aux effets des nanoparticules d'or a considéré un système simpliste, notamment vis-à-vis de la biodistribution des nanoparticules. Plusieurs pistes sont envisagées pour améliorer le modèle, qui prendraient mieux en compte les réalités biologiques.

16. Curriculum Vitae of this thesis

Conferences

International

- **Radiation Research**: Physical, chemical and biological modelling of the radiosensitizing effect of high-Z nanoparticles, *Manchester, England, August 2019*
- **ARGENT**: Impact of gold nanoparticles on nanodosimetry and radical production, *Gif-sur-Yvette, France, January 2018*
- **CIRLAF13**: Modélisation biophysique de l'effet radiosensibilisant des nanoparticules à élément lourd, *Lyon, France, December 2017*
- **MCMA 2017**: Biophysical modelling of the radiosensitizing effect of gold nanoparticles (GNP), *Naples, Italy, October 2017*
- **Nanotech France 2017**: Biophysical modelisation of gold nanoparticle (GNP) radiosensitizing effect, *Paris, France, June 2017*

National

- **Journées scientifiques du pôle de radiobiologie** : Simulation de l'impact des nanoparticules sur la nanodosimétrie et la production de radicaux libres, *Lyon, October 2017*
- **LabEx PRIMES assemblée générale** : Biophysical modelling of high-Z nanoparticles radiosensitizing effect, *Lyon, October 2017*
- **LabEx PRIMES communication** : Biophysical modelling for innovative therapy, Grenoble, *February 2017*
- **Séminaire** : Modélisation biophysique pour thérapies innovantes, *Lyon, May 2017*
- **Journées CLARA** : Modélisation biophysique des effets radiosensibilisants des nanoparticules, *Lyon, April 2016*

Poster

- **Ecole de formation NanoMed** : Physical, chemical and biological modeling of gold nanoparticle-aided radiation therapy: towards a better understanding and optimization of the radiosensitizing effect, *Semur-en-Auxois, France, June 2018*
- **Journées CLARA** : Physical, chemical and biological modeling of gold nanoparticle-aided radiation therapy: towards a better understanding and optimization of the radiosensitizing effect, *Lyon, France, April 2018*
- **Journées CLARA** : Biophysical modeling of radiosensitizing effects of nanoparticles, *Lyon, France, April 2016 + April 2017*

Awards

- **Colloque Santé@LabEx 2019**: second award of the best poster.
- **Journées Jeunes Chercheurs de l'ARC 2018** : First Kerner award. The participation to this price consisted in writing an article and making an illustration of your PhD work for a large public. More info: `https://www.fondation-arc.org/le-prix-kerner-2018`.
- **Journées CLARA 2018**: award of the best poster.

Media

- 2019. Invited of the 18/19 on the French radio RCF, to discuss about nanoparticles in radiotherapy. To listen to the podcast: link.
- 2019. Participation to the French regional TV news. To watch the streaming: link

Illustration for the Kerner Award

La **nanomédecine** s'intéresse aux **nanoparticules**, dont la taille est jusqu'à 1 milliard de fois plus petite que le mètre. Elles sont plus petites que nos cellules, et aussi grosses que certains virus ou notre ADN. Elles sont utilisées dans de nombreux domaines, dont le **traitement du cancer par radiothérapie.**

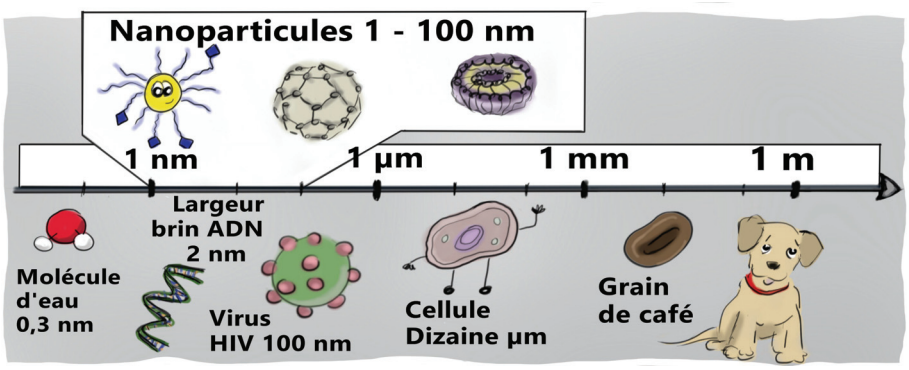

Lorsqu'elles sont injectées dans le sang, **les nanoparticules** ont tendance à naturellement s'accumuler **dans la tumeur**, en raison de ses vaisseaux sanguins malformés. C'est le **ciblage passif (A)**. On peut aussi greffer des molécules aux nanoparticules, pour qu'elles reconnaissent les cellules cancéreuses. C'est le **ciblage actif (B)**.

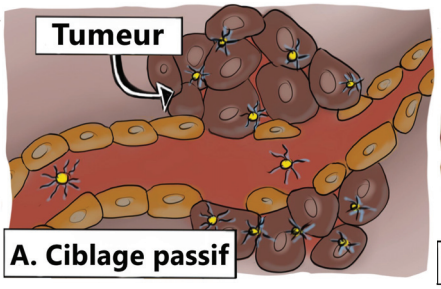

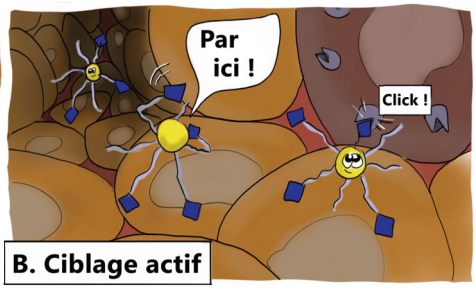

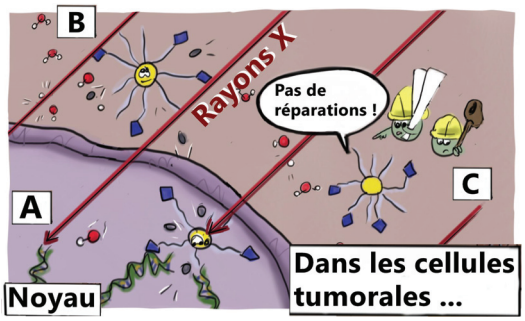

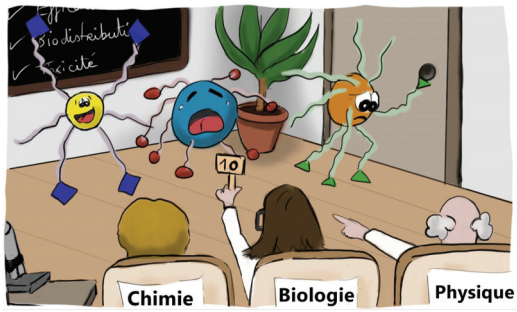

Une fois les nanoparticules dans les cellules tumorales, les rayonnements sont envoyés. En traversant ces cellules, ceux-ci vont détruire l'ADN ou produire des espèces chimiques toxiques en réagissant avec les molécules de nos cellules, notamment les molécules d'eau. En présence de nanoparticules, ces mécanismes sont renforcés par des **voies physiques (A), chimiques (B) et biologiques (C).** Cela rend la destruction de la tumeur plus efficace. C'est **l'effet radio-sensibilisant des nanoparticules**.

Ensemble, des physiciens, chimistes, biologistes et médecins étudient différentes nanoparticules afin de comprendre ces mécanismes pour trouver les nanoparticules les plus efficaces, et ainsi **optimiser ce traitement innovant**.

17. Acronyms

Numbers
3CCA: Coumarin-3-Carboxylic Acid

A
AET: cysteamine
ATM: Ataxia Telangiectasia Mutates
ATP: Adenosine Triphosphate
ATR: Ataxia Telangiectasia RAD3 Related

B
BEB: Binary-Encounter-Bethe
BSA: Bovine Serum Albumin

C
C: Coumarin
CAT: Catalase
CDER: Cytoplasm Dose Enhancement Ratio
CDKs: Cyclin-Dependent Kinases
CS: Cross Section

D
DCS: Differential Cross Section
DEF: Dose Enhancement Factor
DFT: Density Functional Theory
DIMFP: Differential Inverse Mean Free Path
DLS: Dynamic Light Scattering
DMSO: DiMethyl SulfOxide
DNA: DeoxyriboNucleic Acid
DSBs: DNA Double-Strand Breaks

E
EADL: Evaluated Atomic Data Library
EDTA: EthyleneDiamineTetraacetic Acid
EF: Enhancement Factor
EPR: Enhanced Permeation and Retention
ER: Endoplasmic Reticulum

F

FDA: Food and Drug Administration
FBS: Foetal Bovine Serum

G

Gal: Galactose
GdNP: Gadolinium NanoParticle
Glu: Glucose
GNP: Gold NanoParticle
GNPs: Gold NanoParticles
GSH: monomeric glutathione
GSSG: glutathione disulfite

H

Hscen2: Human centrin 2
HPLC: High-Performance Liquid Chromatography
HR: Homologous Recombination
HSA: Human Serum Albumin

I

IGRT: Image-Guided Radiation Therapy
IMFP: Inverse or Inelastic Mean Free Path
IMRT: Intensity Modulated Radiation Therapy
IR: IRradiation
IT: Intra-Tumoural
IV: Intra-Venous

L

L: Linear
LEM: Local Effect Model
LET: Linear Energy Transfer
LMP: Lysosomal Membrane Permeabilization
LQ: Linear Quadratic

M

Mabs: Monoclonal antibodies
MC: Monte Carlo
MDEF: Macroscopic Dose Enhancement Ratio
MID: Mean Inactivation Dose
MRI: Magnetic Resonance Imaging
MTT: 3-(4,5 diMethythiazol-2-yl)-2,5-diphenyl TeTrazolium bromide

N

NADPH: Nicotinamide Adenine Dinucleotide PHosphate
NDER: Nuclear Dose Enhancement Ratio
NHEJ: Non-Homologous End-Joining
NMs: NanoMaterials
NP: NanoParticle

NPs: NanoParticles

OER

OER: Oxygen Enhancement Ratio
OC: Open Circular

P

PBS: Phosphate-Buffered Saline
PC: Protein Corona
PDI: Protein Disulphide Isomerase
PE: Plating Efficiency
PEG: PolyEthylene Glycol
PER: Probability Enhancement Ratio
PIXE: Particle-Induced X-ray Emission
Prx: Peroxiredoxins
PVA: Poly(Vinyl Alcohol)
PVP: Poly(N-Vinyl Pyrrolidone)

R

RBE: Relative Biological Effectiveness
RES: reticuloendothelial system
RNA: ribonucleic acid
RNS: reaction nitrogen species
ROS: reactive oxygen species
RS: radiosensitivity

S

SC: SuperCoiled
scDNA: supercoiled plasmid DNA
SEF: Survival Enhancement Factor
SF: Surviving Fraction
SOBP: Spread-Out Bragg Peak
SOD: SuperOxide Dismustase
SSBs: DNA Single-Strand Breaks

T

TCS: Total Cross Section
TE buffer: tris-EDTA buffer
TEM: Transmission Electron Microscopy
TMA: Trimethylammonium
TNR: tumour necrosis factor
TRIS: hydroxymethyl
Trx: thioredoxin
TrxR1: thioredoxin reductase 1

V

VDAs: Vascular Disrupting Agents

W

WNP: Water NanoParticle

Bibliography

[1] S. Agostinelli et al. GEANT4: A simulation toolkit. *Nucl. Instrum. Meth.*, A506:250–303, 2003. doi: 10.1016/S0168-9002(03)01368-8.

[2] S. Akhter, I. Ahmad, M. Z. Ahmad, F. Ramazani, A. Singh, Z. Rahman, F. J. Ahmad, G. Storm, and R. J. Kok. Nanomedicines as cancer therapeutics: current status. *Current cancer drug targets*, 13(4):362–378, 2013.

[3] K. O. Al-Ahmad and D. E. Watt. Stopping powers and extrapolated ranges for electrons (1-10 kev) in metals. *Journal of Physics D: Applied Physics*, 16(11):2257, 1983. URL `http://stacks.iop.org/0022-3727/16/i=11/a=028`.

[4] A. Alkafri, Y. Ichikawa, R. Shimizu, and K. Goto. Transmission measurement of the absolute cma; simulation and experiments. *Journal of Surface Analysis*, 14(1):2–8, 2007.

[5] E. Amato, A. Italiano, S. Leotta, S. Pergolizzi, and L. Torrisi. Monte carlo study of the dose enhancement effect of gold nanoparticles during x-ray therapies and evaluation of the anti-angiogenic effect on tumour capillary vessels. *Journal of X-ray Science and Technology*, 21(2):237–247, 2013.

[6] E. Amato, A. Italiano, and S. Pergolizzi. Gold nanoparticles as a sensitising agent in external beam radiotherapy and brachytherapy: a feasibility study through monte carlo simulation. *International Journal of Nanotechnology*, 10(12):1045–1054, 2013.

[7] P. A. Anderson. Work Function of Gold. *Physical Review*, 115:553–554, Aug. 1959. doi: 10.1103/PhysRev.115.553.

[8] F. Antunes, E. Cadenas, and U. T. BRUNK. Apoptosis induced by exposure to a low steady-state concentration of h2o2 is a consequence of lysosomal rupture. *Biochemical Journal*, 356 (2):549–555, 2001.

[9] S. Arora, J. M. Rajwade, and K. M. Paknikar. Nanotoxicology and in vitro studies: the need of the hour. *Toxicology and applied pharmacology*, 258(2):151–165, 2012.

[10] S. Asadi, M. Vaez-zadeh, S. F. Masoudi, F. Rahmani, C. Knaup, and A. S. Meigooni. Gold nanoparticle-based brachytherapy enhancement in choroidal melanoma using a full monte carlo model of the human eye. *Journal of applied clinical medical physics*, 16(5):344–357, 2015.

[11] J. Ashley. Interaction of low-energy electrons with condenced matter: stopping powers and inelastic mean free paths from optical data. *Journal of Electrorn Spectroscopy and Related Phenomena*, 46:199–214, 1988.

[12] J. Ashley. Energy loss rate and inelastic mean free path of low-energy electrons and positrons

in condenced matter. *Journal of Electrorn Spectroscopy and Related Phenomena*, 50:323–334, 1990.

[13] J. Ashley, J. Cowan, R. Ritchie, V. Anderson, and J. Hoelzl. Straggling and plasmon excitation in the energy loss spectra of electrons transmitted through carbon. *Thin Solid Films*, 60 (3):361 – 370, 1979. ISSN 0040-6090. doi: http://dx.doi.org/10.1016/0040-6090(79)90082-8. URL `http://www.sciencedirect.com/science/article/pii/0040609079900828`.

[14] G. Baldacchino, T. Maeyama, S. Yamashita, M. Taguchi, A. Kimura, Y. Katsumura, and T. Murakami. Determination of the time-dependent oh-yield by using a fluorescent probe. application to heavy ion irradiation. *Chemical Physics Letters*, 468(4-6):275–279, 2009.

[15] D. M. Bartels, A. R. Cook, M. Mudaliar, and C. D. Jonah. Spur decay of the solvated electron in picosecond radiolysis measured with time-correlated absorption spectroscopy. *The Journal of Physical Chemistry A*, 104(8):1686–1691, 2000.

[16] R. Baskar, K. A. Lee, R. Yeo, and K.-W. Yeoh. Cancer and radiation therapy: current advances and future directions. *International journal of medical sciences*, 9(3):193, 2012.

[17] R. I. Berbeco, W. Ngwa, and G. M. Makrigiorgos. Localized dose enhancement to tumor blood vessel endothelial cells via megavoltage x-rays and targeted gold nanoparticles: new potential for external beam radiotherapy. *International Journal of Radiation Oncology Biology Physics*, 81(1):270–276, 2011.

[18] M. Berger, J. Hubbell, S. Seltzer, J. Chang, J. Coursey, R. Sukumar, D. Zucker, and K. Olsen. Xcom: Photon cross section database (version 1.5), national institute of standards and technology, gaithersburg, md, 2010. *Google Scholar*, 2011.

[19] M. Bernal, M. Bordage, J. Brown, M. Davídková, E. Delage, Z. El Bitar, S. Enger, Z. Francis, S. Guatelli, V. Ivanchenko, et al. Track structure modeling in liquid water: a review of the geant4-dna very low energy extension of the geant4 monte carlo simulation toolkit. *Physica Medica*, 31(8):861–874, 2015.

[20] M. Beuve. Formalization and theoretical analysis of the local effect model. *Radiation research*, 172(3):394–402, 2009.

[21] M. Beuve, M. Caron, P. Fainstein, M. Galassi, B. Gervais, R. Rivarola, and H. Rothard. Monte Carlo simulation of electron emission induced by swift highly charged ions: beyond the linear response approximation. *The European Physical Journal D-Atomic, Molecular, Optical and Plasma Physics*, 21(2):125–135, 2002.

[22] M. Beuve, G. Alphonse, M. Maalouf, A. Colliaux, P. Battiston-Montagne, P. Jalade, E. Balanzat, A. Demeyer, M. Bajard, and C. Rodriguez-Lafrasse. Radiobiologic parameters and local effect model predictions for head-and-neck squamous cell carcinomas exposed to high linear energy transfer ions. *International Journal of Radiation Oncology* Biology* Physics*, 71(2):635–642, 2008.

[23] M. Beuve, A. Colliaux, D. Dabli, D. Dauvergne, B. Gervais, G. Montarou, and E. Testa. Statistical effects of dose deposition in track-structure modelling of radiobiology efficiency. *Nuclear Instruments and Methods in Physics Research Section B: Beam Interactions with Materials and Atoms*, 267(6):983–988, 2009.

[24] S. Biswas and V. P. Torchilin. Nanopreparations for organelle-specific delivery in cancer. *Advanced drug delivery reviews*, 66:26–41, 2014.

[25] L. Bobyk. *Renforcement de la dose par rayonnement synchrotron et atomes lourds dans le cadre du traitement des gliomes*. PhD thesis, 2010. URL `http://www.theses.fr/s123655`. Thèse de doctorat dirigée par Jean-luc Ravanat et Helene Elleaume.

[26] L. Bobyk, M. Edouard, P. Deman, M. Vautrin, K. Pernet-Gallay, J. Delaroche, J.-F. Adam, F. Estève, J.-L. Ravanat, and H. Elleaume. Photoactivation of gold nanoparticles for glioma treatment. *Nanomedicine: Nanotechnology, Biology and Medicine*, 9(7):1089–1097, 2013.

[27] L. Bodgi and N. Foray. The nucleo-shuttling of the atm protein as a basis for a novel theory of radiation response: resolution of the linear-quadratic model. *International journal of radiation biology*, 92(3):117–131, 2016.

[28] T. Böhlen, F. Cerutti, M. Chin, A. Fassò, A. Ferrari, P. Ortega, A. Mairani, P. R. Sala, G. Smirnov, and V. Vlachoudis. The fluka code: developments and challenges for high energy and medical applications. *Nuclear Data Sheets*, 120:211–214, 2014.

[29] E. Boisselier and D. Astruc. Gold nanoparticles in nanomedicine: preparations, imaging, diagnostics, therapies and toxicity. *Chemical society reviews*, 38(6):1759–1782, 2009.

[30] J. F. Briesmeister et al. *MCNP–A general Monte Carlo code for neutron and photon transport*. Los Alamos National Laboratory, 1986.

[31] I. Bronstein and B. Fraiman. Vtorichnaya elektronnaya emissiya. *Moskva: Nauka*, 1969.

[32] J. M. Brown and F. J. Currell. A local effect model-based interpolation framework for experimental nanoparticle radiosensitisation data. *Cancer nanotechnology*, 8(1):1, 2017.

[33] J. M. Brown, G. G. Hanna, N. Lampe, B. Villagomez-Bernabe, J. R. Nicol, J. A. Coulter, and F. J. Currell. Towards photon radiotherapy treatment planning with high z nanoparticle radiosensitisation agents: the relative biological effective dose (rbed) framework. *Cancer nanotechnology*, 9(1):9, 2018.

[34] E. Brun and C. Sicard-Roselli. Could nanoparticle corona characterization help for biological consequence prediction? *Cancer nanotechnology*, 5(1):7, 2014.

[35] E. Brun and C. Sicard-Roselli. Actual questions raised by nanoparticle radiosensitization. *Radiation Physics and Chemistry*, 128:134–142, 2016.

[36] E. Brun, P. Duchambon, Y. Blouquit, G. Keller, L. Sanche, and C. Sicard-Roselli. Gold nanoparticles enhance the x-ray-induced degradation of human centrin 2 protein. *Radiation Physics and Chemistry*, 78(3):177–183, 2009.

[37] E. Brun, L. Sanche, and C. Sicard-Roselli. Parameters governing gold nanoparticle x-ray radiosensitization of dna in solution. *Colloids and Surfaces B: Biointerfaces*, 72(1):128–134, 2009.

[38] K. Butterworth, J. Wyer, M. Brennan-Fournet, C. Latimer, M. Shah, F. Currell, and D. Hirst. Variation of strand break yield for plasmid dna irradiated with high-z metal nanoparticles. *Radiation research*, 170(3):381–387, 2008.

[39] K. Butterworth, J. Coulter, S. Jain, J. Forker, S. McMahon, G. Schettino, K. Prise, F. Currell, and D. Hirst. Evaluation of cytotoxicity and radiation enhancement using 1.9 nm gold particles: potential application for cancer therapy. *Nanotechnology*, 21(29):295101, 2010.

[40] K. T. Butterworth, S. J. McMahon, F. J. Currell, and K. M. Prise. Physical basis and biological mechanisms of gold nanoparticle radiosensitization. *Nanoscale*, 4(16):4830–4838, 2012.

[41] K. T. Butterworth, S. J. McMahon, L. E. Taggart, and K. M. Prise. Radiosensitization by gold nanoparticles: effective at megavoltage energies and potential role of oxidative stress. *Translational Cancer Research*, 2(4):269–279, 2013.

[42] B. C. R. C., F. Jean-M, D.-B. Xochitl, S. Mika, et al. Towards reliable quantification of hydroxyl radicals in the fenton reaction using chemical probes. *RSC Advances*, 8(10): 5321–5330, 2018.

[43] Z. Cai, J.-P. Pignol, N. Chattopadhyay, Y. L. Kwon, E. Lechtman, and R. M. Reilly. Investigation of the effects of cell model and subcellular location of gold nanoparticles on nuclear dose enhancement factors using monte carlo simulation. *Medical physics*, 40(11), 2013.

[44] I. Canton and G. Battaglia. Endocytosis at the nanoscale. *Chemical Society Reviews*, 41 (7):2718–2739, 2012.

[45] J. D. Carter, N. N. Cheng, Y. Qu, G. D. Suarez, and T. Guo. Nanoscale energy deposition by x-ray absorbing nanostructures. *The Journal of Physical Chemistry B*, 111(40):11622–11625, 2007.

[46] R. Castaing, P. Deschamps, and J. Philibert. *Optique des rayons X et microanalyse*. Hermann, 1966.

[47] J. Chang, R. D. Taylor, R. A. Davidson, A. Sharmah, and T. Guo. Electron paramagnetic resonance spectroscopy investigation of radical production by gold nanoparticles in aqueous solutions under x-ray irradiation. *The Journal of Physical Chemistry A*, 120(18):2815–2823, 2016.

[48] M.-Y. Chang, A.-L. Shiau, Y.-H. Chen, C.-J. Chang, H. H.-W. Chen, and C.-L. Wu. Increased apoptotic potential and dose-enhancing effect of gold nanoparticles in combination with single-dose clinical electron beams on tumor-bearing mice. *Cancer science*, 99(7): 1479–1484, 2008.

[49] N. Chattopadhyay, Z. Cai, Y. L. Kwon, E. Lechtman, J.-P. Pignol, and R. M. Reilly. Molecularly targeted gold nanoparticles enhance the radiation response of breast cancer cells and tumor xenografts to x-radiation. *Breast cancer research and treatment*, 137(1):81–91, 2013.

[50] N. Chen, W. Yang, Y. Bao, H. Xu, S. Qin, and Y. Tu. Bsa capped au nanoparticle as an efficient sensitizer for glioblastoma tumor radiation therapy. *RSC Advances*, 5(51):40514–40520, 2015.

[51] N. N. Cheng, Z. Starkewolf, R. A. Davidson, A. Sharmah, C. Lee, J. Lien, and T. Guo. Chemical enhancement by nanomaterials under x-ray irradiation. *Journal of the American Chemical Society*, 134(4):1950–1953, 2012.

[52] B. D. Chithrani and W. C. Chan. Elucidating the mechanism of cellular uptake and removal

of protein-coated gold nanoparticles of different sizes and shapes. *Nano letters*, 7(6):1542–1550, 2007.

[53] B. D. Chithrani, A. A. Ghazani, and W. C. Chan. Determining the size and shape dependence of gold nanoparticle uptake into mammalian cells. *Nano letters*, 6(4):662–668, 2006.

[54] D. B. Chithrani. Intracellular uptake, transport, and processing of gold nanostructures. *Molecular membrane biology*, 27(7):299–311, 2010.

[55] D. B. Chithrani, S. Jelveh, F. Jalali, M. van Prooijen, C. Allen, R. G. Bristow, R. P. Hill, and D. A. Jaffray. Gold nanoparticles as radiation sensitizers in cancer therapy. *Radiation research*, 173(6):719–728, 2010.

[56] S. H. Cho. Estimation of tumour dose enhancement due to gold nanoparticles during typical radiation treatments: a preliminary monte carlo study. *Physics in Medicine & Biology*, 50 (15):N163, 2005.

[57] S. H. Cho, B. L. Jones, and S. Krishnan. The dosimetric feasibility of gold nanoparticle-aided radiation therapy (gnrt) via brachytherapy using low-energy gamma-/x-ray sources. *Physics in Medicine & Biology*, 54(16):4889, 2009.

[58] V. Cobut, Y. Frongillo, J. Patau, T. Goulet, M. Fraser, and J. Jay-Gerin. Monte carlo simulation of fast electron and proton tracks in liquid water-i. physical and physicochemical aspects. *Radiation Physics and Chemistry*, 51(3):229–244, 1998.

[59] A. Colliaux, B. Gervais, C. Rodriguez-Lafrasse, and M. Beuve. O2 and glutathione effects on water radiolysis: a simulation study. In *Journal of Physics: Conference Series*, volume 261, page 012007. IOP Publishing, 2011.

[60] A. Colliaux, B. Gervais, C. Rodriguez-Lafrasse, and M. Beuve. Simulation of ion-induced water radiolysis in different conditions of oxygenation. *Nuclear Instruments and Methods in Physics Research Section B: Beam Interactions with Materials and Atoms*, 365:596–605, 2015.

[61] A. Collins, G. Makrigiorgos, and G. Svensson. Coumarin chemical dosimeter for radiation therapy. *Medical physics*, 21(11):1741–1747, 1994.

[62] B. R. Cooper, H. Ehrenreich, and H. R. Philipp. Optical properties of noble metals. ii. *Phys. Rev.*, 138:A494–A507, Apr 1965. doi: 10.1103/PhysRev.138.A494. URL `https://link.aps.org/doi/10.1103/PhysRev.138.A494`.

[63] D. R. Cooper, D. Bekah, and J. L. Nadeau. Gold nanoparticles and their alternatives for radiation therapy enhancement. *Frontiers in chemistry*, 2:86, 2014.

[64] C. Corbo, R. Molinaro, A. Parodi, N. E. Toledano Furman, F. Salvatore, and E. Tasciotti. The impact of nanoparticle protein corona on cytotoxicity, immunotoxicity and target drug delivery. *Nanomedicine*, 11(1):81–100, 2016.

[65] J. Coulter, W. Hyland, J. Nicol, and F. Currell. Radiosensitising nanoparticles as novel cancer therapeuticsâ€"pipe dream or realistic prospect? *Clinical Oncology*, 25(10):593–603, 2013.

[66] J. A. Coulter, S. Jain, K. T. Butterworth, L. E. Taggart, G. R. Dickson, S. J. McMahon, W. B. Hyland, M. F. Muir, C. Trainor, A. R. Hounsell, et al. Cell type-dependent uptake, localization, and cytotoxicity of 1.9 nm gold nanoparticles. *International journal of nanomedicine*, 7:2673, 2012.

[67] L. Cui, P. Zahedi, J. Saraceno, R. Bristow, D. Jaffray, and C. Allen. Neoplastic cell response to tiopronin-coated gold nanoparticles. *Nanomedicine: Nanotechnology, Biology and Medicine*, 9(2):264–273, 2013.

[68] L. Cui, K. Tse, P. Zahedi, S. M. Harding, G. Zafarana, D. A. Jaffray, R. G. Bristow, and C. Allen. Hypoxia and cellular localization influence the radiosensitizing effect of gold nanoparticles (aunps) in breast cancer cells. *Radiation research*, 182(5):475–488, 2014.

[69] M. Cunha, C. Monini, E. Testa, and M. Beuve. NanOx, a new model to predict cell survival in the context of particle therapy. *Physics in Medicine & Biology*, 62(4):1248, 2017.

[70] M. Cunha, E. Testa, M. Beuve, J. Balosso, and A. Chaikh. Considerations on the miniaturization of detectors for in vivo dosimetry in radiotherapy: A monte carlo study. *Nuclear Instruments and Methods in Physics Research Section B: Beam Interactions with Materials and Atoms*, 399:20–27, 2017.

[71] Z. Czyzewski, D. O. MacCallum, A. Romig, and D. C. Joy. Calculations of mott scattering cross section. *Journal of Applied Physics*, 68(7):3066–3072, 1990. doi: http://dx.doi.org/10.1063/1.346400. URL `http://scitation.aip.org/content/aip/journal/jap/68/7/10.1063/1.346400`.

[72] E. L. da Rocha, G. F. Caramori, and C. R. Rambo. Nanoparticle translocation through a lipid bilayer tuned by surface chemistry. *Physical Chemistry Chemical Physics*, 15(7): 2282–2290, 2013.

[73] M.-C. Daniel and D. Astruc. Gold nanoparticles: assembly, supramolecular chemistry, quantum-size-related properties, and applications toward biology, catalysis, and nanotechnology. *Chemical reviews*, 104(1):293–346, 2004.

[74] J. Daniels. PhD thesis, Hambourg, 1969.

[75] R. A. Davidson and T. Guo. Average physical enhancement by nanomaterials under x-ray irradiation. *The Journal of Physical Chemistry C*, 118(51):30221–30228, 2014.

[76] R. A. Davidson and T. Guo. multiplication algorithm for combined physical and chemical enhancement of x-ray effect by nanomaterials. *The Journal of Physical Chemistry C*, 119 (33):19513–19519, 2015.

[77] N. Del Fatti, C. Voisin, M. Achermann, S. Tzortzakis, D. Christofilos, and F. Vallée. Nonequilibrium electron dynamics in noble metals. *Physical Review B*, 61(24):16956, 2000.

[78] R. Delorme. *Radiothérapie par Photoactivation de Nanoparticules : modélisation Ã l'Échelle Sub-Micrométrique et Comparaison Expérimentale*. PhD thesis, 2013. URL `http://www.theses.fr/2013PA112028`. Thèse de doctorat dirigée par Champion, Christophe Physique médicale Paris 11 2013.

[79] Z.-J. Ding. Self-energy in surface electron spectroscopy: Ii. surface excitation on real metal

surfaces. *Journal of Physics: Condensed Matter*, 10(8):1753, 1998. URL `http://stacks.iop.org/0953-8984/10/i=8/a=010`.

[80] Z.-J. Ding and R. Shimizu. A monte carlo modeling of electron interaction with solids including cascade secondary electron production. *Scanning*, 18(2):92–113, 1996. ISSN 1932-8745. doi: 10.1002/sca.1996.4950180204. URL `http://dx.doi.org/10.1002/sca.1996.4950180204`.

[81] Z. J. Ding, X. D. Tang, and R. Shimizu. Monte carlo study of secondary electron emission. *Journal of Applied Physics*, 89(1):718–726, 2001. doi: http://dx.doi.org/10.1063/1.1331645. URL `http://scitation.aip.org/content/aip/journal/jap/89/1/10.1063/1.1331645`.

[82] Z. J. Ding, H. M. Li, K. Goto, Y. Z. Jiang, and R. Shimizu. Energy spectra of backscattered electrons in auger electron spectroscopy: comparison of monte carlo simulations with experiment. *Journal of Applied Physics*, 96(8):4598–4606, 2004. doi: 10.1063/1.1791752. URL `http://dx.doi.org/10.1063/1.1791752`.

[83] T. A. Doll, S. Raman, R. Dey, and P. Burkhard. Nanoscale assemblies and their biomedical applications. *Journal of The Royal Society Interface*, 10(80):20120740, 2013.

[84] S. M. Douglas, I. Bachelet, and G. M. Church. A logic-gated nanorobot for targeted transport of molecular payloads. *Science*, 335(6070):831–834, 2012.

[85] M. Douglass, E. Bezak, and S. Penfold. Monte carlo investigation of the increased radiation deposition due to gold nanoparticles using kilovoltage and megavoltage photons in a 3d randomized cell model. *Medical physics*, 40(7), 2013.

[86] M. Durante, R. Orecchia, and J. S. Loeffler. Charged-particle therapy in cancer: clinical uses and future perspectives. *Nature Reviews Clinical Oncology*, 14(8):483, 2017.

[87] C. Eggeling, L. Brand, and C. Seidel. Laser-induced fluorescence of coumarin derivatives in aqueous solution: Photochemical aspects for single molecule detection. *Bioimaging*, 5(3): 105–115, 1997.

[88] M. El Gomati, C. Walker, A. Assa'd, and M. Zadražil. Theory experiment comparison of the electron backscattering factor from solids at low electron energy (250–5,000 ev). *Scanning*, 30(1):2–15, 2008.

[89] T. Elsässer and M. Scholz. Improvement of the local effect model (lem)â€"implications of clustered dna damage. *Radiation protection dosimetry*, 122(1-4):475–477, 2006.

[90] T. Elsässer and M. Scholz. Cluster effects within the local effect model. *Radiation research*, 167(3):319–329, 2007.

[91] H.-J. Fitting. Transmission, energy distribution, and se excitation of fast electrons in thin solid films. *physica status solidi (a)*, 26(2):525–535, 1974.

[92] E. A. Foley, J. D. Carter, F. Shan, and T. Guo. Enhanced relaxation of nanoparticle-bound supercoiled dna in x-ray radiation. *Chemical communications*, (25):3192–3194, 2005.

[93] Z. Francis, S. Incerti, M. Karamitros, H. Tran, and C. Villagrasa. Stopping power and ranges of electrons, protons and alpha particles in liquid water using the geant4-dna package.

Nuclear Instruments and Methods in Physics Research Section B: Beam Interactions with Materials and Atoms, 269(20):2307–2311, 2011.

[94] S. Friberg and A. M. Nyström. Nanotechnology in the war against cancer: new arms against an old enemy–a clinical view. *Future Oncology*, 11(13):1961–1975, 2015.

[95] W. Friedland, M. Dingfelder, P. Kundrát, and P. Jacob. Track structures, dna targets and radiation effects in the biophysical monte carlo simulation code partrac. *Mutation Research/Fundamental and Molecular Mechanisms of Mutagenesis*, 711(1):28–40, 2011.

[96] W. Friedland, M. Dingfelder, P. Kundrát, and P. Jacob. Track structures, dna targets and radiation effects in the biophysical monte carlo simulation code partrac. *Mutation Research/Fundamental and Molecular Mechanisms of Mutagenesis*, 711(1):28–40, 2011.

[97] T. Friedrich, U. Scholz, T. Elsässer, M. Durante, and M. Scholz. Systematic analysis of RBE and related quantities using a database of cell survival experiments with ion beam irradiation. *J. Radiat. Res.*, 54(3):494–514, Dec. 2012. ISSN 0449-3060, 1349-9157. doi: 10.1093/jrr/rrs114.

[98] Y. Frongillo, T. Goulet, M. Fraser, V. Cobut, J. Patau, and J. Jay-Gerin. Monte carlo simulation of fast electron and proton tracks in liquid water-ii. nonhomogeneous chemistry. *Radiation Physics and Chemistry*, 51(3):245–254, 1998.

[99] P. P. Fu, Q. Xia, H.-M. Hwang, P. C. Ray, and H. Yu. Mechanisms of nanotoxicity: generation of reactive oxygen species. *Journal of food and drug analysis*, 22(1):64–75, 2014.

[100] W. G. and D. J. R. Approximation of range in materials as a function of incident electron energy. *IEEE Transactions on Plasma Science*, 40(2):291–297, 2012. URL `http://ieeexplore.ieee.org/document/6127915/`.

[101] S. M. Gadoue, P. Zygmanski, and E. Sajo. The dichotomous nature of dose enhancement by gold nanoparticle aggregates in radiotherapy. *Nanomedicine*, (0), 2018.

[102] H. Gao, W. Shi, and L. B. Freund. Mechanics of receptor-mediated endocytosis. *Proceedings of the National Academy of Sciences*, 102(27):9469–9474, 2005.

[103] H. Garnica-Garza. Treatment planning considerations in contrast-enhanced radiotherapy: energy and beam aperture optimization. *Physics in Medicine & Biology*, 56(2):341, 2010.

[104] F. Geng, K. Song, J. Z. Xing, C. Yuan, S. Yan, Q. Yang, J. Chen, and B. Kong. Thio-glucose bound gold nanoparticles enhance radio-cytotoxic targeting of ovarian cancer. *Nanotechnology*, 22(28):285101, 2011.

[105] B. Gervais, M. Beuve, G. Olivera, M. Galassi, and R. Rivarola. Production of ho2 and o2 by multiple ionization in water radiolysis by swift carbon ions. *Chemical physics letters*, 410 (4-6):330–334, 2005.

[106] B. Gervais, M. Beuve, G. Olivera, and M. Galassi. Numerical simulation of multiple ionization and high LET effects in liquid water radiolysis. *Radiation Physics and Chemistry*, 75:495–513, 2006. doi: 10.1016/j.radphyschem.2005.09.015. URL `http://hal.in2p3.fr/in2p3-00409741`.

[107] M. Ghita, S. J. McMahon, L. E. Taggart, K. T. Butterworth, G. Schettino, and K. M.

Prise. A mechanistic study of gold nanoparticle radiosensitisation using targeted microbeam irradiation. *Scientific reports*, 7:44752, 2017.

[108] M. Gilles. *Quantification des espèces radicalaires produites en présence de nanoparticules dâ€™or soumises à un rayonnement ionisant*. PhD thesis, 2015. URL `http://www.theses.fr/2015PA112120`. Thèse de doctorat dirigée par Sicard-Roselli, Cécile Chimie Paris 11 2015.

[109] M. Gilles, E. Brun, and C. Sicard-Roselli. Gold nanoparticles functionalization notably decreases radiosensitization through hydroxyl radical production under ionizing radiation. *Colloids and Surfaces B: Biointerfaces*, 123:770–777, 2014.

[110] M. Gilles, E. Brun, and C. Sicard-Roselli. Quantification of hydroxyl radicals and solvated electrons produced by irradiated gold nanoparticles suggests a crucial role of interfacial water. *Journal of colloid and interface science*, 525:31–38, 2018.

[111] K. Goto, N. Sakakibara, Y. Takeichi, Y. Numata, and Y. Sakai. True auger spectral shapes: A step to standard spectra. *Surface and interface analysis*, 22(1-12):75–78, 1994.

[112] N. Green, M. Pilling, S. Pimblott, and P. Clifford. Stochastic modeling of fast kinetics in a radiation track. *Journal of Physical Chemistry*, 94(1):251–258, 1990.

[113] B. Grosswendt and E. Waibel. Transport of low energy electrons in nitrogen and air. *Nuclear Instruments and Methods*, 155(1):145 – 156, 1978. ISSN 0029-554X. doi: http://dx.doi.org/10.1016/0029-554X(78)90198-2. URL `http://www.sciencedirect.com/science/article/pii/0029554X78901982`.

[114] H. A. Hagelin-Weaver, J. F. Weaver, G. B. Hoflund, and G. N. Salaita. Electron energy loss spectroscopic investigation of polycrystalline au, pd and a pd–au alloy. *Journal of alloys and compounds*, 393(1):93–99, 2005.

[115] J. F. Hainfeld, D. N. Slatkin, and H. M. Smilowitz. The use of gold nanoparticles to enhance radiotherapy in mice. *Physics in Medicine & Biology*, 49(18):N309, 2004.

[116] J. F. Hainfeld, F. A. Dilmanian, D. N. Slatkin, and H. M. Smilowitz. Radiotherapy enhancement with gold nanoparticles. *Journal of Pharmacy and Pharmacology*, 60(8):977–985, 2008.

[117] J. F. Hainfeld, F. A. Dilmanian, Z. Zhong, D. N. Slatkin, J. A. Kalef-Ezra, and H. M. Smilowitz. Gold nanoparticles enhance the radiation therapy of a murine squamous cell carcinoma. *Physics in Medicine & Biology*, 55(11):3045, 2010.

[118] J. F. Hainfeld, H. M. Smilowitz, M. J. Oâ€™connor, F. A. Dilmanian, and D. N. Slatkin. Gold nanoparticle imaging and radiotherapy of brain tumors in mice. *Nanomedicine*, 8(10):1601–1609, 2013.

[119] E. J. Hall, A. J. Giaccia, et al. *Radiobiology for the Radiologist*, volume 6. Lippincott Williams & Wilkins Philadelphia, 2006.

[120] D. Hanahan and R. A. Weinberg. The hallmarks of cancer. *cell*, 100(1):57–70, 2000.

[121] D. Hanahan and R. A. Weinberg. Hallmarks of cancer: the next generation. *cell*, 144(5):646–674, 2011.

[122] C. He and J. Chow. Gold nanoparticle dna damage in radiotherapy: A monte carlo study. *AIMS Bioengineering*, 3:352–61, 2016.

[123] W. He, Y.-T. Zhou, W. G. Wamer, X. Hu, X. Wu, Z. Zheng, M. D. Boudreau, and J.-J. Yin. Intrinsic catalytic activity of au nanoparticles with respect to hydrogen peroxide decomposition and superoxide scavenging. *Biomaterials*, 34(3):765–773, 2013.

[124] S. Her, D. A. Jaffray, and C. Allen. Gold nanoparticles for applications in cancer radiotherapy: Mechanisms and recent advancements. *Advanced drug delivery reviews*, 109:84–101, 2017.

[125] D. M. Herold, I. Das, C. Stobbe, R. Iyer, and J. Chapman. Gold microspheres: a selective technique for producing biologically effective dose enhancement. *International journal of radiation biology*, 76(10):1357–1364, 2000.

[126] C. Huang, Q. Bao, D. Hunting, Y. Zheng, and L. Sanche. Conformation-dependent dna damage induced by gold nanoparticles. *Journal of biomedical nanotechnology*, 9(5):856–862, 2013.

[127] L. Hull, D. Farrell, and P. Grodzinski. Highlights of recent developments and trends in cancer nanotechnology researchâ€"view from nci alliance for nanotechnology in cancer. *Biotechnology advances*, 32(4):666–678, 2014.

[128] H.-J. Hunger and L. Küchler. Measurements of the electron backscattering coefficient for quantitative epma in the energy range of 4 to 40 kev. *physica status solidi (a)*, 56(1), 1979.

[129] B. Hvolbæk, T. V. Janssens, B. S. Clausen, H. Falsig, C. H. Christensen, and J. K. Nørskov. Catalytic activity of au nanoparticles. *Nano Today*, 2(4):14–18, 2007.

[130] S. Incerti, B. Suerfu, J. Xu, V. Ivantchenko, A. Mantero, J. Brown, M. Bernal, Z. Francis, M. Karamitros, and H. Tran. Simulation of auger electron emission from nanometer-size gold targets using the geant4 monte carlo simulation toolkit. *Nuclear Instruments and Methods in Physics Research Section B: Beam Interactions with Materials and Atoms*, 372:91–101, 2016.

[131] A. Jablonski. Angular distribution of elastic electron backscattering from surfaces: determination of the electron inelastic mean free path. *Journal of Physics D: Applied Physics*, 47(5):055301, 2014. URL `http://stacks.iop.org/0022-3727/47/i=5/a=055301`.

[132] A. Jablonski. Analytical theory of elastic electron backscattering from elements, alloys and compounds: Comparison with experimental data. *Journal of Electron Spectroscopy and Related Phenomena*, 206:24 – 45, 2016. ISSN 0368-2048. doi: http://dx.doi.org/10.1016/j.elspec.2015.10.006. URL `http://www.sciencedirect.com/science/article/pii/S0368204815002637`.

[133] A. Jablonski and P. Jiricek. Elastic electron backscattering from surfaces at low energies. *Surface and Interface Analysis*, 24(11):781–785, 1996. ISSN 1096-9918. doi: 10.1002/(SICI)1096-9918(199610)24:11<781::AID-SIA187>3.0.CO;2-K. URL `http://dx.doi.org/10.1002/(SICI)1096-9918(199610)24:11<781::AID-SIA187>3.0.CO;2-K`.

[134] S. Jain, J. A. Coulter, A. R. Hounsell, K. T. Butterworth, S. J. McMahon, W. B. Hyland, M. F. Muir, G. R. Dickson, K. M. Prise, F. J. Currell, et al. Cell-specific radiosensitization

by gold nanoparticles at megavoltage radiation energies. *International Journal of Radiation Oncology Biology Physics*, 79(2):531–539, 2011.

[135] S. Jain, J. A. Coulter, K. T. Butterworth, A. R. Hounsell, S. J. McMahon, W. B. Hyland, M. F. Muir, G. R. Dickson, K. M. Prise, F. J. Currell, et al. Gold nanoparticle cellular uptake, toxicity and radiosensitisation in hypoxic conditions. *Radiotherapy and Oncology*, 110(2):342–347, 2014.

[136] F. Jean-M, D.-B. Xochitl, S. Mika, et al. Towards reliable quantification of hydroxyl radicals in the fenton reaction using chemical probes. *RSC Advances*, 8(10):5321–5330, 2018.

[137] J. Jeevanandam, A. Barhoum, Y. S. Chan, A. Dufresne, and M. K. Danquah. Review on nanoparticles and nanostructured materials: history, sources, toxicity and regulations. *Beilstein journal of nanotechnology*, 9:1050, 2018.

[138] J. Jeynes, M. Merchant, A. Spindler, A. Wera, and K. Kirkby. Investigation of gold nanoparticle radiosensitization mechanisms using a free radical scavenger and protons of different energies. *Physics in Medicine & Biology*, 59(21):6431, 2014.

[139] H. Y. Jia, Y. Liu, X. J. Zhang, L. Han, L. B. Du, Q. Tian, and Y. C. Xu. Potential oxidative stress of gold nanoparticles by induced-no releasing in serum. *Journal of the American Chemical Society*, 131(1):40–41, 2008.

[140] D. Y. Joh, L. Sun, M. Stangl, A. Al Zaki, S. Murty, P. P. Santoiemma, J. J. Davis, B. C. Baumann, M. Alonso-Basanta, D. Bhang, et al. Selective targeting of brain tumors with gold nanoparticle-induced radiosensitization. *PloS one*, 8(4):e62425, 2013.

[141] M. C. Joiner. Quantifying cell kill and cell survival. *Basic clinical radiobiology*, 4:42–55, 2009.

[142] B. L. Jones, S. Krishnan, and S. H. Cho. Estimation of microscopic dose enhancement factor around gold nanoparticles by monte carlo calculations. *Medical physics*, 37(7Part1): 3809–3816, 2010.

[143] Y. Ju-Nam and J. R. Lead. Manufactured nanoparticles: an overview of their chemistry, interactions and potential environmental implications. *Science of the total environment*, 400 (1-3):396–414, 2008.

[144] T. Kamada, H. Tsujii, E. A. Blakely, J. Debus, W. De Neve, M. Durante, O. Jäkel, R. Mayer, R. Orecchia, R. Pötter, et al. Carbon ion radiotherapy in japan: an assessment of 20 years of clinical experience. *The Lancet Oncology*, 16(2):e93–e100, 2015.

[145] H. Kanter. Slow-electron mean free paths in aluminum, silver, and gold. *Phys. Rev. B*, 1: 522–536, Jan 1970. doi: 10.1103/PhysRevB.1.522. URL `https://link.aps.org/doi/10.1103/PhysRevB.1.522`.

[146] Ö. F. Karataş, E. Sezgin, Ö. Aydın, and M. Çulha. Interaction of gold nanoparticles with mitochondria. *Colloids and Surfaces B: Biointerfaces*, 71(2):315–318, 2009.

[147] C. P. Karger and P. Peschke. Rbe and related modeling in carbon-ion therapy. *Physics in Medicine & Biology*, 63(1):01TR02, 2017.

[148] H. Kaur, G. Pujari, M. K. Semwal, A. Sarma, and D. K. Avasthi. In vitro studies on

radiosensitization effect of glucose capped gold nanoparticles in photon and ion irradiation of hela cells. *Nuclear Instruments and Methods in Physics Research Section B: Beam Interactions with Materials and Atoms*, 301:7–11, 2013.

[149] N. Khlebtsov and L. Dykman. Biodistribution and toxicity of engineered gold nanoparticles: a review of in vitro and in vivo studies. *Chemical Society Reviews*, 40(3):1647–1671, 2011.

[150] K. Khoshgard, B. Hashemi, A. Arbabi, M. J. Rasaee, and M. Soleimani. Radiosensitization effect of folate-conjugated gold nanoparticles on hela cancer cells under orthovoltage superficial radiotherapy techniques. *Physics in Medicine & Biology*, 59(9):2249, 2014.

[151] E. Kieft and E. Bosch. Refinement of Monte Carlo simulations of electron–specimen interaction in low-voltage SEM. *Journal of Physics D: Applied Physics*, 41(21):215310, 2008.

[152] B. Y. Kim, J. T. Rutka, and W. C. Chan. Nanomedicine. *New England Journal of Medicine*, 363(25):2434–2443, 2010.

[153] Y.-K. Kim and M. E. Rudd. Binary-encounter-dipole model for electron-impact ionization. *Phys. Rev. A*, 50:3954–3967, Nov 1994.

[154] Y.-K. Kim, J. P. Santos, and F. Parente. Extension of the binary-encounter-dipole model to relativistic incident electrons. *Physical Review A*, 62(5):052710, 2000.

[155] C. Kirkby and E. Ghasroddashti. Targeting mitochondria in cancer cells using gold nanoparticle-enhanced radiotherapy: A monte carlo study. *Medical physics*, 42(2):1119–1128, 2015.

[156] K. Kobayashi, N. Usami, E. Porcel, S. Lacombe, and C. Le Sech. Enhancement of radiation effect by heavy elements. *Mutation Research/Reviews in Mutation Research*, 704(1):123–131, 2010.

[157] B. Koger and C. Kirkby. A method for converting dose-to-medium to dose-to-tissue in monte carlo studies of gold nanoparticle-enhanced radiotherapy. *Physics in Medicine & Biology*, 61(5):2014, 2016.

[158] B. Koger and C. Kirkby. Optimization of photon beam energies in gold nanoparticle enhanced arc radiation therapy using monte carlo methods. *Physics in Medicine & Biology*, 61(24):8839, 2016.

[159] T. Kong, J. Zeng, J. Yang, Y. Yao, X. Wang, P. Li, A. Yang, W. Roa, J. Xing, and J. Chen. Surface modifications of gold-nanoparticles to enhance radiation cytotoxicity. In *Life Science Systems and Applications Workshop, 2007. LISA 2007. IEEE/NIH*, pages 265–268. IEEE, 2007.

[160] T. Kong, J. Zeng, X. Wang, X. Yang, J. Yang, S. McQuarrie, A. McEwan, W. Roa, J. Chen, and J. Z. Xing. Enhancement of radiation cytotoxicity in breast-cancer cells by localized attachment of gold nanoparticles. *small*, 4(9):1537–1543, 2008.

[161] M. O. Krause and J. Oliver. Natural widths of atomic K and L levels, K α x-ray lines and several KLL Auger lines. *Journal of Physical and Chemical Reference Data*, 8(2):329–338, 1979.

[162] H. F. Krug and P. Wick. Nanotoxicology: an interdisciplinary challenge. *Angewandte Chemie International Edition*, 50(6):1260–1278, 2011.

[163] D. Kwatra, A. Venugopal, and S. Anant. Nanoparticles in radiation therapy: a summary of various approaches to enhance radiosensitization in cancer. *Translational Cancer Research*, 2(4):330–342, 2013.

[164] S. Lacombe, E. Porcel, and E. Scifoni. Particle therapy and nanomedicine: state of art and research perspectives. *Cancer nanotechnology*, 8(1):9, 2017.

[165] P. Lai, Z. Cai, J.-P. Pignol, E. Lechtman, S. Mashouf, Y. Lu, M. A. Winnik, D. A. Jaffray, and R. M. Reilly. Monte carlo simulation of radiation transport and dose deposition from locally released gold nanoparticles labeled with 111in, 177lu or 90y incorporated into tissue implantable depots. *Physics in Medicine & Biology*, 62(22):8581, 2017.

[166] M. Laprise-Pelletier, Y. Ma, J. Lagueux, M.-F. Côté, L. Beaulieu, and M.-A. Fortin. Intratumoral injection of low-energy photon-emitting gold nanoparticles: A microdosimetric monte carlo-based model. *ACS nano*, 12(3):2482–2497, 2018.

[167] E. Lechtman. *A Monte Carlo-based model of gold nanoparticle radiosensitization*. Theses, University of Toronto, 2013.

[168] E. Lechtman. *A Monte Carlo-based model of gold nanoparticle radiosensitization*. PhD thesis, 2013.

[169] E. Lechtman and J.-P. Pignol. Interplay between the gold nanoparticle sub-cellular localization, size, and the photon energy for radiosensitization. *Scientific Reports*, 7(1):13268, 2017.

[170] E. Lechtman, N. Chattopadhyay, Z. Cai, S. Mashouf, R. Reilly, and J. Pignol. Implications on clinical scenario of gold nanoparticle radiosensitization in regards to photon energy, nanoparticle size, concentration and location. *Physics in Medicine & Biology*, 56(15):4631, 2011.

[171] E. Lechtman, S. Mashouf, N. Chattopadhyay, B. Keller, P. Lai, Z. Cai, R. Reilly, and J. Pignol. A monte carlo-based model of gold nanoparticle radiosensitization accounting for increased radiobiological effectiveness. *Physics in Medicine & Biology*, 58(10):3075, 2013.

[172] W. R. Leo. *Techniques for nuclear and particle physics experiments: a how-to approach*. Springer Science & Business Media, 2012.

[173] M. K. Leung, J. C. Chow, B. D. Chithrani, M. J. Lee, B. Oms, and D. A. Jaffray. Irradiation of gold nanoparticles by x-rays: Monte carlo simulation of dose enhancements and the spatial properties of the secondary electrons production. *Medical physics*, 38(2):624–631, 2011.

[174] S. Li, S. Penninckx, L. Karmani, A.-C. Heuskin, K. Watillon, R. Marega, J. Zola, V. Corvaglia, G. Genard, B. Gallez, et al. Let-dependent radiosensitization effects of gold nanoparticles for proton irradiation. *Nanotechnology*, 27(45):455101, 2016.

[175] Y. Lin, S. J. McMahon, M. Scarpelli, H. Paganetti, and J. Schuemann. Comparing gold nano-particle enhanced radiotherapy with protons, megavoltage photons and kilovoltage photons: a monte carlo simulation. *Physics in Medicine & Biology*, 59(24):7675, 2014.

[176] Y. Lin, S. J. McMahon, H. Paganetti, and J. Schuemann. Biological modeling of gold nanoparticle enhanced radiotherapy for proton therapy. *Physics in Medicine & Biology*, 60 (10):4149, 2015.

[177] Y. Lin, H. Paganetti, S. J. McMahon, and J. Schuemann. Gold nanoparticle induced vasculature damage in radiotherapy: comparing protons, megavoltage photons, and kilovoltage photons. *Medical physics*, 42(10):5890–5902, 2015.

[178] C.-J. Liu, C.-H. Wang, C.-C. Chien, T.-Y. Yang, S.-T. Chen, W.-H. Leng, C.-F. Lee, K.-H. Lee, Y. Hwu, Y.-C. Lee, et al. Enhanced x-ray irradiation-induced cancer cell damage by gold nanoparticles treated by a new synthesis method of polyethylene glycol modification. *Nanotechnology*, 19(29):295104, 2008.

[179] C.-J. Liu, C.-H. Wang, S.-T. Chen, H.-H. Chen, W.-H. Leng, C.-C. Chien, C.-L. Wang, I. M. Kempson, Y. Hwu, T.-C. Lai, et al. Enhancement of cell radiation sensitivity by pegylated gold nanoparticles. *Physics in Medicine & Biology*, 55(4):931, 2010.

[180] R. Liu. Adsorption and dissociation of h2o on au (1 1 1) surface: A dft study. *Computational and Theoretical Chemistry*, 1019:141–145, 2013.

[181] R. Liu, Y. Wang, Q. Yuan, D. An, J. Li, and X. Gao. The au clusters induce tumor cell apoptosis via specifically targeting thioredoxin reductase 1 (trxr1) and suppressing its activity. *Chemical Communications*, 50(73):10687–10690, 2014.

[182] Y. Liu, X. Liu, X. Jin, P. He, X. Zheng, Z. Dai, F. Ye, T. Zhao, W. Chen, and Q. Li. The dependence of radiation enhancement effect on the concentration of gold nanoparticles exposed to low-and high-let radiations. *Physica Medica*, 31(3):210–218, 2015.

[183] G. Louit, S. Foley, J. Cabillic, H. Coffigny, F. Taran, A. Valleix, J. P. Renault, and S. Pin. The reaction of coumarin with the oh radical revisited: hydroxylation product analysis determined by fluorescence and chromatography. *Radiation Physics and Chemistry*, 72(2-3):119–124, 2005.

[184] B. M., R. J, J. O., and P. J. Electron emission at very low electron impact energy : experimental and monte-carlo results. Technical report, ONERA, 2013.

[185] L. Maggiorella, G. Barouch, C. Devaux, A. Pottier, E. Deutsch, J. Bourhis, E. Borghi, and L. Levy. Nanoscale radiotherapy with hafnium oxide nanoparticles. *Future oncology*, 8(9): 1167–1181, 2012.

[186] J. Marill, N. M. Anesary, P. Zhang, S. Vivet, E. Borghi, L. Levy, and A. Pottier. Hafnium oxide nanoparticles: toward an in vitro predictive biological effect? *Radiation Oncology*, 9 (1):150, 2014.

[187] M. P. Martinov and R. M. Thomson. Heterogeneous multiscale monte carlo simulations for gold nanoparticle radiosensitization. *Medical physics*, 44(2):644–653, 2017.

[188] D. Mateo, P. Morales, A. Ávalos, and A. I. Haza. Oxidative stress contributes to gold nanoparticle-induced cytotoxicity in human tumor cells. *Toxicology mechanisms and methods*, 24(3):161–172, 2014.

[189] R. Mayol and F. Salvat. Total and transport cross sections for elastic scattering of electrons by atoms. *Atomic Data and Nuclear Data Tables*, 65(1):55 – 154, 1997. ISSN 0092-640X.

doi: http://dx.doi.org/10.1006/adnd.1997.0734. URL `http://www.sciencedirect.com/science/article/pii/S0092640X97907348`.

[190] S. J. McMahon, M. H. Mendenhall, S. Jain, and F. Currell. Radiotherapy in the presence of contrast agents: a general figure of merit and its application to gold nanoparticles. *Physics in Medicine & Biology*, 53(20):5635, 2008.

[191] S. J. McMahon, W. Hyland, M. Muir, and et al. Biological consequences of nanoscale energy deposition near irradiated heavy atom nanoparticles. *Scientific report*, 1:18, 2011.

[192] S. J. McMahon, W. B. Hyland, E. Brun, K. T. Butterworth, J. A. Coulter, T. Douki, D. G. Hirst, S. Jain, A. P. Kavanagh, Z. Krpetic, et al. Energy dependence of gold nanoparticle radiosensitization in plasmid dna. *The Journal of Physical Chemistry C*, 115(41):20160–20167, 2011.

[193] S. J. McMahon, W. B. Hyland, M. F. Muir, J. A. Coulter, S. Jain, K. T. Butterworth, G. Schettino, G. R. Dickson, A. R. Hounsell, J. M. O Sullivan, et al. Nanodosimetric effects of gold nanoparticles in megavoltage radiation therapy. *Radiotherapy and Oncology*, 100(3): 412–416, 2011.

[194] S. J. McMahon, H. Paganetti, and K. M. Prise. Optimising element choice for nanoparticle radiosensitisers. *Nanoscale*, 8(1):581–589, 2016.

[195] A. McNamara, W. Kam, N. Scales, S. McMahon, J. Bennett, H. Byrne, J. Schuemann, H. Paganetti, R. Banati, and Z. Kuncic. Dose enhancement effects to the nucleus and mitochondria from gold nanoparticles in the cytosol. *Physics in Medicine & Biology*, 61 (16):5993, 2016.

[196] C. McQuade, A. Al Zaki, Y. Desai, M. Vido, T. Sakhuja, Z. Cheng, R. J. Hickey, D. Joh, S.-J. Park, G. Kao, et al. A multifunctional nanoplatform for imaging, radiotherapy, and the prediction of therapeutic response. *Small*, 11(7):834–843, 2015.

[197] H. N. McQuaid, M. F. Muir, L. E. Taggart, S. J. McMahon, J. A. Coulter, W. B. Hyland, S. Jain, K. T. Butterworth, G. Schettino, K. M. Prise, et al. Imaging and radiation effects of gold nanoparticles in tumour cells. *Scientific reports*, 6:19442, 2016.

[198] A. Mesbahi, F. Jamali, et al. Effect of photon beam energy, gold nanoparticle size and concentration on the dose enhancement in radiation therapy. *BioImpacts: BI*, 3(1):29, 2013.

[199] M. Michaud and L. Sanche. Absolute vibrational excitation cross sections for slow-electron (1–18 ev) scattering in solid h 2 o. *Physical Review A*, 36(10):4684, 1987.

[200] M. Michaud, A. Wen, and L. Sanche. Cross sections for low-energy (1–100 ev) electron elastic and inelastic scattering in amorphous ice. *Radiation research*, 159(1):3–22, 2003.

[201] Y. Mikami, A. Dhakshinamoorthy, M. Alvaro, and H. Garcia. Catalytic activity of unsupported gold nanoparticles. *Catalysis Science & Technology*, 3(1):58–69, 2013.

[202] C. Monini, E. Testa, and M. Beuve. NanOx predictions of cell survival probabilities for three cell lines. *Acta Phys. Pol. B*, 48(10):1653, 2017.

[203] C. Monini, M. Cunha, L. Chollier, E. Testa, and M. Beuve. The nanox description of local lethal events. Under submission, 2018.

[204] C. Monini, M. Cunha, E. Testa, and M. Beuve. Study of the influence of NanOx parameters. *Cancers*, 10(4):87, 2018.

[205] C. Monini, M. Cunha, E. Testa, and M. Beuve. The new theoretical framework NanOx to predict cell survival in the context of particle therapy: Formalism and implementation. UNDER REVISION, 2018.

[206] M. Montenegro, S. N. Nahar, A. K. Pradhan, K. Huang, and Y. Yu. Monte carlo simulations and atomic calculations for auger processes in biomedical nanotheranostics. *The Journal of Physical Chemistry A*, 113(45):12364–12369, 2009.

[207] Y. Muroya, J. Meesungnoen, J.-P. Jay-Gerin, A. Filali-Mouhim, T. Goulet, Y. Katsumura, and S. Mankhetkorn. Radiolysis of liquid water: an attempt to reconcile monte-carlo calculations with new experimental hydrated electron yield data at early times. *Canadian journal of chemistry*, 80(10):1367–1374, 2002.

[208] A. Nel, T. Xia, L. Mädler, and N. Li. Toxic potential of materials at the nanolevel. *science*, 311(5761):622–627, 2006.

[209] G. Neubert and S. Rogaschewski. Backscattering coefficient measurements of 15 to 60 kev electrons for solids at various angles of incidence. *physica status solidi (a)*, 59(1):35–41, 1980.

[210] G. L. Newton and J. R. Milligan. Fluorescence detection of hydroxyl radicals. *Radiation Physics and Chemistry*, 75(4):473–478, 2006.

[211] W. Ngwa, G. M. Makrigiorgos, and R. I. Berbeco. Applying gold nanoparticles as tumor-vascular disrupting agents during brachytherapy: estimation of endothelial dose enhancement. *Physics in Medicine & Biology*, 55(21):6533, 2010.

[212] W. Ngwa, G. M. Makrigiorgos, and R. I. Berbeco. Gold nanoparticle-aided brachytherapy with vascular dose painting: Estimation of dose enhancement to the tumor endothelial cell nucleus. *Medical physics*, 39(1):392–398, 2012.

[213] W. Ngwa, R. Kumar, S. Sridhar, H. Korideck, P. Zygmanski, R. A. Cormack, R. Berbeco, and G. M. Makrigiorgos. Targeted radiotherapy with gold nanoparticles: current status and future perspectives. *Nanomedicine*, 9(7):1063–1082, 2014.

[214] H. Ouerdane, B. Gervais, H. Zhou, M. Beuve, and J.-P. Renault. Radiolysis of water confined in porous silica: a simulation study of the physicochemical yields. *The Journal of Physical Chemistry C*, 114(29):12667–12674, 2010.

[215] B. Pastina, J. A. LaVerne, and S. Pimblott. Dependence of molecular hydrogen formation in water on scavengers of the precursor to the hydrated electron. *The Journal of Physical Chemistry A*, 103(29):5841–5846, 1999.

[216] N. Pauly and S. Tougaard. Determination of the effective surface region thickness and of begrenzungs effect. *Surface Science*, 603(13):2158 – 2162, 2009. ISSN 0039-6028. doi: http://dx.doi.org/10.1016/j.susc.2009.04.023. URL `http://www.sciencedirect.com/science/article/pii/S0039602809003094`.

[217] S. Penninckx, A.-C. Heuskin, C. Michiels, and S. Lucas. The role of thioredoxin reductase in gold nanoparticle radiosensitization effects. *Nanomedicine*, (00), 2018.

[218] S. Penninckx, A.-C. Heuskin, C. Michiels, and S. Lucas. Thioredoxin reductase activity predicts gold nanoparticle radiosensitization effect. *Nanomaterials*, 9(2):295, 2019.

[219] S. T. Perkins, M. H. Chen, D. E. Cullen, and J. Hubbell. *Tables and graphs of atomic subshell and relaxation data derived from the LLNL Evaluated Atomic Data Library (EADL), Z=1-100*. Lawrence Livermore Nat. Lab., Livermore, CA, 1991. URL `https://cds.cern.ch/record/236347`.

[220] H. L. Persson, T. Kurz, J. W. Eaton, and U. T. Brunk. Radiation-induced cell death: importance of lysosomal destabilization. *Biochemical Journal*, 389(3):877–884, 2005.

[221] J. Pierron, C. Inguimbert, M. Belhaj, T. Gineste, J. Puech, and M. Raine. Electron emission yield for low energy electrons: Monte carlo simulation and experimental comparison for al, ag, and si. *Journal of Applied Physics*, 121(21):215107, 2017.

[222] S. M. Pimblott and J. A. LaVerne. Molecular product formation in the electron radiolysis of water. *Radiation research*, 129(3):265–271, 1992.

[223] E. Polo, M. Collado, B. Pelaz, and P. del Pino. Advances toward more efficient targeted delivery of nanoparticles in vivo: understanding interactions between nanoparticles and cells. *ACS nano*, 11(3):2397–2402, 2017.

[224] K. M. Prise, G. Schettino, M. Folkard, and K. D. Held. New insights on cell death from radiation exposure. *The lancet oncology*, 6(7):520–528, 2005.

[225] W. N. Rahman, N. Bishara, T. Ackerly, C. F. He, P. Jackson, C. Wong, R. Davidson, and M. Geso. Enhancement of radiation effects by gold nanoparticles for superficial radiation therapy. *Nanomedicine: Nanotechnology, Biology and Medicine*, 5(2):136–142, 2009.

[226] W. N. Rahman, S. Corde, N. Yagi, S. A. A. Aziz, N. Annabell, and M. Geso. Optimal energy for cell radiosensitivity enhancement by gold nanoparticles using synchrotron-based monoenergetic photon beams. *International journal of nanomedicine*, 9:2459, 2014.

[227] G. S. R. Raju, L. Benton, E. Pavitra, and J. S. Yu. Multifunctional nanoparticles: Recent progress in cancer therapeutics. *Chemical Communications*, 51(68):13248–13259, 2015.

[228] E. Reichert. Die winkelverteilung im bereich 30 bis 155° von elastisch an golddampf gestreuten elektronen mit energien zwischen 150 und 1900 ev. *Zeitschrift für Physik*, 173 (4):392–401, 1963. ISSN 0044-3328. doi: 10.1007/BF01380701. URL `http://dx.doi.org/10.1007/BF01380701`.

[229] L. Reimer and H. Drescher. Secondary electron emission of 10-100 kev electrons from transparent films of al and au. *Journal of Physics D: Applied Physics*, 10(5):805, 1977. URL `http://stacks.iop.org/0022-3727/10/i=5/a=022`.

[230] J. A. Reisz, N. Bansal, J. Qian, W. Zhao, and C. M. Furdui. Effects of ionizing radiation on biological moleculesâ€"mechanisms of damage and emerging methods of detection. *Antioxidants & redox signaling*, 21(2):260–292, 2014.

[231] P. Retif, A. Reinhard, H. Paquot, V. Jouan-Hureaux, A. Chateau, L. Sancey, M. Barberi-

Heyob, S. Pinel, and T. Bastogne. Monte carlo simulations guided by imaging to predict the in vitro ranking of radiosensitizing nanoparticles. *International journal of nanomedicine*, 11:6169, 2016.

[232] P. Richardson, J. Eland, P. Fournier, and D. Cooper. Spectrum and decay of the doubly charged water ion. *The Journal of chemical physics*, 84(6):3189–3194, 1986.

[233] R. Ritchie. Interaction of charged particles with a degenerate fermi-dirac electron gas. *Phys.Rev.*, 114:644–654, 1959.

[234] R. H. Ritchie. Plasma losses by fast electrons in thin films. *Phys. Rev.*, 106:874–881, Jun 1957. doi: 10.1103/PhysRev.106.874. URL `https://link.aps.org/doi/10.1103/PhysRev.106.874`.

[235] W. Roa, X. Zhang, L. Guo, A. Shaw, X. Hu, Y. Xiong, S. Gulavita, S. Patel, X. Sun, J. Chen, et al. Gold nanoparticle sensitize radiotherapy of prostate cancer cells by regulation of the cell cycle. *Nanotechnology*, 20(37):375101, 2009.

[236] S. Rosa, C. Connolly, G. Schettino, K. T. Butterworth, and K. M. Prise. Biological mechanisms of gold nanoparticle radiosensitization. *Cancer nanotechnology*, 8(1):2, 2017.

[237] J. Roupie, O. Jbara, T. Tondu, M. Belhaj, and J. Puech. The study of electron emission from aluminum in the very low primary energy range using monte carlo simulations. *Journal of Physics D: Applied Physics*, 46(12):125306, 2013. URL `http://stacks.iop.org/0022-3727/46/i=12/a=125306`.

[238] D. Sakata, S. Incerti, M. Bordage, N. Lampe, S. Okada, D. Emfietzoglou, I. Kyriakou, K. Murakami, T. Sasaki, H. Tran, et al. An implementation of discrete electron transport models for gold in the geant4 simulation toolkit. *Journal of Applied Physics*, 120(24):244901, 2016.

[239] D. Sakata, I. Kyriakou, S. Okada, H. N. Tran, N. Lampe, S. Guatelli, M.-C. Bordage, V. Ivanchenko, K. Murakami, T. Sasaki, et al. Geant4-dna track-structure simulations for gold nanoparticles: The importance of electron discrete models in nanometer volumes. *Medical physics*, 45(5):2230–2242, 2018.

[240] F. Salvat, A. Jablonski, and C. J. Powell. Elsepa - dirac partial-wave calculation of elastic scattering of electrons and positrons by atoms, positive ions and molecules. *Computer Physics Communications*, 165:157–190, 2005.

[241] F. Salvat-Pujol and W. S. Werner. Surface excitations in electron spectroscopy. Part i: dielectric formalism and Monte Carlo algorithm. *Surface and Interface Analysis*, 45(5): 873–894, 2013.

[242] V. Sanna, N. Pala, and M. Sechi. Targeted therapy using nanotechnology: focus on cancer. *International journal of nanomedicine*, 9:467, 2014.

[243] D. Schardt, T. Elsässer, and D. Schulz-Ertner. Heavy-ion tumor therapy: Physical and radiobiological benefits. *Reviews of modern physics*, 82(1):383, 2010.

[244] M. Scholz, A. Kellerer, W. Kraft-Weyrather, and G. Kraft. Computation of cell survival in heavy ion beams for therapy. *Radiation and environmental biophysics*, 36(1):59–66, 1997.

[245] J. Schuemann, R. Berbeco, D. B. Chithrani, S. H. Cho, R. Kumar, S. J. McMahon, S. Sridhar, and S. Krishnan. Roadmap to clinical use of gold nanoparticles for radiation sensitization. *International Journal of Radiation Oncology* Biology* Physics*, 94(1):189–205, 2016.

[246] M. Schwake, B. Schröder, and P. Saftig. Lysosomal membrane proteins and their central role in physiology. *Traffic*, 14(7):739–748, 2013.

[247] M. Seah and G. Smith. Quantitative aes and xps: Determination of the electron spectrometer transmission function and the detector sensitivity energy dependencies for the production of true electron emission spectra in aes and xps. *Surface and interface analysis*, 15(12):751–766, 1990.

[248] J. Sempau, E. Acosta, J. Baro, J. FernÃ¡ndez-Varea, and F. Salvat. An algorithm for monte carlo simulation of coupled electron-photon transport. *Nuclear Instruments and Methods in Physics Research Section B: Beam Interactions with Materials and Atoms*, 132(3):377 – 390, 1997. ISSN 0168-583X. doi: http://dx.doi.org/10.1016/S0168-583X(97)00414-X. URL `http://www.sciencedirect.com/science/article/pii/S0168583X9700414X`.

[249] J. Sempau, J. FernÃ¡ndez-Varea, E. Acosta, and F. Salvat. Experimental benchmarks of the monte carlo code penelope. *Nuclear Instruments and Methods in Physics Research Section B: Beam Interactions with Materials and Atoms*, 207(2):107 – 123, 2003. ISSN 0168-583X. doi: http://dx.doi.org/10.1016/S0168-583X(03)00453-1. URL `http://www.sciencedirect.com/science/article/pii/S0168583X03004531`.

[250] R. Shimizu and D. Ze-Jun. Monte carlo modelling of electron-solid interactions. *Reports on Progress in Physics*, 55(4):487, 1992.

[251] C. Sicard-Roselli, E. Brun, M. Gilles, G. Baldacchino, C. Kelsey, H. McQuaid, C. Polin, N. Wardlow, and F. Currell. A new mechanism for hydroxyl radical production in irradiated nanoparticle solutions. *small*, 10(16):3338–3346, 2014.

[252] S. Simonet. *Radiosensitizing effect of AGuIXÂ® in Head and Neck Squamous Cell Carcinoma (HNSCC) : from cellular uptake to subcellular damage*. PhD thesis, 2018. URL `http://www.theses.fr/2018LYSE1042`. Thèse de doctorat dirigée par Ardail, Dominique et Rachidi, Walid Biologie cellulaire et oncologie Lyon 2018.

[253] N. Sinha, G. Cifter, E. Sajo, R. Kumar, S. Sridhar, P. L. Nguyen, R. A. Cormack, G. M. Makrigiorgos, and W. Ngwa. Brachytherapy application with in situ dose painting administered by gold nanoparticle eluters. *International Journal of Radiation Oncology Biology Physics*, 91(2):385–392, 2015.

[254] Z. Somosy. Radiation response of cell organelles. *Micron*, 31(2):165–181, 2000.

[255] K. Song, P. Xu, Y. Meng, F. Geng, J. Li, Z. Li, J. Xing, J. Chen, and B. Kong. Smart gold nanoparticles enhance killing effect on cancer cells. *International journal of oncology*, 42(2): 597–608, 2013.

[256] M. Sotiropoulos, N. T. Henthorn, J. W. Warmenhoven, R. I. Mackay, K. J. Kirkby, and M. J. Merchant. Modelling direct dna damage for gold nanoparticle enhanced proton therapy. *Nanoscale*, 9(46):18413–18422, 2017.

[257] V. Stagni, C. Cirotti, and D. Barilà. Ataxia-telangiectasia mutated kinase in the control of

oxidative stress, mitochondria, and autophagy in cancer: a maestro with a large orchestra. *Frontiers in oncology*, 8:73, 2018.

[258] S. T. Stern, P. P. Adiseshaiah, and R. M. Crist. Autophagy and lysosomal dysfunction as emerging mechanisms of nanomaterial toxicity. *Particle and fibre toxicology*, 9(1):20, 2012.

[259] A. Subiel, R. Ashmore, and G. Schettino. Standards and methodologies for characterizing radiobiological impact of high-z nanoparticles. *Theranostics*, 6(10):1651, 2016.

[260] W. Sung, S.-J. Ye, A. L. McNamara, S. J. McMahon, J. Hainfeld, J. Shin, H. M. Smilowitz, H. Paganetti, and J. Schuemann. Dependence of gold nanoparticle radiosensitization on cell geometry. *Nanoscale*, 9(18):5843–5853, 2017.

[261] L. Taggart, S. McMahon, K. Butterworth, F. Currell, G. Schettino, and K. Prise. Protein disulphide isomerase as a target for nanoparticle-mediated sensitisation of cancer cells to radiation. *Nanotechnology*, 27(21):215101, 2016.

[262] L. E. Taggart, S. J. McMahon, F. J. Currell, K. M. Prise, and K. T. Butterworth. The role of mitochondrial function in gold nanoparticle mediated radiosensitisation. *Cancer nanotechnology*, 5(1):5, 2014.

[263] Y. Takeichi and K. Goto. True auger electron spectra measured with a novel cylindrical mirror analyser (au, ag and cu). *Surface and interface analysis*, 25(1):17–24, 1997.

[264] F. Taupin. *Nanoparticules et rayonnement synchrotron pour le traitement des tumeurs cÃ©rÃ©brales*. PhD thesis, 2013. URL `http://www.theses.fr/2013GRENS021`. ThÃ¨se de doctorat dirigÃ©e par Elleaume, HÃ©lÃ¨ne et Ravanat, Jean-Luc Biotechnologie, Instrumentation, Signal et imagerie pour la mÂ´edecine, la biologie et lâ€™environnement Grenoble 2013.

[265] S. Tedesco, H. Doyle, J. Blasco, G. Redmond, and D. Sheehan. Oxidative stress and toxicity of gold nanoparticles in mytilus edulis. *Aquatic Toxicology*, 100(2):178–186, 2010.

[266] V. Tessaro, F. Poignant, M. Beuve, B. Gervais, and M. Galassi. Theoretical study of w-values for particle impact on water. *Nuclear Instruments and Methods in Physics*, 2018.

[267] S. Tougaard. Low energy inelastic electron scattering properties of noble and transition metals. *Solid State Communications*, 61(9):547 – 549, 1987. ISSN 0038-1098. doi: http://dx.doi.org/10.1016/0038-1098(87)90166-9. URL `http://www.sciencedirect.com/science/article/pii/0038109887901669`.

[268] J. Tournebize, A. Sapin-Minet, G. Bartosz, P. Leroy, and A. Boudier. Pitfalls of assays devoted to evaluation of oxidative stress induced by inorganic nanoparticles. *Talanta*, 116: 753–763, 2013.

[269] H. Tran, M. Karamitros, V. Ivanchenko, S. Guatelli, S. McKinnon, K. Murakami, T. Sasaki, S. Okada, M. Bordage, Z. Francis, et al. Geant4 monte carlo simulation of absorbed dose and radiolysis yields enhancement from a gold nanoparticle under mev proton irradiation. *Nuclear Instruments and Methods in Physics Research Section B: Beam Interactions with Materials and Atoms*, 373:126–139, 2016.

[270] S.-J. Tu, P.-Y. Yang, J.-H. Hong, and C.-J. Lo. Quantitative dosimetric assessment for

effect of gold nanoparticles as contrast media on radiotherapy planning. *Radiation Physics and Chemistry*, 88:14–20, 2013.

[271] K. Unfried, C. Albrecht, L.-O. Klotz, A. Von Mikecz, S. Grether-Beck, and R. P. Schins. Cellular responses to nanoparticles: target structures and mechanisms. *Nanotoxicology*, 1 (1):52–71, 2007.

[272] F. Van den Heuvel, J.-P. Locquet, and S. Nuyts. Beam energy considerations for gold nano-particle enhanced radiation treatment. *Physics in Medicine & Biology*, 55(16):4509, 2010.

[273] A. Z. Wang and J. E. Tepper. Nanotechnology in radiation oncology. *Journal of Clinical Oncology*, 32(26):2879, 2014.

[274] A. Z. Wang, R. Langer, and O. C. Farokhzad. Nanoparticle delivery of cancer drugs. *Annual review of medicine*, 63:185–198, 2012.

[275] C. Wang, X. Li, Y. Wang, Z. Liu, L. Fu, and L. Hu. Enhancement of radiation effect and increase of apoptosis in lung cancer cells by thio-glucose-bound gold nanoparticles at megavoltage radiation energies. *Journal of nanoparticle research*, 15(5):1642, 2013.

[276] P. Wang, X. Wang, L. Wang, X. Hou, W. Liu, and C. Chen. Interaction of gold nanoparticles with proteins and cells. *Science and technology of advanced materials*, 16(3):034610, 2015.

[277] C. Wehenkel. Mise au point d'une nouvelle méthode d'analyse quantitative des spectres de pertes d'énergie d'électrons rapides diffusés dans la direction du faisceau incident : application à l'étude des métaux nobles. *Journal de Physique*, 36(2):199–213, 1975. doi: 10.1051/jphys:01975003602019900. URL `https://hal.archives-ouvertes.fr/jpa-00208245`.

[278] W. S. Werner, M. Novák, F. Salvat-Pujol, J. Zemek, and P. Jiricek. Electron supersurface scattering on polycrystalline au. *Physical review letters*, 110(8):086110, 2013.

[279] A. Wicki, D. Witzigmann, V. Balasubramanian, and J. Huwyler. Nanomedicine in cancer therapy: challenges, opportunities, and clinical applications. *Journal of controlled release*, 200:138–157, 2015.

[280] T. Wolfe, D. Chatterjee, J. Lee, J. D. Grant, S. Bhattarai, R. Tailor, G. Goodrich, P. Nicolucci, and S. Krishnan. Targeted gold nanoparticles enhance sensitization of prostate tumors to megavoltage radiation therapy in vivo. *Nanomedicine: Nanotechnology, Biology and Medicine*, 11(5):1277–1283, 2015.

[281] B. G. Wouters and A. C. Begg. Irradiation-induced damage and the dna damage response. *Basic clinical radiobiology*, 4:11–26, 2009.

[282] F. Xiao, Y. Zheng, P. Cloutier, Y. He, D. Hunting, and L. Sanche. On the role of low-energy electrons in the radiosensitization of dna by gold nanoparticles. *Nanotechnology*, 22 (46):465101, 2011.

[283] W. Xie, W. Friedland, W. Li, C. Li, U. Oeh, R. Qiu, J. Li, and C. Hoeschen. Simulation on the molecular radiosensitization effect of gold nanoparticles in cells irradiated by x-rays. *Physics in Medicine & Biology*, 60(16):6195, 2015.

[284] S. Yamashita, G. Baldacchino, T. Maeyama, M. Taguchi, Y. Muroya, M. Lin, A. Kimura,

T. Murakami, and Y. Katsumura. Mechanism of radiation-induced reactions in aqueous solution of coumarin-3-carboxylic acid: Effects of concentration, gas and additive on fluorescent product yield. *Free radical research*, 46(7):861–871, 2012.

[285] C. Yang, M. Neshatian, M. van Prooijen, and D. B. Chithrani. Cancer nanotechnology: enhanced therapeutic response using peptide-modified gold nanoparticles. *Journal of nanoscience and nanotechnology*, 14(7):4813–4819, 2014.

[286] X. Yao, C. Huang, X. Chen, Y. Zheng, and L. Sanche. Chemical radiosensitivity of dna induced by gold nanoparticles. *Journal of biomedical nanotechnology*, 11(3):478–485, 2015.

[287] H. Yasui, R. Takeuchi, M. Nagane, S. Meike, Y. Nakamura, T. Yamamori, Y. Ikenaka, Y. Kon, H. Murotani, M. Oishi, et al. Radiosensitization of tumor cells through endoplasmic reticulum stress induced by pegylated nanogel containing gold nanoparticles. *Cancer letters*, 347(1):151–158, 2014.

[288] S. X. Zhang, J. Gao, T. A. Buchholz, Z. Wang, M. R. Salehpour, R. A. Drezek, and T.-K. Yu. Quantifying tumor-selective radiation dose enhancements using gold nanoparticles: a monte carlo simulation study. *Biomedical microdevices*, 11(4):925, 2009.

[289] X. Zhang, J. Z. Xing, J. Chen, L. Ko, J. Amanie, S. Gulavita, N. Pervez, D. Yee, R. Moore, and W. Roa. Enhanced radiation sensitivity in prostate cancer by gold-nanoparticles. *Clinical & Investigative Medicine*, 31(3):160–167, 2008.

[290] X.-D. Zhang, H.-Y. Wu, D. Wu, Y.-Y. Wang, J.-H. Chang, Z.-B. Zhai, A.-M. Meng, P.-X. Liu, L.-A. Zhang, and F.-Y. Fan. Toxicologic effects of gold nanoparticles in vivo by different administration routes. *International journal of nanomedicine*, 5:771, 2010.

[291] X.-D. Zhang, D. Wu, X. Shen, J. Chen, Y.-M. Sun, P.-X. Liu, and X.-J. Liang. Size-dependent radiosensitization of peg-coated gold nanoparticles for cancer radiation therapy. *Biomaterials*, 33(27):6408–6419, 2012.

[292] X.-D. Zhang, J. Chen, Z. Luo, D. Wu, X. Shen, S.-S. Song, Y.-M. Sun, P.-X. Liu, J. Zhao, S. Huo, et al. Enhanced tumor accumulation of sub-2 nm gold nanoclusters for cancer radiation therapy. *Advanced healthcare materials*, 3(1):133–141, 2014.

[293] Y. Zheng and L. Sanche. Gold nanoparticles enhance dna damage induced by anti-cancer drugs and radiation. *Radiation research*, 172(1):114–119, 2009.

[294] Y. Zheng, P. Cloutier, D. J. Hunting, and L. Sanche. Radiosensitization by gold nanoparticles: comparison of dna damage induced by low and high-energy electrons. *Journal of Biomedical Nanotechnology*, 4(4):469–473, 2008.

[295] Y. Zheng, D. J. Hunting, P. Ayotte, and L. Sanche. Radiosensitization of dna by gold nanoparticles irradiated with high-energy electrons. *Radiation research*, 169(1):19–27, 2008.

[296] C.-d. Zhu, Q. Zheng, L.-x. Wang, H.-F. Xu, J.-l. Tong, Q.-a. Zhang, Y. Wan, and J.-q. Wu. Synthesis of novel galactose functionalized gold nanoparticles and its radiosensitizing mechanism. *Journal of nanobiotechnology*, 13(1):67, 2015.

[297] P. Zygmanski, B. Liu, P. Tsiamas, F. Cifter, M. Petersheim, J. Hesser, and E. Sajo. Dependence of monte carlo microdosimetric computations on the simulation geometry of gold nanoparticles. *Physics in Medicine & Biology*, 58(22):7961, 2013.

Part VI.

Appendices

A. State of the art

A.1. List of *in vitro* experimental conditions and measurements

				Biodistribution					Biological endpoint					
Ref.	NP	Beam	Cell line	Concentration before incubation	Time of incubation	Intra-cellular concentration	Extra-cellular medium washed	Localisation	α	β	Dose for fixed survival	Survival for fixed dose	MID	Additional info
AuroVist^{TM} GNP														
225	AuroVist^{TM} 1.9 nm GNP	80 kVp 1 Gy/min	BAEC	2.5×10^5 nM of gold (0.05 mg/mL)	24h	Fully internalized		Cytoplasm, clustered			SF 0.9 **DER = 4.0**			Viability of ≈ 85 % Increase cell death
225	AuroVist^{TM} 1.9 nm GNP	80 kVp 1 Gy/min	BAEC	5×10^5 nM of gold (0.1 mg/mL)	24h	Fully internalized		Cytoplasm, clustered			SF 0.9 **DER = 20.0**			Viability of ≈ 76 %
225	AuroVist^{TM} 1.9 nm GNP	80 kVp 1 Gy/min	BAEC	10^6 nM of gold (0.2 mg/mL)	24h	Fully internalized		Cytoplasm, clustered			SF 0.9 **DER = 24.6**			Viability of ≈ 75 %
225	AuroVist^{TM} 1.9 nm GNP	150 kVp 1 Gy/min	BAEC	5×10^5 nM of gold (0.1 mg/mL)	24h	Fully internalized		Cytoplasm, clustered			SF 0.9 **DER = 1.4**			Viability of ≈ 76 %
225	AuroVist^{TM} 1.9 nm GNP	150 kVp 1 Gy/min	BAEC	10^6 nM of gold (0.2 mg/mL)	24h	Fully internalized		Cytoplasm, clustered			SF 0.9 **DER = 2.2**			Viability of ≈ 75 %
225	AuroVist^{TM} 1.9 nm GNP	Electron 6 MeV 1 Gy/min	BAEC	2.5×10^5 nM of gold (0.05 mg/mL)	24h	Fully internalized		Cytoplasm, clustered			SF 0.9 **DER = 2.7**			Viability of ≈ 85 %
225	AuroVist^{TM} 1.9 nm GNP	Electron 6 MeV 1 Gy/min	BAEC	5×10^5 nM of gold (0.1 mg/mL)	24h	Fully internalized		Cytoplasm, clustered			SF 0.9 **DER = 2.9**			Viability of ≈ 76 %
225	AuroVist^{TM} 1.9 nm GNP	Electron 6 MeV 1 Gy/min	BAEC	10^6 nM of gold (0.2 mg/mL)	24h	Fully internalized		Cytoplasm, clustered			SF 0.9 **DER = 4.0**			Viability of ≈ 75 %
225	AuroVist^{TM} 1.9 nm GNP	Electron 12 MeV 1 Gy/min	BAEC	5×10^5 nM of gold (0.1 mg/mL)	24h	Fully internalized		Cytoplasm, clustered			SF 0.9 **DER = 3.7**			Viability of ≈ 76 %
225	AuroVist^{TM} 1.9 nm GNP	Electron 12 MeV 1 Gy/min	BAEC	10^6 nM of gold (0.2 mg/mL)	24h	Fully internalized		Cytoplasm, clustered			SF 0.9 **DER = 4.1**			Viability of ≈ 75 %
39	AuroVist^{TM} 1.9 nm GNP	160 kVp 0.625 Gy/min	MDA-231-MB	2.4×10^3 0.1 mg/mL	No		No (removed after IR)					4 Gy (SF 0.5) **SER = 1.4**		Toxicity GNP only: 92 % survival
39	Control	160 kVp 0.625 Gy/min	MDA-231-MB									4 Gy (SF 0.70)		
39	AuroVist^{TM} 1.9 nm GNP	160 kVp 0.625 Gy/min	MDA-231-MB	2.4×10^3 0.1 mg/mL	30 mins		No (removed after IR)					4 Gy (SF 0.59) **SER = 1.1**		Toxicity GNP only: 92 % survival
39	Control	160 kVp 0.625 Gy/min	MDA-231-MB									4 Gy (SF 0.67)		
39	AuroVist^{TM} 1.9 nm GNP	160 kVp 0.625 Gy/min	MDA-231-MB	2.4×10^2 0.01 mg/mL	1h		No (removed after IR)		0.15 ± 0.05	0.03 ± 0.01	SF at 2 Gy (control) **DER = 1.67** *SF 0.1 (6.6 Gy)* ***DER = 1.11***		*(3.33)* ***Ratio = 1.17***	Toxicity GNP only: 91 % survival
39	AuroVist^{TM} 1.9 nm GNP	160 kVp 0.625 Gy/min	MDA-231-MB	2.4×10^3 0.1 mg/mL	1h		No (removed after IR)		0.27 ± 0.06	0.02 ± 0.01	SF at 2 Gy (control) **DER = 1.11** *SF 0.1 (5.9 Gy)* ***DER = 1.24***	4 Gy (SF 0.24) **SER = 2.3**	*(2.76)* ***Ratio = 1.42***	Toxicity GNP only: 82 % survival
39	Control	160 kVp 0.625 Gy/min	MDA-231-MB						0.09 ± 0.03	0.03 ± 0.01	*SF 0.1 (7.3 Gy)*	4 Gy (0.55)	*(3.90)*	
39	AuroVist^{TM} 1.9 nm GNP	160 kVp 0.625 Gy/min	MDA-231-MB	2.4×10^3 0.1 mg/mL	2h		No (removed after IR)					4 Gy (SF 0.30) **SER = 1.8**		Toxicity GNP only: 94 % survival
39	Control	160 kVp 0.625 Gy/min	MDA-231-MB									4 Gy (SF 0.53)		
39	AuroVist^{TM} 1.9 nm GNP	160 kVp 0.625 Gy/min	MDA-231-MB	2.4×10^3 0.1 mg/mL	4h		No (removed after IR)					4 Gy (SF 0.20) **SER = 2.75**		Toxicity GNP only: 74 % survival
39	Control	160 kVp 0.625 Gy/min	MDA-231-MB									4 Gy (SF 0.55)		
39	AuroVist^{TM} 1.9 nm GNP	160 kVp 0.625 Gy/min	MDA-231-MB	2.4×10^3 0.1 mg/mL	8h		No (removed after IR)					4 Gy (SF 0.18) **SER = 2.7**		Toxicity GNP only: 73 % survival
39	Control	160 kVp 0.625 Gy/min	MDA-231-MB									4 Gy (SF 0.48)		
39	AuroVist^{TM} 1.9 nm GNP	160 kVp 0.625 Gy/min	AGO-1552B	2.4×10^2 0.01 mg/mL	1h		No (removed after IR)		0.30 ± 0.06	0.05 ± 0.01	SF at 2 Gy (control) **DER = 1.16** *SF 0.1 (4.4 Gy)* ***DER = 1.14***		*(2.13)* ***Ratio = 1.16***	Toxicity GNP only: 75 % survival
39	AuroVist^{TM} 1.9 nm GNP	160 kVp 0.625 Gy/min	AGO-1552B	2.4×10^3 0.1 mg/mL	1h		No (removed after IR)		0.68 ± 0.19	< 0.04	SF at 2 Gy (control) **DER = 1.97** *SF 0.1 (2.9 Gy)* ***DER = 1.72***		*(1.29)* ***Ratio = 1.91***	Toxicity GNP only: 63 % survival
39	Control	160 kVp 0.625 Gy/min	AGO-1552B						0.25 ± 0.11	0.04 ± 0.02	*SF 0.1 (5 Gy)*		*(2.47)*	

Table A.1.: In vitro experimental results from literature. Unless stated otherwise, the beam particles are photons. Regarding biological endpoint, only cell survival and DNA damages are reported. Control data reported here represent the cell response in absence of GNP injection. DER = dose enhancement ratio, SER = survival enhancement ratio. *Note that in [134,25,26,68] the cell survival with GNP was renormalized to the cell survival with GNP at 0 Gy, to account for GNP toxicity. E_{av} stands for average energy and E_{eq} stands for equivalent energy.

				Biodistribution					Biological endpoint					
Reference	NP	Beam	Cell line	Concentration before incubation	Time of incubation	Intra-cellular concentration	Extra-cellular medium washed	Localisation	α	β	Dose for fixed survival	Survival for fixed dose	MID	Additional info
[39]	AuroVist^{TM} 1.9 nm GNP	160 kVp 0.625 Gy/min	Astro	2.4×10^2 0.01 mg/mL	1h		No (removed after IR)		0.40 ± 0.04	0.09 ± 0.02	SF at 2 Gy (control) **DER = 1.04** *SF 0.1 (3.3 Gy)* ***DER = 1.06***		*(1.59)* ***Ratio = 1.07***	Toxicity GNP only: 99.9 % survival
[39]	AuroVist^{TM} 1.9 nm GNP	160 kVp 0.625 Gy/min	Astro	2.4×10^3 0.1 mg/mL	1h		No (removed after IR)		0.23 ± 0.14	0.16 ± 0.03	SF at 2 Gy (control) **DER = 0.96** *SF 0.1 (3.1 Gy)* ***DER = 1.13***		*(1.65)* ***Ratio = 1.04***	Toxicity GNP only: 80 % survival
[39]	Control	160 kVp 0.625 Gy/min	Astro						0.37 ± 0.14	0.08 ± 0.03	*SF 0.1 (3.5 Gy)*		(1.71)	
[39]	AuroVist^{TM} 1.9 nm GNP	160 kVp 0.625 Gy/min	DU-145	2.4×10^2 0.01 mg/mL	1h		No (removed after IR)		0.05 ± 0.04	0.04 ± 0.01	SF at 2 Gy (control) **DER = 0.98** *SF 0.1 (7 Gy)* ***DER = 1.03***		*(3.87)* ***Ratio = 1.05***	Toxicity GNP only: 87 % survival
[39]	AuroVist^{TM} 1.9 nm GNP	160 kVp 0.625 Gy/min	DU-145	2.4×10^3 0.1 mg/mL	1h		No (removed after IR)		0.04 ± 0.05	0.04 ± 0.01	SF at 2 Gy (control) **DER = 0.81** *SF 0.1 (6.9 Gy)* ***DER = 1.01***		*(3.97)* ***Ratio = 1.03***	Toxicity GNP only: 82 % survival
[39]	Control	160 kVp 0.625 Gy/min	DU-145						0.03 ± 0.05	0.04 ± 0.01	*SF 0.1 (7.2 Gy)*		*(4.08)*	
[39]	AuroVist^{TM} 1.9 nm GNP	160 kVp 0.625 Gy/min	L132	2.4×10^2 0.01 mg/mL	1h		No (removed after IR)		0.11 ± 0.04	0.03 ± 0.01	SF at 2 Gy (control) **DER = 0.86** *SF 0.1 (3.69)* ***DER = 0.99***		*(3.69)* ***Ratio = 0.97***	Toxicity GNP only: 83 % survival
[39]	AuroVist^{TM} 1.9 nm GNP	160 kVp 0.625 Gy/min	L132	2.4×10^3 0.1 mg/mL	1h		No (removed after IR)		0.05 ± 0.03	0.04 ± 0.01	SF at 2 Gy (control) **DER = 0.87** *SF 0.1 (7 Gy)* ***DER = 1***		*(3.87)* ***Ratio = 0.93***	Toxicity GNP only: 71 % survival
[39]	Control	160 kVp 0.625 Gy/min	L132						0.12 ± 0.05	0.03 ± 0.01	*SF 0.1 (7 Gy)*		(3.60)	
[39]	AuroVist^{TM} 1.9 nm GNP	160 kVp 0.625 Gy/min	MCF-7	10 µg/mL	1h		No (removed after IR)		0.28 ± 0.01	0.07 ± 0.04	SF at 2 Gy (control) **DER = 1.41** *SF 0.1 (4 Gy)* ***1.02***		*(2.01)* ***Ratio = 0.94***	Toxicity GNP only: 79 % survival
[39]	AuroVist^{TM} 1.9 nm GNP	160 kVp 0.625 Gy/min	MCF-7	2.4×10^3 0.1 mg/mL	1h		No (removed after IR)		0.24 ± 0.05	0.08 ± 0.02	SF at 2 Gy (control) **DER = 1.09** *SF 0.1 (4 Gy)* ***DER = 1.02***		*(2.06)* ***Ratio = 0.92***	Toxicity GNP only: 83 % survival
[39]	Control	160 kVp 0.625 Gy/min	MCF-7						0.46 ± 0.13	0.02 ± 0.03	*SF 0.1 (4.1 Gy)*		*1.89*	
[39]	AuroVist^{TM} 1.9 nm GNP	160 kVp 0.625 Gy/min	PC-3	2.4×10^2 0.01 mg/mL	1h		No (removed after IR)		0.29 ± 0.08	0.03 ± 0.01	SF at 2 Gy (control) **DER = 1.07** *SF 0.1 (5.1 Gy)* ***DER = 1.02***		*(2.44)* ***Ratio = 1.15***	Toxicity GNP only: 97 % survival
[39]	AuroVist^{TM} 1.9 nm GNP	160 kVp 0.625 Gy/min	PC-3	2.4×10^3 0.1 mg/mL	1h		No (removed after IR)		0.21 ± 0.1	0.03 ± 0.02	SF at 2 Gy (control) **DER = 1.02** *SF 0.1 (5.9 Gy)* ***DER = 0.90***		*(2.89)* ***Ratio = 0.97***	Toxicity GNP only: 43 % survival
[39]	Control	160 kVp 0.625 Gy/min	PC-3						0.12 ± 0.06	0.06 ± 0.01	*SF 0.1 (5.3 Gy)*		*(2.80)*	
[39]	AuroVist^{TM} 1.9 nm GNP	160 kVp 0.625 Gy/min	T98G	2.4×10^2 0.01 mg/mL	1h		No (removed after IR)		0.14 ± 0.07	0.02 ± 0.01	SF at 2 Gy (control) **DER = 1.3** *SF 0.1 (7.8 Gy)* ***DER = 1.04***		*(3.86)* ***Ratio = 1.17***	Toxicity GNP only: 92 % survival
[39]	AuroVist^{TM} 1.9 nm GNP	160 kVp 0.625 Gy/min	T98G	2.4×10^3 0.1 mg/mL	1h		No (removed after IR)		0.06 ± 0.07	0.02 ± 0.01	SF at 2 Gy (control) **DER = 1.91** *SF 0.1 (9.3 Gy)* ***DER = 0.87***		*(4.97)* ***Ratio = 0.90***	Toxicity GNP only: 58 % survival
[39]	Control	160 kVp 0.625 Gy/min	T98G						0.04 ± 0.05	0.03 ± 0.01	*SF 0.1 (8.1 Gy)*		*(4.50)*	

Table A.2.: Same as Tab. A.1.

				Biodistribution					Biological endpoint					
Reference	NP	Beam	Cell line	Concentration before incubation	Time of incubation	Intra-cellular concentration	Extra-cellular medium washed	Localisation	α	β	Dose for fixed survival	Survival for fixed dose	MID	Additional info
[134]	AuroVist^{TM} 1.9 nm GNP	160 kVp 0.69 Gy/min	MDA-MB-231	$\approx 2 \times 10^2$ nM 0.008 mg/mL	24 h		No					4 Gy **SER* = 0.9**		
[134]	AuroVist^{TM} 1.9 nm GNP	160 kVp 0.69 Gy/min	MDA-MB-231	$\approx 1 \times 10^3$ nM 0.04 mg/mL	24 h		No					4 Gy **SER* = 1.1**		
[134]	AuroVist^{TM} 1.9 nm GNP	160 kVp 0.69 Gy/min	MDA-MB-231	$\approx 2 \times 10^3$ nM 0.08 mg/mL	24 h		No					4 Gy **SER* = 1.6**		
[134]	AuroVist^{TM} 1.9 nm GNP	160 kVp 0.69 Gy/min	MDA-MB-231	$\approx 6 \times 10^3$ nM 0.25 mg/mL	24 h		No					4 Gy **SER* = 1.6**		
[134]	AuroVist^{TM} 1.9 nm GNP	160 kVp 0.69 Gy/min	MDA-MB-231	$\approx 24 \times 10^3$ nM 1 mg/mL	24 h		No					4 Gy **SER* = 2.0**		
[134]	AuroVist^{TM} 1.9 nm GNP	160 kVp 0.69 Gy/min	MDA-MB-231	$\approx 12 \times 10^3$ nM 0.5 mg/mL	24 h	≈ 4 µg/mL 96 nM	No	Cytoplasmic lysosomes	0.091 ± 0.031	0.093 ± 0.011	*SF 0.1 (4.5 Gy)* ***DER = 1.42***	4 Gy (SF 0.15) **SER* = 1.8**	**Ratio = 1.41**	Toxicity GNP alone : survival 81.3 %
[134]	Control	160 kVp 0.69 Gy/min	MDA-MB-231						0.019 ± 0.025	0.052 ± 0.007	*SF 0.1 (6.4 Gy)*	4 Gy (SF 0.386)		
[134]	AuroVist^{TM} 1.9 nm GNP	160 kVp 0.69 Gy/min	DU145	12×10^3 nM 0.5 mg/mL	24 h	≈ 3 µg/mL 72 nM	No						**Ratio = 0.92**	Toxicity GNP alone : survival 83 %
[134]	AuroVist^{TM} 1.9 nm GNP	160 kVp 0.69 Gy/min	L132	12×10^3 nM 0.5 mg/mL	24 h	≈ 1.5 µg/mL 36 nM	No						**Ratio = 1.05**	Toxicity GNP alone : survival 95 %
[134]	AuroVist^{TM} 1.9 nm GNP	6 MV 3.55 Gy/min	MDA-MB-231	12×10^3 nM 0.5 mg/mL	24 h	≈ 4 µg/mL 96 nM	No	Cytoplasmic lysosomes	0.104 ± 0.040	0.098 ± 0.011	*SF 0.1 (4.3 Gy)* ***DER = 1.25***	4 Gy (SF 0.12)	**Ratio = 1.29**	Toxicity GNP alone : survival 81.3 %
[134]	Control	6 MV 3.55 Gy/min	MDA-MB-231						0.002 ± 0.022	0.079 ± 0.007	*SF 0.1 (5.4 Gy)*	4 Gy (SF 0.28)		
[134]	AuroVist^{TM} 1.9 nm GNP	6 MV 3.55 Gy/min	DU145	12×10^3 nM 0.5 mg/mL	24 h	≈ 3 µg/mL 72 nM	No						**Ratio = 1.13**	Toxicity GNP alone : survival 83 %
[134]	AuroVist^{TM} 1.9 nm GNP	6 MV 3.55 Gy/min	L132	12×10^3 nM 0.5 mg/mL	24 h	≈ 1.5 µg/mL 36 nM	No						**Ratio = 1.08**	Toxicity GNP alone : survival 95%
[134]	AuroVist^{TM} 1.9 nm GNP	15 MV 3.85 Gy/min	MDA-MB-231	12×10^3 nM 0.5 mg/mL	24 h	≈ 4 µg/mL 96 nM	No	Cytoplasmic lysosomes	0.061 ± 0.050	0.121 ± 0.018	*SF 0.1 (4.1 Gy)* ***DER = 1.34***	4 Gy (SF 0.16)	**Ratio = 1.16** *Calculated 1.31*	Toxicity GNP alone : survival 81.3 %
[134]	Control	15 MV 3.85 Gy/min	MDA-MB-231						0.083 ± 0.027	0.059 ± 0.008	*SF 0.1 (5.5 Gy)*	4 Gy (SF 0.27)		
[134]	AuroVist^{TM} 1.9 nm GNP	Electrons 16 MeV 4 Gy/min	MDA-MB-231	12×10^3 nM 0.5 mg/mL	24 h	≈ 4 µM 0.17 mg/mL	No	Cytoplasmic lysosomes	0.180 ± 0.036	0.015 ± 0.012		4 Gy (SF 0.18)	**Ratio = 1.35**	Toxicity GNP alone : survival 81.3 %
[134]	Control	Electrons 16 MeV 4 Gy/min	MDA-MB-231						-0.038 ± 0.027	0.079 ± 0.008		4 Gy (SF 0.34)		
[25+26]	AuroVist^{TM} 1.9 nm GNP	Synchrotron 50 keV (0.5 Gy/s)	F98	2.4×10^5 10 mg/mL	No		No	Mostly extracellular	0.29504	0.04471	SF 0.1 (4.59 Gy) **DER* = 1.92**		*(2.21)* ***Ratio = 1.99***	
[25+26]	AuroVist^{TM} 1.9 nm GNP	Synchrotron 50 keV (0.5 Gy/s)	F98	2.4×10^5 10 mg/mL	24 h		Yes	Only intracellular	0.25086	0.00958	SF 0.1 (7.19 Gy) **DER* 1.22**		*(3.27)* ***Ratio = 1.36***	Toxic: 80 % survival
[25+26]	Control	Synchrotron 50 keV (0.5 Gy/s)	F98						0.11395	0.01674	SF 0.1 (8.8 Gy)		*(4.44)*	
[25+26]	AuroVist^{TM} 15 nm GNP	Synchrotron 50 keV (0.5 Gy/s)	F98	2.4×10^5 10 mg/mL	No		No	Mostly extracellular	0.03974	0.06771	SF 0.1 (5.54 Gy) **DER* = 1.40**		*(3.13)* ***Ratio = 1.24***	Toxic: 96 % survival
[25+26]	AuroVist^{TM} 15 nm GNP	Synchrotron 50 keV (0.5 Gy/s)	F98	2.4×10^5 10 mg/mL	3h40		Yes	Only intracellular	0.1246	0.03272	SF 0.1 (6.69 Gy) **DER* = 1.16**		*(3.45)* ***Ratio = 1.13***	Toxic: 80 % survival
[25+26]	Control	Synchrotron 50 keV (0.5 Gy/s)	F98						0.13131	0.02118	SF 0.1 (7.77 Gy)		*(3.90)*	
[25+26]	AuroVist^{TM} 15 nm GNP	200 kVp (E_{rmav} = 70 keV)	F98	2.4×10^5 10 mg/mL	15 min		No	Mostly extracellular			SF 0.1 (4.37 Gy) **DER* = 1.58**			
[25+26]	Control	200 kVp (E_{rmav} = 70 keV)	F98								SF 0.1 (6.91 Gy)			
[135]	AuroVist^{TM} 1.9 nm GNP	160 kVp 0.69 Gy/min	MDA-MB-231	12×10^3 nM 0.5 mg/mL	24 h	7.0×10^7 GNP/cell 4.85 pg	No	Aggregated in lysosomes (diameter 200 - 300 nm)	0.126 ± 0.053	0.002 ± 0.005	*SF 0.1 (14.7 Gy)* ***DER = 1.22***	4 Gy (SF 0.61)	(8.12) **Ratio = 1.1**	Hypoxia condition (0.1 % O_2)
[135]	Control	160 kVp 0.69 Gy/min	MDA-MB-231						0.021 ± 0.018	0.006 ± 0.002	*SF 0.1 (17.9 Gy)*	4 Gy (SF 0.833)	(8.97)	Hypoxia condition (0.1 % O_2) No significant radiosensitization
[135]	AuroVist^{TM} 1.9 nm GNP	160 kVp 0.69 Gy/min	MDA-MB-231	12×10^3 nM 0.5 mg/mL	24 h	1.1×10^8 GNP/cell 7.62 pg	No	Aggregated in lysosomes (diameter 200 - 300 nm)	0.107 ± 0.036	0.098 ± 0.011	*SF 0.1 (4.3 Gy)* ***DER = 1.23***	4 Gy (SF 0.344)	(3.21) **Ratio = 1.39**	Hypoxia condition (1 % O_2)
[135]	Control	160 kVp 0.69 Gy/min	MDA-MB-231						0.003 ± 0.025	0.079 ± 0.007	*SF 0.1 (5.3 Gy)*	4 Gy (SF 0.638)	(4.48)	Hypoxia condition (1 % O_2)
[135]	AuroVist^{TM} 1.9 nm GNP	160 kVp 0.69 Gy/min	MDA-MB-231	12×10^3 nM 0.5 mg/mL	24 h	1.3×10^8 GNP/cell 9.01 pg	No	Aggregated in lysosomes (diameter 200 - 300 nm)	0.091 ± 0.031	0.093 ± 0.011	*SF 0.1 (4.5 Gy)* ***DER = 1.42***	4 Gy (SF 0.15)	(2.45) **Ratio = 1.41**	Normoxia condition (21 % O_2)
[135]		160 kVp 0.69 Gy/min	MDA-MB-231						0.019 ± 0.025	0.052 ± 0.007	*SF 0.1 (6.4 Gy)*	4 Gy (SF 0.386)	(3.46)	Hypoxia condition (21 % O_2)

Table A.3.: Same as Tab. A.1.

				Biodistribution					Biological endpoint					
Reference	NP	Beam	Cell line	Concentration before incubation	Time of incubation	Intra-cellular concentration	Extra-cellular medium washed	Localisation	α	β	Dose for fixed survival	Survival for fixed dose	MID	Additional info
[135]	AuroVist^{TM} 1.9 nm GNP	160 kVp 0.69 Gy/min	DU145	12×10^3 nM 0.5 mg/mL	24 h	4.7×10^7 GNP/cell 3.26 pg	No	Aggregated in lysosomes (diameter 200 - 300 nm)						Hypoxia condition (0.1 % O_2)
[135]	AuroVist^{TM} 1.9 nm GNP	160 kVp 0.69 Gy/min	DU145	12×10^3 nM 0.5 mg/mL	24 h	1.6×10^8 GNP/cell 11 pg	No	Aggregated in lysosomes (diameter 200 - 300 nm)						Normoxia condition (21 % O_2)
[135]	AuroVist^{TM} 1.9 nm GNP	160 kVp 0.69 Gy/min	L132	12×10^3 nM 0.5 mg/mL	24 h	5.5×10^7 GNP/cell 3.81 pg	No	Aggregated in lysosomes (diameter 200 - 300 nm)						Hypoxia condition (0.1 % O_2)
[135]	AuroVist^{TM} 1.9 nm GNP	160 kVp 0.69 Gy/min	L132	12×10^3 nM 0.5 mg/mL	24 h	1.0×10^8 GNP/cell 6.93 pg	No	Aggregated in lysosomes (diameter 200 - 300 nm)						Normoxia condition (21 % O_2)
[262] + [66]	AuroVist^{TM} 1.9 nm GNP	225 kVp	MDA-MB-231	12×10^3 nM 0.5 mg/mL	24h	1.3×10^8 GNP/cell 9.01 pg 6.9 mg/mL		Mostly aggregated in large lysosomes			SF at 2 Gy (control) **DER = 1.23 ± 0.14** SF at 4 Gy (control) **DER = 1.20 ± 0.06** SF at 8 Gy (control) **DER = 1.17 ± 0.02**			Reduced mitochondrial membrane polarization with GNP alone + mitochondrial oxidation + increase in G1 phase (GNP alone)
[262] + [66]	AuroVist^{TM} 1.9 nm GNP	225 kVp	DU145	12×10^3 nM 0.5 mg/mL	24h	1.6×10^8 GNP/cell 11.1 pg 8.4 mg/mL		Mostly aggregated in large lysosomes			SF at 2 Gy (control) **DER = 1.01 ± 0.2** SF at 4 Gy (control) **DER = 1.06 ± 0.1** SF at 8 Gy (control) **DER = 1.1 ± 0.04**			Reduced mitochondrial membrane polarization with GNP alone + mitochondrial oxidation + increase in G1 phase (GNP alone)
[262] + [66]	AuroVist^{TM} 1.9 nm GNP	225 kVp	T98G	12×10^3 nM 0.5 mg/mL	24h						SF at 2 Gy (control) **DER = 1.90 ± 0.22** SF at 4 Gy (control) **DER = 1.57 ± 0.08** SF at 8 Gy (control) **DER = 1.35 ± 0.03**			Reduced mitochondrial membrane polarization with GNP alone
[226]	AuroVist^{TM} 1.9 nm GNP	Synchrotron 30 keV 9 Gy/min	BAEC	4.7×10^3 nM 0.197 mg/mL					0.060 ± 0.006	-0.003 ± 0.001	SF 0.9 **DER = 1.74**			
[226]	Control	Synchrotron 30 keV 9 Gy/min	BAEC						0.038 ± 0.006	-0.002 ± 0.001				
[226]	AuroVist^{TM} 1.9 nm GNP	Synchrotron 40 keV 9 Gy/min	BAEC	4.7×10^3 nM 0.197 mg/mL					0.070 ± 0.012	-0.001 ± 0.001	SF 0.9 **DER = 3.47**			
[226]	Control	Synchrotron 40 keV 9 Gy/min	BAEC						0.013 ± 0.007	0.001 ± 0.0003				
[226]	AuroVist^{TM} 1.9 nm GNP	Synchrotron 50 keV 9 Gy/min	BAEC	4.7×10^3 nM 0.197 mg/mL					0.088 ± 0.011	-0.006 ± 0.001	SF 0.9 **DER = 2.77**			
[226]	Control	Synchrotron 50 keV 9 Gy/min	BAEC						0.034 ± 0.003	-0.001 ± 0.0004				
[226]	AuroVist^{TM} 1.9 nm GNP	Synchrotron 60 keV 9 Gy/min	BAEC	4.7×10^3 nM 0.197 mg/mL					0.069 ± 0.008	-0.001 ± 0.001	SF 0.9 **DER = 3.06**			
[226]	Control	Synchrotron 60 keV 9 Gy/min	BAEC						0.003 ± 0.004	0.004 ± 0.001				
[226]	AuroVist^{TM} 1.9 nm GNP	Synchrotron 70 keV 9 Gy/min	BAEC	4.7×10^3 nM 0.197 mg/mL					0.026 ± 0.004	0.003 ± 0.001	SF 0.9 **DER = 1.3**			
[226]	Control	Synchrotron 70 keV 9 Gy/min	BAEC						0.025 ± 0.004	0.001 ± 0.001				
[226]	AuroVist^{TM} 1.9 nm GNP	Synchrotron 81 keV 9 Gy/min	BAEC	4.7×10^3 nM 0.197 mg/mL					0.065 ± 0.011	-0.004 ± 0.002	SF 0.9 **DER = 2.58**			
[226]	Control	Synchrotron 81 keV 9 Gy/min	BAEC						0.022 ± 0.005	-0.0001 ± 0.001				
[226]	AuroVist^{TM} 1.9 nm GNP	Synchrotron 100 keV 9 Gy/min	BAEC	4.7×10^3 nM 0.197 mg/mL					0.031 ± 0.012	0.001 ± 0.002	SF 0.9 **DER = 1.35**			
[226]	Control	Synchrotron 100 keV 9 Gy/min	BAEC						0.016 ± 0.004	0.002 ± 0.001				
[261]	AuroVist^{TM} 1.9 nm GNP		MDA-MB-231	12×10^3 nM 0.5 mg/mL	24 h	1.6×10^8 GNP/cell 11.1 pg					SF at 2 Gy (control) **DER = 1.52 ± 0.03** SF at 4 Gy (control) **DER = 1.27 ± 0.01** SF at 8 Gy (control) **DER = 1.14 ± 0.01**			
[261]	AuroVist^{TM} 1.9 nm GNP		DU-145	12×10^3 nM 0.5 mg/mL	24 h	9.2×10^7 GNP/cell 6.32 pg					SF at 2 Gy (control) **DER = 1.82 ± 0.01** SF at 4 Gy (control) **DER = 1.59 ± 0.01** SF at 8 Gy (control) **SER = 1.36 ± 0.01**			
[261]	AuroVist^{TM} 1.9 nm GNP		T98G	12×10^3 nM 0.5 mg/mL	24 h	2.2×10^8 15.2 pg					SF at 2 Gy (control) **SER = 1.92 ± 0.05** SF at 4 Gy (control) **SER = 1.53 ± 0.01** SF at 8 Gy (control) **SER = 1.33 ± 0.01**			
Tiopronin-GNP														
[68]	Tiopronin-GNP 2.7 nm	225 kVp, 3.47 Gy/min or 2.97 Gy/min	MDA-MB-231	1 610 nM 0.2 mg/mL	1h	26.5 pg 1.33×10^8 GNP/cell	No	Cytoplasm, clusterized in vacuoles in perinuclear region	0.99 ± 0.08	1.35×10^{-16}	SF 0.1 **DER** = 1.31 ± 0.05		*(1.11)* ***Ratio = 1.31***	Oxic condition
[68]	Control	225 kVp, 3.47 Gy/min or 2.97 Gy/min	MDA-MB-231						0.66 ± 0.07	0.033 ± 0.012			*(1.46)*	Oxic condition
[68]	Tiopronin-GNP 2.7 nm	225 kVp, 3.47 Gy/min or 2.97 Gy/min	MDA-MB-231	1 610 nM 0.2 mg/mL	4h	53.3 pg 2.68×10^8 GNP/cell	No	Cytoplasm, clusterized in vacuoles in perinuclear region	1.03 ± 0.08	4.07×10^{-14}	SF 0.1 **DER** = 1.26 ± 0.01	4 Gy **SER* = 2.38**	*(0.97)* ***Ratio = 1.31***	Oxic condition No toxicity
[68]	Control	225 kVp, 3.47 Gy/min or 2.97 Gy/min	MDA-MB-231						0.73 ± 0.08	0.022 ± 0.014			*(1.28)*	Oxic condition
[68]	Tiopronin-GNP 2.7 nm	225 kVp, 3.47 Gy/min or 2.97 Gy/min	MDA-MB-231	1 610 nM 0.2 mg/mL	8h	68.1 pg 3.42×10^8 GNP/cell	No	Cytoplasm, clusterized in vacuoles in perinuclear region	0.90 ± 0.12	0.023 ± 0.022	SF 0.1 **DER** = 1.44 ± 0.02		*(1.06)* ***Ratio = 1.50***	Oxic condition Toxic: 80 % survival
[68]	Control	225 kVp, 3.47 Gy/min or 2.97 Gy/min	MDA-MB-231						0.50 ± 0.10	0.047 ± 0.018			*(1.59)*	Oxic condition

Table A.4.: Same as Tab. A.1.

				Biodistribution					Biological endpoint					
Reference	NP	Beam	Cell line	Concentration before incubation	Time of incubation	Intra-cellular concentration	Extra-cellular medium washed	Localisation	α	β	Dose for fixed survival	Survival for fixed dose	MID	Additional info
[68]	Tiopronin-GNP 2.7 nm	225 kVp, 3.47 Gy/min or 2.97 Gy/min	MDA-MB-231	1 610 nM 0.2 mg/mL	16h	53.1 pg 2.67×10^8 GNP/cell	No	Cytoplasm, clusterized in vacuoles in perinuclear region	0.69 ± 0.07	0.068 ± 0.013	SF 0.1 **DER** $= 1.33 \pm 0.08$		*(1.20)* ***Ratio = 1.34***	Oxic condition
[68]	Control	225 kVp, 3.47 Gy/min or 2.97 Gy/min	MDA-MB-231						0.47 ± 0.06	0.056 ± 0.010			*(1.61)*	Oxic condition
[68]	Tiopronin-GNP 2.7 nm	225 kVp, 3.47 Gy/min or 2.97 Gy/min	MDA-MB-231	1 610 nM 0.2 mg/mL	24h	44.3 pg 2.23×10^8 GNP/cell	No	Cytoplasm, clusterized in vacuoles in perinuclear region	0.58 ± 0.06	0.082 ± 0.010	SF 0.1 **DER** $= 1.31 \pm 0.06$		*(1.31)* ***Ratio = 1.41***	Oxic condition Toxic: 40 % survival
[68]	Control	225 kVp, 3.47 Gy/min or 2.97 Gy/min	MDA-MB-231						0.33 ± 0.09	0.073 ± 0.017			*(1.85)*	Oxic condition
[68]	Tiopronin-GNP 2.7 nm	225 kVp, 3.47 Gy/min or 2.97 Gy/min	MDA-MB-231	1 610 nM 0.2 mg/mL	48h	38.15 pg 1.92×10^8 GNP/cell	No	Cytoplasm, clusterized in vacuoles in perinuclear region						Oxic condition
[68]	Tiopronin-GNP 2.7 nm	225 kVp, 3.47 Gy/min or 2.97 Gy/min	MDA-MB-231	3 210 nM 0.4 mg/mL	1h	53.6 pg 2.69×10^8 GNP/cell	No	Cytoplasm, clusterized in vacuoles in perinuclear region						Oxic condition
[68]	Tiopronin-GNP 2.7 nm	225 kVp, 3.47 Gy/min or 2.97 Gy/min	MDA-MB-231	3 210 nM 0.4 mg/mL	4h	92.7 pg 4.66×10^8 GNP/cell	No	Cytoplasm, clusterized in vacuoles in perinuclear region	1.02 ± 0.17	1.57×10^{-16}	SF 0.1 **DER** $= 1.41 \pm 0.08$	4 Gy **SER* = 4.34**	*(0.98)* ***Ratio = 1.41***	Oxic condition
[68]	Tiopronin-GNP 2.7 nm	225 kVp, 3.47 Gy/min or 2.97 Gy/min	MDA-MB-231	3 210 nM 0.4 mg/mL	4h	92.7 pg 4.66×10^8 GNP/cell	Yes	Cytoplasm, clusterized in vacuoles in perinuclear region	1.00 ± 0.13	1.50×10^{-16}	SF 0.1 **DER** $= 1.39 \pm 0.07$		*(1.00)* ***Ratio = 1.38***	Oxic condition
[68]	Tiopronin-GNP 2.7 nm	225 kVp, 3.47 Gy/min or 2.97 Gy/min	MDA-MB-231	3 210 nM 0.4 mg/mL	0h (no incubation)	–	No	Cytoplasm, clusterized in vacuoles in perinuclear region	0.74 ± 0.04	0.019 ± 0.007	SF 0.1 **DER** $= 1.09 \pm 0.01$		*(1.27)* ***Ratio = 1.09***	Oxic condition
[68]	Control	225 kVp, 3.47 Gy/min or 2.97 Gy/min	MDA-MB-231						0.69 ± 0.02	0.012 ± 0.004			*(1.39)*	Oxic condition
[68]	Tiopronin-GNP 2.7 nm	225 kVp, 3.47 Gy/min or 2.97 Gy/min	MDA-MB-231	3 210 nM 0.4 mg/mL	8h	114.2 pg 5.74×10^8 GNP/cell	No	Cytoplasm, clusterized in vacuoles in perinuclear region						Oxic condition Toxic: 60 % survival
[68]	Tiopronin-GNP 2.7 nm	225 kVp, 3.47 Gy/min or 2.97 Gy/min	MDA-MB-231	3 210 nM 0.4 mg/mL	16h	98.3 pg 4.94×10^8 GNP/cell	No	Cytoplasm, clusterized in vacuoles in perinuclear region						Oxic condition
[68]	Tiopronin-GNP 2.7 nm	225 kVp, 3.47 Gy/min or 2.97 Gy/min	MDA-MB-231	3 210 nM 0.4 mg/mL	24h	85.8 pg 4.31×10^8 GNP/cell	No	Cytoplasm, clusterized in vacuoles in perinuclear region						Oxic condition Toxic: < 20 % survival
[68]	Tiopronin-GNP 2.7 nm	225 kVp, 3.47 Gy/min or 2.97 Gy/min	MDA-MB-231	3 210 nM 0.4 mg/mL	48h	74.5 pg 3.75×10^8 GNP/cell	No	Cytoplasm, clusterized in vacuoles in perinuclear region						Oxic condition
[68]	Tiopronin-GNP 2.7 nm	225 kVp, 3.47 Gy/min or 2.97 Gy/min	MDA-MB-231	321 nM 0.04 mg/mL	4h	8.6 pg 4.32×10^7 GNP/cell	No	Cytoplasm, clusterized in vacuoles in perinuclear region				4 Gy **SER* = 1.39**		Oxic condition
[68]	Tiopronin-GNP 2.7 nm	225 kVp, 3.47 Gy/min or 2.97 Gy/min	MDA-MB-231	321 nM 0.04 mg/mL	4h	3.37 pg 1.69×10^7 GNP/cell	No	Cytoplasm, clusterized in vacuoles in perinuclear region						Acute hypoxia
[68]	Tiopronin-GNP 2.7 nm	225 kVp, 3.47 Gy/min or 2.97 Gy/min	MDA-MB-231	321 nM 0.04 mg/mL	4h	3.37 pg 1.69×10^7 GNP/cell	No	Cytoplasm, clusterized in vacuoles in perinuclear region						Chronic hypoxia
[68]	GNP 2.7 nm	225 kVp, 3.47 Gy/min or 2.97 Gy/min	MDA-MB-231	642 nM 0.07 mg/mL	4h	19 pg 9.55×10^7 GNP/cell	No	Cytoplasm, clusterized in vacuoles in perinuclear region				4 Gy **SER* = 1.72**		Oxic condition
[68]	Tiopronin-GNP 2.7 nm	225 kVp, 3.47 Gy/min or 2.97 Gy/min	MDA-MB-231	642 nM 0.07 mg/mL	4h	7.04 pg 3.54×10^7 GNP/cell	No	Cytoplasm, clusterized in vacuoles in perinuclear region						Acute hypoxia
[68]	Tiopronin-GNP 2.7 nm	225 kVp, 3.47 Gy/min or 2.97 Gy/min	MDA-MB-231	642 nM 0.07 mg/mL	4h	10.1 pg 5.08×10^7 GNP/cell	No	Cytoplasm, clusterized in vacuoles in perinuclear region						Chronic hypoxia
[68]	Tiopronin-GNP 2.7 nm	225 kVp, 3.47 Gy/min or 2.97 Gy/min	MDA-MB-231	1 610 nM 0.2 mg/mL	4h	53.6 pg 2.69×10^8 GNP/cell	No	Cytoplasm, clusterized in vacuoles in perinuclear region				4 Gy **SER* = 2.38**		Oxic condition
[68]	Tiopronin-GNP 2.7 nm	225 kVp, 3.47 Gy/min or 2.97 Gy/min	MDA-MB-231	1 610 nM 0.2 mg/mL	4h	23.6 pg 1.19×10^8 GNP/cell	No	Cytoplasm, clusterized in vacuoles in perinuclear region						Acute hypoxia
[68]	Tiopronin-GNP 2.7 nm	225 kVp, 3.47 Gy/min or 2.97 Gy/min	MDA-MB-231	1 610 nM 0.2 mg/mL	4h	21.1 pg 1.06×10^8 GNP/cell	No	Cytoplasm, clusterized in vacuoles in perinuclear region						Chronic hypoxia
[68]	Tiopronin-GNP 2.7 nm	225 kVp, 3.47 Gy/min or 2.97 Gy/min	MDA-MB-231	3 210 nM 0.4 mg/mL	4h	92.4 pg 4.65×10^8 GNP/cell	No	Cytoplasm, clusterized in vacuoles in perinuclear region				4 Gy **SER* = 4.35**		Oxic condition

Table A.5.: Same as Tab. A.1.

				Biodistribution					Biological endpoint					
Reference	NP	Beam	Cell line	Concentration before incubation	Time of incubation	Intra-cellular concentration	Extra-cellular medium washed	Localisation	α	β	Dose for fixed survival	Survival for fixed dose	MID	Additional info
[68]	Tiopronin-GNP 2.7 nm	225 kVp, 3.47 Gy/min or 2.97 Gy/min	MDA-MB-231	3 210 nM 0.4 mg/mL	4h	29.4 pg 1.48×10^8 GNP/cell	No	Cytoplasm, clusterized in vacuoles in perinuclear region						Acute hypoxia
[68]	Tiopronin-GNP 2.7 nm	225 kVp, 3.47 Gy/min or 2.97 Gy/min	MDA-MB-231	3 210 nM 0.4 mg/mL	4h	28.2 pg 1.42×10^8 GNP/cell	No	Cytoplasm, clusterized in vacuoles in perinuclear region						Chronic hypoxia
[68]	Tiopronin-GNP 2.7 nm	225 kVp, 3.47 Gy/min or 2.97 Gy/min	MDA-MB-231	4820 nM 0.6 mg/mL	4h	99.5 pg 5.00×10^8 GNP/cell	No	Cytoplasm, clusterized in vacuoles in perinuclear region				4 Gy **SER* = 3.45**		Oxic condition
[68]	Tiopronin-GNP 2.7 nm	225 kVp, 3.47 Gy/min or 2.97 Gy/min	MDA-MB-231	4820 nM 0.6 mg/mL	4h	38.3 pg 1.93×10^8 GNP/cell	No	Cytoplasm, clusterized in vacuoles in perinuclear region						Acute hypoxia
[68]	Tiopronin-GNP 2.7 nm	225 kVp, 3.47 Gy/min or 2.97 Gy/min	MDA-MB-231	4820 nM 0.6 mg/mL	4h	34.6 pg 1.74×10^8 GNP/cell	No	Cytoplasm, clusterized in vacuoles in perinuclear region						Chronic hypoxia
[68]	Tiopronin-GNP 2.7 nm	225 kVp, 3.47 Gy/min or 2.97 Gy/min	MDA-MB-231	6420 nM 0.8 mg/mL	4h	100.1 pg 5.03×10^8 GNP/cell	No	Cytoplasm, clusterized in vacuoles in perinuclear region				4 Gy **SER* = 3.33**		Oxic condition
[68]	Tiopronin-GNP 2.7 nm	225 kVp, 3.47 Gy/min or 2.97 Gy/min	MDA-MB-231	6420 nM 0.8 mg/mL	4h	38.6 pg 1.94×10^8 GNP/cell	No	Cytoplasm, clusterized in vacuoles in perinuclear region						Acute hypoxia
[68]	Tiopronin-GNP 2.7 nm	225 kVp, 3.47 Gy/min or 2.97 Gy/min	MDA-MB-231	6420 nM 0.8 mg/mL	4h	40.4 pg 2.03×10^8 GNP/cell	No	Cytoplasm, clusterized in vacuoles in perinuclear region						Chronic hypoxia
Citric-acid stabilized GNP														
[55]	Citric-acid stabilized GNP 14 nm	220 kVp 2.3 Gy/min	HeLa	0.01 nM 2×10^{-4} mg/mL	24h + 3h	$\approx$ 1500 NP/cell 0.042 pg	No	Small vesicles (300-500 nm) close to nucleus			SF 0.1 **DER = 1.2**			Uptake reach plateau at 10h incubation
[55]	Citric-acid stabilized GNP 50 nm	220 kVp 2.3 Gy/min	HeLa	0.01 nM 9×10^{-3} mg/mL	24h + 3h	$\approx$ 6000 NP/cell 7.58 pg	No	Small vesicles (300-500 nm) close to nucleus	0.352 ± 0.005	0.041 ± 0.002	SF 0.1 **DER = 1.4**		*(2.04)* ***Ratio = 1.48***	Uptake reach plateau at 10h incubation
[55]	Citric-acid stabilized GNP 74 nm	220 kVp 2.3 Gy/min	HeLa	0.01 nM 3×10^{-2} mg/mL	24h + 3h	$\approx$ 3000 NP/cell 12.3 pg	No	Small vesicles (300-500 nm) close to nucleus			SF 0.1 **DER = 1.25**			Uptake reach plateau at 10h incubation
[55]	Control	220 kVp 2.3 Gy/min	HeLa						0.150 ± 0.004	0.041 ± 0.001			*(3.01)*	
[55]	Citric-acid stabilized GNP 50 nm	105 kVp 4.7 Gy/min	HeLa	0.01 nM 9×10^{-3} mg/mL	24h + 3h	$\approx$ 6000 NP/cell 7.58 pg	No	Small vesicles (300-500 nm) close to nucleus	0.528 ± 0.007	0.054 ± 0.003	SF 0.1 ($\approx$ 3.3 Gy) **DER = 1.66**		*(1.50)* ***Ratio = 1.68***	
[55]	Control	105 kVp 4.7 Gy/min	HeLa						0.237 ± 0.005	0.041 ± 0.002	SF 0.1 ($\approx$ 5.2 Gy)		*(2.51)*	
[55]	Citric-acid stabilized GNP 50 nm	137Cs 88 cGy/min	HeLa	0.01 nM 9×10^{-3} mg/mL	24h + 3h	$\approx$ 6000 NP/cell 7.58 pg	No	Small vesicles (300-500 nm) close to nucleus	0.259 ± 0.011	0.030 ± 0.003	SF 0.1 ($\approx$ 5.3 Gy) **DER = 1.18**		*(2.60)* ***Ratio = 1.26***	
[55]	Control	137Cs 88 cGy/min	HeLa						0.119 ± 0.013	0.040 ± 0.003	SF 0.1 ($\approx$ 6.2 Gy)		*(3.26)*	
[55]	Citric-acid stabilized GNP 50 nm	6 MV 600 MU/min	HeLa	0.01 nM 9×10^{-3} mg/mL	24h + 3h	$\approx$ 6000 NP/cell 7.58 pg	No	Small vesicles (300-500 nm) close to nucleus	0.191 ± 0.002	0.031 ± 0.001	SF 0.1 ($\approx$ 7 Gy) **DER = 1.17**		*(2.99)* ***Ratio = 1.25***	
[55]	Control	6 MV 600 MU/min	HeLa						0.110 ± 0.008	0.029 ± 0.002	SF 0.1 ($\approx$ 6 Gy)		*(3.74)*	
[182]	Citrate-capped GNP (14.8 ± 1.6) nm	50 kVp 0.57 Gy/min	HeLa	0.08 nM 1.5×10^{-3} mg/mL	24h	$\approx$ 0.14 pg 4×10^3 GNP/cell	Yes	In cytoplasm, gathered in few lysosomes			SF 0.5 (2.52 Gy) **DER = 1.14**			
[182]	Citrate-capped GNP (14.8 ± 1.6) nm	50 kVp 0.57 Gy/min	HeLa	0.4 nM 7.5×10^{-3} mg/mL	24h	$\approx$ 0.72 pg 22×10^3 GNP/cell	Yes	In cytoplasm, gathered in few lysosomes			SF 0.5 (1.00 Gy) **DER = 2.88**			
[182]	Citrate-capped GNP (14.8 ± 1.6) nm	50 kVp 0.57 Gy/min	HeLa	0.8 nM 15×10^{-3} mg/mL	24h	$\approx$ 1.48 pg 45×10^3 GNP/cell	Yes	In cytoplasm, gathered in few lysosomes			SF 0.5 (1.55 Gy) **DER = 1.86**			
[182]	Control	50 kVp 0.57 Gy/min	HeLa								SF 0.5 (2.88 Gy)			
[182]	Citrate-capped GNP (14.8 ± 1.6) nm	Carbon ions 70 keV/µm, 0.6 Gy/min	HeLa	0.08 nM 1.5×10^{-3} mg/mL	24h	$\approx$ 0.14 pg 4×10^3 GNP/cell	Yes	In cytoplasm, gathered in few lysosomes			SF 0.5 (0.44 Gy) **DER = 1.27**			
[182]	Citrate-capped GNP (14.8 ± 1.6) nm	Carbon ions 70 keV/µm, 0.6 Gy/min	HeLa	0.4 nM 7.5×10^{-3} mg/mL	24h	$\approx$ 0.72 pg 22×10^3 GNP/cell	Yes	In cytoplasm, gathered in few lysosomes			SF 0.5 (0.39 Gy) **DER = 1.44**			
[182]	Citrate-capped GNP (14.8 ± 1.6) nm	Carbon ions 70 keV/µm, 0.6 Gy/min	HeLa	0.8 nM 15×10^{-3} mg/mL	24h	$\approx$ 1.48 pg 45×10^3 GNP/cell	Yes	In cytoplasm, gathered in few lysosomes			SF 0.5 (0.42 Gy) **DER = 1.33**			
[182]	Control	Carbon ions 70 keV/µm, 0.6 Gy/min	HeLa								SF 0.5 (0.56 Gy)			

Table A.6.: Same as Tab. A.1.

				Biodistribution					Biological endpoint					
Reference	NP	Beam	Cell line	Concentration before incubation	Time of incubation	Intra-cellular concentration	Extra-cellular medium washed	Localisation	α	β	Dose for fixed survival	Survival for fixed dose	MID	Additional info
Thioglucose capped GNP														
159	Thioglucose capped Glu-GNP 7.2 nm	200 kVp 1.19 Gy/min	Paca-2	15 nM 0.03 mg/mL	4h		Yes	Lysosomes				10 Gy (SF 0.531) **SER = 1.64**		No toxicity
159	Thioglucose capped Glu-GNP 7.2 nm	200 kVp 1.19 Gy/min	Paca-2	7.5 nM 0.02 mg/mL	4h		Yes	Lysosomes				10 Gy (SF 0.532) **SER = 1.64**		No toxicity
159	Thioglucose capped Glu-GNP 7.2 nm	200 kVp 1.19 Gy/min	Paca-2	3.75 nM 0.003 mg/mL	4h		Yes	Lysosomes				10 Gy (SF 0.585) **SER = 1.47**		No toxicity
159	Thioglucose capped Glu-GNP 7.2 nm	200 kVp 1.19 Gy/min	Paca-2	1.8 nM 0.004 mg/mL	4h		Yes	Lysosomes				10 Gy (SF 0.676) **SER = 1.27**		No toxicity
159	TGS (neutral) GNP 7.2 nm	200 kVp 1.19 Gy/min	Paca-2	7.5 nM 0.02 mg/mL	4h	Less than Glu-GNP	Yes	Lysosomes				10 Gy (SF 0.60) **SER = 1.44**		No toxicity
159	Control	200 kVp 1.19 Gy/min	Paca-2									10 Gy (SF 0.868)		
289	Glucose-GNP 7.2 nm	200 kVp	DU-145	15 nM 0.03 mg/mL	2h	$(6.73 \pm 0.67) \times 10^4$ GNP/cell 0.254 pg	Yes	Cytoplasm						
289	TGS (neutral) GNP 7.2 nm	200 kVp	DU-145	15 nM 0.03 mg/mL	2h	$(2.06 \pm 0.24) \times 10^4$ GNP/cell 0.08 pg	Yes	Cytoplasm						
235	Glu-GNP 10.8 nm	137Cs (662 keV) 1.32 Gy/min	DU145	15 nM 0.1 mg/mL	2h	$(6.3 \pm 0.67) \times 10^4$ 0.80 pg	Yes	Mostly in cytoplasm				2 Gy (SF 0.36) **SER = 2.8**		Cellular uptake peak at 4h , G2/M phase 29.9 %, change when combining IR + GNP
235	Control	137Cs (662 keV) 1.32 Gy/min	DU145									2 Gy (SF 1)		G2/M phase 18.4 %
104	Glu-GNP 14.37 ± 2.49 nm	90 kVp	SK-OV-3	5 nM 0.09 mg/mL	24h	1.6×10^5 GNP/cell 4.8 pg	Yes					5 Gy (SF 0.45) **SER = 1.42**		Use of heat-inactivated fetal bovine serum
104	Control	90 kVp	SK-OV-3									5 Gy (SF 0.64)		
104	Glu-GNP 14.37 ± 2.49 nm	6 MV	SK-OV-3	1.25 nM 0.02 mg/mL	24h		Yes					5 Gy (SF 0.61) **SER = 1.05**		Use of heat-inactivated fetal bovine serum
104	Glu-GNP 14.37 ± 2.49 nm	6 MV	SK-OV-3	2.5 nM 0.05 mg/mL	24h		Yes					5 Gy (SF 0.60) **SER = 1.07**		Use of heat-inactivated fetal bovine serum
104	Glu-GNP 14.37 ± 2.49 nm	6 MV	SK-OV-3	5 nM 0.09 mg/mL	24h	1.6×10^5 GNP/cell 4.8 pg	Yes					5 Gy (SF 0.58) **SER = 1.38**		Use of heat-inactivated fetal bovine serum
104	Control	6 MV	SK-OV-3									5 Gy (SF 0.80)		
148	Glucose-capped GNP 5-9 nm	60Co 1.1 + 1.3 MeV	HeLa	5.5×10^3 nM 7.0 mg/mL	6 h		Yes	Agglomerated in 50-60 nm	0.321 ± 0.017	0.008 ± 0.003	SF 0.1 (6.2 Gy) DER = 1.52		*(2.77)* ***Ratio = 1.56***	Heat-inactivated media
148	Control	60Co 1.1 + 1.3 MeV	HeLa						0.181 ± 0.025	0.007 ± 0.003	SF 0.1 (9.4 Gy)		*(4.30)*	
148	Glucose-capped GNP 5-9 nm	62 MeV $^{6+}$C	HeLa	5.5×10^3 nM 7.0 mg/mL	6 h		Yes	Agglomerated in 50-60 nm	1.011 ± 0.017	0.024 ± 0.025	SF 0.1 (2.2 Gy) DER = 1.39		*(0.95)* ***Ratio = 1.50***	Heat-inactivated media
148	Control	62 MeV $^{6+}$C	HeLa						0.691 ± 0.021	0.005 ± 0.006	SF 0.1 (3.1 Gy)		*(1.42)*	
275	Glu-GNP 13 nm	6 MV	A549	5 nM 0.07 mg/mL	24 h	$(11.8 \pm 0.78) \times 10^4$ GNP/cell 2.62 pg	Yes	In vesicles in cytoplasm						
275	Glu-GNP 13 nm	6 MV	A549	20 nM 0.3 mg/mL	24 h		In vesicles in cytoplasm	Yes				2 Gy (0.498) **SER:** 1.38	(1.52) **Ratio:** 1.49	GNP medium without fetal bovine serum Toxicity GNP alone: 93.58 % survival Increased apoptosis
275	Control	6 MV	A549									2 Gy (0.686)	(2.27)	
276	Glu-GNP 16 nm	6 MV	MDA-MB-231	5 nM 0.1 mg/mL	24 h	$(5.31 \pm 0.25) \times 10^4$ GNP/cell 2.2 pg	Yes	In vesicles in cytoplasm						
276	Glu-GNP 16 nm	6 MV	MDA-MB-231	20 nM 0.5 mg/mL	24 h		Yes	In vesicles in cytoplasm				2 Gy (0.51) **SER:** 1.39	**Ratio:** 1.49	No toxicity In G2/M phase: GNP only 4.18 %, GNP + IR 22.55 %
276	Glu-GNP 49 nm	6 MV	MDA-MB-231	5 nM 4 mg/mL	24 h	$(9.46 \pm 0.43) \times 10^4$ GNP/cell 3.92 pg	Yes	In vesicles in cytoplasm						
276	Glu-GNP 49 nm	6 MV	MDA-MB-231	20 nM 14 mg/mL	24 h		Yes	In vesicles in cytoplasm				2 Gy (0.36) **SER:** 1.97	**Ratio:** 1.86	No toxicity In G2/M phase: GNP only 7.57 %, GNP + IR 32.14 %
276	Control	6 MV	MDA-MB-231									2 Gy (0.71)	(2.27)	In G2/M phase: no IR 1.99 %, IR 7.07 %

Table A.7.: Same as Tab. A.1.

				Biodistribution					Biological endpoint					
Reference	NP	Beam	Cell line	Concentration before incubation	Time of incubation	Intra-cellular concentration	Extra-cellular medium washed	Localisation	α	β	Dose for fixed survival	Survival for fixed dose	MID	Additional info
PEG-coated GNP														
[178]	PEG-GNP 4.7 nm	6 MV 2.4 Gy/min	CT-26	160 nM 0.1 mg/mL	48h	5×10^5 GNP/cell 0.52 pg	No	Vesicles, agglomerated				1 Gy (SF 0.58) **SER = 1.58** 2 Gy (SF 0.48) **SER = 1.33**		No toxicity
[178]	Control	6 MV 2.4 Gy/min	CT-26									1 Gy (SF 0.92) 2 Gy (SF 0.64)		
[179]	PEG-GNP 6.1 ± 1.9 nm	160 kVp E_{av} = 73 keV 0.037 Gy/s	EMT-6	60 nM 0.08 mg/mL	48h							2 Gy (SF 0.58) **SER = 1.26** 4 Gy (SF 0.35) **SER = 1.37**		
[179]	Control	160 kVp E_{av} = 73 keV 0.037 Gy/s	EMT-6									2 Gy (SF 0.73) 4 Gy (SF 0.48)		
[179]	PEG-GNP 6.1 ± 1.9 nm	Cu-Kα_1 (8.048 keV) 0.029 Gy/s	EMT-6	72 nM 0.1 mg/mL	48h							2 Gy (SF 0.54) **SER = 1.31** 4 Gy (SF 0.26) **SER = 1.30**		
[179]	Control	Cu-Kα_1 (8.048 keV) 0.029 Gy/s	EMT-6									2 Gy (SF 0.71) 4 Gy (SF 0.34)		
[179]	PEG-GNP 6.1 ± 1.9 nm	Synchrotron (6.5 keV) 0.26 Gy/s	EMT-6	72 nM 0.1 mg/mL	48h							1.5 Gy (SF 0.53) **SER = 1.34** 2.5 Gy (SF 0.41) **SER = 1.41**		
[179]	Control	Synchrotron (6.5 keV) 0.26 Gy/s	EMT-6									1.5 Gy (SF 0.71) 2.5 Gy (SF 0.58)		
[179]	PEG-GNP 6.1 ± 1.9 nm	6 MV 0.04 Gy/s	EMT-6	72 nM 0.1 mg/mL	48h							1 Gy (SF 0.61) **SER = 1.52** 3 Gy (SF 0.27) **SER = 1.48**		
[179]	PEG-GNP 6.1 ± 1.9 nm	6 MV 0.04 Gy/s	EMT-6	145 nM 0.2 mg/mL	48h							1 Gy (SF 0.50) **SER = 1.86** 3 Gy (SF 0.21) **SER = 1.90**		
[179]	Control	6 MV 0.04 Gy/s	EMT-6									1 Gy (SF 0.93) 3 Gy (SF 0.40)		
[291]	PEG-GNP 4.8 nm	137Cs (662 keV)	HeLa	C1: 15×10^3, 10 mg/mL C2 : 30×10^3, 20 mg/mL	24h	Less internalized than bigger GNPs					SF 0.5 **DEF C1 = 1.41** **DEF C2 = 1.46**			Increase in necrosis and apoptosis
[291]	PEG-GNP 12.1 nm	137Cs (662 keV)	HeLa	C1: 9×10^2, 10 mg/mL C2 : 2×10^3, 20 mg/mL	24h						SF 0.5 **DER C1 = 1.65** **DER C2 = 2.07**			Increase in necrosis and apoptosis
[291]	PEG-GNP 27.3 nm	137Cs (662 keV)	HeLa	C1: 81 nM, 10 mg/mL C2 : 160 nM, 20 mg/mL	24h						SF 0.5 **DER C1 = 1.58** **DER C2 = 1.86**			Increase in necrosis and apoptosis
[291]	PEG-GNP 46.6 nm	137Cs (662 keV)	HeLa	C1: 16 nM, 10 mg/mL C2 : 32 nM, 20 mg/mL	24h						SF 0.5 **DER C1 = 1.42** **DER C2 = 1.52**			Increase in necrosis and apoptosis
[171] + [169] + [168]	PEG-GNP 30 nm	100 kVp E_{av} = 33 keV	PC-3	12 nM 2 mg/mL	24 h	$(2.27 \pm 1.4) \times 10^4$ GNP/cell 6.19 pg 0.84 mg/mL	No	In vesicles in cytoplasm					**Ratio:** 1.51 ± 0.16	No loss of clonogenecity
[171] + [169] + [168]	PEG-GNP 30 nm	300 kVp E_{av} = 100 keV	PC-3	12 nM 2 mg/mL	24 h	$(2.27 \pm 1.4) \times 10^4$ GNP/cell 6.19 pg 0.84 mg/mL	No	In vesicles in cytoplasm	0.345 (0.288, 0.402)	0.037 (0.017, 0.057)	*SF 0.1 (4.4 Gy)* ***DER = 1.16***		(2.11 ± 0.10) **Ratio:** 1.21 ± 0.13	No loss of clonogenecity
[171] + [169] + [168]	PEG-GNP 5 nm	300 kVp E_{av} = 100 keV	PC-3	2×10^2 nM 2 mg/mL	24 h	$(2.15 \pm 0.37) \times 10^6$ GNP/cell 2.72 pg 0.38 mg/mL	No	In vesicles in cytoplasm					**Ratio:** 1.36 ± 0.16	No loss of clonogenecity
[171] + [169] + [168]	Control	300 kVp E_{av} = 100 keV	PC-3						0.217 (0.141, 0.293)	0.044 (0.016, 0.072)			(2.56 ± 0.25)	
[171] + [169] + [168]	PEG-GNP 30 nm	300 kVp E_{av} = 100 keV	SK-BR-3	1 nM 0.2 mg/mL	24 h	$(1.19 \pm 0.44) \times 10^3$ GNP/cell 0.32 pg 0.14 mg/mL	No	In vesicles in cytoplasm					**Ratio:** 1.05 ± 0.19	No loss of clonogenecity
[171] + [169] + [168]	PEG-GNP 30 nm	300 kVp E_{av} = 100 keV	SK-BR-3	12 nM 2 mg/mL	24 h	$(1.02 \pm 0.21) \times 10^4$ GNP/cell 2.78 pg 1.19 mg/mL	No	In vesicles in cytoplasm					**Ratio:** 1.40 ± 0.22	No loss of clonogenecity
[171] + [169] + [168]	Control	300 kVp E_{av} = 100 keV	SK-BR-3						0.274 (0.125, 0.0423)	0.035 (-0.023, 0.092)	*SF 0.1 (5.1 Gy)*			

Table A.8.: Same as Tab. A.1.

				Biodistribution					Biological endpoint					
Reference	NP	Beam	Cell line	Concentration before incubation	Time of incubation	Intra-cellular concentration	Extra-cellular medium washed	Localisation	α	β	Dose for fixed survival	Survival for fixed dose	MID	Additional info
Functionalized GNP														
[49] + [43]	HER-2 GNP 30 nm	100 kVp (E_{av} = 33 keV) 2.71/3.53 Gy/min	MDA-MB-361	15 nM 2.4 mg/mL	Overnight	Cytoplasm: $(7.7 \pm 0.9) \times 10^3$ GNP/cell (2.10 pg) Surface: $(2.8 \pm 1.4) \times 10^5$ GNP/cell (76.40 pg) Extracell: $(1.9 \pm 0.2) \times 10^4$ GNP/cell (5.18 pg)	No		0.15 ± 0.016	0.068 ± 0.004	SF 0.1 (4.8 Gy) **DER = 1.6**		*(2.53)* ***Ratio = 1.37***	
[49] + [43]	PEG-GNP 30 nm	100 kVp (E_{av} = 33 keV) 2.71/3.53 Gy/min	MDA-MB-361	15 nM 2.4 mg/mL	Overnight	Cytoplasm: $(1.0 \pm 0.3) \times 10^3$ GNP/cell (0.27 pg) Surface: $(1.6 \pm 0.2) \times 10^5$ GNP/cell (43.66 pg) Extracell: $(1.9 \pm 0.2) \times 10^4$ GNP/cell (5.18 pg)	No		0.13 ± 0.003	0.04 ± 0.001	SF 0.1 (5.9 Gy) **DER = 1.3**		*(3.18)* ***Ratio = 1.09***	
[49] + [43]	Control	100 kVp (E_{av} = 33 keV) 2.71/3.53 Gy/min	MDA-MB-361						0.23 ± 0.065	0.01 ± 0.013	SF 0.1 (7.6 Gy)		*(3.45)*	
[138]	FBS-GNP 50 nm (+ 10 nm proteins)	250 kVp	RT112	7×10^{-3} nM 5.5×10^{-3} mg/mL	4 h	1000 GNP/cell 1.26 pg	Yes	In lysosomes (diameter 150 - 350 nm) ≈ 135 per cell	0.229 ± 0.032	0.023 ± 0.007	*SF 0.1 (6.1 Gy)* ***DER = 1.25***	5 Gy (0.18 ± 0.09) **SER = 1.7**	*(2.95)* ***Ratio = 1.43***	
[138]	TAT-GNP 50 nm (+ 30 nm TAT)	250 kVp	RT112	7×10^{-3} nM 5.5×10^{-3} mg/mL	4 h	5000 GNP/cell 6.32 pg	Yes	In lysosomes				5 Gy (0.08 ± 0.02) **SER = 3.8**		
[138]	Control	250 kVp	RT112						0.048 ± 0.042	0.033 ± 0.007	*SF 0.1 (7.6 Gy)*	5 Gy (0.31 ± 0.10)	*(4.23)*	
[138]	FBS-GNP 50 nm (+ 10 nm proteins)	250 kVp	RT112	7×10^{-3} nM 5.5×10^{-3} mg/mL	4 h	1000 GNP/cell 1.26 pg	Yes	In lysosomes (diameter 150 - 350 nm) ≈ 135 per cell				5 Gy (0.25 ± 0.06) **SER = 1.0**		Add DMSO
[138]	TAT-GNP 50 nm (+ 30 nm TAT)	250 kVp	RT112	7×10^{-3} nM 5.5×10^{-3} mg/mL	4 h	5000 GNP/cell 6.32 pg	Yes	In lysosomes				5 Gy (0.48 ± 0.12) **SER = 1.9**		Add DMSO
[138]	Control	250 kVp	RT112									5 Gy (0.47 ± 0.16)		Add DMSO
[150]	PEG-GNP (2 kDa) 47 ± 8.2 nm	120 kVp, E_{eq} = 37.2 keV 1.85 Gy/min	HeLa	50×10^3 nM 31×10^3 mg/mL	24 h	6800 GNP/cell 7.13 pg						2 Gy **SER = 1.40 ± 0.07**		No toxicity
[150]	PEG-GNP (2 kDa) 47 ± 8.2 nm	180 kVp, E_{eq} = 48.1 keV 3.43 Gy/min	HeLa	50×10^3 nM 31×10^3 mg/mL	24 h	6800 GNP/cell 7.13 pg						2 Gy **SER = 1.43 ± 0.07**		No toxicity
[150]	PEG-GNP (2 kDa) 47 ± 8.2 nm	200 kVp, E_{eq} = 62.3 keV 2.67 Gy/min	HeLa	50×10^3 nM 31×10^3 mg/mL	24 h	6800 GNP/cell 7.13 pg						2 Gy **SER = 1.39 ± 0.05**		No toxicity
[150]	PEG-GNP (2 kDa) 47 ± 8.2 nm	200 kVp, E_{eq} = 74.7 keV 1.71 Gy/min	HeLa	50×10^3 nM 31×10^3 mg/mL	24 h	6800 GNP/cell 7.13 pg						2 Gy **SER = 1.37 ± 0.03**		No toxicity
[150]	PEG-GNP (2 kDa) 47 ± 8.2 nm	250 kVp, E_{eq} = 84.1 keV 2.38 Gy/min	HeLa	50×10^3 nM 31×10^3 mg/mL	24 h	6800 GNP/cell 7.13 pg						2 Gy **SER = 1.39 ± 0.03**		No toxicity
[150]	PEG-GNP (2 kDa) 47 ± 8.2 nm	Co-60, 1250 keV 1.18 Gy/min	HeLa	50×10^3 nM 31×10^3 mg/mL	24 h	6800 GNP/cell 7.13 pg						2 Gy **SER = 1.03 ± 0.01**		No toxicity
[150]	Folic acid 4ATP-GNP 52 ± 11.5 nm	120 kVp, E_{eq} = 37.2 keV 1.85 Gy/min	HeLa	50×10^3 nM 43×10^3 mg/mL	24 h	31 000 GNP/cell 44.05 pg						2 Gy **SER = 1.68 ± 0.08**		No toxicity
[150]	Folic acid 4ATP-GNP 52 ± 11.5 nm	180 kVp, E_{eq} = 48.1 keV 3.43 Gy/min	HeLa	50×10^3 nM 43×10^3 mg/mL	24 h	31 000 GNP/cell 44.05 pg						2 Gy **SER = 1.76 ± 0.09**		No toxicity
[150]	Folic acid 4ATP-GNP 52 ± 11.5 nm	200 kVp, E_{eq} = 62.3 keV 2.67 Gy/min	HeLa	50×10^3 nM 43×10^3 mg/mL	24 h	31 000 GNP/cell 44.05 pg						2 Gy **SER = 1.63 ± 0.05**		No toxicity
[150]	Folic acid 4ATP-GNP 52 ± 11.5 nm	200 kVp, E_{eq} = 74.7 keV 1.71 Gy/min	HeLa	50×10^3 nM 43×10^3 mg/mL	24 h	31 000 GNP/cell 44.05 pg						2 Gy **SER = 1.61 ± 0.07**		No toxicity
[150]	Folic acid 4ATP-GNP 52 ± 11.5 nm	250 kVp, E_{eq} = 84.1 keV 2.38 Gy/min	HeLa	50×10^3 nM 43×10^3 mg/mL	24 h	31 000 GNP/cell 44.05 pg						2 Gy **SER = 1.58 ± 0.06**		No toxicity
[150]	Folic acid 4ATP-GNP 52 ± 11.5 nm	Co-60, 1250 keV 1.18 Gy/min	HeLa	50×10^3 nM 43×10^3 mg/mL	24 h	31 000 GNP/cell 44.05 pg						2 Gy **SER = 1.05 ± 0.03**		No toxicity
[285]	BSA-peptide GNP, 14 nm	225 kVp	HeLa	10 nM 0.17 mg/mL	3h	(2500 GNP/cell (0.07 pg) for 8h incubation)		In cytoplasm and nucleus				2 Gy (0.05) **SER = 4.4**		
[285]	Non-targeted GNP 14 nm	225 kVp	HeLa	10 nM 0.17 mg/mL	3h	(1000 GNP/cell (0.03 pg) for 8h incubation)		In cytoplasm				2 Gy (0.175) **SER = 1.26**		
[285]	Control	225 kVp	HeLa									2 Gy (0.22)		
[296]	Galactose PEG-GNP 20 nm (core) 34 nm altogether	6 MV	HepG2	0.02 nM 0.001 mg/mL	24 h	2.2×10^4 GNP/cell 1.78 pg		In mitochondria			SF 0.37 **DER:** 1.95			Very little toxicity Accumulation in G2/M phase after IR (27.03 %) Decreased activity of CAT, SOD, GSH
[296]	Citrate-capped GNP 20 nm (core)	6 MV	HepG2	0.02 nM 0.001 mg/mL	24 h	8.2×10^3 GNP/cell 0.66 pg		In mitochondria			SF 0.37 **DER:** 1.46			Very little toxicity Accumulation in G2/M phase after IR (20.26 %) Decreased activity of CAT, SOD, GSH
[296]	Control	6 MV	HepG2											In G2/M phase post IR 8.09 %
[174]	Amine-PEG GNP 5 nm GNP	Proton beam 4 MeV, 10 keV/µm	A431	66 nM 0.05 mg/mL	24 h	24×10^4 GNP/cell 0.30 pg		In cytoplasm and in nucleus nearby nucleus membrane	0.22 ± 0.03	0.15 ± 0.006	*SF 0.1 (3.2 Gy)* ***1.06***		*(1.71)* ***Ratio = 1.06***	
[174]	Amine-PEG GNP 10 nm GNP	Proton beam 4 MeV, 10 keV/µm	A431	8 nM 0.05 mg/mL	24 h	7.7×10^4 0.78 pg		In cytoplasm	0.21 ± 0.02	0.15 ± 0.02	*SF 0.1 (3.2 Gy)* ***DER = 1.07***		*(1.73)* ***Ratio = 1.05***	
[174]	Control	Proton beam 4 MeV, 10 keV/µm	A431						0.19 ± 0.05	0.14 ± 0.01	*SF 0.1 (3.4 Gy)*		*(1.82)*	
[174]	Amine-PEG GNP 5 nm GNP	Proton beam 1.3 MeV, 25 keV/µm	A431	66 nM 0.05 mg/mL	24 h	24×10^4 GNP/cell 0.30 pg		In cytoplasm and in nucleus nearby nucleus membrane	1.37 ± 0.03	–	SF 0.1 **DER = 1.08**	3 Gy **SER = 1.33**	*(0.73)* ***Ratio = 1.08***	
[174]	Amine-PEG GNP 10 nm GNP	Proton beam 1.3 MeV, 25 keV/µm	A431	8 nM 0.05 mg/mL	24 h	7.7×10^4 0.78 pg		In cytoplasm	1.45 ± 0.04	–	SF 0.1 **DER = 1.14**	3 Gy **SER = 1.67**	*(0.69)* ***Ratio = 1.14***	
[174]	Control	Proton beam 1.3 MeV, 25 keV/µm	A431						1.27 ± 0.04	–			*(0.79)*	

Table A.9.: Same as Tab. A.1.

B. Monte Carlo simulation of low-energy electrons in metals - Benchmarking of electron gold interaction

B.1. Energy loss function fitting from optical data

For bulk plasmons, the optical energy loss function is expanded into a sum of several terms of the Drude-type energy loss function. The DIMFP reads

$$\frac{d\lambda_{b,\infty}^{-1}}{d\omega} = \frac{1}{\pi E_{\text{kin},1}} \int_{q-}^{q+} \frac{dq}{q} \sum_i A_i \times \frac{\gamma_i \omega}{(\omega^2 - (\omega_{b,i} + \frac{q^2}{2})^2)^2 + (\omega\gamma_i)^2} \tag{B.1}$$

with A_i a weight factor, $\omega_{b,i}$ is the resonance energy and γ_i represents the full width at half maximum of the mode i. A_i, $\omega_{b,i}$ and γ_i were obtained by fitting the energy loss function of the medium of interest. The final parameters are given in Appendix B.4 in the case of gold. As shown in the work by Ashley *et al.*[13], A_i is constrained and must respect the sum rule given in Eq. B.2,

$$\sum_i A_i = 4\pi n_e = 4\pi N_e n_a, \tag{B.2}$$

where N_e is the number of valence electrons per atom, and n_a the number of atoms per volume unit.

Each mode i can be expressed independently, and the DIMFP for one mode is given by Eq. B.3,

$$\frac{d\lambda_{b,\infty}^{-1}, i}{d\omega} = \frac{1}{\pi E_{\text{kin},1}} \int_{q-}^{q+} \frac{dq}{q} A_i \times \frac{\gamma_i \omega}{(\omega^2 - (\omega_{b,i} + \frac{q^2}{2})^2)^2 + (\omega\gamma_i)^2}. \tag{B.3}$$

As it is shown by Eq. B.2, A_i is constrained by the number of electrons considered as valence electrons for gold. This choice determines the limit between the solid state-like model, which takes into account the collective effect and the atomic like model that neglects it. If deep subshells, such as the K and L levels, can clearly be identified as atomic shells, and the 11 outer-most electrons can clearly be described as valence electrons, there is an uncertainty regarding the intermediate shells, such as $5p^6$. Their binding energies are smaller than 100 eV, and it is rather difficult to consider them *a priori* as weekly-bound electrons or core electrons. The key point to our strategy relies in finding a good fit for experimental data, which are available up to energies of about 100 eV. A fit was done without constraints on the A_i coefficients, and the number of electrons contributing to collective effects was then deduced. In this fit, the energies up to the 4f shells were considered, for which the binding energy is about 97 eV. Using 9 fitting Lorenz profiles, 17.3 valence electrons per atom were effectively included in the dielectric function. This number

represents the 11 outer-most electrons, the 4 electrons of the subshell $5p^6_{3/2}$ (binding energy of 61 eV), the 2 electrons of the subshell $5p^6_{1/2}$ (binding energy of 78 eV) and a fraction of the electrons from the subshells $5s^2$ and $4f^{14}$. These results are overall very consistent: as the fit is done up to about 100 eV, it includes the subshells that have their binding energies in this range. The final fit is shown in Fig. B.1.

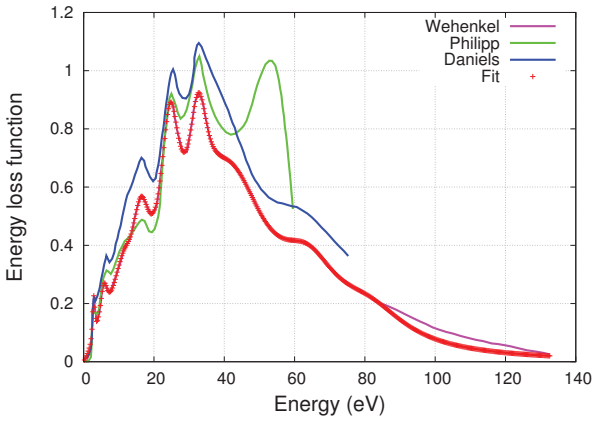

Figure B.1.: Bulk energy loss function $\Im\left\{\frac{-1}{\varepsilon(0,\omega)}\right\}$ as a function of the energy loss (eV). The experimental data were taken from Wehenkel *et al.*[277], Philipp *et al.*[62] and Daniels *et al.*[74]. The final fit was done using the experimental data of Wehenkel *et al.*[277] .

B.2. Position dependent free path Monte Carlo procedure

For an uniform homogeneous medium, the free path s of a projectile between two successive interaction events obeys an exponential law of probability distribution,

$$p(s) = \lambda^{-1} \exp\left(\frac{-s}{\lambda}\right), \tag{B.4}$$

where λ is the total mean free path, and λ^{-1} is determined as the sum of the IMFPs for all the processes considered. Introduction of surface excitation modes in our model leads to the dependence of MFPs on the position of the particle $\vec{r}\ (s)$. As a consequence, sampling the free path by using the distribution (B.4) is no longer valid, and must be replaced by

$$p(s) = \lambda^{-1}(\vec{r}\ (s)) \exp(-U(s)), \tag{B.5}$$

with $U(s) = \int_0^s \lambda^{-1}(\vec{r}\ (s'))\mathrm{d}s'$

To evaluate the dependence of $\lambda^{-1}(\vec{r}\ (s))$ on the current position of the particle, the geometry given in the Fig. B.2 is considered. We assume that locally the surface is planar. At the initial position $s = 0$, the distance to the surface is given by $z = z_0$, and at the position $\vec{r}\ (s)$ the distance to the surface is given by $z(s)$. Given the normal vector to the surface $\vec{n}$, and the velocity of the particle $\vec{v}$, at any position $\vec{r}\ (s)$ along the trajectory, we have

$$z(s) = z_0 + s\cos(\theta), \tag{B.6}$$

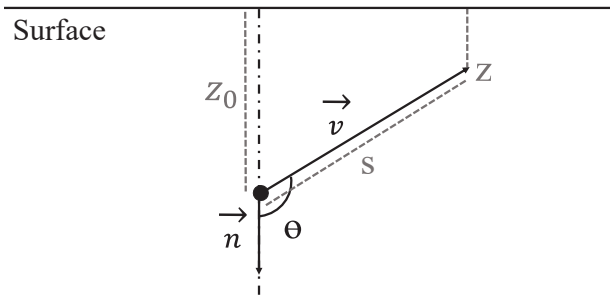

Figure B.2.: Geometry of the system: the electron passes a distance s with velocity $\vec{v}$, starting at an initial position at z_0 from the surface.

$$\cos(\theta) = \frac{\vec{n} \cdot \vec{v}}{\left\|\vec{v}\right\|}. \tag{B.7}$$

At a given position $\vec{r}$ (s), the inverse mean free path $\lambda^{-1}(z(s))$ is equal to

$$\lambda^{-1}(z(s)) = \lambda^{-1}_{\text{surf}} \exp(-z/z_{\text{eff}}) + \lambda^{-1}_{\text{bulk}}(1 - \exp(-z/z_{\text{eff}})) + \sum_i \lambda_i^{-1}, \tag{B.8}$$

where $\lambda^{-1}_{\text{surf}}$ is associated to surface excitation modes, $\lambda^{-1}_{\text{bulk}}$ is associated to bulk modes, and $\sum_i \lambda_i^{-1}$ are associated to all the other interaction without position dependence.

The probability density of having an interaction is therefore given by:

$$p(s) = \lambda^{-1}(z(s)) \exp[-\lambda^{-1}_{\text{surf}} F(s, z_0, \cos\theta) + (\lambda^{-1}_{\text{bulk}} + \lambda_i^{-1})s - \lambda^{-1}_{\text{bulk}} F(s, z_0, \cos\theta)], \tag{B.9}$$

where

$$F(s, z_0, \cos\theta) = \frac{z_{\text{eff}} \exp(\frac{-z_0}{z_{\text{eff}}})}{\cos(\theta)} (1 - \exp\left(\frac{\cos(\theta)s}{z_{\text{eff}}}\right)). \tag{B.10}$$

To sample the free path s, a rejection method is used, using the density of probability $p(s)$. Once s is sampled, the new position is calculated and used to sample the next interaction process. Then, the sampling of the type of interaction i which an electron undergoes is done by the standard MC procedure described for instance in the work by Ding. *et al.*[80], using the different IMFPs λ_i^{-1}. We emphasize that λ_i^{-1} depends on the position, and has therefore to be calculated at the position of the interaction.

B.3. Differential elastic cross section

Fig. B.3 and B.4 show differential elastic cross section obtained with our model and other theoretical and experimental data.

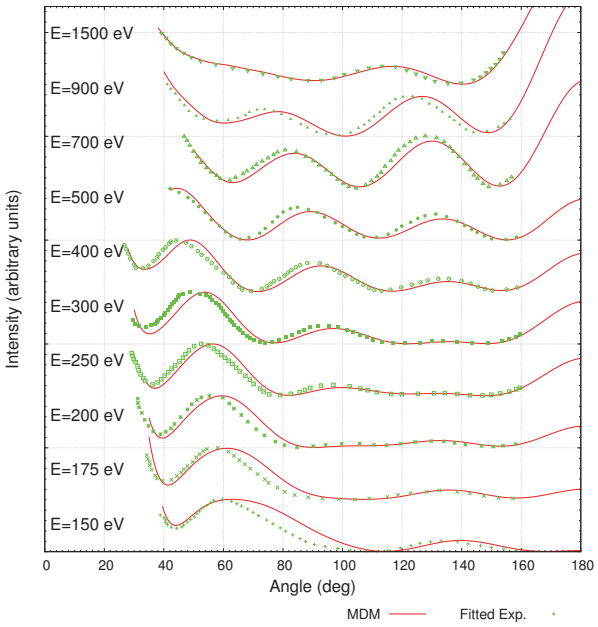

Figure B.3.: Comparison of the differential elastic cross section obtained with MDM with experimental data from Reichert *et al.*[228] for different electron energies. Results were normalized to the maximum intensity.

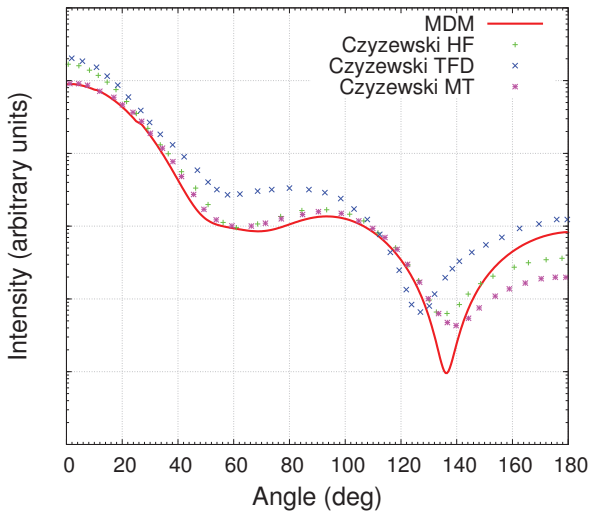

Figure B.4.: Comparison of the differential elastic cross section with theoretical results for different atomic potentials (HF = Hartree-Fock, TFD = Thomas-Fermi-Dirac, MT = Muffin-tin) from Czyzewski *et al.*[71] The energy of the projectile electron was equal to 100 eV. Simulation results were normalized to have the same intensity of the highest peak.

B.4. Optical data fit parameters for dielectric-based interaction

Tab. B.1 presents the parameters obtained for the fitting of the optical data, used for plasmon cross sections.

Mode	A_i	$\omega_{b,i}$	$\omega_{s,i}$	γ_i	e^-	C_0	**Eff.** e^-
1	0.054	0.1069	0.0707	0.029	0.0043	4.	0.0171
2	0.349	0.2158	0.1526	0.098	0.0278	1.	0.0278
3	2.531	0.4279	0.3026	0.201	0.2014	1.	0.2014
4	4.937	0.6093	0.4308	0.231	0.3929	1.	0.3929
5	14.442	0.9117	0.6446	0.244	1.1493	1.	1.1493
6	14.253	1.2047	0.8518	1.205	1.1342	1.	1.1342
7	96.933	1.5994	1.1309	0.961	7.7137	1.	7.7137
8	45.313	2.3735	1.6783	0.785	3.6059	1.	3.6059
9	38.425	3.0205	2.1358	0.974	3.0578	1.	3.0578
				TOT.	17.29		17.30

Table B.1.: Energy loss function fit: parameters obtained. A_i is the amplitude of the mode i, $\omega_{b,i}$ (resp. $\omega_{s,i}$) the resonance energy of the bulk (resp. surface) mode i, and γ_i the dissipation constant. Eff. e^- represents the total number of electrons described by the mode i following Eq. B.2 and Eq. 8.17. All the results are given in atomic units. As the results obtained for electron energy loss clearly showed an underestimation of the surface plasmon peak intensity for the mode 1, its cross section was multiplied by 4.

B.5. Parameters for core-ionization

Tab. B.2 presents the parameter set-up for the core-ionization model based on Kim *et al.*[153].

Shell	**Sub-shell**	**Label**	**Spin**	**B**	$\langle E_{e^-} \rangle$	ΔB	n_{e^-}	c	**Eff.** e^-	**Index**
K	$1s^2$	K	$1s_{1/2}$	2975.4	4 779	0.02	2		2	1
L	$2s^2$	L1	$2s_{1/2}$	526.87	1 107.5	0.02	2		2	2
	$2p^6$	L2L3	$2p_{1/2}$	506.28	1 346	0.02	2		2	3
			$2p_{3/2}$	438.15	732.8	0.02	4		4	4
M	$3s^2$	M1	$3s_{1/2}$	125.01	342.8	0.02	2		2	5
	$3p^6$	M2M3	$3p_{1/2}$	115.556	400.7	0.02	2		2	6
			$3p_{3/2}$	100.48	248.4	0.02	4		4	7
	$3d^{10}$	M4M5	$3d_{3/2}$	84.55	543.7	0.02	4		4	8
			$3d_{5/2}$	81.3	224.7	0.02	6		6	9
N	$4s^2$	N1	$4s_{1/2}$	27.47	108.5	0.02	2		2	10
	$4p^6$	N2N3	$4p_{1/2}$	23.38	118.7	0.02	2		2	11
			$4p_{3/2}$	19.75	79.	0.02	4		4	12
	$4d^{10}$	N4N5	$4d_{3/2}$	13.0	71.	0.02	4		4	13
			$4d_{5/2}$	12.32	65.7	0.02	6		6	14
	$4f^{14}$	N6N7	$4f_{5/2}$	3.58	51.2	0.184	6	0.981	5.886	15
			$4f_{7/2}$	3.43	49.7	0.184	8	0.981	7.848	16
O	$5s^2$	O1	$5s_{1/2}$	4.24	24.6	0.184	2	0.981	1.962	17
	$5p^6$	O2O3	$5p_{1/2}$	2.89	23.44	0.368	2		0.	18
			$5p_{3/2}$	2.26	15.67	0.368	4		0.	19
O+P	$5d^{10}$ + $6s^1$	0405 + P1	$6s_{1/2}$	0.269	8.6	0.2	11		0.	Weakly bound
						TOTAL	79		61.7	

Table B.2.: Parameters used for the BEB model and Auger decay. All the results are given in atomic units. B is the binding energy. $\langle E_{e^-} \rangle$ is the average kinetic energy of the bound electron and ΔB the binding energy broadening that is effectively used for Auger electron emission. n_{e^-} is the number of electrons per shell, which is effectively used for the Auger cascade, while c is a scaling coefficient as introduced in section 8.3.2.5. Eff. e^- represents the final numbers of electrons accounted for in each shell for the BEB model. It might be corrected for relativistic effects and for improved oscillator strengths[154].

C. Nanodosimetry

C.1. Energy conventions for gold an water

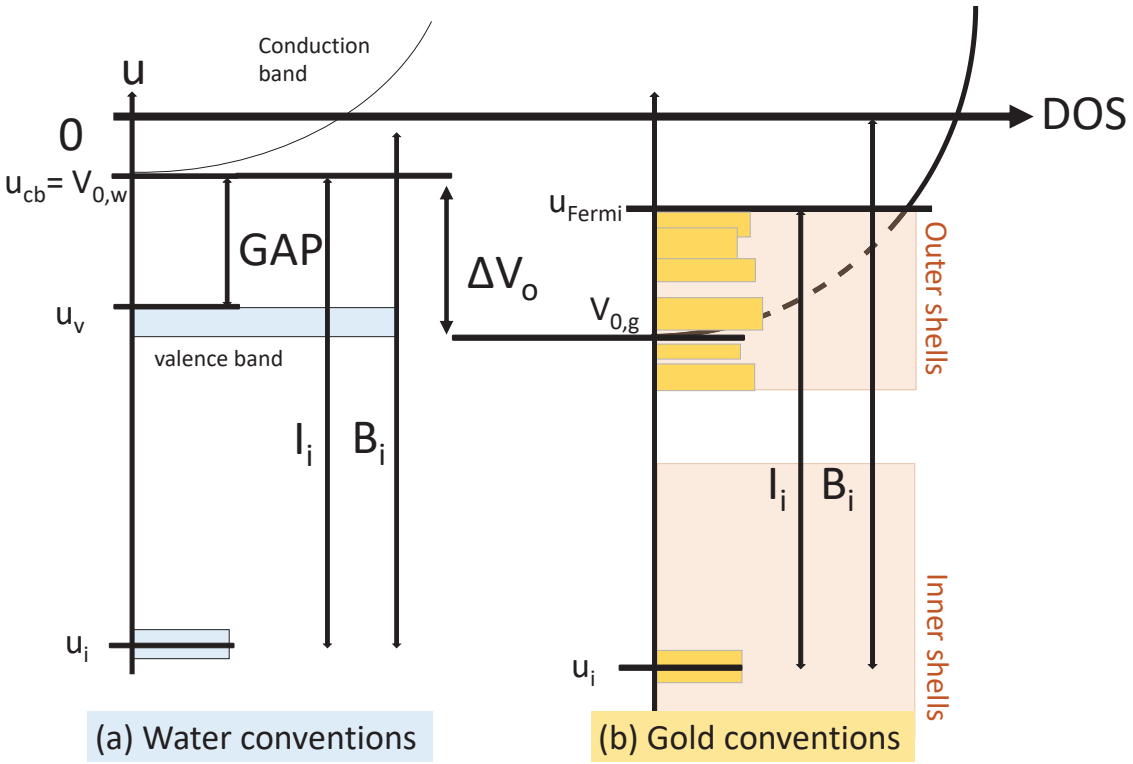

Figure C.1.: Scheme of the density of state (DOS) for water (panel A) and gold (panel B). The occupied states are represented by colored bands. The parabolic density of states corresponds to the final state representation (plane wave approximation). The values of the mesoscopic potential energies V_0 for each material are also displayed (e.g. $V_{0,\mathrm{W}}$ for water and $V_{0,\mathrm{g}}$ for gold). The core levels i are characterized by the binding energies B_i and the ionization energies I_i. The water excited states are not represented here. u_{Fermi} is the Fermi level, u_{cb} (resp. u_{v}) is the bottom of the conduction band (resp. top of the valence band) in water.

C.2. Track by track method for restricted specific energy calculation

We estimated that the calculation of a probability distribution of specific energies would take, without any optimization, at least 500 centuries in the best conditions, where the energy is 20 keV, for a standard computer (Intel© Xeon© CPU W3565 @ 3.20 GHz). This is due to the large volume of water considered, the nanometric size of the GNP making the probability of interaction extremely small, and the fact that we study a distribution of energy deposition inside targets of very small volume, for which most of the time there is no energy deposition. To optimize the calculation and obtain a reasonable computing time, a few simplifications and approximations were mandatory. We assumed that the probability that a nanotarget received energy from two distinct tracks was negligible. Such approximation is reasonable provided that the dose of irradiation is low enough, and the size of the nanotarget is small enough. For the former, such condition corresponds to standard irradiation conditions for which the dose of irradiation is below 10 Gy. For the later, the nanotarget was modeled as a cylinder of radius and height set at 10 nm. In pure water and for low energy (keV) photon irradiation, the probability of hitting a nanotarget was about 4×10^{-4} for one Gy. Therefore, the probability for a nanotarget to received any dose at all is low, and consequently the probability that a nanotarget receives energy from two tracks is negligible.

Using these conditions, our optimization consisted in calculating separately the restricted specific energy from the 3 sub-contributions (W, W+NP, NP), referred to as (1, 2, 3). The specific energy was decomposed as a sum of the 3 sub-contributions as follows:

$$S(\vec{r}, z) = S_1(\vec{r}, z) + S_2(\vec{r}, z) + S_3(\vec{r}, z) \tag{C.1}$$

Each of these contributions (S_1, S_2 or S_3) was decomposed as a linear combination of single-track spectra, $S_1^1(\vec{r}, z)$, $S_2^1(\vec{r}, z)$ and $S_3^1(\vec{r}, z)$. Thus, Eq. C.1 becomes,

$$S(\vec{r}, z) = n_1(D)S_1^1(\vec{r}, z) + n_2(D)S_2^1(\vec{r}, z) + n_3(D)S_3^1(\vec{r}, z) \tag{C.2}$$

$n_1(D) = n_2(D)$ is the mean number of photon interactions in water for a given prescribed dose D in water. $n_3(D)$ is the mean number of photon interactions with the GNP. This results in the following system:

$$\begin{cases} n_1(D) = n_2(D) = F(D)(V - V_{\mathrm{NP}})\sigma_{\mathrm{W}}\rho_{\mathrm{W}} \\ n_3(D) = F(D)V_{\mathrm{NP}}\sigma_{\mathrm{NP}}\rho_{\mathrm{NP}} \end{cases} \tag{C.3}$$

with $F(D)$ the fluence of incoming photons in cm^{-2} which is linear with the dose D, V the total volume in cm^3, V_{NP} the volume of one GNP in cm^3, σ_x the total cross section for interaction in the medium x in $\mathrm{cm}^2{\cdot}\mathrm{g}^{-1}$ and ρ_x the density of the medium x in $\mathrm{g{\cdot}cm}^{-3}$. Each spectrum $S_i^1(\vec{r}, z)$ ($i \in [1, 2, 3]$) is now given per primary photon interaction and is calculated independently, by MC. It contains in particular the details of the physical processes that follow photon interaction. To speed up the calculation, we applied various methods of biasing, to obtain high statistics of rare events within constrained computing time conditions. Such algorithms did not require any further approximation, and therefore will not be described here as this is beyond the scope of this work. Using these approximations and optimized algorithms, the restricted specific energy distributions were obtained in about 2 days for a system $E_{\mathrm{photon}}/\ R_{\mathrm{NP}}$.

C.3. Spectra of electron emission out of a GNP irradiated by photons

Fig. C.2, C.3 and C.4 represent energy distribution of electrons emitted from a GNP irradiated by a monoenergetic photon beam. The GNP was put in vacuum and the beam radius was set to be the same as the GNP radius. The distributions were normalized per incoming photon. On Fig. C.2 the spectra were broken down in sub-contributions depending on the origin of the creation of the electron: the photoelectric contribution refers to electrons ejected after a photo-electric effect, and the entire induced electron cascade. Likewise, the Compton contribution refers to the electrons ejected after a Compton effect and the electronic cascade. Finally, Auger electrons refer to the electrons ejected after the recombination of the initial vacancy created by a photon interaction in the GNP, and the subsequent electronic cascade. It may be noticed that electrons with energy lower than 20 keV are mainly coming from the Auger effect while electrons with larger energies are mainly coming from the photo-electric effect. The Compton effect remains negligible at these energies. We also added the energy distribution of fluorescence photons. Their number remains low compared to emitted electrons. On Fig. C.3, the intensity of the distribution increases with the size of the NP for a fixed energy, due to the higher number of gold atoms per GNP, hence a higher probability of hitting it. For a fixed radius, the intensity tends to be higher at low energy as the probability of a photon to interact with gold decreases with increasing energy, and emitted secondary electrons have lower energies. In particular, when focusing on very low energies ($<$ 2 keV) as shown in Fig. C.4, the number of low energy electrons is approximately 4 to 5 times higher at 20 keV than 70 keV. An exception may be noted for 90 keV, whose intensity is higher than 70 keV due to the K-edge at 80.7 keV and the increased photoelectric cross-section at this energy.

Such energy spectra explain the variation of the restricted specific energy distribution with regard to the size of the GNP. While the volume of the GNP is increasing, the probability of having a photon interaction inside the GNP becomes larger. As a consequence, for a fixed dose D, the intensity of the electron emission distribution increases and more electrons are emitted from the GNP. However, as R_{NP} increases, the probability for a secondary electron to escape decreases and part of the energy is absorbed. Therefore, the amplification does not scale with the number of gold atoms. Besides, as the NP is larger, electrons can interact more before leaving the GNP, potentially leading to the creation of more secondary electrons. Additionally, photoelectrons or Auger electrons leave the GNP with less energy and hence are more likely to deposit strong concentrations of energy in the vicinity of the GNP. For low energy particularly (20 keV), the photoelectron contribution is negligible for small NPs but becomes important for larger GNPs. For larger energies (50 keV), the energy deposition is dominated by Auger electrons no matter how large the GNP is. An exception is to be noted for 90 keV. Due to a high probability of fluorescence recombination, the overall photoelectron energy is reduced leading to a non negligible dose deposition within a few nanometers around the GNP.

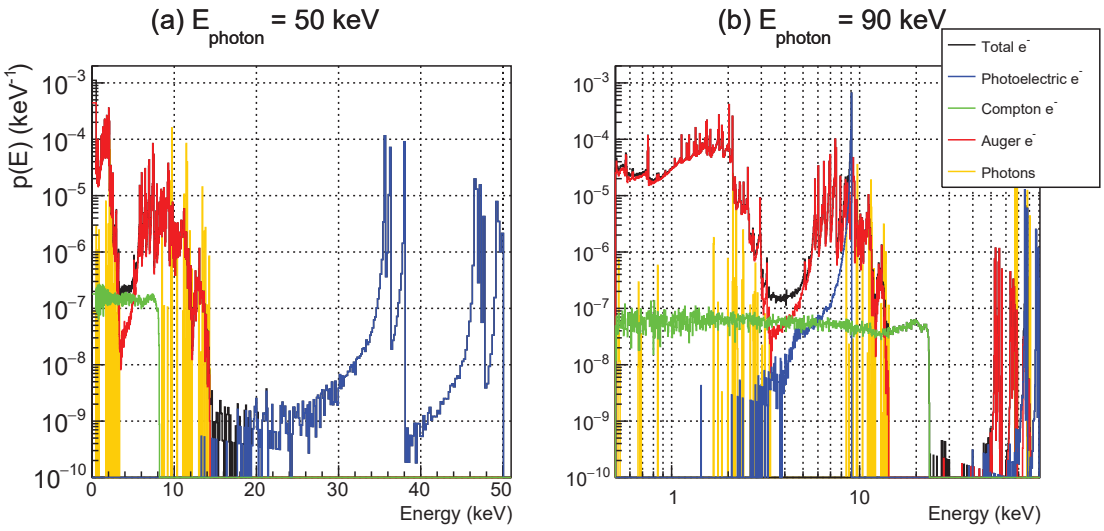

Figure C.2.: Energy distribution of electrons and fluorescence photons leaving a gold NP irradiated in vacuum by a monoenergetic photon beam of diameter set to be as large as the NP diameter, set here at 10 nm. The relative intensity (in keV^{-1}) is given per incoming photon. The electron distributions were broken down into 3 sub-contributions: the contribution of (1) the photoelectric process, (2) the Compton process, (3) Auger process. On the left, the photon energy is set at 50 keV and on the right it is set at 90 keV.

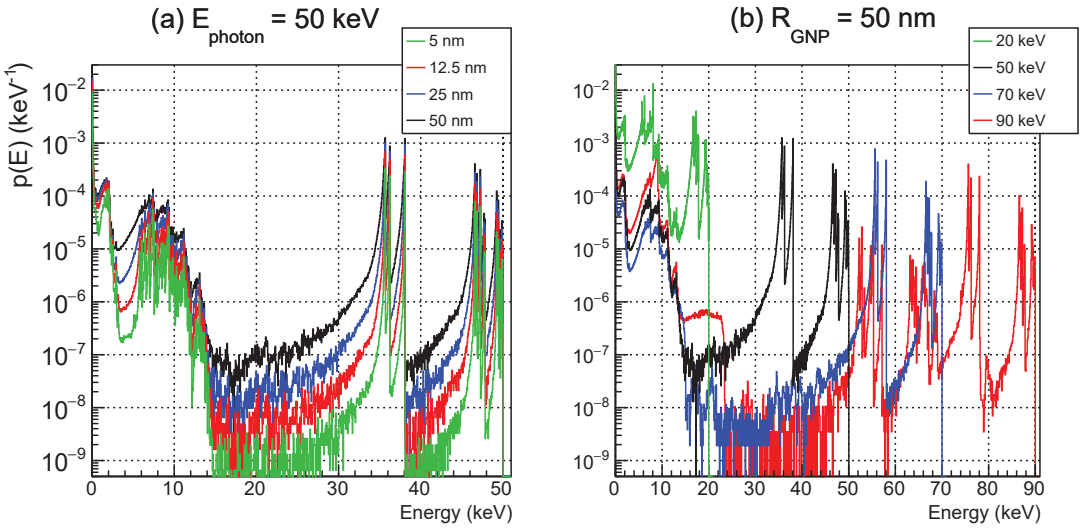

Figure C.3.: Energy distribution of electrons leaving a gold NP irradiated in vacuum by a monoenergetic beam of diameter set to be as large as the NP. The relative intensity (in keV^{-1}) is given per incoming photon. On the left (a), the results are shown for a fixed photon energy (50 keV) and 4 different GNP radii (5nm, 12.5 nm, 25 nm and 50 nm). On the right (b), the results are shown for a fixed NP radius (50 nm) and 4 different photon energies (20 keV, 50 keV, 70 keV and 90 keV).

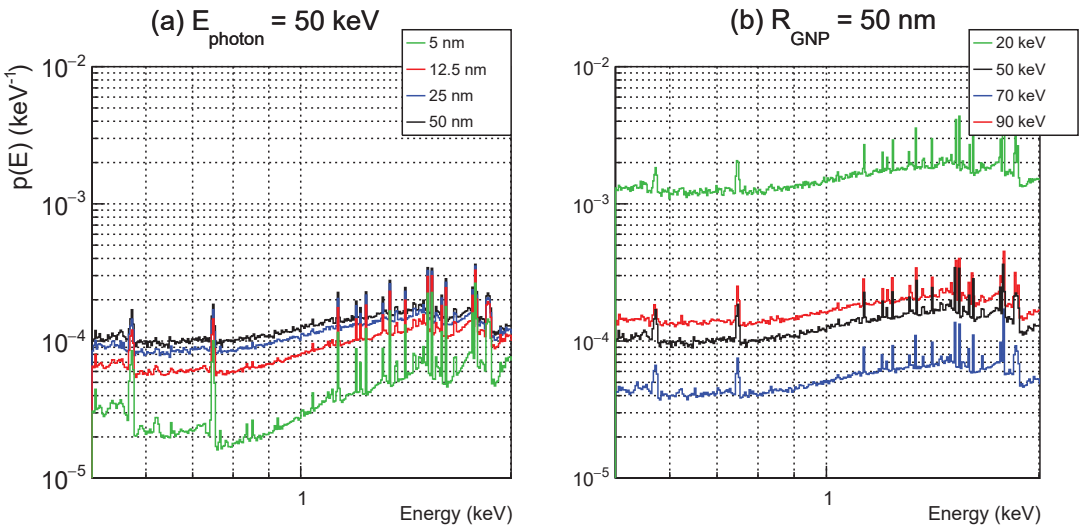

Figure C.4.: Same as Fig. C.3 with a focus on the energy range [0.1-2] keV.

D. Chemical modelling: macroscopic scale

D.1. Track by track methodology

While the expression of the coefficients $n_i(D)$ is straightforward (see Eq. 10.3), the calculation of $R^1_{X,i}$ (see Eq. 10.4) requires MC simulations. As Monte Carlo simulations rely on first degree Markov chains, each track t may be described by $(I_0, \vec{r_0}, s)$, where I_0 is the original event, defined by the photo-electron velocity and the subsequent Auger electrons velocities, $\vec{r_0}$ is the position of the primary photon interaction, and s is a series of random number determining totally the Markov chain. As mentioned in section 10.2.3.1, we decomposed the production of chemical species X, for a given irradiation dose D, as a linear combination of the chemical species produced by isolated tracks of types i, $R^1_{X,i}$, where i refers either to a track type W, W+NP and NP (i.e. 1, 2 and 3). We expose thereafter the method we used, first for a photon interacting in water and then interacting in a GNP.

We define $V_W = V - X_{\mathrm{NP}} V_{\mathrm{NP}}$, the volume occupied by water for a total volume V containing X_{NP} (number of GNP per cm^3) of volume V_{NP}. Then, the average number of chemical species per photon interaction in water is given by,

$$R^1_{X,1\cup 2} = \sum_{I_0,s} \int_{V_{\mathrm{W}}} \mathrm{d}\,\vec{r_0}\, \frac{\sigma_{I_0}}{\sigma_{\mathrm{W}}} \rho(\vec{r_0}) R^1_{X,I_0,\vec{r_0},s} \tag{D.1}$$

σ_{I_0} is the cross section for a photon interaction that leads to an initial event I_0, σ_{W} is the total cross section of photon interaction in water, and, by definition, $\sum_{I_0} \frac{\sigma_{I_0}}{\sigma_{\mathrm{W}}} = 1$. $\rho(\vec{r_0})$ is the probability distribution that the initial event I_0 occurs at the position $\vec{r_0}$. We assume the distribution uniform, thus $\rho(\vec{r_0}) = \frac{1}{V_{\mathrm{W}}}$. $R_{X,T_0,\vec{r_0},s}$ is the number of chemical species X induced by the track t defined by $(I_0, \vec{r_0}, s)$.

To differentiate the contributions W and W+NP, we introduce two functions,

$$\begin{cases} \delta_{I_0,\vec{r_0},s,1} = 1 \text{ if } t = (I_0, \vec{r_0}, s) \in T_1,\ 0 \text{ if } t = (I_0, \vec{r_0}, s) \in T_2 \\ \delta_{I_0,\vec{r_0},s,2} = 0 \text{ if } t = (I_0, \vec{r_0}, s) \in T_1,\ 1 \text{ if } t = (I_0, \vec{r_0}, s) \in T_2 \end{cases} \tag{D.2}$$

As a photon interaction in water leads either to the track type 1 or 2 (i.e. the track either interacts with a GNP or not), we find,

$$R^1_{X,1\cup 2} = \sum_{I_0,s} \frac{\sigma_{I_0}}{\sigma_{\mathrm{W}}} \int_{V_{\mathrm{W}}} \mathrm{d}\,\vec{r_0} \left(\delta_{I_0,\vec{r_0},s,1} + \delta_{I_0,\vec{r_0},s,2} \right) \rho(\vec{r_0}) R^1_{X,I_0,\vec{r_0},s} \tag{D.3}$$

We introduce,

$$\begin{cases} P_{I_0,s,1} = \int\limits_{V_{\mathrm{W}}} \delta_{I_0,s,1}\rho(\vec{r_0})\mathrm{d}\ \vec{r_0} \\ P_{I_0,s,2} = \int\limits_{V_{\mathrm{W}}} \delta_{I_0,s,2}\rho(\vec{r_0})\mathrm{d}\ \vec{r_0} \end{cases} \tag{D.4}$$

For a track defined by an origin I_0 and the series of numbers s defining all the secondary particles, $P_{I_0,s,1}$ (respectively $P_{I_0,s,2}$) represents the probability that any track characterized by I_0,s has no secondary electron hitting a GNP (respectively has at least one electron hitting a GNP). Note that $P_{I_0,s,1} + P_{I_0,s,2} = 1$. We further introduce,

$$\begin{cases} R^1_{X,I_0,s,1} = \frac{1}{P_{I_0,s,1}} \int\limits_{V_{\mathrm{W}}} \mathrm{d}\ \vec{r_0}\ \delta_{I_0,s,1} \cdot \rho(\vec{r_0}) \cdot R^1_{X,I_0,\vec{r_0},s} \\ R^1_{X,I_0,s,2} = \frac{1}{P_{I_0,s,2}} \int\limits_{V_{\mathrm{W}}} \mathrm{d}\ \vec{r_0}\ \delta_{I_0,s,2} \cdot \rho(\vec{r_0}) \cdot R^1_{X,I_0,\vec{r_0},s} \end{cases} \tag{D.5}$$

Then Eq. D.3 becomes,

$$R^1_{X,1\cup 2} = R^1_{X,1} + R^1_{X,2} \tag{D.6}$$

with

$$\begin{cases} R^1_{X,1} = \sum\limits_{I_0,s} \frac{\sigma_{I_0}}{\sigma_{\mathrm{W}}} \cdot P_{I_0,s,1} \cdot R^1_{X,I_0,s,1} \\ R^1_{X,2} = \sum\limits_{I_0,s} \frac{\sigma_{I_0}}{\sigma_{\mathrm{W}}} \cdot P_{I_0,s,2} \cdot R^1_{X,I_0,s,2} \end{cases} \tag{D.7}$$

The estimation of the probability that a secondary particle hit a GNP is not straightforward when having a given number of GNPs, C_{NP} (number of particle per cm^3). We introduced the number nanoparticles X_{NP} in the volume V ($X_{\mathrm{NP}} = C_{\mathrm{NP}}V$, and the probability that a track hit a GNP when there is only a single GNP in the volume V, $p_{I_0,s,2}$. Given a low concentration of GNP, and assuming that they are homogeneously distributed, the probability of not hitting a GNP, in the presence of X_{NP} GNPs, follows a binomial distribution,

$$P_{I_0,s,1} = 1 - P_{I_0,s,2} = \binom{0}{X_{\mathrm{NP}}} (1 - p_{I_0,s,2})^{X_{\mathrm{NP}}} (p_{I_0,s,2})^0 \tag{D.8}$$

Considering a small dose (low track density), and a low radical diffusion ($t \leq 10^{-6}$ s), the probability that a track interacts with the GNP is low, ($p_{I_0,s,2} \ll 1$). Thus, one has,

$$(1 - p_{I_0,s,2})^{X_{\mathrm{NP}}} \sim 1 - X_{\mathrm{NP}} p_{I_0,s,2} \tag{D.9}$$

Therefore, for X_{NP} GNPs in the volume V, $P_{I_0,s,1}$ and $P_{I_0,s,2}$ may be estimated with the probability that a track I_0, s hits one GNP as follows,

$$\begin{cases} P_{I_0,s,1} \sim 1 - C_{\mathrm{NP}} \cdot V \cdot p_{I_0,s,2} \\ P_{I_0,s,2} \sim C_{\mathrm{NP}} \cdot V \cdot p_{I_0,s,2} \end{cases} \tag{D.10}$$

For each track (T_0, s) generated, we estimated $p_{I_0,s,2}$, from which we derived $P_{I_0,s,1}$ and $P_{I_0,s,2}$. Concretely, to estimate $R^1_{X,1}$ (resp. $R^1_{X,2}$), we generated many primary events I_0. s is described by the seed of the pseudo-random generator. $p_{I_0,s,1}$ and $R^1_{X,I_0,s,1}$ (resp. $R^1_{X,I_0,s,2}$) are determined for each couple I_0, s, by generating randomly numerous GNP positions in the volume V.

For the track type NP (i.e. 3), the determination of its contribution was more straightforward. The calculation of $R^1_{X,3}$ consisted of generating a sufficient number of primary photons interaction within the GNP to reach a statistically accurate value of chemical yields.

D.2. Chemical yields at 1 µs as a function of the energy of an electron beam

Fig. D.1 represents the chemical yields of H_2O_2 and $^\bullet$OH, normalized to the maximum, as a function of the primary electron energy (in keV), at 1 µs post-irradiation. The maximum reaches 109 nmol·J^{-1} for H_2O_2 and 246 nmol·J^{-1} for $^\bullet$OH. At very low energies (< 300 eV), there is first an increase of H_2O_2 production. Then, as the energy of the primary electron increases, the H_2O_2 yield first dramatically decreases up to $\sim$ 20 keV due a lower recombination probability with increasing energy, before reaching a plateau at 70 % of the maximum value at 90 keV. On the contrary, $^\bullet$OH first dramatically decreases from the maximum down to $\sim$ 50 % of its maximal value at 1 keV, before increasing again and reaching $\sim$ the maximal value at 90 keV.

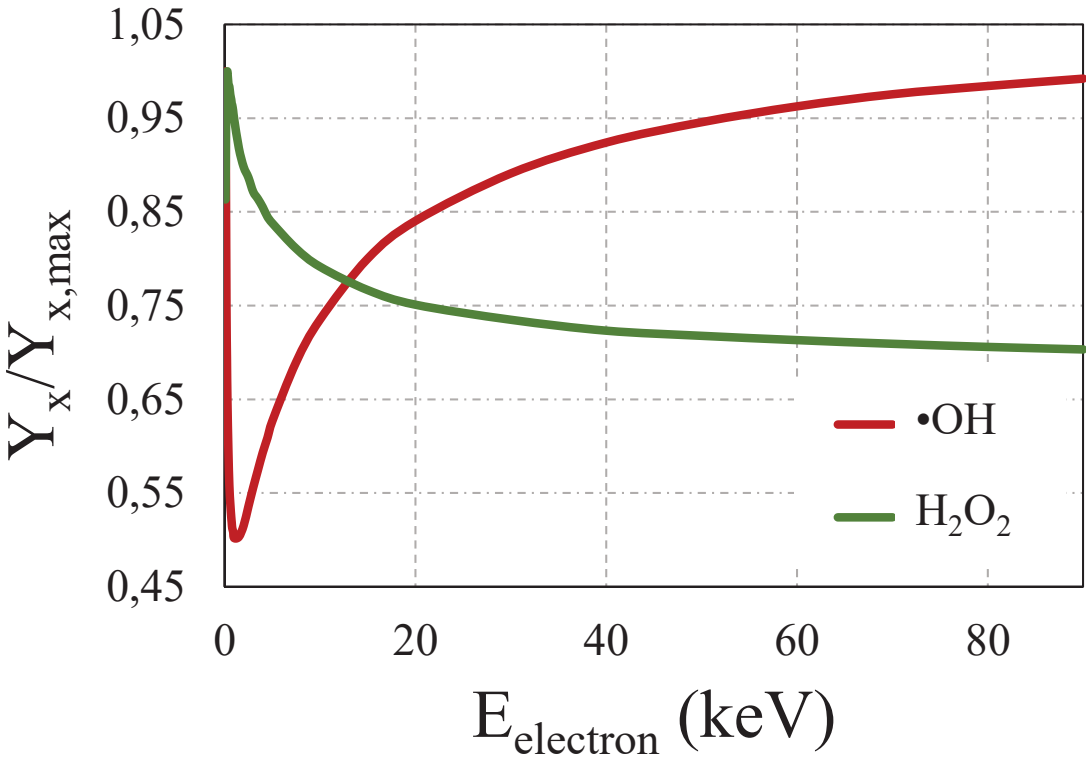

Figure D.1.: Chemical yields of H_2O_2 and $^\bullet$OH as a function of the primary electron energy, at 1 µs, normalized to the maximum.

D.3. Average energy conversion per ionized GNP

Fig. D.2 represents the average energy conversion per GNP ionization, as a function of the incident photon energy E_{photon}. E_{trans} represents the average energy transferred to the medium by the primary photon during an interaction with the GNP, E_{res} represent the average restricted energy deposited per GNP ionization in water, E_{NP} the average energy loss in the GNP, and E_{fluo} the average energy transmitted to fluorescent photons. On the left absolute energies are given in keV, and on the right relative energies are displayed with regard to primary photon energy or E_{trans}. Note that fluorescent photons are not counted as interacting particles and hence do not lead to any energy deposition. As the photo-electric effect dominates, the photon loses most of its energy during an interaction. As the energy of the primary photon increases, the restricted energy deposited in water increases per ionization as the energy of the photo-electron increases. An exception can be noted for 90 keV, for which electrons from the K-shell are ionized, leading to the emission of fluorescent photons which bring along 60 % of the photon energy loss. When E_{photon} increases from 20 keV to 80 keV, the relative restricted energy deposited in water with regard to E_{trans} increases while the relative energy deposited in the GNP decreases. As expected, small GNPs induce less energy auto-absorption: at 20 keV, 25 % of E_{trans} is converted into energy deposition inside the GNP for large (50 nm diameter GNP), while it represents only 5 % for small (5 nm diameter) GNPs.

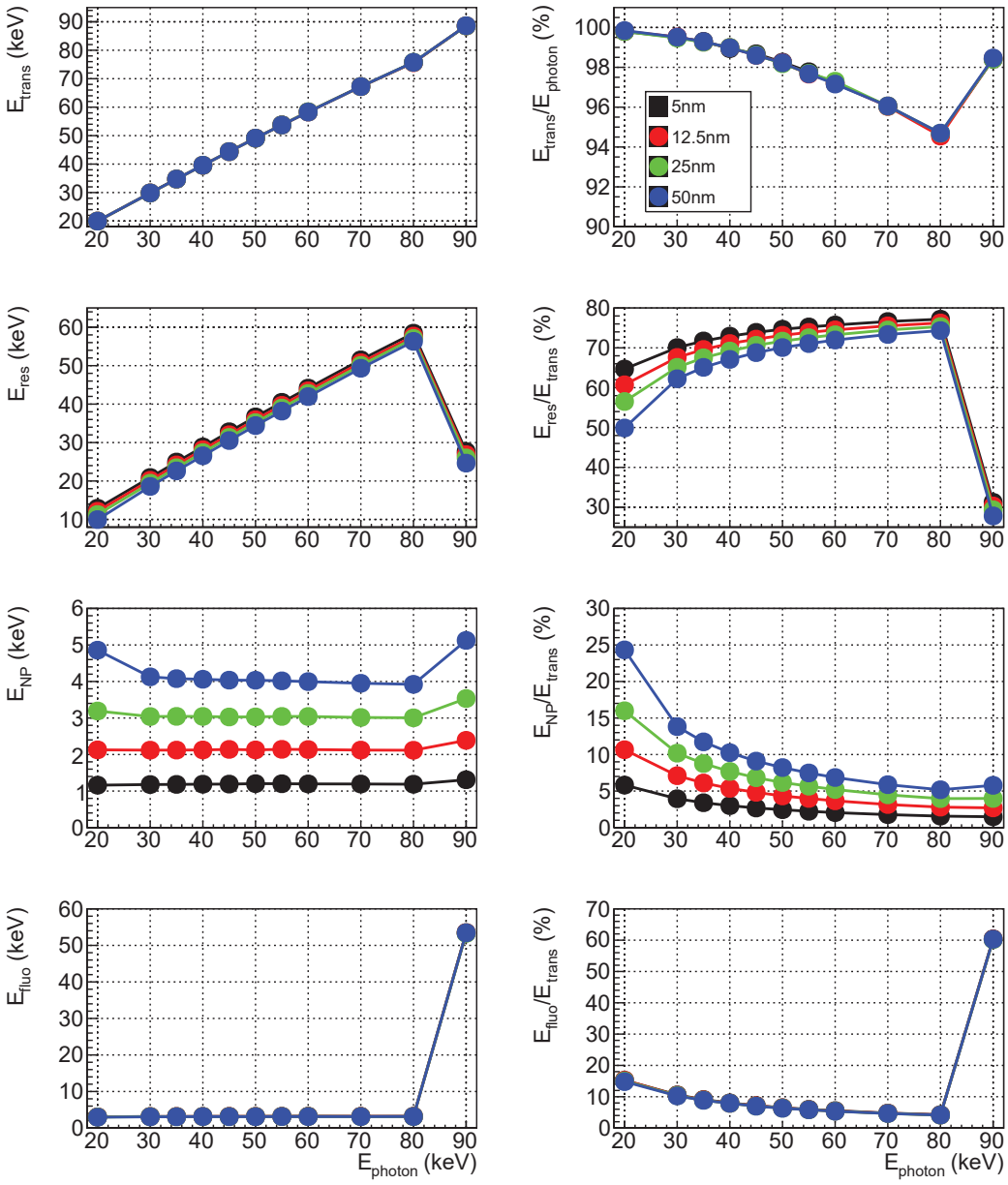

Figure D.2.: Average energy conversion per GNP ionization as a function of the incident photon energy E_{photon}, after direct interaction of the photon with the GNP, for 4 GNP radii.

E. Coumarin

E.1. Spatial distribution of chemical species after a GNP ionization

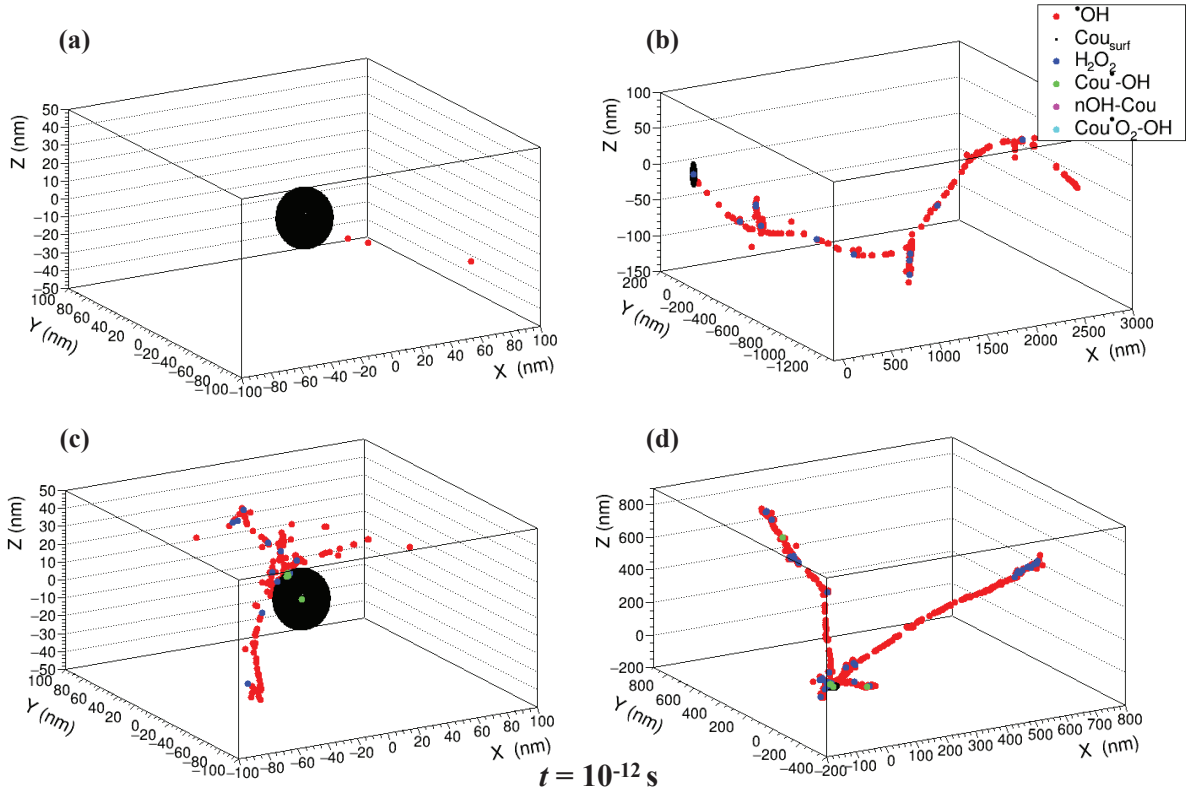

Figure E.1.: Spatial distribution of the chemical species after a GNP ionization at $t = 10^{-12}$ s after the ionization. Panels (a) and (b) (respectively (c) and (d)) represent the same track, with (a) (respectively (c)) a zoom around the GNP.

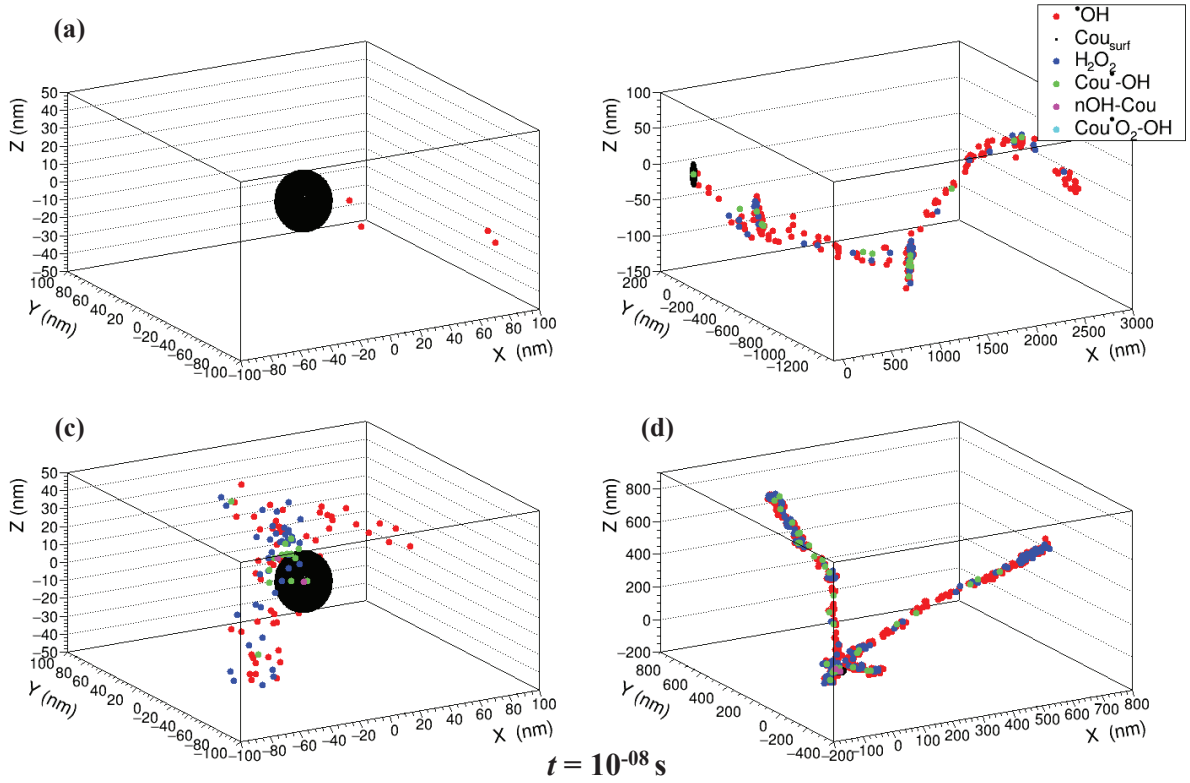

Figure E.2.: Spatial distribution of the chemical species after a GNP ionization at $t = 10^{-8}$ s after the ionization. Panels (a) and (b) (respectively (c) and (d)) represent the same track, with (a) (respectively (c)) a zoom around the GNP.

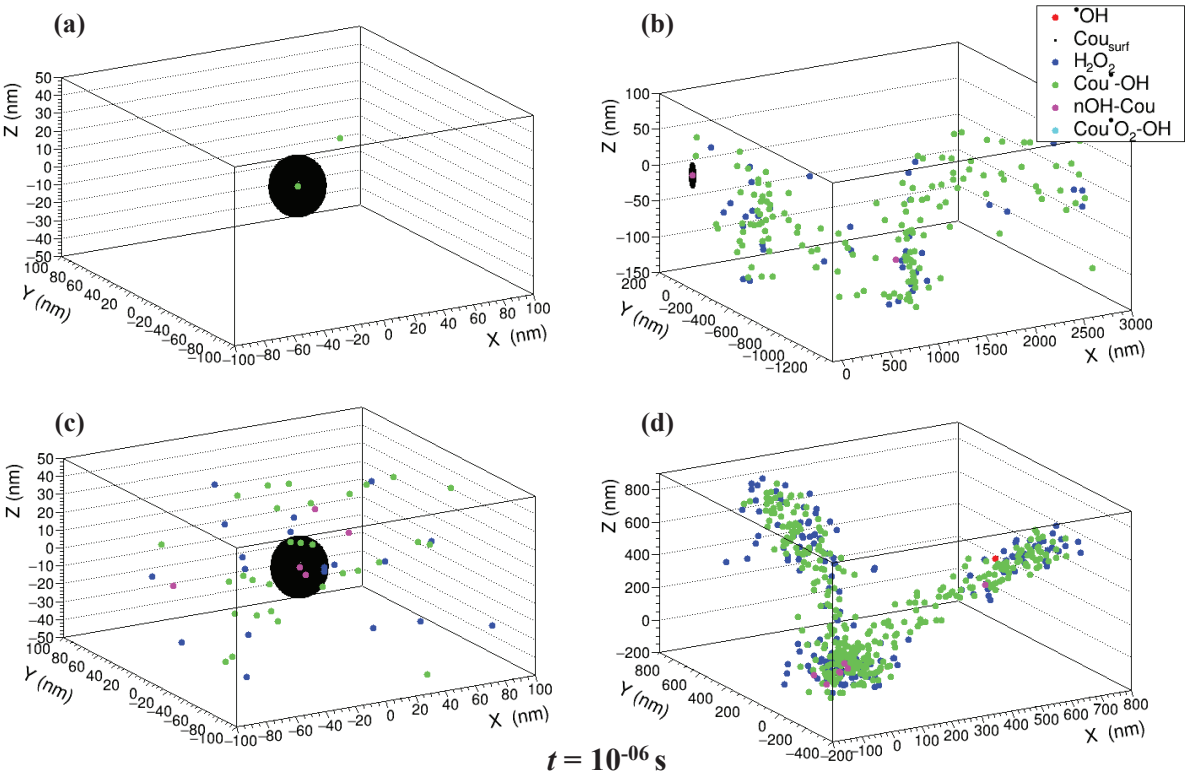

Figure E.3.: Spatial distribution of the chemical species after a GNP ionization at $t = 10^{-6}$ s after the ionization. Panels (a) and (b) (respectively (c) and (d)) represent the same track, with (a) (respectively (c)) a zoom around the GNP.

F. NanOx

F.1. Local events with GNPs

To calculate the number of local lethal events, we assumed that NPs contained in the sensitive volume V_s had an impact on the restricted specific energy in the nanotargets, while any NPs outside of the volume did not. Such assumption is reasonable as we showed a limited effect of GNPs on the restricted specific energy for a distance between the GNP and the radius larger than 200 nm. This is much lower than the size of the sensitive volume. As the number of impacts K remained high, both for impacts originating from photon-water interaction and photon-gold interaction (***justifier), that each target was equivalent and homogeneously distributed in V_s, and each NP was identical, the survival to local lethal events in the presence of NPs can be expressed similarly to the case without NPs, as in Eq. 13.12 and Eq. 13.13. Following the volume decomposition introduced in Eq. 13.15, and similarly to what is done for hadrontherapy[205], the survival to local events for a dose D with NPs may be written as follows,

$$S_{\mathrm{L}}(Z') = \exp(-\alpha_{\mathrm{NP,\,L}} \cdot Z_{\mathrm{NP}} - \alpha_{\mathrm{W,\,L}} \cdot Z_{\mathrm{W}}) \tag{F.1}$$

with Z_{NP} and Z_{W} the restricted specific energy in the microscopic volumes V_{NP} and $V_{\mathrm{W,s}}$ respectively. The distribution of the restricted specific energy in nanotargets depends on the position of the target with respect to the GNP surface. The quantity $\frac{\mathrm{d}P}{\mathrm{d}z'}(z'|\mathbf{r}, D)$ is the differential probability of having a specific energy z' in the nanotarget given the nanotarget is located at $\mathbf{r} = \vec{r}$. We introduce $\frac{\mathrm{d}P}{\mathrm{d}\mathbf{r}}$, the probability density function to have a target at a position $\mathbf{r}$ ($\int_\infty \frac{\mathrm{d}P}{\mathrm{d}\mathbf{r}}\mathrm{d}\mathbf{r} = 1$). As we assumed that the target was homogeneously distributed in the volume V_s, we find at any position $\mathbf{r}$,

$$\frac{\mathrm{d}P}{\mathrm{d}\mathbf{r}} = \begin{cases} \frac{1}{V_s}, & \text{if } \mathbf{r} \in V_s \\ 0, & \text{otherwise.} \end{cases} \tag{F.2}$$

For the contribution of lethal events coming from $V_{\mathrm{W,s}}$, we approximate that the restricted specific energy distribution does not depend on the position of the nanotarget $\mathbf{r}$. Therefore, for a nanotarget located in $V_{\mathrm{W,s}}$, we find,

$$\frac{\mathrm{d}P}{\mathrm{d}z'}(z'/\mathbf{r}) = \frac{\mathrm{d}P}{\mathrm{d}z'}. \tag{F.3}$$

In turns, for a homogeneous distribution of the targets, we find,

$$
\begin{aligned}
\alpha_{\mathrm{W,\,L}} &= \int_{\mathbf{r}\in V_{\mathrm{W,s}}} \frac{\mathrm{d}P}{\mathrm{d}\mathbf{r}}\mathrm{d}\mathbf{r}\cdot\frac{1}{\langle Z_{\mathrm{W}}\rangle}\int_0^{+\infty}\frac{\mathrm{d}P}{\mathrm{d}z'}F(z')\mathrm{d}z' \\
&= \frac{V_{\mathrm{W,s}}}{V_{\mathrm{s}}}\cdot\frac{1}{\langle Z_{\mathrm{W}}\rangle}\int_0^{+\infty}\frac{\mathrm{d}P}{\mathrm{d}z'}F(z')\mathrm{d}z' \\
&\approx \frac{V_{\mathrm{W,s}}}{V_{\mathrm{s}}}\cdot\frac{1}{\langle Z\rangle}\int_0^{+\infty}\frac{\mathrm{d}P}{\mathrm{d}z}F(z)\mathrm{d}z \\
&= \frac{V_{\mathrm{W,s}}}{V_{\mathrm{s}}}\cdot\alpha_{\mathrm{L}}.
\end{aligned}
\tag{F.4}
$$

$F(z')$ is the effective local lethal function as previously defined by Eq. 13.7. In Eq. F.4, we hence approximate that anywhere outside the region of interest, the coefficient α_{L} is the same as in pure water (e.g. without GNPs), as defined in Eq. 13.13.

Due to the several simplifications we introduced, the restricted specific energy distribution for a nanotarget near one GNP is identical to the restricted specific energy around another NP. The number of lethal events coming from V_{NP} then reads,

$$
\begin{aligned}
\alpha_{\mathrm{NP,\,L}} &= \frac{1}{\langle Z_{\mathrm{NP}}\rangle}\int_0^{\infty}\int_{\mathbf{r}\in V_{\mathrm{NP}}}\frac{\mathrm{d}P}{\mathrm{d}\mathbf{r}}\cdot\frac{\mathrm{d}P}{\mathrm{d}z'}(z'/\mathbf{r})\cdot F(z')\mathrm{d}\mathbf{r}\mathrm{d}z' \\
&= \frac{C_{\mathrm{NP}}V_{\mathrm{s}}}{\langle Z_{\mathrm{NP}}\rangle}\int_0^{\infty}\int_{\mathbf{r}\in V_{\mathrm{i}}}\frac{\mathrm{d}P}{\mathrm{d}\mathbf{r}}\cdot\frac{\mathrm{d}P}{\mathrm{d}z'}(z'/\mathbf{r})\cdot F(z')\mathrm{d}\mathbf{r}\mathrm{d}z'.
\end{aligned}
\tag{F.5}
$$

As the GNPs are defined spherical, we assumed that there was a radial symmetry for $\mathrm{d}P/\mathrm{d}\mathbf{r}$. We therefore have,

$$
\frac{\mathrm{d}P}{\mathrm{d}\mathbf{r}}\mathrm{d}\mathbf{r} = \frac{\mathrm{d}P}{\mathrm{d}r}r^2\mathrm{d}r\sin(\theta)\mathrm{d}\theta\mathrm{d}\phi, \tag{F.6}
$$

with r the radial distance from the GNP center, ϕ the azimuthal angle ($\in[0,2\pi]$) and θ the polar angle ($\in[0,\pi]$). Eq. F.5 then becomes:

$$
\begin{aligned}
\alpha_{\mathrm{NP,\,L}} &= \frac{1}{\langle Z_{\mathrm{NP}}\rangle}C_{\mathrm{NP}}V_{\mathrm{s}}\int_0^{\infty}\int_0^{r_{\mathrm{i}}}\int_0^{\pi}\int_0^{2\pi}\frac{\mathrm{d}P}{\mathrm{d}r}\cdot r^2\cdot\sin(\theta)\cdot\frac{\mathrm{d}P}{\mathrm{d}z'}(z'/\mathbf{r})\cdot F(z')\mathrm{d}\phi\mathrm{d}\theta\mathrm{d}r\mathrm{d}z' \\
&= \frac{1}{\langle Z_{\mathrm{NP}}\rangle}C_{\mathrm{NP}}V_{\mathrm{s}}\int_0^{\infty}4\pi F(z')\int_0^{r_{\mathrm{i}}}\frac{\mathrm{d}P}{\mathrm{d}r}\cdot r^2\frac{\mathrm{d}P}{\mathrm{d}z'}(z'/r)\mathrm{d}r\mathrm{d}z'
\end{aligned}
\tag{F.7}
$$

where r_{i} is the radius of the region of interest and,

$$\frac{\mathrm{d}P}{\mathrm{d}z'}(z|r', D) = \frac{1}{\langle Z_{\mathrm{NP}} \rangle} \int_0^{\pi} \int_0^{2\pi} \frac{\mathrm{d}P}{\mathrm{d}z'}(z'/\mathbf{r}) \frac{\sin(\theta)}{4\pi} \mathrm{d}\phi \mathrm{d}\theta. \tag{F.8}$$

As previously stated, we also assumed that the targets are homogeneously distributed within V_{s}. Using Eq. F.8, Eq. F.7 becomes,

$$\alpha_{\mathrm{NP,\,L}} = \frac{1}{\langle Z_{\mathrm{NP}} \rangle} C_{\mathrm{NP}} V_{\mathrm{s}} \int_0^{\infty} \frac{4\pi}{V_{\mathrm{s}}} F(z') \int_0^{r_{\mathrm{i}}} r^2 \cdot \frac{\mathrm{d}P}{\mathrm{d}z'}(z'/r) \mathrm{d}r \mathrm{d}z'. \tag{F.9}$$

The restricted specific energy distribution was calculated in discrete concentric shells of thickness set at 2 nm (see chapter 9), normalized to the dose of irradiation D. The resulting specific energy distribution for each shell j of volume V_j reads,

$$\frac{\mathrm{d}P}{\mathrm{d}z}(z|j) = \int_{r_j}^{r_{j+1}} 4\pi r^2 \frac{\mathrm{d}P}{\mathrm{d}z}(z/r) \frac{1}{V_j} \mathrm{d}r \tag{F.10}$$

In turns, using Eq. F.9 and Eq. F.10, for a discrete approximation of the target position inside a concentric shell, $\alpha_{\mathrm{NP,\,L}}$ reads,

$$\alpha_{\mathrm{NP,\,L}} \approx \frac{1}{\langle Z_{\mathrm{NP}} \rangle} C_{\mathrm{NP}} V_{\mathrm{s}} \sum_j \int_z \frac{\mathrm{d}P}{\mathrm{d}z}(z|j) F(z) \frac{V_j}{V_{\mathrm{s}}} \mathrm{d}z. \tag{F.11}$$